PHYSICAL ASPECTS AND DETERMINATION OF EVAPORATION IN DESERTS APPLYING REMOTE SENSING TECHNIQUES

COVER: colour composite of LANDSAT bands 6 (red), 5 (green) and 4 (blue); 26 September 1978. The area shown is 185 by 185 km (see Map of geographical locations of satellite images).

The dunes of the Idehan Awbari are bordered in the North by the Qarqaf highland and in the South by the Hamadat Marzuq. Along the boundary between Qarqaf and Idehan Awbari playas (dark) are present. Also visible are a few smaller ones at the bottom right in the Idehan Awbari dunes. At the bottom center a sprinkling irrigation scheme near Awbari is visible.

STELLINGEN

I

A clear-cut threshold to mark the transition from liquid to vapour flow in soils cannot be established.

Dit proefschrift

II

Vapour and heat flows in soils can have contrary directions.

Dit proefschrift

III

Use of one-dimensional point-related simulation models to infer regional patterns of energy fluxes at the earth surface from remotely sensed data is theoretically incorrect. If feasible the accuracy of such models must be assessed case by case.

CAMILLO, P. J., R. J. GURNEY and T. J. SCHMUGGE. 1983. A soil and atmospheric boundary layer model for evapotranspiration and soil moisture studies. Water Resour. Res. 19(2) : 371-380.

Dit proefschrift

IV

Water evaporates from any desert surface at a non-zero rate.

ITALCONSULT. 1975. Fezzan land reclamation project. Wadi Shatti - Eshkeda area. Hydrogeological survey. Part 2. Min. Agric. Dev., Tripoli. 70 p.

V

The practical application of regional water management in arid zones requires an accuracy of the water balance terms that cannot be achieved by presently available techniques.

VI

The procedure applied by ROSEMA (1982) to calculate actual evaporation from satellite data requires that two contradictory hypotheses are accepted.

ROSEMA, A. 1982. Actual soil evaporation and germination mapping. In: Group Agromet Monitoring Project (GAMP), Final Report.

VII

The use of numerical radiation transfer models to correct remotely sensed data for atmospheric effects does not improve the accuracy of a specific set of these data.

Dit proefschrift

VIII

Accounting for reduced evaporation from a drying soil only by increasing the surface resistance, is incorrect.

BARTON, J. 1979. A parametrization of the evaporation from non-saturated surfaces. J. Appl. Meteor. 18: 43-47.

IX

Scope for improvement in the efficiency of irrigation systems lies at farm-inlet level rather than in constructional improvements of the main delivery system.

CHAMBOULEYRON, J., M. MENENTI, L. FORNERO, J. MORABITO and L. STEFANINI. 1983. Evaluación y optimización del uso del agua en grandes redes de riego. Instituto Italo-Latino Americano (IILA), Rome. 176 p.

X

Economic optimization of irrigation water use without due account of the operational constraints of the actual irrigation network, yields inaccurate management criteria.

CHAMBOULEYRON, J., M. MENENTI, L. FORNERO, J. MORABITO and L. STEFANINI. 1983. Evaluación y optimización del uso del agua en grandes redes de riego. Instituto Italo-Latino Americano (IILA), Rome. 176 p.

XI

Potential crop production may be improved by modifying optical properties of plant leaves in a pre-determined way by means of genetic manipulation.

XII

Measurement of the short term variability of sensible and latent heat flux in greenhouses can clarify the fundamental interrelationship between heat storage in and stomatal resistance of plants.

HOPMANS, P. A. M. 1971. Rhythms in stomatal opening of bean leaves. Meded. Landbouwhogeschool, Wageningen 71-3. 88 p.

XIII

Inaccurate editing is the most probable explanation for the 3 to 5 Mega-watt$\cdot$cm$^{-2}\cdot$sr^{-1} presented as emittance of the bare soils studied by ABDEL-HADY and KARBS (1971).

ABDEL-HADY, J. and H. H. KARBS. 1971. Depth to ground-water table by remote sensing. Journal of the Irrigation and Drainage Division, ASCE 97 (IR 3): 355-367.

XIV

In a room with stagnant air, smoke goes from the smoker towards the non-smoker.

M. MENENTI
Physical aspects and determination of evaporation in deserts, applying remote sensing techniques
Wageningen, 16 maart 1984

M. Menenti

PHYSICAL ASPECTS AND DETERMINATION OF EVAPORATION IN DESERTS APPLYING REMOTE SENSING TECHNIQUES

CURRICULUM VITAE

Massimo Menenti was born in Rome on 9 July, 1949, where he attended High School from 1963 to 1968. In 1972 he obtained (cum laude) the degree of Dottore in Fisica at the University of Rome with, in partial fulfill- ment, a thesis on the water balance of the river Po watershed. From 1973 to 1974 he attended a post graduate school on Physics of the Solid and Liquid State, while working at the Office of Agricultural Ecology of the Italian Ministry of Agriculture and Fisheries. He then joined TECNECO, a state-owned engineering company dealing with management of water resources and environment. There he contributed to a number of projects, both in Italy and abroad, among which an experimental study on the water require- ments of natural vegetation (1975-1976), an advisory mission to the Venezuelan Ministry of Environment at Caracas (1979) and an Italo - Argen- tinian joint research project (1977-1982) on the optimization of irriga- tion water use. In 1977 he became involved under contract from the state- owned engineering company Aquater in the study of the West-Libyan aquifer system. In 1979, in the framework of this study, he was seconded for nine months to the Institute for Land and Water Management Research (ICW). From 1 September 1980 he is Senior Scientist in the Department of Water Manage- ment of the ICW.

A Cecilia per aver condiviso il disegno dell' emigrazione
e della vita intensa di questi anni.

Ai miei genitori, nella speranza che la partecipazione all'
esito di questi anni di lavoro, possa compensare la lontananza.

ABSTRACT

Menenti, J. 1984. Physical aspects and determination of evaporation
in deserts applying remote sensing techniques. Report 10 (special issue),
Inst. Land Water Manag. Res. (ICW), Wageningen, The Netherlands. (XII) +
202 p., 250 eqs., 55 tables, 8 plates in colour, 117 figs., 381 refs.,
Eng. and Dutch summaries.
Also: Doctoral thesis, Agricultural University, Wageningen, The Netherlands.

In the deserts of the world groundwater losses by evaporation are
shown to be a very important and almost unknown quantity in the water bal-
ance of aquifers present.

After establishing a new combination formula to calculate actual evap-
oration from within the soil, the evaporational soil physical aspects are
discussed in detail. It is shown that under specified conditions vapour
flow can take place against the direction of heat flow. A new, fundamental,
definition of evaporation sites is given and its bearing on a model of heat
and moisture flow is discussed. A theory of heat exchange at the soil - air
interface is presented in terms of the apparent soil thermal admittance.
Equations to relate the latter soil property to soil layering and to the
frequency of the surface temperature wave are given. A theory of evaporation
in terms of multi-dimensional geometry is proposed and it is shown how to
derive approximate formulae to calculate actual evaporation by making use
of satellite data only. For more accurate results point ground reference
measurements have been used to calibrate the satellite-based calculations.

After describing a particular desert area in Libya, the accuracy of a
number of satellite data of that area is discussed on the basis of ground
reference measurements and numerical correction procedures.

Finally, the theory is combined with satellite and point ground refer-
ence data to calculate the different terms of the surface energy balance
and the actual evaporation for some 36,000 km^2 of the Libyan desert.

UDC: 528.88:556.131(252.3) 631.436 536.423.1 551.52:556.131(252.3)
551.435.77(612)
Free descriptors: regional evaporation, remote sensing, dry soils, heat flow,
energy balance, deserts, Libya

PREFACE

'Nunc de partibus, quamquam infinitum id quoque existimatur nec temere sin aliqua reprehensione tractatum, ...'

(PLINIUS, Naturalis Historia, Liber III:1)

This story began during a cold, snowy January in the Po delta. Then I used to spend my time afloat on a raft placed somewhere in a marsh, one of the very few left in that region. The idea was to measure the energy balance terms of that surface, with special attention to the latent heat flux. Then somebody decided that such a working experience was quite suited to solve the particular problems of ex-marshes (= playas!) in the Libyan desert.

To be sure the above is only part of the prologue. To a great extent this Report is the outcome of my relation with the Institute for Land and Water Management Research (ICW) at Wageningen. As long ago as 1976 I went to comply with my duties as a serviceman with some publications of the ICW as part of my personal belongings. There were two papers by Reinder Feddes about the very interesting complications around bi-dimensional plant roots. That was a revealing accident, indeed. Little did I know at that time that I had been reached by the propaganda arm of 'mijnheer Schierbeek'. The trickling stream of ICW-publications which I received from a colleague in Rome, clearly conveyed the image of an outstanding scientific institution. That many years ago it also was unknown to me how much of the burden of producing those instructive reports was being carried by the remarkable professional skills of Mieke van Dijk. The whole thing was definitely worth a trip.

An opportunity to make it came from Libya in 1977. The Libyan Secretariat of Agricultural Reclamation and Land Development entrusted the Italian engineering company Aquater to carry out a hydrogeological study of the Fezzan area. Thermal infrared remote sensing was considered to be the best possible technique to estimate total groundwater losses by evaporation from the playas in the Wadi Ash Shati basin. The following five years of work were to prove that the matter was not that straightforward. At the ICW they were at that time actively engaged in research into the hydrological capabilities of thermal infrared remote sensing. The outcome of all this was that the ICW became involved in the Libyan project.

This Report is an attempt to answer some of the questions into which I bumped during the first phase of the study performed under the Libyan government contract.

CONTENTS

1. INTRODUCTION

'... *harenis circumdati, puteos tamen haut difficile binum fere cubitorum altitudine inveniunt, ibi restagnantibus Mauretaniae aquis.*'

(PLINIUS, Naturalis Historia, Liber V:34)

1.1. GROUNDWATER LOSSES THROUGH THE SURFACE OF DESERTS

In the Pleistocene ice ages the climate of North-African deserts was characterized by higher rainfall than nowadays (SELLERS, 1965). The limit of the area with a rainfall regime now typical of middle latitudes, was displaced towards the equator by the extended ice caps. Thus to a great extent the present hydrography of desert regions is the outcome of the last Pluvial periods, dating around 11,000 year B.P. (Makalian Pluvial) and 4500 year B.P. These figures find support from age determinations of groundwater samples. During the evolution to drier conditions potential evaporation became much higher than rainfall; this gave a gradual modification of the surface

properties which allows for lower evaporation rates.

For detailed information about deserts, see McGINNIES et al. (1968), McGINNIES and GOLDMAN (1969), McKEE (1979). In Fig. 1.1 a map of desert and arid areas in the world is presented. For a more detailed classification of desert climates see MEIGS (1953). A wealth of specific data, with as basic mapping tool LANDSAT imagery and covering fifteen major desert areas was gathered by the US Geological Survey (McKEE, 1979). A map showing these 15 areas is given in Fig. 1.2.

During the last ten years irrigation schemes were developed in the arid and desert areas of the world and many are still being set up or designed. This went together with a strong increase in groundwater exploi-

■ deserts (where it might not rain for more than one year)
▨ arid areas (where rainfall is less than evapotranspiration)
▤ FEZZAN area
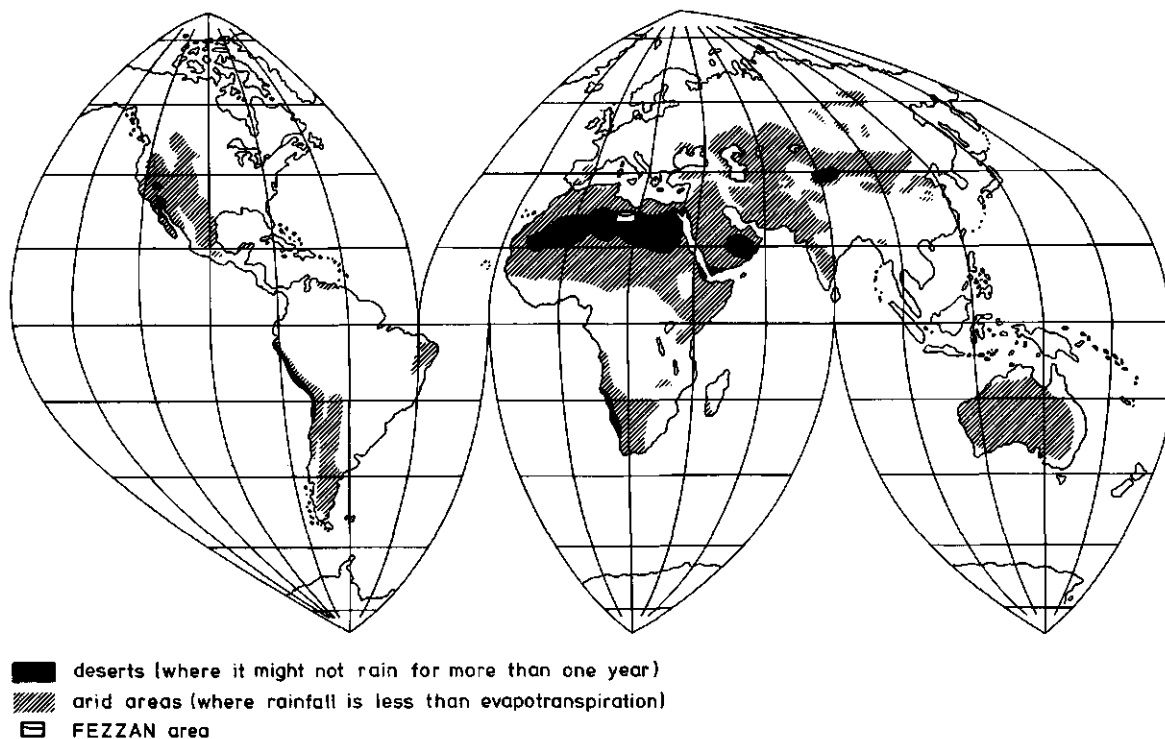
Fig. 1.1. Deserts and arid zones of the world

1
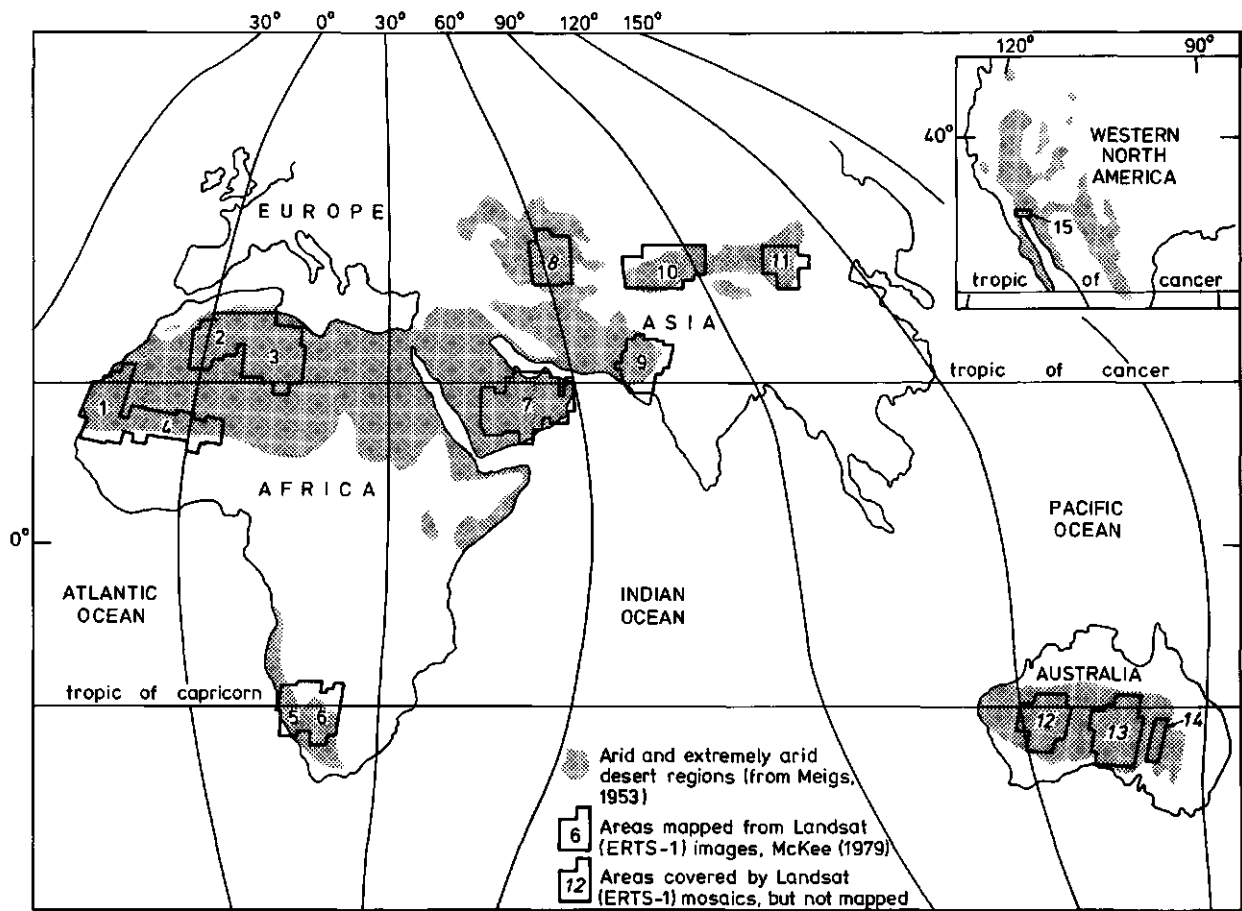
Fig. 1.2. Principal desert and semidesert regions. 1, Western Sahara, Mauritania and Senegal; 2, Northern Sahara (Grand Erg Occidental and Grand Erg Oriental), Algeria; 3, Northern Sahara, Libya; 4, Southern Sahara and Sahel, Mauritania, Mali, and Niger; 5, Namib Desert, South-West Africa; 6, Kalahari Desert, South-West Africa, Botswana, and South Africa; 7, Rub' al Khali, Saudi Arabia, United Arab Emirates, Oman, and Yemen; 8, Peski Karakumy and Peski Kyzylkum, USSR; 9, Thar Desert, India and Pakistan; 10, Takla Makan, People's Republic of China; 11, Ala Shan Desert, People's Republic of China; 12, Great Sandy Desert, Australia; 13, Great Victoria Desert, Australia; 14, Simpson Desert, Australia; 15, Algodones Desert and Gran Desierto, USA and Mexico (after McKee, 1979)

tation. In the oil-rich countries of the Middle East and North Africa the rush for new oil fields made it necessary to collect information and data to understand the structure and nature of groundwater basins with sizes between 10^5 and 10^6 km^2. The water requirements of drilling activities made the search for productive water wells necessary, along with careful, although local, determination of the hydraulic characteristics of the aquifers. The oil revenues allowed agricultural development, even when non-profitable. The exceptional circumstances did not call for a gradual approach. However, after only a few years it now is evident that the risks of mining groundwater resources were not fully understood or assessed. Even in other regions of the world where oil did not play a relevant role, the increase of groundwater exploitation clashed with the fast rising energy costs for pumping. In many instances it was realized that earlier studies relating to the appraisal of groundwater

resources had not been carried out with the proper detail and duration. Especially the time period allowed for a single study was often set by the overall pace in growth of a country's economy.

A positive point scored by the oil production development is the availability of financial resources to undertake new and comprehensive hydro-geological studies. The enormous groundwater basins of North Africa are presently known with a reasonable detail because of a number of hydro-geological studies which were conceived and financed at a feasibility level of integrated regional planning. Even if state-of-the-art technology and knowledge was usually applied in these projects, it was realized that the accuracy achieved in estimating the various terms of the water balance could not be accepted as satisfying for the feasibility assessment.

It appears that the accuracy required to judge projected water consumptions is generally not fully

2

appreciated. For example a figure of 10^8 $m^3 \cdot a^{-1}$ is considered as representative of the gross water requirement of new irrigation systems in the Fezzan in North Africa. A conservative figure for the extension of outcrops in that aquifer system is 10^4 km^2. Hence the corresponding surface water exchange rate is 0.03 $mm \cdot d^{-1}$, which rate can only be measured by very accurately weighing lysimeters. In feasibility studies the difference between 'groundwater mining' and 'managing a renewable resource' therefore is a rather thin one. There is probably no way of determining the water balance of large expanses with the accuracy specified above. Scope for improvement is greater when dealing with more restricted areas where the actual evaporation rate is larger, 1 $mm \cdot d^{-1}$ say. Since volumetric quantities are needed, the characteristics of the surface to which a given evaporation rate applies must be defined and its area estimated. With the available knowledge and technology this is not an easy task.

A detailed discussion of the impossibility for a straightforward application to arid and desert areas of known hydrological principles can be found in FAO (1981) and EVANS and THAMES (1981). The preceding remarks show that in deserts a scope for both useful applications and scientific improvement is evident. Now it is required to establish:

- which kind of water consumption is quantitatively the most important;
- in which direction research on water consumption evaluation will be most effective.

Groundwater resources of desert regions are being used, and to some extent wasted, in different ways. Groundwater losses through the surface of deserts occur because of transpiration of natural vegetation, bare soil evaporation and pumping. The following categories of groundwater losses through the surface of deserts are to be considered:

- Industrial and domestic water consumption. Broadly speaking the quantities of water involved in this category of use are smaller than the water requirements in agriculture. However, many examples could be put forward to show that groundwater consumed by industries and towns in deserts is not only essential for the life in those cities but also relevant to the water balance of the desert aquifers.
- Traditional large surface irrigation schemes with a size of the order of 10^5 ha. The analysis of the water balance is intricate because of losses in the distribution system. A detailed knowledge of the efficiency

of the system is essential for any prediction of the water balance terms. Net average water requirements can be evaluated from weather data. The issue in this category is to reduce the difference between gross water consumption and net water requirement. This goal can be pursued by gathering detailed data about the operation of the irrigation system and by matching simulation and optimization models to those data. Two examples of this approach have been presented by CHAMBOULEYRON et al. (1983). Whether operation procedures in a particular irrigation system can accommodate the improvements following from a very detailed knowledge of actual evaporation over short time periods, is a matter open to question.

- Modern irrigation schemes by sprinkling with a size between 10^3 and 10^4 ha. When establishing a groundwater management plan, the details of the operation of a new irrigation system are either unknown or rigidly specified. More often than not a forthcoming irrigation system is specified in terms of a lumped gross water consumption and the geographical location of the project. There is plenty of literature and data on almost any possible aspect of modern irrigation schemes in general. It is far from sure, however, as noted by STANHILL (1973), that use can be made of this literature for water consumption evaluation. The reason for this inconvenience also stems from the extremely high production rate of formal publications on evaporation of two a day around 1975, again according to Stanhill. Thus the second requirement mentioned above cannot be met. It must be noted that the impact of modern irrigation schemes on the water balance is heavy, especially in the desert areas of North Africa and the Middle East.
- Natural vegetation. When estimating evaporation losses a relevant difference exists between the relatively small oases and the extensive regions with low soil cover percentage. Even in the latter case the rôle of vegetation in the water balance can be relevant because of its extension. It should be mentioned that a main problem is found in the assessment of the possible damage to vegetation due to an increase in groundwater extraction. An estimation of groundwater losses can be also rather difficult since little is known about actual evaporation of single species and ground coverage is variable and difficult to estimate. Results from a number of case studies are reported in FAO (1981). The relationship between a number of specific phreatophytes and groundwater consumption has been studied by MEINZER (1927) and ROBINSON (1958).
- Bare soils. Within short periods from rain-

fall events bare soils may discharge runoff water or groundwater. Runoff water - after being concentrated in water courses - may infiltrate further downstream. The combination of geographical extent, variability of landforms and hydrological processes is very intricate.

An important feature for planning groundwater development is that natural discharge areas from groundwater reservoirs may show the long term evolution of groundwater basins. The different characteristics and composition of evaporites in these large areas may provide valuable information about the response of the reservoir to climate fluctuations. The undoubtedly important rôle and extent of such natural discharge areas are not fully understood. It appears that little is known on transport processes in the soils being present in these areas. Thus bare soil evaporation is a most promising candidate to fulfill both earlier mentioned requirements.

1.2. PLAYAS

In desert areas evaporation takes place in bare soil depressions which may have quite different sizes and characteristics. In American literature often the term 'playa' is used for these depressions. Most of the largest playas were lakes during the last pluvial periods, while the smallest ones originated by erosion.

Although the classification of playa surfaces is by no means definitive and supported by a majority of authors, see for example KERR and LANGER (1965) and MOTTS (1965), the present author is of the opinion that the most efficient classification of playas should be based upon the different surface characteristics. The following description of playas has been summarized from NEAL (1965a, 1969, 1972). Four different types of surfaces may be considered:

- H a r d , d r y c r u s t. It shows very little microrelief, except from what was created by shrinkage of mud. The typical surface consists of small mud polygons, about 10 cm across. Minor amounts of calcium carbonate or sodium chloride are common surface constituents. Hard, dry crusts usually have some fine material (clay and silt) binding the particles together. In former lakes the clay content can be as high as 90%. When the salt content is somewhat higher, 5% say, the surface is less hard. Vegetation is rather uncommon on these surfaces.
- S o f t , f r i a b l e s u r f a c e. It is a kind of self-rising ground. Capillary rise up to the surface can be relevant, but the upper 15 cm of soil

usually is dry and loose; microrelief shows elements 5 to 8 cm high with a varying hardness. Groundwater discharge by evaporation is relevant and depends on the water transmitting capacity of the soil, including the modifications due to salt accumulation. Salt content can be as high as 25% in the upper 30 cm and drop to less than 5% a meter deeper. When the groundwater level draws down, the salts can eventually be flushed out by rainfall.

- S o f t , s t i c k y w e t s u r f a c e. The groundwater table is at or near the surface. When the water table is at a shallow depth, the surface is very smooth, while only a slight drawdown may allow for the development of pressure ridge polygons, with higher salt contents and a whitening of the surface. Playas in interdune depressions have a higher sand content and therefore are not as sticky as clayey playas.
- H a r d e v a p o r i t e c r u s t s. Thick accumulations of salt, gypsum and other materials occur at the surface. Such deposits require long periods of evaporative concentration of near-surface brines; thicknesses can reach many meters (Salar Grande in Chile). The relation between the strength of the crust, its salt content and groundwater table depth appears to be well established. Where the salt is relatively pure and the saturated zone is situated at a meter or more deep, the crusts are extremely hard. With intermediate groundwater table depths salt-ridged and rugged crusts develop, with a microrelief between a few centimeters and a meter. At some places the crusts show an impressive roughness (Salar de Atacama in Chile and the Idri playas in Libya).

The last three categories of playa surfaces may show varying characteristics, but a relation with the amount and quality of groundwater discharge always exists. Mineralogical knowledge of these landforms is fairly good, mainly because of commercial exploitation. However, it is rather difficult to establish clear cut definitions since the variability of groundwater levels and rainfall amounts produce important modifications of the characteristics.

The structure and evolution of the crusts also depend on their mineral composition. In a clay soil, the platelets may behave in a different way due to the presence of different salts. Forces developing during crystallization apply different stresses on the soil matrix according to the salts present in the brine.

Properties of crusts in playas were studied and described by LANGER and KERR (1966), EUGSTER and SMITH (1965) and VERGOUWEN (1981). A regular observation of

Table 1.1. Regional playa nomenclature (after Neal, 1969)

Locale	General terms	Clay-silt playas	Saline playas
United States	playa, dry lake alkali flat	dry playa, clay playa	salt flat, salt marsh, salina
Mexico	laguna, salina	laguna	salina
Chile	–	–	salina (moderate salt) salar (much salt)
Australia	playa, lake	clay pan	salt pan, salina
Russia	pliash	takir	tsidam
Mongolia	gobi, nor	takyr	tsaka, nor
Iran	daryacheh	daqq	kavir
South Africa	pan, vloer, mbuga	clay pan, kalpfannen	salt pan, Kalahari
North Africa	sebkha	garaet, qarat	sebkha, chott
Arabia	–	khabra	mamlahah (salt flat) sabkhah (coastal salt flat)
Jordan	ghor	qa	–
Iraq	hawr	faydat	sabkhat
India	rei	–	–
Pakistan	hamun	–	–

the variability of playa surfaces, also in time, such as by satellite, appears to be essential for a better understanding of the relationship with groundwater discharge. An example is a study by NEAL (1965b, 1972) on surface features in playas.

Groundwater table depth controls not only the evaporation at the surface but also erosive processes, since the consistence of the surface depends on its moisture content. As an example it can be mentioned that bush mounds develop only where the water table is at a proper depth and of a proper quality to allow for the growth of the soil retaining plants. When these plants die, water discharge through them is replaced by discharge through the soil capillaires, with the consequent appearance of puffy surface characteristics. More details about this subject have been given by UTEPBERGENOV (1980) and UMURZAKOV (1980).

The rate of the groundwater table drawdown also has an effect on surface features. When the drawdown rate is rather low and steady, very large dessication polygons may develop; at Rogers playa (California) they reached 75 m across (NEAL, 1969). Since different terms used for playas are being used in each part of the world, a list is given in Table 1.1 (after NEAL, 1969). In the present publication the term playa will be used as general name. A brief summary of the quantities and location of playas is:

North African playas. In North Africa more than a thousand playas are scattered from western Sahara to Sudan, with sizes of 1 km^2 to more than 3000 km^2. It must be noted that in North Africa many playas may belong to the same groundwater basin and that they are discharge areas from large artesian basins. Hard, dry crusts are rather

uncommon in this region; a possible explanation can be found in the climatic history different from more northern regions. It seems reasonable to believe that the North African climate was never as humid as to maintain permanent lakes. Many large depressions are present in the Libyan desert, including the wide Qattara depression (15,000 km^2).

Coastal salt flats. In some regions they occupy large areas, such as the Rann of Kutch in India and the Trucial Coast of Arabia.

Iranian playas. An impressive portion of the country shows playa features and extremely large playa systems occur (SZABOLCS, 1979). The Dasht-e-Kavir reaches an extension of 45,000 km^2, even if it cannot be taken as one playa, since it rather is a group of different playas.

South African playas. These are known as 'pans' and, when occurring in groups as 'panneveld' and their size is in the range between 1 and 250 km^2. Hundreds of small playas occur in troughs between ridges of sand in the Wankie National Park of extreme western Zimbabwe.

Chilean playas. They occur north of latitude 27°30' S and cover an area of 7300 km^2 in a number of about 100.

North American playas. In North America there are some 300 playas exceeding 5 km^2 in size; almost all of them are located in the states of California, Oregon, Nevada, Arizona, Utah and New Mexico. Many smaller playas are present in the southern High Plains of eastern New Mexico and West Texas, numbering in the hundreds. They are also numerous in the semi-arid areas of Wyoming, Idaho, Colorado and Kansas. Several dozens of playas also occur in extreme southern Canada (Alberta, Saskatchewan and Manitoba). Details of specific playas in the US can be found in

5

NEAL (1965b) and CABANISS (1965). Many playas are also present in Mexico with surface characteristics similar to those of the southern United States. A u s t r a l i a n   p l a y a s. Three types can be considered: a, clay and silt floored playas, most common in the southern part of West Australia and in South Australia, covering an area of 50,000 km²; b, salt-encrusted playas, Lake Eyre is one of the largest playas in the world and, together with Lake Torrens and Lake Gardiner, shows some evidence of marine origin in its deposits; c, rock floored playas, they have been described in Australia by JUTSON (1918).

On the ground of the preceding overview it can be concluded that evaporation from playas is of world wide importance in the water management of desert regions. When evaporation losses are comparable with exploitational use from a given aquifer, the long term appraisal of the available groundwater resource eventually depends on the reduction in evaporation losses from the playas due to a lowering of the water table because of pumping. The long term evolution of the water quality depends on salt and water transfer processes in playas. A few examples of the quantative relationship of evaporation of playas with groundwater exploitation are reported to support these statements:

From data found in INTERAGENCY TASK FORCE ON IRRIGATION EFFICIENCIES (1979), the gross water requirement of $2.6 \cdot 10^6$ ha irrigated land in California can be estimated as being $3.4 \cdot 10^{10}$ m³·a⁻¹, with $1.7 \cdot 10^{10}$ m³·a⁻¹ being groundwater exploitation. Many playas are present in California, especially in the southern part. According to LANGER and KERR (1966) and NEAL and MOTTS (1967) there are as many as 20 large ones. Their total area can be estimated by graphical map integration as 1300 km² approximately. An estimation of actual evaporation is rather hard to give, but as a yearly average a figure of 2 mm·d⁻¹ can be considered to apply (support for this figure will be given in Chapter 8). Accordingly total groundwater losses by evaporation can be estimated to be 10^9 m³·a⁻¹. Thus evaporation losses amount to 6% of gross groundwater exploitation.

Another example can be drawn from UNESCO (1972) that deals with the hydro-geological study of the Algerian - Tunisian Sahara. The pool of experts in charge of the study fully realized the rôle of playas (chotts in this region) on the long term trend of groundwater availability at reasonable costs. These playas discharge water from a system of two overlapping aquifers covering an area of 800,000 km². The most relevant playas are close to the sea: Chott

Table 1.2. Evaporation, exploitation and recharge of the 'Complexe Terminale' aquifer in the Algerian - Tunisian Sahara (after Unesco, 1972)

Year	Evaporation (10^6 m³·a⁻¹)	Exploitation (10^6 m³·a⁻¹)	Recharge (10^6 m³·a⁻¹)
1950	315	268	583
1970	280	397	583

Melrhir and Chott Djerid, and belong to the upper aquifer, the 'Complexe Terminale'. In Table 1.2 figures relating to evaporation, exploitation and recharge are presented. The expected trends of evaporation and exploitation do not compensate each other. These values are estimates with recharge and evaporation much less accurate than exploitation. Especially the evaporation amount may be a rather rough guess, since it was determined as the amount to be included as a boundary condition of a simulation model of the aquifer, to match a given piezometric distribution. As is shown, the increase in exploitation is much larger than the estimated decrease in evaporation. It is not easy to think of a definitive argumentation to account for this result, since the lowering of the water table in the evaporating areas does not depend on exploitation only, but also on the transmissivity and the distance from the areas where water is being pumped out. This is the reason why the relationship between areas of evaporation and extraction should be investigated taking into account their mutual position. The latter statement also applies to water quality related problems. The possibility for a saline water flow to take place from the chotts to neighbouring wells has also been discussed in UNESCO (1972). It was estimated that in the zone North of the Wadi Rhir, excessive salinization of pumped water could be irreversible within a time span of 100 to 500 year, because of flow coming from the Chotts Merouane and Melrhir. It appears that the situation is much worse around the Chott Djerid, where contamination was expected to develop within 30 years.

Interrelations between exploitation, evaporation

Table 1.3. Water balance of the Sedjoumi basin (after Ennabli, 1981)

	Recharge (dm³·s⁻¹)		Discharge (dm³·s⁻¹)
Infiltration	209	Pumping	113.5
Inflow		'Valley of Tunis'	26.5
through		Playa evaporation	111.0
boundaries	42		
Total	251		251.0

and salinization of groundwater reservoirs was analyz-
ed in detail for the playa Sedjoumi (Tunisia). A
hydro-geological study was presented by WEIMAN (1963)
and a simulation study by a numerical model was de-
scribed by ENNABLI (1981). The latter author emphasiz-
ed the risk of salt pollution of the fresh groundwa-
ter supply to the Tunis urban area, because of out-
flow from the playa phreatic aquifer. As shown in
Table 1.3 evaporation from the playa represents a 45%
share of discharge from the whole reservoir. Thus it
can be concluded that evaporation from playas can be
quite relevant as a driving process in the behaviour
of groundwater reservoirs in desert regions.

It is impossible to give here even a short syn-
thesis of the literature on geological and hydrologic-
al playa features. However, a few references should
be mentioned: DUTCHER and THOMAS (1967) who studied
the water balance of a wadi system in Tunisia; HUNT
(1960), NEAL (1975) and MOLINEUX et al. (1971) who
analyzed surface features of playas in relation to
their hydro-geological behaviour.

The only actual measurements of the evaporation
rate in playas that are available were performed on
two days in 1969 (PIKE, 1970). Another study perform-
ed in 1938-1939 and presented by BLANEY (1957) does
not strictly relate to playa evaporation, even though
being useful because of the data collected on pan and
lake evaporation in a true desert environment.

Dealing with the estimation of groundwater losses
by surface evaporation in deserts, the task becomes
harder in those areas where rainfall is not extremely
low because in those areas the groundwater table depth
in playas changes over short periods, with a related
effect on evaporation. It must also be pointed out
that estimating the recharge of aquifers is as tricky
as estimating losses by evaporation, as they are
strictly related to each other. As far as at least one
of these two terms in the water balance is not measured
as directly as possible, there is little hope to
achieve a good reliability in the appraisal of ground-
water reservoirs.

1.3. AQUIFER SYSTEMS IN WEST-LIBYA

In Section 1.2 only a general outline of playas
and the water balance of groundwater reservoirs in
deserts was given, but a specific example is needed
when both structure and geographical extent of an
aquifer system in which playas play a rôle are to be
illustrated. For this purpose the rôle of the West-
Libyan playas has been chosen.

The importance of the West-Libyan aquifer has

Fig. 1.3. Itinerary (broken line with arrows) of the
journey of Lucius Cornelius Balbus in 20-19 B.C. when
pursuing the Garamantes into the Phazania (Fezzan),
presented on a DMSP-satellite image (0.4-1.1 μm; 21
September 1978). Also shown is the boundary of the
West-Libyan aquifer (dotted line)

been recognized for a long time. PLINIUS (77) in his
'Naturalis Historia - Liber V' describes the war be-
tween a Roman army and the Garamantes, the earlier
inhabitants of Phazania (the present Fezzan). In
20-19 B.C. Lucius Cornelius Balbus was able to lead
an army of 20,000 men from Sabratah on the Mediterra-
nean coast (some 70 km West of Tripoli) to Garama
(the present Jarmah) some 20 km East of Awbari. The
army followed a natural track on the West-Libyan aqui-
fer (Fig. 1.3) from Sabratah to Cidamus (Ghadames).
Then they headed for the Hamada al Hamra to reach
Dedris (most probably present-day Idri). The final leg
of the trip brought the army to Garama, the capital of
the Kingdom of the Garamantes. The indications given
about the distance from Cidamus to Garama suggest that
the army had to cross the Idehan Awbari marching along
the track still in use from Idri to Awbari. In the ac-
count given by PLINIUS (77) it is stated that the
Garamantes inhabited a region encircled by sand. The
'restagnantes Mauretaniae aquae', however, provided
the Roman army with a water supply from very shallow
wells (~0.9 m below the surface).

Knowledge about groundwater reservoirs in Libya
dramatically improved only in recent years. A meaning-
ful amount of geological data was unavailable to ear-
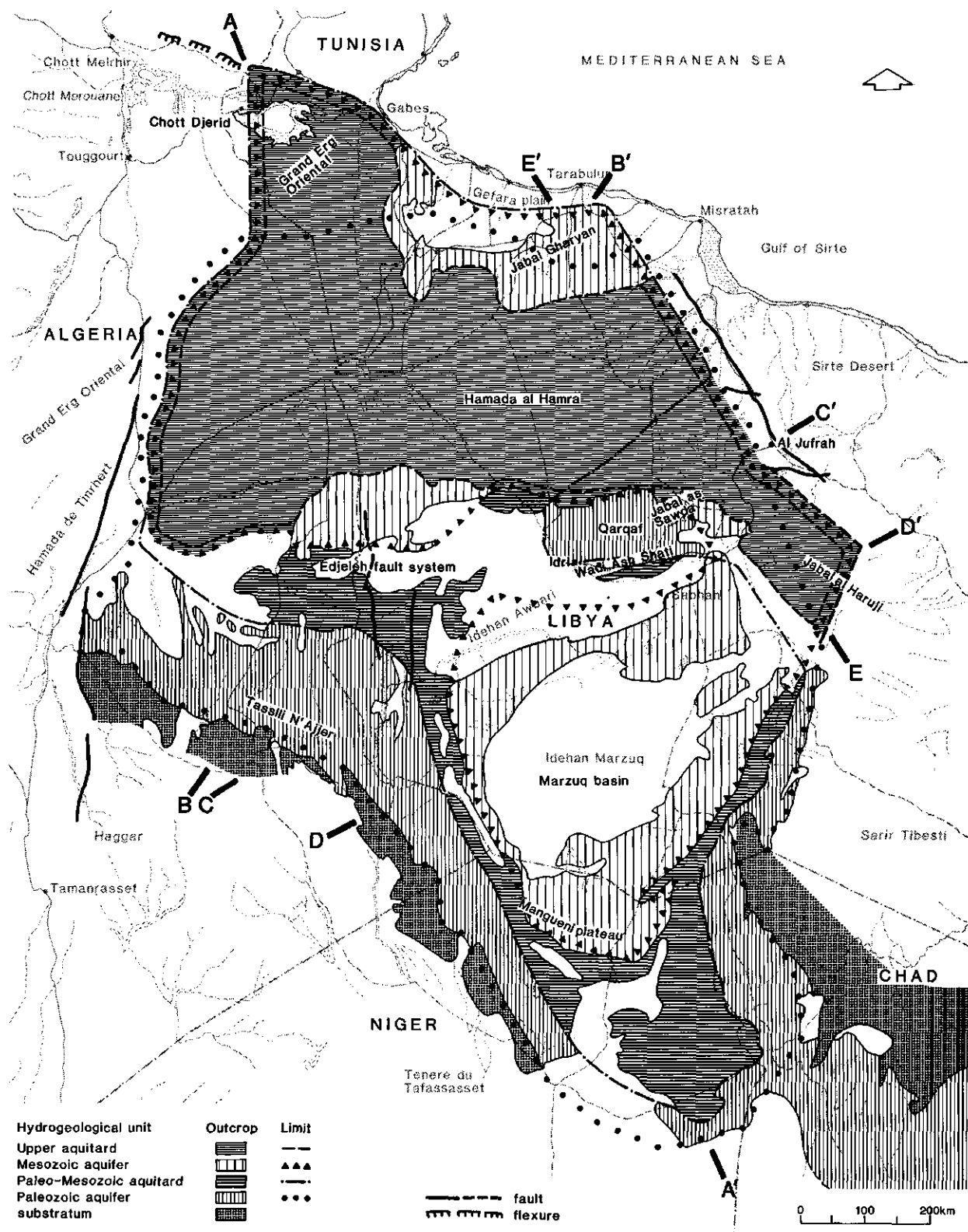
Fig. 1.4. Schematic structure of the West-Libyan aquifer system (after Pizzi and Pone, 1978). For cross sections A - A' etc. see Fig. 1.5
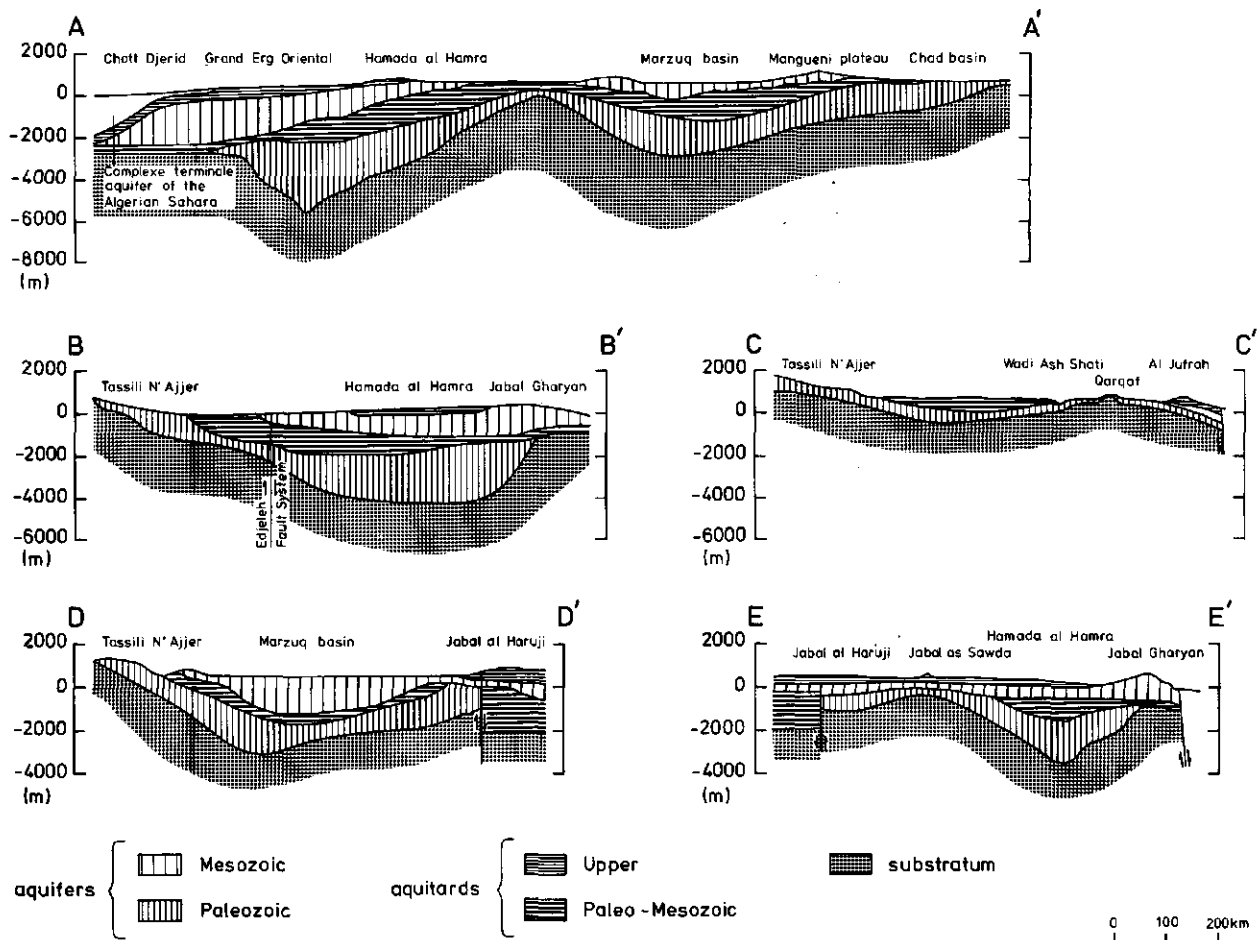
Fig. 1.5. Schematic cross sections (see Fig. 1.4) of the West-Libyan aquifer system (after Pizzi and Pone, 1978)

lier authors, thus studies and reports heavily relied on intuition. Reports from WHITCOMB (1956), JONES (1964, 1971) and TIBBITS (1966) represented first efforts to define the hydro-geology of the known groundwater reservoirs in West-Libya. However, the proposed structural units were mainly derived from surface features.

The playas in the surroundings of Idri were studied by GOUDARZI (1962, 1970). In this study the complexity of the hydro-geological problem was completely overlooked. Very little attention was paid to the origin of the thick (0.4 m) salt crust, which was considered-to be valuable for commercial exploitation. A number of samples of the crust were analyzed for NaCl, K_2O, $MgCl_2$, while samples of the brine underlying the crust were analyzed for Na, K, Cl, SO_4, Mg, HCO_3. Evaporation tests were performed to assess the yield capacity in crystallized salts.

According to PIZZI and PONE (1978) the aquifer system (Fig. 1.4) extends over 800,000 km^2 in West-Libya, Tunisia, Algeria, Niger and Chad. It consists of two main aquifers hydraulically linked by an interbedded aquitard. The deeper aquifer is contained in

Paleozoic formations (Paleozoic aquifer). The aquitard is built up of Upper Devonian, Carboniferous and Triassic semipervious formations (Paleo-Mesozoic aquitard). The upper aquifer is contained in Mesozoic formations (Mesozoic aquifer).

In Fig. 1.5 five schematic cross sections (for their location see Fig. 1.4) of the regional aquifer system are presented. The limits of the Paleozoic aquifer (Fig. 1.6) are the base outcrops (South), the Amguid fault system (West) and the Bu Nghem - Hun graben (East). The northern boundary of the Paleozoic aquifer is represented by the limit of the Paleozoic formations lying approximately along the 32° parallel.

The limits of the Mesozoic aquifer (Fig. 1.7) are the Paleo-Mesozoic aquitard outcrops in Marzuq and Polignac basins, the Amguid fault system (West), the Homs fault system and the Atlas flexure (North), the Bu Nghem - Hun graben (East). The Mesozoic aquifer consists of two groundwater basins geographically separated by the Qarqaf uplift axis. The only contact between the northern and southern zone of the Mesozoic aquifer occurs eastward in the Al Jufrah - Al Fuqaha area. As can be seen in Fig. 1.5 C-C', the Paleozoic

Fig. 1.6. Distribution of the piezometric head (in m above Ordnance Datum) of the Paleozoic aquifer (after Pizzi and Pone, 1978); location of playas also is indicated. Ordnance Datum is for practical purposes equal to sea level
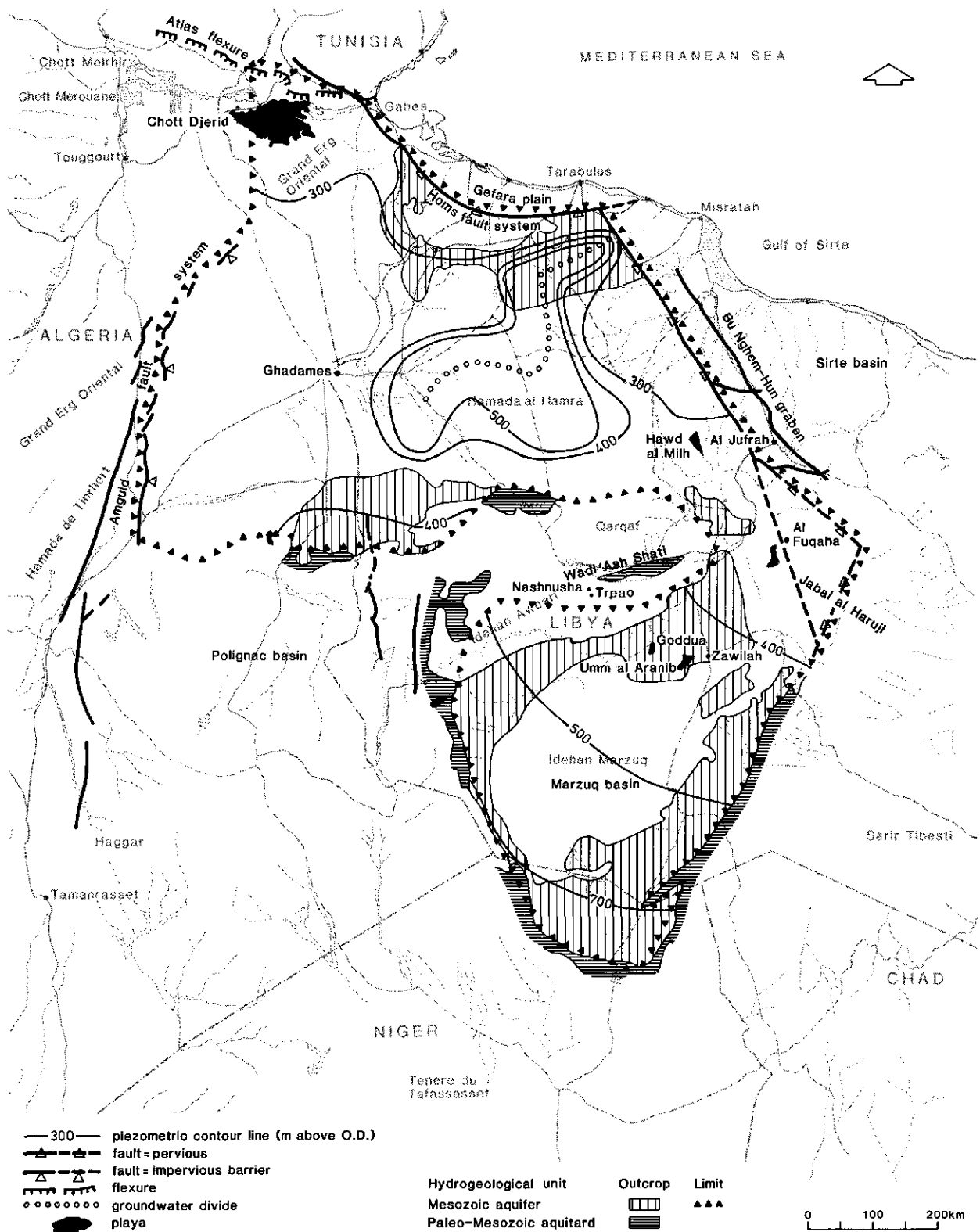
Fig. 1.7. Distribution of the piezometric head (in m above Ordnance Datum) of the Mesozoic aquifer (after Pizzi and Pone, 1978); location of playas also is indicated

aquifer crops out in the Wadi Ash Shati basin. Thus evaporation of groundwater will occur and the relatively lower elevation allows for groundwater supply. The effect of natural discharge into the area is shown quite clearly by the distribution of piezometric heads in Fig. 1.6, South of the Qarqaf highland.

The large-scale flow pattern is quite clear: groundwater flow takes place across the Bu Ghem - Hun graben towards the Sirte basin. In the southern zone of the area a groundwater divide exists and South of this divide, the groundwater flow is directed towards the Chad basin. In Fig. 1.7 the iso-piezometric lines of the Mesozoic aquifer show two different distributions for the Marzuq and the Ghadames basins. The main features of the flow pattern are:

- outgoing groundwater flow from the Hamada al Hamra;
- vertical water exchange from the Mesozoic aquifer
  to the Complexe Terminale aquifer (see UNESCO,
  1972) of the Algerian Sahara in the region of Chott
  Djerid.

The above given sketch of flow patterns in both the Paleo- and Mesozoic aquifers helps to understand the rôle of natural discharge areas in the region investigated. Natural groundwater discharge takes place:

- on and near the outcrops of the Paleozoic and Mesozoic aquifers in the form of evaporation from playas;
- along the Bu Nghem - Hun graben and the Jabal al Haruji region where groundwater moves across the fault system from the Paleozoic and the Mesozoic aquifers to the Sirte basin water-bearing formations;
- in the southern zone of the Paleozoic aquifers where the groundwater flow is directed towards the Chad basin;
- along the Homs fault where groundwater moves across the fault system, from the Mesozoic aquifer to the Gefara water-bearing formations;
- in the playa region of Tunisia where an important leakage from the Mesozoic aquifer to the Complexe Terminale (UNESCO, 1972) aquifer exists.

About playa surface features it suffices to say that examples of all four classes described in Section 1.2 are present in the area. In the Idehan Marzuq and Idehan Awbari even small lakes exist.

1.4. SCOPE OF THE PRESENT INVESTIGATIONS

In Section 1.1 the scope for further research into groundwater losses by evaporation from deserts has been briefly discussed. It was concluded that bare soil evaporation is a relatively unknown term in the water balance of aquifer systems in deserts. It also was stressed that the accuracy in the determination of this term required by real-world water management problems in deserts, is badly underrated. The scope for a deeper insight in the physical aspects of evaporation in nearly dry soils and for application of new data-gathering techniques, fitting the regional nature of water management in deserts, has been emphasized.

In Section 1.2 a general description of playa surface characteristics has been given. The different surface crusts, with their variable flow-transmitting properties are of main importance in any investigation dealing with transport phenomena in desert soils. Theory and methods applied to reach the investigation goal must be shaped to cope with the difficulties brought about by the structure of those crusts. In Sections 1.2 and 1.3 it was stated that evaporation areas in deserts are scattered over a large expanse. Thus the second component to be solved is the capability of translating point data or results into regional ones.

The scope of the present investigations can be described as the development of an approach to estimate groundwater losses by evaporation combining point experiments with regional data.

After the overview given in Chapter 1, the application of formulae involving the use of meteorological data to estimate actual evaporation rates will be discussed in Chapter 2.

To establish a clear separation between potential and actual evaporation, a new combination formula applying to actual evaporation will be derived. Then potential evaporation is defined by taking the limit of the new combination equation for a zero-depth of the evaporation front. It is also shown that unless constant and known heat and moisture flow properties can be assumed in the top soil layer, little scope is left for that approach.

The equations presented in Chapter 2, will be applied in Chapter 8, after illustrating in Chapter 3 how the required transport coefficients can be determined and which kind of physical schematization of the transfer processes in the soil can be accepted. A problem left open in Chapter 2 is the finding of a physically meaningful content for the evaporation-front concept.

In Chapter 3 particular aspects of transport phenomena being specific for (both dry and playa) desert soils are discussed at length. It is shown that thermal convective air movement in the soil may arise and that, because of the air humidity gradient in the soil, vapour transport may take place against the tempera-

ture gradient. These processes greatly enhance the transport coefficients for both heat and vapour as needed to determine the actual evaporation from the soil. A new definition of evaporation sites in the soil is given, relying on the Knudsen flow concept. This definition, aside from fulfilling the requirement put forward above in relation to Chapter 2, will be applied in Chapter 8 to map the areas where evaporation takes place from below the soil surface. For this purpose remotely sensed data can be applied as will be discussed in Chapters 5 and 7.

In Chapter 3 also methods are presented to determine the apparent soil thermal diffusivity, including the contribution of convective flow, together with procedures to account for the effect of salts and temperature on soil hydrological properties.

In Chapter 4 the relationship between the apparent thermal properties of a bare soil surface and the frequency of the surface temperature wave is established. This relationship explicitly relates the thermal properties and thickness of the different soil layers to the thermal behaviour of the soil surface. Since the latter can be studied by means of satellite measured surface radiation temperatures, as discussed in the Chapters 5 and 7, the theory presented in Chapter 4 is a suitable tool for the quantitative use of thermal infrared satellite data.

The heat flux into the soil is a very important term in the determination of the energy balance at the soil surface. In first instance, the surface apparent thermal properties necessary to calculate this heat flux from surface temperature data are unknown. So the soil heat flux is to be determined in a preliminary step of the procedure. This can be achieved by making use of the definition of the evaporation front (Chapter 3) and of the theory of heat and vapour transfer (Chapter 3). The procedures to be followed in this respect are described in Chapter 5, the data available of a specific desert area are analyzed in Chapter 7, while in a part of Chapter 8 the procedure to obtain the heat flux into the soil and the surface apparent thermal properties is given.

In Chapter 5 various possibilities are analyzed to measure or estimate terms in the surface energy balance equation. The geometrical interpretation of this equation is given and applied to establish relationships between the actual evaporation rate and the other variables present in the equation. Such a schematic analysis of the surface energy balance has a two-fold goal. Simplified relationships are to be established to make proper use of satellite data which, at best, provide surface temperature and surface reflectance. Secondly, using the geometrical interpretation, criteria can be set to select the

kinds of surfaces to be considered for the collection of specified ground reference data.

In Chapter 6 a conspectus of the data concerning the playas in West-Libya, where the case study is situated, is given. The experiments performed for the specific needs of the investigations are briefly described.

In Chapter 7 the remotely sensed data, as surface radiation temperature and surface reflectance, of the test area in West-Libya are evaluated. Two main points are adressed. Firstly it is assessed to which extent the atmospheric effects discussed in Chapter 5 actually are relevant and whether the data can be corrected, with a better accuracy than the data themselves, for such atmospheric effects by theoretically based calculation methods. Secondly the accuracy and the meaning of the satellite data is established by comparing them with the ground reference measurements. In particular the consequences of the very different areal resolution of the different data are analyzed.

In Chapter 8 the practical application of the procedures presented in Chapter 2 through 5, with the data discussed in Chapters 6 and 7, is given. It will be shown that the definition of evaporation sites given in Chapter 3, together with the relationship between surface reflectance and surface moisture content, as established in Chapter 5, greatly facilitates the partition of the available radiative energy between latent and sensible heat flux, necessary to be able to calculate the actual evaporation rate.

Finally the regional actual evaporation from the Wadi Ash Shati and Qarqaf area in West-Libya is calculated and an estimate is given of the net depletion of the groundwater reservoir as result of the evaporation losses. In the summary of Chapter 8 (Section 8.5), a flowchart (Fig. 8.16) gives the interrelation of the contents of various chapters, sections and paragraphs as applied to reach this end.

2. CALCULATION OF EVAPORATION IN DESERTS WITH METEOROLOGICAL DATA

'... fontem eius, mergique in cuniculos ipsum amnem vapore anhelantem fumidis cautibus ubi conditur;...'

(PLINIUS, Naturalis Historia, Liber V:55)

2.1. GENERAL

According to FAO (1981) many concepts and definitions in hydrology cannot straightaway be transposed to arid zones. It appears that of the definitions relating to evaporative phenomena only the one given for actual evapotranspiration remains meaningful: '... is the sum of evaporation and transpiration occurring from any natural or cultivated terrain'.

Potential evapotranspiration is: '... the theoretical evapotranspiration which would occur from an infinite expanse of natural or cultivated terrain, adequately supplied with moisture when exposed to specified climatic conditions which remain unaltered by the evapotranspiration itself'. Deserts, however, are defined as areas where only locally an adequate amount of moisture is supplied. Furthermore, the differences between the actual conditions and the conditions specified in the definition of potential evapotranspiration are very much smaller in humid climates than in arid ones. In deserts an adequate moisture supply changes it to a wetland with dramatically different physiographical features. Even less dramatic changes are to be considered because of their effect on the relationship between local climate and evaporation. For example the reflectance of a wet surface is quite different from the dry case, thus the available radiant energy also changes.

Remarks similar to those in FAO (1981) also can be found in STANHILL (1965) and SUTCLIFFE and SWAN (1970). Notwithstanding this, it has been a rather common practice to estimate crop water requirements in desert areas by methods as described in FAO (1975, 1977).

A few experimental investigations into actual evaporation losses in desert areas have been reported in the literature. Data collected from May 1938 to April 1939 at the Silver Lake - Mojave Desert (California) were presented by BLANEY (1957). During that period the class-A pan evaporation was 3245 mm and the ratio of the evaporation of open water (free lake surface) to pan evaporation was 0.6. Maximum daily (24 hr) pan evaporation was measured to be 24.8 $mm \cdot d^{-1}$. In Central Iraq, WARTENA (1959) observed with a class-A pan a value of 26.2 $mm \cdot d^{-1}$ as a monthly average.

Difficulties already arise in calculating open water evaporation in deserts by formulae involving meteorological data. It can be expected that similar problems arise when calculating evaporation from crops. The manner of obtaining reference data (with a class-A or a Colorado-B pan) is very important, as was found by AL-NAKSHABANDI and KIJNE (1974) who determined the wind function relating to the class-A pan and the (sunken) Colorado-B pan in Central Iraq and they were not able to choose a definite suitable formula to calculate crop water requirements in arid climates.

An important contribution to desert evaporation comes from evapotranspiration by phreatophytes. Experimental results as obtained during a six year experiment on saltcedar (Tamarix pentandra) have been presented by van HYLCKAMA (1970). Actual evapotranspiration was observed to change remarkably with the ion concentration in the water supply. When the electric conductivity (EC) of the water supply was 4 $S \cdot m^{-1}$ the evapotranspiration was 500 $mm \cdot a^{-1}$, and with an EC of 1 $S \cdot m^{-1}$, 3000 $mm \cdot a^{-1}$. A review of experimental investigations into water losses from phreatophytes can be found in FAO (1981). There, however, a few important literature references are missing. Accumulation of salts in the leaves of saltcedar has been studied by HEM (1967) who presented the results of very detailed analyses of plant samples. Actual evapotranspiration of phreatophytes has been measured by the soil water balance method by ROBINSON and WAANANEN (1970) and van HYLCKAMA (1974). Micrometeorological methods have been shown to succeed better than the soil water balance approach by van HYLCKAMA (1980). Results obtained by the last mentioned approach at different sites have been presented by EVANS et al. (1981).

Results relating to bare soil evaporation are even scarcer than for open water and crops. The results presented by PIKE (1970) seem to be the most valuable for the present study. He determined evaporation (during two days) in a coastal playa in Saudi Arabia by the Bowen ratio - energy balance method.

2.2. CALCULATION OF POTENTIAL EVAPOTRANSPIRATION

Procedures to calculate potential evapotranspiration from meteorological data have been reviewed in a number of publications as WARD (1971), FAO (1975, 1977, 1981). It appears that the physical nature of the formulae used is much closer to a specialized climatological index than to a measurable quantity. This concept is quite evident in the approach applied to estimate crop water requirements (FAO, 1975, 1977).

The possibility of applying formulae to calculate potential evapotranspiration from usual meteorological data in arid and desert climates has been ruled out by GAY (1981).

In deserts surface types are present where water availability is unlimited. As already mentioned, according to the definition of potential evapotranspiration, it there cannot be defined as 'potential' because of the restricted extension of these surfaces. As examples one can think of irrigated plots and free water or wet soil surfaces of the size of 10 to 10^2 ha. However, it was shown by van BAVEL (1966) that the combination formula for potential evapotranspiration:

$$LE = -\frac{s(R_n + G_0) + \rho_a c_p (e_{sat} - e_a)/r_a}{s + \gamma} \quad \begin{array}{l} (W \cdot m^{-2}) \\ (2.1) \end{array}$$

where R_n $(W \cdot m^{-2})$ is net radiation, G_0 $(W \cdot m^{-2})$ soil heat flux at the surface, ρ_a $(kg \cdot m^{-3})$ air density, c_p $(J \cdot kg^{-1} \cdot K^{-1})$ air specific heat (at constant air pressure), e_{sat} (mbar) saturation vapour pressure, e_a (mbar) actual vapour pressure, s $(mbar \cdot K^{-1})$ the slope of the saturation vapour pressure curve, γ $(mbar \cdot K^{-1})$ the psychrometric constant and r_a $(s \cdot m^{-1})$ the aerodynamic resistance for heat and vapour transfer from the surface to a reference height z_{ref}, allows for accurate estimates of actual evaporation rates. The term $\rho_a c_p (e_{sat} - e_a)/r_a$ is often indicated as the aerodynamic term, E_a. Actual evaporation was measured in the arid climate of Arizona (van BAVEL, 1966) by weighing lysimeters in small plots containing samples of kinds of surfaces adequately supplied with moisture. Van Bavel's results proved that horizontal advection of sensible heat can be accounted for by using observations when they are collected at small heights

above the surface, i.e. when they are collected inside the inner boundary layer. An inner boundary layer grows in height downwind from the edge between the dry and wet area, thus a fetch requirement can be established by dividing z_{ref} by the chosen ratio of that height to the distance from the edge of wet and dry area. A theoretical explanation of the findings presented by van BAVEL (1966) has been given by ITIER (1977). With the approach applied by Itier errors in the potential evapotranspiration as established by eq. (2.1) caused by a particular choice of z_{ref} at a particular distance from the upwind edge of a sample plot can be estimated. For example when the measuring site is at d/3, where d is the size of the sample plot, and the reference height is 2 m, the error in the evaporation calculated with eq. (2.1) would be 2% with d = 100 m.

Analyses of sensitivity to the different meteorological variables for various procedures to estimate evapotranspiration were presented by McCUEN (1974) and COLEMAN and de COURSEY (1976). Results presented by McCUEN (1974) for a number of weather stations in the USA show that variations in sensitivity of different methods to the same variables are comparable with the scatter in sensitivity between the different stations.

Saline water is a most likely occurrence in playas and the effect of salts on evaporation of open water must be accounted for. Saturation vapour pressure in air at equilibrium with a salt solution of known concentration is, at constant temperature, a function of the concentration itself. Hence, e_{sat} in eq. (2.1) is to be replaced by $U(\chi_i)e_{sat}$ and s by $U(\chi_i)s$, where U is air relative humidity at the salt concentration χ_i. HARBECK (1955) has shown how to account for the effect of salinity on open water evaporation, including explicit relationships with meteorological data. Effects of salts on density, viscosity and surface tension of the solution will be discussed in Sections 3.2 and 3.5.

Air thermal stratification above deserts may vary from strongly stable to strongly unstable. Stability effects on the aerodynamic resistance r_a may be accounted for as shown by THOM and OLIVER (1977).

2.3. A NEW COMBINATION EQUATION AND ITS LIMIT FOR ZERO DEPTH OF THE EVAPORATION FRONT

Evaporation from a bare soil will take place either at the soil surface or below it. A combination formula applying to the entire range of possibilities now will be derived. At zero depth of the evaporation front the limit of the formula applying to evap-

oration taking place inside the soil will be shown to be the eq. (2.1) for potential evaporation of bare soil.

In a drying soil the existence of a dry top layer was observed in a number of cases. Transition from nearly dry to moist soil is much sharper in soils of coarse texture (sand) than in soils of fine texture. The boundary between the upper and lower layer has been called: 'location of evaporation sites' by PHILIP (1957), 'site of evaporation' by WIEGAND and TAYLOR (1961), 'evaporation zone' by MARSHALL and HOLMES (1979), and 'drying front' by HILLEL (1980). The subject is going to be treated in Section 3.1, 3.3 and 3.4, here it suffices to mention the definition given by Philip. This author considered the dependence of q_v/q_{mo}, where q_{mo} is moisture flux and q_v vapour flux, on moisture content θ. He showed that for Yolo clay q_v/q_{mo} changes from 0 to 1 in a narrow moisture range, namely from $\theta = 0.09$ to 0.07 vol.% corresponding to relative humidities U of 0.965 and 0.945, respectively. In Section 3.3 a new definition of evaporation zone will be proposed, because the assumption $(q_v/q_{mo}) = (D_v/D_{mo})$, where D_{mo} is the total moisture diffusivity, is not as straightforward as it looks (see Section 3.2). For the moment it is enough to say that an evaporation zone inside the soil can exist and can consistently be defined. The nearly dry soil layer above the evaporation front has a definite effect on the vapour flow rate, thus any calculation procedure must include a proper parametrization for heat and vapour transfer in that soil layer. To calculate actual evaporation many formulae were presented as extensions of combination methods like the ones discussed in Section 2.2. Formulae presented by TANNER and FUCHS (1968) and MONTEITH (1981) essentially are similar. To account for effects of the dry layer on vapour flow they include only a soil resistance to vapour transport. It will be shown in the Sections 3.1 and 3.4 that also heat flow should explicitely be included, because a proper heat supply is needed to keep up with a given vaporization rate. An approach different from that applied by Tanner and Fuchs, and Monteith has been presented by van BAVEL and HILLEL (1976) who calculated the actual evaporation rate from a bare drying soil by applying a simplified numerical simulation model describing fluxes of heat and water in the top soil.

A further complicating circumstance in calculating evaporation from a drying surface arises because the transfer coefficients for heat and water vapour depend not only on a reference height z_{ref}, but also on air temperature and vapour pressure (see Section 2.5). Hence, in principle, a description of the ver-

tical profiles of these variables is necessary, if transfer coefficients are to be calculated. Sensible heat and vapour fluxes can tentatively be related to vertical gradients by:

$$H = \rho_a c_p k u_* z \phi_h^{-1} \frac{\partial T_a}{\partial z} \quad (W \cdot m^{-2}) \qquad (2.2)$$

$$LE = \rho_a L k u_* z \phi_v^{-1} \frac{\partial q_a}{\partial z} \quad (W \cdot m^{-2}) \qquad (2.3)$$

where

ρ_a = air density $(kg \cdot m^{-3})$
c_p = air specific heat at constant pressure $(J \cdot kg^{-1} \cdot K^{-1})$
L = latent heat of vaporization of water $(J \cdot kg^{-1})$
k = Von Karman's constant
u_* = friction velocity $(m \cdot s^{-1})$
z = height above surface (m)
q_a = air specific humidity
ϕ_h = Monin-Obukhov's function for heat transfer
ϕ_v = Monin-Obukhov's function for vapour transfer
T_a = air temperature (K)

The eqs. (2.2) and (2.3) are useful as far as the ϕ-functions are 'universal' and the data required to calculate their value are available. Usually this is not the case. It appears that the calculation of fluxes from gradients would be much easier if the condition $\phi_h = \phi_v$ applies. For particular and simplified cases BOWEN (1926) has shown that this relationship holds true. The equations considered by BOWEN (1926) were not in the form of eq. (2.2) and eq. (2.3). Some remarks about Bowen's findings will be given in Section 2.5. In the same section different determinations of ϕ_h and ϕ_v will be presented to discuss the equality $\phi_h = \phi_v$. Here the ratio of sensible to latent heat flux will be considered in connection with eqs. (2.2) and (2.3).

According to eqs. (2.2) and (2.3) the ratio (H/LE) can be written as:

$$\beta = \frac{H}{LE} = \frac{c_p}{L} \frac{\phi_h^{-1}}{\phi_v^{-1}} \frac{(\partial T_a/\partial z)}{(\partial q_a/\partial z)} \quad (-) \qquad (2.4)$$

This so-called Bowen ratio β depends on the gradients only when $\phi_h = \phi_v$. This latter condition can be checked against a number of known ϕ-functions. As shown in Section 2.5 the inherent experimental indetermination of the ϕ-functions does not allow to achieve a clear cut conclusion. If evaporation occurs at the soil surface only, the equation for the energy balance at the soil surface reads:

$$R_n + G_0 + LE + H = 0 \quad (W \cdot m^{-2}) \qquad (2.5)$$
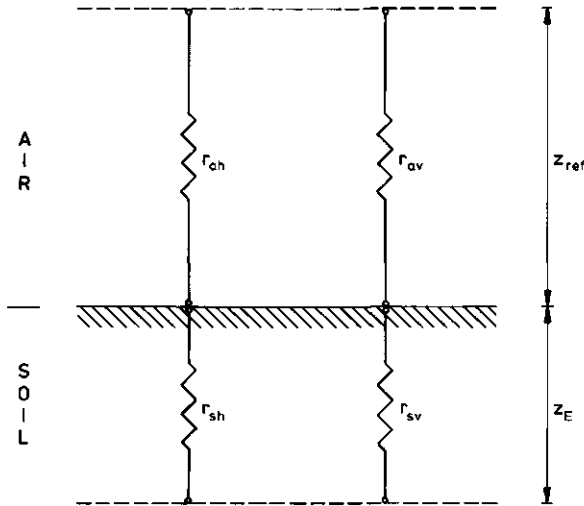
Fig. 2.1. Scheme of heat and vapour transport when evaporation takes place inside the soil. Resistances to flow according to eq. (2.25) are indicated. z_E is the depth of the evaporation front and z_{ref} is the reference height above the soil surface

where fluxes towards the surface where an energy balance equation is derived are counted positive. It can be reduced to the form:

$$LE = -\frac{R_n + G_0}{1 + \beta} \qquad (W \cdot m^{-2}) \qquad (2.6)$$

which provides a method to measure LE when β can be determined by measurements, $\phi_h = \phi_v$ and heat and vapour fluxes can be related to vertical gradients. The method is known in the literature as Bowen Ratio Energy Balance method. This method was applied to measurements taken at the sites listed in Section 6.2 and the results will be presented in Section 8.2.

In the following pages it will be shown that a combination equation can be obtained which applies to a soil profile with evaporation occurring from a front at some depth in the soil (Fig. 2.1). It will also be shown that this equation approaches the known equation for wet soil when the evaporation depth approaches zero.

The energy balance equation at the soil surface, where now no phase transition occurs (LE = 0), eq. (2.5) then reduces to:

$$R_n + H + G_0^{in} = 0 \qquad (W \cdot m^{-2}) \qquad (2.7)$$

where G_0^{in} is the heat flux reaching the soil surface.

The energy balance equation at the evaporation front, where phase transition occurs, can be formulated as:

$$G_E^{in} + LE + G_E^{out} = 0 \qquad (W \cdot m^{-2}) \qquad (2.8)$$

where G_E^{in} is the heat flux reaching the evaporation front and G_E^{out} is the heat flux leaving it. The flux G_E^{in} is related to the flux leaving the soil surface by:

$$G_E^{in} = G_0^{out} - \int_0^{z_E} \rho_s(z) c_s(z) \frac{\partial T_s(z,t)}{\partial t} dz \qquad \begin{array}{c} (W \cdot m^{-2}) \\ (2.9) \end{array}$$

where z_E is the depth of the evaporation front, T_s the soil temperature, c_s soil specific heat and ρ_s soil bulk density. The integral term accounts for heat storage which for a given harmonic fluctuation can be relevant for time intervals shorter than a complete period.

Note that eq. (2.9) implies that the heat flux leaving the soil surface, G_0^{out}, is positive when directed downwards, i.e. the sign is opposite to that in eq. (2.7) in accordance with the given sign convention, so:

$$G_0^{out} = -G_0^{in} \qquad (W \cdot m^{-2}) \qquad (2.10)$$

If heat storage between $z = 0$ and $z = z_E$ is neglected, eq. (2.8) can be rewritten as:

$$G_0^{in} - LE - G_E^{out} = 0 \qquad (W \cdot m^{-2}) \qquad (2.11)$$

Then from eq. (2.7):

$$R_n + H = -(LE + G_E^{out}) \qquad (W \cdot m^{-2}) \qquad (2.12)$$

This latter equation can be rewritten by substitution of $H = \beta LE$ (eq. 2.4) and by writing G_E for G_E^{out}:

$$R_n + G_E = -(1 + \beta)LE \qquad (W \cdot m^{-2}) \qquad (2.13)$$

or

$$LE = -\frac{R_n + G_E}{1 + \beta} \qquad (W \cdot m^{-2}) \qquad (2.14)$$

Note that eq. (2.14) is formally identical to eq. (2.6) which holds for actual evaporation which takes place at the wet soil surface. However, some basic differences hold: G_E is the soil heat flux at the evaporation front [positive when directed towards the plane at $z = z_E$ to which the energy balance equation (2.8) relates] and in eq. (2.14) the latent heat flux LE in the air must be equal to the corresponding flux in the soil. These restrictions can be cast in the form of a set of transport equations of which the meaning is that in the soil layer between $z = 0$

and $z = z_E$ a trade off must be established between the soil capability in carrying heat and vapour. When $G_E \neq 0$ the partition of energy at the evaporation front will be limited by the lowest flow rate either of vapour or of heat in the soil. The result then is that a net flux G_E remains.

The transport equation for sensible heat in air is:

$$H = - \frac{\rho_a c_p}{r_{ah}} \left[T(0) - T(z) \right] \qquad (W \cdot m^{-2}) \qquad (2.15)$$

where $\rho_a c_p$ is the thermal capacity of air, r_{ah} the resistance for sensible heat transport in air.

For heat transport from the soil surface to the evaporation front applies:

$$G_0^{in} = \lambda \, \frac{T_E - T(0)}{z_E} = \frac{T_E - T(0)}{r_{sh}} \qquad (W \cdot m^{-2}) \qquad (2.16)$$

where λ is the soil thermal conductivity $(W \cdot m^{-1} \cdot K^{-1})$.

The resistance for heat transport r_{sh} is defined as:

$$r_{sh} = \frac{z_E}{\lambda} \qquad (W^{-1} \cdot m^2 \cdot K) \qquad (2.17)$$

For transport of latent heat in air, we have:

$$LE = - \frac{\rho_a c_p}{\gamma r_{av}} \left[e(0) - e(z) \right] \qquad (W \cdot m^{-2}) \qquad (2.18)$$

where r_{av} is the resistance for vapour transport in air.

For transport of latent heat in soil air holds:

$$LE = - \frac{\rho_a c_p}{\gamma r_{sv}} \left[e_{sat}(T_E) - e(0) \right] \qquad (W \cdot m^{-2}) \qquad (2.19)$$

where r_{sv} is the resistance for vapour transport in the soil.

Note that according to the given definition of the evaporation front the actual vapour pressure there closely approaches the saturation value at temperature T_E. When salts are present, a value of the relative humidity U can be assigned at z_E as already indicated in Section 2.2.

Eqs. (2.18) and (2.19) can be rewritten as:

$$r_{av} = - \frac{\rho_a c_p}{\gamma LE} \left[e(0) - e(z) \right] \qquad (s \cdot m^{-1})$$

$$(2.20)$$

$$r_{sv} = - \frac{\rho_a c_p}{\gamma LE} \left[e_{sat}(T_E) - e(0) \right] \qquad (s \cdot m^{-1})$$
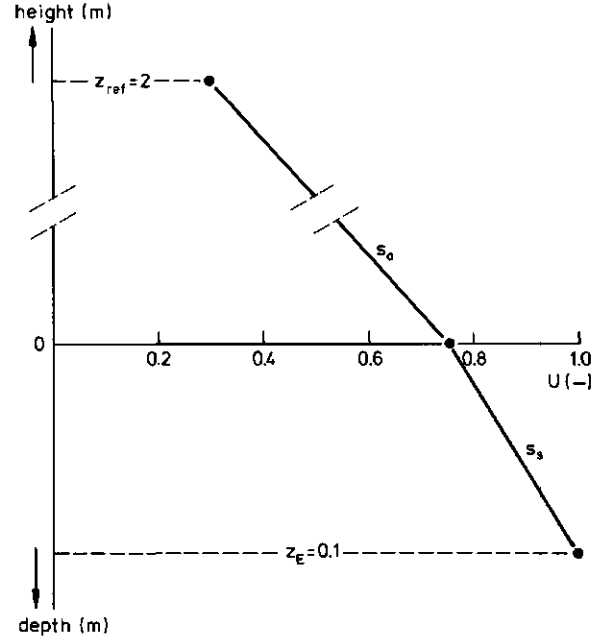
Fig. 2.2. Variation of air relative humidity U inside the soil and above it. The slope s_s of saturation vapour pressure curve $e_{sat}(T)$ is calculated at the average temperature in the soil layer from $z = 0$ and $z = z_E$, while in air s_a applies to the average temperature between $z = 0$ and $z = z_{ref}$

which can be summed while eliminating $e(0)$:

$$r_{av} + r_{sv} = - \frac{\rho_a c_p}{\gamma LE} \left[e_{sat}(T_E) - e(z) \right] \qquad (s \cdot m^{-1}) \quad (2.21)$$

The saturation vapour pressure at the evaporation front can be expressed as a function of the saturation vapour pressure in air at height z:

$$e_{sat}(T_E) = e_{sat}(T(z)) + s_a \left[T(0) - T(z) \right] + s_s \left[T_E - T(0) \right]$$

$$\text{(mbar)}$$
$$(2.22)$$

where s is the slope of $e_{sat}(T)$. Two different values must be considered (Fig. 2.2) at least in principle: s_a is the value applying to the air (corresponding with the value calculated at the mean temperature between $z = 0$ and $z = z_{ref}$, while s_s applies to the soil, i.e. calculated at the mean temperature between $z = 0$ and $z = z_E$.

Eqs. (2.15), (2.16), (2.11), (2.7) can be substituted in eq. (2.22):

$$e_{sat}(T_E) = e_{sat} \left[T(z) \right] + \frac{s_a r_{ah}}{\rho_a c_p} (R_n + G_E) + s_s r_{sh} G_E +$$

$$+ (s_a \frac{r_{ah}}{\rho_a c_p} + s_s r_{sh}) LE \qquad \text{(mbar)} \qquad (2.23)$$

which can be substituted in eq. (2.21):

18

$$-\tilde{\gamma}(r_{av} + r_{sv})LE = \rho_a c_p\left[e_{sat}(T(z)) - e(z)\right] +$$

$$+ s_a r_{ah}(R_n + G_E) + s_s \rho_a c_p r_{sh} G_E +$$

$$+ s_s r_{ah} LE + s_s \rho_a c_p r_{sh} LE \qquad (2.24)$$

and, finally:

$$LE = -\frac{\rho_a c_p\left[e_{sat}(z) - e(z)\right] + s_a r_{ah}(R_n + G_E)}{\tilde{\gamma}(r_{av} + r_{sv}) + s_a r_{ah} + s_s \rho_a c_p r_{sh}} +$$

$$+ \frac{s_s \rho_a c_p r_{sh} G_E}{\tilde{\gamma}(r_{av} + r_{sv}) + s_a r_{ah} + s_s \rho_a c_p r_{sh}} \qquad \begin{matrix}(W \cdot m^{-2})\\(2.25)\end{matrix}$$

which is the combination equation looked for. In Chapters 3 and 4 attempts will be made to determine the coefficients involved and in Chapter 8 use will be made of this equation.

It should be noted that this equation approaches the known combination equation for wet soil, when $r_{sh} \rightarrow 0$, i.e. $z_E \rightarrow 0$ since the case $\lambda \rightarrow \infty$ has no practical meaning. Note that $r_{sv} \rightarrow 0$ also holds since $T_E \rightarrow T(0)$ when $z_E \rightarrow 0$ (see eq. 2.20) and that $G_E = G_0$, since now $z_E = 0$. Taking the limit of eq. (2.25) as $z_E \rightarrow 0$ yields:

$$LE_0 = -\frac{\rho_a c_p\left[e_{sat}(z) - e(z)\right] + s_a r_{ah}(R_n + G_0)}{\tilde{\gamma} r_{av} + s_a r_{ah}} \qquad \begin{matrix}(W \cdot m^{-2})\\(2.26)\end{matrix}$$

and with the usual assumption $r_{av} = r_{ah}$ and furthermore $s = s_a$:

$$LE_0 = -\frac{s(R_n + G) + \rho_a c_p\left[e_{sat}(z) - e(z)\right]/r_a}{s + \tilde{\gamma}} \qquad \begin{matrix}(W \cdot m^{-2})\\(2.27)\end{matrix}$$

which is the usual combination equation for wet soil as already presented as eq. (2.1).

Note that when the evaporation front displaces itself towards deeper depths, an important change in the soil surface properties occurs. A wet soil surface has very little in common with the case where the evaporation front lies within the soil: the reflectance of the surface is quite different, thus the available radiant energy also is. In Section 5.3 and 7.5 it will be shown that the function $\alpha(\theta)$, describing the dependence of bare soil reflectance α on surface moisture content θ, can be predicted by a simple model.

2.4. EXTRAPOLATION OF ENVIRONMENTAL POINT VALUES TO AREAL VALUES

A conspectus of different approaches to estimate regional actual evapotranspiration from weather data can be found in MONTEITH (1981).

With eq. (2.25) in mind the following remarks can be given. If soil physical properties and meteorological data were known for each sub-area where an actual evaporation rate is to be assigned, then that formula would yield in principle the required figure for the volume of water evaporated. Such a knowledge seems a rather unlikely occurrence.

Of the needed meteorological data only net radiation can be estimated by a reasonably consistent procedure. Global incoming shortwave radiation is uniform over large areas, thus a map of surface reflectance (for example by remote sensing) allows to calculate net shortwave radiation. Global incoming shortwave radiation can also be estimated from sunshine hours, cloud cover or cloudiness observations.

Net longwave radiation can be calculated from turbidity, cloud height and amount, surface and air temperature, and air humidity. Density of weather stations in deserts is very low, however, thus some extrapolation cannot be avoided, even when not justified. It will be shown that relevant differences in air temperature and humidity exist even within an area of 10^2 km^2 because of microscale effects. However, there seems to be no alternative but to apply the same routine weather observations to areas as large as 10^4 to 10^5 km^2.

As far as the resistances in eq. (2.25) are concerned detailed maps of land use and soil types can in principle be applied to estimate the relevant figures within each 'homogeneous' area. According to THOM and OLIVER (1977) the effect of surface roughness on $r_a = r_{ah} = r_{av}$ is not too relevant. Thus simple empirical relationships between roughness length z_0 and height of roughness elements z, such as $z_0 = bz$ can be helpful. A useful empirical equation for r_a was given by FEDDES (1971). Difficulties relating to the extrapolation of weather data, however, cannot be overcome, and calculation of corrections to account for air stratification effects on r_a always will be a risky affair.

As regards the soil physical aspects the estimation of r_{sv} and r_{sh} in eq. (2.25) is even more difficult. Only when a number of simplifying hypotheses can be accepted, typical values can be assigned according to the soil type encountered. A similar remark applies to the soil heat flux G_E in eq. (2.25).

A partial alternative to combination equations involving surface resistances is the concept of actual and potential evapotranspiration being complementary quantities as proposed by BOUCHET (1963). This author proposed different approaches to estimate a

term relating to large scale advection, which appears in his procedure. MORTON (1978) determined the advection term and the vapour transfer coefficient from the sum of potential and actual evaporation. Accounting for large scale advection as required by the Bouchet concept, BRUTSAERT and STRICKER (1979) applied the argument proposed by SLATYER and McILROY (1961) on the aerodynamic term E_a in eq. (2.1).

It must be noted that the best possible outcome of the Bouchet approach is a correct value of actual evaporation at the site where a weather station is present. This implies that because of poor coverage of weather stations the same evaporation rate must be applied to large areas. Therefore eq. (2.25) has an advantage in that the explicit use of transfer coefficients (resistances) clearly indicates the surface related local effects.

Procedures presented in the above mentioned references to calculate actual regional evaporation, make use of meteorological data routinely collected at ground stations. Because of the low measuring height (2 m say), such data relate to meteorological phenomena of a small length scale.

To determine regional evaporation a generalization of the profile method, e.g. eqs. (2.2) and (2.3), has been proposed by BRUTSAERT and MAWDSLEY (1976). The idea is that by applying upper air data the resultant effect of any, complicated, pattern of actual evaporation at ground level, is being measured.

A different approach, also requiring upper air data, has been applied by PEIXOTO et al. (1976, 1981) who calculated from upper air data the atmospheric water balance.

It appears that neither a clear operational definition of regional actual evaporation nor a feasible method to determine it, are available. The latter implies that reference data for the calculations presented in Chapter 8 cannot be obtained.

2.5. FEASIBILITY OF THE METEOROLOGICAL APPROACH

Difficulties arising with the extrapolation of calculated values because of non-optimal quantity and quality of areal data already were discussed. However, the restrictions on the use of both the Bowen ratio - energy balance method (eq. 2.14) and the combination formula (eq. 2.25) have yet to be properly defined.

The first approach (eq. 2.14) seems to be fairly close to a direct measuring procedure, because only the hypothesis $(\phi_h/\phi_v) = 1$ is involved. However, some difficulties arise in measuring the soil heat flux G_E. When evaporation is taking place inside the soil, a proper determination of G_E is paramount to the deter-

mination of actual evaporation. Full attention to this point will be given in the Sections 3.4 and 4.1, but it can be anticipated that the main trouble concerns the soil thermal conductivity λ. Knowledge of λ is needed to calculate G_E from temperature measurements or to correct measurements obtained by soil heat flux transducers. Since λ turns out to be dependent on soil air humidity and vapour flow rate, it is difficult to settle on a simplifying hypothesis, without biasing the final result for the evaporation rate E.

A second problem relates to the ratio (ϕ_h/ϕ_v) in eq. (2.4) being different from unity. The ϕ-functions account for the variation of transfer coefficients with air thermal stratification. Because of the typically large amplitude of soil and air temperature in deserts, that variation also is large.

Variability of the relationship between fluxes and the corresponding gradients (Monin-Obukhov's ϕ-functions) according to air thermal stratification was studied by many authors in experiments. A given condition of thermal stratification can be defined by Monin-Obukhov parameter $\zeta = (z/L)$ where L is the Obukhov's length:

$$L = - \frac{u_*^3 \overline{T}_a}{k g \overline{w'T'}_a} \quad (m) \qquad (2.28)$$

where w is the vertical wind velocity $(m \cdot s^{-1})$, or by the Richardson number Ri:

$$Ri = \frac{g(\partial \overline{T}_a/\partial z)}{\overline{T}_a(\partial \overline{u}/\partial z)^2} \quad (-) \qquad (2.29)$$

Therefore it appears not too difficult, at least in principle, to account for deviations of ϕ_h/ϕ_v from unity, since the particular functions ϕ_h and ϕ_v can be chosen and applied to calculate the ratio for a given ζ or Ri. However, the matter is not so straightforward because of intrinsic experimental variability in the ϕ-functions. A number of different ϕ-functions can be found in literature. The subject was reviewed by PRUITT et al. (1973), DYER (1974), YAGLOM (1977) and BRUTSAERT (1982). In Fig. 2.3 some of the $\phi_{h,v}(\zeta)$ are plotted: for stable conditions in the upper half and unstable conditions in the lower half of the figure. It appears that the difference between ϕ_h and ϕ_v is comparable with the intrinsic variability inherent to the separate values of ϕ_h and ϕ_v. A similar result is found in Fig. 2.4 where ϕ_m-functions are plotted versus Ri, as listed by PRUITT et al. (1973). It can also be seen that the experimental indetermination increases both with higher values of $|\zeta|$ and $|Ri|$. Thus, it can be concluded, as in YAGLOM (1977), that $\phi_h = \phi_v$ for the entire range of ζ and Ri covered by the experiments performed insofar.

ϕ_h resp ϕ_v (—)

$\phi_h = (1+7\zeta)$
$\phi_v = (1+5.2\zeta)$
$\phi_v = (1+5\zeta)$
$\phi_h = (0.74+4.7\zeta)$
$\phi_h = 0.93(1-1.56\zeta)^{-0.5} [0 \leq |\zeta| < 0.15]$
$\phi_h = 0.38(-\zeta)^{-1/3} [0.15 \leq |\zeta| \leq 1.2]$
$\phi_v = (1-9\zeta)^{-0.5}$
$\phi_v = (1-16\zeta)^{-0.5}$
$\phi_v = (1-15\zeta)^{-0.55}$
$\phi_h = 0.74(1-9\zeta)^{-0.5}$
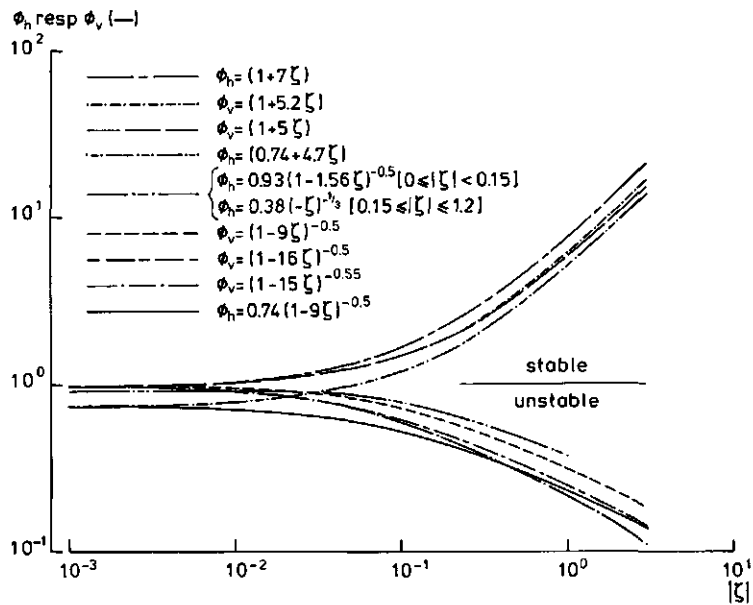
Fig. 2.3. Comparison of Monin-Obukhov's ϕ-functions as given by various authors. ϕ_h is the relationship between the vertical gradient of air temperature and sensible heat flux; ϕ_v the relationship between the vertical gradient of air specific humidity and water vapour flux; $\zeta = z/L$ is the Monin-Obukhov's stability parameter

ϕ_m (—)

$\phi_m = (1+10 Ri)^{0.5}$
$\phi_m = (1+16 Ri)^{1/3}$
$\phi_m = (1+38 Ri)^{0.25}$
$\phi_m = (1+18 Ri)^{0.25}$
$\phi_m = (1-18 Ri)^{-0.25}$
$\phi_m = (1-38 Ri)^{-0.25}$
$\phi_m = (1-16 Ri)^{-1/3}$
$\phi_m = (1-9 Ri)^{-0.5}$
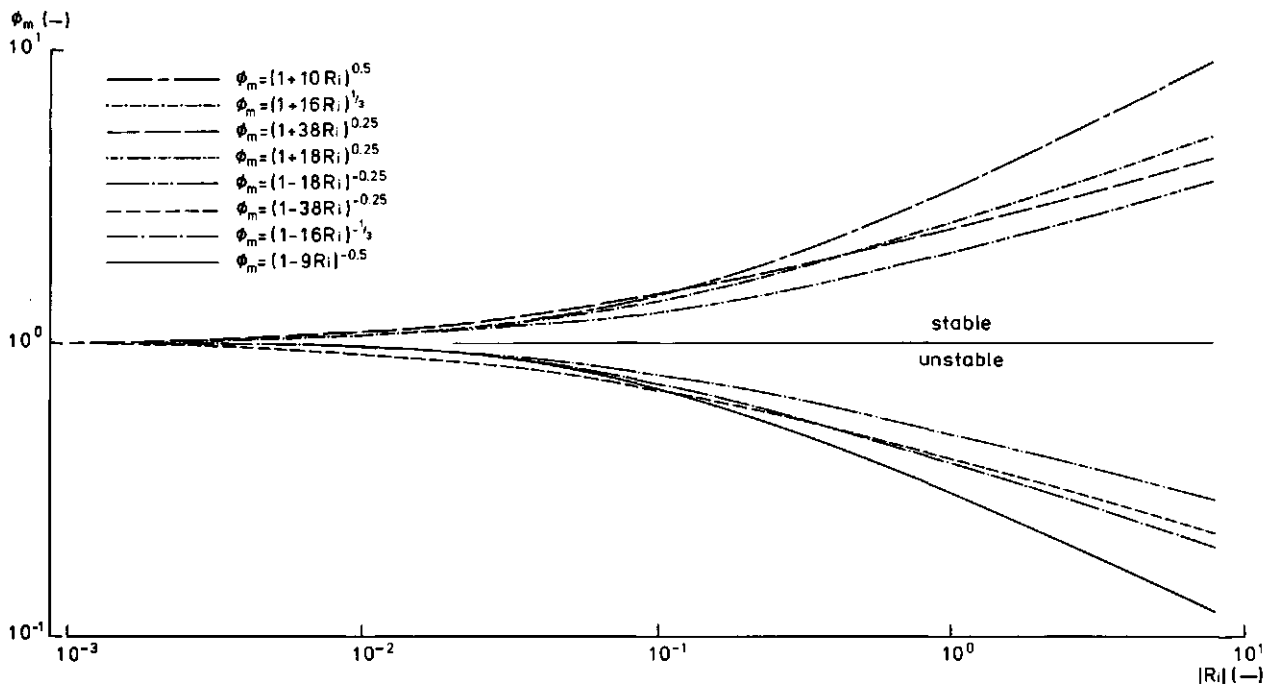
Fig. 2.4. As Fig. 2.3, but ϕ_m is the relationship between the vertical gradient of horizontal wind velocity and momentum flux; Ri is the Richardson number

The intrinsic variability of the ϕ-functions means that the corrections applied according to stability conditions in calculating fluxes from gradients depend on the particular choice of these functions. The risk of calculating fluxes from gradients in very stable or very unstable conditions must also fully be appreciated. Due attention should always be paid to the range of ζ or Ri actually observed in the experiments to which the applied ϕ-functions relate.

A different approach, not based on the ϕ-functions, but on a more general definition of the transfer coefficients in air for heat $\hat{K}_h$ and vapour $\hat{K}_v$, namely:

$$H = -\hat{K}_h \rho_a c_p \frac{\partial T_a}{\partial z} \quad (W \cdot m^{-2}); \quad LE = -\hat{K}_v L \frac{\partial \rho_v}{\partial z} \quad (W \cdot m^{-2})$$

$$(2.30)$$

can be applied. Again the so-called Bowen ratio β can

easily be calculated from gradients when $\hat{K}_h = \hat{K}_v$. Conditions in which the latter holds have been established by WARHAFT (1976). That author considered second order equations for heat and moisture transport and did give the ratio $\hat{K}_h/\hat{K}_v$ as:

$$\frac{\hat{K}_h}{\hat{K}_v} = \frac{1 - \frac{1}{2}\frac{g}{\overline{w'^2}}(\frac{\overline{T_a'^2}}{\overline{T}_a} + 0.61\overline{T_a'q_a'})(\frac{\partial \overline{T}_a}{\partial z})^{-1}}{1 - \frac{1}{2}\frac{g}{\overline{w'^2}}(0.61\overline{q_a'^2} + \frac{\overline{T_a'q_a'}}{\overline{T}_a})(\frac{\partial \overline{q}_a}{\partial z})^{-1}} \quad (-) \quad (2.31)$$

When a deterministic relationship between q_a and T_a holds, such as

$$q_a = \overline{q}_a + q_a' = b_1 T_a + b_2 = b_1\overline{T}_a + b_1 T_a' + b_2 \quad (2.32)$$

where b_1 and b_2 are any constant, it can easily be shown that eq. (2.31) yields $\hat{K}_h/\hat{K}_v = 1$. From eq. (2.32) it can be found that $\overline{q}_a = b_1\overline{T}_a + b_2$ and $q' = b_1 T_a$ and substitution of these relationships in (2.31) yields $\hat{K}_h = \hat{K}_v$ without any influence of the gradients and of the values of b_1 and b_2. If r (r being the correlation coefficient between T_a and q_a) is different from unity, the hypothesis $\hat{K}_h = \hat{K}_v$ is affected by an error that increases with decreasing r, and that varies with the gradients.

In the preceding pages the possible deviations of ϕ_h/ϕ_v and $\hat{K}_h/\hat{K}_v$ from unity were discussed for a horizontally homogeneous ground surface. When there exists a horizontal variability in surface properties over relatively short distances, then the vertical stratification in the lowest few meters of an air mass is also varying along some horizontal directions. An important consequence of this phenomenon is that then all the results presented insofar about the relationship between fluxes and gradients in terms of ϕ-functions, do not hold. Namely horizontally homogeneous conditions are a primary requirement in experiments performed to determine the ϕ-functions. In such cases use may still be made of the Bowen ratio.

It appears, however, that a clarification is needed here on the term 'Bowen ratio'. The dependence on stability of the ratio H/LE, as defined by eq. (2.4) has little to do with the ratio as considered by BOWEN (1926). That author namely assumed in the first place that the coefficients $\hat{K}_h$ and $\hat{K}_v$ were constant and independent from shear stress and secondly that no buoyancy of air could take place. That is to say that wind movement only contributes to horizontal transport. Remarkably enough BOWEN (1926) considered advection of air from land to a lake as a simpler case than airflow over a homogeneous surface. This because

the initial values of air temperature T_a and vapour pressure e are easier identified in the advection case. Bowen reasoned that when advection of air from land to lake takes place T_a and e changed from the values applying to the air layer overland to the values of the air layer in direct contact with the water. It appears that the system land plus water plus air could be described by Bowen in relatively simple terms, because of the very simple choice of the transfer coefficients. Therefore no direct relationship exists between Bowen's findings and the dependence of the so-called 'Bowen ratio' and air thermal stratification.

Analyses of measurements of the transfer coefficients for heat and vapour under advective and non-advective conditions have been presented by MOTHA et al. (1979a). Under advective conditions a shift towards higher frequencies occurred in the wind velocity and temperature spectra. The experiments of Motha et al. included runs for non-advective conditions, i.e. two with leaf area index LAI = 1.0 and one with LAI = 5.0, and runs for advective conditions, i.e. with LAI = 2.5. Thus, next to a variation in atmospheric conditions a second important variation occurred in the experimental set-up. Such variation in LAI was observed by Motha et al. to yield different humidity spectra: the flux carried by high-frequency eddies disappeared with full crop cover. From the same data-set, MOTHA et al. (1979b) drew the conclusion that $\hat{K}_h > \hat{K}_v$ under advective conditions.

Comments on the results of Motha et al. have been given by BROST (1979) and HICKS and EVERETT (1979). These latter authors showed that the difference ($\hat{K}_h > \hat{K}_v$) between $\hat{K}_h$ and $\hat{K}_v$ observed by MOTHA et al. (1979b) could be accounted for by a difference in displacement heights between the T_a and q_a-profiles. This is just another way of saying that the way crop structure determines the vertical distribution of sources and sinks is not necessarily the same for heat and vapour. Therefore the results shown by Motha et al. do not seem to be conclusive about the turbulent structure of the atmosphere under advective conditions as being definitely different from that under non-advective conditions.

Difficulties involved in the application of the combination formula, eq. (2.25), now can be considered. The formula can be applied only to time periods in which heat storage can be neglected. Problems relating to the ϕ-functions are essentially the same as with the Bowen ratio approach. In practical applications the outlook can be somewhat better, because only the integrals of the ϕ-functions are needed. The resistances given in eq. (2.25) for transport in air can be written in terms of ϕ-functions and specificities as in MONTEITH (1981):

$$r_x = \int_{z_1}^{z_2} \left[\hat{K}_x(z)\right]^{-1} dz = b_x^{-1} \int_{z_1}^{z_2} (u_* z)^{-1} \phi_x dz \qquad \begin{array}{c}(s \cdot m^{-1}) \\ (2.33)\end{array}$$

where x, a specificity, is one of the entities of which the transport from z_1 to z_2 is considered, and b_x a constant appearing in the expression for its flux. The units of $\int_{z_1}^{z_2}(u_* z)^{-1}\phi_x dz$ are $s \cdot m^{-1}$, the usual ones for resistances.

The combination formula eq. (2.25) may appear even more difficult to apply than the Bowen ratio approach because resistances for transport inside the soil are involved. However, it should be noted that there can be a large difference in the numerical value of the various resistances. As typical values can be considered: $r_{ah} = r_{av} = 2 \cdot 10^2$ s$\cdot$m^{-1}, $r_{sv} = 2 \cdot 10^3$ s$\cdot$m^{-1} with $z_E = 5 \cdot 10^{-2}$ m, $\rho_a c_p r_{sh} = 2 \cdot 10^2$ s$\cdot$m^{-1}. Thus the process limiting evaporation is vapour transport in the top soil layer from $z = z_E$ to $z = 0$. If, in connection with their relative magnitude, r_{ah}, r_{av}, $\rho_a c_p r_{sh}$ are neglected eq. (2.25) reduces to eq. (2.18), the equation for vapour transport from the evaporation front to the soil surface.

The value $r_{sv} = 2 \cdot 10^3$ (s$\cdot$m^{-1}) mentioned above was obtained as $r_{sv} = \int_0^{z_E} D_v^{-1} dz$ with D_v supposed to equal D_{va} the water vapour diffusion coefficient in air $D_{va} = 0.24 \cdot 10^{-4}$ m$^2 \cdot$s^{-1}. As will be shown in Chapter 3, it is by no means obvious that this supposition gives a reasonable approximation.

A further complication in the determination of the resistance to transport in soils stems from the dependence of heat and vapour transport coefficients on moisture content. This point will be properly discussed in Chapter 3, but here it will be shown how the transport coefficients shape the moisture profile in the top soil layer.

In a number of cases it was observed that moisture distribution during drying was a parabolic function of depth. A review of experimental observations relating to this aspect can be found in WIEGAND and TAYLOR (1961). The concept of a characteristic drying curve, as presented by KEEY and SUZUKI (1974), can be applied to show the interrelation between the shape of the moisture profile and the transport coefficients. Beneath the evaporation front moisture flow may be described by a diffusion-like equation:

$$LE = -L\rho_s D_\theta \frac{\partial \theta}{\partial z} \qquad (W \cdot m^{-2}) \qquad (2.34)$$

where ρ_s is soil bulk density (kg$\cdot$m^{-3}), D_θ the diffusion coefficient for liquid moisture (m$^2 \cdot$s^{-1}) and θ is moisture content on weight basis (kg$\cdot$kg^{-1}). If

moisture distribution is assumed to be parabolic, then $\theta(z)$ is of the form:

$$\theta = \theta^* + b(1 - \frac{z}{z^*})^2 \qquad (kg \cdot kg^{-1}) \qquad (2.35)$$

where z^* is some reference soil depth and θ^* the moisture content at z^*, b any constant.

The $\partial \theta / \partial z$ term in (2.34) can be obtained explicitly from (2.35). Hence the following relation at the evaporation front, $z = z_E$ can be derived:

$$\frac{2b}{z^*}(1 - \frac{z_E}{z^*}) = \frac{LE}{L\rho_s D_\theta} \qquad (m^{-1} \cdot kg^{-1}) \qquad (2.36)$$

Now the transport coefficients in the soil layer above the evaporation front and in the air can be included explicitly in eq. (2.36) by substitution of LE from eq. (2.25). Preliminarly eq. (2.26) for LE_0 can be substituted in eq. (2.25), and the result reads:

$$LE = \frac{(\bar{\gamma} r_{av} + s_a r_{ah})LE_0 + s_s \rho_a c_p r_{sh} G_E}{[\bar{\gamma}(r_{av} + r_{sv}) + s_a r_{ah} + s_s \rho_a c_p r_{sh}]} \qquad \begin{array}{c}(W \cdot m^{-2}) \\ (2.37)\end{array}$$

By substitution of LE obtained with eq. (2.37) into eq. (2.36) one obtains for the factor b:

$$b = \frac{z^*}{2L\rho_s D_\theta (1 - \frac{z_E}{z^*})} \cdot \frac{(\bar{\gamma} r_{av} + s_a r_{ah})LE_0 + s_s \rho_a c_p r_{sh} G_E}{[\bar{\gamma}(r_{av} + r_{sv}) + s_a r_{ah} + s_s \rho_a c_p r_{sh}]}$$

$$\begin{array}{c}(-) \\ (2.38)\end{array}$$

Eq. (2.38) and eq. (2.35) show how moisture content in the top soil layer reacts to the different transfer processes. I t i s u n d e r s t o o d t h a t a w a y o u t o f t h e l o o p e v a p - o r a t i o n r a t e → t r a n s f e r c o e f f i - c i e n t s → m o i s t u r e d i s t r i b u t i o n → e v a p o r a t i o n r a t e c a n n o t e a s - i l y b e f o u n d. According to the remarks on the magnitude of the different resistances given above, a deeper knowledge of actual flow mechanisms is needed to decide about possible simplifications. When transport coefficients can be estimated eq. (2.25) can be helpful for calculations of evaporation from bare desert surfaces on a daily basis, and the Bowen ratio - energy balance method for shorter periods.

It might be of interest that the intimate relationship between heat supply and deep evaporation has been noted long ago. In the quotation at the beginning of this chapter, the effect of hot rocks on the subsurface stream of the Upper Nile is mentioned.

23

2.6. SUMMARY

In Section 2.1 the practical and conceptual difficulties involved in the calculation of evaporation from deserts by means of meteorological data are discussed. In literature very few results have been reported, thus making it rather difficult to establish terms of reference for the results of the present investigations.

In Section 2.2 the immaterial nature of the potential evaporation concept was pointed out. The influence of sensible heat advection and of salts on potential evaporation was discussed in short. The conclusion was that for the specific purpose of the present investigation a much clearer separation between actual and potential evaporation is badly needed.

To establish such a separation, in Section 2.3 a new combination equation (2.25) was derived, which describes actual evaporation when it takes place inside the soil. It was shown that the limit of this equation for zero depth of the evaporation front, is the usual combination equation for potential evaporation of bare soil. In this manner the difference between actual and potential evaporation was firmly established.

At this stage a physically meaningful concept for the evaporation front still must be found and then a suitable technique is to be developed to define, for the large desert expanses, the boundaries of areas where the evaporation takes place at the surface, respectively below it. The first point will be treated in Chapter 3, while the second is dealt with in Chapter 5. The equations (2.6), (2.14), (2.15), (2.18) and (2.25) derived in Section 2.3 will be adapted in Chapter 5 to make use of areal satellite data and they will be applied in Chapter 8 for the calculation of soil actual evaporation.

In Section 2.4 some methods to calculate regional actual evaporation were briefly recalled, to conclude that they ultimately rely on the rationale that enough weather stations are present in a given area. Such a working hypothesis crumbles when large desert expanses are to be dealt with, where a single weather station is by necessity representative for 10^5 km^2 or for an even larger area. The conclusion is that to make good use of areal data, as satellite data, the equations must be modified. A solution in this direction is given in Chapter 5, while in Chapter 8 the application to data described in Chapter 6 and analyzed in Chapter 7, is presented.

In Section 2.5 it was shown that the Bowen ratio -

energy balance method described in Section 2.3 can be applied under the conditions present in deserts. As far as the transfer coefficients for heat and vapour in a turbulent atmosphere have been treated in literature, no definitive evidence has been reported that the involved hypothesis of their equality is not correct. A much more serious bottle-neck relates to the explicit interrelation, derived in Section 2.5, between the transfer coefficients for heat and vapour in the soil and the evaporation rate itself. It was therefore concluded that a thorough, in-depth study of heat and vapour transport in the soil is needed, before moving to a practical use of the methods being proposed.

This in-depth study is presented in Chapter 3, while in Chapter 4 a theory of heat exchange at the soil - air interface is developed, which is explicitly designed to take advantage of the areal satellite data. In Chapter 8 the required transfer coefficients will be obtained from field measurements and applied to calculate actual soil evaporation.

3. HEAT AND WATER FLOW IN DESERT SOILS

'... adfuso fonte a medio die ad mediam noctem aquis ferventibus totidemque horis ad medium diem rigentibus, ...'

(PLINIUS, Naturalis Historia, Liber V:36)

3.1. GENERAL

3.1.1. Peculiar aspects of heat and moisture flow in playa soils

Desert climate and playas provide rather uncommon experimental conditions. The large oscillations in surface temperature, the very low relative air humidity and the large radiant energy flux create conditions seldom studied in soils. The almost absent rainfall allows soil moisture to attain steady state conditions during very long time periods. Because of the shallow groundwater table in playas, soil moisture often changes from saturation to air dryness across a small soil depth interval. The characteristics of playa soils, as described in Section 1.2, add to the entangled character of heat and moisture flow processes. The occurrence of clayey soils with cracks and salts of different composition complicates the identification of the most relevant processes.

The rendition of the combination of playa environment and playa soils by the model expressed in the eq. (2.25), is not easily achieved. The scope of the present chapter is to identify the dominant transfer processes and to show how these processes can be reduced to the simplified model of eq. (2.25).

Two problems have to be solved:

A. to establish a suitable definition of the evaporation front;
B. to evaluate the heat and moisture transfer coefficients from evaporation front, situated at a depth z_E, to soil surface.

A d A. It is intuitively clear that the transition from prevalent liquid to prevalent vapour flow in a particular soil takes place at some specific moisture content θ_E. Such a moisture content θ_E belongs to the θ-range where the vapour diffusivity becomes larger than liquid diffusivity. In this respect it is necessary to clarify some of the terminology involved. Actual evaporation inside the soil here is intended as

the net vapour flow out of a particular soil layer. Such a net vapour flow becomes larger than liquid flow, when vapour diffusivity becomes larger than liquid diffusivity. The definitions of vapour and liquid diffusivities are somewhat loose, because they rely on particular moisture flow models (out of the many proposed) and on particular experimental techniques.

It might be useful to anticipate here that three different conceptual steps must be considered to establish the required definition of the evaporation front:

- definition of the drying front;
- definition of the evaporation site;
- definition of the evaporation front.

A d B. When the moisture content θ_E corresponding to the evaporation front is established, the soil depth z_E can in principle be detected. Then the heat and moisture transfer coefficients, thus the resistances r_{sh} and r_{sv} in eq. (2.25), can be determined. For the latter, the quantitative effect of a number of transfer processes must be evaluated. As regards playa soils and playa environmental conditions these processes include flow of water vapour, of adsorbed and liquid water, heat conduction and convection. Two issues should systematically be adressed:

- applicability of theoretical and experimental results available in literature, to the extreme environmental conditions present in playas;
- capability of the different experimental techniques to measure either the required transfer coefficients directly or other variables in order to calculate such coefficients.

It must be stressed here that the theoretical and experimental difficulties relating to the vapour and liquid diffusivities make it not practical to define the evaporation front directly on the basis of the dependence of these diffusivities on θ, as mentioned under Ad A above.

It is anticipated that soil temperature measurements, which can be local and accurate, can show whether conduction or convection is the dominant heat transfer process. Furthermore, that the same soil temperature measurements can be used to estimate r_{sv}, because of the close relationship between heat flow towards the evaporation front and vapour flow away from it.

As a concluding note in this introduction to Chapter 3, the following is to be added. The practical difficulties with the problems mentioned above stem only in part from the practical aspects of particular experimental techniques. A more relevant source of troubles is that one has to deal with the most fundamental aspects of soil and water interactions, as for example the evaporation of adsorbed water in small pores taking also into account salt and temperature effects. The wealth of published results is not easily translated into clear-cut conclusions and reference values, because of the loosely defined terminology and the interrelation of terminology, experimental technique and scope of the results. It may be of interest to mention that according to MORROW (1970) eleven different terms for the energy status of water in porous media were used in the literature. Furthermore, as shown by CHU et al. (1983) in relation to the coupling between heat flow and total water content: 'a unique definition of the heat flux vector in a coupled flow process is not possible within the context of thermodynamics of irreversible processes'. As can be understood this makes it difficult to use many published results on the combined flow of heat and moisture. The positive consequence of the theoretical work of CHU et al. (1983) is, that any physically sound model to relate heat flux with gradients in moisture content must be compatible with the general theoretical framework of thermodynamics of irreversible processes.

As regards literature on heat and moisture flow extensive and general reviews about these flows in drying soils have been presented by WIEGAND and TAYLOR (1961) and BRUTSAERT (1981). A clear-cut statement about theoretical pitfalls specifically applying to desert soils has been given by JURY et al. (1981): 'This deficiency is the result of inadequate experimental work and because the physical conditions (large temperature gradients; high temperatures and dry soils) are outside the assumptions used in most theoretical investigations'. A specific discussion on the assumptions involved in diffusion-like models of vapour flow has been given by NAKANO and MIYAZAKI (1979). The application of the water balance method to calculate actual evaporation in deserts has been presented

by EVANS et al. (1981), within the framework of a broader discussion by EVANS and THAMES (1981) on water-related aspects of ecological processes in deserts.

3.1.2. Scope of this chapter

To overcome the difficulties mentioned in the previous paragraph a number of basic equations are needed which will be given in Section 3.2. This section deals with liquid and vapour flow; more specifically the issues to be adressed are:

- the effect of temperature and salt concentration on water flow;
- the meaning and determination of liquid and vapour diffusivities;
- the water flow regime in the top soil and in the soil layer close to the groundwater table.

In Section 3.3 a definition of the evaporation front will be given, as based on the equations given in Section 3.2. The outcome of this definition is that evaporation in the soil will be considered to take place at a particular depth z_E in the soil, where soil moisture attains a specific value θ_E. This implies that even a homogeneous soil now is considered to be a two-layered system: a top layer above z_E and a lower layer below this depth.

With this model in mind, in Section 3.4 the relative contribution of conduction and convection to heat transport in playa soils is discussed. It will be shown that in hot soils convection of moist air above the evaporation front can transport heat downwards and vapour upwards. Furthermore, a simple equation to estimate the apparent soil thermal conductivity is derived. Finally transfer processes, the effect of which may be lumped into values of apparent soil thermal diffusivity, as obtained from field measurements of soil temperature, briefly are discussed.

The outcome of Section 3.4 is a simplified procedure to estimate the resistances r_{sh} and r_{sv} in eq. (2.25). To use this procedure the apparent soil thermal diffusivity has to be known. In Section 3.5 procedures to determine the apparent soil thermal diffusivity from soil temperature data, as collected in the field, are given. Methods to determine soil hydrological properties are discussed and equations are given to account for variations in these properties, as caused by differences in soil temperature and salt concentration between laboratory and field conditions.

In Section 3.6 the contributions of the flow processes discussed in the preceding sections are summarized by proposing the concept of the critical ground-

water table depth. This is the maximum groundwater table depth which allows evaporation to take place at a given steady rate through a particular soil system under specified boundary conditions at the soil surface.

3.2. LIQUID AND VAPOUR FLOW

As mentioned in Paragraph 3.1.2, the following items here will be discussed:

- the effect of temperature and salt concentration on flow of liquid water; the results of this analysis will be applied in Paragraph 8.2.1 to calculate the soil water balance from field measurements;
- the meaning and determination of liquid and vapour diffusivities; in Section 3.3 a definition of the evaporation front will be given as relying on the equations presented in this Section 3.2;
- the flow regime in the top soil and in the soil layer close to the groundwater table; the outcome of this analysis will be applied in Section 8.2 to calculate actual soil evaporation.

3.2.1. Effect of soil temperature and salt concentration on liquid flow

It was suggested by RICHARDS (1931), taking also into account the earlier work of BUCKINGHAM (1907), that Darcy's equation could be extended to unsaturated soils in the form:

$$v_w = -\kappa(h)\left(\frac{\partial h}{\partial z} - 1\right) \qquad (m \cdot s^{-1}) \tag{3.1}$$

with v_w being the water flux density and h the pressure head (negative in unsaturated soil). The pressure heads to be expressed in unit length of water column.

The pressure head h is a function of moisture content θ, κ is the capillary conductivity and in eq. (3.1) only vertical flow (with z positive downwards) is considered. It must be noted that eq. (3.1) is a definition of $\kappa(h)$, thereby implying that any experimental procedure to determine $\kappa(h)$ has to rely on the same equation. The more so when it is recalled that the macroscopic pressure head h as it appears in eq. (3.1), is not necessarily equal to the instrumental pressure head as measured by a tensiometer, as has been discussed by BEAR et al. (1968, Chapter 4).

The essentially experimental foundation of eq. (3.1) has practical consequences when this equation is to be applied to soils with structure and skeleton. As stressed by PHILIP (1975) v_w and h in eq. (3.1) are mean variables, so they remain local in character

only when the soil has very small structural elements. If the latter does not apply, e.g. for the playa soils considered in Section 8.2, the combined use of eq. (3.1) and field measurements implies schematizations which cannot be fully appreciated. Similar difficulties arise with heat flow, as to be discussed in Section 3.4. The determination of the soil hydrological properties $h(\theta)$ and $\kappa(h)$ will be discussed in Section 3.5.

To describe the behaviour of soil moisture θ, eq. (3.1) is combined with the continuity equation:

$$\frac{\partial \theta}{\partial t} = \frac{\partial}{\partial z} \kappa(h)\left(\frac{\partial h}{\partial z} - 1\right) \qquad (s^{-1}) \tag{3.2}$$

Eq. (3.2) can be rewritten as a diffusion-type equation (see for example PHILIP, 1975):

$$\frac{\partial \theta}{\partial t} = \frac{\partial}{\partial z} D(\theta) \frac{\partial \theta}{\partial z} - \frac{d\kappa}{d\theta} \frac{\partial \theta}{\partial z} \qquad (s^{-1}) \tag{3.3}$$

where $D(\theta) = \kappa(dh/d\theta)$. The discussion on the drying and evaporation front given in Section 3.3 will be based on eq. (3.3).

It should be noted that eqs. (3.1) and (3.2) are often intended to describe the flow of liquid water only, with $\theta = \theta_\ell$ the liquid water content. In this case $\kappa(h)$ and $h(\theta)$ relate to liquid water only and additional equations have to be applied to describe the flow of water vapour. This issue is adressed in Paragraph 3.2.2. Eq. (3.3), conversely, is usually applied to describe 'moisture' diffusion, that is the flow of both liquid and vapour.

To account for the effect of soil temperature T_s and salt concentration χ_i on the Darcian flow, as described by eq. (3.1), partial derivatives of that equation can explicitly be calculated. In this Report eq. (3.1) will be considered to apply to liquid flow only.

It is recalled that the actual temperature and salt concentration dependence of v_w in soils, may be different from the one implied by the bulk properties of liquid water. The purpose now is to derive equations to calculate the variation δv_w of v_w in eq. (3.1) because of the difference in bulk properties of liquid water due to T_s and χ_i, between pure water at 20 C in the laboratory and the water found under field conditions in the desert. It is therefore implicit that eqs. (3.1) and (3.2) can only be used in a range of θ where surface effects at soil particles are negligible.

The expression for $\delta v_{T_s,\chi_i}$, the variation of v_w due to temperature and salt concentration is:

$$\delta v_{T_s,\chi_i} = \frac{\partial v_w}{\partial T_s} \delta T_s + \frac{\partial v_w}{\partial \chi_i} \delta \chi_i \qquad (m \cdot s^{-1}) \tag{3.4}$$

where the derivatives can be calculated by using eq. (3.1) and the variations are:

$$\frac{\partial v_w}{\partial T_s} \delta T_s = - \frac{\partial \kappa(h)}{\partial T_s} \delta T_s (\frac{\partial h}{\partial z} - 1) - \kappa(h) \frac{\partial}{\partial T_s} (\frac{\partial h}{\partial z} - 1) \delta T_s$$

and $\qquad\qquad\qquad$ $(m \cdot s^{-1})$ (3.5)

$$\frac{\partial v_w}{\partial \chi_i} \delta \chi_i = - \frac{\partial \kappa(h)}{\partial \chi_i} \delta \chi_i (\frac{\partial h}{\partial z} - 1) - \kappa(h) \frac{\partial}{\partial \chi_i} (\frac{\partial h}{\partial z} - 1) \delta \chi_i$$

The unsaturated hydraulic conductivity can be written as:

$$\kappa(h) = b(h)\kappa_{sat} = b(h)\rho_w g \frac{K}{\eta_w} \qquad (m \cdot s^{-1}) \qquad (3.6)$$

where K (m^2) is the soil specific permeability and $b(h)$ is the relative unsaturated capillary conductivity. The viscosity η_w and the density ρ_w of liquid water depend on temperature T and electrolyte concentration χ_i, namely decreasing with increasing T and increasing with increasing χ_i.

Under the restrictive conditions as specified above, the main contribution to the vertical gradient of pressure head h is due to the matric pressure head h_m, which for relatively moist conditions can be expressed as:

$$h_m = \frac{1}{\rho_w g} (\frac{2\sigma_{wa}}{r_m}) \qquad (m) \qquad (3.7)$$

where r_m (m) is the mean radius of curvature of the solid surface enclosing the meniscus and σ_{wa} $(N \cdot m^{-1})$ is the surface tension of water against air. Note that since eq. (3.7) is written with r_m, the mean pore (or capillary) radius, it is strictly implied that surface effects at the wall - liquid interface are absent.

The effect of salts on the pressure head h is two-fold. Firstly, the osmotic pressure head h_o can be calculated from the salt concentration χ_i; h_o contributes to h as a simple additive term. Furthermore vertical gradients of h_o can arise only in particular situations, i.e. only if either a semipervious soil layer is present or χ_i changes with z in a single soil profile. A second contribution of salts, which is usually neglected, arises from the dependence of the surface tension of water on χ_i. According to TSCHAPEK et al. (1978) the surface tension of water against air σ_{wa} decreases with increasing organic matter content and concentration of NH_4OH, HNO_3 and HCl, while it increases with the content of other inorganic solutes. The derivative $(\partial \sigma_{wa}/\partial T)$ is $-0.16 \cdot 10^{-3}$ $N \cdot m^{-1} \cdot K^{-1}$ and for NaCl in water at 293 K the derivative $(\partial \sigma_{wa}/\partial \chi_i)$ is $2.2 \cdot 10^{-3}$ $N \cdot m^{-1}$ $(mol \cdot l^{-1})^{-1}$. When it is considered

that brine is present in playas, the soil solution is maintained at saturation (6.1 mol·l^{-1} for NaCl) with a surface tension of $87 \cdot 10^{-3}$ $N \cdot m^{-1}$ at 293 K, quite different from that of pure water: $72.7 \cdot 10^{-3}$ $N \cdot m^{-1}$ at 293 K.

The expressions for the partial derivatives of $\kappa(h)$ and h (h $\simeq$ h_m as defined by eq. 3.7) are:

$$\frac{\partial \kappa(h)}{\partial T_s} = \frac{\rho_w g K}{\eta_w} \frac{\partial b(h)}{\partial h} \frac{\partial h}{\partial T_s} + gKb(h) \frac{\partial}{\partial T_s} (\frac{\rho_w}{\eta_w})$$

and $\qquad\qquad\qquad\qquad\qquad$ (3.8)

$$\frac{\partial \kappa(h)}{\partial \chi_i} = \frac{\rho_w g K}{\eta_w} \frac{\partial b(h)}{\partial h} \frac{\partial h}{\partial \chi_i} + gKb(h) \frac{\partial}{\partial \chi_i} (\frac{\rho_w}{\eta_w})$$

and

$$\frac{\partial h}{\partial T_s} = \frac{\rho_w h}{\sigma_{wa}} \frac{\partial}{\partial T_s} (\frac{\sigma_{wa}}{\rho_w})$$

and $\qquad\qquad\qquad\qquad\qquad$ (3.9)

$$\frac{\partial h}{\partial \chi_i} = \frac{\rho_w h}{\sigma_{wa}} \frac{\partial}{\partial \chi_i} (\frac{\sigma_{wa}}{\rho_w})$$

so:

$$\frac{\partial}{\partial T_s} (\frac{\partial h}{\partial z} - 1) = \frac{\partial}{\partial z} \frac{\rho_w h}{\sigma_{wa}} \frac{\partial}{\partial T_s} (\frac{\sigma_{wa}}{\rho_w})$$

and $\qquad\qquad\qquad\qquad\qquad$ (3.10)

$$\frac{\partial}{\partial \chi_i} (\frac{\partial h}{\partial z} - 1) = \frac{\partial}{\partial z} \frac{\rho_w h}{\sigma_{wa}} \frac{\partial}{\partial \chi_i} (\frac{\sigma_{wa}}{\rho_w})$$

The eqs. (3.4) to (3.10) can also be applied to estimate the contribution to liquid water flow of vertical gradients in temperature and salt concentration. Namely, the variations δT_s, $\delta \chi_i$ can be written in terms of gradients:

$$\delta T_s = \frac{\partial T_s}{\partial z} \delta z \quad (K) \qquad \delta \chi_i = \frac{\partial \chi_i}{\partial z} \delta z \quad (mol) \quad (3.11)$$

Then eq. (3.4) can be applied to determine δv_w of eq. (3.1).

Further applications of eqs. (3.4) through (3.10) to calculate the variations of $\kappa(h)$ and $h(\theta)$ due to T_s and χ_i will be presented in Section 3.5.

3.2.2. Liquid and vapour diffusivities

The moisture diffusivity $D(\theta)$ in eq. (3.3) has a peculiar 'hooked' shape due to the different depen-

$D(\Theta)$ $(cm^2 \cdot s^{-1})$
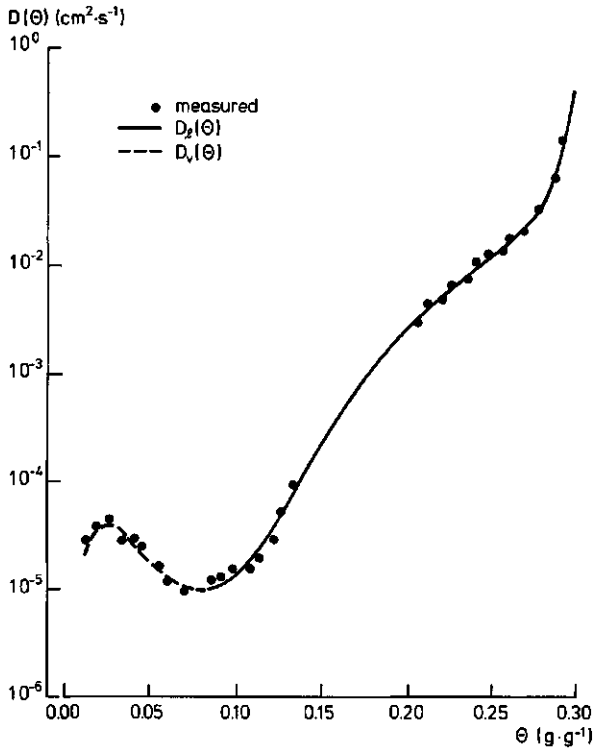
Fig. 3.1. Soil water diffusivity D versus soil moisture content θ as measured and calculated. The branches of the $D(\theta)$-curve contributed by the liquid diffusivity $D_\ell(\theta)$ respectively the vapour diffusivity $D_v(\theta)$ are indicated (adapted from Jackson et al., 1974)

dence of the liquid diffusivity $D_\ell(\theta)$ and the vapour diffusivity $D_v(\theta)$ on θ. In Fig. 3.1 the $D(\theta)$ curve is presented as measured by JACKSON et al. (1974) for Avondale clay loam. Such a hooked shape plays an essential rôle in establishing the shape of the drying front, as discussed in Section 3.3. The dependence of D_ℓ and D_v on θ will now be considered.

The total moisture flux $\tilde{q}_{mo}$ can be written as:

$$\tilde{q}_{mo} = \tilde{q}_\ell + \tilde{q}_v = -D_\ell(\theta) \frac{\partial \theta}{\partial z} - D_v(\theta) \frac{1}{\rho_a} \frac{\partial \rho_v}{\partial z} \qquad (m \cdot s^{-1}) \atop (3.12)$$

The expression for $D_\ell(\theta)$ under isothermal conditions has already been given in connection with eq. (3.3). When soil temperature gradients are present, an additional contribution to liquid flow must be taken into account. Assuming that $\kappa(h)$ relates to liquid flow only, as done in Paragraph 3.2.1, the contribution to the flux density v_w can be calculated by means of eqs. (3.4) through (3.11). The same approach has been applied by ROSE (1968) and JACKSON et al. (1974) to calculate thermal liquid flow, i.e. due to soil temperature gradients, from field measurements. The underlying assumption is that soil - water interactions, as accounted for by $\kappa(\theta)$ are temperature-inde-

pendent, so the only effect of variations in T is to change η_w, ρ_w and σ_{wa}. This is a rather far-reaching hypothesis when dealing with relatively dry soils, the more so if clay and salt contents are high. A number of authors have compared measurements of soil water properties with the expected values of $\kappa(h)$ and $h(\theta)$ as predicted from bulk water properties: e.g. FRITTON et al. (1970) for Webster silty clay loam, JURY and MILLER (1974) for Plainfield sand, LOW (1979) for montmorillonite-water systems and CONSTANZ (1982) for Oakley sand and Hanford sandy loam. All of them found large differences between measurements and theory. It is interesting to recall that LOW (1979) ascribed the observed deviations to changes of the intermolecular bonding of H_2O in the free (bulk) respectively the surface-affected state. Furthermore, CONSTANZ (1982) who measured the temperature dependence of η_w of the Oakley sand saturation extracts, stressed that the temperature dependence of the in-situ η_w may be much greater than of the saturation extract η_w.

According to the above it can be concluded that to calculate soil actual evaporation (see Paragraph 8.2.1) the water balance method only is reliable when applied to measurements of $\theta(z)$, $h(\theta)$ and $\kappa(h)$ at relatively high θ and relating to soil layers where temperature is relatively constant.

The dependence of D_v on θ and T can now be discussed. Vapour flux in soils q_v can tentatively be written as:

$$q_v = -D_v \frac{\partial \rho_v}{\partial z} = \rho_v u_{zv} \qquad (kg \cdot m^{-2} \cdot s^{-1}) \qquad (3.13)$$

The relationship between ρ_v and θ can easily be found:

$$\rho_v = \rho_{v,sat}(T) \exp(-g|h|M/\hat{R}T) \qquad (kg \cdot m^{-3}) \qquad (3.14)$$

where M is the mass of a mole of water and $\hat{R}$ is the gas (molar) constant. Since $h = h(\theta)$, the combination of eq. (3.14) with eq. (3.13) yields the required expression for $D_v(\theta)$:

$$\frac{q_v}{\rho_w} = -\frac{D_v}{\rho_w} \frac{\partial \rho_v}{\partial h} \frac{\partial h}{\partial \theta} \frac{\partial \theta}{\partial z} = -D_v(\theta) \frac{\partial \theta}{\partial z} \qquad (m \cdot s^{-1}) \qquad (3.15)$$

The relationship $D_v(\theta)$ is usually termed the 'isothermal' vapour diffusivity. Furthermore the diffusivity D_v can be related to the molecular interdiffusion coefficient of water vapour in air D_{va}:

$$D_v = f(\chi_a)D_{va} \qquad (m^2 \cdot s^{-1}) \qquad (3.16)$$

where χ_a is the air-filled pore volume and f accounts

for porosity and tortuosity. Finally, D_{va} depends on temperature and pressure as (KRISCHER and ROHNALTER, 1940):

$$D_{va}(T) = \frac{23.3}{P} \left(\frac{T}{273}\right)^{2.3} \quad (cm^2 \cdot s^{-1}) \quad (3.17)$$

with P in mbar and T in K.

A systematic theory of vapour transport in soils has been presented by PHILIP and de VRIES (1957), while a more general formulation based on thermodynamics of irreversible processes has been given by CARY and TAYLOR (1962a,b). JURY et al. (1981) have pointed out that if the Clausius-Clapeyron equation applies, the thermodynamic equations and the Philip - de Vries model can be derived one from the other.

The issues now to be discussed are:

- the temperature dependence of $D_v(\theta,T)$ in relation with the hooked shape of $D(\theta)$;
- the contribution of vapour flow under temperature gradients to heat flow.

The thermal vapour diffusivity is obtained from eq. (3.13) by differentiating ρ_v as given by eq. (3.14) with respect to temperature:

$$\frac{D_{v,T}}{\rho_w} = (U \frac{\partial \rho_{v,sat}}{\partial T} + \rho_{v,sat} \frac{\partial U}{\partial T}) \frac{D_v}{\rho_w} \quad \begin{array}{c}(m^2 \cdot s^{-1} \cdot K^{-1})\\ (3.18)\end{array}$$

where U, the soil air relative humidity, depends on h:

$$U = \exp(-g|h|M/\hat{R}T) \quad (-) \quad (3.19)$$

The derivative $\partial U/\partial T$ was taken by PHILIP and de VRIES (1957) and JACKSON et al. (1974) to be zero. To the present author's knowledge there is at least one instance of $\rho_{v,sat}(\partial U/\partial T) \neq 0$ and comparable with $U(\partial \rho_{v,sat}/\partial T)$. Namely, SHARMA et al. (1969) measured the adsorption isotherms of Wahiawa clay and Molokai clay at different temperatures. From their data therefore it is possible to calculate the second term at the right hand side of eq. (3.18), i.e. $\rho_{v,sat}(\partial U/\partial T)$ = $3.5 \cdot 10^{-4}$ $kg \cdot m^{-3} \cdot K^{-1}$ for the Wahiawa soil and $6.7 \cdot 10^{-4}$ $kg \cdot m^{-3} \cdot K^{-1}$ for the Molokai clay. As the term $U(\partial \rho_{v,sat}/\partial T) \cong 7.3 \cdot 10^{-4}$ $kg \cdot m^{-3} \cdot K^{-1}$, this second term in eq. (3.18) is quite comparable with the first term.

The reason for this discrepancy with the usual assumption of $\partial U/\partial T = 0$, is to be sought in the contribution of surface effects to the free energy of soil water. The concentration of vapour depends on the total potential energy of the vapour molecules:

$$p = Pr\{N|U_N\} \propto \exp(-U_N/kT) \quad (-) \quad (3.20)$$

where p is the probability of finding N molecules with energy U_N; this probability given by the exponential Maxwell-Boltzmann distribution. Let $\tilde{E}$ be the (negative) free energy of a liquid wedge in the soil and $\tilde{h}$ the free energy per unit weight. Then the vapour pressure in the surroundings of the liquid wedge is:

$$e = e_0 \exp(-|\tilde{E}|/\hat{R}T) = e_0 \exp(-g|\tilde{h}|M/\hat{R}T) \quad (mbar)(3.21)$$

If the reference state for $\tilde{E}$, as usual, is chosen to be that of open salt-free water, then the reference vapour pressure e_0 is e_{sat}. The dependence of e_{sat} on T can approximately be described by means of the Clausius-Clapeyron equation (see also FERMI, 1968), so $e_{sat}(T) = e_{sat}^0 \exp$ -LM/$\hat{R}T$, and the equation for the relative humidity of soil air reads:

$$U = \exp -(L + g|\tilde{h}|)M/\hat{R}T \quad (-) \quad (3.22)$$

The difference between eq. (3.19) and eq. (3.22) is that in the former the temperature dependence of h, so of U as needed in eq. (3.18), is considered to be that specified by eq. (3.9). This approach has been applied by PHILIP and de VRIES (1957) and JACKSON et al. (1974), which implies, however, that the temperature dependence of $\tilde{E}$ is only due to the temperature dependence of the bulk water properties (see Paragraphs 3.2.1 and 3.5.3). In principle it is well possible to obtain $\partial U/\partial T$ from measured data, as done above with the data of SHARMA et al. (1969). Then adsorption isotherms must be measured at different temperatures for the particular soil of interest.

Two conclusions can be drawn from the above:

- The hooked shape of $D(\theta)$ is enhanced at higher temperatures, because $D_v(\theta)$ increases with increasing T more than $D_\ell(\theta)$ does. Accordingly a more sharply defined front is to be expected, as will be shown in Section 3.3.
- The calculation of $D_{v,T}(\theta)$ for playa soils is reliable only when adsorption isotherms are measured at different temperatures. This is a serious drawback for regional hydrological studies as presented in this Report. The more so, when it is recalled that the simulation of heat and moisture flow in the top soil layer constitutes a bottle-neck of models as applied in the interpretation of remotely sensed thermal infrared data (see also Sections 5.4 and 5.5).

3.2.3. Unsaturated water flow close to the groundwater table and in the top soil

From the remarks presented in the preceding paragraphs two feasible approaches to determine soil evap-

oration in playas can be recognized:

A. applying eq. (3.1) or (3.2) at high θ-values (wet range);
B. taking advantage of the close relation between water vapour and heat flow at low θ-values (dry range).

A d A. It appears that to calculate moisture fluxes one can better consider a deeper soil layer close to the shallow groundwater table in playas, where moisture contents are relatively high. Flow can safely be assumed to be in the liquid phase and eq. (3.1) applies. Thus the flux can be calculated from measured pressure heads through the $\kappa(h)$-curve, or from measured moisture contents through the $\kappa(h)$- and $h(\theta)$-curves. When a shallow water table is present, a very convenient procedure is by measuring moisture contents close close to the water table and considering steady state solutions of eq. (3.1) for different constant fluxes $v_{w,i}$ (negative when upwards). Assuming that the $h(\theta)$-curve of a particular soil is known, the following equation can be applied:

$$z(h) - z_{gw} = - \int_0^h \frac{\kappa(\tau)}{v_{w,i} - \kappa(\tau)} d\tau \qquad (m) \qquad (3.23)$$

Note that the difference $\left[z(h) - z_{gw}\right]$ is negative and eq. (3.23) yields depths $z(h)$ above the water table depth z_{gw}, where $h_m(z_{gw}) = 0$.

Eq. (3.23) has widely been applied to estimate moisture extraction from shallow water tables: see PHILIP (1957), FEDDES (1971), HADAS and HILLEL (1972), HILLEL and HADAS (1972). It was also applied by de RIDDER and EREZ (1977) for a tentative estimation of evaporation losses from playas in the Varamin plain (Iran). The $\kappa(h)$ and $h(\theta)$ must be corrected to account for variations in temperature and salt concentration (see Paragraph 3.2.1) according to the procedure presented in the Paragraph 3.5.3.

Eq. (3.23) will be applied in Paragraph 8.2.1 to calculate the mean actual soil evaporation in the Idri playas (Fezzan, Libya).

A d B. As shown in Paragraph 3.2.2, at very low θ-values moisture flow takes place in the vapour phase only. A very strict relationship exists between heat flow and both vapour diffusion and soil air convection. So measured values of apparent soil thermal conductivity (see Sections 3.4 and 3.5) can be related to the vapour diffusivity D_v. Finally the resistance r_{sv} in eq. (2.25) can be estimated as z_E/D_v.

When vapour flow takes place by diffusion, the following equations apply. The apparent thermal con-

ductivity λ' of a gas-filled pore can be written (de VRIES, 1963):

$$\lambda' = \lambda_a + U\lambda_{v,sat} \qquad (W \cdot m^{-1} \cdot K^{-1}) \qquad (3.24)$$

with $\lambda_{v,sat}$ being (KRISCHER and ROHNALTER, 1940):

$$\lambda_{v,sat} = \frac{LD_{va}P}{RT(P - e_{sat})} \frac{de_{sat}}{dT} \qquad (W \cdot m^{-1} \cdot K^{-1}) \qquad (3.25)$$

where the vapour diffusion coefficient D_{va} depends on temperature and pressure according to eq. (3.17).

The apparent soil thermal conductivity can finally be calculated from soil composition and soil moisture content by means of formulae given in Paragraph 3.5.1. When convection applies the relationship between vapour flow D_v and the mean convection velocity u_{zv} has been given in eq. (3.13), while a relationship between the apparent soil thermal conductivity and the convection velocity of soil air will be given in Section 3.4.

3.3. THE EVAPORATION FRONT

The analysis presented in the previous section on liquid and vapour flow, with special regard to $D_v(\theta)$, $D_\ell(\theta)$ and the resulting shape of $D(\theta)$, makes it possible to establish a suitable definition of the evaporation front. Such a definition will have to allow for the depth z_E to be determined, as required for the application of the approach presented in Chapter 2.

In the following pages the concepts of drying and evaporation front will be recalled and their relationship discussed. Afterwards the available experimental evidence on the existence of the evaporation front will be summarized. Finally a new definition of the evaporation front will be proposed, as relying on the known interrelation between fluid flow regime in porous media and pore size.

3.3.1. The concepts of drying front and evaporation front

The concept of the drying front can be illustrated by recalling the analytical solution of eq. (3.3) given by PHILIP (1969, 1975). Under the conditions:

$$t = 0 \qquad z > 0 \qquad \theta = \theta_i$$
$$t > 0 \qquad z = 0 \qquad \theta = \theta_0 \qquad (3.26)$$

where θ_i is the initial moisture content and θ_0 is the assigned value at the soil surface, the solution at large t is:
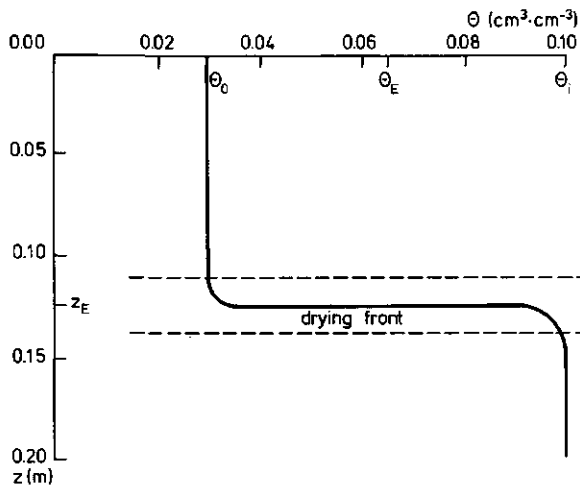
Fig. 3.2. Profile of soil moisture content $\tilde{z}(\theta)$, see eq. (3.27); the position of the drying front is indicated. θ_E is a particular choice for the soil moisture content at the evaporation front, located at a depth z_E

$$z(\theta,t) = (t - t_0)v + \tilde{z}(\theta) \qquad (m) \qquad (3.27)$$

where the velocity v of the profile $\tilde{z}(\theta)$ is given by:

$$v = \frac{\kappa(\theta_0) - \kappa(\theta_i)}{\theta_0 - \theta_i} \qquad (m \cdot s^{-1}) \qquad (3.28)$$

The solution $z(\theta,t)$ applies to infiltration, but in principle can also be considered to describe bare soil evaporation. The issue is that the conditions (3.26) are not that realistic for the evaporation case (e.g. θ_0 may not be constant). The point to be made relates only to the shape of the profile $\tilde{z}(\theta)$ and to its constant downward velocity. The shape of $\tilde{z}(\theta)$ is given in Fig. 3.2. It here is recalled that van KEULEN and HILLEL (1974) simulated soil drying by numerically solving eq. (3.3) under the conditions (3.26) with $\theta_i > \theta_0$. They indeed found that the solution was of the kind given by eq. (3.27) and hence it also applied to soil drying.

It can, therefore, be concluded that the conceptual basis for the drying front model stems from the shape of $\tilde{z}(\theta)$, namely from the steep transition from low to higher θ-values over a small soil depth. The drying front can be defined as that thin soil layer where θ decreases from θ_i to θ_0. As depicted in Fig. 3.2 the position of the drying front can also be specified by the depth z_E at which the soil moisture content attains the value θ_E. For the moment it is suffi-
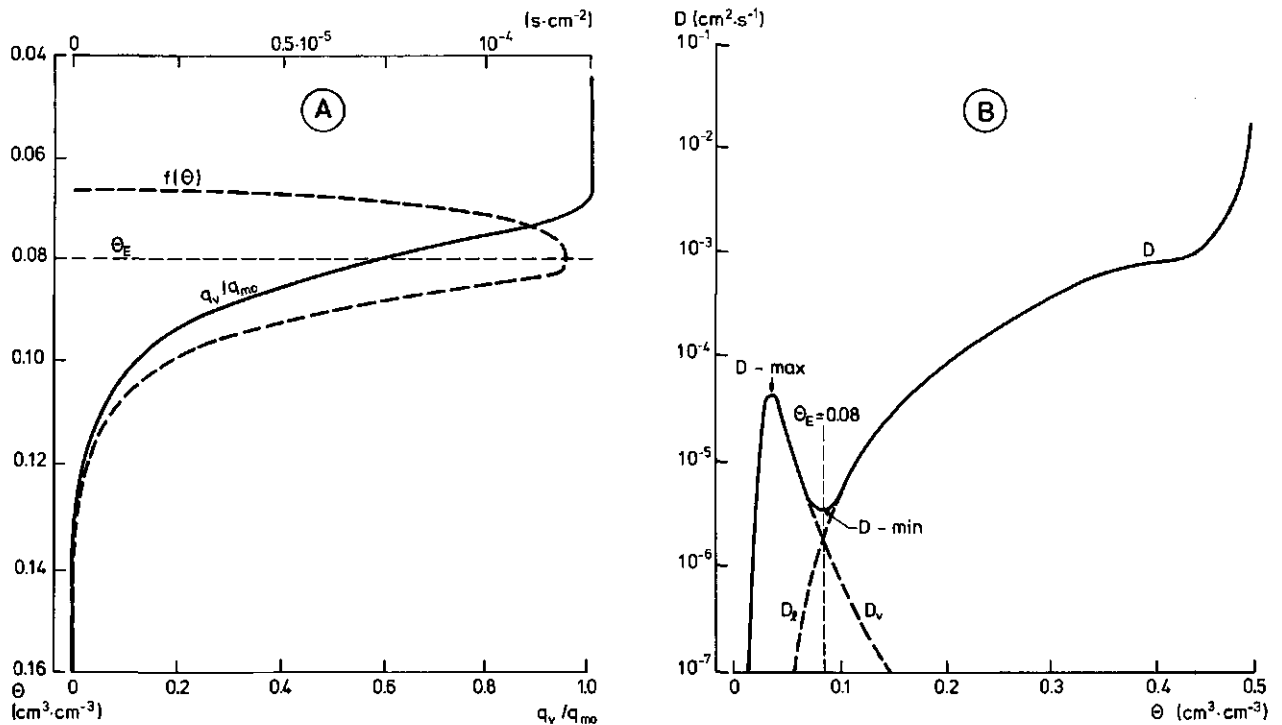
Fig. 3.3. A. Phase transformation within soil: ratio of vapour flux to moisture flux q_v/q_{mo} versus moisture content θ; relative intensity of evaporation $f(\theta) = -D(\theta)^{-1}\partial(q_v/q_{mo})/\partial\theta$; θ_E is the moisture content at the evaporation front. B, Moisture diffusivity D, liquid diffusivity D_ℓ and vapour diffusivity D_v at 20^oC versus moisture content θ; θ_E is the moisture content at the evaporation front; the relative minimum D-min respectively maximum D-max of the moisture diffusivity $D(\theta)$ at low moisture contents also are indicated (after Philip, 1957)

cient to consider θ_E as being $(\theta_i + \theta_0)/2$.

As it was anticipated in Paragraph 3.2.2, there is a close relationship between the steepness of the transition from θ_i to θ_0 (see Fig. 3.2) and the shape of $D(\theta)$. The simulation exercise by van KEULEN and HILLEL (1974) did show that the hook of $D(\theta)$ at low θ, due to the contribution of $D_v(\theta)$ to $D(\theta)$, made the difference between a smooth, parabolic shape of $\tilde{z}(\theta)$ and a sharper graph. This result intuitively is clear. Since $D(\theta)$ decreases with θ decreasing down to θ', say, and increases afterwards (see Fig. 3.1), as soon as the soil surface dries just beyond this θ'-value the drying rate will be larger in the drier top soil than in the lower moisture soil layer. The outcome is a moisture content profile of the shape depicted in Fig. 3.2.

The relation between the drying front concept, i.e. a thin soil slab as indicated in Fig. 3.2, and the evaporation front concept can now be discussed. A seemingly reasonable starting point is the definition of relative intensity of evaporation given by PHILIP (1957). According to this author the relative intensity of evaporation within the soil is $-D(\theta)^{-1}\partial(q_v/q_{mo})/\partial\theta$. This function is plotted in Fig. 3.3A, and compared with the $D(\theta)$ curve (Fig. 3.3B) as applied by Philip. It clearly appears that the maximum intensity of evaporation is attained at $\theta = 0.08$, which value corresponds to the relative minimum of $D(\theta)$, i.e. just before the hook originating from $D_v(\theta)$. Thus the connection between the intensity of evaporation within the soil and the shape of the $D(\theta)$-curve is well established. It might, therefore, appear that the evaporation front can be defined as that surface $z_E(x,y)$ where $\theta = \theta_E$, the latter being the moisture content corresponding to the relative minimum of $D(\theta)$. There is, however, a very serious shortcoming in such a definition. The $D_v(\theta)$ and $D_\ell(\theta)$ curves cannot be measured exactly as aptly shown by the scarcity of published data. To the present author's knowledge the only measured $D_v(\theta)$ have been given by JACKSON (1964a,b) for Adelanto loam, Pachappa loam and Pine silty clay, and by JACKSON et al. (1974) for Avondale clay loam. Moreover, an implicit definition of the evaporation front relying on the concept of relative intensity of evaporation, with severe experimental requirements, would not be of much help in the estimation of regional evaporation from playas.

In Paragraph 3.3.3 a new definition of evaporation front will be proposed to allow a more direct estimation of θ_E.

3.3.2. Experimental evidence for the evaporation front

Many authors have studied the location of the drying and evaporation sites by means of experiments. Quite different experimental techniques have been applied and widely different drying periods were allowed. So it can be understood that large differences in the depth of the evaporation sites were observed. The results to be mentioned in this paragraph, however, show that the formation of an evaporation front has indeed been observed.

According to the concepts presented in the previous paragraph, the existence of a drying front can experimentally be confirmed by measuring $\theta(z)$-profiles during steady drying. The expected $\tilde{z}(\theta)$ shape was observed by FRITTON et al. (1970) in soil columns of Webster silty clay loam. It should be noted that the direct observation of the $\tilde{z}(\theta)$ profile requires local measurements of θ, which are rather difficult to obtain with non-destructive techniques.

The evaporation front can be somewhat easier to detect than the drying front. A number of parameters relate to the intensity of evaporation and may be used as tracers of the evaporation front: the relative humidity of soil air, the salt concentration and the vertical divergence of soil heat flux. A cruder method to trace the evolution of the evaporation front is the choice of an arbitrary θ_E-value.

If it is assumed that $\theta_E = 0.01$ in sandy soils, then the data as given by GUPTA (1979) show a drawdown of the evaporation front of 22 cm during a 4 month dry season. DINCER et al. (1974) observed that the soil moisture profile in desert sand dunes hardly did change during one year and they concluded that the evaporation front was located at a depth of 55 cm. ONCHUKOV (1957) took the wet bulb depression of soil air temperature as a criterion for the relative importance of vapour and liquid flow and concluded that most evaporation occurred inside the top 5 cm layer. The best way to locate the evaporation front is probably by looking at salt accumulation. RICHARDS et al. (1956) observed in a field plot (bare, fine sandy loam) that the evaporation front was located between 15 and 30 cm depth. HELLWIG (1974, 1979) concluded that evaporation in sand could take place at a depth of 50 cm. On the other hand from laboratory experiments HASSAN and GHAIBEH (1977) concluded that the evaporation front reached 3 cm depth after a drying period of a few days. NAKAYAMA et al. (1973) observed under field conditions that the salt concentration in the 1 to 2 cm layer began to increase after 25 days.

Divergence of soil heat flux was related by GARDNER and HANKS (1966) to the depth of the evapora-

tion front in a sample of Loveland fine sandy loam. They found that the evaporation front was at a depth of 3 cm after an 18-day drying period. By means of a similar procedure, FRITTON et al. (1970) concluded that the evaporation front reached 5 cm depth after a 28-day drying period. It must be mentioned here that soil heat flux G is difficult to measure accurately (see Section 4.1), thus div G is rather unreliable as a measurement of LE. It can, however, safely be considered as a reliable indication of the occurrence of either evaporation or condensation.

The downward displacement of the drying front and the hooked shape of $D(\theta)$ also have a bearing on the actual evaporation rate during soil drying. Three stages have been observed in the evolution of bare soil evaporation, e.g. by IDSO et al. (1974). The characteristic feature of the third stage is the low, quasi-constant evaporation rate. This would seem to be in contrast with the concept expressed by eq. (2.19), at least if r_{sv} and $e(0)$ were constant. It appears that the latter is not the case. The diffusivity $D_v(\theta)$ increases with decreasing θ, as shown in Figs. 3.1 and 3.3B, the resistance z_E/D_v therefore may remain constant even with increasing z_E, at least in the θ-range where D_v increases. Furthermore, it is also not straightforward that $e(0)$ remains constant in real-world soil drying. The $\theta(z)$ profile in the top soil will always have a relatively smooth shape (see eq. 2.38), so the surface moisture content $\theta(0)$ and vapour pressure $e(0)$ would gradually decrease with increasing z_E. It therefore can be concluded that the actual evaporation rate during the third stage must not by necessity decrease as sharply as eq. (2.19) with constant D_v and $\left[e_{sat}(T_E) - e(0)\right]$ would predict.

With the preceding concepts in mind the literature data recalled earlier in this paragraph, have
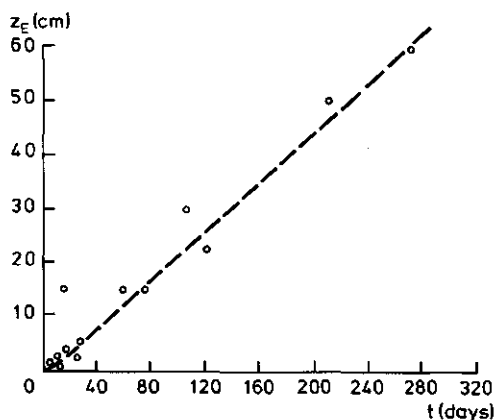
been plotted in Fig. 3.4. These data should be fitted by a downward bent curve, i.e. a function $z_E(t)$ apt to describe the expected slowdown in the drawdown of the evaporation front. A straight line has been drawn by eye through these points, however, to obtain a rough estimation of the terminal evaporation rate (third drying stage). The slope of the straight line in Fig. 3.4 gives the constant downward velocity of the drying front. Accordingly it is found that $\dot{z}_E = 2.2 \cdot 10^{-3}$ m·d^{-1} multiplied by $\theta_E = 0.05$ say, gives a terminal evaporation rate of 0.1 mm·d^{-1}. This figure is in reasonable agreement with the value observed by JACKSON (1973), i.e. 0.5 mm·d^{-1}, and by IDSO et al. (1974), i.e. 0.7 mm·d^{-1}. The more so when it is recalled that the data presented by these authors relate to shorter drying periods than most of the data points in Fig. 3.4.

3.3.3. A new definition of the evaporation front

In Paragraph 3.3.1 it has been shown how the onset of a drying front relates to the shape of $D(\theta)$ and which difference there is between drying front and evaporation front. When presenting those comments on the shape of $D_v(\theta)$, two points intentionally were left out:

- the size of pores contributing to $D_v(\theta)$ and, particularly, those ones relating to the minimum respectively maximum value of $D(\theta)$ at low θ-values (see also Fig. 3.3B);
- the relationship between vapour diffusivity, at a particular r_m, and pore size distribution, which yields the shape of the measured $D_v(\theta)$.

In Table 3.1 the equivalent pore radii calculated by means of eq. (3.7) from $D(\theta)$- and $h(\theta)$-curves as given by different authors, are reported. It appears that the transition from D-min to D-max takes place when the radius of the largest water-filled pores decreases from

Fig. 3.4. Depth z_E (cm) of the evaporation front versus duration (days) of the drying period as obtained from literature references (see text) for different soil types

Table 3.1. Soil moisture content θ and equivalent pore radius r_m, according to eq. (3.7), corresponding to the minimum, D-min, respectively maximum, D-max, values of moisture diffusivity $D(\theta)$ (see also Fig. 3.3B), as measured by different authors

θ(D-min) (cm^3·cm^{-3})	r_m (m)	θ(D-max) (cm^3·cm^{-3})	r_m (m)	Reference
0.135	$7.5 \cdot 10^{-8}$	0.075	$0.1 \cdot 10^{-8}$	Adelanto loam, Jackson (1973)
0.175	$7.5 \cdot 10^{-8}$	0.075	$<0.1 \cdot 10^{-8}$	Webster silty clay loam, Fritton et al. (1970)
0.08	$5 \cdot 10^{-8}$	0.03	$0.2 \cdot 10^{-8}$	Yolo light clay, Philip (1957)
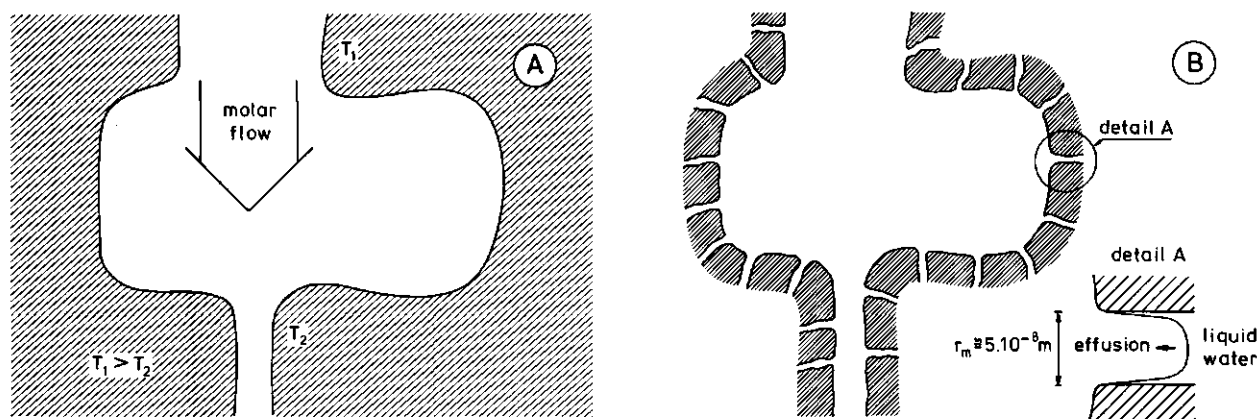
Fig. 3.5. A, molar gas flow in a macropore under a temperature gradient: T_1 is higher than T_2; B, sketch of effusion (Knudsen diffusion) of water vapour at atmospheric pressure and a temperature of 300 K; water molecules 'jump out' of pores with a radius $r_m \cong 5 \cdot 10^{-8}$ m, i.e. comparable with ℓ_m the mean free path of water vapour under the specified conditions

10^{-7} m to 10^{-9} m say. As can be seen the (relative) minimum of $D(\theta)$ relates to pore radii between $5 \cdot 10^{-8}$ m and $7.5 \cdot 10^{-8}$ m. Now the mean free path ℓ_m of water vapour at atmospheric pressure and 300 K is $4.7 \cdot 10^{-8}$ m. It appears too remarkable a coincidence for it being accidental. Let us therefore draw an interim conclusion about the existence of experimental evidence for the relationship between gas kinetics and the shape of the $D(\theta)$-curve. This would imply that there is also a relationship between gas kinetics and the onset of the drying (and evaporation) front.

Before proceeding further, a few remarks are due about the model of vapour flow in soils, which was taken for granted in the preceding paragraphs. The problem lies not so much in the diffusivity type eq. (3.3), which essentially is an assumption, as in the validity of Fick's diffusion equation, i.e. eq. (3.13). According to the EGELSTAFF (1967) rendition of the Einstein's random-walk theory, it can be shown that the Fick's diffusion equation can only be obtained when it is assumed that a large number of (gas) molecular collisions have taken place. In micropores with $r_m \cong \ell_m$ this is clearly impossible because of the high frequency of gas - wall collisions. One is, therefore, left without any firm ground for the models of vapour flow in soils under temperature gradients (see Paragraph 3.2.2). In this respect it should also be recalled that the gas flow regime changes in porous media with decreasing pore size (see for example CARMAN, 1956; LUIKOV, 1966). In pores comparable in size with ℓ_m, or smaller, gas flow is of the Knudsen type (see CARMAN, 1956; LUIKOV, 1966; DULLIEN, 1979). Under these conditions, gas - wall collisions are dominant over gas - gas collisions. This points to another difficulty. Inside a micropore in soils the gas - wall collision cannot be modeled as such for the obvious reason

that there is a film of adsorbed water on the surface of the soil particle. Especially in playas where clayey and salty soils are present, these fundamental aspects have practical consequences for the magnitude of vapour flux.

In Figs. 3.5 and 3.6 an attempt has been made to depict the processes mentioned above. In Fig. 3.5A one pore, large enough for the vapour in it not to be affected by surface effects at the walls, is depicted. Fick's diffusion equation applies to gas molar flow and, accordingly, the models of thermal vapour flow also apply. In Fig. 3.5B a closer view of the same pore is presented. The micropores present around the boundary of the macropore in Fig. 3.5A, have a radius $r_m \cong \ell_m$ and gas flow is of the Knudsen type. The outflow of water vapour molecules is much larger than it would be according to Fick's diffusion equation, since the relevant velocity at the micropore exit, is the mean molecular velocity.

In such small pores there are more microphysical processes which affect water and vapour flow. Some of these processes now will briefly be mentioned.

The extent of the diffuse double layer at low liquid contents has been discussed by BOLT (1976). The thickness of that layer varies between $2 \cdot 10^{-9}$ and $2 \cdot 10^{-8}$ m. In soils with a large specific surface the amount of water in the adsorbed phase can be considerable. The specific surface of playa soils (see Section 1.2) often will be large. As shown by KERR and LANGER (1965): when clay content in playa soils is less than 35%, the content in salt crystals increases. The structure and size of salt minerals has been studied by scanning electron microscopy by VERGOUWEN (1981), who also emphasized the effect on evaporation of metastable salt minerals.

A qualitative picture relating to these processes
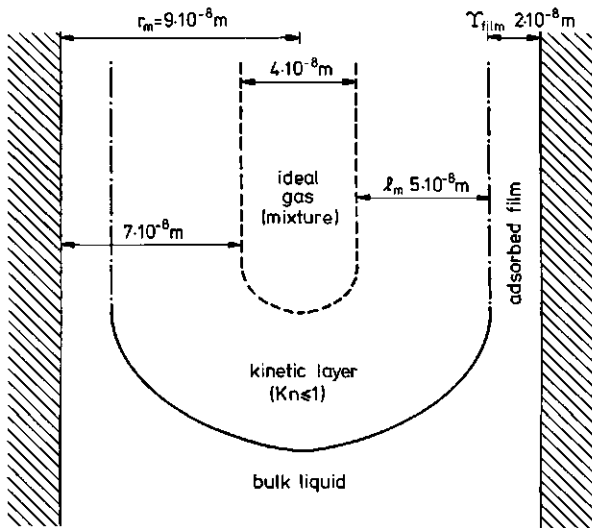
Fig. 3.6. Qualitative sketch of co-existing phases inside a micropore of radius $r_m \cong 9 \cdot 10^{-8}$ m, say; $\ell_m \cong 5 \cdot 10^{-8}$ m is the mean free path of water vapour at 300 K and atmospheric pressure; $T_{film} \cong 2 \cdot 10^{-8}$ m is the thickness of the adsorbed water film; Kn is the Knudsen number equal to the characteristic length divided by ℓ_m

is given in Fig. 3.6, whose only scope is to give an idea of the length-scales of the different components simultaneously existing in such a micropore. Fig. 3.6 shows a further magnification of the micropore of Fig. 3.5B. First of all there is no physical boundary between the adsorbed film, the kinetic layer and the vapour; as a matter of fact the absence of such a barrier is the problem one has to cope with. The thickness of the adsorbed film has been chosen to be representative of the thickness of the diffuse double layer at low moisture contents.

The flow rate of the not-surface-bound molecules can be calculated at the pore exit by means of equations given by CARMAN (1956), as applying to the flow transition range and to Knudsen flow in short capillaries. Accordingly the 'apparent linear flow rate' would be in the range 1 to $5 \cdot 10^{-2}$ m·s^{-1}.

The data in Table 3.1 indicate that the pores relevant for the onset of the drying front are of the type depicted in Fig. 3.6. It can, therefore, be concluded that a suitable model of evaporation within a soil must deal explicitly with the adsorbed film and the kinetic layer. Such a model is especially needed to gain a better insight of temperature effects on both the liquid - vapour transition and vapour flow. It is here recalled that the known models for the coupled heat and vapour flow in soils do not include a parametrization of the phase transition. On the other hand a suitable model of the liquid - vapour phase transition and vapour kinetics inside a single pore has been giv-

en by LUIKOV et al. (1974). These authors could not model the interaction between pores. To describe vapour flow through a porous body they had to resort to the 'dusty gas' model of MASON et al. (1967). LUIKOV et al. (1974), however, derived an important conclusion about the evolution of the moisture distribution at pore scale towards equilibrium. That conclusion will be applied later in this paragraph.

By now it has become clear that in relation with the intensity of the liquid - vapour transition, the relevant pore size class is from 10^{-7} m to 10^{-9} m. The question to be answered next can be put as follows. At a given $\hat{\theta}$, do all the air filled pores of radius $r_m > r_m(\hat{\theta})$ contribute to $D_v(\hat{\theta})$, or only those ones of $r_m = r_m(\hat{\theta})$? In other words it is to be shown whether $D_v(\theta)$ is of the form:

$$D_v(\hat{\theta}) = \int_{r_m(\hat{\theta})}^{r_m(\theta_{sat})} D_{eff}(r_m') \frac{d}{dr_m'} \chi_a(r_m') dr_m' \qquad (m^2 \cdot s^{-1}) \qquad (3.29)$$

or

$$D_v(\hat{\theta}) = D_{eff}[r_m(\hat{\theta})] \frac{d}{dr_m} \chi_a(r_m) \delta r_m \qquad (m^2 \cdot s^{-1}) \qquad (3.30)$$

where D_{eff} is the effective vapour diffusivity in pores of radius r_m, and $\chi_a(r_m)$ is the total air-filled porosity of pores with radius $\leq r_m$.

When the shape of $D_v(\theta)$, as measured e.g. by JACKSON (1964a,b) for some soils, is recalled it can easily be shown that $D_v(\hat{\theta})$ must be of the form as in eq. (3.30). Were $D_v(\hat{\theta})$ of the form eq. (3.29), it would not decrease with decreasing θ or increasing air-filled porosity. Let us assume that pores of $r_m \leq \tilde{r}_m$ do not contribute to $D_v(\theta)$. Then $D_v(\theta)$ will remain constant according to eq. (3.29) for $\theta \leq \theta(\tilde{r}_m)$. The experimentally observed existence of a peak in $D_v(\theta)$ can, therefore, be consistent only with eq. (3.30).

There are, moreover, two other reasons for $D_v(\theta)$ to be of the form eq. (3.30): the first one stems from theory, the second one from experimental evidence.

It is intuitively clear that vapour transfer across a porous slab will be faster when condensation and evaporation take place at the same time at opposite sides of pores belonging to the water vapour paths in the porous slab. Such an enhancement mechanism was postulated by PHILIP and de VRIES (1957) for vapour flow across the 'liquid islands', also termed pendular rings by VERSLUYS (1916). LUIKOV et al. (1974), by means of their single pore model, could theoretically establish in which pores of a particular porous sample both evaporation and condensation take place. They did show that when the pore radius is larger than its

D_{eff}/D_{va} (—)
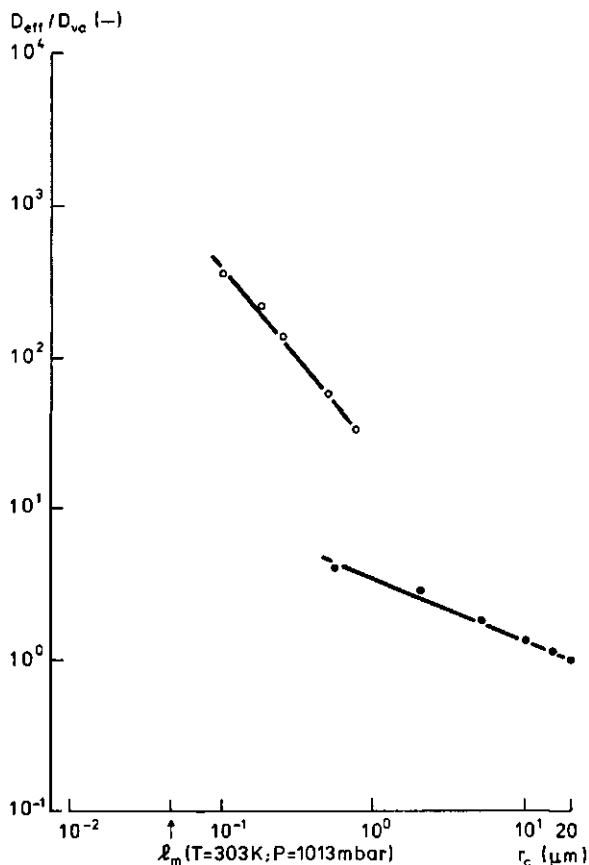
Fig. 3.7. Values of the ratio of the effective water vapour diffusivity D_{eff} to the diffusivity in air D_{va}, versus capillary radius r_c (after Churaev, 1975). The mean free path of water vapour ℓ_m at specified temperature and total pressure also is indicated. The open circles relate to inflow into dry capillaries, while dots relate to evaporation out of wet capillaries

D_v (10^{-7} m^2·s^{-1})

•——• calculated
x— —x measured

Fig. 3.8. Soil vapour diffusivity D_v as calculated by means of eq. (3.30) respectively measured for Pachappa loam by Jackson (1965), versus pore radius r_m; pore size distribution as given by Schoonderbeek et al. (1983)

length, evaporation takes place at both exits of the pore. Conversely when the radius is smaller than the length, evaporation takes place at one pore exit, and condensation at the other one. Therefore, under steady state conditions at a given θ pores belonging to the latter type effectively will shorten the path for water vapour through the porous medium.

Let us now consider a porous material to be a bundle of capillaries of varying radius. The contribution of each capillary size class is specified by $d[\chi_a(r_m)]/dr_m$. The effective vapour diffusivity $D_{eff}(r_c)$ as a function of capillary radius was measured by CHURAEV (1975) and his data are given in Fig. 3.7. The pore size distribution, in the range of radii we are now dealing with, can only be measured by the most advanced techniques. Even then the cut-off of $\chi_a(r_m)$ due to the resolving power of the particular experimental technique is relevant as aptly shown by JONGERIUS and BISDOM (1981). In their Fig. 5 the shift

of the peak in the pore size distribution towards smaller radii is quite remarkable, and only due to the increased resolution.

To give an example of the $D_v(θ)$ obtained by means of eq. (3.30), the data of CHURAEV (1975) in Fig. 3.7 for the desorption branch have been combined by the present author with the air-filled porosity $\chi_a(r_m)$ given by SCHOONDERBEEK et al. (1983), as measured on backscattered electron scanning images by means of a digital image analyzer. In Fig. 3.8 calculated as well as measured $D_v(r_m)$ are presented. The latter as obtained from the $D_v(θ)$ and $h(θ)$ curves applying to Pachappa loam, as given for desorption by JACKSON (1965). It can be seen that eq. (3.30) yields the correct hooked shape and the proper order of magnitude of $D_v(r_m)$. The setback is that the peak of the calculated $D_v(θ)$ is located at too large a radius. The latter is a likely consequence of the cut-off of $\chi_a(r_m)$ due to the presently available experimental techniques.

It is clear that the three curves, i.e. $D_{eff}(r_c)$, measured $\chi_a(r_m)$ and measured $D_v(θ)$, do not belong together. The preceding example, therefore, is meant to be qualitative only. It can, however, be concluded that the agreement in shape and order of magnitude between prediction and measurements does indeed show that eq. (3.30) qualitatively is correct. So the second question proposed at the beginning of the paragraph has also been answered.

S u m m a r y. The main steps considered in the present Section 3.3 now can briefly be summarized.

The onset and the sharpness of the drying front depend on the shape of $D_v(θ)$. That shape determines how reasonable it is to substitute the evaporation front for the drying front (see Fig. 3.2). The substitution will be correct when the transition from D-min to D-max is steep.

37

The shape of $D(\theta)$ relates to the transition in flow regime with decreasing size of air-filled pores: from molar gas flow in the macropores to Knudsen diffusion to film flow in the very small pores. This transition occurs in the size range where pore size is comparable with the mean free path of water vapour ℓ_m.

In this Report, therefore, the θ_E-value, the soil moisture content at the evaporation front, is assumed to be the one contributed by pores with $r_m \cong \ell_m$. By means of eq. (3.7) the value of $h_{m,E}$ is obtained and next θ_E from measured $h(\theta)$-curves. This definition of θ_E yields U-values of the proper magnitude: $U_E = 0.97$. Namely, from the data of PHILIP (1957) and Fig. 3.3A, one finds that the evaporation front corresponds to the U-range between 0.945 and 0.965, which is comparable with the above mentioned one.

It finally is stressed that the evaporation front as defined above is an intrinsic property, i.e. specific, of each soil type. The evaporation front will be more or less easily observed under actual field conditions. At least two processes tend to make direct detection difficult:

A. the shape of the $h(\theta)$-curve;
B. weather variability.

A d A. The transition from higher to lower moisture contents, i.e. from below the evaporation front to above it, will be the sharper the steeper the $h(\theta)$-curve of the particular soil type. So a less sharp evaporation front is to be expected in clayey soils.

A d B. Rainfall and nocturnal condensation obviously will blur the distinction of the evaporation front. More difficult to assess is the relevance in this respect of thermally induced vapour flow, with eventual condensation, as is likely to occur during the cold desert nights.

3.4. HEAT TRANSPORT ABOVE THE EVAPORATION FRONT

3.4.1. General

In Paragraph 3.1.1 it was anticipated that the main goal of the present chapter is to establish a procedure to estimate the transport coefficients for heat and vapour between evaporation front and soil surface. These transport coefficients are related to the resistances r_{sh} and r_{sv} in eq. (2.25). Preliminarly a suitable definition for the evaporation front was needed; this requirement has been fulfilled in Section 3.3.

The approach to be followed will be to determine r_{sh} first and then r_{sv} from r_{sh} by means of simplified equations relating vapour flow to heat flow. The resis-

tance $r_{sh} = z_E/\lambda$, see eq. (2.17), and therefore the soil thermal conductivity is needed. By applying the procedures presented in Paragraph 3.5.1, the soil thermal diffusivity $a = \lambda/\rho c$ is obtained. To infer λ from a the soil heat capacity preliminarly must be calculated, e.g. from soil composition and moisture content (see Paragraph 3.5.1). This approach will be applied in Paragraph 8.2.2.

Because of the presence of cracks in playa soils, thermal convection of soil air may take place (Paragraphs 3.4.3 and 3.4.4) above the evaporation front. To establish conditions for the onset of thermal convection, the evaporation front will be considered as a physical boundary, which is not completely true. The physical basis proposed for the evaporation front in Paragraph 3.3.3 indicates that it has a finite thickness.

3.4.2. Heat conduction and convection

The relevance of convective heat transport in soils is easily assessed by mentioning a few references.

Vapour losses of triallate (a herbicide) were measured in absence and presence of water evaporation by JURY et al. (1980). The upward flow of triallate in San Joaquin sandy loam in the vapour phase was enhanced by water vapour flow. Transport of radon (^{222}Rn) across depths of a few tens of meters in a fault zone was studied by MOGRO-CAMPERO and FLEISCHER (1977). They suggested that only thermal convective air movement inside the earth skin could account for the observed spatial pattern and the behaviour in time of the ^{222}Rn concentration prevailing at the soil surface.

Experiments on evaporation from cracks in soils provide additional and interesting references. Measured evaporation rates from crack openings only, have been calculated by the present author from data of ADAMS et al. (1969) in an artificial crack made of ceramic plates, of SELIM and KIRKHAM (1970) in Edina silt loam,

Table 3.2. Evaporation from cracks E $(mm \cdot d^{-1})$ as calculated from some literature references. Vapour velocity v_{zv} $(cm \cdot s^{-1})$ corresponding to E was calculated by eq. (3.37)

E $(mm \cdot d^{-1})$	v_{zv} $(cm \cdot s^{-1})$	Reference
9.5	0.5	Adams et al. (1969)
30	0.6	Selim and Kirkham (1970)
17	1.2	Selim and Kirkham (1970)
8	0.7	Ritchie and Adams (1974)
19	1.5	Ritchie and Adams (1974)

Edina mixed loam and Hagener sand, and of RITCHIE and
ADAMS (1974) in Houston black clay. A few examples
are presented in Table 3.2, where the evaporation rate
E (mm·d^{-1}) from crack openings is compared with the
vapour velocity v_{zv}. This latter velocity has been
calculated by means of eq. (3.37) as the velocity that
under steady state conditions is required for the giv-
en evaporation rate at the liquid - vapour interface.
The actual concentration of water vapour inside the
cracks has been inferred or calculated by the present
author from the data provided by the different authors.
It appears that the actual flow rate could be as much
as two orders of magnitude larger than expected for a
diffusion-like process. In Selim-Kirkham's case vapour
flow even was taking place against steep temperature
gradients.

Perhaps the most self-explaining results were
presented by HADAS (1977a) who measured soil thermal
conductivity, λ, by two methods i.e. in the field and
under laboratory conditions. Under steady state con-
ditions it was found that, except at low moisture con-
tents, the method presented by de VRIES (1963) predict-
ed λ with a very good accuracy. Under unsteady state
conditions the de Vries method badly underestimated
the measured values during part of the day. Thus HADAS
(1977a) concluded that the assumptions underlying the
method had to be revised. He suggested that free con-
vection within air filled pores could explain the be-
haviour observed.

In the following pages a non-structured soil will
be considered, with the evaporation front $z_E(x,y)$ be-

ing a plane surface. It is understood that this does
not apply to cracked soils, unless an apparent soil
thermal diffusivity can be determined. The distribution
of evaporation sites in the soil can be approximated
by a surface whose shape depends on the soil structure.
In a homogeneous soil the evaporation sites lie on
some horizontal plane at depth z_E. When cracks are
present, the evaporation sites will lie on a surface
of different shape, approximating the shape of the
cracks. In Fig. 3.9, for example, the soil moisture
distribution as measured by RITCHIE and ADAMS (1974)
around a crack is presented. In more general terms it
can be stated that small elements of the surface that
envelops the evaporation sites, are normal to the max-
imum vapour transfer coefficient when the latter is
defined as a vector.

Fluid convection in porous media usually is de-
scribed by means of macroscopic equations, as for ex-
ample given by COMBARNOUS and BORIES (1975):

$$(\rho c)^* \frac{\partial T}{\partial t} = \lambda^* \text{div}(\text{grad } T) - (\rho c)_f \vec{v} \cdot \text{grad } T \qquad \begin{matrix}(W \cdot m^{-3}) \\ (3.31)\end{matrix}$$

where λ^* is the isotropic effective thermal conductiv-
ity of the porous medium when no fluid convection takes
place, $\vec{v}$ the vectorial flux density and $(\rho c)^*$ the ef-
fective heat capacity, as given by:

$$(\rho c)^* = \chi_{so}(\rho c)_{so} + \chi_f(\rho c)_f \qquad (J \cdot m^{-3} \cdot K^{-1}) \qquad (3.32)$$

where χ_{so} is the fraction of the porous volume occupied
by the solid, χ_f by the fluid, $(\rho c)_{so}$ the heat capacity
of the solid and $(\rho c)_f$ of the fluid.

To derive an equation which allows for an apparent
soil thermal conductivity to be calculated from field
measurements (see Paragraph 8.2.2), a simple case will
now be envisaged.

Fig. 3.9. Deviation of the soil moisture distribution
from horizontal symmetry, because of the presence of
a crack (after Ritchie and Adams, 1974)
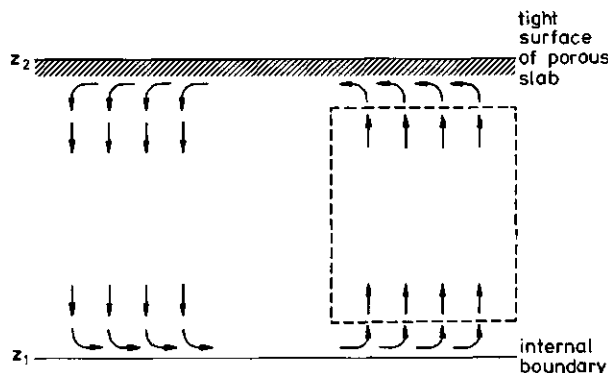
Fig. 3.10. Conceptual scheme of a thermal convective
coil inside a porous slab. Eq. (3.33) applies to the
region within the broken line

A portion of a porous medium large enough for the continuum limit to apply, but restricted to include only the upward branch of a thermal convective coil (Fig. 3.10) will be considered. As discussed by BEUKEMA (1980) the same concept applies to thermal convection inside a cylinder in contact with air at top and bottom, since the downward convective flow takes place outside the cylinder. Within the broken line depicted in Fig. 3.10 a temperature gradient is present only in the vertical direction, thus $(\partial T/\partial x) = (\partial T/\partial y) = 0$, furthermore $(\partial T/\partial z) = $ constant. Under these conditions $v_x = v_y = 0$ and v_z depends on $(\partial T/\partial z)$ only. In this manner a one-dimentional heat balance equation is obtained, applying to the region within the broken line of Fig. 3.10:

$$(\rho c)^* \frac{\partial T}{\partial t} = \lambda^* \frac{\partial^2 T}{\partial z^2} - (\rho c)_f v_z \frac{\partial T}{\partial z} \qquad (W \cdot m^{-3}) \qquad (3.33)$$

It should be noted that v_z is the vertical component of the flux density and not of the actual fluid velocity.

It will be shown in Paragraphs 3.4.3 and 3.4.4 that thermal convection of soil air may take place above the evaporation front, while below it heat transfer will take place by conduction. So the one-dimensional heat balance equation reads:

$$\frac{\partial T}{\partial t} = a \frac{\partial^2 T}{\partial z^2} \qquad (K \cdot s^{-1}) \qquad (3.34)$$

where the thermal diffusivity $a = \lambda^*/(\rho c)^*$ $(m^2 \cdot s^{-1})$. The eqs. (3.31), (3.33) and (3.34) apply to homogeneous soils, so they involve spacial mean quantities. For a discussion about such a conceptual schematization see for example de VRIES (1975). These difficulties are very similar to those mentioned in Paragraph 3.2.1 concerning the eqs. (3.1), (3.2) and (3.3).

ATMOSPHERE
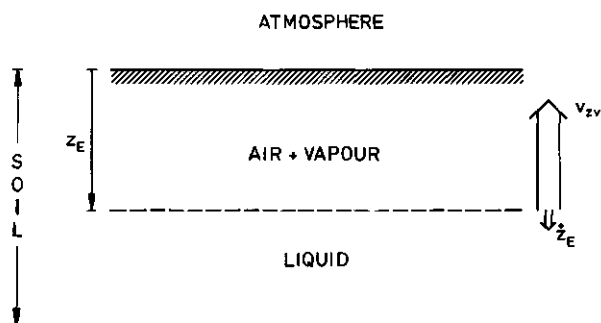
Fig. 3.11. Conceptual scheme of a moving liquid - vapour interface; z_E is the depth of the evaporation front and $\dot{z}_E$ the velocity of its displacement; v_{zv} is the velocity of vapour, away from the interface

The onset of an evaporation front will make a two-layered soil out of a homogeneous one. The system we are dealing with can, accordingly, be schematically depicted as in Fig. 3.11.

As regards the heat balance aspect the interface problem should be handled by considering explicitly soil heat flux in the upper soil layer (G_u), i.e. above the evaporation front, and in the lower soil layer (G_ℓ), i.e. below the evaporation front. The two layers are connected by the boundary condition (CARSLAW and JAEGER, 1959, Chapter XI):

$$G_u - G_\ell = L\rho_w \theta \dot{z}_E \qquad (W \cdot m^{-2}) \qquad (3.35)$$

or

$$-\lambda_u \frac{\partial T_s}{\partial z}\Big|_{z_E^-} - (-\lambda_\ell \frac{\partial T_s}{\partial z}\Big|_{z_E^+}) = L\rho_w \theta \dot{z}_E \qquad (W \cdot m^{-2}) (3.36)$$

where λ_u is the soil thermal conductivity of the upper soil layer and λ_ℓ of the lower one. Soil depths are positive downwards, therefore z_E^- is above the evaporation front, and z_E^+ in the lower soil layer, i.e. below the evaporation front.

As regards the vapour flow aspect another boundary condition must be considered, relating to the difference in densities of water vapour and liquid water. When evaporation E is expressed as a water depth, the downward velocity of the vapour - liquid interface is $\dot{z}_E = E/\theta_E$ where θ_E is the moisture content at z_E (Fig. 3.11). When the interface moves downward with velocity $\dot{z}_E$ water molecules are dispersed (in moist air) with a density ρ_v which is much lower than the density of liquid water ρ_w. Thus the molecules, released when the interface moves (per unit time) a distance z_E downwards, must be dispersed over a distance per unit time $(\theta_E \rho_w/\chi_{a,E}\rho_v)\dot{z}_v$ away from the interface, i.e. upwards. The resulting velocity of water vapour is in the coordinate system with the origin at the soil surface:

$$v_{zv} = \dot{z}_E - \frac{\theta_E \rho_w}{\chi_{a,E}\rho_v} \dot{z}_E = (1 - \frac{\theta_E \rho_w}{\chi_{a,E}\rho_v})\dot{z}_E \qquad (m \cdot s^{-1}) (3.37)$$

The flux is directed away from the evaporating interface, since $\rho_w \gg \rho_v$. If water is supplied to the interface from the lower zone at the same rate, the interface will not move but the previous equation holds with $\rho_w \theta_E \dot{z}_E$ being the rate of water supply to the evaporation front.

It might appear that the coupled heat and moisture flow could be described by means of the equations mentioned in this paragraph and in Paragraph 3.2.1. In the present author's opinion the experimental require-

ments of such an approach make it hardly viable at a laboratory or field scale, as indicated by the conflicting literature on the subject. Furthermore, for the specific purpose of the present investigation (see Section 1.4), the measurements of soil properties needed make the approach not feasible for the regional study presented in this Report. It would be possible to apply rough estimates of the soil properties, but the accuracy of the results would be low and comparable with that achieved by simpler procedures. In this respect it may be mentioned that CAMILLO et al. (1983) applied a moisture - heat flow simulation model to the analysis of remotely sensed thermal infrared data and concluded that only a range of λ-values could be determined. In their approach the determination of thermal conductivity λ is an intermediate step towards the estimation of soil moisture content.

The equations given in this paragraph, however, provide the theoretical basis needed in the discussion presented in the following paragraphs. The forthcoming analysis is necessary to explain the results obtained from field measurements; the results themselves will be given and discussed in Chapter 8.

3.4.3. Conditions for vapour and heat flow in soils to be contrary

It may appear that the conditions required to enhance upward vapour transport contrast with those required for downward heat transport. According to condition (3.36) there must be a net heat supply to the vapour - liquid interface, to provide the energy needed for evaporation.

When $(\partial T/\partial z)|_{z_E^+}$ is positive, i.e. heat flux below the interface is upwards, the temperature gradient favours both heat transport and moisture flow. However, during heating of the soil layer above the interface, it appears that the temperature gradient reduces the flow rate when vapour flow is diffusive in character (see also eqs. 3.13 and 3.18). However, since in principal thermal convection is possible the difference between the densities of moist and dry air must be taken into account, the more so because of the high soil temperatures observed in deserts. The easiest way in doing this is by applying the definition of virtual temperature T_{vi}:

$$T_{vi} = \frac{(1 + \tilde{r}/\varepsilon)}{1 + \tilde{r}} T_a \qquad (K) \qquad (3.38)$$

where $\tilde{r}$ is the mixing ratio (grams of water vapour per gram of dry air) and ε the ratio of molecular weight of water vapour and dry air. An approximate expression for T_{vi} involving only the vapour pressure

(see MONTEITH, 1973) is:

$$T_{vi} = (1 + 0.38 \frac{e}{P}) T_a \qquad (K) \qquad (3.39)$$

with e the vapour pressure (mbar) and P (mbar) the total air pressure. The virtual temperature T_{vi} is that temperature which dry air must have in order to have the same density as moist air at the same P, with given T_a and mixing ratio $\tilde{r}$. When the evaporation front is situated at a depth of a few centimeters, soil air at the surface will be nearly as dry as the air above it. Thus at the surface T_{vi} will be not too different from T_a, while at the evaporation front at high temperatures the difference between T_{vi} and T_s (in the soil local thermal equilibrium is assumed) will be very large. Data presented by SELIM and KIRKHAM (1970) already recalled in Paragraph 3.4.2 help in presenting an example.

Inside an artificially cracked soil sample temperatures of 60°C were measured during drying by radiation, while at the surface the temperature was 70°C. At the crack opening vapour density can safely be assumed to have been close to that of the experimental room, whose temperature was controlled at 25°C and the relative humidity (U) at 50%. By taking into account the temperature at the crack opening, the virtual temperature T_{vi} there can be calculated by eq. (3.39) as being 75°C. At the evaporation front, where $T_a = T_s = 60°C$ and the relative humidity $U \approx 0.98$, $T_{vi} \approx 87°C$, thus a driving force for thermal convection exists. Under these conditions water vapour losses from the crack opening only, were measured as being between 10 and 14 $mm \cdot d^{-1}$ according to soil type. Hence opposite fluxes of heat (downward) and vapour (upward) are well established in this case.

The onset of thermal convection under a temperature drop δT (K) inside a porous slab of thickness δz (m) is usually established by evaluating the Rayleigh number:

$$Ra = \frac{\rho_f g \beta_f \delta T \delta z K}{\eta_f \hat{a}} \qquad (-) \qquad (3.40)$$

where β_f (K^{-1}) is the thermal expansion coefficient, K (m^2) the specific permeability of the porous medium, η_f $(N \cdot s \cdot m^{-2})$ the viscosity of the involved fluid and according to KATTO and MASUOKA (1967) $\hat{a} = \lambda^*/(\rho c)_f$ is the hybrid thermal diffusivity to be used in eq. (3.40). Critical values Ra_{cr} define thresholds corresponding to different specifications of the boundary conditions at both sides of the slab. Values of Ra_{cr} for particular cases have been presented and were discussed by WEBER (1973, 1974) and BEUKEMA (1980).

A state-of-the-art review on thermal convection in porous media was presented by COMBARNOUS and BORIES (1975); they also have given a detailed table of Ra for different boundary conditions, as taken from NIELD (1968).

Boundary conditions of the flow regime applying to the soil layer between soil surface and evaporation front have yet to be defined. For the moment it is assumed that the soil surface does not restrict air flow and that the temperature is specified and uniform. At the evaporation front the same boundary conditions may apply when air density further decreases below it. When the minimum density, e.g. because of maximum T_{vi}, is found at the evaporation front, the latter can be considered to be impervious to air flow. If the lower boundary, i.e. the evaporation front, is considered to be pervious, and both lower and upper boundaries isothermal, then $Ra_{cr} = 0$ and any gradient of virtual temperature T_{vi} will induce thermal convection. Conversely, if the lower boundary is impervious, then $Ra_{cr} = 27.1$ (NIELD, 1968). It must be emphasized that the conceptual model of evaporation and flow of moist air in a porous medium, as given in this section, is highly idealized.

It appears that the dichotomy pervious - impervious to characterize the permeability of the layer enclosing the porous slab, although being clear, is not of direct use. As a matter of fact the contrast between the two terms is relative in some way, since they relate to the difference in permeability between the bulk of a porous slab and the layers enclosing it (Fig. 3.12). According to ANDERSON and SKILBECK (1980), and GARTLING (1982) an enclosure has a sealing effect
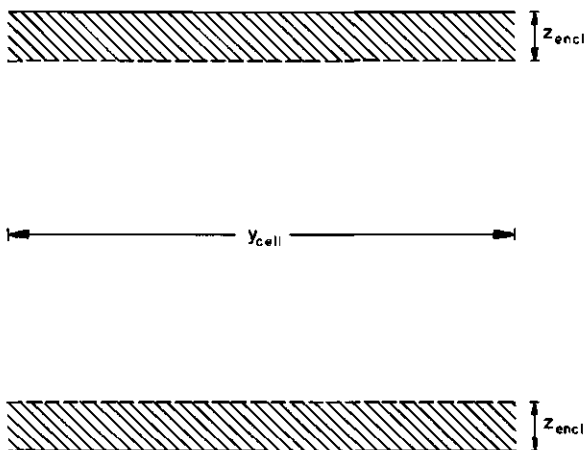
Fig. 3.12. Scheme of a convective cell in a porous slab bounded by two enclosing layers of lower specific permeability; the thickness z_{encl} of each enclosure and the width y_{cell} of the convective cell are indicated

on thermal convective flow, if:

$$\frac{K_{encl}}{z_{encl}} < \frac{\pi}{y_{cell}} K_{slab} \qquad (m) \qquad (3.41)$$

After the work published by FARRELL et al. (1966) several authors (e.g. FEDDES, 1971) considered air turbulence just above the soil surface as being effective on the gas exchange between the top soil and the atmosphere. Both experimental results and theoretical findings support this concept. According to SCOTTER and RAATS (1969) evaporation through a dry mulch (randomly packed spheres) can increase over molecular diffusion by a factor 2 to 3 under those circumstances. However, this enhancement is strongly dependent on particle size, which has to be large enough anyhow. A similar result was also given by SCOTTER et al. (1967), who found in Parc silt loam that by air turbulence vapour flow increased by 60% over diffusion. The experimental results of KIMBALL (1973) and KIMBALL and LEMON (1971a) bring further support to this reasoning. The effect could even have been smoothed by their relatively long sampling time in relation to the frequency of the pressure fluctuations: 30 minutes and 1 minute respectively. Hence it is not possible to dismiss the effect of air turbulence on soil evaporation occurring at a few centimeter depth inside the top soil.

Penetration of pressure waves into the soil was studied theoretically by KIMBALL and LEMON (1971b). Pressure fluctuations at high frequency (>1 Hz) induce relatively large air velocity, but are quickly damped out. With decreasing frequencies of pressure waves, the Darcy-type air velocity also decreases, but air displacement increases. Because of the very low frequency, behaviour of pressure waves induced by oscillations in (virtual) temperature will be quite different. Air velocities associated with such pressure fluctuations are low, but high enough to satisfy the condition (3.37).

It can be concluded that depending on the type of soil, meaningful soil air velocities may or may not occur. A proper criterion to make a decision is the Rayleigh number according to (3.40), but it should be kept in mind that theoretical derivations of Ra_{cr} assume constant and not oscillating temperatures at both boundaries of the porous slab.

3.4.4. Thermal convection of moist air above the evaporation front

The theoretical background of thermal convection in soils has been summarized in the preceding paragraphs. The onset of thermal convection above the evaporation front now can be considered in more detail.

The concepts underlying the definition of the evaporation front (Section 3.3) have to be kept in mind to properly choose the boundary conditions.

The soil layer between evaporation front and soil surface can definitely be said to be pervious to air flow at the upper boundary. There temperature and pressure can fluctuate freely. The lower boundary, i.e. the evaporation front as defined in Paragraph 3.3.3, is to be considered impervious to air only if the virtual temperature has a maximum at the evaporation front.

Temperature can be considered to be constant at both boundaries over short time intervals. Under such conditions (see Paragraph 3.4.3) $Ra_{cr} = 0$. When a porous slab is considered to have an impervious lower boundary and a pervious upper boundary, both at constant pressure, $Ra_{cr} = 17.1$ according to RIBANDO and TORRANCE (1976). Note that even when the lower boundary is impervious and at constant pressure, it may well be that $Ra_{cr} = 0$ when the upper boundary is pervious with temperature and pressure free to fluctuate.

It must be recalled that the known theoretical derivations of Ra_{cr} rely on three assumptions:

- the inertia term $v \cdot \nabla(\rho\vec{v})$ is neglected in the equation for momentum transport, which assumption does not appear to be reasonable close to the evaporative interface, since $\nabla(\rho\vec{v})$ is expected to be large;
- viscous heating is neglected in the equation for energy transport, because of the low soil air velocities prevailing above the evaporation front;
- the Boussinesq's approximation applies: the density of the fluid is constant, with the exception of the buoyancy term (momentum equation). Some difficulties arise with gas mixtures, such as air plus vapour. It was shown by LAWSON and YANG (1975) that it was not possible to define a homogeneous fluid equivalent

to the mixture, by calculating the properties from mixture composition. With a fifty-fifty mixture of He and N_2 it was found that $Ra_{cr} = 20$, instead of the theoretically expected value of 39.5.

With the preceding remarks in mind, the Rayleigh number as applying to the porous layer above and to the one below the evaporation front can be evaluated. Three different schemes may eventually apply (Figs. 3.13A, B, C):

A, air circulates into and out of the top soil layer, with convective coils partly located in the air above soil surface;
B, air circulates within a thicker layer, between the evaporation front at $z_E \simeq 5$ cm and the groundwater table at $z_{gw} \simeq 1$ m;
C, air circulates between a deep evaporation front at $z_E \simeq 2$ m and the soil surface.

The Rayleigh number can be evaluated as in eq. (3.40) with the following numerical values: $\eta_a = 1.89 \cdot 10^{-5}$ N·s·m^{-2}, $\hat{a} = 2.5 \cdot 10^{-4}$ m^2·s^{-1}, $\beta_a = (1/T) = 3.1 \cdot 10^{-3}$ K^{-1}, $\rho_a = $ air $= 1.1$ kg·m^{-3}, K = specific permeability $= 10^{-10}$ to 10^{-6} m^2.

C a s e A. The temperature difference can be taken as δT_{vi}: the difference in virtual temperature T_{vi} between the evaporation front and a reference level z_{ref} at 50 cm height where air temperature and vapour pressure are assumed to be measured. A value $\delta T_{vi} = 15$ K will be considered as applying to the early afternoon and $\delta T_{vi} = 5$ K to the early morning. Accordingly $Ra = 5.6 \cdot 10^{-3}$ to 56 for $\delta T_{vi} = 15$ K and $Ra = 1.8 \cdot 10^{-3}$ to 18 (in accordance with the selected range of K) for $\delta T_{vi} = 5$ K.
C a s e B. This case applies to transport of moist air from the groundwater table to the evaporation
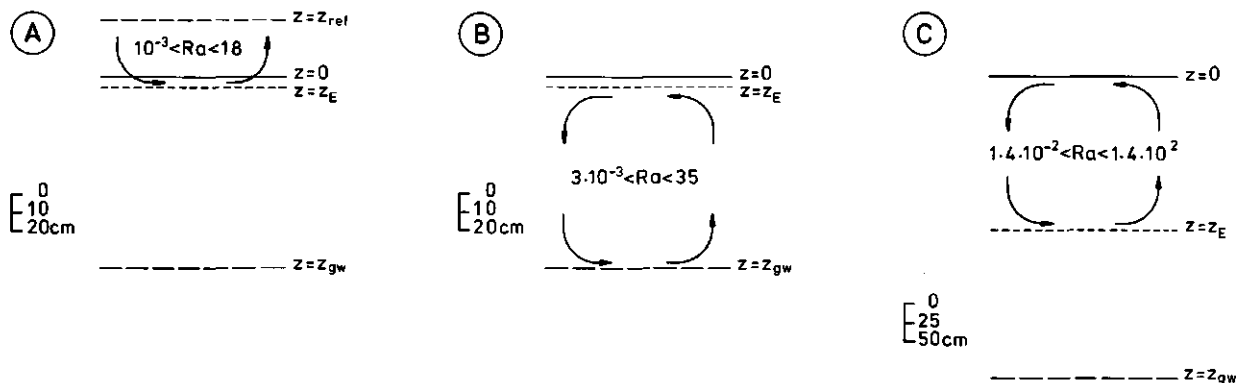
Fig. 3.13. A, air circulates into and out of the top soil layer, with the convective coils partly located in the air above the soil surface; B, air circulates within a thicker layer between the evaporation front and the groundwater table; C, air circulates between the evaporation front and the soil surface. In each case the range of values obtained for the Rayleigh number is indicated

front. Since relative humidity would be quite close
to 1 in the entire layer, differences in virtual tem-
perature will be close to differences in soil air tem-
perature. A first consequence is that because of the
daily warming - cooling cycle of the top soil, con-
vection of soil air can only arise during the night
or early morning (see the quotation of Plinius at the
beginning of this chapter!). To fix thoughts δT_a can
be taken as $5^{\circ}C$ and $\delta z = 1$ m and Ra $= 3.5 \cdot 10^{-3}$ to 35
(in accordance with the selected range of K). It must
be noted, however, that $\kappa_a(\theta) = (K/\eta_a)f(\theta)$ decreases
at deeper depths, since the liquid moisture content
increases. For given values of δT_a, z_{gw}, z_E the par-
ticular value of Ra will be or will not be higher than
Ra_{cr}, according to the average κ_a in the soil layer
between z_E and z_{gw}. The lower the liquid moisture
content in that layer, the higher the average soil
permeability to air flow. Hence it can be concluded
that convection may take place, but only in very
coarse soils, where K is high and liquid moisture con-
tent only increases close to the groundwater table.
C a s e C. This case applies to the downward dis-
placement of the evaporation front and to the kind of
moisture profile observed by the present author in
desert sand dunes above a relatively shallow water
table. Soil moisture contents were observed to be con-
stant with time across a soil layer of 4 m thickness
from groundwater table to soil surface. The evapora-
tion front was situated at 2 m depth. The virtual
temperature at that depth can be estimated to have
been $30^{\circ}C$, while at the soil surface T_{vi} varied be-
tween $21^{\circ}C$ and $51^{\circ}C$. Hence convection may only arise
in the early morning. The Rayleigh number relating to
the minimum virtual temperature at the soil surface
ranges from $1.4 \cdot 10^{-2}$ to $1.4 \cdot 10^2$ with K varying between
10^{-10} to 10^{-6} m^2.

The theoretical argument developed insofar finds
a surprisingly good confirmation in the results pub-
lished by HELLWIG (1973, 1978). The presence (case C)
of an early morning peak in evaporation (hourly values)
from a sandy soil with the water table 0.6 m deep was
observed by him during an experiment from May 1967 to
August 1968. He realized that the temperature differ-
ence between z_{gw} and air at z_{ref} was the main driving
force, with vapour pressure also playing a relevant
rôle. To gather more specific data about the sunrise
peak, he performed a second experiment over 847 days
(during 1969-1971) with hourly measurements. In a
sand mixture with 98% of the particles within the
range >0.1 mm, it was observed that when the water
table depth dropped below 30 cm the sunrise evapora-
tion peak was the only one left. Statistical analyses
were performed by him on the 1967-1968 evaporation
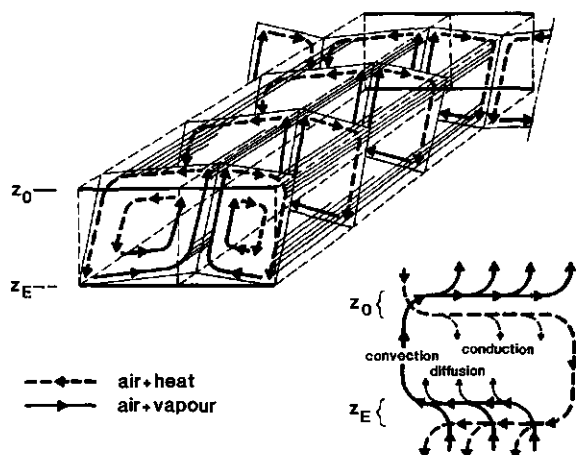
Fig. 3.14. Conceptual scheme of simultaneous upward
vapour transport and downward heat transport as a re-
sult of thermal convection of soil air; two neighbour-
ing coils are shown (see text)

data and he did show that there was a good correla-
tion with the temperature difference between water
table and air at z_{ref}, but only for night-time data.
When full 24-hour periods were considered, correla-
tion coefficients dropped sharply. He also observed
that the sunrise evaporation peak was clearly related
to the vapour pressure difference between z_{gw} and air
at z_{ref}, even matching the peak of this latter differ-
ence in four out of eight cases. Especially with the
deeper water table depths, vapour pressure at the
water table was higher (+15 mbar) than in the air at
20 cm height, with the larger differences observed in
the early morning. The huge amount of data from the
1969-1971 experiments confirmed beyond any reasonable
doubt the results of the first experiment. It is re-
grettable that Hellwig did not consider the connection
between temperature and vapour pressure as expressed
by the virtual temperature T_{vi} (see eq. 3.39).

In Fig. 3.14 a sketch is presented to depict the
rôle of thermal convection in both heat and water va-
pour transfer between the evaporation front and the
soil surface. The soil surface (z = 0) is at tempera-
ture T_a^0 and virtual temperature T_{vi}^0. At the evapora-
tion front (z = z_E), where the temperature $T_a^E < T_a^0$
and virtual temperature $T_{vi}^E > T_{vi}^0$, water vapour is
being released into the coils. An amount of heat is
extracted, in part, from the heat transported down-
wards by the descending branches of the two neigh-
bouring convective coils. Heat can be transported
downwards because $T_a^0 > T_a^E$ and vapour upwards because
$T_{vi}^E > T_{vi}^0$. At the soil surface vapour is removed from
the two thermal convective coils. Heat and vapour
transfer between the soil surface and the turbulent
atmosphere above it, is much faster than the transfer
between the evaporation front and the soil surface.

Vapour density at the soil surface will, therefore, almost immediately reach equilibrium with the vapour density in air.

In this paragraph it has been shown that thermal convection of soil air may indeed take place in playa soils. The more so when it is recalled that large K-values are easily attained, because of the large and deep cracks so often found in such soils. It appears hardly possible to perform reasonably accurate experiments under field conditions to assess directly the relevance of the effects described insofar. The results to be given in Paragraph 8.2.2, however, show that thermal convection of soil air indeed does take place. Such a flow regime explains the relatively large evaporation rate and the large apparent soil thermal diffusivity, observed in the Libyan playas.

3.4.5. Effective and apparent soil thermal properties

In Paragraph 3.4.2 heat balance equations have been given for the cases of convection, eq. (3.31), and conduction, eq. (3.34). There the effective soil thermal conductivity λ^* and effective heat capacity $(\rho c)^*$ were defined. These properties account for the overall effect of soil structure, composition and moisture content on the conductive heat flow.

Vapour diffusion and convection of soil air can contribute to heat flow, while soil water - soil particle interactions may add to $(\rho c)^*$ especially at low moisture contents. The microphysical aspects of these processes are very complicated and to some extent not exactly known, beginning with the actual structure of soil water. Even for those cases where a reasonably accurate microphysical model is known, such as vapour flow in macropores, the required experimental data are not easily available; at least not for the needs of a regional study as the one presented in this Report. Therefore it was decided to apply the concept of apparent soil thermal properties. The apparent soil thermal diffusivity $a = \lambda'/(\rho c)'$ can be obtained from soil temperature measurements by means of the procedures to be presented in Paragraph 3.5.1. Here equations that account for the contribution to λ' arising from soil air thermal convection will be given. The contribution of vapour diffusion to λ' has already been discussed in Paragraph 3.2.3, eqs. (3.24) and (3.25).

The same temperature field as described by eq. (3.33) can also be described by a conduction-like equation:

$$(\rho c)^* \frac{\partial T}{\partial t} = \frac{\partial}{\partial z} \lambda' \frac{\partial T}{\partial z} \qquad (\text{W·m}^{-3}) \qquad (3.42)$$

where λ' is the apparent thermal conductivity, including heat transport by fluid convection. An example can be worked out to show which kind of relation exists between λ^*, v_z and λ'.

A relatively dry soil will be considered, with the fluid being moist air; it is also assumed that $\lambda_s^* = \text{const}$, $T_s = bz + T_0$. The latter statement appears quite reasonable for small depths $\delta z = z$ with $b = (\partial \tilde{T}_s/\partial z)$ and $\tilde{T}_s(z)$ any soil temperature profile. Substitution of the assumed linear temperature profile in the eqs. (3.33) and (3.42) yields:

$$\frac{\partial}{\partial z} \lambda_s' = -\rho_a c_p v_{za} \qquad (\text{W·m}^{-2}\text{·K}^{-1}) \qquad (3.43)$$

or, by considering small increments, i.e. $z = \delta z$:

$$\lambda_s'(\delta z) - \lambda_s'(0) = -\rho_a c_p v_{za} \delta z \qquad (\text{W·m}^{-1}\text{·K}^{-1}) \qquad (3.44)$$

When $v_{za} = 0$, the eqs. (3.33) and (3.42) must be identical and $\lambda_s'(\delta z) = \lambda_s'(0)$ holds according to eq. (3.44). Therefore $\lambda_s'(\delta z) = \lambda_s'(0) = \lambda_s^*$ and a solution of eq. (3.43) is:

$$\lambda_s' = -\rho_a c_p v_{za} \delta z + \lambda_s^* \qquad (\text{W·m}^{-1}\text{·K}^{-1}) \qquad (3.45)$$

Eq. (3.45) can be rewritten by relating the air velocity v_{za} to pressure differences according to Darcy's equation. Again only part of the porous body bounded by the broken line as shown in Fig. 3.10 will be considered. Since Darcy's equation applies only at low Reynolds numbers (Re), the present example also relates only to low Re. Darcy's equation for air flow in a porous medium of specific permeability K reads:

$$v_{za} = -\frac{K}{\eta_a} \frac{\partial}{\partial z} (P - \rho_a gz) \qquad (\text{m·s}^{-1}) \qquad (3.46)$$

where P (N·m^{-2}) is the total pressure depending on virtual temperature as specified by eq. (3.48), K (m^2) is the intrinsic permeability of the soil, η_a (N·s·m^{-2}) the air viscosity. The remarks of CHILDS (1969, pages 166-167) about the possibility of discerning a solid related (through K) and a fluid-related (through η) contribution to fluid flow in soils, should be given proper consideration. Moreover the high frequency fluctuations in the intensity of turbulent transfer in the atmospheric surface layer (see Section 7.6) are likely to affect soil air flow in the top soil (see Paragraph 3.4.3).

If eq. (3.46) is accepted as it is written, then the permeability for air can be obtained from the soil saturated conductivity for water κ_{sat} (m·s^{-1}) according to:

45

$$\frac{K}{\eta_a} = \frac{\eta_w}{\eta_a} \frac{\kappa_{sat}}{\rho_w g} \qquad (kg^{-1} \cdot m^3 \cdot s) \qquad\qquad (3.47)$$

When the virtual temperature concept is applied, the gas law for the moist soil air reads $P = R_a \rho_a T_{vi}$. Effects of gas thermal expansion on convective flow have been partly neglected by accepting Boussinesq's approximation (see Paragraph 3.4.4; COMBARNOUS and BORIES, 1975). Because of the steep gradients of T_{vi} in the top soil above the evaporation front and of the very small pressure gradients required to enhance soil air flow, the entire issue deserves some more attention. It is understood that the partial pressure of (dry) air is kept constant in the soil layer above the evaporation front by the thermal convective flow, as depicted in Figs. 3.10 and 3.14. Without such a mechanism vertical flow of soil air, as eventually induced by a pressure increase at the evaporation front, would only last for very short periods.

Accordingly the pressure gradient can be written as:

$$\frac{\partial P}{\partial z} = R_a \frac{\partial}{\partial z} (\rho_a T_{vi}) \qquad (N \cdot m^{-3}) \qquad\qquad (3.48)$$

where R_a is the gas constant for dry air $(N \cdot m \cdot kg^{-1} \cdot K^{-1})$. Note that in eq. (3.48) $\rho_a = \rho_a(z)$ and that local thermal equilibrium in the soil is assumed.

The eqs. (3.48) and (3.46) can be substituted in (3.45):

$$\lambda'_s = \rho_a c_p \frac{K}{\eta_a} \left[R_a \frac{\partial}{\partial z} (\rho_a T_{vi}) - \rho_a g - gz \frac{\partial \rho_a}{\partial z} \right] \delta z + \lambda^*_s$$

$$(W \cdot m^{-1} \cdot K^{-1})$$
$$(3.49)$$

Eq. (3.49) will later be applied in Paragraph
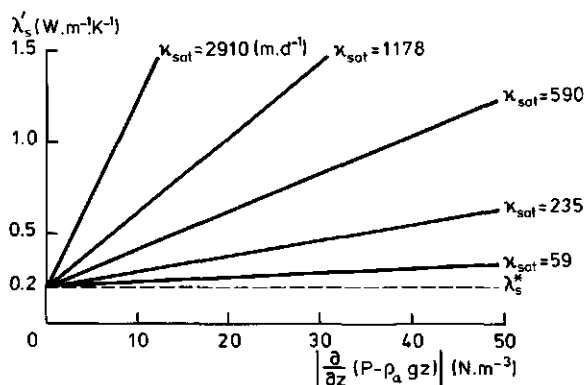
Fig. 3.15. Apparent soil thermal conductivity λ'_s as affected by convection of soil air. Five different soils are considered, i.e. with a saturated hydraulic conductivity between 59 m·d^{-1} and 2910 m·d^{-1}. The gradient term varies between 0 en 0.5 mbar·m^{-1} (50 N·m^{-3})

8.2.2 to estimate the resistance r_{sh}, as needed in eq. (2.25) to calculate the latent heat flux LE. Values of λ'_s are plotted in Fig. 3.15, as calculated by means of eq. (3.49). Specific permeability K varies between $0.7 \cdot 10^{-10}$ and $3.5 \cdot 10^{-9}$ m^2, i.e. κ_{sat} between 59 and $2.9 \cdot 10^3$ m·d^{-1}, from very coarse sand to fine gravel according to BEAR et al. (1968, page 60). The specific gas constant for air $R_a = 2.87 \cdot 10^2$ N·m·kg^{-1}·K^{-1}; $\eta_a = 1.89 \cdot 10^{-5}$ N·s·m^{-2}; the effective thermal conductivity (λ^*_s) of dry sand is 0.2 W·m^{-1}·K^{-1}. The latter value is intended to be representative of the peculiar structure of soils in playas. There cracks allow for high permeabilities, although the thermal conductivity of the solid soil phase remains low.

The apparent soil heat capacity as lumped in the value $a = \lambda'_s/(\rho c)'_s$, may also include contributions which do not relate to actual heat storage, i.e. $(\rho c)'_s \neq (\rho c)^*_s$. Let us assume that the soil heat capacity has been measured by the calorimetric method for a volume which includes the evaporation front. So the value obtained for the apparent soil heat capacity will in addition to heat storage relate to the evaporation rate:

$$(\rho c)'_s = (1 + \frac{L\rho_w (\partial \theta/\partial z)\dot{z}_E}{\dot{Q}})(\rho c)^*_s \qquad (J \cdot m^{-3} \cdot K^{-1}) \quad (3.50)$$

where $\dot{Q}$ is the heating rate $(J \cdot m^{-3} \cdot s^{-1})$.

In the discussion presented above two complicating factors have not been mentioned. First of all the rate of removal of water vapour away from the evaporation front may be lower than the value required by:

$$v_{zv} = (1 - \frac{\theta_E \rho_w}{\chi_{a,E} \rho_v})\dot{z}_E \qquad\qquad (3.37)$$

for a particular evaporation rate. Secondly, Darcy's equation may not apply to air flow in soils with relatively large specific permeabilities. These two difficulties will now be discussed.

Boundary condition eq. (3.37) requires that a specific mean velocity of water vapour away from the evaporation front is achieved. This implies that for a given evaporation rate either the thermal convective velocity is large enough or pressure will tend to increase locally. It will be shown that this process can slightly enhance air flow in the low range of the K-values considered in Paragraph 3.4.4 and in this one. Once again it should be recalled that the conceptual model of flow processes in the soil applied here has been depicted in Fig. 3.10: a top soil layer where convection may take place is separated from the underlying soil by the evaporation front. One-dimensional equations, such as eq. (3.33), can only be ap-

plied to the region within the broken line in Fig. 3.10.

An a-priori reason for the synergism of phase transition and transfer of momentum is provided by Curie's principle (see LUIKOV, 1966, Chapter 1). If one dimensional (vertical) flow applies, the air flow velocity can in principle be calculated by Darcy's equation (3.46). This approach has often been used to study engineering applications of drying processes in porous slabs. The porous slab concept applies to the soil layer between evaporation front and soil surface under the condition that thermal convective flow (see Figs. 3.10 and 3.14) supplies dry air to the evaporation front.

An approximate model for the evolution of the pressure distribution during evaporation inside a semi-infinite porous medium has been presented by CROSS et al. (1979). Gas flow velocity was related to pressure by means of Darcy's equation and the proper boundary condition (identical to eq. 3.37) at the evaporation front was applied. A simplified analytical solution was presented, as applying to relatively low temperature differences between the air and the evaporation front and taking into account the permeability of the particular medium. That solution allowed these authors to conclude that the maximum pressure always occurs at the evaporation front. Namely the increase δp of pressure over P is in direct proportion with $(T_a^2 - T_E^2)$, where T_a is air temperature and T_E temperature at the evaporation front. This increase in pressure is inversely proportional to the specific permeability of the porous medium.

The equation given by CROSS et al. (1979) cannot straightaway be applied to calculate the enhancement due to δp of moist air flow, because these authors did not include a continuity equation for air. As far as one-dimensional flow in a porous slab is considered the approximation is correct, since an unrestricted air supply is available at the lower boundary of the slab. When a soil layer above the evaporation front is considered, a gradient in total pressure can last only if a thermal convective circulation of soil air takes place (see Fig. 3.10). The order of magnitude of the maximum pressure increase at the evaporation front can be calculated by the equation given by Cross et al., as being $1 \cdot 10^{-2}$ N·m^{-2} with K = 10^{-8} m^2 and 110 N·m^{-2} with K = 10^{-12} m^2. Both values calculated for T_a = 50°C and T_E = 30°C. If values of z_E are selected, air flow velocities corresponding with the values above can be calculated.

The onset of a pressure gradient in a porous body, as due to phase transition has also been studied by CHO (1975) and MIKHAILOV (1975). Transport equa-

tions describing the simultaneous evolution of the temperature, moisture and pressure fields were presented by HUANG (1979) along with proper figures for the constants involved in the equations. Results of numerical integration of those equations were presented by HUANG et al. (1979) as applying to transfer processes in concrete slabs (K = 10^{-14} m^2). The temperature range was kept between 21 and 26°C and natural drying was considered. The results presented as functions of the depth in the slab show an initial pressure build-up at the evaporation front, while the pressure gradient decreases along with the drying rate. In this experiment the boundary condition was set at atmospheric pressure on both sides of the slab. After 30 hours of drying the pressure drop was about 10 N·m^{-2} across 10^{-1} m so a gradient of 100 N·m^{-3}; temperature increased during drying, but it remained constant across the slab.

It should be realized that the eventual pressure increase, as due to vapour release at the evaporation front, is a consequence of boundary condition (3.37). When a particular soil evaporation rate is measured which cannot be achieved by diffusion only, then other transfer processes must be present to satisfy eq.
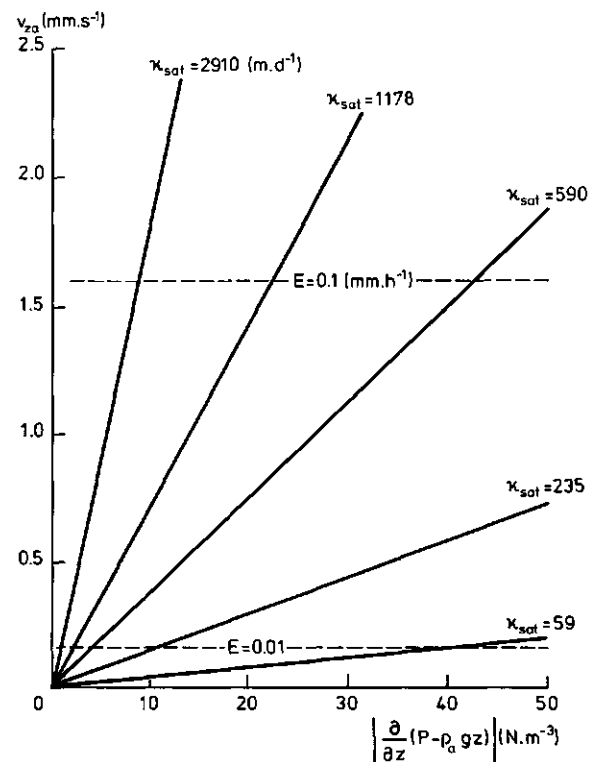
Fig. 3.16. Darcy-type soil air velocity (v_{za}) calculated by eqs. (3.46) and (3.48) for five different soils, i.e. with saturated hydraulic conductivities between 59 m·d^{-1} and 2910 m·d^{-1}. The gradient term varies between 0 and 0.5 mbar·m^{-1} (50 N·m^{-3}). The horizontal broken lines show the vapour velocity (v_{zv}) required to match the evaporation rate shown on each line

(3.37). Once again it should be mentioned that thermal convection of soil air has been treated in Paragraphs 3.4.3 and 3.4.4, while here a possible, additional, enhancement process directly due to vapour production has been considered.

To illustrate the relationship between the velocity of soil air and evaporation rate, values of v_{za} have been calculated by means of eq. (3.46) with $\partial P/\partial z$ given by eq. (3.48), and plotted in Fig. 3.16. There the v_{zv}-values, as required by eq. (3.37) to achieve two particular evaporation rates also are indicated. When comparing the values of v_{za} in Fig. 3.16 with the v_{zv}-values in Table 3.2 it can be concluded that the evaporation rates mentioned in that table are to be explained by means of eq. (3.46).

With regard to the range of validity of Darcy's equation it must be recalled that eq. (3.46) does not include an inertial term, i.e. depending on v^2, and that it only applies to low Reynolds numbers. The transition from Darcy to non-Darcy flow takes place at a critical Reynolds number Re_{cr}, which is known to be dependent on pore structure and surface roughness of pore walls. According to DULLIEN (1979) a reasonably good criterion is:

$$1 < \frac{Re_{cr}}{1 - \chi} < 10 \qquad (3.51)$$

According to the definition of $Re = (dv\rho/\eta)$, where d is a length scale, it is found that only with $K \lesssim 10^{-8}$ m^2 the air flow regime is of the Darcy-type, with air velocity v_a as required by eq. (3.37) for a reasonable evaporation rate. If $K > 10^{-8}$ m^2 a different flow equation must be applied, which includes an inertial term. Such an equation, widely applied and tested, is the Ergun equation presented by ERGUN (1952):

$$\frac{\delta P}{\delta z} = \frac{1 - \chi_a}{d\chi_a^3} \left[\frac{150(1 - \chi_a)}{Re} + 1.75 \right] \rho_a v_a^2 \qquad (N \cdot m^{-3}) \ (3.52)$$

By now it will have become clear that an exact theoretical description of air, vapour and heat flow is not available. A number of particular aspects of these flow processes are fairly well known, but they cannot univocally be related with each other and, therefore, the required heat transfer coefficients cannot theoretically be derived. As already anticipated, therefore, from now on measured values of soil thermal properties will be considered to be apparent quantities and relating to the Fourier-like equation:

$$\lambda_s' \frac{\partial^2 T}{\partial z^2} = (\rho c)_s' \frac{\partial T}{\partial t} \qquad (W \cdot m^{-3}) \qquad (3.53)$$

3.5. SOIL PHYSICAL PROPERTIES

The analysis will be restricted to those soil physical properties which appear in the eqs. (3.2), (3.34) and (3.53).

3.5.1. Thermal properties

Soil thermal properties may be derived from the composition of the soil, i.e. from the volumetric fraction and the thermal property of each constituent. A full description of the method can be found in de VRIES (1963, 1975). The effective heat capacity per unit volume of soil $(\rho c)_s^*$ can be calculated from:

$$(\rho c)_s^* = \Sigma_i \chi_{si} \rho_{si} c_{si} + \chi_w \rho_w c_w + \chi_a \rho_a c_a \qquad \begin{matrix} (J \cdot m^{-3} \cdot K^{-1}) \\ (3.54) \end{matrix}$$

where χ is the volumetric fraction of each constituent and the subscripts si, w and a stand for the different soil minerals and organic material, water and air respectively. The thermal conductivity λ_s^* can be calculated according to de Vries from:

$$\lambda_s^* = \frac{\chi_w \lambda_w + \Sigma_i \mu_{si} \chi_{si} \lambda_{si} + \mu_a \chi_a \lambda_a}{\chi_w + \Sigma_i \mu_{si} \chi_{si} + \mu_a \chi_a} \qquad \begin{matrix} (W \cdot m^{-1} \cdot K^{-1}) \\ (3.55) \end{matrix}$$

where μ_{si} and μ_a are weighing coefficients accounting for the shape of each kind of constituent particle as well as for the ratio between thermal conductivities of each constituent and the surrounding medium. In eq. (3.48) it is assumed that water occupies the largest volumetric fraction. With lower moisture contents, either the soil or the air has to be considered as the continuous surrounding medium. A different empirical formula was given by WOODSIDE and MESSMER (1961). HADAS (1977b) has compared λ_s-values as computed with both the formula of Woodside and Messmer, and of de Vries, with measured λ_s-values. He concluded that the Woodside - Messmer formula proved to be somewhat better, but that both methods failed with increasing aggregate size.

Underlying eq. (3.55) is a schematization (de VRIES, 1952) of heat transfer in the gaseous phase, which neglects the presence inside the soil pores of the adsorbed film in the transition layer between the gaseous and the solid soil phase (Fig. 3.6). Especially in the small pores the adsorbed water plays an essential rôle in the pore-scale microphysics of soil - fluid interactions. Furthermore convection of soil air at very low Rayleigh numbers, as described by PHILIP (1982a,b), also is neglected. So it can be concluded that eq. (3.55), although useful, is not of general applicability.

Thermal properties can be measured directly, e.g. with the method of the needle probe. Analytical solutions of particular heat conduction problems can be applied to derive the values of λ_s. As shown by van HANEGHEM (1981), when a layered wall cylinder model is considered for the probe, the method can be applied in unsteady state conditions to determine both $\rho_s c_s$ and $(\lambda_s \rho_s c_s)^{\frac{1}{2}}$. For a discussion on the different methods and on the possibility to estimate soil moisture contents through the eqs. (3.47) and (3.48) see STIGTER (1969), for an evaluation of the so-called contact or block method, see HADAS (1973).

For a comparison of different methods to estimate the apparent soil thermal diffusivity near the surface, see HORTON (1982) and HORTON et al. (1983).

Three procedures which are suitable for the determination of apparent soil thermal properties will now be described. The meaning of apparent soil thermal properties is as specified by eq. (3.53).

P r o c e d u r e A. The solution of the equation for heat conduction, as obtained with a sinusoidal boundary condition at the soil surface is applied. When this upper boundary condition is expressed as:

$$T(0,t) = \bar{T} + A_0 \sin \omega t \qquad (K) \qquad (3.56)$$

with $\bar{T}$ being the average temperature (K), A_0 the amplitude at the surface (K), ω the angular frequency (rad·s^{-1}) and t is time (s), the solution for the differential heat conduction equation (3.53) in a homogeneous soil is (CARSLAW and JAEGER, 1959, page 64):

$$T(z,t) = \bar{T} + A(z) \sin(\omega t - z/d) \qquad (K) \qquad (3.57)$$

where the amplitude of the oscillation in half a period at depth z is:

$$A(z) = A_0 e^{-z/d} \qquad (K) \qquad (3.58)$$

and the damping depth d is:

$$d = (2a/\omega)^{\frac{1}{2}} \qquad (m) \qquad (3.59)$$

with a (m^2·s^{-1}) being the apparent soil thermal diffusivity, i.e. $a = \lambda_s'/(\rho c)_s'$. In order to yield values of a, eq. (3.58) can be rewritten as:

$$a = \frac{\omega}{2} z^2 / \left[\ln A_0 - \ln A(z)\right]^2 \qquad (m^2 \cdot s^{-1}) \qquad (3.60)$$

which is the formula to be applied in practice.

The heat flowing into the soil during the period $[t_1, t_2]$ when the surface temperature increases from $(\bar{T} - A_0)$ to $(\bar{T} + A_0)$, i.e. from $\omega t_1 = -\pi/4$ to $\omega t_2 = 3\pi/4$, can be obtained from the relationship:

$$Q = \sqrt{2} \; \rho_s c_s d A_0 \qquad (J \cdot m^{-2}) \qquad (3.61)$$

The eqs. (3.56), (3.57), (3.58) provide other ways than by eq. (3.60) to infer the thermal diffusivity a. The phase angle $\Omega = -z/d$ in eq. (3.57) can in principle be determined by plotting soil temperature measurements at different depths versus time t. This method is difficult to apply in practice, because soil temperature maxima are not well defined, unless very shallow soil depths and very large temperature amplitudes are considered. WIERENGA et al. (1969) rewrote eq. (3.53) in finite difference form for different sets of depth intervals, obtaining a system of equations which could be solved for the thermal diffusivity a. They also determined a from the phase shift, i.e. eq. (3.57), and by plotting ln A(z) vs. depth, i.e. eq. (3.58). The results were found by Wierenga et al. to be quite comparable with each other and with calculations by eqs. (3.54) and (3.55). FEDDES (1971) approximated measured soil temperatures by the first six terms of a Fourier series and then attempted to determine a by plotting the amplitude and phase of the first harmonic versus depth. In his experiments he observed a clear dependence on depth of soil thermal properties. Such a trend was confirmed by direct determinations of $\rho_s c_s$, by the calorimetric method, and of λ_s, by the needle probe technique.

It should be realized that the advantage residing in eqs. (3.56) through (3.61) is their relative simplicity, which allows quick checks of data reliability, before more accurate (and more complicated) procedures are applied or before further interpretations are worked out.

P r o c e d u r e B. A different method to evaluate a was proposed by CHUDNOVSKII (1962, page 62), who applied the Green function of eq. (3.53). An average value of a can then be obtained from vertical temperature profiles measured at different time instants. A transformed temperature function T'(z',t') can be obtained from the actual T(z,t) by the substitutions:

$$z' = z - \tilde{z}, \quad t' = t - \tilde{t}$$

where $\tilde{z}$ and $\tilde{t}$ are particular depth and time values respectively. The following constraints apply to T'(z',t'):

$$\lim_{t' \to 0} T'(z',t') = 0$$

and

$$\lim_{z' \to 0} T'(z',t') = T(z_0,t - \tilde{t}) - T(z_0,\tilde{t})$$

These constraints plainly mean that $T'(z',t')$ should match the actual temperature profile at $t = \tilde{t}$ and that $T'(z',t')$ should match the actual temperature difference at two different times (i.e. $t,\tilde{t}$) at any depth (i.e. $\tilde{z}$). The required solution $T'(z',t')$ is:

$$T'(z',t') = \frac{z'}{2\sqrt{a\pi}} \int_0^{t'} T(0,\tau) - T(0,0) \cdot$$

$$\cdot \frac{\exp[-z'^2/4a(t' - \tau)]}{(t' - \tau)^{3/2}} \, d\tau \qquad (3.62)$$

From eq. (3.62) Chudnovskii obtained a suitable relationship to determine the thermal diffusivity by multiplying both sides of eq. (3.62) by dz' and integrating:

$$a^{\frac{1}{2}} = \frac{\pi \int_0^{\infty} \left[T(z',t') - T(z',0)\right] dz'}{\int_0^{t'} \frac{\left[T(0,\tau) - T(0,0)\right]}{(t' - \tau)^{\frac{1}{2}}} \, d\tau} \qquad (m \cdot s^{-\frac{1}{2}}) \qquad (3.63)$$

The numerator can be determined by graphical integration of measured temperature profiles, with z' varying from $z = 0$ to a depth where $T'(z',t') = 0$. The denominator requires further treatment. The actual soil temperature at depth $\tilde{z}$ can be described by a linear piecewise function $f(t') = b_i t' + b_{0i}$ for each interval (t'_{i-1}, t'_i). Then the denominator of eq. (3.63) can be split up in a number of terms relating to the time intervals (t'_{i-1}, t'_i), where b_{0i}, b_i can be calculated from the temperature record.

P r o c e d u r e   C. The Laplace transform of eq. (3.53) has been applied by van WIJK and de BRUIJN (1964) and by van WIJK and DERKSEN (1966) to derive the thermal diffusivity a. Mathematical constraints on the temperature record slightly different from those in Procedure B are required for the Laplace transform method. The initial values of the function $T'(z',t')$ must be equal to the initial actual soil temperature, instead of its limit as in the previous case. Furthermore $T'(z',t')$ must be zero at infinite depth; this condition was not required for eq. (3.62) and a corresponding approximation is accepted when calculating the denominator of eq. (3.63).

The most important difference between Procedure C and Procedure B (eq. 3.63) is that by the latter equation only a single value of a is obtained from temperature measurements at a number of depths. The eq. (3.63) namely requires the integration with depth of the temperature profile at different time instants,

while Procedure C allows to determine thermal diffusivity of different soil layers.

The eq. (3.53) is solved by the Laplace transform method, taking λ'_s and $(\rho c)'_s$ as constant. The solution found reads:

$$LT'(z',t') = B \exp -z'(p/a)^{\frac{1}{2}} \qquad (3.64)$$

where $T'(z',t')$ is the Laplace transform of the temperature record $T'(z',t')$ defined as:

$$LT'(z',t') = \int_0^{\infty} e^{-p\tau} T(z',\tau) d\tau \qquad (3.65)$$

where p is any positive number, while B is a constant depending on the heat flux at the surface. When eq. (3.64) is written down for two different depths, the following relationship can be obtained by dividing right and left hand sides:

$$\frac{LT'(z'_1,t')}{LT'(z'_2,t')} = \exp -(z'_1 - z'_2)(p/a)^{\frac{1}{2}} \qquad (3.66)$$

The method is most suitable for transient variations of soil temperature at different depths. Eq. (3.66) is valid for all values of p, therefore in principle any value of p can be used in eq. (3.65), but it has to be chosen according to the measured temperature records. The Laplace transform of a temperature record is calculated in practice by considering a finite time period, up to t', say. Accordingly the particular choice of p, affects the value of a as obtained by eq. (3.66). According to van WIJK and DERKSEN (1966) for daily fluctuations a suitable value is $p = 10^{-4} \, s^{-1}$.

The scope of Procedure C has been somewhat restricted by van WIJK and de BRUIJN (1964). They argued that the only transformation allowed on the time - depth temperature pattern is to reduce it to a zero initial value by subtraction of a constant. According to these authors such transformation is allowed because only a different zero of the measuring scale is implied.

The present author is convinced (see also CARSLAW and JAEGER, 1959) that the constraints on the temperature record can be fulfilled in a much more general class of cases, as discussed below. The point to be considered is that any solution of eq. (3.53) can be separated into a time-independent part and a time-dependent one with zero initial value.

A solution of the heat conduction equation in the form:

$$\frac{\partial^2}{\partial z^2} T(z,t) - \frac{1}{a} \frac{\partial T(z,t)}{\partial t} = S(z) \qquad (3.67)$$

where S is a source term, can be sought as:

$$T(z,t) = u(z) + w(z,t)$$

under the following conditions:

$$T(z,0) = f_1(z) \qquad \text{initially}$$
$$T(z,t) = f_2(z,t) \quad \text{at the surface}$$

The terms $u(z)$ and $w(z,t)$ are solutions of the following system, equivalent to eq. (3.67):

$$\frac{\partial^2}{\partial z^2} u(z) = S(z) \qquad (3.68)$$

with $u = f_1(z)$ initially and $u = 0$ at the surface; note that $\partial u/\partial t = 0$ and

$$\frac{\partial^2}{\partial z^2} w(z,t) - \frac{1}{a} \partial w(z,t)/\partial t = 0 \qquad (3.69)$$

with $w(z,t) = 0$ initially and $w(z,t) = f_2(z,t)$ at the surface; note that $\partial w(z,t)/\partial t = \partial(w + u)/\partial t = \partial T(z,t)/\partial t$.

When the time - depth pattern of soil temperature is measured, $T_m(z,t)$, the solution of eq. (3.67) is known by definition.

Since $T_m(z,t)$ is a solution of (3.67), $T'_m(z,t) = T_m(z,t) - T_{0m}(z)$ is another one, where T_{0m} is some initial value of $T_m(z,t)$. Thus, by substitution of $T'_m(z,t)$ in (3.67) and splitting the equation into the system:

$$\frac{\partial^2}{\partial z^2} T_{0m}(z) = S(z) \qquad (3.70)$$

$$\frac{\partial^2}{\partial z^2} T'_m(z,t) - \frac{1}{a} \frac{\partial}{\partial t} T'_m(z,t) = 0 \qquad (3.71)$$

Eqs. (3.70) and (3.71) operate under the same set of conditions as in the eqs. (3.68) and (3.69):

$$u = T_{0m}(z) \text{ initially and } u = 0 \text{ at the surface}$$

$$w(z,0) = T'_m(z,0) = T_m(z,0) - T_{0m}(z) = 0 \qquad \text{initially}$$

$$w(0,t) = T'_m(0,t) = T_m(0,t) - T_{0m}(0,0) \text{ at the surface}$$

Therefore eq. (3.66) can be applied to the estimation of the thermal diffusivity a, and the experimental problems originating from the requirement of a homogeneous initial soil temperature, as pointed out by van WIJK and DERKSEN (1966) and FEDDES (1971), can be overcome. The initial profile of $T'_m(z,t)$ is homo-

geneous by definition since:

$$T'_{0m}(z,0) = T_{0m}(z,0) - T_{0m}(z) = 0 \qquad (3.72)$$

It should be noted that any value of a as obtained from eq. (3.60), (3.63) or (3.66) may depend on the data-handling applied to a given set of measured temperatures. SINGH and SINA (1977) presented a method to calculate a, by specifying an analytical function to fit temperature data at the soil upper boundary. The choice of a particular function was shown to affect the inferred value of a.

The results of these approaches will be applied.

3.5.2. Extreme variations of soil thermal properties

Soil thermal conductivity λ_s is known to be quite sensitive to soil temperature, especially at intermediate moisture contents. Measured thermal conductivities at $25°C$ and $45°C$, a temperature range typical of desert conditions, vs. moisture content were presented by SEPASKHAH and BOERSMA (1979). At the higher temperature, λ_s was three times as large as the value at $25°C$. The effect of water flow on apparent thermal properties was studied by ERH et al. (1971), who observed a 2-fold increase in λ_s with a flow velocity varying from $3 \cdot 10^{-6}$ m·s^{-1} to $7 \cdot 10^{-5}$ m·s^{-1} at $30°C$. The same effect was hardly detected when the temperature was set at $10°C$. In many instances mass flow was accounted for by a mass enhancement factor, needed to match calculations to measurements. HADAS (1977a) reported a mass enhancement factor between 1 and 5, and suggested that free convection of soil air could have been responsible for the deviations. It is interesting to note in connection with the argument presented in Paragraph 3.4.4 that the largest deviations from the expected values were observed by Hadas in the early morning and late afternoon. It should also be recalled that an oscillating surface temperature induces pressure waves (see eqs. 3.46 and 3.48). This circumstance was pointed out by HADAS (1969), who noticed that the heat flux waves he produced also produced pressure waves with an amplitude of 22 mbar. Values of mass enhancement factors higher than 10 were reported by ROSE (1968).

A peculiarity of very dry soils is the possible influence of adsorbed water on the exchange of heat. The adsorbed phase may have an enthalpic content varying with the relative humidity of soil air. This property implies that the adsorbed phase can either store or release heat when the relative humidity of the soil air changes. The magnitude of this phenomenon can be evaluated for any soil, when its adsorption

isotherm and the proper relationship between enthalpy and relative humidity are known. This effect is likely to be relevant in playa soils, because of the particle size and the chemical interactions at the surface of particles and salt crystals. The basic thermodynamic quantities that relate to the process can be determined by laboratory experiments.

In order to show the variation in enthalpy of different soils, the results published by SHARMA et al. (1969) for a Molokai clay and by CARY et al. (1964) for a Milville loam will be used. In Fig. 3.17A the enthalpy of the adsorbed phase is presented as a function of the relative humidity of the soil air for the two soils mentioned. The difference between the two soils is striking and, as remarked by SHARMA et al. (1969), for the Molokai clay probably due to the chemical interaction between water and particles. It should also be noted that the two curves get close together and that they are nearly constant when relative humidity equals 0.6 or higher. Here the enthalpy is close to the latent heat of vaporization of pure free water. The different structure of the two soils is also evi-

dent in Fig. 3.17B where the corresponding adsorption isotherms are given. It is evident that the Molokai clay has a higher quantity of water in the adsorbed phase. In Fig. 3.17A the energy is given per mole of adsorbed water. To obtain the energy per unit volume of soil, the amount of vapour per unit volume of soil, i.e. the proper adsorption isotherm in Fig. 3.17B, and the soil bulk density also must be known. The corresponding curves in the Figs. 3.17A and 3.17B have been combined by the present author to obtain Fig. 3.17C. There the amount of heat stored in the adsorbed phase of water per unit soil volume is plotted as a function of the relative humidity. The different shape of the two curves implies an important difference in behaviour of the two soil types. When vapour is added to the soils, the Molokai clay releases heat, while the Milville loam stores heat. Since in both cases these heat amounts are not negligible, the heat capacity of such soils cannot be determined by considering only the sum of the volumetric heat capacities of the solid material, the water and the air as in eq. (3.54). The problem can be illustrated with the following example.
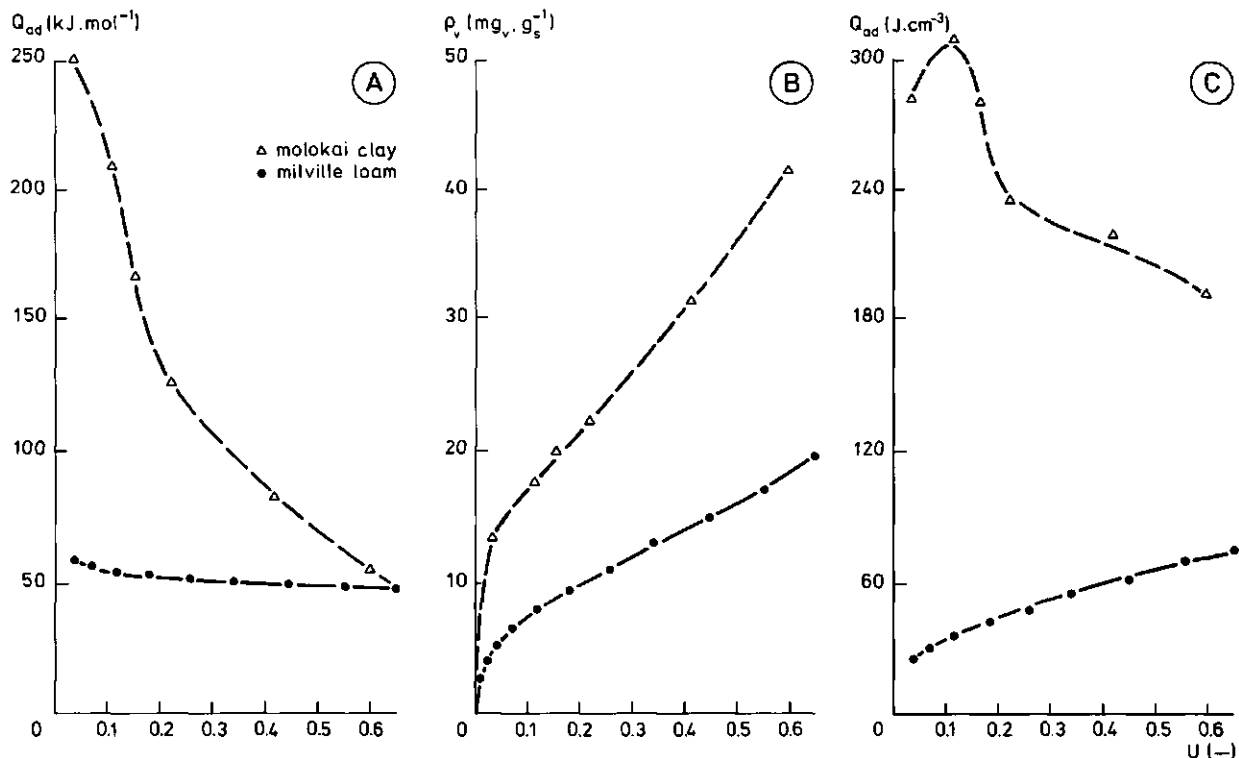
Fig. 3.17. A, enthalpy of adsorbed soil water Q_{ad} for Molokai clay (after Sharma et al., 1969) and Milville loam (after Cary et al., 1964) versus relative humidity U of soil air at equilibrium with water adsorbed in the particular soil sample; B, adsorption isotherms of these soils; C, enthalpy of adsorbed soil water Q_{ad} per unit soil volume, as calculated for each soil with the aid of the two figures at the left, plotted versus relative humidity U of soil air

It can be assumed that in an upper thin dry soil layer of 1 mm, say, the moisture content and temperature remain in equilibrium with surrounding air of varying relative humidity and temperature. Thus the enthalpy Q_{ad} of the adsorbed phase will change according to Fig. 3.17C. A reasonable daily range of relative humidity for desert climates is between 0.2 and 0.6. Accordingly over this range in Molokai clay an enthalpy amount $\delta Q_{ad} = 7.5 \cdot 10^4$ J·m^{-2} is released, while in Milville loam $\delta Q_{ad} = 2.9 \cdot 10^4$ J·m^{-2} is stored. To assess the effect of such heat amounts on soil surface temperature, in first instance the soil heat capacity is determined without taking the rôle of adsorbed water into account. Accordingly the soil heat capacity of both soils is estimated from eq. (3.54) as being $\rho_s c_s = 1.05 \cdot 10^6$ J·m^{-3}·K^{-1} with U = 0.2, and $\rho_s c_s = 1.2 \cdot 10^6$ J·m^{-3}·K^{-1} with U = 0.6. Thus some average value $\rho_s c_s = 1.1 \cdot 10^6$ J·m^{-3}·K^{-1} can be applied. A representative daily amplitude for the surface temperature can be chosen as being 30°C. Hence the heat amount released from the storage as defined by the heat capacity obtained from eq. (3.54) $\delta Q = \rho_s c_s \cdot \delta T = -3.3 \cdot 10^4$ J·m^{-2}, which figure must be compared with the $-7.5 \cdot 10^4$ J·m^{-2} and $+2.9 \cdot 10^4$ J·m^{-2} given above.

Since in Fig. 3.17A $Q_{ad} \cong L$ at high relative humidities it can also be concluded that at high relative humidities, i.e. at the evaporation front, the vapour is in equilibrium with free water. The use of eq. (3.7), therefore, has been correctly applied in Paragraph 3.3.3.

It will be understood that for some playa soils the contribution of the adsorbed phase to soil heat capacity must be taken into account. For sandy soils the effect depicted above is probably not relevant, because of their small specific surface. Thermodynamic properties of adsorption of water on quartz were studied by WHALEN (1961).

It was shown by FINK and JACKSON (1973) that to describe adsorption isotherms for a large number of soils one single analytical function can be applied.

3.5.3. Hydrological properties

As discussed in Section 3.2, the main problem in describing water flow is the proper and accurate determination of the soil hydrological properties which appear in eq. (3.2), i.e. the unsaturated hydraulic conductivity $\kappa(h)$ and the moisture retention curve $h(\theta)$. An overview of experimental methods can be found in textbooks on soil physics, see for instance MARSHALL and HOLMES (1979). A comprehensive review of available techniques to measure $\kappa(h)$ or $\kappa(\theta)$ was

presented by KLUTE (1972). Because of the inherently limited range of tensiometers, values of $\kappa(h)$ cannot be obtained at $|h| > 850$ cm, and more often than not, a value of 300 to 400 cm cannot be exceeded. The hot-air method proposed by ARYA et al. (1975) to measure $\kappa(\theta)$-curves, can in principle be applied to extend the θ-range. As remarked by EHLERS (1976), however, the method is less accurate than the usual evaporation - tensiometer method. Difficulties are to be expected when the total water diffusivity changes during each measuring run. The latter circumstance is most likely to occur in coarse as well as in structured soils, because of vapour flow at low moisture contents.

The meaning of the experimental determination of $\kappa(\theta)$ can be made clear on the ground of a statistical model for hydraulic conductivity as given by CHILDS and COLLIS-GEORGE (1950). The conductivity at a given saturation is calculated from a distribution function assigning the probability that water in a given pore size class crosses an infinitesimal porous slab either by changing to a different pore size class or staying in the upstream one. According to this concept a measured $\kappa(h)$ specifies for any given saturation the integral of that distribution function.

It appears that when the general mathematical form of any model for hydraulic conductivity can be specified, experimental difficulties can be reduced because of the fewer degrees of freedom in $\kappa(h)$. Different equations for hydraulic conductivity have been proposed in literature.

For the purpose of the large scale hydrological study here being reported variability of hydrological properties is a most relevant problem. It appears that when the $\kappa(h)$ and $h(\theta)$ curves have to be measured as such for each soil type in the area, the experimental work needed is not feasible. It must also be noted that at field scale an intrinsic variability of hydrological soil properties exist, even in homogeneous soils as shown by NIELSEN et al. (1973).

To define a common reference for the hydrological properties of the different soils in the study area three possible main approaches can be distinguished:

- assume that the $\kappa(h)$ and $h(\theta)$ for any given soil are proportional to the properties of a standard reference medium (similar media concept);
- derive a general expression for a class of statistical models for hydrological properties;
- apply for simplified boundary conditions an analytical solution of the θ-dependent diffusion-type equation (eq. 3.3).

Results obtained according to the first approach can be found in REICHARDT et al. (1972) and WARRICK et al. (1977). The second approach was applied by MUALEM (1976) to some 45 soils, while the theoretical generalization was presented by MUALEM and DAGAN (1978). Many examples of the third approach can be found in the literature. BRUTSAERT (1979), following earlier work of BRUTSAERT (1976), suggested that a number of the known solutions can be reduced to one single (universal) expression. Later the same author (BRUTSAERT, 1981) restricted the scope of the preceding results, however, by suggesting that the constants involved in the expression given for $\kappa(\theta)$ were not 'universal', but varying over a certain but limited range.

The effect of the variability at field scale of soil hydrological properties on the soil water balance has been presented by BRESLER et al. (1979).

Of importance might be the hysteresis in the $h(\theta)$ relationship. Sandy soils have a small specific surface, but hysteresis is due to pore geometry. The experimental field data on fine sand presented by ROYER and VACHAUD (1975) show considerable effects. In Fig. 2 of their paper a hysteretic loop is presented with the main drying and wetting branches closing up at a capillary pressure head of -400 cm. This loop is wider than in other results for finer soils with much larger specific surface also presented by them. The reliability of the hysteretic $h(\theta)$ relationship shown by Royer and Vachaud is questionable as the drying branch appears to be drawn from only two data points. To be complete it must be recalled that adsorption isotherms also may be hysteretic as shown by CARMAN and RAAL (1951), JACKSON (1964c).

In the present author's opinion κ-values can only be accurately measured and safely applied to playa desert conditions, in the wet range of moisture content. In this range κ-values, as obtained in the laboratory at $20^\circ C$ and solute concentration $\chi_i = 0$, can be corrected to account for the effect of temperature and salt concentration on the liquid phase of water.

For a fine textured soil, salts induce permanent modifications in hydraulic conductivity because of the displacement of clay particles. This is most likely primarily due to clogging of a certain percentage of pores. The reduction of hydraulic conductivity may be irreversible as has been shown by the experimental results of DANE and KLUTE (1977). The effect may even be important in sandy soils as shown by PUPISKY and SHAINBERG (1979). In the present investigation it was assumed that salt effects on soil structure were irreversible, and accounted for by measurements perform-

ed on undisturbed soil columns, while differences in fluid properties between laboratory and field conditions were taken into account.

As shown in Paragraph 3.2.1 the curves $\kappa(h)$ and $h(\theta)$ depend on fluid properties, i.e. density ρ, viscosity η and surface tension σ, which in turn depend on temperature T and solute concentration χ_i. According to eqs. (3.8) and (3.9) the relevant derivatives, written in shorthand, are:

$$\frac{\partial}{\partial T, \chi_i} \frac{\rho_w}{\eta_w} \quad \text{and} \quad \frac{\partial}{\partial T, \chi_i} \frac{\sigma_{wa}}{\rho_w} \tag{3.73}$$

which can explicitly be written in terms of variations as:

$$\frac{\partial}{\partial T, \chi_i} \frac{\rho_w}{\eta_w} \doteq \left[(\eta_w \delta_T \rho_w - \rho_w \delta_T \eta_w) + (\eta_w \delta_{\chi_i} \rho_w - \rho_w \delta_{\chi_i} \eta_w) \right] /$$

$$\eta_w^2 \tag{3.74}$$

and

$$\frac{\rho_w h}{\sigma_{wa}} \left[\frac{\partial}{\partial T} \frac{\sigma_{wa}}{\rho_w} + \frac{\partial}{\partial \chi_i} \frac{\sigma_{wa}}{\rho_w} \right] \doteq$$

$$\doteq \frac{h}{\rho_w \sigma_{wa}} \left[(\rho_w \delta_T \sigma_{wa} - \sigma_{wa} \delta_T \rho_w) + \right.$$

$$\left. + (\rho_w \delta_{\chi_i} \sigma_{wa} - \sigma_{wa} \delta_{\chi_i} \rho_w) \right] \tag{3.75}$$

As shown by eqs. (3.74) and (3.75) it is misleading to account only for effects due to variations in one or two of the fluid properties ρ_w, η_w, σ_{wa}. An example will be given, but it will be seen that variations with temperature compensate each other, while the net effect of the solute concentration depends on the particular type of solute. For inorganic solutes the values of the properties ρ_w, η_w and σ_{wa} of the solution increase with increasing concentration, but decrease with increasing temperature. So there will be a compensation between the effect of temperature and solute concentration. For organic solutes, both derivatives in eq. (3.73) will change in the same direction according to eqs. (3.74) and (3.75). A meaningful variation of h and $\kappa(h)$, therefore, would occur at lower solute concentrations than for inorganic solutes. Organic solutes are of no importance in playa soils, however.

To show according to eqs. (3.74) and (3.75) the magnitude of variations in $\kappa(\theta)$ an example will be given. Cases will be considered with temperatures respectively equal to $20^\circ C$ and $50^\circ C$, and solute concentrations being zero and equal to the value at saturation. As solute NaCl will be considered with $\chi_i =$

Table 3.3. Density ρ, viscosity η and surface tension σ of pure water and of a NaCl-saturated solution at 293 and 323 K. In the rightmost column, the average variation of the unsaturated hydraulic conductivity $\kappa(\theta)$ is given

Case	T (K)	χ_i (mol·l⁻¹)	ρ_w (kg·m⁻³)	η_w (N·s·m⁻²)	σ_{wa} (N·m⁻¹)	$\dfrac{\kappa_i(\theta)}{\kappa_A(\theta)}$
A	293	0	$0.9982 \cdot 10^3$	$1.005 \cdot 10^{-4}$	$7.275 \cdot 10^{-2}$	A/A = 1
B	323	0	$0.9888 \cdot 10^3$	$0.55 \cdot 10^{-4}$	$6.791 \cdot 10^{-2}$	B/A = 1.9
C	293	6	$1.273 \cdot 10^3$	$1.63 \cdot 10^{-4}$	$8.698 \cdot 10^{-2}$	C/A = 0.85
D	323	6	$1.13 \cdot 10^3$	$1.09 \cdot 10^{-4}$	$8.214 \cdot 10^{-2}$	D/A = 1.1

6 mol·l^{-1} at saturation. Values of ρ_w, η_w, σ_{wa} for each case are given in Table 3.3. As a reference the $\kappa(\theta)$ given for fine sand by RIJTEMA (1969) will be taken. The results for the cases A through D are shown in Fig. 3.18. It must be noted that the ratio of $\kappa(\theta)$ for case D and reference case A (laboratory conditions) is 1.1 only, instead of 1.9 which would have been found by accounting only for the effect of T on ρ_w, η_w and σ_{wa}. The change in $\kappa(\theta)$ is higher than as estimated by accounting only for the reduced viscosity at the higher temperature. As shown in Table 3.3 for $\delta T = 30°C$, $\delta\eta_w = -0.456 \cdot 10^{-4}$ N·s·m^{-2}, thus the term $\rho_w g K / \eta_w$ in eq. (3.8) will increase with a factor $\delta\eta_w/\eta_w$ or with 45%. This latter percentage must be compared with the 90% as in the η_w-ratio (A - B)/B.

WEEKS et al. (1968) gave the 'golden number' of 1.61 as a coefficient to apply to $\delta\eta_w/\eta_w$ to obtain the actual correction to be applied to $\kappa(\theta)$ to account for temperature variation. These authors did not give reasons for the 1.61 correction but referred to personal communications with Doering and Gardner. According to these authors one should, therefore, multiply $\delta\eta_w/\eta_w = 0.45$ with 1.61 giving 0.72. This result is somewhat closer to the 0.90 mentioned above and it indicates a likely origin of the 'golden number'.

From Fig. 3.18 the maximum range for the correction on $\kappa(\theta)$ for the NaCl saturated solution can be estimated: the correction will not be larger than -14% at 20°C and -10% at 50°C.

3.6. CRITICAL GROUNDWATER TABLE DEPTH FOR EVAPORATION

The relevance of a number of water transfer processes has been discussed in detail in the preceding sections. Here it will be discussed how these different processes of different phases of water combine.

As specifically relevant to the goal of the present investigation, it will also be discussed whether it is possible or not to establish the maximum groundwater table depth at which a specific evaporation rate still occurs in playas. Accordingly a few comments will be given on:

- published results of field experiments showing the complex physical aspects of water flow in nearly dry soils;
- suitable range of water contents and the approach for the determination of water fluxes;
- possibility of mutual enhancement between different water transfer processes.

Water flow in the top, drying, soil layer was observed by JACKSON et al. (1973) to be a very dynamic process both in intensity and direction. In this respect the possible relationship with the high frequency of variation in turbulent heat and vapour flux in the atmospheric surface layer must be mentioned here (see also Section 7.6). Variability in time gradually dis-

Fig. 3.18. Variations of the unsaturated hydraulic conductivity of fine sand due to variations of temperature T and salt concentration χ_i; for the definition of the cases A, B, C, D, see Table 3.3

appeared at deeper depths and the drying rate tended to a constant value. The same data also indicated three different drying stages in relatively thin upper soil layers.

The three stages can be characterized according to the varying evaporation rate: potential evaporation rate in the first stage, decreasing evaporation rate in the second one and finally a low, relatively constant rate in the third stage. The transition between the different stages has been established by IDSO et al. (1974) by measuring surface reflectance. The conclusion which can be drawn is that calculating water fluxes in the top soil layer proves to be a more demanding task than measuring the fluxes themselves. This statement can be supported by referring to data and procedures presented by JACKSON et al. (1974).

In playa soils where the groundwater table depth is 1 m or deeper, water transfer processes as described by eqs. (3.46), (3.13) and (3.2) occur simultaneously and at different soil depths. It must, therefore, be established to which extent they enhance

each other. In a soil profile where water content changes from saturation to air dryness, one should think of a series type combination of flow mechanisms. The final result of the assessment is a critical depth for a given water flow rate. Note that when the proper sequence (with depth!) of equations is established, it can also be decided which process is the rate-limiting one under the given conditions.

A qualitative example can be given by applying eq. (3.46) for convective air flow, eq. (3.13) for vapour diffusion, and eq. (3.23) for liquid flow by capillary rise. If it is assumed that pressure in eq. (3.46) and vapour concentration in eq. (3.13) change linearly with z, the maximum depth corresponding to a given gradient and flux can be estimated. Namely eq. (3.46) can be rewritten as:

$$\delta z_{conv} \quad - \frac{\kappa_a \delta (R_a \rho_a T_{vi})}{v_{za}} \quad \text{(m)} \tag{3.76}$$

The virtual temperature difference is obtained from the difference in vapour pressure between the
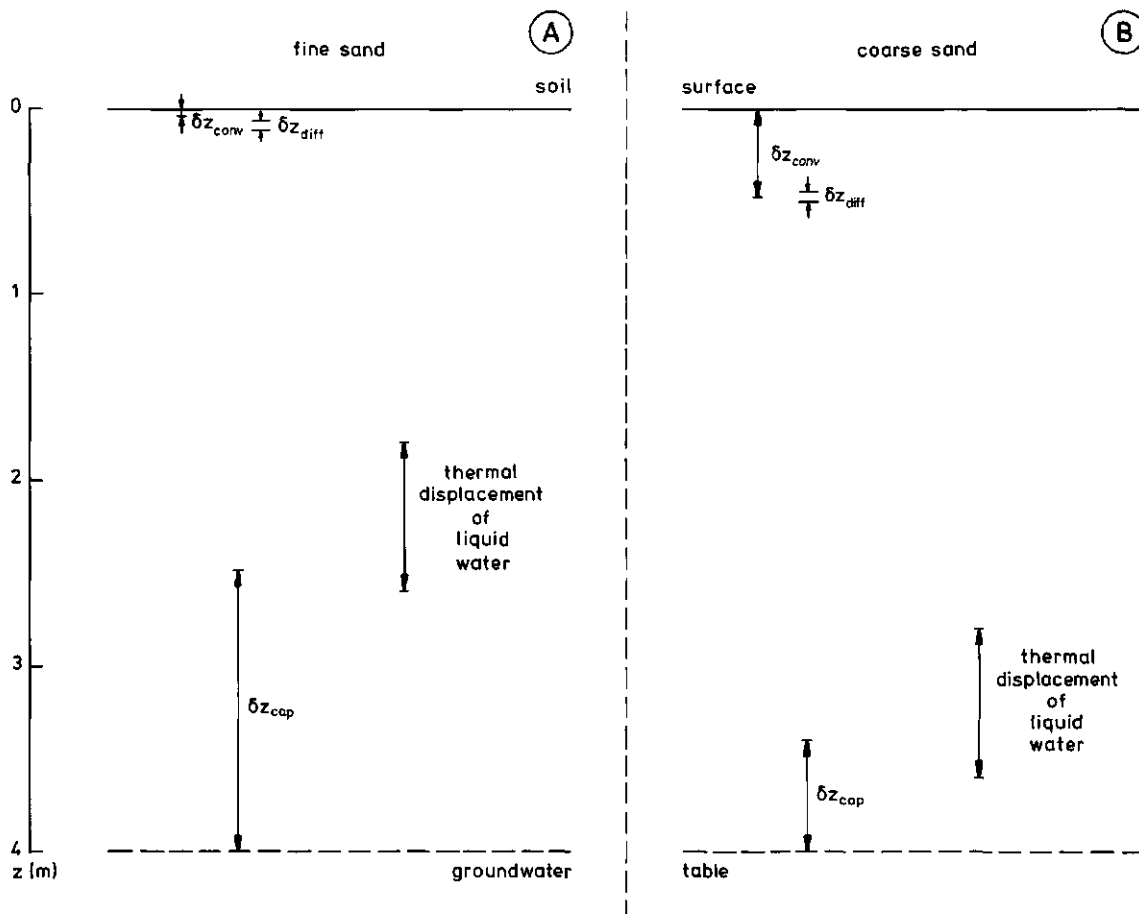
Fig. 3.19. Combination of different moisture transfer processes at different depths in A, a fine sand and B, a coarse sand. For symbols, see text

evaporation front and the air above soil surface.

Eq. (3.13) can be rewritten as:

$$\delta z_{dif} = - \frac{D_v \delta \rho_v}{q_v} \quad (m) \quad (3.77)$$

When temperature, air relative humidity and vapour flux are assigned, eqs. (3.23), (3.76) and (3.77) can be applied to establish whether or not the assigned q_v will actually reach the soil surface. The condition to be fulfilled is:

$$\delta z_{dif} + \delta z_{conv} + \delta z_{cap} = \tilde{z}_{gw} \quad (m) \quad (3.78)$$

where $\tilde{z}_{gw}$ is the critical groundwater table depth. In Fig. 3.19A a fine sand (RIJTEMA, 1969; κ_{sat} = 0.5 m·d^{-1}, or K = 5.9·10^{-13} m^2) is considered with z_{gw} = 4 m, T = 303 K, U = 0.4 and q_v = 1.16·10^{-5} kg·m^{-2}·s^{-1} or E = 1 mm·d^{-1}. The maximum distance from the groundwater table where that flux can be maintained by capillary rise is 1.5 m. Since eq. (3.76) yields δz_{conv} = 2.2·10^{-2} m and eq. (3.77) δz_{dif} = 3.9·10^{-2} m, the critical depth according to eq. (3.78) is 1.56 m. In Fig. 3.19B the corresponding results for coarse sand (RIJTEMA, 1969; κ_{sat} = 11.2 m·d^{-1}, or K = 1.3·10^{-11}) are shown. For coarse sand δz_{cap} = 0.6 m, δz_{dif} = 3.9·10^{-2} m and δz_{conv} = 0.48 m, thus the critical $\tilde{z}_{gw}$ = 1.12 m. It is understood that cracks in the top soil layer may dramatically increase δz_{conv}. Because of the many assumptions involved in the presented reasoning the meaning of Fig. 3.19, which gives an indication of the transfer processes, is essentially qualitative. This figure, however, helps in pointing at a possible rôle of thermal liquid transport during the yearly warming - cooling cycle. For the given z_{gw} = 4 m both Fig. 3.19A and 3.19B show that a flux of 1 mm·d^{-1} from the groundwater table cannot be maintained from diffusion, soil air convection and capillary rise alone ($\tilde{z}_{gw} < z_{gw}$). However, eq. (3.5) with δT_s = $(\partial T_s/\partial z)\delta z$ shows that a temperature gradient induces thermal liquid flow. Hence eq. (3.5) describes liquid waves induced by traveling temperature waves. Even if velocities are low, displacement of water becomes important because it may fill the gap between $\tilde{z}_{gw}$ and z_{gw}. In other words to establish the critical depth for a mean moisture flux the thermal displacement of liquid water must also be estimated. According to ROSE (1968) the velocity of thermal liquid flow is somewhere between 10^{-7} and 10^{-8} m·s^{-1} for the daily temperature wave. When the same velocity is assumed for the yearly wave, the displacement in a half-period will be from 0.16 to 1.6 m, such a value should be added to the critical depths previously given.

When the groundwater table is very deep as in

the outcropping water bearing formations of the West-Libyan aquifer (see Section 1.3), the critical depth as established above will be a negligible quantity. Then, however, surface diffusion of the adsorbed water can still build-up losses by evaporation which may be comparable with the accuracy (see Section 1.1) required in the calculation of the aquifer water balance.

3.7. FEASIBILITY OF OTHER THEORETICAL APPROACHES

As a concluding remark, it is pointed out that two other theoretical approaches could have been developed along the same lines as followed in this chapter. Traveling wave solutions could have been sought to a diffusion-like equation as in CRANK (1956), Chapter 13, eq. (13.16). In the notation used by the present author, in the mentioned equation of Crank the independent variable is the linear combination $(c_1 \chi_v + c_2 T_a)$, quite similar to the virtual temperature as applied in Section 3.4 to describe soil air flow. The Crank equation describes the simultaneous transport of heat and moisture.

Another possibility would have been to derive steady state solutions for flow in more complex force fields, as shown by SMIRNOFF and HRIBAR (1970)

The difficulty with both approaches is that the independent variable cannot directly be measured, as it is possible to do with surface temperature. It therefore was decided to make use of the apparent thermal properties as defined by eq. (3.53) to account for the combined transport of heat and moisture. Building on this concept, the approach, presented in Chapter 4, has been developed.

3.8. SUMMARY

To illustrate the necessity for the analysis of heat and water flow processes, as given in the present chapter, the peculiar characteristics of playa soils and playa environment were recalled.

For the approach presented in Chapter 2 to be feasible, two successive results had to be achieved. A suitable definition of evaporation front had to be established and furthermore the heat and water transfer coefficients between the evaporation front and the soil surface had to be determined.

After having given an outline of the difficulties to be overcome, the approach to be followed in the present report was briefly summarized.

In Section 3.2 it was pointed out that the equa-

tions as usually applied to describe water flow, draw their reliability from experimental evidence. The relationship between water flow rate, soil temperature and salt concentration was discussed and equations to account for differences in soil temperature and salt concentration between field and laboratory conditions were derived.

These equations were used in Section 3.5 to derive equations to correct soil hydrological properties as measured in the laboratory.

As discussed in Paragraph 3.2.2 a main difficulty in dealing with water flow in a relatively dry soil is the difficult separation between liquid and vapour flow. Neither theory nor experiments yield a clear cut threshold marking the transition from liquid to vapour flow. This conclusion is of obvious relevance in the process of establishing a definition of the evaporation front. The conclusion drawn in Section 3.2 was that in playa soils reliable predictions of water flow can only be obtained close to the water table (liquid flow) and in the top soil (vapour flow). In Section 3.3 a new definition of the evaporation front was given.

It was shown that under constant drying conditions both the shape of the water content profile and the intensity of phase transition inside the soil, depend on the typically hooked shape of the moisture diffusivity $D(\theta)$. Such a shape arises from the contribution at low water contents of the vapour diffusivity $D_v(\theta)$. It was shown that the equivalent pore radii corresponding to these low water contents are comparable with the mean free path of water vapour. In such small pores vapour flow will be of the Knudsen-type rather than of the Fick's diffusion type.

An important conclusion reached in Section 3.3 was that the shape of $D_v(\theta)$ implies that, at a given moisture content, only a particular class of pores contributes to vapour flow. An example was worked out to show that the equation proposed by the present author to estimate $D_v(\theta)$ yields values of the proper order of magnitude. The pitfall in that equation is that pore size distributions at very small radii ($<10^{-7}$ m) cannot yet be determined with the presently existing experimental techniques.

Finally the evaporation site was defined as corresponding to pores of radius comparable with the mean free path of water vapour.

In Chapter 5 it will be shown how the definition of evaporation sites facilitates the calculation of the partition of the available radiative flux into the latent and sensible heat flux. In Chapter 8 a specific example of application will be presented by mapping the areas of subsurface evaporation from satel-

lite data. In Chapter 8 it also will be shown that the measured values of actual evaporation confirm the theoretical conclusions on the possibility of vapour flow being contrary to heat flow.

In Section 3.4 the contribution of soil air convection to heat transport in the top layer of playa soils was discussed.

It was shown that literature data on actual evaporation rate from crack openings indicate that the measured rates cannot be explained by vapour diffusion only. A few simplified equations have been given to describe convection of soil air in the top soil above the evaporation front. It was emphasized that a great deal of conceptual schematization is implied in the two-layer plus interface model of heat transfer in playa soils. In this scheme, the evaporation front is considered to be the lower boundary of a porous slab, with the soil surface as upper boundary. Within this slab thermal convection may arise and a one-dimensional model was proposed, by specifying to which part of the thermal convective coil it applies. It was shown that at the high soil temperatures present in deserts, the decrease in soil air density due to the presence of water vapour is large enough for flows of heat and vapour to be of contrary direction. The conditions for this phenomenon to happen were specified. The relationship between the liquid - vapour phase transition and the corresponding vapour velocity was discussed as a mechanism for enhanced evaporation.

Finally it was pointed out that bulk soil thermal properties should be termed 'effective', in absence of vapour and liquid water movement, since they account for the overall contribution of an extremely complicated system. When fluid convection takes place in a soil of which the bulk thermal properties are intended to be determined by experiments, the soil thermal properties should be termed 'apparent'. A simplified equation was derived to calculate the apparent soil thermal conductivity, which accounts for both the conductive and convective contribution. It was shown that in soils having a relatively high specific permeability, as cracked playa surfaces, the convective term is the most important one.

The equation for the apparent soil thermal conductivity will be applied in Chapter 8 to calculate first the soil heat flux and next the actual soil evaporation by means of the methods presented in Chapter 2. In Chapter 4 it will be shown how to account for the effect of the thermal convective slab concept on the apparent soil thermal admittance as defined at the soil surface.

In Section 3.5 three procedures to determine the apparent soil thermal diffusivity from soil tempera-

ture measurements were described. On the basis of
literature data the rôle of extreme variations in soil
thermal properties was briefly discussed. In particular
it was shown that large deviations have been observed
of the dependence of vapour pressure on temperature
in comparison with the expected behaviour of vapour in
equilibrium with free water. The favourable conclusion
was reached that under the conditions applying to the
evaporation site, as defined in Section 3.4, anomalies
have not been found. The equations given in Section
3.2 have been elaborated to give an actual example of
the extent to which soil hydrological properties change
with temperature and salt concentration of the soil
liquid phase.

In Section 3.6 the critical groundwater table
depth for a specific soil evaporation rate under steady
state conditions, has been defined by combining, in a
somewhat qualitative manner, the flow processes de-
scribed in Chapter 3. At a particular actual evapora-
tion rate this critical depth has been evaluated for
two specific soil types.

Finally, in Section 3.7, the feasibility of other
theoretical approaches to define apparent soil proper-
ties to account for the combined transport of heat and
vapour has been discussed, with negative result.

4. FREQUENCY DEPENDENT APPARENT SOIL THERMAL ADMITTANCE

*'... per solitudines nigri pulveris, eminentibus interdum velut exustis cautibus, loca
inhabitabilia fervore, quamquam hiberno tempore experto.'*

4.1. HEAT FLUX AT THE SOIL SURFACE

4.1.1. General

After the analysis presented in Chapter 3, it is
clear that the heat flux in the top soil layer must
be known, if evaporation is to be determined when it
takes place inside the soil.

According to the conclusions reached in the sec-
tions 3.2, 3.3 and 3.4 a number of transfer processes
are effective in the simultaneous transport of heat
and moisture in the top soil layer. The most common
method of measuring the soil heat flux by plate trans-
ducers may prove to be inaccurate, because of distur-
bances induced by the transducers in the flow regime.
How important the error can be, is easily shown by
the equation given by PHILIP (1961) for the ratio of
the heat flux through a transducer, G_{me}, over the ac-
tual flux in the soil, G_s. For thin plates, i.e. of
a thickness much smaller than the other dimensions,
the equation reads:

$$\frac{G_{me}}{G_s} = \frac{1}{1 - b(1 - r^{-1})} \qquad (-) \qquad (4.1)$$

where b is a constant equal to 1.7 times the ratio of
mean transducer thickness in the flow direction to
the square root of the transducer mean cross section
normal to the flow direction. The value of 1.7 implies
that transducer shape is assumed to be that of an ob-
late spheroid. The variable r in eq. (4.1) stands for
the ratio of transducer to soil thermal conductivity.
It should be noted here that the relationship between
the apparent thermal conductivity λ_s' and the thermal
convective velocity v_{za} (eq. 3.45) implies that a
variable time dependent correction, i.e. by eq. (4.1),
should be applied to measured soil heat fluxes.

Procedures to calibrate soil heat flux plates
were described by PORTMAN (1958), FUCHS and TANNER
(1968), OVERGAARD MOGENSEN (1970), CARY (1971), HANKS
and TANNER (1972) and IDSO (1972).

It has already been noted in Chapter 3 that of

the soil thermal properties involved in the heat con-
duction equation, only the heat capacity can be mea-
sured independently from the equation itself. Thus it
appears that better measurements of the heat flux
could be achieved by determining variations in the
heat content, or at least in soil temperatures. Such
a calorimetric method was proposed by HANKS and TANNER
(1972) in combination with the use of heat transducers
deeply placed in order to reduce differences in ther-
mal conductivity between transducer and top soil. A
similar method was applied by KIMBALL and JACKSON
(1975).

According to Chapter 3 it must be recalled that
the theory presented by PHILIP (1961) (see eq. 4.1),
which is based on an equation given by CARSLAW and
JAEGER (1959, page 427), relates to a purely conduc-
tive temperature field. The latter condition implies
that the transport of latent heat is not taken into
account, since this transport is not proportional to
the temperature gradient. In a conduction-like equa-
tion vapour flow can be accounted for by introducing
an apparent thermal conductivity (see eq. 3.53).

Use of soil heat transducers in relation to wa-
ter vapour flow was studied by CARY (1979). The ac-
tual heat flux through a soil slab was measured by a
calorimeter along with the temperature at both sides
of the slab. He compared values of thermal conductiv-
ity as obtained from these heat flux and temperature
measurements, with results obtained by different pro-
cedures, namely heat flux plate, transient (needle)
thermal conductivity probe and the calculation method
presented by de VRIES (1963). The conclusion reached
by Cary was that all three methods tend to give too
low values of the thermal conductivity. Note that,
because of possible differences in the flow regime,
even the value found by the calorimeter is not nec-
essarily the same as would apply to the same soil
under field conditions. A last remark is due about
the method presented by HANKS and TANNER (1972). This
method relies on the concept that heat capacity can
be calculated with pretty good accuracy from soil

composition and moisture content. However, in a rather dry soil water in the adsorbed phase may eventually play an important rôle as was shown in Paragraph 3.5.2. Thus one should also be careful in determining the heat flux in the top dry soil layer from temperature and calculated heat capacity (eq. 3.54). Some additional details and references about the methods described can be found in BRUTSAERT (1981).

The rationale for presenting the remarks above, was to show that suitable determination of the heat flux at the soil surface can be achieved by applying two different methods. The first possibility would be to go deep into the microphysical aspects of both flow processes in pores and surface phenomena. Some kind of a 'more exact' equation in principle could be written down and the properties included in it measured. The large amount of scientific literature appears to suggest that this approach would not be an easy task. The second possibility is to include implicitly the microscale aspects of the flow mechanism in simpler equations. The overall rôle of microscopic processes can then be accounted for by 'apparent' thermal properties such as the thermal diffusivity a, which comes out of the procedures described in Paragraph 3.5.1. Difficulties can be expected only when these properties are to be applied in a heat conduction equation with a scale different from that applied to estimate thermal diffusivity a. The second approach has been chosen in the present paper.

4.1.2. Thermal admittance of a semi-infinite homogeneous soil

For the purpose of the present investigation it would be very convenient to establish an explicit relationship between surface temperature and heat flux into the soil. Such a relationship can be sought in the form:

$$G_0(t) = y_0 T_0(t) \tag{4.2}$$

with y_0 being termed thermal admittance, because of the resemblance of eq. (4.2) with the relationship between voltage and electric current. To find a relationship between G_0 and T_0 a traveling wave solution of eq. (3.53) can be sought. Traveling wave solutions of a wide class of physical problems have been found. Solutions relating to saturated - unsaturated flow were presented by NAKANO (1980) and to water and air flow by NAKANO (1981).

A traveling wave solution of eq. (3.53) will be sought in the form:

$$T(z,t) = A_0 \exp(b_1 + ib_2)z \exp i(\omega t - \Omega) \tag{4.3}$$

For A_0 see eq. (3.58). By substitution in eq. (3.53), it is found that:

$$b_1 = b_2 = \pm(\omega/2a)^{\frac{1}{2}} \tag{4.4}$$

Note that $(2a/\omega)^{\frac{1}{2}}$ is the damping depth as defined in eq. (3.59).

The most general form of eq. (4.3) is a linear combination of two terms for positive and negative values of b_1 and b_2, which reads:

$$T(z,t) [\exp i(\omega t - \Omega)]^{-1} = c_1 A_0 \exp -(b_1 + ib_2)z +$$
$$+ c_2 A_0 \exp(b_1 + ib_2)z \tag{4.5}$$

By recalling the definitions of sinh, cosh and with the notation $b_1 + ib_2 = (1 + i)(\omega/2a)^{\frac{1}{2}} = \gamma$ eq. (4.5) can be rewritten as:

$$T(z,t) [\exp i(\omega t - \Omega)]^{-1} = c_1 A_0(\cosh \gamma z - \sinh \gamma z) +$$
$$+ c_2 A_0(\cosh \gamma z + \sinh \gamma z) \tag{4.6}$$

or, with $(c_1 A_0 + c_2 A_0) = C$ and $(c_2 A_0 - c_1 A_0) = D$:

$$T(z,t) [\exp i(\omega t - \Omega)]^{-1} = C \cosh \gamma z + D \sinh \gamma z \tag{4.7}$$

The heat flux in the soil is, by definition:

$$G(z,t) = -\lambda \frac{\partial T(z,t)}{\partial z} \tag{4.8}$$

and, according to the expression given for $T(z,t)$ in eq. (4.7):

$$G(z,t) = -\lambda\gamma(C \sinh \gamma z + D \cosh \gamma z)\exp i(\omega t - \Omega) \tag{4.9}$$

In the expressions given for $T(z,t)$, $G(z,t)$ a homogeneous medium with thermal diffusivity a has been assumed. Now to determine C and D two boundary conditions have to be specified. As a first step a semi-infinite soil will be considered having a harmonic temperature wave at the upper boundary, and a heat flux $G(z,t)$ damping out with depth z. The two boundary conditions can respectively be written as:

$$T(0,t) = A_0 \exp i(\omega t - \Omega) \tag{4.10}$$

and

$$\lim_{z \to \infty} G(z,t) = 0 \tag{4.11}$$

By substitution of eq. (4.7) for $T(z,t)$ in eq. (4.10) and of eq. (4.9) for $G(z,t)$ in eq. (4.11) and recalling that $\lim_{z \to \infty} \sinh z = \lim_{z \to \infty} \cosh z = \infty$, it can be found that $C = A_0$ and $D = -C = -A_0$.

When these results are substituted in eqs. (4.7) and (4.9) it is found:

$$T(z,t) = A_0(\cosh \gamma z - \sinh \gamma z) \exp i(\omega t - \Omega) \quad (4.12)$$

and

$$G(z,t) = \lambda \gamma A_0(\cosh \gamma z - \sinh \gamma z) \exp i(\omega t - \Omega) \quad (4.13)$$

Now the flux $G(z,t)$ can be written by substitution of eq. (4.12) as:

$$G(z,t) = \lambda \gamma T(z,t) \quad (4.14)$$

The complex variable $\lambda \gamma$ can by definition of γ be written as:

$$\lambda \gamma = \lambda(1 + i)(\omega/2a)^{\frac{1}{2}} \quad (4.15)$$

or

$$\lambda \gamma = (1 + i)(\lambda \rho c \omega/2)^{\frac{1}{2}}$$

and finally:

$$\lambda \gamma = (2\pi \lambda \rho c/P)^{\frac{1}{2}} \exp i\pi/4 \quad (4.16)$$

Because of the analogy between eq. (4.14) and the relation between current and voltage in electric circuits (CARSLAW and JAEGER, 1959, page 69), the parameter $(2\pi \lambda \rho c/P)^{\frac{1}{2}} \exp i\pi/4$ can be defined as the thermal admittance y ($W \cdot m^{-2} \cdot K^{-1}$). The term $\exp i\pi/4$ accounts for the phase shift between flux and temperature waves of period P, while the modulus $(2\pi \lambda \rho c/P)^{\frac{1}{2}}$ accounts for the ratio between the amplitudes. Therefore eq. (4.14) can be written for the soil surface as:

$$G_0(t) = y_0 T_0(t) \quad (4.17)$$

which has the form required by eq. (4.2) with y_0 being the thermal admittance at the surface of a semi-infinite homogeneous soil.

It should be noted that the thermal admittance y_0 appears to be a handy synthesis of the heat conduction equation (3.53) and of the boundary conditions eqs. (4.10) and (4.11). It also appears that the explicit dependence of y_0 on the frequency of the applied temperature wave ω does not bring too much trouble. Namely, the time behaviour of the soil temperature can be described with good accuracy by the first few terms, n say, of a Fourier series. Thus the follow-

ing relationship between the fluctuations of temperature and heat flux at the soil surface can be given:

$$G_0(t) = \sum_{1}^{n} j y_j A_j \exp i(\omega_j t - \Omega_j) \quad (4.18)$$

where the index j relates to the harmonic of frequency ω_j. Eq. (4.18) has been obtained in a simple way by writing eq. (4.17) at different temperature wave frequencies ω_j with $T_0(t)$ given by eq. (4.10) and then by summation of, respectively, right and left hand sides. It is understood that the thermal admittance can be calculated from eq. (4.16) for any frequency ω_j, when thermal conductivity λ and heat capacity ρc are known. Therefore eq. (4.18) allows for calculating the heat flux at the soil surface from the first n terms of a Fourier series approximating the surface temperature $T_0(t)$.

The close interrelation between evaporation, soil heat flux and vertical homogeneity of soil thermal properties has been discussed in detail by FUCHS and HADAS (1972). These authors applied a harmonic analysis of measured soil heat flux and temperature at different depths to determine the thermal properties of an inhomogeneous soil under wet and dry conditions. By means of substitution in the heat conduction equation these authors derived analytical relationships between the first n harmonics of a Fourier series and the thermal properties λ_s and $\rho_s c_s$ at different depths. For the present investigation such an approach is not suitable, because thermal infrared remotely sensed data only relate to properties defined at the soil surface. The thermal behaviour of the soil surface, therefore, must be explicitly related to the properties at different soil depths. The latter is achieved through the thermal admittance concept and the equations presented in this chapter.

The case of a semi-infinite soil was considered first to give an explanation of the scope of thermal admittance.

4.1.3. Thermal admittance of a two-layered soil

As discussed in Sections 3.2 and 3.4 there always will be a difference in thermal properties between the soil layers above and below the evaporation front. The system depicted in Fig. 4.1 therefore is to be considered. The top layer extends from $z = 0$ to $z = z_1$, while from $z = z_1$ to $z \to \infty$ a semi-infinite homogeneous soil is considered.

By applying boundary conditions different from those in eqs. (4.10) and (4.11), the thermal admittance at the surface of the composite system can be obtain-

ed from eqs. (4.7) and (4.9). The coefficients C and D in those equations can be derived by assigning soil temperature T_0 and heat flux G_0 at the surface and T_1, G_1 at $z = z_1$ and by seeking a solution $T(z,t)$ such that:

$$T(z,t) = T_0(t) \text{ at } z = 0 \qquad (4.19)$$

and

$$T(z,t) = T_1(t) \text{ at } z = z_1 \qquad (4.20)$$

Thus at $z = 0$ eq. (4.7) respectively (4.9) read:

$$C = T_0(t) \left[\exp i(\omega t - \Omega)\right]^{-1} \qquad (4.21)$$

$$D = -G_0(t)(\lambda\gamma)^{-1} \left[\exp i(\omega t - \Omega)\right]^{-1} \qquad (4.22)$$

These results can be substituted in the eqs. (4.7) and (4.9) giving for $z = z_1$:

$$T_1 = T_0 \cosh \gamma z_1 - (G_0 \sinh \gamma z_1)/\lambda\gamma \qquad (4.23)$$

$$G_1 = -\lambda\gamma T_0 \sinh \gamma z_1 + G_0 \cosh \gamma z_1 \qquad (4.24)$$

Since the temperature T_0 actually is needed, the eqs. (4.23) and (4.24) must be inverted. When considering that the exchange of z_1 with $-z_1$ yields a corresponding exchange of index 0 with index 1 for T and G this procedure is straightforward. Remembering that $\sinh(-z) = -\sinh z$, this gives:

$$T_0 = T_1 \cosh \gamma z_1 + (G_1 \sinh \gamma z_1)/\lambda\gamma \qquad (4.25)$$

$$G_0 = \lambda\gamma T_1 \sinh \gamma z_1 + G_1 \cosh \gamma z_1 \qquad (4.26)$$
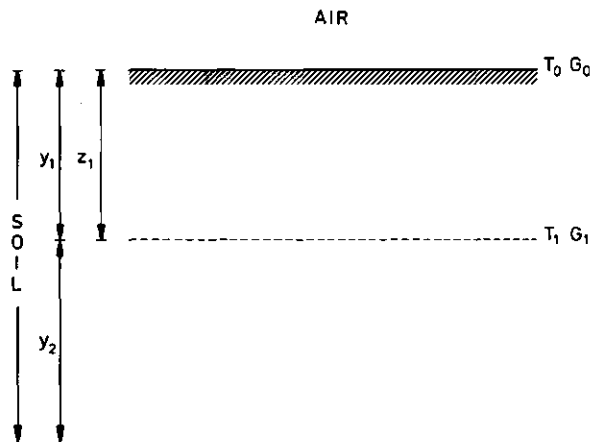
Fig. 4.1. Sketch of a two-layered soil: a top layer of thickness z_1 overlies a homogeneous semi-infinite soil. T, temperature; G, heat flux; y, thermal admittance

The required expression for the thermal admittance at the soil surface of a two-layered soil (Fig. 4.1) can be obtained by dividing eq. (4.26) by eq. (4.25) and writing the outcome as:

$$G_0 = \left(\frac{\lambda\gamma T_1 \sinh \gamma z_1 + G_1 \cosh \gamma z_1}{T_1 \cosh \gamma z_1 + G_1 \sinh \gamma z_1/\lambda\gamma}\right)T_0 \qquad (4.27)$$

which in the form of eq. (4.2) reads:

$$G_0(t) = y_0 T_0(t) \qquad (4.28)$$

where y_0 is the thermal admittance at the surface of a two-layered soil.

Taking z_1 to be the thickness of the upper layer and $\lambda\gamma = (2\pi\lambda\rho c/P)^{\frac{1}{2}} \exp i\pi/4$ with λ and ρc being the thermal properties of the upper layer one obtains:

$$\frac{y_0}{\lambda\gamma} = \frac{y_2/\lambda\gamma + \tanh \gamma z_1}{y_2 \tanh (\gamma z_1)/\lambda\gamma + 1} \qquad (4.29)$$

In eq. (4.29) y_0 is the apparent thermal admittance of the two-layered soil, while $\lambda\gamma = y_1$ is the thermal admittance that would be measured at the surface of the top soil, if it had an infinite thickness. Finally y_2 is the thermal admittance of the homogeneous semi-infinite soil beginning at z_1. Accordingly, eq. (4.29) allows for an easy estimation of the minimum depth z_1 at which there is no distinction between the two-layered system of Fig. 4.1 and a homogeneous semi-infinite soil with the same thermal characteristics as the upper layer. Since in eq. (4.29) the thermal admittance is a complex function of a complex variable it will be helpful to write eq. (4.29) in a form where the real and imaginary parts are explicitly separated. By recalling that:

$$\tanh z = \frac{\sinh 2p + i \sin 2q}{\cosh 2p + \cos 2q} \qquad (4.30)$$

and that $z = p + iq = b_1 z_1 + ib_2 z_1$ for the top layer in Fig. 4.1, where according to eq. (4.4) $b_1 = b_2 = b = |\gamma|$ and finally taking $c = |y_2|/|y_1|$, eq. (4.29) reads:

$$\frac{y_0}{y_1} = \frac{\begin{aligned}&[(c + 1)\exp 2bz_1 + (c - 1)\exp(-2bz_1) + \\ &+ 2c \cos 2bz_1 + 2i \sin 2bz_1]\end{aligned}}{\begin{aligned}&[(c + 1)\exp 2bz_1 - (c - 1)\exp(-2bz_1) + \\ &+ 2 \cos 2bz_1 + 2ci \sin 2bz_1]\end{aligned}} \qquad (4.31)$$

From eq. (4.31) a graph for the module and phase of (y_0/y_1) as a function of the thickness z_1 of the upper layer can be obtained. In Fig. 4.2 an example is given that relates to the system of Fig. 4.1 with actual thermal admittances being $|y_1| = 11.1 \text{ W} \cdot \text{m}^{-2} \cdot \text{K}^{-1}$
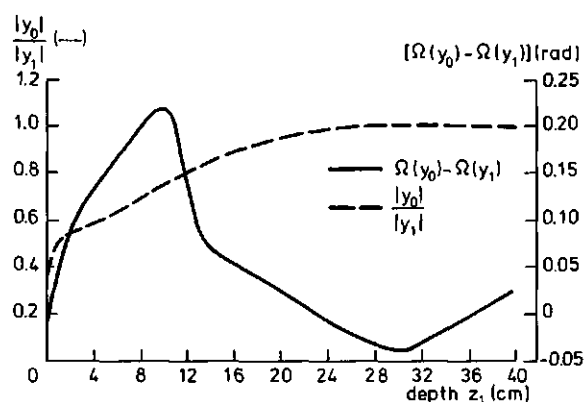
Fig. 4.2. Graph of the ratio of moduli $|y_0|/|y_1|$, left, and difference of phase $[\Omega(y_0) - \Omega(y_1)]$, right, between the apparent thermal admittance y_0 at the surface of a soil as in Fig. 4.1 and the thermal admittance y_1 of the top soil having an infinite thickness. Values are plotted against the thickness z_1 of top soil; $P = 1$ day

for the top layer and $|y_2| = 5.4$ $W \cdot m^{-2} \cdot K^{-1}$ for the homogeneous semi-infinite soil below it, as obtained from experiments performed in Idri playas (Fezzan, Libya) by the present author. In Fig. 4.2 both the ratio of moduli, i.e. $|y_0|/|y_1|$, and the difference of phases, i.e. $\Omega(y_0) - \Omega(y_1)$, are plotted, as is required by y_0 and y_1 being complex variables. According to the graph of $|y_0|/|y_1|$ it appears that when $z = 25$ cm no difference can be observed between the thermal behaviour of the two-layer system and of a semi-infinite soil with the thermal properties of the top soil. Note that a thermal admittance $|y| = 11.1$ $W \cdot m^{-1} \cdot K^{-1}$ is relatively high, thus in moving through the top layer a temperature wave is not damped to a large degree (see also van WIJK and DERKSEN, 1963). Graphs of theoretical values of $|y_0|/|y_1|$ versus z_1 for a few combinations of different two-layered soils can be found in BYRNE and DAVIS (1980).

4.1.4. Amplitude of surface temperature oscillation as related to soil thermal properties

A firmly established notion in the interpretation

of thermal infrared remotely sensed data is that the wetter the soil (higher $\lambda \rho c$), the smaller the amplitude of surface temperature daily oscillations. The thermal admittance concept and the equations given in Paragraphs 4.1.2 and 4.1.3 allow for some criticism of that notion.

Three cases will be considered: evaporation takes place at the surface of a nearly saturated soil (hereafter called case A), or at a few centimeter depth (case B), or there is no evaporation at all (case C). In case B a subdivision in two possibilities will be reviewed: the thermal admittance is rate dependent (case B1) or it is not (case B2).

In each case the apparent thermal admittance y_0 will be specified as that of an equivalent semi-infinite homogeneous soil. For all cases a sandy soil will be considered, e.g. with porosity equal to 0.5. In cases A, B2 and C the thermal properties are as presented by van DUIN (1963). For case B1 the value of $|y_0|$ has been obtained from temperature measurements performed by the present author in the playas around Idri (Fezzan, Libya), i.e. $|y_0| = 11.1$ $W \cdot m^{-2} \cdot K^{-1}$. In Table 4.1 the soil thermal properties taken as well as the quantities obtained through calculations are presented.

In case A the heat flux G_0 into the soil will be a minor component in the surface energy balance: 30 $W \cdot m^{-2}$ say for the daily amplitude ΔG_0. From the given values of λ_s and $(\rho c)_s$, the thermal admittance is calculated by means of eq. (4.16). The temperature gradient $(\partial T_s/\partial z)$ is indicated to give an impression of the thermal soil conditions. The daily amplitude of surface temperature ΔT_0 has been obtained by eq. (4.17), it being 1.6 K.

To discuss the cases B1 and B2 an estimation for ΔG_0 must be obtained first. The soil heat flux was chosen somewhat higher than the values measured by GARDNER and HANKS (1966) in a soil layer above the evaporation front, where they observed an evaporation rate of 7 $mm \cdot d^{-1}$. Since in both cases B1 and B2 the top soil layer would be nearly dry the heat capacity is small and will be the same in both cases. The thermal conductivity for case B2 has been estimated by eq.

Table 4.1. Apparent thermal admittance, $|y_0|$, amplitude of surface temperature, ΔT_0, and of heat flux, ΔG_0, relating to the behaviour of a sandy soil with porosity 0.5, during evaporation. Heat capacity, $(\rho c)_s$, thermal conductivity, λ_s, damping depth, d, and vertical temperature gradient, $\partial T_s/\partial z$, are also given. $P = 1$ day

Case	$(\rho c)_s$ $(J \cdot m^{-3} \cdot K^{-1})$	λ_s $(W \cdot m^{-1} \cdot K^{-1})$	d (m)	$|y_0|$ $(W \cdot m^{-2} \cdot K^{-1})$	ΔG_0 $(W \cdot m^{-2})$	$\frac{\partial T_s}{\partial z}$ $(K \cdot m^{-1})$	$\frac{\partial T_s}{\partial z}$ $(°C \cdot cm^{-1})$	ΔT_0 (K)
A (saturated sand)	$3 \cdot 10^6$	1.7	0.12	19.3	30	17.5	0.2	1.6
B1 (dry sand, y dependent)	$0.96 \cdot 10^6$	1.7	0.22	11.1	150	107	1.1	13.5
B2 (dry sand, y independent)	$0.96 \cdot 10^6$	0.2	0.08	3.7	150	750	7.5	40.5
C (dry sand, no evaporation)	$0.96 \cdot 10^6$	0.2	0.08	3.7	40	200	2.0	10.8

(3.55) for a dry soil, while for B1 it was obtained from $|y_0|$ and $(\rho c)_s$ as applied in the example of Fig. 4.2. The temperature gradients for both cases B1 and B2 have been obtained from ΔG_0 and λ_s. The resulting amplitudes of surface temperature are $\Delta T_0 = 13.5$ K for case B1 and $\Delta T_0 = 40.5$ K for case B2. As it appears by considering the values of ΔT_0 and $|(\partial T_s/\partial z)|$, case B2 is rather unrealistic, especially when it is recalled that $\Delta T_0 = 40.5$ implies that T_0 would oscillate between $\overline{T_0} - 40.5$ and $\overline{T_0} + 40.5$ (see eq. 4.10 with $A_0 = \Delta T_0$).

In case C the values given for λ_s and $(\rho c)_s$ are as applying to a dry soil. The vertical temperature gradient was established as an independent variable, namely that gradient which would be expected for a very high energy supply to the soil surface and no evaporation. A vertical temperature gradient of 2 $K \cdot cm^{-1}$ was observed by DINCER et al. (1974) in sand dunes in Saudi Arabia. The amplitude ΔG_0 of the soil heat flux will be somewhat higher than in the wet case A, but not that much, since sensible heat transport to the air will always result in a more efficient heat transfer away from soil surface. Anyhow, the value of ΔG_0 given in Table 4.1 was obtained as λ_s(dry sand)· $(\partial T_s/\partial z)$. Finally the amplitude ΔT_0 has again been obtained by eq. (4.17).

The comparison of the values of ΔT_0 finally obtained between the cases A and C supports the concept mentioned at the beginning of this paragraph: a small amplitude in surface temperature corresponds with a wet soil and a large evaporation rate, while a large amplitude corresponds with a dry soil without evaporation. It is the comparison between case C and B1 which looks disturbing from the conceptual point of view: in case B1 the evaporation occurs, but the amplitude of surface temperature is larger than in case C. The reason is that because the larger thermal admittance can only supply part of the required heat flux, the amplitude of surface temperature must be as large as required by eq. (4.17). Since case B2 appears to be somewhat unrealistic, the possibility should be ruled out that evaporation takes place inside the soil for the soil thermal conditions specified for case B2.

It therefore can be concluded that the relation between the amplitude of surface temperature and the presence of evaporation is not univocal. This circumstance is a complicating factor in the interpretation of thermal infrared remotely sensed data.

4.2. THERMAL ADMITTANCE OF MULTI-LAYERED SOILS

4.2.1. Thermal contrast of soil layers

In Paragraph 4.1.3 the apparent thermal admittance of a specific two-layered soil profile was defined and calculated to estimate the maximum thickness of the top layer that allows to discern the lower layer. In that paragraph specific values of y_1 and y_2 were considered.

It is understood that a decision whether or not a soil seen from above is a layered structure, is a main problem when studying soil thermal behaviour. It should also be noted that because of differences in the heat and moisture flow regime at different depths (see Chapter 3) a soil may appear as a layered structure. A good example of this concept is the soil layer between the evaporation front and the soil surface, in which the thermal conductivity is $\lambda_s' > \lambda_s$ (see eq. 3.45 and Fig. 3.14). Heat transfer through layered systems also relates to a soil which is covered by vegetation.

According to eq. (4.29) the layered structure of a soil is disclosed by the ratio $k = y_0/y_1$, being different from unity. Thus the accuracy in measuring k plays a critical rôle. The ratio k is considered by the present author to be a good measure of the thermal contrast between the apparent thermal behaviour of the surface of a layered soil and the thermal properties of the top soil layer. The ratio $k_1 = y_2/y_1$, accordingly, is considered to be a measure of thermal contrast between the lower and top soil layer.

To show how thick the top soil layer can be without masking the lower layer eq. (4.29) can be rearranged to:

$$\frac{\tanh{(\gamma_1 z_1^*)} + k_1}{\tanh{(\gamma_1 z_1^*)} \cdot k_1 + 1} = k \tag{4.32}$$

where z_1^* is the thickness of the upper layer corresponding to a nearly perfect masking ($k \cong 1$) of the deeper layer. Eq. (4.32) can be rewritten as:

$$z_1^* = \frac{1}{\gamma_1} \text{arctanh} \left(\frac{k - k_1}{1 - kk_1}\right) \tag{4.33}$$

A logarithmic representation is easier to use for calculations, hence:

$$z^* = \frac{d_1}{2} \ln \frac{(k + 1)(1 - k_1)}{(1 - k)(1 + k_1)} \tag{4.34}$$

where d_1 is the damping depth for the upper layer. In
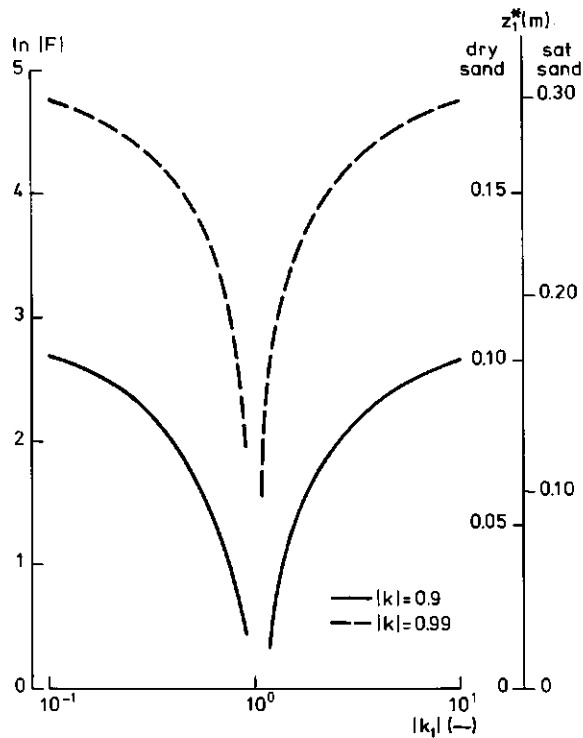
Fig. 4.3. Relationship between the amplification factor, F, and the thermal contrast, k_1, between top soil and lower layer for two values of the thermal contrast, k, between a layered soil and its top layer. On the right-hand axes the maximum not-masking z_1^* of respectively a dry and a saturated sand top soil is given. $P = 1$ day

eq. (4.34) the term d_1 relates to the thermal properties of the upper layer, k_1 to the difference in thermal properties between upper and lower layer and k to the difference which can be sensed between the apparent thermal properties at the surface and those of the upper layer. When in eq. (4.34) one replaces

$[(k + 1)(1 - k_1)] / [(1 - k)(1 + k_1)]$ by F, one obtains:

$$z_1^* = \frac{d_1}{2} \ln F \qquad (4.35)$$

In Fig. 4.3 $\ln |F|$ is plotted versus k_1; as the quantity $\ln F$ is a complex number only its module is plotted. Note that $\ln F$ has the meaning of a gain, since a given combination of y_2, y_1 and k determines a depth z_1^* larger or smaller than d_1. The depth which is actually sensed depends on the magnitude of d_1 as shown by the two vertical scales (right-hand) in Fig. 4.3. The inner scale relates to a typical damping depth for dry sand (see Table 4.1 and eq. 3.59), the outer one for saturated sand.

To illustrate the use that can be made of eq. (4.34) and of Fig. 4.3 an arbitrary example is given. The graphs in Fig. 4.3 for example can be applied to

find out how thick the black (iron containing) dust described by Plinius (see quotation at the beginning of this chapter) can be, without hiding the rocks underneath. Let us presume that Plinius described quartz rocks, i.e. of thermal admittance $|y_2| = 58.5$ $W \cdot m^{-2} \cdot K^{-1}$, and that the black dust has the same thermal properties as dry sand, i.e. $|y_1| = 3.7$. Accordingly $k_1 = 15.8$, which value falls beyond the range indicated in the horizontal scale of Fig. 4.3. Thus eq. (4.34) must be applied, obtaining $z_1^* = 10.8$ cm, with $k = 0.9$, and $z_1^* = 19.7$ cm, with $k = 0.99$. If the black dust was wet, then $k_1 = 3$ and the values of z_1^* can be read on the rightmost scale in Fig. 4.3: $z_1^* = 14.5$ cm with $k = 0.9$ and $z_1^* = 28.7$ cm with $k = 0.99$. It is, therefore, understood that a layer of dry sand 19.7 cm thick, or a layer of wet sand 28.7 cm thick, makes the soil plus rock system when observed from above behave thermally as a semi-infinite sand soil.

Eq. (4.34) shows that there exists an explicit relationship between a particular soil layering and its thermal response. The next step is to formulate and solve the inverse problem. When a set of functions relates the apparent thermal admittance y_0 to a set of different soil layering, then a set of measurements of k would enable one to estimate the thermal admittance and thickness of soil layers. Since the relationship (eq. 4.29) between k (i.e. $y_0/\lambda\gamma = y_0/y_1$) and the frequency ω of the temperature wave (eq. 4.15) is known, the best approach would be to measure k at different ω. The required forcing function, with components of different frequency, is provided by measuring the natural oscillations of surface temperature.

4.2.2. Matrix representation of the thermal admittance operator

Thickness and thermal admittance of the different soil layers will now explicitly be related to the thermal reaction of the soil surface to the forcing functions produced by varying weather conditions. This goal can be achieved by deriving equations like eq. (4.29), but now for a multi-layered system.

It first will be shown that a matrix representation can be given for the thermal admittance operator of a soil slab (see also CARSLAW and JAEGER, 1959, page 111). Then the derivation will be given in some detail for a three-layered system to show how the procedure can be extended to a larger number of layers.

Eqs. (4.25) and (4.26) can be rewritten in matrix form as:

$$\begin{bmatrix} T_0 \\ G_0 \end{bmatrix} = \begin{bmatrix} \cosh \gamma_1 z_1 & \sinh (\gamma_1 z_1)/\lambda_1\gamma_1 \\ \lambda_1\gamma_1 \sinh \gamma_1 z_1 & \cosh \gamma_1 z_1 \end{bmatrix} \begin{bmatrix} T_1 \\ G_1 \end{bmatrix} \qquad (4.36)$$
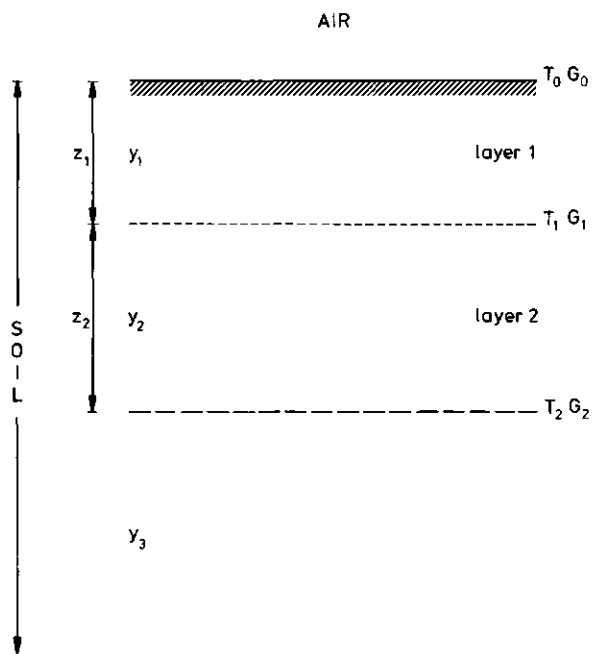
Fig. 4.4. Sketch of a three-layered soil: two layers of thickness z_1 respectively z_2 overlie a homogeneous semi-infinite soil; subscripts of T and G relate to each interface, and subscripts of y to each layer

or: $H_0 = M_{0,1}H_1$

This equation relates to the system depicted in Fig. 4.1. Subscripts to T and G relate to the two interfaces, while subscripts to λ, γ and (later) y relate to the thermal properties of each layer soil. According to this notation the matrix $M_{i-1,i}$ can be written as:

$$M_{i-1,i} = \begin{bmatrix} \cosh\,(\gamma_i z_i) & \sinh\,(\gamma_i z_i)/\lambda_i\gamma_i \\ \lambda_i\gamma_i\,\sinh\,(\gamma_i z_i) & \cosh\,(\gamma_i z_i) \end{bmatrix} \quad (4.37)$$

An equation similar to eq. (4.36) can be written for the system of Fig. 4.4 including two layers overlying a semi-infinite soil by introducing the transfer matrix for the second layer, $M_{1,2}$:

$$H_0 = M_{0,2}H_2 \qquad (4.38)$$

where the elements of the matrix $M_{0,2} = M_{0,1}\cdot M_{1,2}$ can be calculated according to:

$$S = M_{0,2} = \qquad (4.39)$$

$$\begin{bmatrix} (m_{11}^{0;1}m_{11}^{1;2} + m_{12}^{0;1}m_{21}^{1;2}) & (m_{11}^{0;1}m_{12}^{1;2} + m_{12}^{0;1}m_{22}^{1;2}) \\ (m_{21}^{0;1}m_{11}^{1;2} + m_{22}^{0;1}m_{21}^{1;2}) & (m_{21}^{0;1}m_{12}^{1;2} + m_{22}^{0;1}m_{22}^{1;2}) \end{bmatrix}$$

Thus an equation corresponding to eq. (4.36) is obtained:

$$\begin{bmatrix} T_0 \\ G_0 \end{bmatrix} = \begin{bmatrix} s_{11} & s_{12} \\ s_{21} & s_{22} \end{bmatrix} \begin{bmatrix} T_2 \\ G_2 \end{bmatrix} \qquad (4.40)$$

or:

$$T_0 = s_{11}T_2 + s_{12}G_2$$
$$\qquad (4.41)$$
$$G_0 = s_{21}T_2 + s_{22}G_2$$

Dividing left and right hand side of G_0 by T_0:

$$y_0 = \frac{G_0}{T_0} = \frac{s_{22}y_2 + s_{21}}{s_{12}y_2 + s_{11}} \qquad (4.42)$$

where numerator and denominator of the right-hand side have been divided by T_2.

After substitution of the expressions for s_{ij} given in eqs. (4.39) and (4.37), eq. (4.42) becomes:

$$\frac{y_0}{y_1} = \frac{\left[\tanh(\gamma_1 z_1)\dfrac{y_3}{y_2} + \dfrac{y_2}{y_1}\right]\tanh(\gamma_2 z_2) + \dfrac{y_3}{y_1} + \tanh(\gamma_1 z_1)}{\left[\tanh(\gamma_1 z_1)\dfrac{y_2}{y_1} + \dfrac{y_3}{y_2}\right]\tanh(\gamma_2 z_2) + \dfrac{y_3}{y_1}\tanh(\gamma_1 z_1) + 1}$$

$$\qquad (4.43)$$

To simplify the expressions the following notation will be used:

$$c_1 = |y_2|/|y_1| \qquad c_2 = |y_3|/|y_1|$$

$$c_3 = |y_3|/|y_2| \qquad (4.44)$$

Substitution in eq. (4.43) yields:

$$\frac{y_0}{y_1} = \frac{\left[\dfrac{\sinh\,\gamma_1 z_1}{\cosh\,\gamma_1 z_1}c_3 + c_1\right]\dfrac{\sinh\,\gamma_2 z_2}{\cosh\,\gamma_2 z_2} + c_2 + \dfrac{\sinh\,\gamma_1 z_1}{\cosh\,\gamma_1 z_1}}{\left[\dfrac{\sinh\,\gamma_1 z_1}{\cosh\,\gamma_1 z_1}c_1 + c_3\right]\dfrac{\sinh\,\gamma_2 z_2}{\cosh\,\gamma_2 z_2} + c_2\dfrac{\sinh\,\gamma_1 z_1}{\cosh\,\gamma_1 z_1} + 1}$$

$$\qquad (4.45)$$

or

$$\frac{y_0}{y_1} = \frac{\begin{bmatrix}c_3\,\sinh\,\gamma_1 z_1\,\sinh\,\gamma_2 z_2 + c_1\,\cosh\,\gamma_1 z_1\,\sinh\,\gamma_2 z_2 + \\ + c_2\,\cosh\,\gamma_1 z_1\,\cosh\,\gamma_2 z_2 + \sinh\,\gamma_1 z_1\,\cosh\,\gamma_2 z_2\end{bmatrix}}{\begin{bmatrix}c_1\,\sinh\,\gamma_1 z_1\,\sinh\,\gamma_2 z_2 + c_3\,\cosh\,\gamma_1 z_1\,\sinh\,\gamma_2 z_2 + \\ + \cosh\,\gamma_1 z_1\,\cosh\,\gamma_2 z_2 + c_2\,\sinh\,\gamma_1 z_1\,\cosh\,\gamma_2 z_2\end{bmatrix}}$$

$$\qquad (4.46)$$

According to the formulae for the products of hyperbolic sines and cosines, eq. (4.46) can be reduced further, making use of the following notation:

$$b_1 = c_2 + c_3 \qquad b_2 = c_2 - c_3 \qquad b_3 = 1 + c_1$$

$$b_4 = 1 - c_1 \tag{4.47}$$

$$B = |\gamma_1 z_1 + \gamma_2 z_2| \qquad D = |\gamma_1 z_1 - \gamma_2 z_2| \tag{4.48}$$

Thus:

$$\frac{y_0}{y_1} = \frac{\left[b_1 \cosh(B + iB) + b_2 \cosh(D + iD) + b_3 \sinh(B + iB) + b_4 \sinh(D + iD) \right]}{\left[b_3 \cosh(B + iB) + b_4 \cosh(D + iD) + b_1 \sinh(B + iB) + b_2 \sinh(D + iD) \right]} \tag{4.49}$$

In eq. (4.49) the real (Re) and imaginary (Im) parts of numerator N and denominator De can be explicitly separated in the form:

$$\frac{y_0}{y_1} = \frac{Re\ N + i\ Im\ N}{Re\ De + i\ Im\ De} \tag{4.50}$$

where the expressions for each term are:

$Re\ N = b_1 \cosh B \cos B + b_2 \cosh D \cos D +$
$\qquad + b_3 \sinh B \cos B + b_4 \sinh D \cos D$

$Im\ N = b_1 \sinh B \sin B + b_2 \sinh D \sin D +$
$\qquad + b_3 \cosh B \sin B + b_4 \cosh D \sin D$

$Re\ De = b_3 \cosh B \cos B + b_4 \cosh D \cos D +$
$\qquad + b_1 \sinh B \cos B + b_2 \sinh D \cos D$

$Im\ De = b_3 \sinh B \sin B + b_4 \sinh D \sin D +$
$\qquad + b_1 \cosh B \sin B + b_2 \cosh D \sin D$

The definition of hyperbolic sines and cosines can be now substituted in eq. (4.50), making use of the notation indicated in eqs. (4.47) and (4.48). The result reads:

$Re\ N = \left[(b_1 + b_3)e^B + (b_1 - b_3)e^{-B} \right]\cos B +$
$\qquad + \left[(b_2 + b_4)e^D + (b_2 - b_4)e^{-D} \right]\cos D$

$Im\ N = \left[(b_1 + b_3)e^B - (b_1 - b_3)e^{-B} \right]\sin B +$
$\qquad + \left[(b_2 + b_4)e^D - (b_2 - b_4)e^{-D} \right]\sin D$

$Re\ De = \left[(b_1 + b_3)e^B - (b_1 - b_3)e^{-B} \right]\cos B +$
$\qquad + \left[(b_2 + b_4)e^D - (b_2 - b_4)e^{-D} \right]\cos D$

$Im\ De = \left[(b_1 + b_3)e^B + (b_1 - b_3)e^{-B} \right]\sin B +$
$\qquad + \left[(b_2 + b_4)e^D + (b_2 - b_4)e^{-D} \right]\sin D \tag{4.51}$

For soils with more than three layers the non-dimensional number $k = y_0/y_1$ can be obtained by numerical multiplication of the matrices $M_{i-1,i}$, as needed for each layer.

In Section 4.3 it will be shown that the parameters appearing in the eq. (4.50) can be determined by observing the quantity $|y_0|/|y_1|$ at different frequencies.

4.3. SURFACE TEMPERATURE IN RELATION TO GROUNDWATER TABLE DEPTH

The idea of estimating shallow groundwater table depths indirectly by studying the thermal behaviour of the soil surface may look somewhat cumbersome. It should be noted, however, that in extensive desert
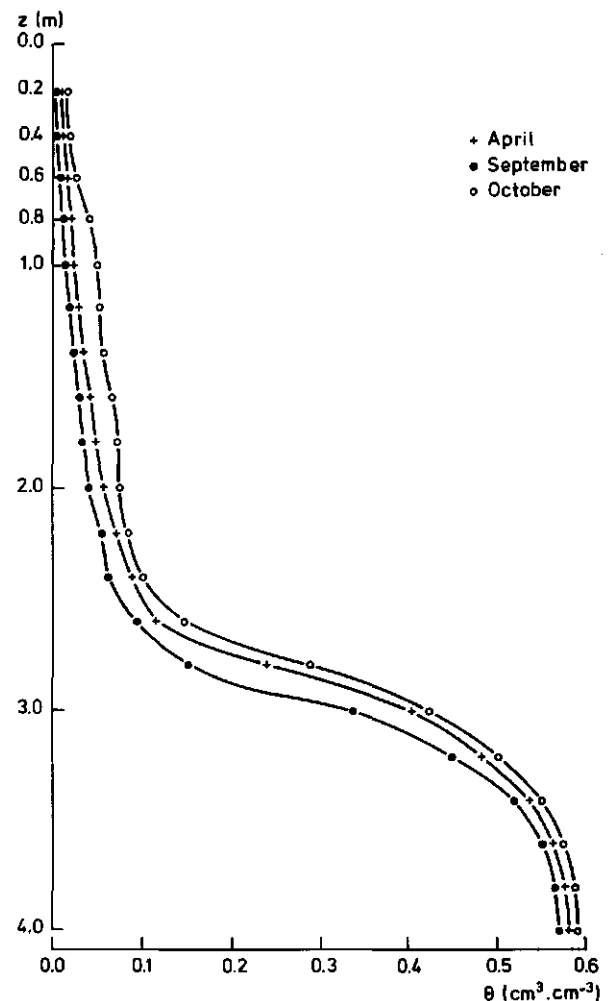
Fig. 4.5. Vertical distribution of moisture content θ in a sand dune in the Idehan Awbari (Fezzan, Libya) some 20 km West of Idri; θ(z)-profiles are shown as measured in April, September and October 1978

areas mapping groundwater table depths and, even more, monitoring water table variations in time can be an endless and very costly affair. A possibility to obtain data on groundwater table depths in and around playas by simply observing the soil surface from above, would be welcome therefore.

The daily temperature wave (see Fig. 4.3) allows sensing layered soils to shallow depths only. To look deeper into the soil measurements of the surface temperature over longer time periods are needed. Ideal sources of such data are the thermal infrared scanners of satellites. It should also be noted that the climatic conditions existing in deserts make this approach feasible. Furthermore, since there is hardly any rainfall, the moisture profile above the water table relates to a quasi-steady state flow regime.

For a sandy soil of a dune in the Idehan Awbari, with the groundwater table at 4 m depth (Fig. 4.5), the vertical distribution of moisture content resembles a typical h(θ) curve of sand. The moisture content θ initially remains low and relatively constant with increasing depth; then a relatively steep increase in θ occurs within a short depth interval. Finally, a wet layer, again of nearly constant θ is found just above the water table. A three layered model for the distribution of thermal admittance with depth (shown in Fig. 4.4) is therefore justified. Moreover, the thermal admittance of each layer determined from temperature measurements, or calculated from soil composition and moisture content (eqs. 3.54 and 3.55), gives a three-layer profile.

To estimate the depth of a shallow groundwater table the ratio $k = y_0/y_1$ in eq. (4.50) can be considered to be a measurable quantity. It can be assumed first that the unknown quantities in eq. (4.50) are z_1 and z_2, which means that the thermal characteristics of the three layers (see Figs. 4.4 and 4.5) separately are known. To determine z_1 and z_2 two possibilities are open. The first possibility is to measure at one frequency of the temperature wave, the modulus $|k|$ and the phase $\Omega(k)$. Thereby providing the two equations to be solved for z_1 and z_2. It appears rather difficult, however, to measure $\Omega(k)$, since it is the deviation of the phase difference between $G_0(t)$ and $T_0(t)$ from $\pi/4$ (see eqs. 4.14 and 4.16). A second and handier possibility is to measure $|k|$ at two different frequencies ω, because only the amplitudes of $G_0(t)$ and $T_0(t)$ are needed.

When the thermal admittance y_3 of the system depicted in Fig. 4.4 is chosen as applying to a saturated soil, the depth $(z_1 + z_2)$ is equal to the groundwater table depth. According to eq. (4.50) the modulus $|k| = |y_0/y_1|$ reads:

Table 4.2. Thermal properties of a layered sandy soil (dune in the Idehan Awbari) with two layers overlying the saturated zone (see also Fig. 4.4). Values of $|\gamma|$ and $|y|$ are presented for two different temperature waves with a period P of 1 day (86,400 s) and 4 days (345,600 s) respectively

Layer	a ($m^2 \cdot s^{-1}$)	λ ($W \cdot m^{-1} \cdot K^{-1}$)	$\|\gamma\|$ (m^{-1})	$\|y\|$ ($W \cdot m^{-2} \cdot K^{-1}$)
$P = 1$ day				
1	$1.4 \cdot 10^{-6}$	1.4	7.2	10.1
2	$0.2 \cdot 10^{-6}$	0.2	19.1	3.8
3	$0.6 \cdot 10^{-6}$	1.7	11.3	19.3
$P = 4$ days				
1			3.6	5.0
2			9.55	1.9
3			5.65	9.6

$$\frac{|y_0|}{|y_1|} = \frac{[(Re\ N)^2 + (Im\ N)^2]^{\frac{1}{2}}}{[(Re\ De)^2 + (Im\ De)^2]^{\frac{1}{2}}} \qquad (4.52)$$

which can be calculated as a function of z_2 for different values of z_1 to construct a nomogram of $|k|$ as a function of $z_1 + z_2 = z_{gw}$.

In Table 4.2 the thermal properties of the three layers (see Fig. 4.4) of the dune in the Idehan Awbari are given. The thermal admittances y_i have been calculated by eq. (4.16) with periods P of 86,400 s (1 day) and respectively 345,600 s (4 days). As can be seen this dune soil is a three layered sandy soil with a top layer z_1, where thermal convection of soil air occurs (see Paragraph 3.4.4), an intermediate nearly dry layer of varying thickness z_2 and a semi-infinite water saturated region. With the possible exception of convective transport, this situation is to be found at the boundary between a playa and the surrounding dunes.

Calculations with eq. (4.52) were performed for two different temperature waves, respectively with a period of one day and of four days (Fig. 4.6). When comparing the two figures with each other it can be seen that $|k| = |y_0|/|y_1|$ varies with the 1-day harmonic between 0.38 and 1.20 and with the 4-day harmonic between 0.37 and 1.49. So the latter gives a somewhat better thermal contrast (see Paragraph 4.2.1) between combinations of z_1 and z_2. The improvement particularly is evident for larger z_1-values, i.e. for a thicker topsoil. When the largest $z_1 = 10$ cm is considered, one notices that $|k|$ varies between 0.67 and 0.99 with the 1-day harmonic, while with the 4-day harmonic the variation is from 0.50 to 1.26. It can also be seen that with a period of 4 days $|k|$ becomes independent from z_2 at 50 cm and, with a period of 1 day at 20 cm. It appears that when these relative-
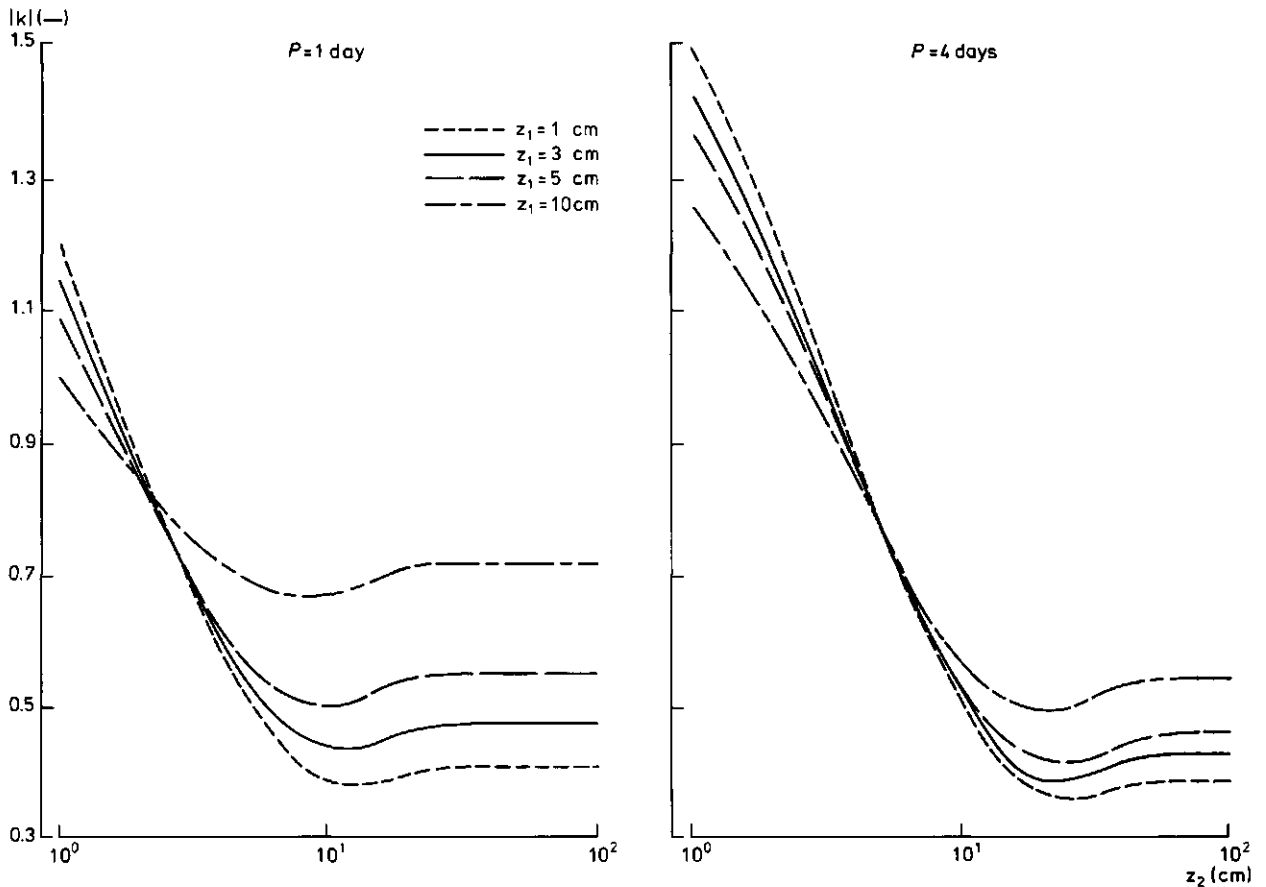
Fig. 4.6. The non-dimensional number k of a three-layered soil (see Fig. 4.4) plotted versus the thickness z_2 of the second layer for different thicknesses z_1 of the upper soil layer and for a temperature wave period $P = 1$ day respectively 4 days

ly high frequency harmonics are considered for the given thermal properties the deepest groundwater table which can be detected through observations of the thermal behaviour of the soil surface is $z_1 + z_2 = 60$ cm. In the example discussed the steepest damping (higher $|\gamma|$) occurs in the second layer, where the thermal admittance is low (Table 4.2). The graphs in Fig. 4.6 show that when the frequency of the temperature wave only slightly differs, the apparent thermal admittance at the soil surface changes considerably.

It appears that the most interesting opportunities in studying the variation of k are in a broader frequency range. Hence calculations were performed for a number of combinations of z_1 and z_2, with both z_1 and z_2 being in the range of 0.01 m to 7 m, and a number of temperature waves, with periods ranging from 1 to 550 days. Thermal properties of the three layers are as given in Table 4.2.

Results are now presented for a few periods as graphs of the ratio $|k|$ versus z_2; in Fig. 4.7 such a graph is presented as relating to $z_1 = 0.2$ m and temperature waves with periods P of 1, 8, 64, 128 and 365 days. As it is seen a falling groundwater table,

i.e. $(z_1 + z_2)$ increasing, brings about remarkable changes in $|k|$ for periods >1 day. Note that for low values of z_2, i.e. a very shallow water table, the apparent thermal admittance increases with P. When z_2 becomes larger, however, the apparent thermal admittance decreases with increasing periods. The latter
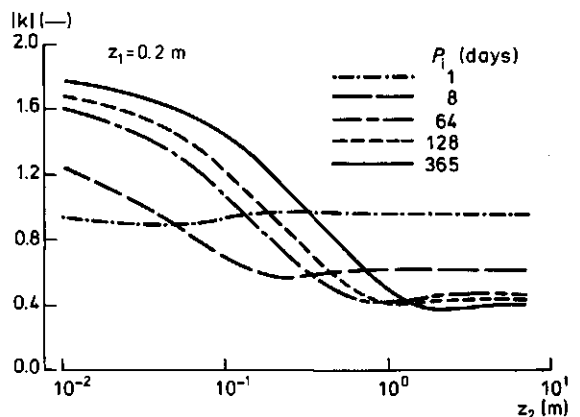
Fig. 4.7. As Fig. 4.6, but for different temperature waves of periods $P_i = 1$, 8, 64, 128 and 365 days and with a thickness z_1 of the top soil layer of 0.2 m
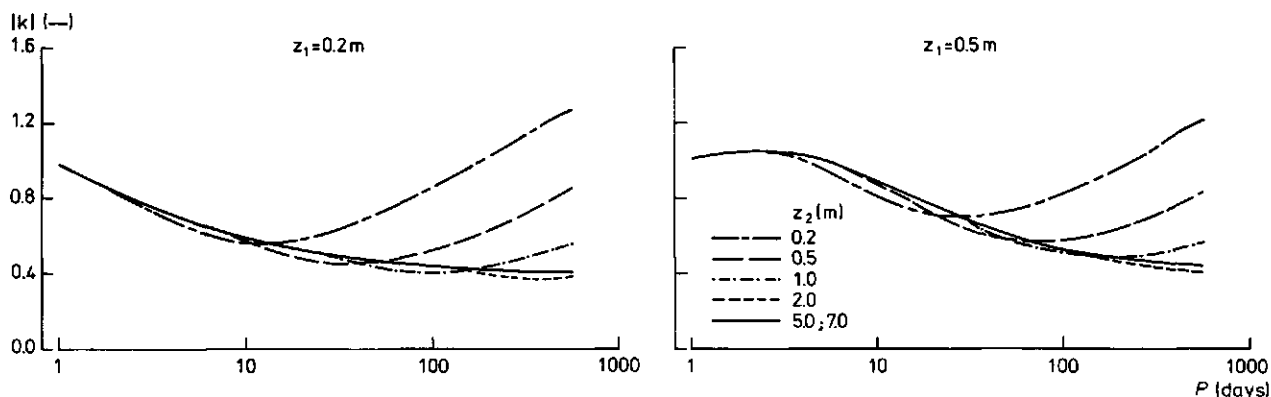
Fig. 4.8. As Fig. 4.6, but $|k|$ plotted versus the period P for different thicknesses z_2 of the second soil layer and respectively $z_1 = 0.2$ m and $= 0.5$ m

is the result of a decreasing penetration of the temperature waves with a decreasing period.

The possibility of studying a water table of time-varying depth can be better discussed by using a different graphic representation for the results obtained. The ratio $|k|$ can be plotted as a function of P for different combinations of z_1 and z_2. Fig. 4.8 relates to $z_1 = 0.2$ m respectively $= 0.5$ m and $z_2 = 0.2, 0.5, 1, 2, 5$ and 7 m. When large period lengths have been taken, the separate curves prove to have a good accordance with the specific thermal admittance graphs, the general shape of which is shown in Fig. 4.9. In Fig. 4.9 the thermal admittances $|y_i|$ of the three layers, as given in Table 4.2 for the daily temperature wave are plotted versus depth z. The curves in Fig. 4.8, therefore, provide a good description of the layering of the soil. It might be useful to emphasize here that the non-dimensional number k does not depend explicitly on the frequency ω of the applied temperature wave, as evident from the definition for y given below eq. (4.16). The dependence of k on ω only
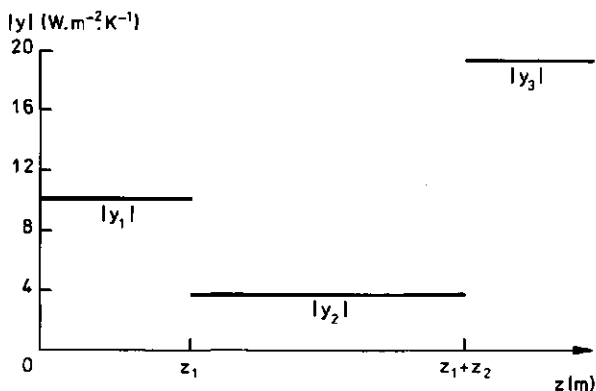
Fig. 4.9. Modulus of thermal admittances at $P = 1$ day of the three soil layers as depicted in Fig. 4.4; see also Table 4.2

is due to soil layering.

Thus plots as in Fig. 4.8 can be applied to estimate z_1 and z_2, as appearing in eq. (4.48) and therefore in eqs. (4.50) and (4.52), from experimentally obtained values of $|k|$ plotted versus period P. Then a curve of the family generated by eq. (4.52) is to be found that fits this experimentally obtained curve. Eventually the unknown z_i variables are obtained as parameters of the curve, best approximating the measured points, giving $z_1 + z_2$ as groundwater table depth (for the thermal properties as given in Table 4.2, up to 2 m depth).

From a conceptual point of view the apparent thermal admittance method is a relative one. Only ratios of amplitudes of temperature and heat flux at the surface are needed. Furthermore, certain categories of errors on these amplitude ratios will not cause major problems. A constant error percentage will only change the absolute value of $k(P)$, but not its shape which still will vary with the groundwater table depth as expected. A normally distributed error over not too large period intervals will place the measured points as well above as below the true curve, which can be overcome in the fitting procedure. A calibration of the experimentally obtained curves can be achieved by comparing some of them with the actual soil layering. This is much easier than calibrating an estimated pattern of surface temperature or soil heat flux. Finally it must be noted that a gradual drawdown of a water table during a relatively long period, will give curves showing a gradual transition of the curve pertaining to the initial groundwater depth and the curve for the groundwater depth finally reached.

Although the procedure was applied to estimate the groundwater table depth $z_{gw} = z_1 + z_2$, the thermal

behaviour of any layered structure can be studied at relatively shallow depths with the same approach. For a more than three layered system, graphs similar to the ones of Fig. 4.8 can be drawn.

4.4. EXTRAPOLATION OF HEAT AND MOISTURE FLUX POINT VALUES TO AREAS

Throughout Chapter 3 a number of processes were considered for their rôle in heat and moisture transfer through nearly dry soils. Problems and opportunities were discussed about approaches to measure or estimate flow rates. A criterion now is to be defined to establish the boundaries of areas which are homogeneous with respect to heat and moisture flux. As discussed in Section 1.1 the error in the determination of areas where actual evaporation has a certain value, is a very important contribution to the total error in the water losses estimated.

It appears that the critical groundwater table depth $\bar{z}_{gw}$ defined by eq. (3.78) in Section 3.6, is a suitable criterion for the homogeneity of evaporation, while the apparent thermal admittance y_0 defines homogeneous areas with respect to heat transfer at the soil surface. It is, however, clear that the determination of $\bar{z}_{gw}$ over very large desert areas is more difficult than of y_0 or, better, k. Furthermore, the coupling between the heat flux at the soil surface and evaporation (Section 2.3 and 3.4) implies that the heat flux itself already represents a reasonable estimation of actual evaporation. Enhancement of vapour transport by means of soil air thermal convection (Paragraph 3.4.4) can be cast in terms of a larger y_1 (Section 4.3). As the thermal admittance y_0 and the matrix $M_{i,j}$ are different representations of the heat conduction differential equation, the theory and the application procedure presented in this chapter have a meaning as general as that equation. It can therefore be concluded that the non-dimensional number k is a suitable criterion of homogeneity with respect to both heat and moisture flux.

According to eq. (4.17), the apparent thermal admittance y_0 can be determined from measured values of temperature and heat fluxes at the soil surface. The most efficient way of obtaining surface temperature over very large areas is by using thermal infrared remotely sensed data. Daily temperature oscillations, thus high frequency, provide information about the top soil layer, while the yearly ones, so low frequencies, disclose the effect of deeper layers. A combined use of remotely sensed data in the visible (0.4 to 1.1 μm) and thermal infrared (8 to 14 μm) spectral band offers a feasible solution, as will be discussed in Chapter 5.

It is recognized that a main difficulty for practical application of the apparent thermal admittance concept lies in the estimation of the soil heat flux G. Procedures to estimate G will be discussed in Section 5.4 and applied in Paragraph 8.2.2.

4.5. SUMMARY

In Section 4.1 the difficulties involved in the determination of the heat flux in the top soil layer were discussed. This soil heat flux is needed to determine the actual evaporation from the soil by means of the methods having been presented in Chapter 2. Thermal convective flow of soil air may greatly enhance heat transfer in soils of high specific permeability, as was described in Chapter 3. The conclusion was reached that there is little scope for the determination of the true thermal conductivity of the solid soil phase, since next to it the soil air flow velocity must also be determined. A much better outlook was recognized in the determination of the apparent soil thermal properties defined in Chapter 3. This concept was strengthened further by deriving an explicit relationship between the bulk thermal properties of a semi-infinite homogeneous soil and the apparent soil thermal admittance, a property defined at the soil surface. Further it has been shown that an explicit relationship can also be derived for a semi-infinite two-layered soil. The masking effect of the top soil was evaluated and a numerical example relating to the daily surface temperature wave was given. An important result for the specific goal of the present investigation has been obtained in Paragraph 4.1.4. There a numerical example has been given to show that the amplitude of the surface temperature does not necessarily bear a straightforward relationship with soil moisture and evaporation from the soil.

In Section 4.2 the concept of thermal contrast between soil layers was introduced. A way of detecting this contrast by means of observations of the thermal behaviour of the soil surface has been presented. For this purpose the thermal admittance of a layered soil was expressed in matrix form and explicitly derived for a semi-infinite three-layered system.

In Section 4.3 it has been shown how to take advantage of the relationship between the thickness and thermal properties of the three soil layers and the apparent thermal admittance at different frequencies of the incoming surface temperature wave, as established in Section 4.2. A how-to example has been worked out to show how groundwater tables at shallow depths (up to some few meters) can be detected by studying the apparent thermal admittance of the soil surface.

In Section 4.4 the point has been made that the apparent soil thermal admittance is a suitable criterion to identify areas which are homogeneous from the point of view of heat exchange at the soil - air interface.

In Chapters 5 and 8 it will be discussed how the apparent thermal admittance can be determined over large areas by means of satellite data. A key step in this procedure is the separation of a territory in areas where evaporation takes place at the soil surface and where inside the soil. Such a separation is made possible by the definition of evaporation sites as given in Chapter 3 and by a relationship between surface reflectance and surface moisture content which will be given in Chapter 5. An example of the procedure to determine the thermal admittance will be given in Chapter 8, where the entire procedure also is summarized. The apparent thermal admittance, together with its dependence on frequency, can accommodate both the enhancement mechanism of heat transport in the top soil as described in Chapter 3 and the heat exchange between soil and air at high frequencies as will be shown in Section 7.6.

5. REMOTE SENSING, ENERGY BALANCE AND EVAPORATION OF DESERTS

*'... et solem orientem occidentemque dira inprecatione contuentur ut exitialem ipsis
agrisque, ...'*

(PLINIUS, Naturalis Historia, Liber V:45)

5.1. RELATIVE WEIGHT OF THE TERMS IN THE SURFACE ENERGY BALANCE EQUATION

In recent years a number of procedures to estimate from satellite data the energy fluxes contributing to the surface energy balance have been proposed, of which a review has been presented by PRICE (1982). Since any given approach must be made to work under a restricted availability of ground data, a number of assumptions implicitly are involved. Therefore a preliminar assessment of the relative weight of each term of the surface energy balance equation is needed.

The soil heat flux is usually assumed to be negligible or is taken to be a fixed percentage, 10% say, of net radiation. As has been discussed in Chapter 3, in nearly dry soils these assumptions are far from correct.

To give an example of the rôle of the soil heat flux, some surface energy balance data will be given as measured in the playa An-Nabiyah, Saudi Arabia, as reported by ITALCONSULT (1969). In Fig. 5.1, left, the data relate to 16 February 1969 and, right, to 14 May
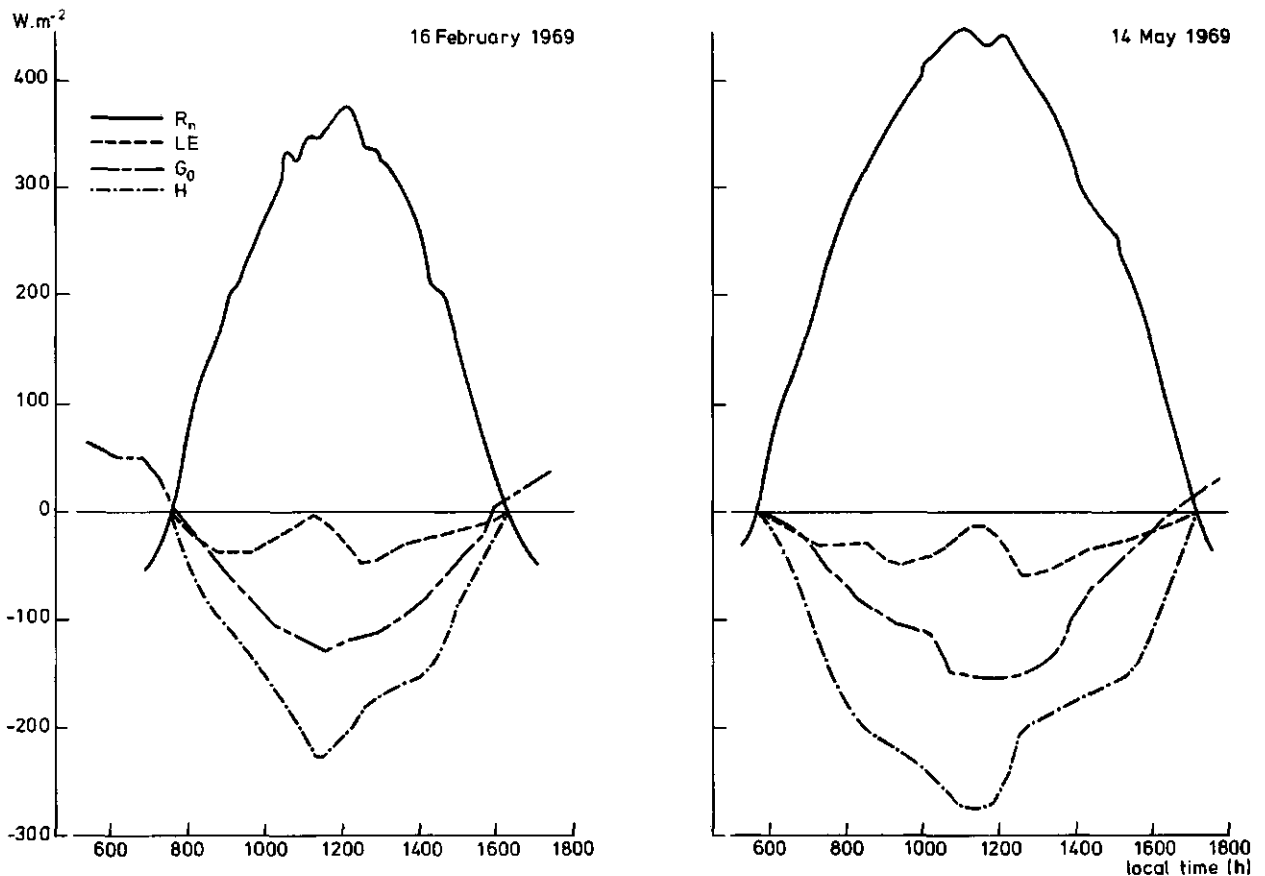
Fig. 5.1. Energy balance of playa An-Nabiyah (Saudi Arabia) as measured on 16 February 1969 and on 14 May 1969. R_n, net radiation; H, sensible heat flux; LE, latent heat flux; G_0, soil heat flux at the soil surface. After Italconsult, 1969

Table 5.1. Relative weight of the terms in $mm \cdot d^{-1}$ equivalent water depth of the surface energy balance equation on 16 February and on 14 May 1969 in playa An-Nabiyah, Saudi Arabia (after Pike, 1970)

Term		16 February 1969	14 May 1969
Net radiation	R_n	+9.40	+15.62
Soil heat flux	G_0	-3.00 (32%)	- 5.00 (32%)
Sensible heat	H	-5.25 (56%)	- 8.84 (57%)
Evaporation	LE	-1.15 (12%)	- 1.78 (11%)

1969. It can be seen that most of the available energy goes into sensible heat H and soil heat flux G_0. Latent heat flux LE is a relatively minor component and the early morning peak (see Paragraph 3.4.4) is quite evident. When around 1100 hours LE decreases, a corresponding increase of H is observed. The relative weights of each energy balance term for the same data sets are given in percent in Table 5.1 (after PIKE, 1970). The most remarkable feature is that on both days the separate percentages are practically constant which is typical for desert climate conditions. The percentages also show that soil heat flux G_0 takes a relevant share of available net radiation. Since G_0 is strongly dependent on soil type, it is likely that over a given area substantial variations in this term may occur. Thus variability in space of the different energy fluxes at the soil surface is a more critical issue than the variability in time.

As an aside it must be mentioned that the data shown in Fig. 5.1 and Table 5.1 were the only measurements of the energy balance of playas available before the present investigation was performed.

To work out a systematic analysis of the weight of each term in the surface energy balance, the equations presented and discussed in Section 2.3 will now be applied.

The energy balance equation at the soil surface (eq. 2.5) and at the evaporation front (eq. 2.8) can be combined to yield:

$$R_n + H + LE + G_E = 0 \qquad (W \cdot m^{-2}) \qquad (5.1)$$

Net radiation can be expressed as the sum of shortwave R_{sw} and longwave (Stefan - Boltzmann law) contributions:

$$R_n = (1 - \alpha_0)R_{sw} + \varepsilon'\sigma T_a^4 - \varepsilon\sigma T_0^4 \qquad (W \cdot m^{-2}) \qquad (5.2)$$

where α_0 is the shortwave surface reflectance, ε' the apparent emissivity of the air, ε the emissivity of the soil surface and σ is the Stefan - Boltzmann constant. The sensible heat flux can now be expressed ac-

cording to eq. (2.15), so eq. (5.1) can be rewritten as:

$$(1 - \alpha_0)R_{sw} + \varepsilon'\sigma T_a^4 - \varepsilon\sigma T_0^4 - \frac{\rho_a c_p}{r_a}(T_0 - T_a) + LE + G_E = 0 \qquad (W \cdot m^{-2}) \qquad (5.3)$$

Eq. (5.3) can be rewritten to define LE as an explicit function of the remaining variables:

$$LE = -(1 - \alpha_0)R_{sw} - \varepsilon'\sigma T_a^4 + \varepsilon\sigma T_0^4 + \frac{\rho_a c_p}{r_a}(T_0 - T_a) - G_E \qquad (W \cdot m^{-2}) \qquad (5.4)$$

Thus LE is a function of six variables (α_0, R_{sw}, T_a, T_0, r_a, G_E). Some of these variables can in principle be measured at each point in any given area (see Section 5.2), while most of them cannot. Because of the very low density of weather stations in desert areas the latter holds especially true for air temperature and wind speed. Shortwave incoming radiation can be considered to be relatively uniform. Surface roughness can be estimated from a land-use or vegetation map.

The approach applied in the present investigation is to approximate LE by means of eq. (5.4), but involving only those variables that can actually be measured over a large area. The remaining variables are to be assigned a constant value typical for the area, but variable with time. Calculation according to eq. (5.4) of partial differentials of LE (α_0, R_{sw}, T_a, T_0, r_a, G_E) makes it possible to establish a linear approximation of LE and also to assess the rôle of each separate term. The partial differentials $D_x(LE)$ read:

$$D_{\alpha_0}(LE) = R_{sw} d\alpha_0 \quad (W \cdot m^{-2}); \quad D_{R_{sw}}(LE) = -(1 - \alpha_0)dR_{sw}$$
$$(W \cdot m^{-2}) \qquad (5.5)$$

$$D_{T_0}(LE) = (4 \varepsilon\sigma T_0^3 + \frac{\rho_a c_p}{r_a})dT_0 \qquad (W \cdot m^{-2}) \qquad (5.6)$$

$$D_{T_a}(LE) = -(4 \varepsilon' T_a^3 + \frac{\rho_a c_p}{r_a})dT_a \qquad (W \cdot m^{-2}) \qquad (5.7)$$

$$D_{r_a}(LE) = -\frac{\rho_a c_p}{r_a^2}(T_0 - T_a)dr_a \qquad (W \cdot m^{-2}) \qquad (5.8)$$

$$D_{G_E}(LE) = -dG_E \qquad (W \cdot m^{-2}) \qquad (5.9)$$

α_0	R_{sw}	T_0	T_a	r_a	G_E	$4\epsilon\sigma$	$\rho_a c_p$	$4\epsilon'\sigma$
-	$W\cdot m^{-2}$	K	K	$s\cdot m^{-1}$	$W\cdot m^{-2}$	$W\cdot m^{-2}\cdot K^{-4}$	$J\cdot m^{-3}\cdot K^{-1}$	$W\cdot m^{-2}\cdot K^{-4}$
0.4	250	305	300	200	100	$2.2\cdot10^{-7}$	$1.147\cdot10^3$	$1.9\cdot10^{-7}$

Table 5.2. Numerical values of variables and constants in the function LE for average conditions in the Libyan desert

	$D_{\alpha_0}(LE)$	$D_{R_{sw}}(LE)$	$D_{T_0}(LE)$	$D_{T_a}(LE)$	$D_{r_a}(LE)$	$D_{G_E}(LE)$
	25.	0.	110.	-22	-15	-50
δx	0.1	0.	10 K	2 K	100 s·m⁻¹	50 W·m⁻²

Table 5.3. Numerical values of partial differentials $D_x(LE)$ $(W\cdot m^{-2})$ for average conditions in the Libyan desert. The assumed regional variation for each independent variable is also shown (δx)

As already mentioned (Section 2.3) the latent heat flux is counted negative when directed outwards of the soil surface, i.e. positive increments imply reductions in evaporation rate.

With respect to the soil heat flux it can be recalled that the transport equation (eq. 2.16) for heat between the soil surface and the evaporation front establishes an additional constraint on LE and G_E:

$$LE + G_E = - \frac{T_0 - T_E}{r_{sh}} = G_0^{in} \qquad (W\cdot m^{-2}) \qquad (5.10)$$

Since $r_{sh} = (z_E/\lambda'_s)$, substitution of eq. (5.10) in eq. (5.4) could only be helpful, if a procedure to estimate r_{sh} over an area is available.

To determine the order of magnitude of each term appearing in the eqs.(5.5) through (5.9), a number of numerical values for the constants and independent variables have been taken as shown in Table 5.2. They relate to field data to be listed in Section 6.2. The results of the calculations are shown in Table 5.3. Since each one of the variables in the LE-function eventually has a characteristic variability range in a given area, the assumed range is also presented in Table 5.3 where R_s has been taken constant over the area, i.e. $dR_s = 0$, and ϵ was given a value of 0.97. More details will be given in Section 5.3.

As shown in Table 5.3 the most significant contributions to the areal variability of LE are due to the variables T_0, G_E and α_0 in this order. Since through eq. (5.10) G_E depends on T_0, T_0 and α_0 will bear most of the information needed to determine LE. It should be noted that this does not imply that the variables R_s, T_a, r_a are unrelevant or should not be measured if this can easily be done. The range of variability, δx, indicates that fewer measuring sites are needed for R_{sw}, T_a, r_a than for T_0, α_0 and G_E.

Surface temperature T_0 and reflectance α_0 can in principle be measured by remote sensors. Hence as far as LE is essentially a function $LE(\alpha_0, T_0)$, a cost-effective calculation procedure using remote sensing data is feasible.

It appears, however, that many effects cannot easily be included. To fix ideas, in Fig. 5.2 a particular function $\tilde{LE} = LE(\alpha_0, T_0)$ is depicted. The point P* represents a particular evaporation state, at a given site on a given instant. Next an increase in G_E will be considered which changes LE, changing G_0^{in} according to eq. (5.10). If only T_0 would change to achieve this, the process could be tracked by measuring T_0 while point P* moves for example to P'. The value of $LE(\alpha_0, T_0)$ would then be $|LE'|$. However, the temperature at the evaporation front T_E or r_{sh} may change (see eq. 5.10) and the outcome could be different, $|LE''|$ say, corresponding to P''. Thus the difference $(LE'' - LE')$ cannot be accounted for by measurements available through satellites and two possibilities are left:
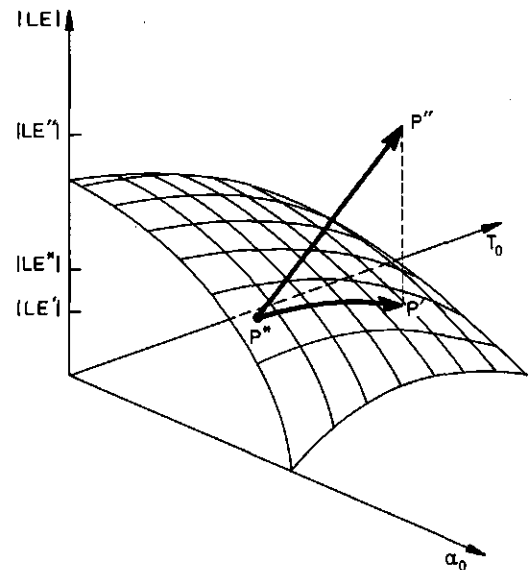
Fig. 5.2. Sketch showing possible errors on estimates of latent heat flux due to approximated formulas of less-than-six dimensionality

- determine in a preliminary step additional properties such as r_a and r_{sh};
- apply measured 'strings' (LE, α_0, R_{sw}, T_0, T_a, r_a, G_E) to establish corrections accounting for effects not included in LE = LE(α_0, T_0).

These possibilities will be discussed in the Sections 5.5 and 5.6.

5.2. REMOTE MEASUREMENT OF SOME TERMS IN THE SURFACE ENERGY BALANCE

Some of the quantities in eq. (5.3), namely R_{sw}, α_0 and $\varepsilon\sigma T_0^4$ can be determined by radiometers in airplanes or satellites. The accuracy of determination, however, is strongly dependent on atmospheric conditions. Atmospheric effects on shortwave (R_{sw} and α_0) and longwave ($\varepsilon\sigma T_0^4$) radiative transfer in a clear atmosphere can be accounted for, but under cloudy conditions more information is badly needed. Opportunities to infer surface-related quantities from remotely sensed data have been summarized by ITTEN (1981) and GRUBER (1981). ITTEN (1981) considers that determination of shortwave reflectance, percentage of cloud cover and surface temperature have already achieved operational status. GRUBER (1981) on the other hand stresses the need to account for scattering and absorption when determining both R_{sw} and α_0 in accordance with the local atmospheric conditions.

5.2.1. Shortwave radiation

R_{sw} can be estimated (not measured!) from satellite data. Two different approaches generally are applied:

- determination of statistical relationships between R_{sw} and cloudiness, in terms of amount and additional parameters relating to cloud type;
- calculation of atmospheric transmittance by a radiative transfer model, where some of the required parameters such as cloudiness, surface reflectance (α_0) and planetary reflectance can be obtained from satellites.

The first approach was applied by TARPLEY (1979) to data from a geostationary satellite (GOES). A statistical model was made by this author to relate R_{sw} to cloud amount and cloud brightness (satellite data), and to precipitable water and surface pressure (ground weather-data). It was found that under clear atmospheric conditions the ground based data were statistically significant in the estimation of R_{sw}. These data did not improve, however, the accuracy of the estimate in

a sensible way. Under cloudy conditions ground weather-data were not statistically significant because of the overwhelming effect of cloud top reflectance. The method was shown to estimate R_{sw} of a 50 by 50 km surface with a 10% accuracy.

According to GRUBER (1981) deterministic methods based on radiative transfer physics achieve a similar accuracy when accurate values of surface reflectance are known. The same conclusion was reached by VONDER HAAR (1980) who compared measurements of planetary reflectance and emitted longwave flux with radiative transfer calculations. Data relating to a 14 year period were considered.

A slightly different approach was applied by HISER and SENN (1980). Ground based data on sunshine, sky cover and shortwave radiation were used to establish empirical relationships. Then satellite-derived maps of sunshine and sky cover could be converted to shortwave radiation maps.

It appears that the key-step in the procedures discussed above is the determination of cloud-cover percentage. For most cloud types a threshold on brightness can be defined as corresponding to a few classes of sky cover percentage. It is, however, difficult to define the boundaries of semi-transparent clouds, such as cirri and fragmented clouds, if satellite data only in the visible spectral region are being used. Then thermal infrared satellite data can be helpful, since clouds have a lower temperature than the ground surface (see PARIKH and BALL, 1980, for examples).

It should be noted that ground-derived relationships between insolation and type and amount of clouds have a limited scope when applied to satellite data. While cloud amount is relatively easy to determine from satellite data, it is very difficult to infer cloud type from satellite imagery as shown by PARIKH and BALL (1980).

Because of the statistics involved in the determination of sky cover, any procedure requiring it to obtain R_{sw} implies a loss in resolution. It appears that the higher the accuracy required on sky cover percentage, the larger the number of pixels involved in a single estimate of that percentage. Thus a coarser distinction in classes of cloud amount would allow for pixel-sized estimates of R_{sw}. The concept can be made clear by recalling the method presented by STANGHELLINI (1981) to estimate the monthly average of sunshine duration N_s from cloudiness. Only three classes, i.e. overcast, partly covered and clear sky, were distinguished and the number of days per class were considered as independent variables. Then sunshine duration is obtained as:

$$N_s = n_1 c_1 + n_2 c_2 + n_3 c_3 \qquad (h) \qquad (5.11)$$

where c_i is the number of days per class. The coefficients n_i are the average sunshine hours per day in each class. An equation similar to eq. (5.11) can be written down to obtain the shortwave radiation averaged over an area:

$$\bar{R}_{sw} = R_{sw}^{I} n_I' + R_{sw}^{II} n_{II}' + R_{sw}^{III} n_{III}' \qquad (W \cdot m^{-2}) \qquad (5.12)$$

where the coefficients R_{sw}^{i} represent the amount of shortwave solar radiation received at the ground respectively under overcast, partly covered and clear sky conditions, while the n_i' are the corresponding fractions in each class of the total number of pixels. The coefficients R_{sw}^{i} can be determined from measurements of R_{sw} at a single point during some period of time. The fractions n' are obtained from satellite imagery, after establishing thresholds to define the three classes. If a map of R_{sw} is required, then the values R_{sw}^{i} are assigned to each pixel according to the particular class of sky cover conditions.

The accuracy of R_{sw} as measured at a weather station is much higher than the accuracy of the e s - t i m a t e d R_{sw} for a given pixel. It must be noted, however, that for the specific purpose of the present investigations, it is the accuracy of areal evaporation losses which is important, rather than the accuracy of a single value for R_{sw}. Calculation of the evaporation pattern at a given instant from satellite imagery involves the extrapolation of R_{sw} to a large area, which can be solved in the above mentioned manner.

5.2.2. Reflectance

It was shown in Section 5.1 that surface reflectance is one of the main factors inducing variability of LE over large areas. Radiometric measurements by remote sensors are a most convenient solution for the determination of areal patterns of surface reflectance. However, KONDRATYEV et al. (1981) were of the opinion that for airborne surveys at flight altitudes higher than 200 m corrections for atmospheric effects already are needed. Under cloudy conditions, with nearly opaque clouds, satellite measurements of the surface reflectance are of course impossible. However, under clear sky conditions reflectance measured from satellites will be only slightly different from values obtained on the ground, at least for desert conditions. Data presented by VONDER HAAR (1980) and KONDRATYEV et al. (1981) can be compared to show how large these differences are. The former author presented the distributions in space and time of reflectance and net

radiation for the earth - atmosphere system as obtained from satellite data. The latter authors presented surface reflectance maps as obtained by applying ground measured values to land use maps and climatological data. The planetary reflectance map of VONDER HAAR (1980) for the summer period gives $\alpha_0 \simeq 0.3$ for the Sahara, while surface reflectance for the same area in July as given by KONDRATYEV et al. (1981) is $\alpha_0 > 0.25$. It appears that figures relating to the North-African deserts are relatively close to each other, especially when considering that the actual figure applied by Kondratyev et al. to desert areas was 0.28. Thus, when data relating to clear sky and low zenith angle are considered, it can be concluded that planetary reflectance, as measured by satellites, is a good estimation of surface reflectance. The value presented by VONDER HAAR (1980) is confirmed by figures of CARLSON and WENDLING (1977), who reported for desert areas a measured planetary reflectance of 0.342 (NOAA 2 SR data) and 0.297 (NOAA 3 VHRR data), both on 30 July 1974.

CARLSON and WENDLING (1977) also did show that reflected radiance increases as a quasi-linear function of aerosol optical depth. It should be recalled that Sahara dust affects radiometric measurements over large areas, not only over the desert itself, but also over the Atlantic Ocean. The relationship between reflectance and dust load changes with wavelength. According to CARLSON and CAVERLY (1977) at wavelengths of 0.5 µm an increase in dust load induces a decrease in reflectance. It must be pointed out that satellite measurements of reflected radiance have been proposed, e.g. by FRASER (1976), as a method to determine dust load, by means of relationships obtained through models of atmospheric scattering. Surface reflectance has to be known very accurately for the dust load to be inferred. Thus one has eventually to decide whether it is easier to measure either α_0 or the dust load, independently from satellite data. How important the value of surface reflectance is for a proper determination of dust load by satellite measurements of radiance, can be appreciated by considering the results presented by FRASER (1976): with an indetermination on α_0 of 0.01 only, a relative error on the calculated radiance of 8% was found.

A detailed analysis of surface reflectances in desert areas as obtained from LANDSAT MSS data has been presented by OTTERMAN and FRASER (1976). Surface reflectances α_0 were obtained from measured planetary reflectances α_p by means of look-up graphs, where the ratios (α_p/α_0) were calculated by means of a radiation transfer model (see FRASER, 1976) and plotted as a function of α_0 for different solar zenith angles and

$\alpha_p (\Phi_{su}, \alpha_0)$ (—)

Φ_{su}
——— 0°
— — — 40°
—·—·— 70°
·—··—·· 80°
——— 90°

α_0 (—)
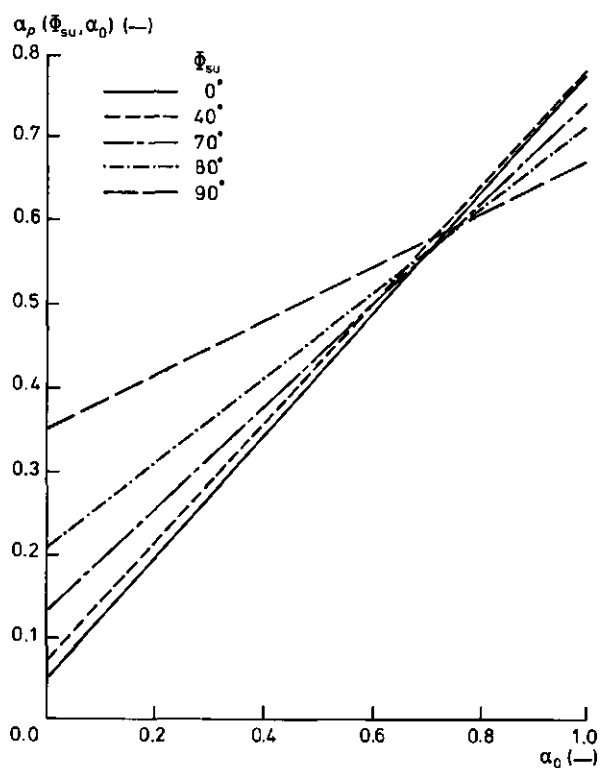
Fig. 5.3. Reflectance α_p at the top of the cloud-free atmosphere as a function of surface reflectance α_0, for several sun zenith angles Φ_{su} (after Nack and Curran, 1978)

atmospheric optical depths (τ). For the surface of the Libyan desert in the spectral range from 0.4 to 1.1 μm α_0-values between 0.53 and 0.58 were found. These results are much higher than those given above, which are generally accepted. The calculation method applied by OTTERMAN and FRASER (1976) required iterative steps on the specific graph of (α_p/α_0) for a particular sun zenith angle Φ_{su}. In the present author's opinion the procedure tends to end in a particular range of α_0 independently of the measured α_p and the true α_0^*, so towards erroneous values of α_0. Accordingly the graphs of α_p versus α_0 presented in Fig. 5.3 after NACK and CURRAN (1978), are sound in contrast with the ones presented by OTTERMAN and FRASER (1976). The graphs in Fig. 5.3 can, therefore, be used to determine α_0 from α_p by applying satellite data.

It can be concluded that satellite measured planetary reflectances provide good estimates of surface reflectances, especially for desert areas, where a relatively large quantity of cloud-free and low zenith angle data are available.

5.2.3. Longwave radiation

Longwave (thermal) radiation $\varepsilon \sigma T_0^4$ emitted by the

surface can in principle be obtained by measuring the emittance in the 8 to 14 μm spectral range. Use of radiometers installed in an airplane or a satellite is a suitable experimental technique which allows the coverage of large areas.

If surface temperature T_0 is to be obtained, two factors have to be accounted for: attenuation due to atmospheric water vapour and dust, and the specific value of the emissivity ε of the surface. The effect of atmospheric water vapour will be discussed first. W a t e r   v a p o u r little absorbes, in principle, in the thermal infrared range of 8 to 14 μm because windows in the H_2O rotational spectrum exist at 8.94, 11.10, 12.01 and 12.67 μm. However, it was shown by BIGNELL (1970) that absorption in the spectral range of 8 to 14 μm can be observed indeed, although no individual line can be clearly identified.

The extinction coefficient for H_2O, Γ, can be written as:

$$\Gamma = N_w c_{self}[e + b(P - e)] \qquad (cm^{-1}) \qquad (5.13)$$

where N_w is the concentration of H_2O molecules (molec·cm^{-3}), c_{self} is molec^{-1}·cm^2·mbar^{-1}, $b = c_{for}/c_{self}$ the ratio of foreign broadening to self broadening coefficient, e vapour pressure (mbar), P total pressure (mbar). The self and foreign broadening of the rotational lines of H_2O was calculated theoretically by BENEDICT and KAPLAN (1964). Their findings were not confirmed by experimental observations in the 8 to 14 μm range. They were in agreement, however, with single line measurements in other ranges. This was essentially the argument to ascribe the absorption observed to be in excess of line contributions, to a water dimer $(H_2O)_2$ responsible for additional interactions. Thus the number of possible energy levels and of the corresponding transitions increases tremendously to yield an absorption continuum. It was shown by MONTGOMERY (1978) that the rôle of continuum absorption decreases with temperature and that at T > 350 K, line broadening is the main process. Absorption by atmospheric water vapour is lowest in the window from 10.5 μm to 12.5 μm, but also in this region absorption has been observed to be in excess of calculations based on line broadening. There is, however, no definitive agreement on the theory and calculation of line broadening, so the previous statement relates to a particular model of line broadening. By deriving a different theoretical model of collision - broadened lines, CLOUGH et al. (1980) concluded that the basis for the excess - absorption concept was not firm. Therefore the amount of the excess depends on

details of the different calculation procedures.

In the application of thermal infrared data it is common practice, however, to calculate the 'atmospheric correction', by applying the excess absorption concept.

A method to estimate the effect of atmospheric water vapour on satellite measured earth surface temperatures can be presented, but as will become clear at the end of this section such calculations cannot be very accurate and trustworthy. The issue is rather the determination of firstly the weight of the several possible uncertainties and secondly of the trend of the atmospheric water vapour effects.

Thermal infrared radiation models. In the application of thermal infrared remotely sensed data, a number of radiation transfer models have been proposed to account for atmospheric absorption. Calculations for specific cases will be presented in Chapter 7 in relation to data collected over the Libyan desert.

The radiant intensity $I_{\tilde{\lambda}}$ in the upward direction through an horizontally homogeneous atmosphere can be written as an integral function of the optical depth τ (LIOU, 1980):

$$I_{\tilde{\lambda}}(\tau) = I_{\tilde{\lambda}}(\tau_{bot})\exp\left[-\ (\tau_{bot} - \tau)\right] +$$

$$+ \int_{\tau}^{\tau_{bot}} B_{\tilde{\lambda}}[T(\tau')]\exp\left[-\ (\tau' - \tau)\right]d\tau'$$

$$(W\cdot m^{-2}\cdot\mu m^{-1}\cdot sr^{-1})$$
$$(5.14)$$

where $I_{\tilde{\lambda}}$ is the spectral radiant intensity $(W\cdot m^{-2}\cdot\mu m^{-1}\cdot sr^{-1})$ at wavelength $\tilde{\lambda}$ (μm), τ_{bot} is the total optical depth to the bottom of the atmosphere and $B_{\tilde{\lambda}}(T)$ $(W\cdot m^{-2}\cdot\mu m^{-1}\cdot sr^{-1})$ is Planck's function at temperature T (K) and wavelength $\tilde{\lambda}$.

The optical depth τ due to the absorbent i is defined as:

$$\tau^i = \int_s^\infty \hat{\Gamma}_i\rho_i ds' \qquad (-) \qquad (5.15)$$

where $\hat{\Gamma}_i$ is the absorption coefficient of absorbent i $(m^2\cdot kg^{-1})$ and ρ_i its density $(kg\cdot m^{-3})$, while s is a generic path length (m). When s is chosen as the vertical distance z, positive upwards, the highest τ is found at the bottom of the atmosphere, i.e. at z = 0. Eq. (5.14) can be rewritten between τ_{bot} and τ = $(\tau_{bot} - d\tau)$, i.e. for a thin layer at the lower boundary of the atmosphere:

$$I_{\tilde{\lambda}}(\tau) = I_{\tilde{\lambda}}(\tau + d\tau)\exp(-d\tau) +$$

$$+ \int_{\tau}^{\tau + d\tau} B_{\tilde{\lambda}}[T(\tau')]\,d[\exp -\ (\tau' - \tau)]$$

$$(W\cdot m^{-2}\cdot\mu m^{-1}\cdot sr^{-1})$$
$$(5.16)$$

which can be considered as a recursive formula suitable to calculate numerically $I_{\tilde{\lambda}}(\tau)$ between the levels n and n - 1. Namely $I_{\tilde{\lambda}}(\tau)$ at level n is obtained by eq. (5.15) from $I_{\tilde{\lambda}}(\tau + d\tau)$ at the lower level n - 1. Before calculations can be performed, a suitable expression for τ must be given. Accordingly, either the absorption coefficient $\hat{\Gamma}_v$ or the extinction coefficient $\Gamma_v = \hat{\Gamma}_v\rho_v$ (m^{-1}) is to be specified to account for the effect of atmospheric water vapour on $I_{\tilde{\lambda}}$. Now the problem is to determine the value of one of these coefficients and its dependence on temperature T, total pressure P and vapour pressure e. To the author's knowledge the most complete overview of the state-of-art of atmospheric water vapour physics has been given by DEEPAK et al. (1980). Available experimental results on absorption by water vapour were summarized by BURCH and GRYVNAK (1980). It appears that no firm explanation exists of the absorption observed in excess of that obtained by calculation of line broadening. Since there is no accepted definition of a reference line absorption, comparison of results from different experiments is somewhat entangled. There is no definitive evidence that the dimer really exists and if so, that it accounts completely for the observed absorption spectrum of water vapour in the 10.5 to 12.5 μm spectral range. Evidence of its existence relies on findings of ROWLINSON (1949), as discussed by EISENBERG and KAUZMANN (1969). It has been shown that the difference between measured values of the second virial coefficient of steam and calculations based on the no-dimer hypothesis could be explained by the existence of the dimer. The energy of formation of a dimer (4.98 kcal·mol^{-1}) was determined and shown to correspond to a physically possible state. Evidence that the dimer could account for the excess absorption was presented by BOHLANDER et al. (1980). These authors calculated theoretically the dimer spectrum by considering vibrations and rigid rotations, but their conclusions did not reach further than saying: 'excess absorption by water vapour is similar in magnitude to predicted dimer absorption and has a similar temperature dependence'. Some of the data presented by these authors support the concept that the water dimer may exist in an excited state in the lowest tropospheric layers (P > 950 mb). Thus the absorption coefficient of wa-

$B'_\lambda(T) / B_\lambda(T)$ (‰)
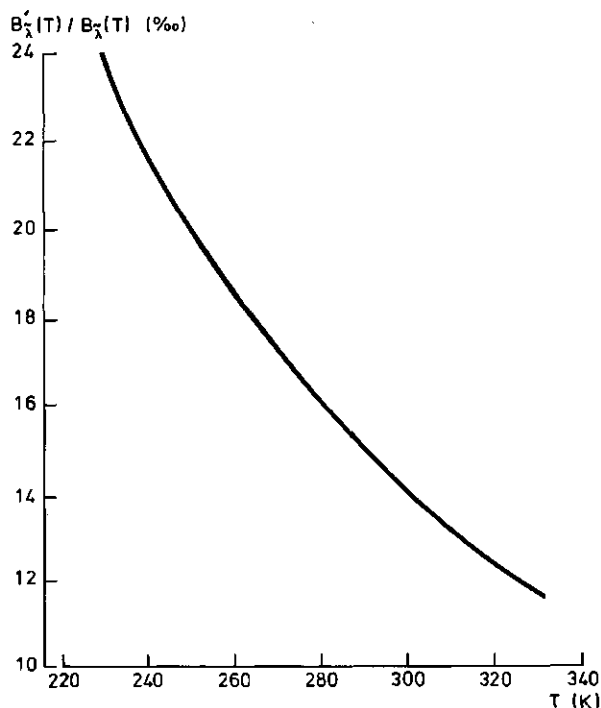
Fig. 5.4. Ratio of the derivative B'_λ, with respect to temperature of Planck's function $B_\lambda(T)$, to $B_\lambda(T)$. The value of this ratio specifies the accuracy required of the radiant intensity at the top of the troposphere to achieve a 1K-accuracy of the satellite-measured temperature

ter vapour may differ in the lower and in the higher levels of the troposphere because a shift in the shape of the absorption spectrum may occur at lower total pressures.

Data on the temperature dependence of the absorption coefficient at lower temperatures has been presented by LLEWELLYN-JONES (1980). It appears that the energy of formation of $(H_2O)_2$ increases at lower temperatures, that is to say that $(H_2O)_2$ is in a lower energy level.

The preceding remarks also give an idea of the fundamental problems involved in calculations of the 'atmospheric correction'. It should be realized that we are still far away from a real operational status of techniques in that field.

The difference between satellite measured (T^0_{top}) and 'true' (T_0) surface temperature can be evaluated from I^{top}_λ-values by inverting Planck's function $B_\lambda(T)$. The accuracy on I^{top}_λ needed to evaluate $(T^0_{top} - T_0)$ with 1K-accuracy can easily be calculated. The derivative $B'_\lambda = \partial B_\lambda(T)/\partial T$ is temperature dependent only, since only one wavelength $\lambda = 11.5$ µm is considered. The ratio (B'_λ/B_λ) specifies the required accuracy on $(T^0_{top} - T_0)$ as intended above. In Fig. 5.4 this ratio is plotted in the temperature range from 240 to 330 K. It should be noted that the accuracy on

I^{top}_λ-values must be 1.9% at 260K, and 1.2% at $T_0 = 330$, if $(T^0_{top} - T_0)$ is to be obtained with the required 1K-accuracy.

Some positive evidence on the magnitude of absorption coefficients of water vapour $\hat{\Gamma}$ is available, although in a rather narrow range of T-, P- and e-values. In addition to results presented by DEEPAK et al. (1980), other literature should be considered: COX (1973), HUNT (1973), LEE (1973), ROBERTS et al. (1976) and MONTGOMERY (1978), to give but a few. As summarized by BOLLE (1982) the final result can be represented by empirical functions relating:

- the absorption coefficient $\hat{\Gamma}^*_v$ at T = 296K to the wave number $\tilde{v}$ (cm^{-1}) as:

$$\hat{\Gamma}^*_v = b_1 + b_2 \exp(-b_3 \tilde{v}) \qquad (cm^2 \cdot atm^{-1} \cdot molec^{-1}) (5.17)$$

where $b_1 = 1.25 \cdot 10^{-22}$ cm$^2 \cdot$atm$^{-1} \cdot$molec^{-1}; $b_2 = 2.34 \cdot 10^{-19}$ cm$^2 \cdot$atm$^{-1} \cdot$molec^{-1}; $b_3 = 8.30 \cdot 10^{-3}$ cm. To express eq. (5.17) in units of cm$^2 \cdot$atm$^{-1} \cdot$g^{-1} the molecular weight of water $(2.99 \cdot 10^{-23}$ g) has to be substituted in the equation;

- the absorption coefficient $\hat{\Gamma}_v$ to temperature T at constant values of P and e:

$$\hat{\Gamma}_v(\tilde{v},T) = \Gamma^*_v(\tilde{v}) \exp[b_4(\frac{1}{T} - \frac{1}{296})] \qquad (cm^2 \cdot atm^{-1} \cdot g^{-1}) \\ (5.18)$$

The value of b_4 varies between 1745 and 2000K, with as best estimate 1800K. The constant b_4 equals the energy of formation of the absorbent divided by the gas constant per mole. When $b_4 = 1800$K is considered, one finds an energy of formation of the absorbent of 3.6 kcal$\cdot$molec^{-1}, a value lower than that found from the second virial coefficient of steam (see also BOHLANDER et al., 1980).

As regards the dependence of $\hat{\Gamma}_v$ on P and e, two relationships have been reported by BOLLE (1982), as obtained by other authors by fitting measurements to functions of the form:

$$\hat{\Gamma}_v = \hat{\Gamma}^{self}_v(\tilde{v}^*,T)(e + bP) \qquad (cm^2 \cdot g^{-1}) \qquad (5.19)$$

or

$$\hat{\Gamma}_v = \hat{\Gamma}^{self}_v(\tilde{v}^*,T)e + \hat{\Gamma}^{for}_v(\tilde{v}^*,T)P \qquad (cm^2 \cdot g^{-1}) (5.20)$$

where $\tilde{v}^* = 869.6$ cm^{-1} if $\lambda = 11.5$ µm, has been considered, $\hat{\Gamma}^{self}_v$ is the self-broadening coefficient, $\hat{\Gamma}^{for}_v$ is the foreign-broadening coefficient, b = $\hat{\Gamma}^{for}_v/\hat{\Gamma}^{self}_v$. The trouble with the eqs. (5.18), (5.19) and (5.20) is that they are semi-empirical in nature and that the range of T, P, e actually covered by

81

measurements of $\hat{\Gamma}_v$, is rather narrow. For this narrow range it has been shown that the dimer indeed can account for the excess absorption. Therefore the present author proposes to calculate the extinction coefficient $\Gamma_v = \hat{\Gamma}_v \rho_v$ (cm^{-1}) of water vapour in the spectral range 10.5 to 12.5 µm as a function of dimer concentration. Namely:

$$\Gamma_v = \hat{\Gamma}_v \rho_v = \hat{\Gamma}_{dim} \rho_{dim} = \hat{\Gamma}_{dim} \xi_{dim} \rho_v \qquad (cm^{-1}) \qquad (5.21)$$

where ξ_{dim} is the molar fraction of the dimer. The improvement is that ξ_{dim} can be related to T, P, e on theoretical grounds as discussed by EISENBERG and KAUZMANN (1969) and COX (1973). The expression for ξ_{dim} then reads:

$$\xi_{dim} = \frac{1}{2} \left\{ (2 + \frac{P \exp(b_5 - b_6/T)}{e}) - \right.$$

$$\left. + \left[(2 + \frac{P \exp(b_5 - b_6/T)}{e})^2 - 4 \right]^{\frac{1}{2}} \right\} \qquad (-) \quad (5.22)$$

where $b_5 = 13.96$, $b_6 = 2878$. The order of magnitude of ξ_{dim} is 10^{-3} $mol_{dim} \cdot mol_{mon}^{-1}$, therefore the concentration of the monomer (H_2O) is almost equal to ρ_v, which can be used in eq. (5.21).

Values for $\hat{\Gamma}_{dim}$ can be obtained from measurements of $\hat{\Gamma}_v$, when the values of T, P and e applying to the particular experiment are known. Then ξ_{dim} can be calculated by means of eq. (5.22) and $\hat{\Gamma}_{dim}$ obtained from eq. (5.21). According to ROBERTS et al. (1976) $\hat{\Gamma}_v$ = 10.3 $cm^2 \cdot atm^{-1} \cdot g^{-1}$ at T = 294K, P = 1013 mb, e = 19.06 mb. Then from eqs. (5.21) and (5.22) one finds $\hat{\Gamma}_{dim}$ = 259 $cm^2 \cdot g^{-1}$.

It must be mentioned again that the approach to calculate the effect of atmospheric water vapour on satellite-measured surface temperatures does not rest on definitely established grounds. There are no measurements of Γ_v in the 10.5 to 12.5 µm range applying to atmospheric conditions at greater heights than the 950 mb level. There is no definitive evidence that the dimer exists. There is no reason to believe that its behaviour, assuming $(H_2O)_2$ is a real entity, in the entire atmospheric range of T, P, e is the same as that of steam and as that observed under ground level atmospheric conditions. The proposal by the present author indicated by eqs. (5.21) and (5.22) is intended to specify the dependence of Γ_v on T, P and e, from what is theoretically known, rather than from experimental findings only.

A few authors have compared calculations of upward radiant intensity $I_{\tilde{\lambda}}$ in the so-called 10 to 12 µm atmospheric window with measurements. HOUGHTON and LEE (1972) showed that calculations with $\hat{\Gamma}_v$ as obtained by an equation in the form of eq. (5.20), where
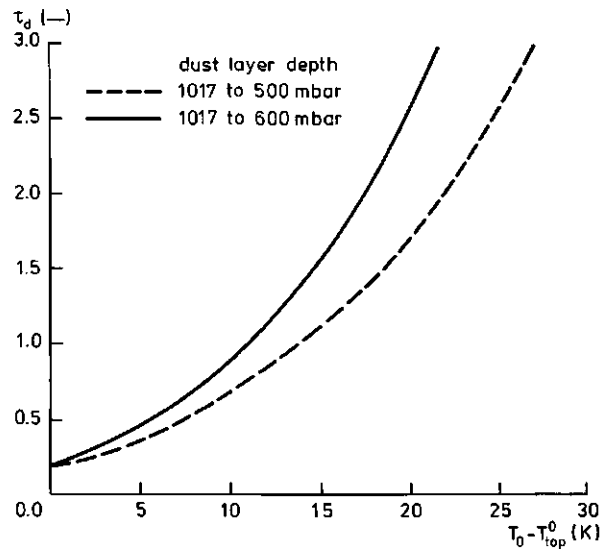
Fig. 5.5. Atmospheric optical depth at $\tilde{\lambda}$ = 0.5 µm due to dust, τ_d, plotted versus the temperature difference, $T_0 - T_{top}^0$, for two thicknesses of the atmospheric layer containing dust (after Carlson and Benjamin, 1980)

$\hat{\Gamma}_v^{self}$ = 10.0 $cm^2 \cdot atm^{-1} \cdot g^{-1}$ and $\hat{\Gamma}_v^{for}$ = 0.0 $cm^2 \cdot atm^{-1} \cdot g^{-1}$ agreed with radiant intensity measurements performed up to heights of 0.6 km within a 5% difference in $I_{\tilde{\lambda}}$ or 5K, say, in T_0 (cf. Fig. 5.4).

S a h a r a n   d u s t   plays a rôle in longwave radiation transfer, as it does in the shortwave region. Atmospheric heating due to Sahara dust has been studied by CARLSON and BENJAMIN (1980). As shown in Fig. 5.5 dust may be responsible for sensible cooling in the longwave spectral region. As has been shown by these authors the effect is irrelevant below a height of 4000 m, thus airplane measurements would not be affected. Satellite data would show a lower (apparent) surface temperature, even though they neglected upper tropospheric and stratospheric aerosols. These authors proposed to use the apparent depression in surface temperature (see Fig. 5.5) to estimate the amount of aerosol from thermal infrared satellite data in the 10 to 12 µm spectral range. A key-assumption was to consider the absorption by water vapour in tropical atmospheres, as being much smaller than the contribution of dust. The discussion given above shows that the matter is not straightforward, and the calculations to be presented in Chapter 7 prove that the effect of water vapour cannot a-priori be neglected. It is, however, clear that the effect of vapour, of dust and of emissivity must be assessed, before thermal infrared satellite data can quantitatively be used. The matter is theoretically rather entangled and only ground-based measurements of T_0 allow to determine $T_0 - T_{top}^0$ (Chapter 7).

Surface effects. Longwave radiation depends on surface temperature T_0 as $\varepsilon \sigma T_0^4$. A radiometer in the thermal infrared region gives the black body equivalent temperature T_0^* as obtained from the Stefan - Boltzmann law, i.e. $\sigma(T_0^*)^4$, with $\varepsilon = 1$ being assumed. Details on surface reflectance and emissivity of bare soils will be given in Section 5.3. The inaccuracy of T_0 resulting from the approximation $\varepsilon = 1$ is additive to those implied in the calculations on atmospheric absorption. According to KONDRATYEV et al. (1981) a typical value $\varepsilon = 0.95$ applies to soils, thus the true T_0 would be obtained as:

$$0.95 \ \sigma T_0^4 = \sigma T_0^{*4} \qquad (W \cdot m^{-2}) \tag{5.23}$$

or

$$T_0 = 1.0129 \ T_0^* \qquad (K) \tag{5.24}$$

which implies that with a measured $T_0^* = 300K$ actually is $T_0 = 303.9K$, which is an important difference. Because of the presence of dust T_0 in eq. (5.24) is likely to be lower than the true surface temperature. If a difference of 5K is considered, then for $T_0^* = 300K$, $T_0 = 308.9$. It should be noted that the correction on T_0^* for ε as accounted for by eq. (5.23) and (5.24) applies to an infinite-bandpass detector. However, it has been shown by SUTHERLAND et al. (1979) that a correction for the finite detector bandpass (8 to 14 μm or 10 to 12 μm) for normal values of ε would be approximately 0.5K.

In the preceding pages it has been shown that opportunities do exist for the remote determination of some terms of the surface energy balance. However, a number of complicating factors have to be considered and their respective rôle is to be assessed. The need for comprehensive ground-reference data therefore is clear. As will be shown in Chapter 7, it is by far easier to assess the actual rôle of the various complicating factors on the basis of relatively few ground measurements, than by applying theoretical calculations involving many parameters which are not exactly known.

5.3. SOIL RADIATIVE PROPERTIES

Problems of interest in the present study mainly relate to the application of eq. (5.4) to calculate the latent heat flux. According to the SMITHSONIAN Meteorological Tables (1951, Table 148) 99% of solar radiation is received in the spectral range $0.3 < \tilde{\lambda} < 1.9$ μm and 83% in the range $0.3 < \tilde{\lambda} < 1.1$ μm. Hence an instrument sensing radiative fluxes in the inter-

val $0.3 < \tilde{\lambda} < 2$ μm provides representative values of reflected radiance. When satellite data are used in the range 0.3 to 1.1 μm, the relation between solar spectrum, soil spectral response and the finite detector bandpass must be taken into account. The radiometer onboard the LANDSAT spacecraft measures reflected radiance from 0.5 to 1.1 μm, that on the HCMM spacecraft from 0.5 to 1.1 μm and the one on the METEOSAT from 0.4 to 1.1 μm.

5.3.1. Shortwave surface reflectance

The soil surface is an imperfect diffuse reflector, although in many cases it has been assumed to be a Lambertian, i.e. perfect, one. Reflection behaviour different from a Lambertian surface implies that the reflected radiance changes not only with view-angle, but also with the relative magnitude of diffuse and direct radiation. For the combined effect of R_{swdf}, the diffuse component of R_{sw}, and of the sun zenith angle Φ_{su}, the expression:

$$\alpha_0 = \alpha_0'[1 + 2.5(1.25 - R_{swdf}/R_{sw})(1 - \alpha_0')\sin \tfrac{3}{2} \Phi_{su}]$$
$$(-) \tag{5.25}$$

as proposed by MAKAROVA et al. (1973) and reported by KONDRATYEV et al. (1981) can be used. In eq. (5.25) α_0' denotes the surface reflectance at $\Phi_{su} = 0$. A simpler formula, which in Section 7.5 will be shown to be satisfactory:

$$\alpha_0 = \alpha_0' \ 2.444 \left[1 - \cos \Phi_{su} \ \ln(1 + \frac{1}{\cos \Phi_{su}})\right] \qquad (-) \tag{5.26}$$
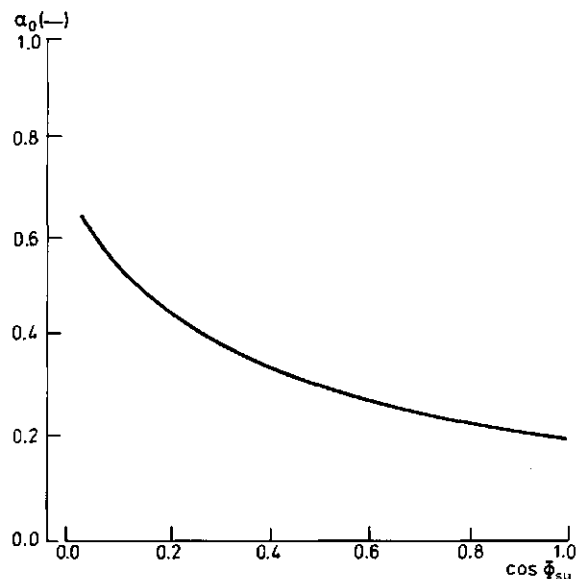
Fig. 5.6. Surface reflectance α_0 (see eq. 5.26) versus the cosinus of the sun zenith angle Φ_{su}

Table 5.4. Shortwave surface reflectance of a number of soil surfaces

Surface type	α_0	Reference
White sand (dry)	0.40	Kondratyev (1969)
White sand (moist)	0.20	Kondratyev (1969)
White sand (dry)	0.34 - 0.40	Kondratyev (1954)
Yellow sand (dry)	0.35	Kondratyev (1954)
Grey sand (dry)	0.18 - 0.23	Kondratyev (1954)
Alluvial soil on sea sediments (dry)	0.12	Oguntoyinbo (1970)
Semi-arid, brown and reddish soils	0.17	Oguntoyinbo (1970)
Red ferrous soils on sand deposits	0.17	Oguntoyinbo (1970)

Fig. 5.7. An example of the spectral reflectance $\alpha_0(\tilde{\lambda})$ for dry and wet sand (after Condit, 1970)

to account for the effect of Φ_{su} only, has been applied by BARTMAN (1980), after LARSON and BARKSTROM (1977), to establish maps of earth reflectance. In Fig. 5.6 α_0 has been plotted for $\alpha_0' = 0.28$, i.e. for a desert surface, against cos Φ_{su}, as computed by eq. (5.26). Because of the daily cycle of Φ_{su}, α_0 will decrease in the morning and increase in the late afternoon. Literature values of the reflectance of different bare soil surfaces are presented in Table 5.4; it should be remembered that for the various values mentioned measuring technique and averaging procedure need not necessarily to be the same. The dependence of α_0 on Φ_{su} has been measured by GUBE (1982) by means of METEOSAT hourly-data. He also did show that satellite-based measurements of α_0 confirmed calculations by a radiative transfer model. Desert surface reflectance was measured by this author as being 0.3 for the Sahara and 0.18 for the Kalahari desert, both figures relating to 12.00 GMT on 24 November 1979. The dependence of α_0 on Φ_{su}, e.g. as described by eq. (5.26), has been observed by ASHBURN and WELDON (1956) for the Mojave desert.

The dependence of α_0 on wavelength $\tilde{\lambda}$ has a twofold relevance for the present investigation. Firstly it should be shown that α_0 in the 0.4 to 1.1 µm spectral range (LANDSAT, HCMM and METEOSAT shortwave band) is representative of the wider solar spectral range of 0.2 to 3.5 µm. Secondly, knowledge of $\alpha_0(\tilde{\lambda})$-curves is helpful in classifying bare soil surfaces from LANDSAT - MSS data and in assessing soil moisture conditions. Selection of optimal wavelengths for soil classification has been discussed by CONDIT (1970) and by MAY and PETERSEN (1975).

Spectral reflectances for different sandy soils have been measured by CONDIT (1970) and in Fig. 5.7 one representative example of his $\alpha_0(\tilde{\lambda})$-curves for a dry and wet sand is given. Spectral reflectances of playas in the broader spectral range of 0.5 to 6.0 µm have been measured by HOVIS (1966) and HOVIS et al.
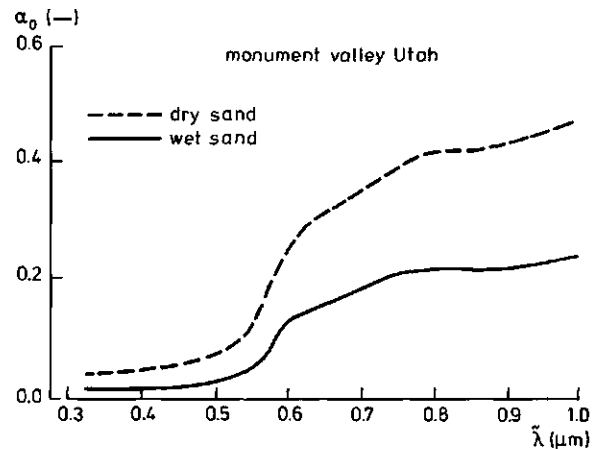
(1968) with the aid of remote sensors. An example is given in Fig. 5.8 as applying to Rosamond Dry Lake (Cal.). The value of α_0 is rather constant in the spectral range 0.7 to 2.2 µm and the decrease of α_0 between 2.2 and 3.0 µm is partly due to the reflectance of calcium carbonate present in the Rosamond Dry Lake soil. According to figures of the type of Figs. 5.7 and 5.8 it can be concluded that broad-band radiometers (spectral range from 0.5 to 1.1 µm) as carried in satellites, allow a good determination of α_0. When dealing with multispectral scanners one should account for the percentage of solar energy in each band to calculate α_0 from the various single band reflectances $\alpha_0(\tilde{\lambda}_i)$.

Shortwave surface reflectance α_0 of bare soil is strongly dependent on soil moisture content θ, i.e. α_0 decreases with increasing moisture content. In Fig. 5.9 $\alpha_0(\tilde{\lambda})$ curves as measured by BOWERS and HANKS (1965) for a silt loam at different moisture contents are shown. ÅNGSTRÖM (1925) already did show that sat-
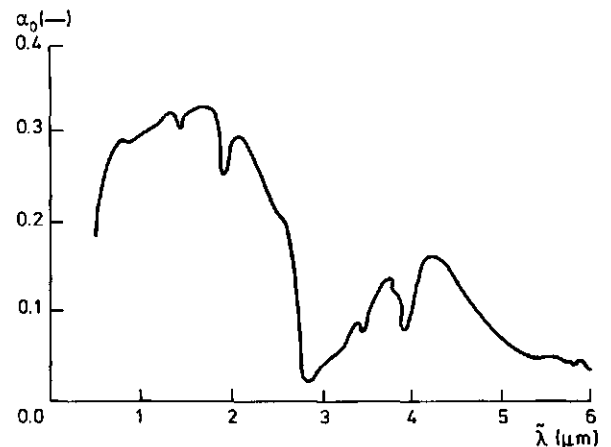
Fig. 5.8. Spectral reflectance $\alpha_0(\tilde{\lambda})$ of a playa soil (Rosamond Dry Lake, Cal.) (after Hovis, 1966)
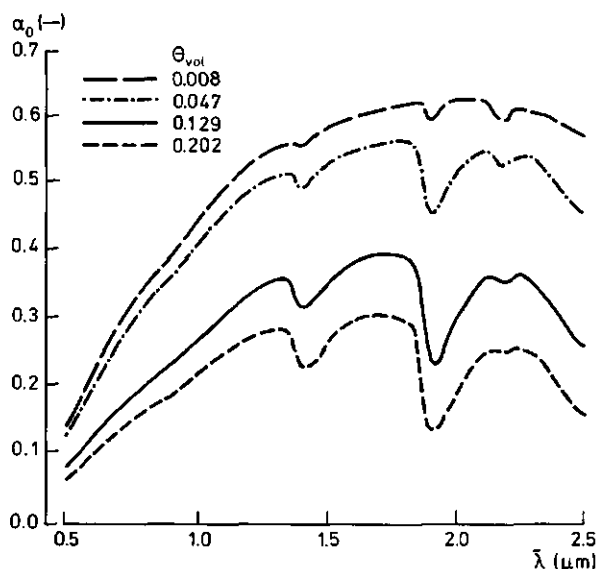
Fig. 5.9. Reflectance α_0 versus wavelength $\tilde{\lambda}$ for different moisture contents θ_{vol}, as indicated for each curve (after Bowers and Hanks, 1965)

urated soil reflectance α_{sat}^0 and the dry soil reflectance α_{dry}^0 can be related to the refraction index n of the saturating liquid as:

$$\alpha_{sat}^0 = \frac{\alpha_{dry}^0}{\left[n^2(1 - \alpha_{dry}^0) + \alpha_{dry}^0\right]} \qquad (-) \qquad (5.27)$$

Eq. (5.27) was supported by experiments of PLANET (1970) who pointed out that n changes with the salt content of the liquid. IDSO et al. (1975) did show that measurements of α_0 were linearly related to measured θ_0 and that a particular θ^* can

be identified above which no further variation in α_0 is observed (Fig. 5.10). It must be noted that this result is not contradictory with the theory of ÅNGSTRÖM (1925). This author assumed that internal reflection takes place, i.e. light reflected on the surface of soil particles is re-reflected at the surface of the water film. It then appears reasonable to assume that the process breaks down at some θ^*, where the water film gets thinner. With $\theta < \theta^*$ the interaction light - soil particles becomes the dominant process, thus the impinging light 'sees' more and more soil particles.

It was shown by van BRAKEL and HEERTJES (1974) that the soil solid fraction is the same when expressed per unit area as when expressed per unit volume. Assuming the same holds true for soil moisture content, the behaviour of α_0 according to the present author is linear between α_{dry}^0 and α_{wet}^0:

$$\alpha_0 = \alpha_{wet}^0 \qquad \text{if } \theta^* < \theta < \theta_{sat}$$

$$\alpha_0 = \alpha_{dry}^0 (\frac{\chi - \theta_0}{\chi}) + \alpha_w \frac{\theta_0}{\chi} \qquad \text{if } \theta \leqslant \theta^* \qquad (5.28)$$

where $\chi = \chi_a + \chi_w$ is the total soil porosity.

In Fig. 5.10 values as calculated with eq. (5.28) are compared with the measured curve of IDSO et al. (1975). In the calculations with eq. (5.28), the $\alpha_{dry}^0 = 0.305$, $\alpha_w = 0.08$ and $\chi = 0.35$.

The relevance of the concept underlying eq. (5.28) lies aside from the possibility to measure θ_0 at the surface by means of α_0, also in the possibility to decide whether or not evaporation takes place at the soil surface. According to the definition of the evap-

Fig. 5.10. Comparison of α_0, as calculated by eq. (5.28), with measured (Idso et al., 1975) α_0-values versus moisture content θ_{vol}
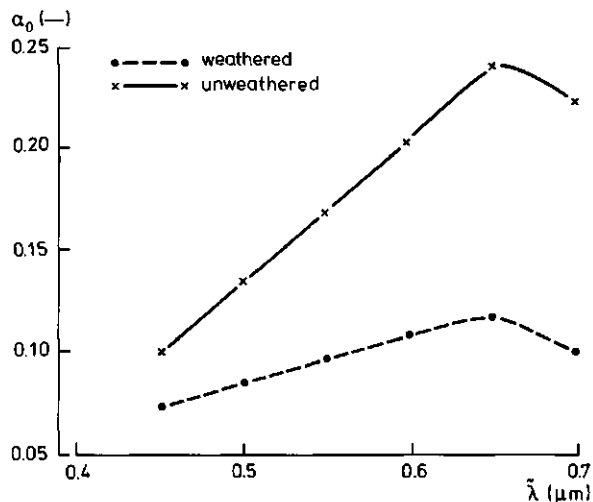
Fig. 5.11. Spectral reflectance $\alpha_0(\tilde{\lambda})$ of weathered and unweathered volcanic rocks (after Reeves et al., 1975)

oration site given in Section 3.3 one can determine the corresponding moisture content θ_E, hence the reflectivity α_{θ_E}, albeit approximate.

It must be pointed out that the observed dependence of α_0 on θ_0, as shown in Fig. 5.10, does not include possible modifications which may take place at the surface of soil particles (e.g. desert varnish). In Fig. 5.11 it is shown how the α_0 of volcanic rock is affected by desert varnish. The interrelation between colour, weathering and reflectance of desert minerals has been applied by McKEE (1979) to study from LANDSAT imagery the movement of sand dunes. Another typical feature of desert (playa) soils is the likely occurrence of salty crusts. Because of the high reflectance of salts, as soon as a crust is established soil reflectance will increase dramatically.

5.3.2. Longwave surface emissivity

A list of emissivities for different surfaces is given in Table 5.5. It appears that a value of $\varepsilon = 0.97$ in the spectral range of 10.4 to 12.6 μm can safely be ascribed to most bare soil surfaces. This value implies that at 300K the black body equivalent temperature is 2K lower than the thermometric temperature, as explained in Paragraph 5.2.3.

The infrared spectral range has in principle a high potential for identification of soil constituents, because of molecular vibrational and roto-vibrational transitions. An excellent and detailed review on infrared spectral lines of soil constituents has been given by STEPANOV (1974). In Table 5.6 a short list of absorption bands in the spectral range between 10.5 and 12.5 μm, the thermal infrared channel of satellite scanners, and in the spectral range from

Table 5.6. Maxima in characteristic absorption bands of minerals in two infrared ranges (after Stepanov, 1974)

10.5 to 13.3 μm	13.3 to 17.4 μm
10.58 - 10.70 μm	13.70 - 13.89 μm
10.75 - 10.99	14.29 - 14.70
11.17 - 11.30	14.70 - 15.38
11.23 - 11.36	14.93 - 15.38
11.69 - 11.83	15.87 - 16.13
11.83 - 11.98	16.13 - 16.39
12.42 and 12.74 (doublet)	15.63 - 16.67
12.5 - 12.82	

13.3 to 17.4 μm is given.

Under actual field conditions, however, different results from those presented in Table 5.6 are to be expected. The blurring effect of surface structures and impurities often overrides the spectral properties of soil minerals. This is a topic of particular relevance in the application of thermal infrared data to study the surface energy balance of playas. Salt crystals and especially halite (NaCl) have a very low emissivity in the thermal infrared spectral range. Therefore, the black body equivalent temperature of such surfaces will be quite different from the thermometric temperature.

Theoretical aspects of absorptions by phonons (quanta of crystal oscillations) in the spectral range where absorption (thus emissivity) is low, have been discussed by LI (1980). This author also reviewed the known measured values of the absorption coefficients of alkali halides (as NaCl) and their dependence on wavelength. In particular he concluded that at low absorptions by the bulk material, the extinction coefficient for surface absorption is a factor 10^3 times the bulk extinction coefficient.

Table 5.5. Emissivity of some bare soil surfaces in particular spectral ranges

Surface type	Spectral range (μm)				Reference
	4 to 100	5 to 15	10.4 to 12.6	9 to 12	
Sand	0.89				Falckenberg (1928)
Sand	0.95				Kawabata et al. (1951)
Loam	0.97				Kawabata et al. (1951)
Clods	0.98				Falckenberg (1928)
Limestone	0.91				Falckenberg (1928)
Gravel	0.91				Falckenberg (1928)
Brown loam		0.97	0.98		Taylor (1979)
Shale and clay		0.97	0.98		Taylor (1979)
Brown loam, brown sand and gravel		0.94	0.97		Taylor (1979)
Grey and brown loam		0.93	0.96		Taylor (1979)
Grey sand		0.91	0.97		Taylor (1979)
Dark sands		0.97	0.98		Taylor (1979)
Fine-grained sand (dry)				0.949	Gaevsky (1951)
Fine-grained sand (saturated)				0.962	Gaevsky (1951)
Loamy sand (dry)				0.954	Gaevsky (1951)
Sandy loam (saturated)				0.968	Gaevsky (1951)
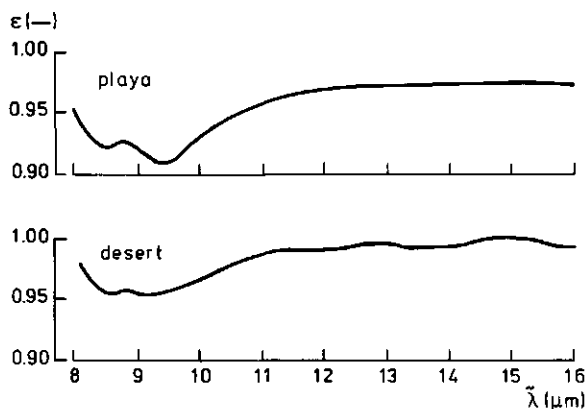
Fig. 5.12. Spectral emissivities of a playa soil, Bristol Dry Lake, and of the desert nearby (after Hovis et al., 1968)

Accordingly it can be concluded that the optical properties of the salty playa crusts will have little in common with those of the salt minerals in their pure state.

The measurements of $\varepsilon(\tilde{\lambda})$ presented by HOVIS et al. (1968) for a number of desert and playa surfaces show that there will not be a very large difference between the black body equivalent temperature and the thermometric temperature. In Fig. 5.12 the spectral emissivity $\varepsilon(\tilde{\lambda})$ of a playa, the Bristol Dry Lake (Cal.), is compared with the $\varepsilon(\tilde{\lambda})$ of the desert nearby. It is seen that the emissivity of the desert is only slightly higher than the one of the playa and both of them are higher than 0.97 in the spectral range 11 to 14 μm.

The conclusion therefore can be drawn that for spectral emissivities in the range of 10.5 to 12.5 μm desert and playa soils have emissivities $\varepsilon \gtrsim 0.97$. Additional data on spectra of natural soil surfaces can be found in HOVIS and CALLAHAN (1966), LYON and PATTERSON (1969), VINCENT (1975) and VINCENT et al. (1975).

On the basis of the preceding reasoning it can be concluded that enough reference values are available to interpret the results of measurements performed in the Libyan desert (as listed in Section 6.2). Literature data and ground measurements allow in turn for validation of satellite-inferred surface temperatures and reflectances (see Section 7.5).

5.4. ESTIMATION OF SOIL HEAT FLUX AT THE SURFACE

5.4.1. General

The soil heat flux at the surface, G_0, is usually assumed to be a minor component of the surface energy balance. However, as shown in Section 5.1 this

holds not always true. The near absence of vegetation cover allows for a close relationship between soil bulk properties and G_0, as discussed in Chapter 4 by means of the apparent thermal admittance concept. A proper estimation of both the distribution of G_0 in space and in time therefore is required.

Surface reflectance α_0 relates to the superficial soil skin rather than to soil bulk properties. Since only the surface temperature T_0 can be remotely sensed, some indirect procedure has to be set up to estimate G_0. It has been pointed out in Paragraph 4.1.1 that the very measurement of G_0 is a difficult task. However, as stated in Section 4.4 one may accept a poor accuracy in the estimation of G_0 when the derived apparent thermal properties can be calibrated against known soil layering at a few sites. It appears that interest lies rather in the possibility of comparing the difference in thermal response of different sites within one region. To estimate the absolute value of the heat flux without carrying out an empirical calibration based on experiments is impossible. When a few calibration experiments are performed, however, the distribution of thermal response as well as the actual value of the heat flux G_0 can be obtained from remotely sensed data in the thermal infrared range.

In the discussion the space and time dependent pattern of surface temperature T_0 will be considered separately. The space dependent pattern here is defined as being the long term average of T_0 and the time dependent part as being the sum of the harmonic components of T_0. Analogous definitions apply to the soil heat flux G_0. The reason for this separation stems from the different kind of information present in the two parts which give information for different applications requiring knowledge of thermal properties at different depths, for example:

- Detection of deeper structural anomalies. The average value of G_0 over a time period long enough to filter out the stronger harmonic components is required.
- Derivation of the apparent soil thermal admittance and application of the interpretation procedure as presented in Chapter 4. Then the amplitude of one or more harmonic components of G_0 is needed.
- Determination of the latent heat flux LE from the surface energy balance equation. Here instantaneous values of G_0 are needed.

It should be realized that the relation between the frequency of the surface temperature wave and the depth which can be sensed, holds true throughout the entire frequency range, up to the continuum component, i.e. the long term average of T_0. This topic

has a direct bearing on the interpretation of thermal infrared imagery.

It can be shown that the mean value $\overline{T}_0$ and the harmonic components present in $T_0(t)$ relate to different thermal properties and to different components of the forcing function G_0. It has already been stated that to achieve a satisfactory accuracy in describing $T_0(t)$ only the first few terms of the Fourier series usually are needed. Let P_X be the longest period which is considered in eq. (4.18). Hence $\overline{T}_0$ relates to periods longer than P_X and over such periods the observed pattern of surface temperature relates in principle to the deep thermal characteristics of the earth skin. This aspect can be discussed in more formal terms; by recalling that the solution of the heat conduction equation (eq. 3.34) can be split up in two terms:

$$T(z,t) = u(z) + w(z,t) \qquad (K) \qquad (5.29)$$

where $u(z = 0) = \overline{T}_0$ according to the definition given above for the space dependent part of the surface temperature pattern and $w(z,t)$ is the harmonic part of T_0, thus the time dependent part of the surface temperature pattern. Over a full period P_X, $\overline{w}(z,t) = 0$ and the $u(z)$ part of the solution relates to the heat source distribution $S(z)$ according to eq. (3.68). If $S(z) = 0$ in a particular stratum, then from eq. (3.68) can be derived:

$$\frac{\partial^2}{\partial z^2} u(z) = 0 \qquad (5.30)$$

hence

$$\frac{\partial}{\partial z} u(z) = b_1 \qquad (5.31)$$

where b_1 is any constant. As discussed in Section 4.3 temperature waves of relatively long periods can only penetrate to a few meters depth. At deeper depths, some tens of meters say, the temperature gradient is the outcome of the upward geothermal flux G_{deep}. Accordingly:

$$G_{deep} = -\lambda_{deep} \frac{\partial}{\partial z} u(z) \qquad (W \cdot m^{-2}) \qquad (5.32)$$

Thus, by substituting eq. (5.32) in eq. (5.31) and integrating:

$$u(z) = -\frac{G_{deep}}{\lambda_{deep}} z + b_2 \qquad (K) \qquad (5.33)$$

The constant b_2 can be obtained by assigning the temperature T_{deep} at some depth z_{deep}, or at the surface (where $u(0) = \overline{T}_0$):

$$T_{deep} = -\frac{G_{deep}}{\lambda_{deep}} z_{deep} + b_2 \qquad (K) \qquad (5.34)$$

or

$$\overline{T}_0 = b_2 \qquad (K) \qquad (5.35)$$

When the time dependent part $w(z,t)$ is described by eq. (4.12) for each harmonic in $T(z,t)$, the following expression for a semi-infinite medium is:

$$T(z,t) = -\frac{G_{deep}}{\lambda_{deep}} z + \overline{T}_0 +$$
$$+ \sum_{j=1}^{n} A_j^0 (\cosh \gamma_j z - \sinh \gamma_j z) \exp i(\omega_j t - \Omega_j)$$
$$(K) \qquad (5.36)$$

Note that $\overline{T}_0$ in eq. (5.36) is related to G_{deep}, λ_{deep} and z_{deep} through eq. (5.34). The harmonic part of $T(z,t)$ is related to the heat flux G_0 through the thermal admittance.

5.4.2. Space dependent part of surface temperature patterns

The bearing of eq. (5.36) on the interpretation of thermal infrared imagery is to be discussed for areas of such limited extension that the dependence on latitude of the yearly average of R_{sw} can be neglected. Under these conditions the sun-induced oscillations of surface temperature will be periodic, thus time dependent only and the mean surface temperature space dependent only, according to the particular combination of T_{deep}, G_{deep} and λ_{deep}.

The application of thermal infrared imagery to detect geothermal areas is a relatively well established technique, see for instance WATSON (1975). A single image is usually applied as observed at a particular time instant when $G_0 \approx 0$; then the effect of the deeper thermal behaviour can be observed at the soil surface. Such a technique will be successful if G_{deep} is not too low, 8 $W \cdot m^{-2}$ say according to WATSON (1975). It is, however, clear that a single thermal infrared image will show differences which also relate to the periodic part of $T_0(t)$, through the phase difference in $T_0(t)$ between different surfaces. The longer the time span covered by a number of thermal infrared images, the better the periodic part of $T_0(t)$ can be filtered out and the finer differences detected in G_{deep}.

As far as the assumption holds true that no harmonic of a period longer than P_X is present in $T(z,t)$, eq. (5.36) is an exact description of the temperature distribution $T(z,t)$. An example will be presented to

Table 5.7. Data applied in the example discussed to illustrate the relation between G_{deep} and T_0, $P = 500$ days

Soil	λ $(W \cdot m^{-1} \cdot K^{-1})$	ρc $(J \cdot m^{-3} \cdot K^{-1})$	d (m)	$\|y\|$ $(W \cdot m^{-2} \cdot K^{-1})$	$A'(G_0)$ $(W \cdot m^{-2})$	$A(T_0)$ (K)	$A''(G_0)$ $(W \cdot m^{-2})$	$A(T_0)$ (K)	$\bar{T}_0$ (K)
1	1	$2 \cdot 10^6$	2.6	0.54	1	1.9	10	19	283
2	2	$3 \cdot 10^6$	3.0	0.93	1	1.1	10	11	288

show how large the differences can be in surface temperature respectively due to the geothermal heat flux and to the sun induced energy flux at the soil surface. Finally the possibility that T_0-fluctuations of period $P > P_x$ would mask the G_{deep}-dependent pattern of T_0, will be discussed. It should be realized that the small magnitude of the geothermal heat flux in comparison with fluxes at the soil surface is no definitive argument to rule out effects on the surface temperature pattern.

A homogeneous layer of two different soils with respectively $\lambda_1 = 1$ $W \cdot m^{-1} \cdot K^{-1}$ and $\lambda_2 = 2$ $W \cdot m^{-1} \cdot K^{-1}$ will be considered separately. The boundary conditions at z_{deep} are specified as: $G_{deep} = -0.05$ $W \cdot m^{-2}$ (so upwards), $T_{deep} = 293$ K at $z_{deep} = 200$ m. According to eq. (5.34) one finds that $\bar{T}_0 = 283$ K at the surface of soil 1 and $\bar{T}_0 = 288$ K at the surface of soil 2, so a difference of 5 K!

To discuss the rôle of temperature waves of period $P > P_x$, let us assume that a fluctuation of $\tilde{P} = 500$ days is present, while the observation period $P_x = 365$. Oscillations with $P \leq P_x$ by definition are assumed to have been filtered out. As an example, two possible amplitudes of heat flux for $P = \tilde{P}$ have arbitrarily been taken: $A'(G_0) = 1$ $W \cdot m^{-2}$ and $A''(G_0) = 10$ $W \cdot m^{-2}$. The corresponding amplitudes of the surface temperature can be calculated by means of the thermal admittance for a homogeneous soil according to eq. (4.17) and for $P = \tilde{P}$. The selected soil thermal properties, amplitudes of the T_0- and G_0-oscillations and mean surface temperature are presented in Table 5.7. As is shown by the value of the damping depth d at $\tilde{P}$

for both soil 1 and soil 2, the temperature T_{deep} is independent from the surface energy balance, because $z_{deep} \gg d_1$ or d_2. At a depth of 12 m for soil 1 and of 13.8 m for soil 2 the surface-related temperature amplitude is 10^{-2} $A(T_0)$.

In Table 5.8 maximum T_x^0 and minimum T_n^0 surface temperatures, as calculated from eq. (5.36) according to the data in Table 5.7, are presented. For each value of $A(G_0)$, i.e. the amplitude of the soil heat flux at the surface, values relating to $G_{deep} = -0.05$ $W \cdot m^{-2}$ and $G_{deep} = 0$ $W \cdot m^{-2}$ are given. It appears that this comparison between $A(G_0)$ and G_{deep} is not a good criterion to establish whether the effect of a particular G_{deep} can be detected at the surface. Although a flux $G_{deep} = -0.05$ $W \cdot m^{-2}$ can be considered definitely negligible in comparison to both 1 and 10 $W \cdot m^{-2}$, the effect of G_{deep} on the pattern of $\bar{T}_0$ cannot be neglected. It should be realized that differences in λ much larger than those between soil 1 and soil 2 in Table 5.7 occur in practice, e.g. between rocks and soil.

The preceding example clearly points out that the time dependent part of T_0, i.e. $w_0(t)$, is modulated by the thermal admittance $\|y\|$. The time independent part, i.e. u_0, is modulated by the thermal conductivity λ only. This difference is important from the application point of view. Information on deeper depths can be obtained from observations on u_0, rather than on $w_0(t)$. As was shown in Sections 4.2 and 4.3 fluctuations of surface temperature T_0 can penetrate only up to relatively shallow depths, even if very low frequencies are considered. On the other hand the steady state pattern dependent on horizontal coordinates x and y of surface temperature $\bar{T}_0(x,y)$ may show

Table 5.8. Mean surface temperature $\bar{T}_0$, and maximum T_x^0 and minimum T_n^0 surface temperatures calculated by eq. (5.36) with the data of Table 5.7 for two different soils and different combinations of $A(G_0)$ and G_{deep}. Temperatures in K

Soil	$A'(G_0) = 1$ $W \cdot m^{-2}$ $G_{deep} = -0.05$ $W \cdot m^2$			$G_{deep} = 0$ $W \cdot m^2$			Soil	$A''(G_0) = 10$ $W \cdot m^{-2}$ $G_{deep} = -0.05$ $W \cdot m^2$			$G_{deep} = 0$ $W \cdot m^2$		
	$\bar{T}_0$	T_x^0	T_n^0	$\bar{T}_0$	T_x^0	T_n^0		$\bar{T}_0$	T_x^0	T_n^0	$\bar{T}_0$	T_x^0	T_n^0
1	283	284	282	285.5	286.5	284.5	1	283	292.5	273.5	285.5	295	276
2	288	288.5	287.5	285.5	286	285	2	288	293.5	282.5	285.5	291	280

important differences because of the variability with x and y of λ_{deep}, the thermal conductivity of deep layers. The conclusion is that the study of $w_0(x,y,t)$ will be of interest for applications in agriculture and hydrology, while the study of $u_0(x,y)$ can provide useful information for geological purposes. It is remarkable that theoretical findings to apply the first and the second possibility have been developed quite independently from each other without reciprocal mention.

To show that the relationship between $G_{deep}(x,y)$, $\lambda_{deep}(x,y)$ and $u_0(x,y)$ can theoretically be handled and that such a relationship has indeed been observed a few references will be given.

Perturbations induced in the regional heat flow G_{deep} have been studied analytically by LEE and HENVEY (1974) and LEE (1975) for a number of cases. Bodies with a thermal conductivity differing from that of the surrounding semi-infinite medium were considered in the shape of ellipsoids, spheres and cylinders. These bodies, or thermal anomalies, were intended to resemble geological structures like sedimentary basins. It has been shown that the theoretically predicted perturbation in the average surface heat flow may extend beyond the anomaly and that the ratio between the heat flux above a buried anomalous body and that above its surrounding medium differs from the ratio of the corresponding thermal conductivities. The effect of a buried sphere has been described explicitly as focussing (or defocussing) of heat flow.

The mentioned authors intended their theory as a helpful tool to reconstruct regional patterns out of spotty measurements of λ_{deep} and G_{deep}. In the opinion of the present author there is scope for a similar theory in the interpretation of thermal infrared imagery since heat flow patterns can be handled by an optics-like theory. Thus the relationship between a geologic system and a thermal image relating to it, is relatively straightforward. The thermal admittance theory, which in Chapter 4 has been restricted to one dimension, could be extended to a three dimensional case to handle the time dependent part of T_0, i.e. $w_0(x,y,t)$. The $u_0(x,y)$ could be handled by an optics-like theory, as mentioned above.

The focussing effect has been observed in at least one case. Von HERZEN et al. (1972) found that the ratio of heat fluxes was larger than the ratio of thermal conductivities between a salt dome and the surrounding medium.

5.4.3. Time dependent part of surface temperature patterns

In Chapter 4 the soil apparent thermal admittance has been defined (eq. 4.2) and it has been shown how to make use of the interrelation between the time behaviour of T_0 and soil layering, to infer the thermal properties of soil layers or their thickness. There soil heat flux G_0 was assumed to be known, while in the Paragraph 5.2.3 it has been shown that T_0 can in principle be measured by remote sensors. The conclusion reached in Section 5.2 was that only some terms of the surface energy balance can be obtained by remote sensors. Since the only alternative to direct measurements is by deriving G_0 from the surface energy balance equation, it has now to be discussed how to combine remotely sensed data with the available equations for the energy fluxes at the soil surface. It should be remembered that the observed surface temperature pattern is the outcome of both the space dependent and the time dependent part of T_0, as discussed in the preceding Paragraphs 5.4.1 and 5.4.2.

A short summary of methods proposed to estimate G_0 by applying remotely sensed data will be given, after which a new procedure will be presented.

A number of methods have been proposed in literature to derive apparent surface thermal properties, such as the thermal inertia $(\lambda\rho c)^{\frac{1}{2}}$. It appears that a combination of different temperature waves, as presented in Section 4.3, and the explicit dependence of y_0 on soil layering (Sections 4.1 and 4.2) have never been considered. Since apparent surface thermal properties are calculated from amplitudes of T_0 and G_0, methods as proposed in literature are compared in terms of G_0.

WATSON (1975) presented one of the first applications of the thermal inertia concept. He, however, neglected in the energy balance equation, e.g. eq. (5.3) when written to apply to the soil surface, both the latent and sensible heat fluxes, LE respectively H. The heat flux G_0 therefore was obtained by him as:

$$G_0 = -(1 - \alpha_0)R_{sw} - \varepsilon'\sigma T_a^4 + \varepsilon\sigma T_0^4 \qquad (W \cdot m^{-2}) \qquad (5.37)$$

always taking the fluxes positive when directed towards the surface (see Chapter 2).

Another formulation of the energy balance equation has been presented by PRICE (1977):

$$G_0 = -(1 - \alpha_0)R_{sw} - \varepsilon'\sigma T_a^4 + \varepsilon\sigma T_0^4 - H - LE \qquad \begin{matrix}(W \cdot m^{-2})\\(5.38)\end{matrix}$$

which was approximated by Price in the form:

$$G_0 = -(1 - \alpha_0)R_{sw} - b_1 T_0 - b_2 \qquad (W \cdot m^{-2}) \qquad (5.39)$$

The coefficients b_1, b_2 were derived by a somewhat cumbersome procedure from the daily averages of the fluxes in eq. (5.38). Price applied daily averages in order to get the energy balance equation, eq. (5.38), to hold with $\bar{G}_0 = 0$. When b_1 and b_2 are known G_0 can be solved from eq. (5.39). Then to get the maximum and minimum values of G_0, eq. (5.39) was calculated for instantaneous values of α_0, R_{sw} and T_0. It should be noted that the hypothesis $\bar{G}_0 = 0$ implies that evaporation cannot take place below the soil surface. When $z_E \neq 0$ and assuming $G_E = 0$, the daily totals of G_0 and LE will be equal. As discussed more generally in Chapter 2 the difference between G_0 and G_E is the energy source for evaporation at z_E. Furthermore the linear form of the surface energy balance, eq. (5.39), indicates a very particular combination of radiative and convective energy transfer. The involved character of the procedure of PRICE (1977), however, does not allow for a clear understanding of the constraints which are actually imposed on the transfer coefficients by the linearization procedures.

An equation similar to eq. (5.38) was proposed by SALTZMAN and ASHE (1976), although these authors considered the equation to hold for monthly averages of meteorological data. Transfer coefficients were calculated as in PENMAN (1948). In a later research PRICE (1980) assumed, in a key-step of his calculations, LE to be zero and calculated H according to eq. (2.15), while PRICE (1982) proposed to calculate the diurnal heat capacity $(\lambda \rho c \omega)^{\frac{1}{2}}$ from the day - night difference in sensible heat flux H (compare Chapter 4). In the same research he calculated a moisture availability factor from the daily average of LE, as obtained by means of a numerical simulation model. The results of the numerical model were resampled to establish a relationship between the variables mentioned above.

ROSEMA et al. (1978) applied a numerical model to simulate the energy balance at the soil surface by considering the following equations:

$$G_0 = -(1 - \alpha_0)R_{sw} - \varepsilon'\sigma T_a^4 + \varepsilon\sigma T_0^4 + \rho_a c_p \frac{T_0 - T_a}{r_a} - LE$$

$$(\text{W}\cdot\text{m}^{-2}) \qquad (5.40)$$

$$LE = L\rho_a \frac{q_a - q_{a0}}{r_a} \qquad (\text{W}\cdot\text{m}^{-2}) \qquad (5.41)$$

$$|G_0| = \lambda_s \frac{\partial T_s}{\partial z} \qquad (\text{W}\cdot\text{m}^{-2}) \qquad (5.42)$$

Note that when heat fluxes are written in the form of eq. (5.42), the sign convention, as it applies to the soil surface, does not hold.

Eq. (5.41) implies that evaporation is taking

place at the soil surface (see Section 2.3). The boundary condition at the soil surface as defined by eq. (5.42) was substituted by these authors with one on T_s at a deeper depth i.e. beyond the reach of the daily cycle, by solving numerically the heat conduction equation (eq. 3.34). The expected improvement is that T_s at that depth is constant on a daily basis, thus easier to be specified than G_0, or than the ratio between LE and H as needed in the procedures proposed by PRICE (1977, 1980, 1982). It is, however, clear that to integrate numerically eq. (3.34), the thermal diffusivity a is needed. The procedure of ROSEMA et al. (1978) is by calculating a look-up table of the daily amplitude of surface temperature for a number of values of thermal inertia $(\lambda_s \rho_s c_s)^{\frac{1}{2}}$. These thermal inertia values can arbitrarily be selected, but for each value the corresponding value of a must be obtained. This implies that either λ_s or $(\rho c)_s$ must be known if the procedure is to be applied correctly. As discussed in Chapter 3 it is usually easier to determine $(\rho c)_s$ than λ_s. The requirement for proper selection of $(\rho c)_s$-values in the procedure of ROSEMA et al. (1978) has been stressed by HUYGEN and REINIGER (1979). Furthermore the procedure of Rosema et al. requires, in principle, the relationship between soil thermal properties and moisture content, to obtain an average θ-value in the top soil. Such relationships, see eqs. (3.54) and (3.55), require the composition of the mineral soil phase to be known. As it is understood from eqs. (5.40) and (5.41) meteorological data (T_a, q_a, r_a) are required to solve the set of equations. The latter implies that the results bear a regional meaning only if the density of weather stations in the territory is high. If such condition is not fulfilled only α_0 and T_0 are actually known for any point in a specific area, because they can be remotely sensed. Finally it must be mentioned that the specific humidity at the surface q_{a0} was obtained by Rosema et al. by iterative calculations of eq. (5.41), while the only coupling being left between LE and the remaining energy fluxes was eq. (5.40). Thus the coupling between the θ-profile (including θ_0 and q_{a0}) in the top soil described by eq. (2.38) is neglected, as well the coupling between heat and vapour transport as discussed in Section 3.4.

In the present author's opinion the involved character of the procedure and the heavy requirement for input data, are not justified by the results which have been presented in the references mentioned above. This opinion is supported by recalling that ROSEMA (1982) applied a very much simplified energy balance equation to estimate LE from METEOSAT data. Furthermore, a number of sensitivity studies on methods to

infer G_0, so $(\lambda\rho c)^{\frac{1}{2}}$, from measurements of T_0 have been published which point in the same direction.

A number of studies on the sensitivity of the estimated thermal inertia $(\lambda\rho c)^{\frac{1}{2}}$ to errors and actual variability of input data and parameters have been presented by QUIEL (1975). This author compared the variations of thermal inertia with the corresponding variations in soil moisture, porosity and thermal conductivity of the mineral soil constituents. For each combination, he calculated λ_s by the WOODSIDE and MESSMER (1961) formula and $(\rho c)_s$ according to eq. (3.54). Quiel found that information on mineral composition can be extracted from thermal infrared data only for water saturated rocks and soils respectively rocks with low porosity. He also showed that the same increase in thermal inertia can be the result of either a decrease from 0.48 to 0.33 in porosity, or an increase from 0.2 to 0.5 in moisture content. Similar results were found by PRATT and ELLYETT (1979).

PRATT (1980) showed that wind speed and surface roughness can be major sources of error in $(\lambda\rho c)^{\frac{1}{2}}$, as also deviations from soil vertical homogeneity. A detailed sensitivity analysis has been presented by SALTZMAN and POLLACK (1977), who calculated explicitly the partial derivatives of a function relating the diurnal range of soil surface temperature to 17 variables, i.e. 10 parametrization constants, 3 mean atmospheric variables and 4 surface-state variables. They used equations given by SALTZMAN and ASHE (1976).

In the opinion of the present author there is a more fundamental reason, in addition to the serious and specific difficulties mentioned above, for the determination of G_0, so $(\lambda\rho c)^{\frac{1}{2}}$, to be highly inaccurate. The main obstacle is to be seen in the determination of the so-called Bowen ratio H/LE. No physically clear method to obtain that ratio has been proposed in the references above mentioned, while the ratio is expected to be obtained by crunching a large number of data. The accuracy of the final results, therefore, strongly depends on that of the data and on their areal density. This point can be made clear by recalling that ROSEMA et al. (1978) obtain the resistances $r_{ah} = r_{av} = r_a$ by an iteration procedure for given values of T_a and u. The resistances include the effect of atmospheric stability as specified for instance by eq. (2.33). Such procedure is inaccurate in two ways. Firstly the selection of a particular ϕ-function is somewhat arbitrary (see Section 2.5) and relevant differences exist between ϕ-functions of the same class (heat, vapour or momentum), as shown in Figs. 2.3 and 2.4. Secondly a single value of T_a must be applied in combination with different T_0-values present in a particular thermal infrared image.

It appears that rather involved procedures hinder, rather than help, a better understanding of the errors that occur. It would be easier to attune the estimates, calculated from remotely sensed data, of individual fluxes appearing in the energy balance equation at the soil surface. Then measured ground data could be applied to compare and calibrate results.

5.4.4. Partition of energy at the soil surface

On the basis of the preceding paragraph a different approach is proposed by the present author. From satellite data α_0 and T_0 are obtained, compared with ground measurements, and corrected. Then night and day-time 'snapshots' of the fluxes are calculated. R_n is calculated according to eq. (5.2); sensible heat flux from eq. (2.15), with r_a calculated from ground measurements. The principle to calculate LE is based on a dichotomy of the possible ways of partitioning the available radiative energy in sensible (H) and latent (LE) heat fluxes.

If evaporation takes place inside the soil, the energy balance equation at the soil surface holds in the form of eq. (2.7):

$$R_n + H + G_0 = 0 \qquad (W \cdot m^{-2}) \qquad (5.43)$$

G_0 is obtained with the aid of eq. (5.43) from R_n and H. Then a first approximation value for LE is obtained by assuming $G_E = 0$, i.e. $LE = G_0$. To additionally obtain the thermal admittance y_0 eq. (4.17) is used.

If evaporation takes place at the soil surface, the energy balance equation holds in the form of eq. (2.5):

$$R_n + LE + H + G_0 = 0 \qquad (W \cdot m^{-2}) \qquad (5.44)$$

LE can be now obtained by eq. (2.18) with $e(0) = e_{sat}(T_0)$ according to the definition of the evaporation site given in Section 3.3.

The resistance $r_a = r_{ah} = r_{av}$ in eqs. (2.15) and (2.18) is calculated as follows. Wind speed and surface roughness have to be known. Then it has to be assessed whether a correction for air thermal stratification is needed. Such correction can be calculated from relationships between fluxes and the corresponding gradients (Section 2.5), when a stability parameter like Monin-Obukhov's ζ, eq. (2.28), or the Richardson number, eq. (2.29), can be determined. To calculate Ri from ground measurements, wind speed at two levels must be measured. Finally G_0 is obtained

from eq. (5.44) and y_0 again from eq. (4.17).

The problem is how a criterion can be defined to decide whether eq. (5.43) or eq. (5.44) applies. The answer lies in the known dependence of soil reflectance α_0 on moisture content θ_0. As shown in Paragraph 5.3.1 the difference in α_0 between wet and dry soil is relevant and a threshold moisture content can be established. Hence a remotely sensed map of α_0 allows to separate areas where the depth of the evaporation front $z_E = 0$ and where $z_E \neq 0$.

5.5. ACTUAL EVAPORATION RATE AND THE ESTIMATED ENERGY BALANCE

In the previous section the calculation of LE from estimates of the other terms in the energy balance equation has already been discussed in connection with the determination of G_0. Now a more systematic analysis is presented.

First a particular threshold for α_0 is taken, $\alpha_0 = 0.2$ say (see Chapter 8), to separate the case with $z_E = 0$ from that with $z_E \neq 0$.

When $\alpha_0 \leq 0.2$, e v a p o r a t i o n takes place a t t h e s o i l s u r f a c e , and two options are available. If only one data set is available for α_0 and T_0, actual evaporation can be calculated by the transport equation for LE eq. (2.18), with the vapour pressure at the soil surface $e(0)$, being equal to $e_{sat}(T_0)$. As shown in Paragraph 3.3.3, if the moisture content at the evaporation front $\theta > \theta_E$, then soil air relative humidity $U \approx 1$. If two data sets are available, the first one is used to estimate y_0 as discussed in Section 5.4. Then G_0 can be determined from the second set and LE calculated by the combination formula eq. (2.27) or by the energy balance equation in the form of eq. (5.4). Note that eq. (5.4) is to be applied with G_0 instead of G_E. In principle both eq. (2.27) and eq. (5.4) should yield the same result.

When $\alpha > 0.2$, then e v a p o r a t i o n takes place b e l o w t h e s o i l s u r f a c e , and the deeper the evaporation front, the more difficult becomes the estimation of LE. As discussed in Section 2.5 the transport coefficients inside the top soil (above z_E) tend to become the dominant factor in establishing the actual evaporation rate. The rate limiting factors are now the apparent thermal conductivity λ'_s, the resistance to vapour transport r_{sv} and the depth of the evaporation front z_E. The variables λ'_s, r_{sv} and z_E are related according eq. (2.17).

The increase of λ'_s as compared with soil thermal

conductivity λ^*_s relates to vapour and air transport in the top soil layer. In principle a relationship exists between the flow rate of soil air (eq. 3.45) and the soil apparent thermal admittance y_0 (eq. 4.16). By means of the procedure presented in Paragraph 5.4.4 y_0 can be estimated and calibrated, and the areas where $|y_0|$ is large in comparison with $|y_1|$ can be detected. However, without a reliable estimation of λ^*_1, the ratio $|y_0|/|y_1|$ will also be inaccurate and it will be difficult to determine z_E with the method developed in Sections 4.2 and 4.3, when this ratio is measured at one frequency. The apparent thermal conductivity λ'_1 (see Chapter 4 for notation) and the thickness of the top soil layer z_E can be inferred from measurements of $|y_0|/|y_1|$ at two frequencies.

For one layer overlying a semi-infinite medium, the thermal conductivity λ_2 is either to be known or to be determined by measuring $|k|$ at an additional frequency. When two layers overlie a semi-infinite medium, z_2 (see Fig. 4.3) also is needed. Finally the flux G_E can be calculated by eq. (4.13) from G_0, λ_1 and z_1. Then LE is obtained as $(G_0 - G_E)$, i.e. by eq. (2.8).

If daily values are required, then eq. (2.25) can be applied after a last effort to obtain r_{sv} and r_{sh}. The latter resistance can be directly obtained from the quantities in the preceding steps. The top soil layer above the evaporation site at z_E is coincident with the first layer in Fig. 4.3, thus $z_E = z_1$ and $r_{sh} = z_1/\lambda_1$, see eq. (2.17). Once λ'_s, λ^*_s and z_E are known, the resistance to vapour transport r_{sv} can be derived. The procedure is somewhat involved, however, and the following two cases have to be considered.

F i r s t c a s e. When convection of soil air takes place in the top soil layer above z_E (see Paragraph 3.4.4) the latent heat flux by means of eq. (3.46) can be written as:

$$LE_{conv} = -Lq_v = -L\tilde{r}_0 \rho_a v_{za} \qquad (W \cdot m^{-2}) \qquad (5.45)$$

where $\tilde{r}_0$ is the mixing ratio of soil air at the surface. The negative sign in eq. (5.45) accounts for the different sign convention a t the soil surface and f o r the z-axis.

An additional equation relates λ'_s to λ^*_s, namely eq. (3.45). By substitution of eq. (3.45) in eq. (5.45) one finds:

$$LE_{conv} = L \frac{\tilde{r}_0(\lambda'_s - \lambda^*_s)}{c_p z_E} \qquad (W \cdot m^{-2}) \qquad (5.46)$$

By comparing $\tilde{LE}_{conv}$ with $LE = G_0 - G_E$ it can be

decided whether air convection plays a rôle or not. Finally r_{sv} can be estimated as v_{za}^{-1}.

S e c o n d   c a s e. If it is concluded from the first case that convection does not play a rôle vapour transport is diffusive in character. Then the relationship between λ_s' and vapour diffusivity is more involved. Instead of taking eq. (5.45), the equation for LE_{diff} (see also eq. 3.13) must be written as:

$$LE_{diff} = LD_{vs} \frac{\delta \rho_v}{z_E} \quad (W \cdot m^{-2}) \tag{5.47}$$

or

$$LE_{diff} = LD_{vs} \frac{\rho_v^{sat}(\overline{T}_s) - \rho_v^0}{z_E} \quad (W \cdot m^{-2}) \tag{5.48}$$

where the sign convention for LE_{diff} is as specified at the soil surface (positive fluxes towards the surface) and $\overline{T}_s$ can be estimated in the top soil layer above z_E as $(T_X^0 - T_n^0)/2$ and D_{vs} calculated according to CURRIE (1960) as $D_{vs} = b_1 (\chi_a)^b D_{va}$, which holds for isothermal vapour diffusion (see also FEDDES, 1971).

In principle a relationship exists between the apparent soil thermal conductivity λ_s' and D_{vs}. Namely eqs. (3.17), (3.24) and (3.25) can be substituted in eq. (3.55), which gives an estimate λ_s'' for the apparent soil thermal conductivity when vapour flow is diffusive. Let us now assume that a value of λ_s', $\tilde{\lambda}_s'$ say, has been independently obtained, e.g. by means of the thermal admittance method. Then $\lambda_s'' = \tilde{\lambda}_s'$ must hold true, which constraint can be solved to obtain U; λ_a' also is obtained and the enhancement factor and D_{vs} can be calculated.

The procedure is rather involved and the expected errors may be large. It is, however, always possible to compare the estimate of $r_{sv} = (z_E/D_{vs})$ with literature data or with experiments.

The procedures described to estimate LE_{conv} and LE_{diff} seem to be rather complicated, so another more realistic approach will be presented in Section 5.6. One should always realize, however, that remotely measured patterns of α_0 and T_0 can be helpful in the calculation of LE. Data on surface status as needed in any combination formula or transport equation can be obtained in this way.

5.6. ACTUAL EVAPORATION AS A LINEAR FUNCTION OF SURFACE TEMPERATURE AND REFLECTANCE

In Section 5.1. it was already anticipated that measured strings (LE, α_0, R_{sw}, T_a, T_0, r_a, $G_E)_i$ could be combined with the energy balance and transport equations to estimate LE.

According to eq. (5.4) any estimator f_1 of LE should be defined on a 6-dimensional space $(\alpha_0$, R_{sw}, T_a, T_0, r_a, $G_E)$ and map it onto a set of LE-values:

$$\{\alpha_0, R_{sw}, T_a, T_0, r_a, G_E\} \xrightarrow{f_1} \{LE\} \tag{5.49}$$

Since only α_0, T_0 and eventually R_{sw} can be determined from remote observations, i.e. all over an area, it appears that the problem of defining an estimator f_2:

$$\{\alpha_0, R_{sw}, T_0\} \xrightarrow{f_2} \{LE\} \tag{5.50}$$

is ill-posed, unless the 6-strings corresponding to the same 3-string can be specified. An estimator f_2' approximating f_2 can only be determined empirically, i.e. from measured 3-strings $\{(\alpha_0, R_{sw}, T_0)_i\}$ and values $\{LE_i\}$:

$$\{(\alpha_0, R_{sw}, T_0)_i\} \xrightarrow{f_2'} \{LE_i\} \tag{5.51}$$

A fully empirical approach tilts towards the pessimistic side, since no use is made of the equations relating the variables mentioned above to each other. The energy balance equation eq. (5.3) and the transport equations eqs. (2.15), (2.16), (2.18) specify a-priori relationships between the variables in the 6-strings. These relationships allow to reduce the amount of measured data, $(\alpha_0, R_{sw}, T_0)_i$ and LE_i, needed to determine f_2'. The approach involving the determination of f_2' is essentially different from the inversion procedures discussed in Sections 5.4 and 5.5. These procedures define an estimator f to calculate from variables defined at a given point $(\tilde{x}, \tilde{y})$ the soil and latent heat fluxes also defined at $(\tilde{x}, \tilde{y})$:

$$\{\alpha_0(\tilde{x}, \tilde{y}), T_0(\tilde{x}, \tilde{y}), \ldots\} \xrightarrow{f} F(\tilde{x}, \tilde{y}) \tag{5.52}$$

On the contrary f_2' is only implicitly dependent on space:

$$\{x,y\} \xrightarrow{f_3} \{\alpha_0(x,y), R_{sw}(x,y), T_0(x,y)\} \xrightarrow{f_2'} \{LE\} \tag{5.53}$$

The dependence on space is specified by the sensor that maps α_0, R_{sw}, T_0, while f_2' relates state variables to each other. This latter circumstance is quite helpful in determining f_2' empirically, since data regardless of space and time can be used.

The determination of f_2' would be much easier if eq. (5.4) could be linearized. It appears that LE is linear in α_0 and R_{sw}, while the dependence on T_0 has

to be investigated further. Everything else being constant LE is a quasi-linear function of T_0, as shown by SOER (1980). The slope of $LE(T_0)$ changes according to eq. (5.6), since r_a is kept constant. Note that it is implied that r_a is a smooth function of air thermal stratification, i.e. of T_0 and T_a. The dependence of LE on r_a is not linear, as shown by eq. (5.8), thus linearity in r_a can be a reasonable approximation only for a limited range of r_a. Accordingly linearity of $LE = LE(\alpha_0, R_{sw}, T_a, T_0, r_a, G_E)$ can be accepted as a first approximation. In a second step corrections can be applied to account for non-linearities in particular ranges of some variables. If LE is a linear function it can be expressed as the first order term of a Taylor's series:

$$LE = LE_{ref} + D_{\alpha_0}(LE)\delta\alpha_0 + D_{R_{sw}}(LE)\delta R_{sw} + D_{T_a}(LE)\delta T_a +$$

$$+ D_{T_0}(LE)\delta T_0 + D_{r_a}(LE)\delta r_a + D_{G_E}(LE)\delta G_E \quad \begin{array}{c}(W \cdot m^{-2})\\ (5.54)\end{array}$$

where the partial derivatives are given by the eqs. (5.5) through (5.9). Increments are considered from a reference 6-string $(\alpha_0, R_{sw}, T_a, T_0, r_a, G_E)_{ref}$ where the evaporation rate is LE_{ref}.

A linear estimator f_2'' defined on $\{\alpha_0, T_0\}$ can be obtained by casting in matrix form the condition for four points to lie on the same plane:

$$\begin{vmatrix} \alpha_0 - \alpha_0^I & T_0 - T_0^I & LE - LE_I \\ \alpha_0^I - \alpha_0^{II} & T_0^I - T_0^{II} & LE_I - LE_{II} \\ \alpha_0^{III} - \alpha_0^{II} & T_0^{III} - T_0^{II} & LE_{III} - LE_{II} \end{vmatrix} = 0 \quad (5.55)$$

where the coordinates of points $P_1 \equiv (\alpha_0^I, T_0^I, LE_I)$, $P_2 \equiv (\alpha_0^{II}, T_0^{II}, LE_{II})$ and $P_3 \equiv (\alpha_0^{III}, T_0^{III}, LE_{III})$ are known. When numerical values are substituted in eq. (5.55), one finds for LE:

$$LE = b_1\alpha_0 + b_2T_0 + b_3 \quad (W \cdot m^{-2}) \quad (5.56)$$

where the b_j are dimensional constants. The coordinates of the points P_i can be calculated from a reference value LE_{ref} and from the derivatives $D_{\alpha_0}(LE)$ and $D_{T_0}(LE)$. It can be expected that, as discussed at the beginning of this section, points defined in this way are not representative of the actual shape of the LE function (Fig. 5.2). Then one or more measured 3-strings, or points, must be included in eq. (5.55).

If the derivatives eqs. (5.5) and (5.6) are applied to calculate the coordinates of the points P_i, the coefficients b_i in eq. (5.56) will be negative: for specific weather conditions evaporation will be higher at lower surface temperature and reflectance. This re-

mark illustrates the task of a desert farmer: he must fight uphill to increase LE up to a point where a crop can grow. The surface he is trying to build up will have the lower reflectance of plants and a lower surface temperature (for a given T_a), in comparison with the barren desert surface. This fight of farmers against the surface energy balance, is vividly depicted in the quotation from PLINIUS (77) at the beginning of this chapter.

A further improvement in the estimate of LE can be achieved by applying corrections to account for the effect of those variables (T_a, r_a and G_E) which cannot be observed areally.

Finite increments can be calculated by integration of the partial derivatives in eq. (5.54). For example for the derivative, eq. (5.8), with respect to r_a:

$$\delta_{r_a}(LE)\begin{vmatrix} P_j \\ \\ P_i \end{vmatrix} = -\rho_a c_p(T_0 - T_a)\int_{P_i}^{P_j} \frac{1}{r_a^2}dr_a \quad (W \cdot m^{-2}) \quad (5.57)$$

which equation accounts for the difference in actual evaporation due to the difference in the transport coefficient between point P_i and P_j. The correction $\delta_{r_a}(LE)$ can be calculated from measured 3-strings P_i or estimated by making use of the knowledge about the area that is available. Corrections for effects dependent on other variables than r_a can be calculated by equations similar to eq. (5.57). A detailed description of the procedure can be found in MENENTI (1980).

The semi-empirical nature of the method should not be considered as a shortcoming, since the data needed to rigorously apply deterministic procedures (see Sections 5.4 and 5.5) cannot be made available all over a region. It is also noteworthy that the most successful attempt up to date to calculate evapotranspiration from remotely sensed data relied on a fully empirical procedure. In the framework of the Gila River Phreatophyte Project, JONES (1977) established the relationship:

$$LE = f(R)\tilde{g} \quad (mm \cdot d^{-1}) \quad (5.58)$$

where the factor $\tilde{g}$ is proportional to the Blaney-Criddle consumptive-use factor. Evapotranspiration, as measured by the water balance method, in this way was related to the radiance R obtained by colour-infrared photography.

5.7. SUMMARY

In Section 5.1 the relative weight of the differ-

ent terms in the surface energy balance has been eval-
uated by writing simple equations for each term and
then taking the first order differentials of the sim-
plified energy balance equation. This equation has
been re-arranged to express the latent heat flux as
an explicit function of the other variables in the
energy balance equation. To study the relationship
between latent heat flux, surface temperature and
surface reflectance, a geometrical interpretation of
this function has been proposed. The relationships
that were presented in this section are suitable for
the use of satellite data of surface radiation temper-
ature and surface reflectance to calculate actual
evaporation.

In Section 5.2 the possibility of deriving some
of the terms of the surface energy balance equation
from satellite data has been discussed. It was con-
cluded that satellite data can be used to estimate
sky cover percentage and hence solar incoming radia-
tion. Furthermore reflected solar radiation can direct-
ly be measured. The varying atmospheric transmittance
due to the presence of dust, however, represents in
principle a major difficulty. The effect of the sun
zenith angle on satellite measured surface reflectances
has been discussed in detail. As regards the surface
emitted radiative flux, the effect of atmospheric wa-
ter vapour has been studied. A radiation transfer mod-
el has been proposed where this effect is estimated
by explicitly relating the volume concentration of the
water vapour dimer to temperature, pressure and vapour
pressure of the air. The effect of dust on surface
emitted radiation also has briefly been considered. It
has been shown how to account for longwave surface
emissivity when surface temperature ultimately is re-
quired. The conclusion was reached that if the actual
weight of the many complicating factors is to be
assessed, ground-reference data definitely are needed.

In Section 5.3 a selection of available data con-
cerning shortwave surface reflectance and longwave
surface emissivity of desert surfaces have been re-
viewed. As regards surface reflectance the dependence
on sun-zenith angle has been considered and a few lit-
erature data have been given. Of particular relevance
for the present investigation are data relating to
playa surfaces, as also to the dependence of surface
reflectance on surface moisture content and to the ef-
fect of weathering on the surface reflectance of rocks.
A relationship between surface reflectance and surface
moisture content has been presented.

The relationship between surface reflectance and
surface moisture content will be applied in Chapter 8
to map the areas where evaporation takes place inside
the soil, according to the definition of evaporation

sites as has been given in Chapter 3. On the basis of
the data on surface emissivity it has been concluded
that the emissivity of desert and playa surfaces is
that close to unity that remote measurement of surface
radiation temperature is feasible.

In Section 5.4 the determination of heat flux into
the soil (a problem which was left open in Chapter 4)
has been discussed. Preliminarly it has been shown that
in an areal pattern of surface temperature, the time-
dependent part must in principle be separated from the
time-independent one. It has been pointed out that the
soil thermal conductivity relates to the time-indepen-
dent part, while the thermal admittance relates to the
time-dependent part. In relation to this latter part
different models, as proposed in literature to infer
the soil heat flux, have been briefly reviewed. The
conclusion was reached that either some 'heavy-weight'
hypotheses have to be accepted, or many additional data
are to be used (as will be done in Chapter 8) to make
the procedures in estimating the soil heat flux fea-
sible. It has finally been shown that when a partition
of the territory into areas where evaporation takes
place at the soil surface and where inside the soil can
be established, a more straightforward approach can be
applied. This result can be achieved by making use of
the definition of evaporation sites as was given in
Chapter 3, of the relationship between surface reflec-
tance and surface moisture content given in Section
5.3 and of the soil hydrological properties for the
test area as will be described in Chapter 6.

In Section 5.5 it has been discussed how the
latent heat flux can be calculated from the estimates
of the other terms of the surface energy balance,
both for the case of evaporation taking place at the
soil surface and for the one with evaporation occur-
ring inside the soil. If the latter applies the oc-
currence of convective respectively diffusive vapour
flow has been considered.

In Section 5.6 the geometrical interpretation
of the energy balance equation, as proposed in Section
5.1, has been enlarged. The simplifying hypotheses
which are to be accepted to be able to calculate evap-
oration from satellite measured surface radiation
temperature and surface reflectance, have been dis-
cussed. Finally it has been shown how to derive sim-
plified equations to calculate actual evaporation by
combining satellite derived images of surface radia-
tion temperature and surface reflectance.

The procedures presented in this chapter will
be applied in Chapter 8 to the data described in
Chapter 6 and analyzed in Chapter 7.

6. DATA ON PLAYAS IN WEST-LIBYA

'Ultra eum deserta, mox Thelge oppidum Garamantum itemque Dedris adfuso fonte ... eius puteos - qui sunt non alte fodiendi, si locorum notitia adsit - harenis operientibus.'

(PLINIUS, Naturalis Historia, Liber V:36,38)

6.1. AVAILABLE INFORMATION ON THE WEST-LIBYAN AQUIFER SYSTEM

6.1.1. General

In Section 1.3 a brief description of the West-Libyan regional aquifer system has been presented to illustrate the rôle of playas with respect to the water balance of groundwater reservoirs in deserts. In this section more quantitative information will be given, as the theoretical approach given in the earlier chapters will be used in examples taken from West-Libya.

In the period 1977 through 1980 a comprehensive hydrogeological study of that part of the Fezzan region where a rapid development of groundwater irrigated agriculture is to be expected (Al Jufrah area and Wadi Ash Shati basin), was undertaken by the Italian engineering company Aquater.

In the framework of this study by Aquater, much emphasis was placed on the rôle of evaporation from playas. The rationale to undertake such effort, which originated the present investigation, stems from the experience gained in the UNESCO (1972) study of the Algerian - Tunisian groundwater basin. During that study it was realized for the first time how important the rôle of playas in the long term evolution of a desert groundwater basin could be. The interrelation between evaporation from playas and specific water management policies has already been briefly discussed in Sections 1.1 and 1.2. The region of interest for the entire hydrogeological study is shown in Fig. 6.1.

The development planned in the Al Jufrah and Wadi Ash Shati area is a long term one, some 50 years or more. Then the now thinly populated oases will have to bear a heavy pressure on their water resources.

The knowledge available on the West-Libyan aquifer before the Aquater study will now be briefly summarized.

JONES (1971) has presented a map of the so-called groundwater provinces of Libya, which map, however, does not present the complex structure of the Paleozoic and Mesozoic aquifers, as depicted in Section 1.3. A jump in quality and quantity of available data was achieved in the studies performed by ITALCONSULT (1975) and GERMANCONSULT (1975). The former one relates to an area of 111,625 km^2, the latter to 11,520 km^2. Both areas include Brak (in Wadi Ash Shati) and its surroundings, where most of groundwater extraction takes place. A study to calculate the expected drawdown of the water table has been presented by PALLAS (1977). Two different numerical simulation models were applied and water table drawdown from 1976 to the year 2000 was estimated to be in the range of 50 to 80 m (Germanconsult) respectively 30 to 60 m (Italconsult). In the Germanconsult study evaporation from playas was assumed to be zero, while Italconsult estimated it to be 10^8 $m^3.a^{-1}$ when the calculated water table level was higher than ground surface, and zero otherwise.

The studies quoted above were performed to assess the feasibility of two land reclamation projects nearby Brak. After their completion it was realized that the reliability of the results was such, that they could not provide a guarantee solid enough for the future development of the region. Therefore a new hydrogeological study was undertaken with a larger amount and a better quality of data. Next to items like piezometric levels, water quality data, pumping tests and an inventory of exploitation, a number of analyses for Tritium (^3H), Deuterium (^2H), Oxygen 18 (^{18}O) and Carbon 14 (^{14}C), an experimental investigation of evaporation from playas and the drilling of exploration wells were included.

For a description of the setup and results see the report of AQUATER (1980). Here, after a short description of the area, the expected goals will be given.

The study area (Fig. 6.1) covers approximately 120,000 km^2. The area is located in central West-Libya and lies between the highland of Hamada al Hamra to the North, the Idehan Awbari and the Idehan Marzuq sand seas to the West and South respectively, and the Sirte
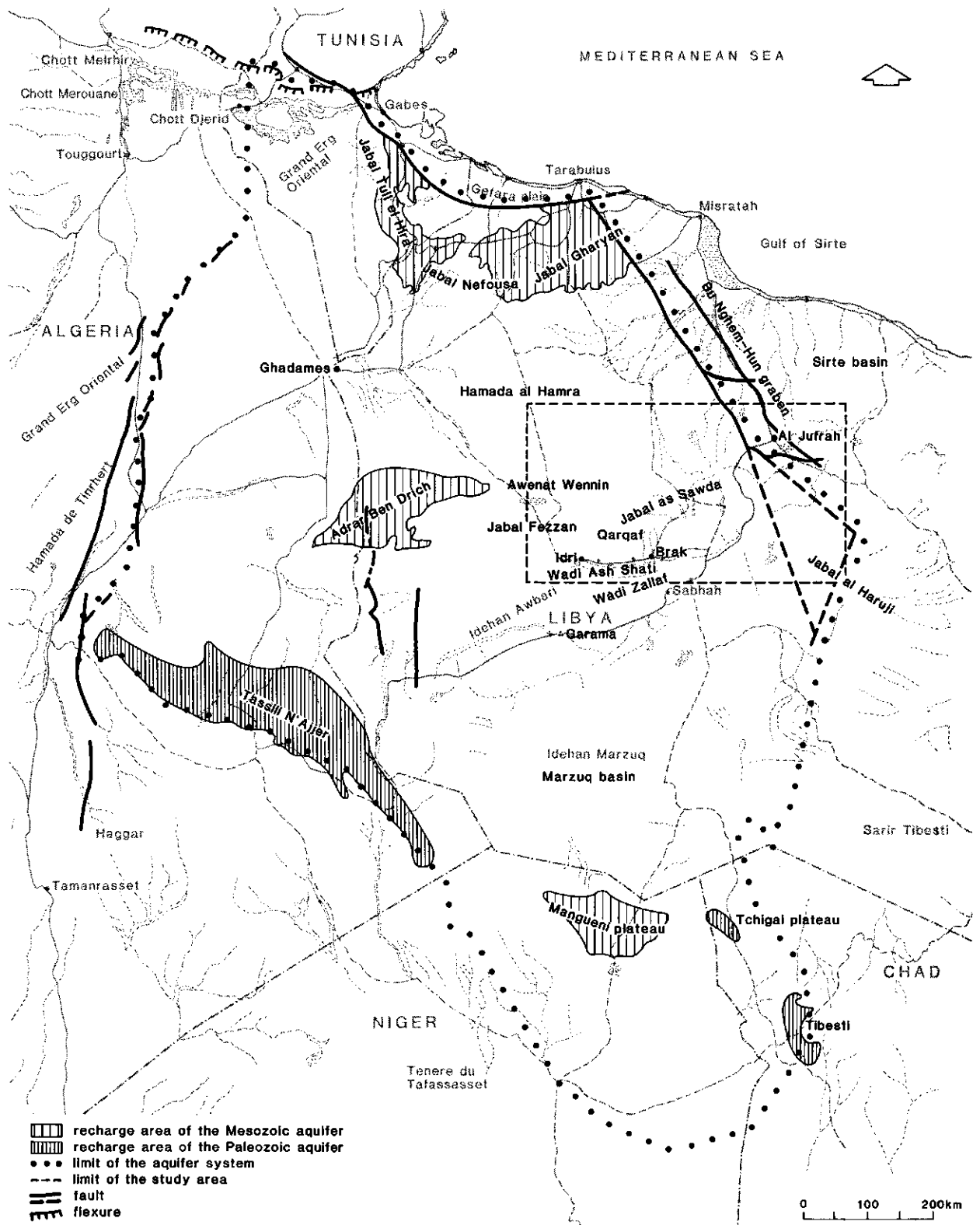
Fig. 6.1. Area covered in the hydrogeological study by Aquater of Wadi Ash Shati, Al Jufrah and Jabal Fezzan area. Also shown the areas of possible recharge of the Mesozoic and Paleozoic aquifers (after Pizzi and Pone, 1978). More detailed maps of the study area are given in Figs. 6.4 and 6.19

basin to the East. Geographically it is bounded by
27° and 29°30' latitude and 12°30' and 17° E longitude.
The main geographic features are:

- mountainous zone in the centre of the area (Jabal
  Fezzan) rising to more than 750 m above mean sea
  level;
- an East - West depression running at the South of
  Jabal Fezzan (Wadi Ash Shati) 350 to 400 m above
  mean sea level;
- a plateau extending farther to the North (Hamada al
  Hamra) limited to the South by an escarpment running
  along the northern flank of Jabal Fezzan, 500 to 600
  m above mean sea level;
- two volcanic massifs: Jabal as Sawda (840 m) at the
  middle northeastern, and Jabal al Haruji (1180 m)
  at the southeastern corner; both built up by lava
  flows;
- the southern part of a NW-SE depression (Hun graben)
  in the northeastern section of the area, 500 m above
  mean sea level.

The study area is characterized in the North and
in the East by a flat morphology. The morphology be-
comes uneven only near major basaltic outcrops (Jabal
as Sawda and Jabal al Haruji). The mid-western part of
the study area, formed by the Qarqaf massif and bor-
dered in the South by the large Wadi Ash Shati depres-
sion, is characterized by an irregular morphology. The
Qarqaf massif is formed by Cambro-Ordovician clastic
rocks. Several remnants of infra-Cambrian rocks crop
out in the middle of this structure.

In the South the Qarqaf massif is connected to
the Wadi Ash Shati depression by several escarpments
situated at gradually lower elevations. This depres-
sion has an East - West direction and has a rather
flat morphology, marked by erosions which indicate the
existence of a well-developed fossil hydrographic sys-
tem. This area is characterized by clayey-sandstone
rocks of an age between Devonian and Carboniferous.
Another important characteristic of Wadi Ash Shati is
the presence of several playas between Brak and Idri
on its southern side. The southern-most part of the
area is formed by the sand sea of Wadi Zallaf and
Idehan Awbari.

The synthesis of available stratigraphic data and
results obtained from wells drilled for the study, in-
creased the geological knowledge of the area. For more
details see the report of AQUATER (1980) which study
mainly deals with the regional Paleozoic aquifer
(Cambro-Ordovician) and its relationship with aquifers
of Mesozoic age (Cretaceous period), as briefly dis-
cussed in Section 1.3.

The goals were:

- to establish a general appraisal of groundwater re-
  sources in the area with particular attention to
  the following problems:

  . relationship between Fezzan, Hamada al Hamra and
    Sirte basin;
  . hydraulic rôle of Jabal Fezzan;
  . history of water exploitation in Wadi Ash Shati
    and Al Jufrah (quantities of water and water lev-
    els);
  . water quality within the western part of Wadi Ash
    Shati;

- to determine the possible interaction between two
  development zones, i.e. Al Jufrah and Wadi Ash Shati
  and the possible additional effect of new develop-
  ment zones;
- to determine possible environmental effects of in-
  tensive water extraction in Wadi Ash Shati and Al
  Jufrah;
- to establish a water development plan in Wadi Ash
  Shati, by taking into account:

  . the requirement of the existing and planned agri-
    cultural projects;
  . the drinking water demand;
  . the requirements of the private farms;
  . the interference of the different extraction areas;
  . the results of previous soil surveys and the pos-
    sibility of extension of the present projects or
    making additional ones;

- to evaluate the hydrologic results of the operation
  of the Al Jufrah projects and to improve the fore-
  casts of the future groundwater drawdown;
- to find out new possible areas of development.

For water management policies environmental fac-
tors are as important as the aquifer structure. Ac-
cordingly a short overview is given, partly taken from
the Aquater report and partly assembled by the present
author, about climate, possible recharge, water use
in agriculture and distribution of natural vegetation.

6.1.2. Climate

A complete insight of the North African climate
has been provided by GRIFFITHS and SOLIMAN (1972),
while an excellent collection of data can be found in
LEBEDEV (1968). The climate of Libya was studied in
depth by FANTOLI (1967). The following conspectus, as
applying to the study area in Fig. 6.1, can be given.

The entire area, including Hamada al Hamra, Al
Jufrah, Qarqaf massif and Wadi Ash Shati is character-
ized by the North African Desert climate, whose main
elements are the following:

- poor and sporadic rainfall;
- very high daytime temperatures;
- high daily and yearly temperature variations;
- low relative humidity;
- intense solar radiation;
- strong and mostly dry winds.

In the study area (Fig. 6.4), two weather stations have been working for a long period: Sabhah and Hun.

R a i n f a l l. Rain occurs quite seldom in the area, as is shown in Table 6.1. The data of Table 6.1

Table 6.1. Number of events with a daily rainfall higher than 5, 10, 20 and respectively 30 mm (weather station Sabhah, 1931 through 1978)

Rainfall (mm)	Number of events
5	17
10	6
20	3
30	2

do not point out the year-to-year variability of rainfall events. For this purpose the maximum monthly rainfall has been compared with the corresponding monthly averages (Table 6.2). One might conclude that the average rainfall does not contribute to the regional water balance. This conclusion can, however, not be reached for the monthly maxima. Rain storms may occur over large areas and may perhaps yield a recharge of the same order of magnitude as groundwater exploitation (see Section 1.1). In the Wadi Ash Shati basin rainfall data were collected at Brak (1932 through 1938) and Idri (1933 through 1939). The over-

all average was 5 mm·a^{-1} only. The observation record is too short, however, to take this figure as more than an indication.

In the Aquater study rainfall data were collected by tipping-bucket recorders at five sites and during different periods from September 1977 to October 1979. In Table 6.3 the maximum rainfall intensity, together with the pertaining daily total and the maximum daily total for each site are presented. The data given in this table are of interest, since for the first time rainfall recorders were used in the region. However, it should be considered that because of the often local character of rainfall events a reasonably accurate raingauge network probably is unfeasible. This subject is discussed at length in FAO (1981).

T e m p e r a t u r e. Some data obtained from weather stations of the Libyan Meteorological Service will be briefly presented. The air temperature data recorded at Sabhah from 1950 through 1970 show that the mean maximum temperatures range from 38.8°C in June to 19.7°C in December, while the mean minimum temperatures range from 5.8°C in December to 23.8°C in June. The absolute minimum and maximum values show variations between -4.4°C in February and 45.9°C in July. At Hun station the mean of the monthly maximum temperatures ranges from 30.7°C in July to 14.0°C in January, while the mean minimum temperatures range from 6.6°C in January to 26.5°C in June. The absolute minimum and maximum values are -6.9°C in January and 47.2°C in May.

W i n d. Wind speed and direction at 10 m height at Sabhah station show mean wind velocities varying from 3 to 5 m·s^{-1}. The highest velocities occur from

Table 6.2. Monthly maximum (R_x) and average (R) rainfall (mm) at weather station Hun (1935-1978)

	Jan.	Feb.	Mar.	Apr.	May	June	July	Aug.	Sept.	Oct.	Nov.	Dec.
R_x	34.4	21.8	13.7	34.4	42.2	4.7	0.0	1.3	20.1	47.3	19.9	22.3
R	2.9	2.9	2.2	2.8	4.7	0.5	0.0	0.1	3.4	6.2	2.1	2.3

Site	Date	Maximum intensity (mm·h^{-1})	Pertaining daily total (mm)	Maximum daily total (mm·d^{-1})
Farjan	14- 2-1978	5.7	1.9	
	5- 9-1979			3.5
Jabal as Sawda	13-12-1977	15.6	1.3	
	5- 9-1979			5.1
Brak	14- 4-1978	41.2	6.6	
	1-11-1978			15.6
Qarqaf	5- 9-1979	10.8	5.4	5.4
Idri	20- 3-1979	16.2	12.2	12.2

Table 6.3. Maximum rainfall intensity, the pertaining daily total and the maximum daily rainfall as observed at different sites in the Fezzan region in the period 1977 through 1979. For the rainfall intensity data, the basic time interval was 10 minutes

Table 6.4. Reference crop evapotranspiration ET0 $(mm \cdot d^{-1})$. Mean monthly values presented for Sabhah after Chin (1977), while for Idri monthly values were calculated from data relating to the period February 1978 through March 1979

Method and station	Feb.	Mar.	Apr.	May	June	July	Aug.	Sept.	Oct.	Nov.	Dec.	Jan.	Feb.	Mar.
Blaney and Criddle														
Sabhah	3.6	4.8	6.5	7.8	8.8	10.2	9.5	7.3	5.0	3.4	2.3	2.6		
Idri	3.4	4.0	6.7	5.9	8.4	7.1	7.1	6.0	4.8	3.8	1.8	2.9	3.2	4.0
Radiation														
Sabhah	4.2	5.8	7.0	8.5	9.6	9.7	9.3	6.9	6.0	3.7	3.0	3.4		
Idri	3.9	4.9	6.8	6.3	8.7	7.6	7.2	6.4	4.8	3.3	2.6	3.2	4.0	4.3
Penman														
Sabhah	4.6	7.5	9.3	9.3	11.	9.8	8.6	8.0	7.0	4.6	3.2	3.1		
Idri	3.4	4.9	6.5	7.9	8.7	7.4	7.3	5.4	5.0	3.3	2.2	2.6	3.9	5.0

March to August. Winds coming from the East generally prevail during summertime and the NE direction during wintertime. An important occurrence is Ghibli, a hot wind from the South which may occur during all seasons. Other data concerning wind velocity and direction are available from Jabal as Sawda station, where the main wind direction is NE.

R e f e r e n c e   e v a p o t r a n s p i r a t i o n. As already discussed in Section 2.2, the formulas used to calculate potential evapotranspiration define a kind of specialized climatological index. Accordingly, calculations of the reference crop evapotranspiration ET0 by the procedures proposed in FAO (1977) are presented here as related to meteorological data collected at the weather stations Sabhah and Idri, the latter having been instituted for the Aquater study. The Blaney and Criddle, Radiation and Penman methods have been applied by the present author to the Idri data, while for Sabhah the results obtained by CHIN (1977) are given. In Table 6.4 are given the mean monthly values of ET0 for Sabhah, while for Idri monthly values have been calculated with the data collected from February 1978 through March 1979. Reference crop evapotranspiration ET0 is found to be higher at Sabhah, independently of the method used. The three methods do show a very close agreement of the results and it can be concluded that simple formulas, e.g. Blaney and Criddle, can safely be used to calculate ET0. It must again be stressed that the relation between ET0 and actual crop water requirements is not straightforward.

6.1.3. Recharge

As in every report dealing with arid zone hydrology, this subject could be introduced by warning about the awkwardness of estimating runoff and recharge in arid areas. A general discussion on the subject can be found in FAO (1981). A few remarks will be made on the known attempts to measure recharge flow.

In the last few years two approaches were attempted. The first approach relies on the known variation in the last 30 years of the concentration of atmospheric tritium due to thermonuclear experiments. The method is suitable for large sized hydrogeological studies since a long-term, time-smoothed effect can be sought by collecting relatively few samples all over an area. The basic idea is that groundwater which originated from rainfall during years with peak tritium concentration can easily be recognized from other water that has a lower tritium concentration. Sampling depths must be properly chosen since the downward velocity of water is likely to be very low. Therefore only the upper few meters of surface materials may be affected by present recharge. VOGEL et al. (1974) collected a number of samples at different sites in South-Africa down to depths varying from 3 to 13 m. The ratio between total percolation and rainfall could be evaluated as being between 2 and 13%. The lowest recorded value relates to a profile in the Kalahari sands, where average yearly rainfall is 450 mm. DINCER et al. (1974) presented results obtained from data collected in the Dahna sand dunes, central Saudi Arabia. Yearly rainfall in the area averages around 80 mm. Samples were collected down to a depth of 6 m at 0.5 m intervals; the peak tritium concentration was found at 4 m. According to the measured soil moisture profile, the yearly average recharge was estimated as being 20 mm, i.e. 25% of rainfall.

The results reported above point out the importance of a proper choice of sites and sampling depths. The downward movement of the water carrying known concentration peaks of tritium is very slow and the amounts of soil moisture involved are rather small. Thus the interpretation of samples collected at deeper depths and below a water table should be done with care.

In the aquifer system of the Sirte and Kufra basins (Libya) a thorough investigation has been perform-

ed between 1967 and 1973. Some results were presented by WRIGHT and EDMUNDS (1971) and the analyses of stable and radio-isotope data were presented by EDMUNDS and WRIGHT (1979). These authors collected at different depths samples for tritium determinations in a number of wells. The average yearly rainfall at Kufra is only 9 $mm \cdot a^{-1}$ (1933-1939, 1949-1959), so the chances of finding some evidence of recharge seem very slight. Possible traces of tritium peaks are most likely smoothed when dilution of the would-be recharge takes place within the water saturated layers. Thus it can be understood that according to Edmunds and Wright, traces of recent water were only found at the phreatic surface in one single shallow well.

The second approach in estimating recharge flow is by measuring percolation in soil monoliths. The results of a detailed experiment were presented by VACHAUD et al. (1981), and VAUCLIN and VACHAUD (1981). They made use of a particular soil profile which can occur in playas: a sandy layer 90 cm thick, overlying a gypsum crust situated between 90 and 110 cm depth. The experiment was performed at a site near Gabes (Tunisia) where the average yearly rainfall is 180 mm. After artificial wetting of the soil monolith with 173 mm water, soil moisture and pressure head profiles were measured during a 160 day drying period. At the end of this period deep percolation amounted to 131 mm. Thus as much as 76% of the artificial rainfall percolated. The result most likely depends on the way of wetting: a constant rainfall intensity of 19 $mm \cdot h^{-1}$ with a duration of 9 hours.

The above mentioned references show that the available evidence of groundwater recharge in deserts is inconclusive and this circumstance should be kept in mind when considering the results presented below.

In the first stage of the hydrogeological study of the Fezzan area some 80 groundwater samples were collected and analyzed for tritium concentration. The samples were collected mainly in the Idehan Awbari and very low tritium contents were found. SALEM and VISSER (1977) suggested that a possible explanation could be found in the origin of the samples, which were collected from free-flowing wells and springs. This suggestion found further support from the results of additional analyses for tritium content during the period 1977 through 1980. Also in this latter case samples were collected from free-flowing springs and wells, with only two exceptions. Two groundwater samples were collected in shallow phreatic reservoirs, one near Awenat Wannin and another one in the Hamada al Hamra. Tritium content was respectively 1.6 and

6.0 TU (tritium units), much higher than in the remaining groundwater samples. Such single findings having also been presented by EDMUNDS and WRIGHT (1979) as mentioned above, may be more than a coincidence. Namely, it might be concluded that groundwater recharge does indeed take place, but the tritium technique can only be applied to groundwater present at shallow depths.

On the ground of the results reported above it does not seem possible to estimate in an accurate way the average amount of recharge. PIZZI and PONE (1978) give a choice equal to 1% and respectively 10% of the average yearly rainfall. In Fig. 6.1 the areas where recharge of the West-Libyan aquifer system is possible, are indicated. As regards the Paleozoic aquifer the most important one is the Tassili N'Ajier. Its area, having an average annual rainfall of 30 mm, is 42,000 km^2 and the potential recharge accordingly is either 0.4 $m^3 \cdot s^{-1}$ or 4 $m^3 \cdot s^{-1}$.

There are four important zones that may recharge the Mesozoic aquifer. In the Ghadames - Hamada al Hamra region they are:

- the Jabal Gharyan - Jabal Nefousa (22,000 km^2, 150 mm of rainfall, 1 to 10 $m^3 \cdot s^{-1}$ of potential aquifer recharge);
- the Jabal Tuil el Hira (13,000 km^2, 65 mm of rainfall, 0.3 to 3 $m^3 \cdot s^{-1}$ of potential aquifer recharge);
- the Adrar Ben Drich (17,500 km^2, 20 mm of rainfall, 0.1 to 1 $m^3 \cdot s^{-1}$ of potential aquifer recharge).

In the Marzuq basin the only possible recharging zone is the Mangueni plateau north of Madama (10,000 km^2, 20 mm of rainfall, 0.06 to 0.6 $m^3 \cdot s^{-1}$ of potential aquifer recharge).

The Mesozoic aquifer is also recharged in the Northwest along 7°45' longitude, where no physical boundary of the regional groundwater system is present (see Section 1.3).

A better determination of the ratio of recharge to rainfall could be achieved by numerical simulation of water flow in unsaturated soil, taking into account soil physical characteristics and different types of rainfall events.

6.1.4. Water use in agriculture

The desert climate of Fezzan requires irrigation for true agricultural crops all over the year, as the average rainfall may be as low as 5 $mm \cdot a^{-1}$.

At present quite different irrigation techniques are used in the area, ranging from modern, large scale, sprinkler irrigation to traditional basin irrigation

Fig. 6.2. Radar image of the eastern part of Wadi Ash Shati and Idehan Awbari (see Fig. 6.4). The Ashkidah sprinkler irrigation scheme is visible at the top of the image, while at the right central-pivot units (some 0.6 km in diameter) can be seen. Image observed during the SIR-A experiment onboard Space Shuttle Columbia, 14 to 18 November 1981

of very small plots (see Fig. 6.2). Water is usually obtained from wells by motor pumps, but some artesian wells with a large discharge also exist. The old technique of raising water by buckets with man or animal power disappeared recently, due to the subsidized purchase of agricultural machinery. An impressive picture of the growing hydrologic impact of irrigation in the Wadi Ash Shati - Sabhah region is provided by the Space Shuttle radar image (SIR-A experiment) presented in Fig. 6.2. The Ashkidah sprinkler irrigation system is shown together with a number of central-pivot units located near Umm al 'Abid.

A study of the ancient irrigation practices in Fezzan has been presented by ELDBLOM (1961) who found that in 1958 these ancient practices were still applied full scale. Groundwater was extracted from shallow wells by a kind of tipping-bucket system, which could supply up to 0.04 $m^3 \cdot min^{-1}$. The water was applied to small parcels, i.e. from 2 to 5 m^2. Shallow wells in these oases were dug by hand and there was no particular protection to prevent the wells from collapsing. It can, therefore, be understood that PLINIUS (77) stated (see quotation at the beginning of this chapter) that most wells were covered by sand. He might have

been wrong, however, about the mischievous intentions of the Garamantes, who just did not have the technology to properly maintain their wells.

For a very long time natural vegetation has been the primary asset of desert inhabitants, while in the near future the actual productivity of natural vegetation may depend on, or at least be influenced by, the large water management schemes being developed. It is felt that this aspect of the effects of water management should also be taken into account when considering different alternatives for development. At present development of natural pastures is being considered as a possibility for the coastal belt in North Africa (RNEA, 1976). Under that scheme wadi beds and coastal playas could be reclaimed by increasing the present density of natural vegetation. Now, because of the to be expected groundwater table drawdowns in the Wadi Ash Shati basin, important oases may be liable to a sharp drop in productivity.

Oases are a common landscape feature in the Wadi Ash Shati, while in the Al Jufrah region they are not that extensive and developed. The Wadi Zallaf shows excellent examples of extensive, natural palm groves, although the ground coverage percentage is low: 14.5% over 130,000 ha. See also Fig. 6.4.

103
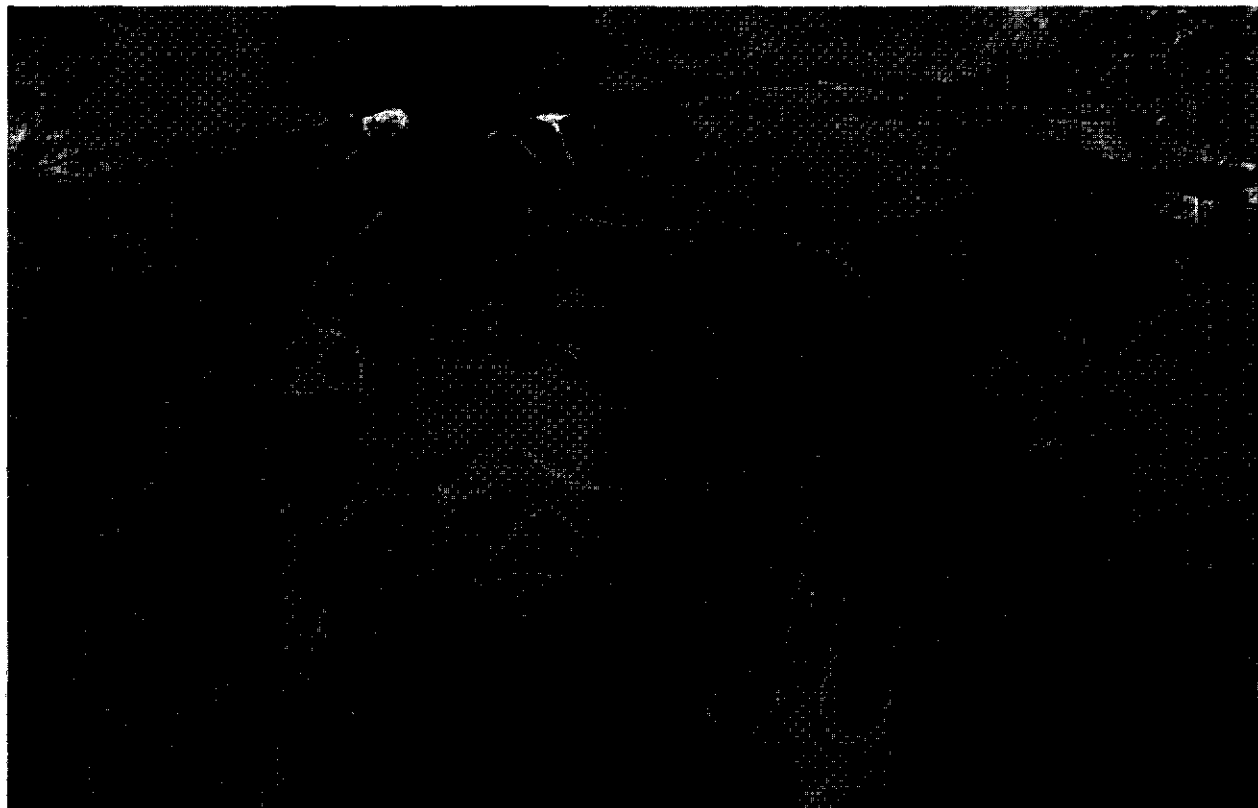
Fig. 6.3. Graffiti found some 20 km NE of Brak; similar animals are featured by graffiti described in other parts of the Sahara. Top: an elephant; bottom: bovine

To depict the rôle of natural vegetation in the past of Fezzan, there is probably no better image than the graffiti shown in Fig. 6.3. These photos show graffiti found some 20 km NE of Brak. According to MAUNY (1961) elephants and bovines (see Fig. 6.3) are a frequent subject of graffiti in this part (Fezzan) of the Sahara; even animals requiring a much more humid climate, such as hippopatami, often are depicted. Again according to this author such a picture of the Sahara applies to some 4000 to 5000 years BC, when natural vegetation did suffice for these animals to live.

The present rangelands are much less productive, but they are still used for nomadic grazing. Rangelands can be endangered by increased groundwater extraction. The corresponding impact on the cattle carrying capacity of the present ecosystem should be quantitatively assessed. A difficulty to achieve this goal is the scarcity of data on the productivity of natural desert vegetation. In Table 6.5 a list is given of irrigated areas in the Fezzan study area that are relevant to the present research (for locations see Fig. 6.4). In total about 9800 ha is irrigated and plans are made for further expansion. The area covered by Fig. 6.4, is the area of the Aquater study

Table 6.5. Gross water requirements ($mm \cdot a^{-1}$) of existing traditional (T) and modern (M) agricultural areas in the Fezzan study area (after Aquater, 1980)

Region	Cropped area (ha)	Gross water requirement ($mm \cdot a^{-1}$)
Wadi Ash Shati area:		
Idri	430 T	1,500
Wanzarich	225 T	2,400
Al Hatiyah Barqan project	?	?
Barqan	195 T	3,150
Quttah	45 T	10,600
Al Mahruqah	485 T	5,100
Brak	980 T	3,200
Umm al Jadawil project	100 M	2,500
Ashkidah	330 T	2,900
Brak – Ashkidah project	3000 M	1,260
Bir Ghalmayah	20 T	7,500
Al Jufrah area:		
Jufrah project	2400 M	810
Sawknah	43 T	1,280
Hamam project	1200 M	550
Hun	184 T	920
Waddan	130 T	960

(see also Fig. 6.1). The evolution of groundwater extraction is shown in Fig. 6.5 for both the Wadi Ash Shati and Al Jufrah areas.
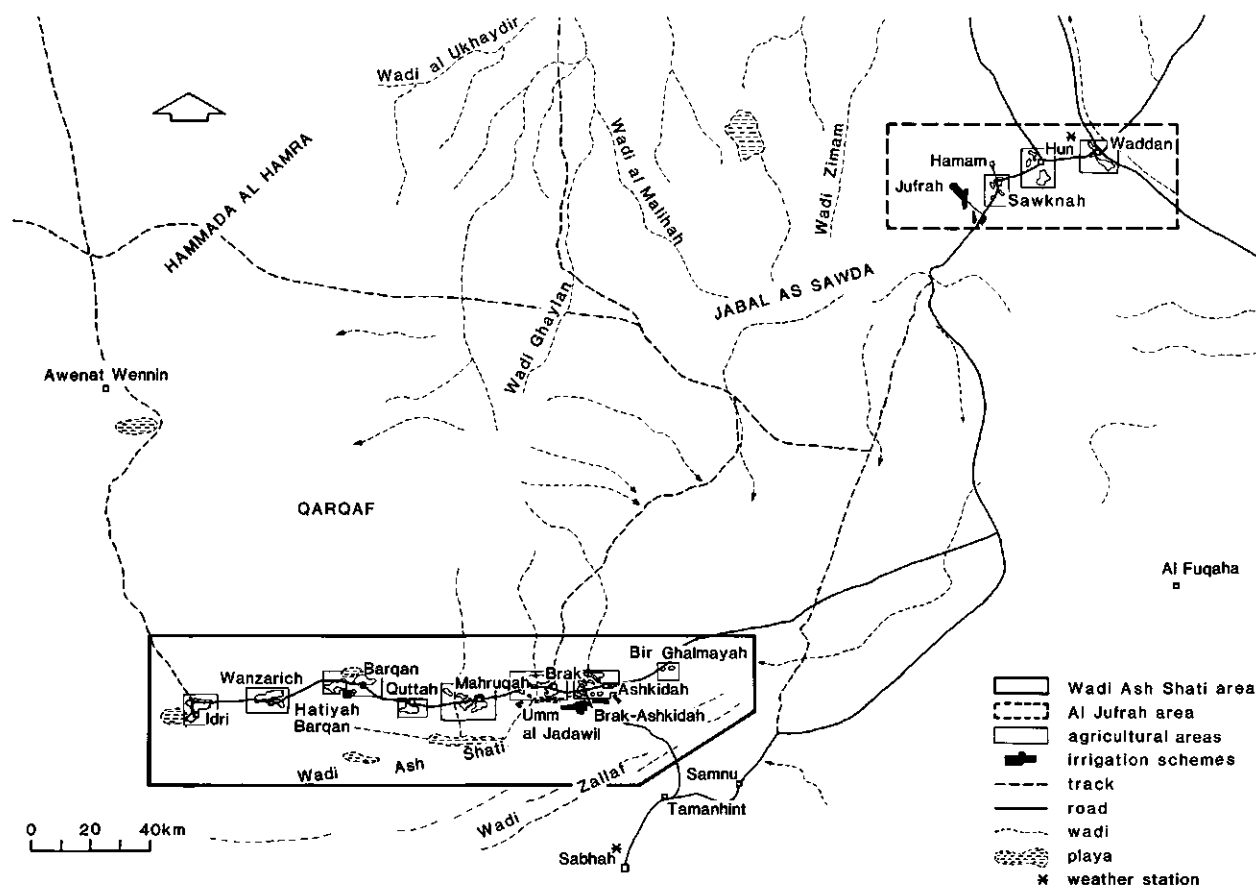
Fig. 6.4. Location of irrigated areas in the Wadi Ash Shati and Al Jufrah regions (after Aquater, 1980), also of some moisture measurement sites (see Table 6.8); see also Fig. 6.19
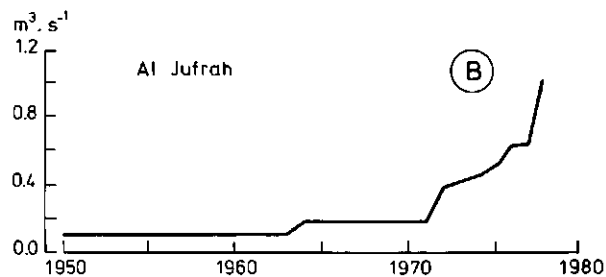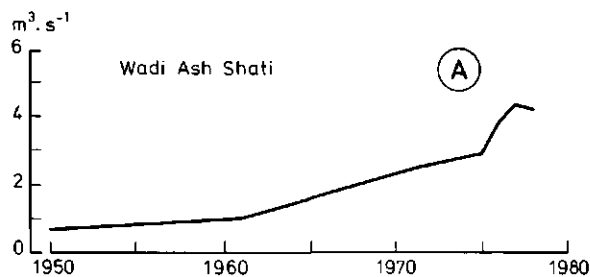
Fig. 6.5. Total artificial groundwater discharge in A: Wadi Ash Shati area and respectively B: Al Jufrah area (after Aquater, 1980)

The tremendous importance of proper water management can be easily seen by comparing data on water requirements in small traditional areas as Quttah and Bir Ghalmayah, with those of modern large schemes as Brak - Ashkidah and Jufrah (see Table 6.5). It must be emphasized that even an area of a few hundred ha has a regional impact on the aquifer water balance due to the ratio of irrigation requirements over rainfall, i.e. 10^3! Note that this ratio implies that the 10^4 irrigated ha (see Table 6.5) have a sensible impact on a region 10^5 km^2 large. From this it can be understood why any appraisal of groundwater reservoirs in deserts is regional in character. A clear impression of the impact of irrigated agriculture in Fezzan, is easily obtained by comparing the increasing amount of groundwater being extracted (Fig. 6.5) with the order of magnitude of recharge given in the Paragraph 6.1.3 (from 1.9 to 19 $m^3 \cdot s^{-1}$). Groundwater losses by evaporation are of the same order of magnitude as groundwater use for irrigation, as will be shown in Chapter 8.

6.2. FIELD INVESTIGATIONS IN THE WADI ASH SHATI BASIN

The Wadi Ash Shati basin (see Fig. 6.4) plays a very important rôle in the behaviour of the aquifer described in Section 6.1, as is clearly illustrated by Fig. 6.5 where it is shown that groundwater extraction is much higher there than in the Al Jufrah area. Furthermore, the particular hydrogeological position of the Wadi Ash Shati basin (see Figs. 1.4 and 1.5) allows evaporation of groundwater stored in Paleozoic formations cropping out in the area. Many efforts were devoted in the framework of the Aquater study to collect data which could be helpful in transforming evaporation results from local experiments to the entire basin (see also Figs. 6.12 and 6.19). These data are of different nature and will be briefly described. Rainfall observations have already been mentioned in Section 6.1.

6.2.1. Hydrological data

Depth of the shallow groundwater is of course an easy criterion to identify areas where evaporation is large. In the Wadi Ash Shati basin a number of areas exist where the groundwater table is present at shallow depths, but the data available were scarce and only for the areas surrounding the oases it was possible to draw a piezometric map. The result is shown in Fig. 6.6. It can be seen that groundwater flow is directed downhill from the Qarqaf highland. At Wanzarich the effect of groundwater extraction is clearly evident. From the piezometric head distribution around the oases of Al Mahruqah and Al Gorda it is clear that over-irrigation in the oases causes much groundwater to be lost towards the dunes of the Idehan Awbari.

By Aquater water samples also were collected and analyzed for the concentration of total dissolved salts. A map was drawn and it is presented in Fig. 6.7. As it easily can be seen the highest salt concentrations are observed in the most important oases: Aqar, Al Mahruqah, Al Gorda, Wanzarich and Idri. In particular it should be noted that the salt concentration increases steeply at the West of Idri, i.e. towards the extensive playa area. The map of Fig. 6.7 clearly points out the need for very careful control of water extraction in the Idri oasis from shallow depths to avoid contamination due to the possible flow of saline water from the playas towards the oasis. According to the concepts discussed in Chapter 3, the salt concentration must also be known to calculate the soil water flow and the humidity of soil air. Par-

Table 6.6. Composition of soluble salts (mass percentage) of Idri deposit (after Goudarzi, 1962)

	NaCl	K_2O	$MgCl_2$
Crust	69.9	3.4	1.6
Undercrust	13.5	0.7	0.4
Brine	11.2	0.6	0.6

QARQAF HIGHLAND
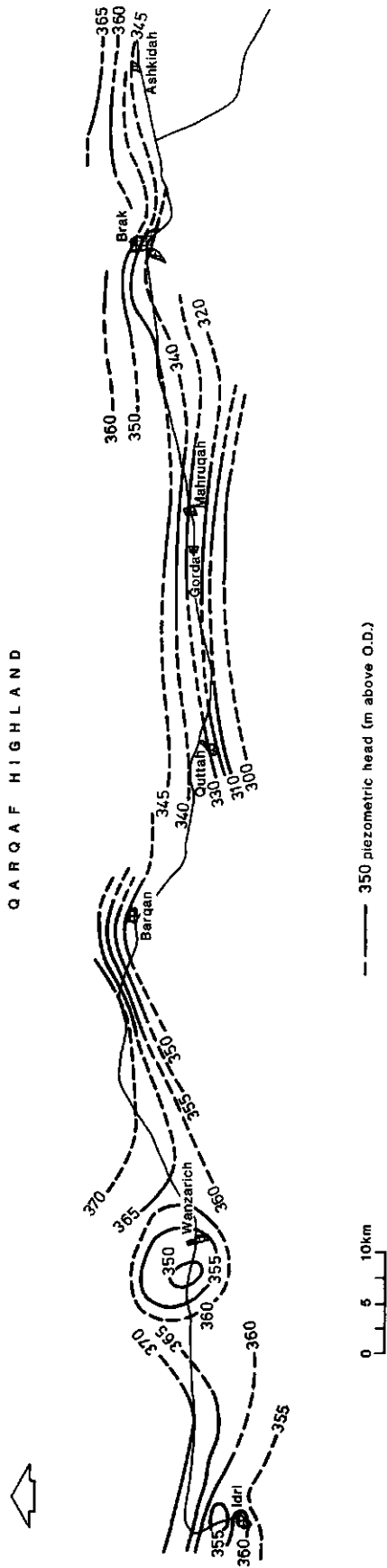
Fig. 6.6. Piezometric head distribution of the shallow water table surrounding the various oases in the Wadi Ash Shati basin (after Aquater, 1980)

——————— 350 piezometric head (m above O.D.)

0   5   10km

QARQAF HIGHLAND
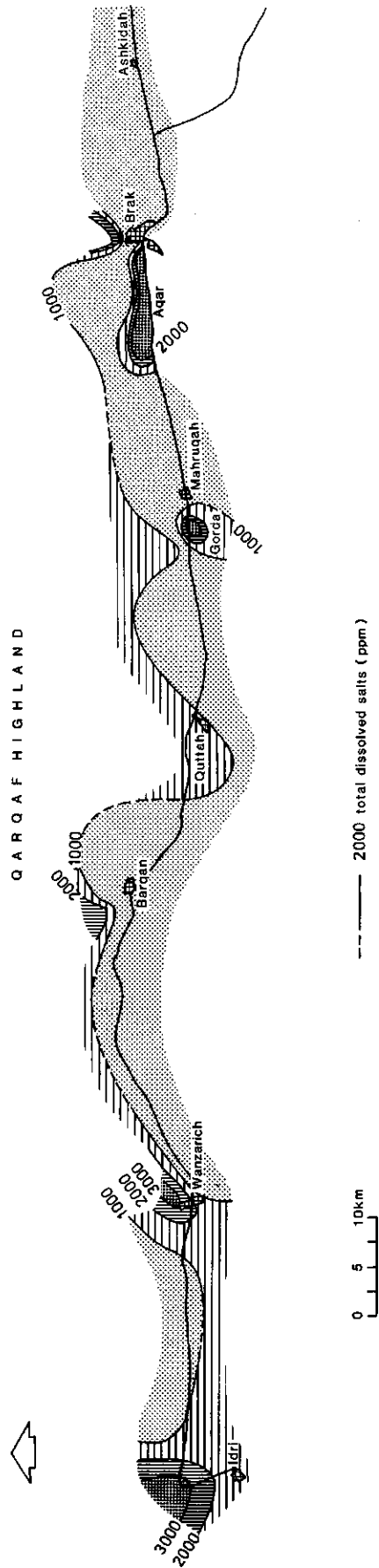
Fig. 6.7. Concentration of total dissolved salts (ppm) in the Wadi Ash Shati basin (after Aquater, 1980)

——————— 2000 total dissolved salts (ppm)

0   5   10km

107

Week	Na	K	Cl	SO$_4$	Mg	HCO$_3$	Solids
1	.721	.097	1.193	.23	.048	.03	
2	.997	.137	1.664	.315	.067	.03	
3	7.003	.776	10.460	1.670	.377	.020	20.420
4	1.232	.222	1.985	.422	.094	.035	4.020
5	1.223	.243	2.127	.442	.096	.036	4.220
6	1.554	.271	2.268	.534	.102	.028	4.800
7	1.524	.278	2.411	.540	.107	.034	4.940
8	1.574	.280	2.660	.564	.115	.033	5.280
9	2.221	.466	2.526	.450	.118	.030	6.016
10	2.090	.432	2.773	.481	.030	.030	5.896
11	1.994	.491	3.120	.584	.125	.040	6.420
12	1.732	.458	2.721	.452	.091	.016	5.540

Table 6.7. Composition of brine (mass percentage) at Idri. Weekly samples collected from May to September 1956 (after Goudarzi, 1962)

ticularly the salt concentration is to be determined in playa soils, crusts and in the brine which is present there.

The results of a study on the characteristics of the Idri salt deposits have been presented by GOUDARZI (1962). Data of this author relating to the crust respectively the brine are presented in Table 6.6 and Table 6.7. These data show that sodium chloride is by far the main salt constituent of the soil and, in the crust at the surface even the main soil constituent (Table 6.6). In Table 6.7 salt concentrations of brine samples collected weekly in pits dug to perform evaporation experiments, are presented. It should be noted that the concentration of the various salts increases only in the first two, three weeks, to remain rather constant afterwards. The difference in concentration between the beginning and the end of the evaporation experiments indicates that the brine was not salt saturated in the original situation.

The playas around Idri show all the surface features described for playas discharging groundwater in Section 1.1 (see Fig. 6.12).

In Figs. 6.8 through 6.11 a few examples of these features are presented. The difference between Fig. 6.8 and 6.9 is most impressive when considering that the variation is probably due to a 20 cm lowering of the water table only. The water table below the bare soil surfaces of Figs. 6.10 and 6.11 lies somewhat deeper. The Idri playas are located in the Wadi Ash Shati basin at approximately 27°30' N latitude at the western side of the village and oasis of Idri (see Figs. 6.6 and 6.7).

Field experiments were carried out mainly in the area around Idri because of the following reasons:

- a wide spectrum of representative surfaces;
- the Paleozoic aquifer reaches the surface (no impervious layers);
- in the western and eastern part of the playa area the influence of wells on evaporation from playas is unimportant, the only possible exception being on the southern side of the oasis.

6.2.2. Meteorological observations

To the present author's knowledge no other weather data (see Paragraph 6.1.2) but rainfall data have been collected in the Wadi Ash Shati basin. Also pan evaporation and solar radiation data are not collected at the meteorological weather station of the Libyan Meteorological Service at Sabhah. Thus a meteorological station of the agrometeorological type was set up by the present author for the Aquater study, near the village of Idri. The position of the station is indicated in Fig. 6.12, while the station itself is shown in Fig. 6.13.

In the period from January 1978 to March 1979 the following data were recorded on paper charts:

- atmospheric pressure;
- air temperature;
- air relative humidity;
- solar radiation;
- class-A pan evaporation, including wind run above the pan edge and water temperature;
- wind velocity, recorded both as wind run and instantaneous value;
- wind direction;
- soil temperature at two soil depths, 30 respectively 90 cm;
- rainfall, in addition to a tipping-bucket recorder, a totalizer raingauge was used.

For a detailed description of the instruments, which were standard meteorological ones, the reader is referred to the final report of the Aquater study (AQUATER, 1980). There the daily totals respectively averages are reported.

6.2.3. Soil water balance data

As discussed in Paragraph 3.2.3 and Section 3.6 evaporation in playas where a groundwater table is present at shallow depths, can reliably be determined by the soil water balance method. The data required are: depth of the groundwater table, soil hydrological

Fig. 6.8. Example of the soil surface of a playa around Idri (Wadi Ash Shati) with a free water surface
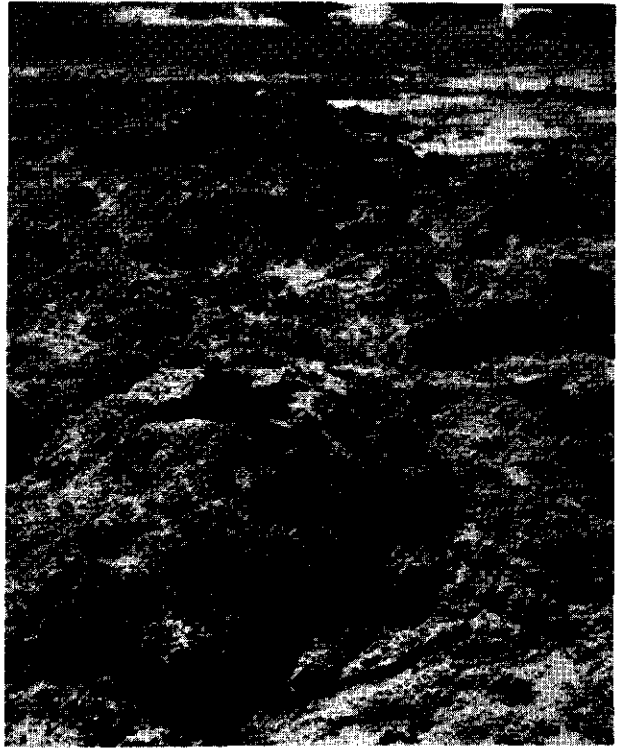
Fig. 6.9. Example of a soil surface of a playa around Idri: a very rugged crust overlying a 20 cm deep groundwater table

Fig. 6.10. Example of a soil surface of a playa around Idri: a smooth, hard, very dry soil surface overlying a 1 m deep groundwater table. The person is holding a thermal infrared radiometer

Fig. 6.11. Example of a soil surface of a playa around Idri: puffy salt crust overlying a 2 m deep groundwater table. Also shown is the neutron probe in one of the access tubes
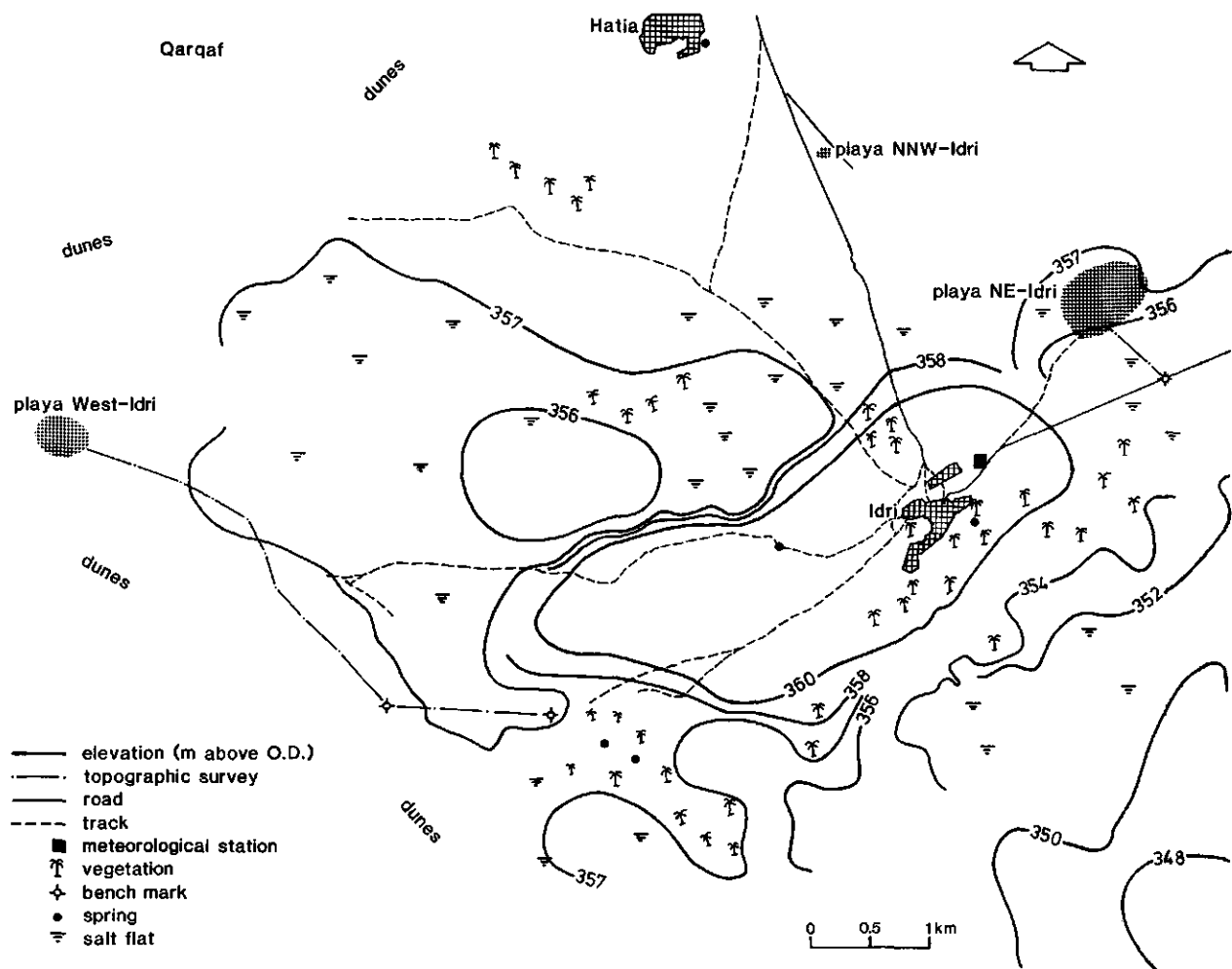
Fig. 6.12. Elevation contour lines, location of wells, springs, palm groves and of the weather station and test sites in the Idri area

Fig. 6.13. The agrometeorological station installed near Idri
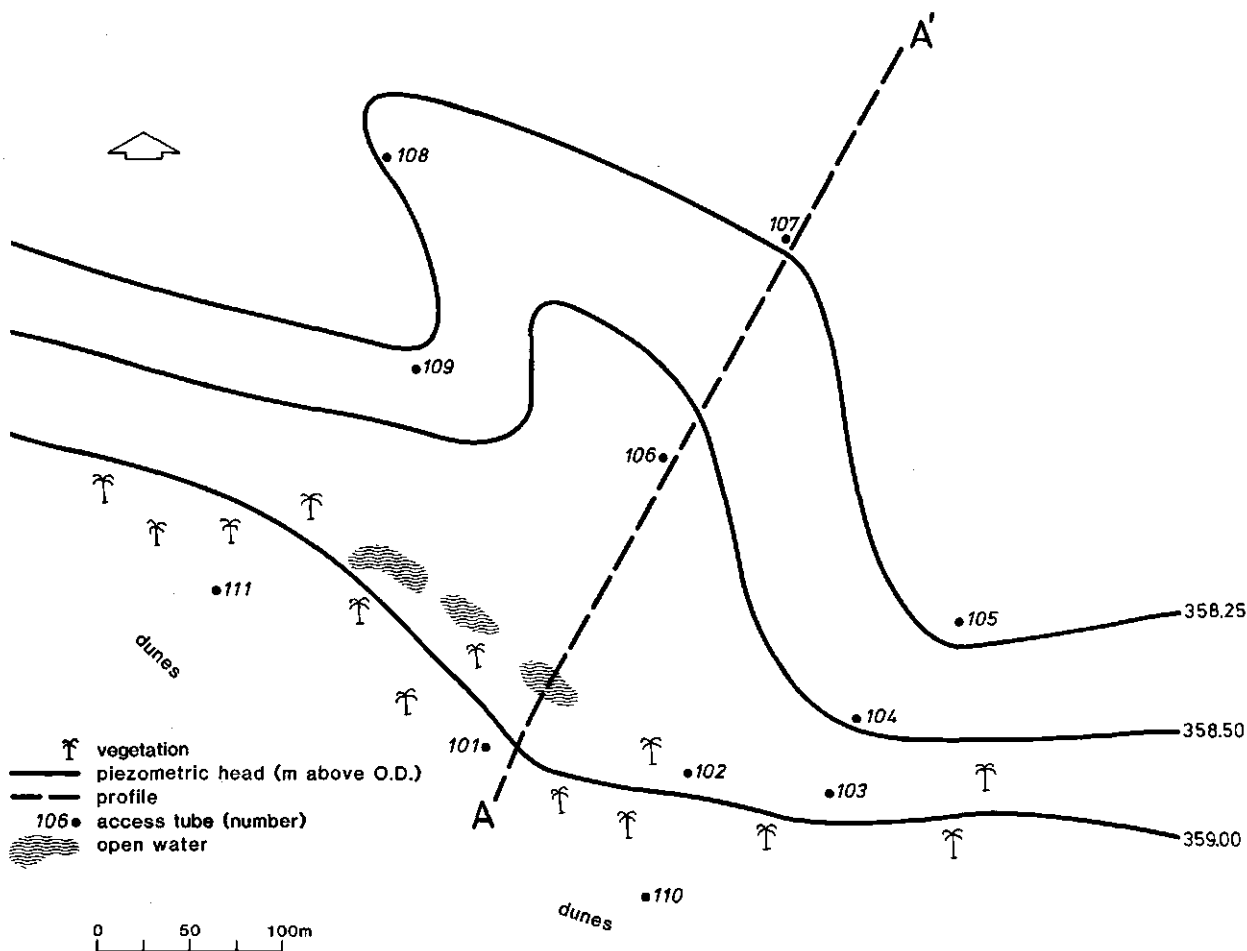
Fig. 6.14. Distribution of the piezometric head of the shallow water table in the playa West-Idri, January 1978 (see Fig. 6.12); for cross section A - A' see Fig. 6.16

properties and soil moisture content. Such data were collected at a number of sites in the playas around Idri. A brief description of the data-gathering programme is given here; the location of the test sites has been indicated in Fig. 6.12.

Groundwater table depth. Topographical surveys have been carried out to pinpoint the test sites by linking them to a previously established (REGWA, 1973) bench mark network. The nominal accuracy of those surveys was 1 cm, thus compatible with the accuracy required for groundwater table depth. Determination of the geographic coordinates of the test sites also is required to compare different remotely sensed data with the ground based measurements. After the topographic maps of the test sites had been obtained, groundwater table depth was measured at a number of points. The map of piezometric head (in m above Ordnance Datum) for the playa West-Idri (see Fig. 6.12), as obtained on 21 January 1978, is presented in Fig. 6.14. It is seen that groundwater flow is directed outwards from the dunes. The

piezometric head distribution observed in the playa West-Idri confirms the overall pattern of groundwater flow in the Wadi Ash Shati, as depicted in Fig. 1.6 for the Paleozoic aquifer. The piezometric heads, as depicted in Fig. 6.15 for the playa NE-Idri, show in detail the groundwater flow pattern in the eastern surroundings of Idri. Fig. 6.15 can be compared with Fig. 6.6 to confirm that flow is directed towards the South, downhill from the Qarqaf. It should be noted that only in the playa West-Idri groundwater table depths have been measured from the very boundary between playas and dunes.

In Fig. 6.16 the variation of groundwater table depth and ground surface level is depicted as applying to the cross section A-A' in Fig. 6.14. Finally the topographic map of the playa NNW-Idri, where one of the experiments on surface energy balance was performed, is presented in Fig. 6.17.

Soil hydrological properties. The $h(\theta)$- and $\kappa(h)$-curves have been measured for two
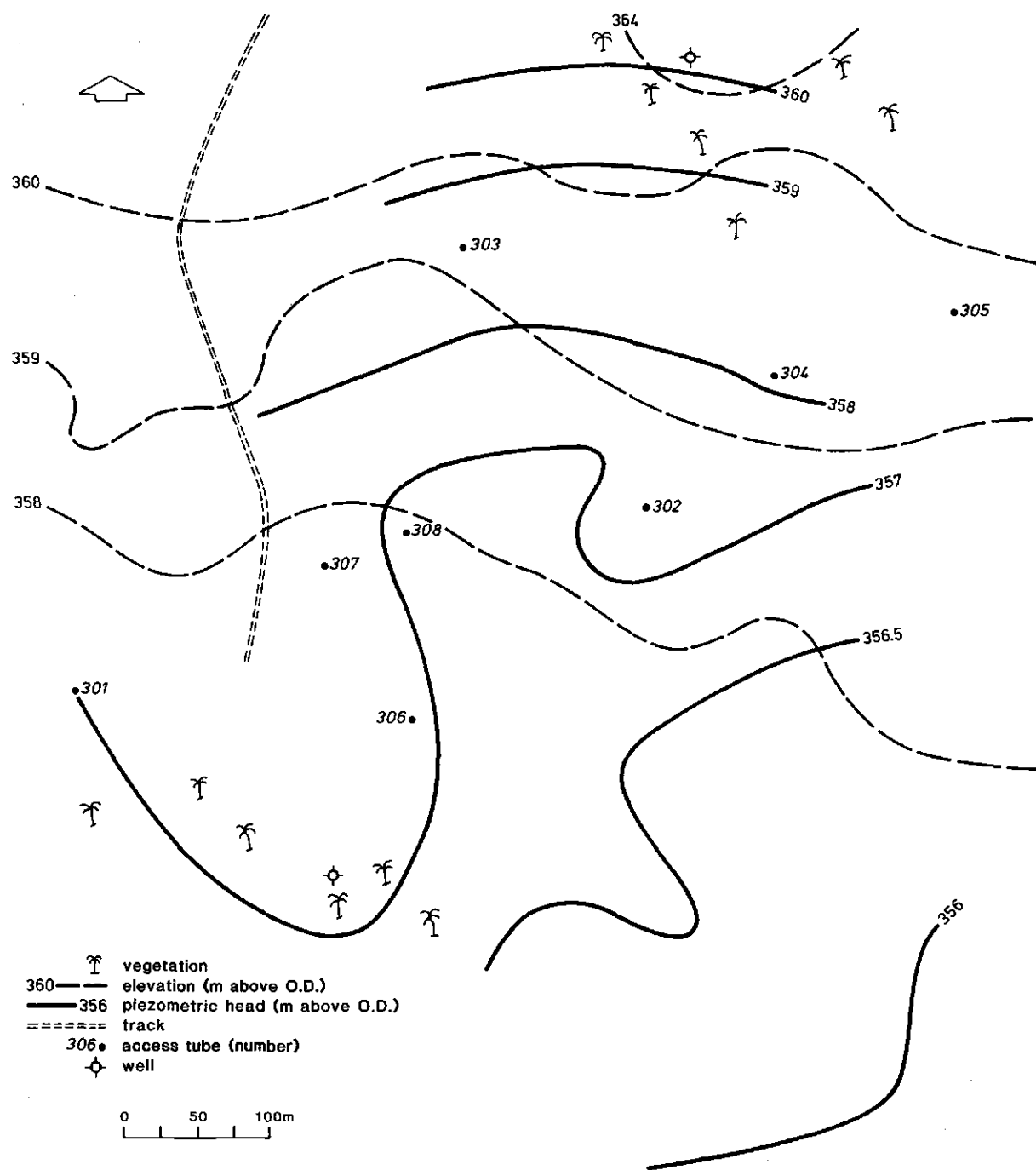
Fig. 6.15. Distribution of the piezometric head of the shallow water table in the playa NE-Idri, January 1978 (see Fig. 6.12)

soil profiles in the Wadi Ash Shati basin: one in the playa NE-Idri and one in the Ashkidah oasis (see Fig. 6.6). The h(θ)-curves were obtained according to the procedure of STAKMAN et al. (1969) and STAKMAN and van der HARST (1969), the κ(h)-curves by means of the soil column apparatus described by BOELS et al. (1978). The sampling scheme was:

h(θ): playa NE-Idri : layers 45, 90, 135, 180 cm (in duplicate)

Ashkidah oasis: layers 10, 40, 60, 75 cm (in duplicate)

κ(h): playa NE-Idri : layer 10-50 cm
layer 60-100 cm

Ashkidah oasis: layer 0-40 cm
layer 40-80 cm

The curves obtained under laboratory conditions have been corrected to account for differences in

elevation (m above O.D.)
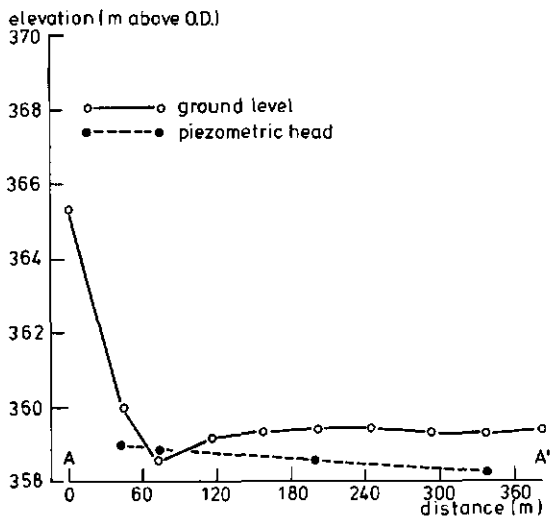
Fig. 6.16. Cross section of piezometric head of the shallow water table and topographic height in the playa West-Idri (see Fig. 6.14)

road
track
363.31• elevation (m above O.D.)
open water
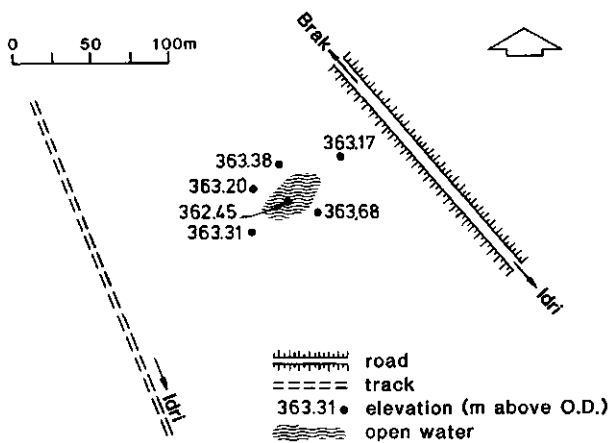
Fig. 6.17. Topographic map of the playa NNW-Idri showing the extension of an open water surface (see Fig. 6.12)

temperature and salt concentration, as described in Paragraph 3.5.3.

S o i l m o i s t u r e c o n t e n t has been measured in the period February to October 1978 at a number of sites and depths in the Wadi Ash Shati basin. A neutron probe was used (see Fig. 6.11), calibrated by comparison of neutron probe readings against measured moisture contents in terms of weight percentage. To transform values on weight basis into moisture contents per unit volume, a number of undisturbed soil samples of known volume were collected. A list of the sites (see Figs. 6.4, 6.14 and 6.15) and depths where moisture content has been measured at 20 cm depth intervals is given in Table 6.8, with the sites where calibration of the neutron probe readings have

Table 6.8. Sites, access tube designations and depths where soil moisture measurements have been performed at 20 cm intervals in the period February through October 1978 (see Figs. 6.4, 6.14 and 6.15). G: at these sites gravimetric moisture determinations for calibration were performed

Site	Access tube	Depth (m)
Playa, West-Idri	101	0.20 - 1.00
	102	0.20 - 1.50
	103	0.20 - 1.60
	104	0.20 - 1.60
	105G	0.20 - 2.20
	106	0.20 - 0.90
	107	0.20 - 1.20
	108	0.20 - 3.50
	109	0.20 - 1.20
	110G	0.20 - 4.20
	111	0.20 - 4.00
	112G	0.20 - 1.20
Playa, NE-Idri	301	0.20 - 1.00
	302G	0.20 - 1.50
	303	0.20 - 1.60
	304	0.20 - 0.90
	305	0.20 - 1.20
	306G	0.20 - 2.20
	307	0.20 - 1.50
	308	0.20 - 1.40
Palms on dunes, Idri	401G	0.20 - 2.70
	402	0.20 - 1.80
Irrigated palms, Idri	501	0.20 - 2.20
Alfalfa, Idri	601G	0.20 - 1.60
Tamarix, Tamanhint	701G	0.20 - 3.50
Calligonum, Quttah	801G	0.20 - 3.70
Alfalfa, Ashkidah project	901G	0.20 - 3.70
Imperata cilindrica, Quttah	1001G	0.20 - 3.50
Alagi Maurorum, Quttah	1101G	0.20 - 2.50
Alfalfa, Aqar	1201G	0.20 - 1.10
Tamarix, Idri	1301G	0.20 - 1.80

been carried out.

The results of the measurements described in this paragraph will be presented in Chapter 8.

6.2.4. Surface energy balance experiments

To study the energy balance of different surfaces, a number of experiments have been carried out in February and September 1978. In Fig. 6.18 a view is given of part of the Playa West-Idri in winter and in summer. The following data were collected:

- net radiation by a Funk-type net radiometer with forced ventilation of the two domes;
- soil heat flux by heat flux plates at 1 cm depth;
- shortwave solar radiation (0.3 to 2.5 μm) both incident and reflected, by means of dome solarimeters;
- surface temperature by hand-held thermal infrared (8 to 14 μm) radiometers (see Fig. 6.10);
- soil temperature at five depths by Cu-constantan thermocouples;
- air temperature and vapour pressure at two levels within 3 m above ground surface, by means of Assmann psychrometers with thermometers and a similar thermocouple - psychrometric system;

113

Fig. 6.18. View of the playa West-Idri, site of two energy balance experiments. Top: wet soil, wintertime; bottom: extremely dry surface, summertime
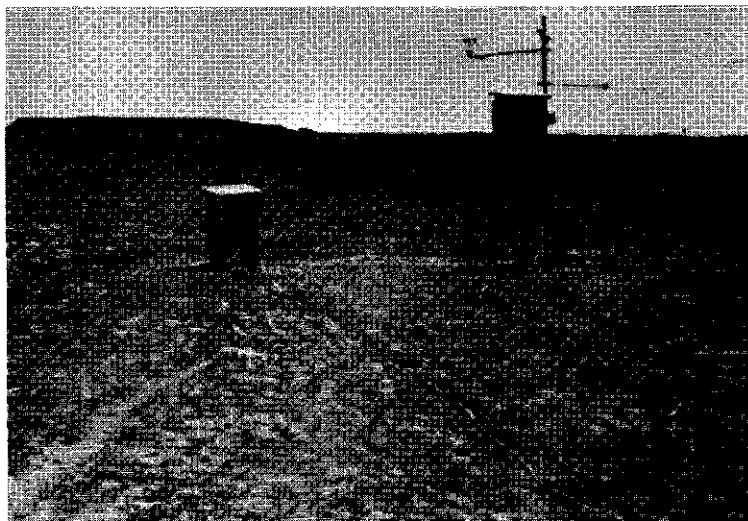
Site	Period			
	winter		summer	
Playa West-Idri (wet soil)	6 - 28 Feb.			
Playa West-Idri (extremely dry surface)			27 Aug. - 21 Sept.	
Playa NE-Idri	12 - 17 Feb.		30 Aug. - 4 Sept.	
Playa NNW-Idri	6 - 12 Feb.		9 - 12 Sept.	
Palms on dunes, Idri	17 - 20 Feb.		5 - 8 Sept.	
Irrigated palms, Idri	20 - 24 Feb.			
Alfalfa, Idri	24 - 28 Feb.			
Tamarix, Idri			15 - 18 Sept.	
Calligonum, Brak			19 - 20 Sept.	
Alfalfa, Ashkidah project			21 - 23 Sept.	

Table 6.9. Sites and periods of the energy balance evaluation survey in 1978 (see Figs. 6.4 and 6.12)

- wind speed at two levels within 3 m above ground surface by cup-anemometers of the light chopper or Sheppard type.

Net radiation, soil heat flux and, in some cases, psychrometric and soil temperature data were obtained on paper charts by voltage analog recorders. Solar radiation data were integrated over different time periods (mostly one hour) and both printed and hand-written by the on-site operator. Soil temperatures

usually were read each hour. Psychrometric data from
the Assmann psychrometers, of which the level and
site regularly were changed, were read by the oper-
ator. Wind speed was obtained as wind run in a 1- or
2-minute interval and written down; only in a few ex-
periments they were printed out.

The data listed above have been used to apply
the approaches described in Chapter 2. The soil tem-
perature data, furthermore, allowed for the determina-
tion of apparent soil thermal diffusivity according
to the procedures described in the Paragraph 3.5.1.
The results will be discussed in Chapter 8. Further-
more the data will be used in Chapter 7 to check the
remotely sensed data.

The list of sites and time periods relating to
the here presented survey of the surface energy bal-
ance in the Wadi Ash Shati basin is given in Table
6.9.

6.2.5. Remotely sensed data

The potentially helpful rôle of remotely sensed
data to study soil layering, surface energy balance
and evaporation in deserts has already been mentioned
in the preceding Chapters 4 and 5. Such data have
been collected over the Wadi Ash Shati basin by dif-
ferent platforms and in different spectral ranges.
They will very briefly be described; a thorough anal-
ysis will be presented in Chapter 7.

It is pointed out beforehand that the kind of
data collected on the ground and described in the
previous part of Section 6.2 represent an essential
body of information for the proper and efficient use,
as described above, of remotely sensed data.

Data in the Wadi Ash Shati have been remotely
sensed by airplane and a number of satellites. The
airborne thermal infrared survey is described first.

To establish the detailed flight programme of
the airborne I n f r a R e d L i n e S c a n -
n i n g (IRLS) survey, two kinds of information were
preliminarly gathered: an empirical, unchecked clas-
sification of surface types and the daily variability
of surface temperature and heat flux for different
surfaces. The classification of surface types was
based on LANDSAT-MSS digital data, while temperature
and heat flux data were provided by the experiments
described in Paragraph 6.2.4. The final scheme of the
flight is presented in Fig. 6.19, where the main bare
soil surface types in playas have also been indicated.
The duration and sequence of the different flight
sections is indicated in Table 6.10. The flight cov-
ered a 1500 km^2 area plus two smaller areas including
the test sites, i.e. the playas West and NE-Idri.
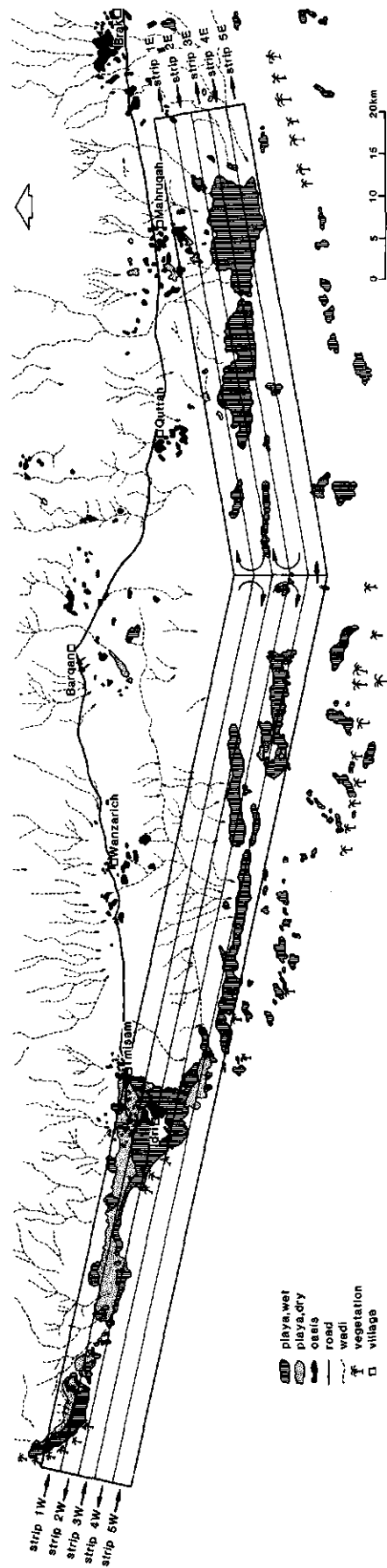
Fig. 6.19. Area covered by and flight programme of the IRLS survey performed in the Wadi Ash Shati basin in February 1978 (after Aquater 1980)

Area	Afternoon	Predawn
Test sites	16 Feb. 12.36 and 14.59	17 Feb. 5.12 and 7.43
Strip 1W	16 Feb. 12.58 to 13.22	17 Feb. 5.42 to 6.12
2W	16 Feb. 13.22 to 13.57	17 Feb. 6.12 to 6.40
3W	16 Feb. 13.57 to 14.22	17 Feb. 6.40 to 7.05
4W	16 Feb. 14.22 to 14.59	17 Feb. 7.05 to 7.43
Test sites	17 Feb. 12.43	18 Feb. 5.15
Strip 5W	17 Feb. 13.04 to 13.32	18 Feb. 5.37 to 6.05
5E	17 Feb. 13.32 to 13.48	18 Feb. 6.05 to 6.20
4E	17 Feb. 13.48 to 14.11	18 Feb. 6.20 to 6.45
3E	17 Feb. 14.11 to 14.26	18 Feb. 6.45 to 7.00
2E	17 Feb. 14.26 to 14.43	18 Feb. 7.00 to 7.18
1E	17 Feb. 14.43	18 Feb. 7.18

Table 6.10. Time-table (Standard Libyan Time) showing duration and scheme of the IRLS survey on 16, 17 and 18 February 1978 (after Aquater, 1980)

The flight height was 7500 m over the entire area and 4000 m over the test sites. The instrument was a Daedalus DS-1230 thermal infrared line scanner, with two infrared channels, 3.0 to 5.5 μm and 8.0 to 12.0 μm, and with an instantaneous field of view equal to $1.7 \cdot 10^{-3}$ rad. Resolution, therefore was 6.8 m for the test site coverage and 11.9 m for the entire area.

Duration and time of execution have been selected for the western (W) and eastern (E) parts (see Table 6.10) of the flight on the basis of the temperature and heat flux measurements at the soil surface. Fairly constant values of these variables were observed in the early morning before sunrise, while the early afternoon flights could not be restricted, for operational reasons, to time periods short enough to guarantee the constancy of surface temperature within each flight section.

S a t e l l i t e   d a t a have been collected by the present author with two goals in mind:

- to assess weather conditions and their variability during the period of execution of the field experi-

ments from photographic products;
- to measure surface temperature and reflectivity according to the concepts discussed in Chapter 5, by using digital products.

For the different satellite systems the reader is referred to the pertinent official documentation. For an overview of the characteristics of these satellite systems see for instance CORNILLON (1982). In Table 6.11 the type of data, the spectral range, the ground resolution, the period and the time interval between two subsequent coverages are given for the particular satellite data. As regards the METEOSAT data it should be added that the time interval figure is a nominal value since some of the data were missing. Furthermore, the data obtained from the SIR-A experiment, carried out during the flight of the Space Shuttle Columbia, are listed among the satellite data, which classification is not correct.

Table 6.11. List of satellite data collected for the present investigation of the Wadi Ash Shati basin

Satellite	Type of data	Spectral range	Ground resolution	Period	Time interval
Space Shuttle Columbia (SIR-A)	photographic	23 cm	40 m	15 Nov. 1981	single
LANDSAT	MSS, digital	0.5 - 1.1 μm	79 m	12 Mar. 1978	single
				26 Sept. 1978	single
NOAA-5	VHRR-TIR, photographic	11.5 - 12.5 μm	1.1 km	1 - 28 Feb. 1978	one day
				15 Aug. - 30 Sept. 1978	one day
HCMM	VIS, digital	0.55 - 1.1 μm	0.5 km	18 Sept. 1978	single
HCMM	TIR, digital	10.5 - 12.5 μm	0.6 km	16 and 18 Sept. 1978	60 hrs
DMSP	VIS, photographic	0.4 - 1.1 μm	0.6 km	15 through 25 Feb. 1978	one day
				12 through 23 Sept. 1978	one day
DMSP	TIR, photographic	8 - 13 μm	0.6 km	(as for VIS-data)	
METEOSAT	VIS, digital	0.4 - 1.1 μm	2.5 km	17 through 18 Feb. 1978	9 hrs
METEOSAT	TIR, digital	10.5 - 12.5 μm	5 km	16 through 18 Feb. 1978	6 hrs
				16 through 18 Sept. 1978	6 hrs
				15 June through 15 July 1978	12 hrs
				22 Dec. 1978 through 22 Jan. 1979	12 hrs

7. ANALYSIS OF REMOTELY SENSED DATA OF THE WADI ASH SHATI BASIN

'Ab his mons longo spatio in occasum ab ortu tendit, Ater nostris dictus a natura, adusto similis aut solis repercussu accensus.'

(PLINIUS, Naturalis Historia, Liber V:35)

7.1. GENERAL

The Libyan desert and the Fezzan region offer ideal conditions for application of remotely sensed data. In addition to the very high percentage of clear days, the sharp contrast between the Qarqaf highland and the Idehan Awbari allows the use of data with different characteristics and resolution.

ZUIDAM (1971) compared images taken by the TIROS, Nimbus, ESSA and ITOS-1 meteorological satellites and drew a geomorphological map of the Libyan desert from a GEMINI XI (1966) image. WALKER (1979) pointed out that a GEMINI XI colour photograph of the Idehan Awbari proved that sand redness increased in the direction of transport. Sand colour is useful for estimating the distance travelled by dunes, because the time required to achieve a specified colour depends on slow chemical processes. FRYBERGER (1979) established from LANDSAT images that the linear dunes in Wadi Zallaf lie parallel to the expected drift direction according to weather data at Sabhah. BREED et al. (1979) drew maps of the morphology and distribution of eolian sands from LANDSAT imagery. It appeared that when both Wadi Zallaf and Idehan Awbari are considered, in a large part of the area two dune patterns are superimposed. The same authors published an excellent colour photograph of Idehan Marzuq from the Skylab mission.

The conclusion to be drawn is that in the Fezzan region satellite imagery has already been found to be a very helpful tool. It should be recalled that medium and large scale maps of the region are either not available or of poor accuracy. It is interesting to compare the DMSP (Defense Meteorological Satellite Program of US Air Force) visible image on 19-9-1978 (see Fig. 1.3) with the schematic structure of the West-Libyan aquifer system in Fig. 1.4 as drawn by combining available documents and stratigraphic data. It appears that use of the image of Fig. 1.3 could both have saved a considerable amount of work and improved the accuracy of the final product. The boundaries of the aquifer system in Fig. 1.3 are clear, especially

the Amguid fault system which shows up as a sharply edged scar in the top left.

To the author's knowledge there exist no previous applications of thermal infrared imagery relating to the Fezzan region. However, many applications of thermal infrared remote sensing in the world relate to the geology of deserts, many of them dealing with playas. NEAL (1972) gave an overview on the latter subject. The first example are Nimbus 1 images (1964) of NW-Nevada and South-Iran, where playas appear as the brightest surface types. Playa surface features in Iran as detected by the Nimbus 1 image were compared by Neal with GEMINI V photos (1965). Observed differences were related to soil type and occurrence of groundwater discharge, as at playa Lavar Maidan. According to Neal the first airborne infrared (4.5 to 5.5 μm) survey of a playa was carried out at Harper Lake (California) in 1967. Large daily amplitudes of surface temperature were observed in soft, friable surfaces where groundwater discharge occurred. Small amplitudes were observed in hard, dry, clayey crusts. Two explanations of this behaviour can be put forward by the present author: either the puffy surface had a poor thermal contact with the soil underneath, thus a low $|y_0|$ (see Chapter 4), or the clay crust had an air humidity dependent heat of wetting (see Paragraph 3.5.2). Since that early investigation, it has been realized that the interpretation of thermal infrared data becomes quite difficult when surface reflectance changes across the scene.

Van DIJK et al. (1971) presented the results of an airborne thermal infrared survey performed in Oman in combination with soil temperature measurements down to a depth of 2 m. Below a few centimeters depth soil temperature remained constant. In the two soil profiles where measurements were carried out a seemingly contrasting behaviour was observed. The differences in mean temperature were consistent with the differences in thermal conductivity of the two soils, while surface temperature amplitudes were nearly identical at the two sites. The authors explained

the large temperature amplitude of clay pans by poor
thermal contact between crust and bulk soil.

The investigations of van Dijk et al. were aimed
at detecting salt domes. The general idea was to per-
form flights at such times that the soil heat flux
$G_0 = 0$. Absolute calibration of thermal imagery and a
quantitative comparison between successive flights was
ruled out by the poor technique used in recording of
data. Notwithstanding these inconveniences, a previous-
ly unknown salt dome was discovered. Also an area
with a shallow water table was detected, as confirm-
ed by ground observations.

EL-SHAZLI et al. (1973) presented the interpreta-
tion of a number of night-time airborne thermal infra-
red surveys over the western desert in Egypt. Identi-
fication of wadis by thermal imagery was found to be
much easier than by aerial photographs.

The first quantitative interpretation of surface
properties by thermal infrared data, was carried out
by POHN et al. (1974). A thermal inertia map of Oman
was drawn by determining surface reflectance from
Nimbus III (11 November 1969) visible data and surface
temperature from Nimbus IV (15 May 1970) thermal infra-
red data. Unknown geological features or ones wrongly
located on existing geological maps, were discovered.
An essentially identical procedure was computer-coded
and applied to airborne data from the Mojave desert by
GILLESPIE and KAHLE (1977). They concluded that ther-
mal inertia alone was not sufficient to identify spe-
cific surface materials.

A combined application of visible and thermal
infrared METEOSAT data of poor resolution with LANDSAT
data of West-Africa has been presented by BARDINET et
al. (1982). These authors also concluded that thermal
inertia as provided by standard HCMM data products is
too crude an indicator of surface types. The procedure
neglects latent and sensible heat fluxes, longwave ra-
diation balance and variability in atmospheric trans-
mittance (see Section 5.2 and Paragraph 5.4.3). It was
suggested by Bardinet et al. that a better discrimina-
tion of surface types could be obtained by making a
two-dimensional classification based on one image of
mean surface temperature and one image of surface tem-
perature amplitude.

The preceding short overview calls for a few com-
ments:

- satellite imagery has already proved to be a useful
  mapping tool in desert regions;
- thermal infrared imagery fits rather well with the
  size and environmental conditions of desert areas;
- differences between remotely sensed surface tempera-
  tures and actual ones are not that severe that they
  prevent meaningful results of remote sensing;

- to take full advantage of the potential capabilities
  of available remote sensing techniques accurate geo-
  graphic registration of imagery is essential;
- in the interpretation of remotely sensed data great
  care must be exercised in defining the physical mod-
  el to be applied, because different explanations can
  fit the same behaviour, given the relatively poor
  accuracy of the data.

7.2. EARTH LOCATING DIGITAL SATELLITE DATA

The satellite data available for the Wadi Ash
Shati basin and Fezzan region have been listed in Ta-
ble 6.11. Imagery from the polar orbiting satellites
LANDSAT, HCMM and the geostationary satellite METEOSAT
was available in the form of computer compatible tape
(CCT). Accurate mutual registration of images obtain-
ed from different satellites is necessary for the
proper combined use of such data. Geographic regis-
tration of satellite data, furthermore, is needed to
check the interpretation with ground-based observations
and data.

Accuracy requirements, in terms of pixels, of
the registration procedure increase with decreasing
resolution of data. On the one hand one may feel frus-
trated by the detail of low altitude airborne data,
while on the other hand it is hard to translate the
25 km^2 pixels of geostationary satellites (METEOSAT)
into common 'ground level' information.

L A N D S A T   d a t a. LANDSAT standard frames as
delivered in CCT-form have already been corrected for
a number of deformations. Details can be found in
TELESPAZIO (1976) and NASA documents X-563-73-206 and
PHO-TR 543. It suffices here to say that deformations
within a frame are not corrected, while those between
frames are. The average accuracy of spatial registra-
tion between the spectral bands has been found to be
better than one pixel (root mean square), while the
positional accuracy, i.e. with respect to geographic
coordinates, is better than 1 km (root mean square).
The values of parameters involved in the geometric
correction procedure are included in CCT's. The rela-
tively high spatial resolution (80 m) allows for easy
identification of landmarks. Hence errors in estimated
image position can easily be recognized. In the Wadi
Ash Shati region the resolution of LANDSAT data was
sufficient to locate within the image different types
of surfaces.

H C M M   d a t a. Since the HCMM experiment was spe-
cifically designed to study the surface energy balance,
both the visible and thermal infrared data from this
satellite fit rather well the requirements of the

present investigation. This especially applies to the determination of the daily surface temperature amplitude from the daytime respectively night-time thermal infrared data. The mutual registration of these two images is necessary to achieve the best possible accuracy.

According to the data on the satellite's attitude, visible and thermal infrared images of the HCMM satellite have been geometrically corrected on a frame-by-frame basis. According to the User's Guide (NASA, 1980) most data processed by NASA are expanded over their proper width by approximately 6%. When values of attitude parameters exceed a certain design figure, the correction procedure is performed according to these maximum values. The latter case applies to the 16 September 1978 night-time HCMM image of Fezzan. Because by taking maximum instead of actual values the information on the actual satellite attitude data has been lost, the remaining deformation of this image is unknown. An alternative to the application of deterministic corrections according to the geometry of the system, is by establishing a set of tie-points on both the image that has to be corrected and on a reference. As a reference a better image made at another time or a map can be used. The 16 September 1978 night-time HCMM image has been registered by the present author on the 18 September 1978 daytime VIS-image (see Plates 1 and 2). For two reasons the latter image has been chosen as a reference. Firstly, this daytime image underwent nominal processing, i.e. the geometric correction was performed according to the actual attitude data. Secondly, a preliminary control showed that a reasonably consistent relationship could be established between that image and geographic coordinates of control points in the Wadi Ash Shati basin. The daytime thermal infrared image could not be used as reference because of the excessive cloud cover: as discussed in Paragraph 5.2.1 clouds that show up in thermal infrared images may not appear in the VIS-image (0.4 to 1.1 μm).

Given the 0.6 x 0.6 km resolution of the HCMM thermal infrared band and the morphology of the area, it is rather difficult to establish tie-points. The tricky part lies not only in that the area is a desert, thus by definition devoid of vegetation, water bodies and towns. The real difficulty lies in the different nature of VIS and thermal infrared images: there is, in principle, no reason why the two images should very closely resemble each other. This implies that lines, such as wadi beds, and edges will appear different in the two spectral bands or not at all in one of them. As regards the HCMM images of Fezzan, hardly any regularly shaped form with well defined

edges is present. The only exception is the 3000 ha large Ashkidah irrigated area in the Wadi Ash Shati basin (see Fig. 6.4). The village of Idri can also be identified. By relating the geographic coordinates of these two tie-points to their coordinates in the image reference system, i.e. pixel and line number, the apparent pixel size can be calculated from the known geographic coordinates of the frame center. Accordingly from the coordinates of Idri the line width (latitude) has been obtained as 641 m, quite close to the 640.2 relating to the Ashkidah tie-point, while the corresponding pixel widths (longitude) were 619.3 respectively 653.9. Due to the tangent effect the difference is consistent with the expected deformation: the Ashkidah area lies 191 km, or 31% of the satellite height, away from the subsatellite point. The same preliminary check on pixel and line width has been applied to the night-time thermal infrared (TIR) image, to find that this image was expanded as well as rotated.

To tackle this kind of difficulties a polynomial transformation of order N:

$$x' = \sum_0^N{}_p \sum_0^{N-p}{}_q a_{pq} x^p y^q$$

$$y' = \sum_0^N{}_p \sum_0^{N-p}{}_q b_{pq} x^p y^q$$

(7.1)

can be applied. In our case x, y are pixel coordinates in the reference system of the night-time image, while x', y' are the coordinates of pixel x, y in the reference system of the daytime image. The coefficients a_{pq}, b_{pq} are to be determined from known couples $(x,y)_i \rightarrow (x',y')_i$, i.e. the tie-points. It was found that a second order polynomial was needed to rectify the night-time image. Therefore at least six tie-points had to be established. To reduce the error in the transformation, however, a large number of tie-points is needed since errors have to be expected in defining the couples $(x,y)_i$, $(x',y')_i$. In the night-time HCMM image only ten tie-points could reliably be identified. The coefficients a_{pq}, b_{pq}, standard deviation $\tilde{\sigma}$ on x', y', ratios of pixel length (δy'/δy) and width (δx'/δx) between the two images and the average rotations along x(δΦ_x) and y(δΦ_y) directions are given in Table 7.1. The value corresponding to each pixel position (x',y') in the transformed image was obtained by interpolation on the nearest neighbours of (x,y).

The values in Table 7.1 relate to a part of the entire HCMM image. Several attempts were carried out by the present author to improve the accuracy of the transformation. The final result is presented

	x^2	xy	y^2	x	y	Constant
x'	$0.1241 \cdot 10^{-3}$	$0.211 \cdot 10^{-3}$	$0.890 \cdot 10^{-4}$	0.6122	-0.5492	412
y'	$0.3873 \cdot 10^{-3}$	$-0.7191 \cdot 10^{-3}$	$0.1164 \cdot 10^{-3}$	0.3655	1.035	-100.2
$\tilde{\sigma}_{x',y'}$	$(\delta x'/\delta x)$		$(\delta y'/\delta y)$		$\delta\phi_x$	$\delta\phi_y$
5.57	1.12		0.88		$23.6°$	$-15°$

Table 7.1. Values of coefficients a_{pq} respectively b_{pq} in the transformation eq. (7.1) mapping the night-time TIR-image onto the daytime HCMM-VIS image; for explanation of symbols see text

in Plates 1 and 2. In Plate 1 the daytime HCMM-VIS-image relating to a part of Fezzan and in Plate 2 the corrected night-time HCMM-TIR-image is given. It should be noted that the reference system for the images in Plates 1 and 2 now is the same, and this allows further use of the data to study the surface energy balance.

M E T E O S A T d a t a. METEOSAT-1 is a geostationary satellite, and a nominal frame can be defined which is supposed to be imaged 48 times a day, i.e. with the geographic boundaries of the image being constant. Thus a reference image can be established, where a constant and known relationship exists between line and pixel coordinates, and latitude and longitude. In the actual images various distortions are present. The nominal frame allows for a measure of the deformation resulting from these distortions.

The transformation from the actual to the reference frame varies per each actual image (slot) and is provided by ESOC as an additional data set. Direct polynomials from actual to reference and inverse polynomials from reference to actual image, in the form of eq. (7.1) with N = 5, are supplied by ESOC. The coefficients are derived either by prediction from deformation models or from measured values. The method applied has been described by JONES (1981). The description of data provided on image distortions can be found in ESOC (1980a, 1980b). FORTRAN coded routines are also provided to establish the relationship between given geographic coordinates (latitude and longitude), and line and pixel in the reference frame. Variability in geographical position of the images available for Libya (see Table 6.11) could

easily be determined by looking at the coastline of the Gulf of Sirte in terms of actual image coordinates.

7.3. RADIOMETRIC CALIBRATION OF DIGITAL DATA PRODUCTS

L A N D S A T d a t a. Only the calibration of the four LANDSAT bands in the 0.5 to 1.1 μm spectral range will be discussed.

Two radiometric calibration procedures are applied by Telespazio to LANDSAT-CCT digital data products. The standard procedure involves a calibration source being brought in view of the radiometer during each retrace line. The calibration wedge emitted by the calibration source is resampled and correlated with the initial, nominal shape. Accordingly the calibration relationship is obtained. The calibration signal is sampled during each retrace, but the calibration relationship is given per frame.

LANDSAT CCT-images generated at the Fucino ground station (Italy) are calibrated by a second statistical procedure. It is assumed that both the mean and variance of input radiances to each of the six sensors in one band are equal. From the differences in output, relationships can be written which allow for the determination of the calibration equation. More details can be found in TELESPAZIO (1979).

In the present study LANDSAT data have been applied to calculate the surface reflectance α_0. The sensor output in terms of digital count number DN in a single spectral band relates to input radiant intensity $I(\lambda)$ in $W \cdot m^{-2} \cdot sr^{-1} \cdot \mu m^{-1}$ as:

Band	Wavelength	R_i ($W \cdot m^{-2} \cdot sr^{-1}$)				$R_{out,i}$
	(μm)	LANDSAT-1		LANDSAT-2		($W \cdot m^{-2}$)
		min. DN = 0	max. DN = 255	min. DN = 0	max. DN = 255	
MSS-4	0.5 - 0.6	0	24.8	1.0	21.0	192.63
MSS-5	0.6 - 0.7	0	20.0	0.7	15.6	161.49
MSS-6	0.7 - 0.8	0	17.6	0.7	14.0	126.93
MSS-7	0.8 - 1.1	0	46.0	1.4	41.5	246.06

Table 7.2. Reflected radiance R_i in the four LANDSAT MSS-bands; earth - sun distance equal to 1 Astronomical Unit or $1.496 \cdot 10^{11}$ m (after Otterman and Fraser, 1976). Respectively the energy distribution of incoming solar radiation at 1 Astronomical Unit, or $1.496 \cdot 10^{11}$ m, outside the atmosphere $R_{out,i}$ in the four LANDSAT MSS-bands (after Smithsonian Meteorological Tables, 1951)

$$DN = \int_{\lambda_1}^{\lambda_2} A(\tilde{\lambda})I(\tilde{\lambda})d\tilde{\lambda} \qquad (-) \qquad (7.2)$$

where $\tilde{\lambda}_1$, $\tilde{\lambda}_2$ (μm) are the band limits and $A(\tilde{\lambda})$ is the sensor response function. It appears that the larger the variability of $I(\tilde{\lambda})$ within a band, the larger the error in converting DN back to radiance and reflectance. It is also evident that the relation between reflectance in the four LANDSAT bands and the true spectral reflectance as for example given in Paragraph 5.3.1 for bare soils, is not straightforward. However, the mean reflectance calculated by weighting the reflectance in each band will be more accurate than single-band values. Large errors can be expected only for surfaces with marked changes in reflectance beyond $\tilde{\lambda} = 1.1$ μm. In Table 7.2 the relationship between DN and input radiance is presented, as well as the distribution of solar radiation in the four LANDSAT bands. For each band the reflectance from space α_p can accordingly be calculated as:

$$\alpha_{p,i} = \frac{\pi R_i}{R_{out,i} \cos \phi_{su}} \qquad (-) \qquad (7.3)$$

where the index $i = 1, ..., 4$ relates to the four MSS-bands. The weighting coefficients to calculate α_p in the range 0.5 to 1.1 μm therefore are:

$$c_i = \frac{R_{out,i}}{\sum_1^4 {}_i R_{out,i}} \qquad (-) \qquad (7.4)$$

and the reflectance is:

$$\alpha_p = \sum_1^4 {}_i c_i \alpha_{p,i} \qquad (-) \qquad (7.5)$$

Results obtained from LANDSAT-MSS images of the area around Idri in the Wadi Ash Shati are presented in Section 7.5.

H C M M   d a t a. Calibration equations are provided by NASA (1980) for the visible respectively thermal infrared bands. Digital count numbers DN for the visible band (0.5 to 1.1 μm) are normalized to the solar radiance. Hence the reflectance (in %) is found by dividing DN by the full scale count 255 and multiplying by 100, i.e. α_p = (DN/255)·100. For the thermal infrared band (10.5 to 12.5 μm) the following equation is given by NASA:

$$T = 1251.1591/\ln\left[14{,}421.587/(DN + 118.21378) + 1.0\right]$$
$$(K) \qquad (7.6)$$

In the HCMM validation study performed by SUBBARAYUDU (1979) satellite measurements were corrected for atmospheric absorption and then compared with ground data. On the basis of five measurements collected in the first two months after launching, satellite temperatures were found to be 5.5 K too high, after the correction for absorption due to atmospheric water vapour was applied. After the offset of -5.5 K was taken into account, and included in the definitive calibration equation (eq. 7.6), it was found from some new measurements that satellite temperatures were 5.0 K too low (!). The main problem to be solved is, therefore, to establish whether the offset of -5.5 K was correct.

REINIGER (1981) summarized data collected in Europe to check the calibration equation of the HCMM: it was found that during most of the mission lifetime the difference satellite minus ground measured surface temperature was essentially constant and equal to -5.8 K. This author concluded that the offset should not apply to the entire duration of the mission. This conclusion is also supported by the calibration relationships given by REINIGER (1981):

$$\tilde{T}_0 = 7.55 + 0.95 \, T_0 \qquad (^{\circ}C) \qquad (7.7)$$

and

$$\tilde{T}_0 = 6.87 + 0.7 \, T_0 + 0.01 \, (T_0)^2 \qquad (^{\circ}C) \qquad (7.8)$$

where T_0 is the surface temperature as calculated by eq. (7.6) and $\tilde{T}_0$ is the correct value.

It should also be mentioned that the values for the atmospheric water vapour absorption coefficients applied by SUBBARAYUDU (1979), and therefore involved in the determination of the -5.5 K offset, find very little support in the literature (see Paragraph 5.2.3). Furthermore the accuracy on I_λ^{top}, as shown in Fig. 5.4, required to reliably determine the -5.5 K offset is some 6%. It will be shown in Section 7.4 that it is unrealistic to presume that such accuracy can be achieved. Accordingly, the present author decided to ignore the -5.5 K offset and, therefore, the surface temperatures were calculated from HCMM data by adding 5.5 K to the result obtained by eq. (7.6).

M E T E O S A T - 1   d a t a. In the present investigation only the thermal infrared data of this satellite were converted by the present author into calibrated values. Details on the spectral response of the radiometer have been given by ESOC (1981). Data used in the present investigation relate to the most troubled period of the radiometric history of METEOSAT-1. A reasonably accurate calibration can be obtained by applying the on-board black body data.
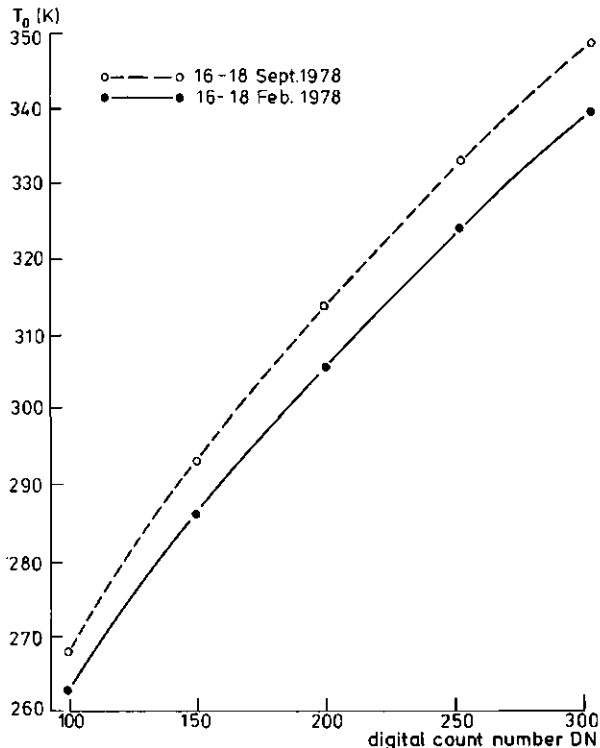
Fig. 7.1. Calibration relationships for thermal infrared data of METEOSAT-1 (second thermal infrared channel) as applying to the periods 16 through 18 February 1978 respectively 16 through 18 September 1978

These data are in principle available twice daily, but the actual rate is much lower. In ESOC (1981) only one value for every 10 days is given (during 1978). The data give the DN-value applying to T = 290 K. Hence the value of B (Planck's function) at this temperature can be calculated. The procedure applied was suggested by calibration studies performed by KÖPKE (1980) and WILLIAMSON and WILKINSON (1980). The final accuracy is probably not better than 1 K. With DN = 2.5 at zero radiance (space view), a linear relationship between DN and B can be obtained. To convert radiances into temperatures a table is provided as obtained by convolution of Planck's function and radiometer spectral response. When an entire image is to be converted into calibrated values, the tabular relationship has to be refitted by means of some analytical function. Because of the shape of the radiometer response function, a good accuracy is not easy to achieve and a second degree function at least is needed.

The following equations have been obtained by the present author for METEOSAT-TIR data for the period 16 through 18 February 1978:

$$T_0 = -8.005 \cdot 10^{-4} \, DN^2 + 0.703 \, DN + 199.006 \quad (K)(7.9)$$

and for the period 16 through 18 September 1978:

$$T_0 = -8.058 \cdot 10^{-4} \, DN^2 + 0.722 \, DN + 203.019 \quad (K)(7.10)$$

The graphs of eqs. (7.9) and (7.10) are presented in Fig. 7.1.

7.4. ATMOSPHERIC EFFECTS ON REMOTELY SENSED DATA

In this section effects of clouds, water vapour and dust on remotely sensed data in the visible and thermal infrared data will be discussed. Although discussed separately, it is by no means intended they can be evaluated independently. A comprehensive assessment will be given in Paragraph 7.4.4.

As regards clouds it will be shown how they can be detected on thermal infrared satellite images and that the use of only visible images is not a reliable procedure. Then calculations of absorption in the 10.5 to 12.5 µm spectral range by atmospheric water vapour will be presented to illustrate the rôle of a number of uncertainties in such calculations. Finally it will be shown that the reliability of calculations on the rôle of dust is even poorer than that on the effect of atmospheric water vapour.

7.4.1. Clouds

Clouds have the most direct atmospheric effect on both visible and thermal infrared data. As already anticipated in Paragraph 5.2.1 the problem here is not so much the correction of satellite derived data, as to identify the cloud contaminated pixels, those giving the temperature of clouds and not of the ground surface. Radiative transfer through clouds has been studied by many authors, e.g. BOLLE (1982), HUNT (1973), etc. Difficulties are overwhelming and not even the most basic properties are exactly known.

In Fig. 7.2 the histogram of a METEOSAT-TIR image of Libya on 16 September 1978 at 10.45 GMT is presented. Aside from the peak at T ≃ 310 K relating to the bulk of the image, two additional peaks are recognized at T ≃ 260 K and T ≃ 294 K. By comparing these values with the radiosonde data from the Sabhah weather station, taken at the same day at 12.00 GMT, it was established that the air layer where T ≃ 260 K was at 6000 m height, and the one where T ≃ 294 K at 1000 m. Thus a first criterion for further analysis is to leave out any pixel showing a radiation temperature T < 297 K, say.

A more refined procedure can be applied by combining infrared and visible data as presented by PLATT (1981). Firstly, cloud fields were located on hard copies of digital data. Then pixels were plotted in a T,α plane. Different positions in these bidimensional histograms were found to correspond with
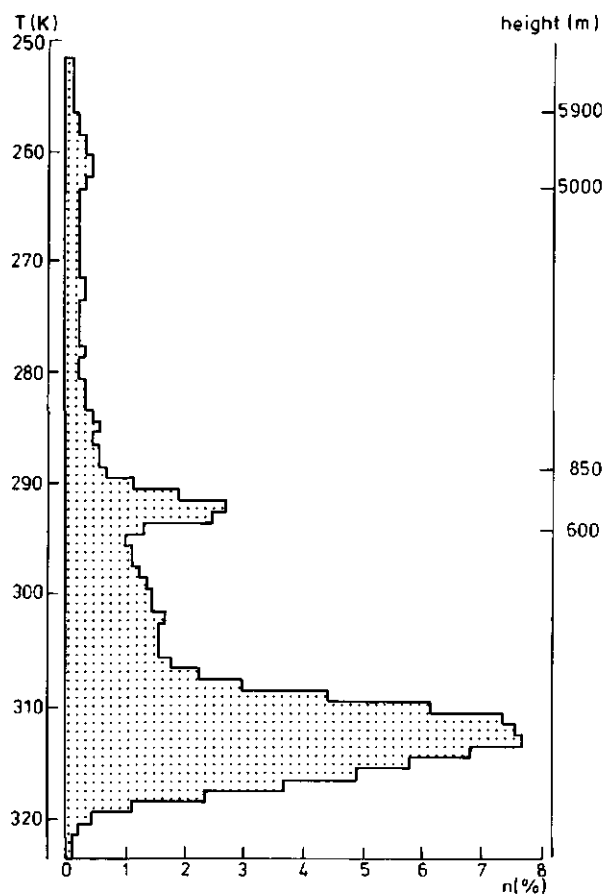
Fig. 7.2. Histogram of radiation temperatures as obtained from the METEOSAT-TIR image on 16 September 1978 (slot 22 or 10.45 GMT). Also shown the estimated heights of the cloud-related histogram peaks; heights applying to specific temperature values were obtained from radiosonde data (Sabhah weather station); n, pixel frequency; the number of pixels is 40,832, i.e. an area of $1.02 \cdot 10^6$ km^2

Fig. 7.3. Scatter diagram, reflectance α_p plotted versus temperature T, of pixels relating to clouds and different ground surfaces, as present in the HCMM-VIS and HCMM-TIR images on 18 September 1978

Fig. 7.3 by the symbol c, it was found that for that image $\overline{T}_c$ = 291. Eventually some measure of the scatter of these T-values, e.g. one standard deviation, can be added to $\overline{T}_c$ to obtain the required threshold. Note that the large spread of α_c-values in Fig. 7.3 is due to the many semi-transparent pixels present in the HCMM colour composite (VIS and TIR) image shown in Plate 3. Especially at the boundaries of the clouds overlying the Wadi Ash Shati basin at the bottom of the image, the ground surface underneath can still easily be recognized.

The cloudy character of a TIR-satellite image is most clearly disclosed by histograms, e.g. as presented in Fig. 7.2. It should, however, be realized that the characteristic shape of such histograms can only be obtained from data of geostationary satellites, i.e. of low resolution and covering very large areas in a single frame. The histogram in Fig. 7.2 relates to a $1.02 \cdot 10^6$ km^2 area. When higher resolution images, such as LANDSAT, are considered the area included in a single frame is likely to appear as either

different cloud types. The present author performed a similar analysis of the daytime HCMM images (visible and thermal infrared) taken on 18 September 1978. Values of α and T for a number of pixels belonging to clouds (c), rocks (r), playas (p) and dunes (d) are plotted in Fig. 7.3. It should be noted that the pixels relating to the different ground surface types are scattered in a relatively narrow range of T, while reflectance α varies somewhat more. For ground surfaces, therefore, visible and thermal infrared data give a comparable quantity of information. For clouds only the thermal infrared data give a reliable indication on whether a particular pixel is cloudy or clear. According to Fig. 7.3 it was decided by the present author, in the interpretation of HCMM and METEOSAT thermal infrared data to consider as cloud-contaminated any pixel with a temperature lower than a critical T-value determined on a subset of cloudy pixels. For example from the subset as indicated in

Fig. 7.4. Histogram of radiation temperatures as obtained from the HCMM-TIR image on 18 September 1978 at 13.45 LMT; image observed under partly cloudy conditions; n, pixel frequency; the number of pixels is 10^5, i.e. an area of $0.036 \cdot 10^6$ km^2

123
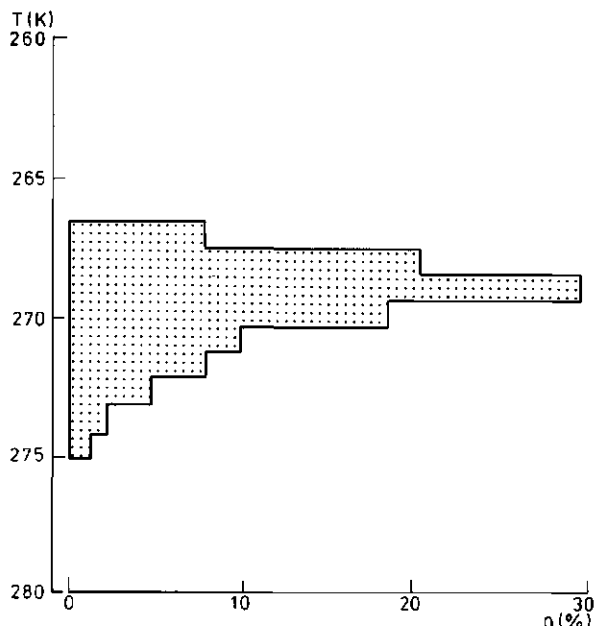
Fig. 7.5. Histogram of radiation temperatures as obtained from the METEOSAT-TIR image on 17 February 1978 at 5.45 GMT; image observed under completely clear sky conditions; n, pixel frequency; the number of pixels is 22,005, i.e. an area of $0.55 \cdot 10^6$ km^2

cloudy or clear. The reason for this phenomenon is the difference between the scale of cloud systems and the pixel size of the different satellites. A proof of this statement is given by Fig. 7.4, where the histogram of the daytime thermal infrared HCMM image on 18 September 1978 is presented. As is evident from Fig. 7.3 and Plate 3, the percentage of cloudy pixels is rather high. However, no peak relating to clouds shows up in Fig. 7.4, where cloudy pixels fall in the tail towards lower temperatures (see also Fig. 7.3). An example of a perfectly clear scene is presented in Fig. 7.5 relating to a METEOSAT-TIR scene on 17 February 1978. All the pixels belong to the rather narrow temperature interval of 8 K. It must be mentioned that this METEOSAT-TIR image and a similar one on 18 February 1978 showed very small differences in surface temperature between these dates. As indicated in Table 6.10, on these two dates the IRLS survey of the Wadi Ash Shati basin was carried out.

7.4.2. Atmospheric water vapour

Under clear sky conditions, atmospheric water

vapour still has a marked influence on radiation transfer in the 10.5 to 12.5 spectral range ('thermal' infrared region or TIR). Theoretical aspects relating to this topic have been discussed in Paragraph 5.2.3. Here it will be shown by means of a numerical radiation transfer model that a number of uncertainties are present in these calculations:

A. variations in the vertical profiles of T_a, P, e, which are measured by radio-soundings, between the site where such observations are carried out and the one where they are required. In the present investigation radiosonde data were obtained from the Sabhah weather station, i.e. some 150 km from the test area at Idri;

B. different possible expressions for the absorption coefficients of atmospheric water vapour.

A d A. Radiosonde data were obtained by the present author from the Libyan Meteorological Service, as observed at 12.00 GMT, Sabhah weather station. The fol-
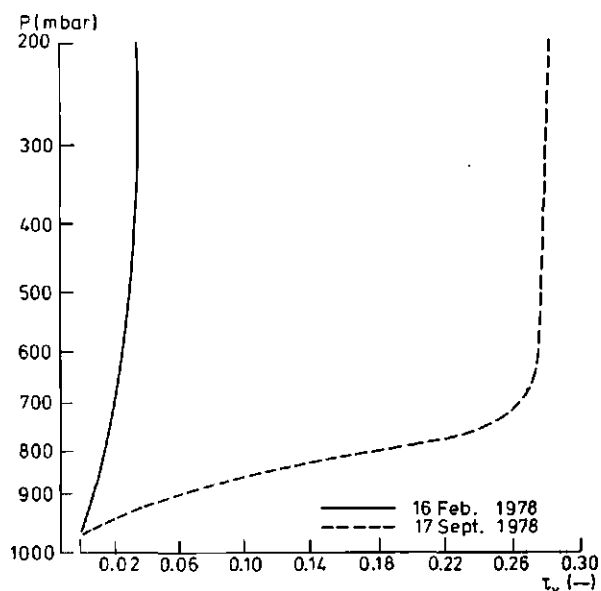
Fig. 7.6. Vertical profile of atmospheric optical depth τ_v in the 10.5 to 12.5 µm spectral range as calculated by a radiation transfer model (only the absorption by water vapour is included). Two profiles are shown: of 16 February 1978 respectively of 17 September 1978

Table 7.3. Precipitable water vapour $\tilde{w}$, spectral radiant intensity I_λ^{top} and optical depth τ_v in the 10.5 to 12.5 µm spectral interval. Values calculated from radiosonde data at Sabhah, Fezzan, Libya

	16 Feb. 1978	18 Feb. 1978	17 Sept. 1978	18 Sept. 1978
$\tilde{w}$ (cm)	0.8	1.50	2.25	2.25
τ_v (-)	0.03	0.12	0.28	0.3
I_λ^{top} (W·m^{-2}·sr^{-1}·µm^{-1})	7.84	8.872	9.154	9.356

Table 7.4. Comparison of surface weather observations at 12.00 GMT, at the Sabhah respectively Idri weather station (Fezzan, Libya)

Date	Sabhah			Idri		
	T (K)	P (mb)	e (mb)	T (K)	P (mb)	e (mb)
16 Feb. 1978	288.4	974.4	4.16	290	977	8.16
18 Feb. 1978	298.2	967.4	14.94	296	970.6	11.56
17 Sept. 1978	302.6	971.0	12.34	305.5	975.5	9.39
18 Sept. 1978	303	970.0	15.15	305	974.7	8.79

lowing dates were considered: 16 and 18 February 1978, because of the IRLS survey (see Table 6.10), and 17 and 18 September 1978, because of the HCMM overpasses (see Table 6.11).

In Table 7.3 an impression of the atmospheric conditions on these four days is presented, the corresponding values of precipitable water vapour $\bar{w}$ (cm) as obtained from the radiosonde data, of optical depth due to atmospheric water vapour τ_v as calculated by the model, and of spectral radiant intensity $I_{\bar{\lambda}}^{top}$ (W·m^{-2}·sr^{-1}·µm^{-1}). Values of $I_{\bar{\lambda}}^{top}$ relate to the highest observed height in the radiosonde data and to a surface temperature equal to the air temperature at the lowest observed height. Furthermore, to point out the large variability in radiation transfer conditions of desert atmosphere, as observed at Sabhah, the calculated vertical profile of τ_v on 16 February respectively 17 September is presented in Fig. 7.6. It can be seen that in summer the effect of atmospheric water vapour can be relevant.

To illustrate the difference in atmospheric conditions between Sabhah and Idri at the time when radio-soundings were carried out, surface observations at the two sites at 12.00 GMT and on the same dates as given in Table 7.3 are presented in Table 7.4. It can be seen that a relevant difference is found in the e-values, while the T- and P-values are much closer to each other for the two stations. Vapour pressure e, as given in Table 7.4 at Idri is the mean of two contemporary data collected at two sites (see Table 6.9).

To assess the effect of such regional differences between meteorological data at Idri and Sabhah, the spectral radiant intensity $I_{\bar{\lambda}}^{top}$ (W·m^{-2}· sr^{-1}·µm^{-1}) and the corresponding black body equivalent

Table 7.6. Difference between T_0 and T_{top} (K) due to the indetermination of T, P, e profiles. Sun zenith angle $\phi_{su} = 0°$, $10°$, $20°$, $30°$. $T_0 = 313$ K; $\Gamma_{dim} = 259$ cm^2·g^{-1}. For cases a, b and c, see text

Case	$\phi_{su} = 0°$	$\phi_{su} = 10°$	$\phi_{su} = 20°$	$\phi_{su} = 30°$
a	5.3	5.4	5.6	6.0
b	5.3	5.4	5.6	6.0
c	4.6	4.6	4.8	5.2

temperature T_{top}^0 (K) have been calculated at the highest observed height in the radio-sounding. Three cases are considered for the T, P, e profiles at Idri between the 850 mb level and ground surface (the results are given in Table 7.5):

a. identical data as observed at Sabhah on 18 September 1978;

b. air temperature interpolated linearly between the temperature at ground level at Idri and the temperature at the 850 mb level in the Sabhah radio-sounding, with U_a constant;

c. same as b, but with ρ_v constant.

Case b is a rather unlikely occurrence since an increase of 0.4 cm in precipitable water vapour $\bar{w}$ is implied (T_a higher and U_a constant). Case c may well occur, although up to lower heights than the 850 mb level considered here. The cases b and c are intended to give upper bound estimates of the variations in T_{top}^0 and $I_{\bar{\lambda}}^{top}$.

It should be noted that the increased absorption (higher $\bar{w}$) in case b due to the higher amount of precipitable water vapour is compensated for by increased emission: the values of $I_{\bar{\lambda}}^{top}$ in cases a and b are identical. The difference in $I_{\bar{\lambda}}^{top}$ between case c and a can be expressed as indetermination of $(T_0 - T_{top}^0)$

Table 7.5. Variability of spectral radiant intensity $I_{\bar{\lambda}}^{top}$ and the corresponding temperature at the top of the troposphere T_{top}^0, as resulting from different T, P, e profiles between 850 mb and ground level; the black-body equivalent temperature at the ground is $T_0 = 313$ K; radiosonde data for case a on 18 Sept. 1978 at Sabhah (see text for explanation of cases a, b, c)

T_0 (K)	$I_{\bar{\lambda}}^{top}$ a (W·m^{-2}·sr^{-1}·µm^{-1})	$I_{\bar{\lambda}}^{top}$ b (W·m^{-2}·sr^{-1}·µm^{-1})	$I_{\bar{\lambda}}^{top}$ c (W·m^{-2}·sr^{-1}·µm^{-1})	T_{top}^0 a (K)	T_{top}^0 b (K)	T_{top}^0 c (K)
313	10.347	10.347	10.448	307.56	307.43	308.18

Plate 1. HCMM-VIS image on 18 September 1978 (see also Table 6.11); the daytime image shows the Qarqaf highland at the top and the Wadi Ash Shati basin below (see Fig. 6.4). Black, red, white respectively low, intermediate, high reflectance. See Paragraph 8.4.1 for detailed comments. For location, see Map of geographical locations of satellite images
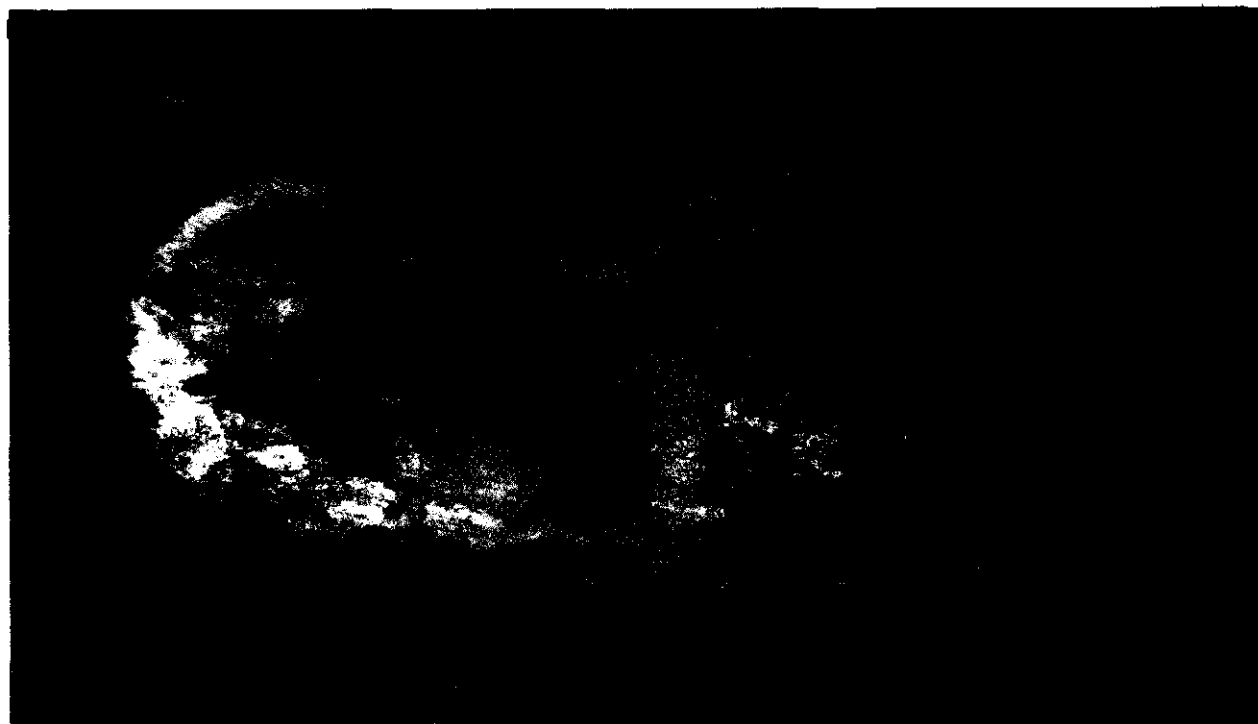
Plate 2. HCMM-TIR image on 16 September 1978 (see also Table 6.11); night-time, the same area of Plate 1 is shown. The night-time image has been registered on the coordinates of the image in Plate 1 (see text). Black, red, white respectively low, intermediate, high radiation temperature. See Paragraph 8.4.1 for detailed comments. For location, see Map of geographical locations of satellite images

Plate 3. Colour composite of the HCMM-VIS (red channel) and HCMM-TIR (green channel) images on 18 September 1978 (see Table 6.11). The southern part of the Qarqaf highland (top) and the Wadi Ash Shati basin (bottom) are shown (see Fig. 6.4). At the bottom-center of the image the clouds are transparent and let the underlying ground surface shine through. Bright red, high reflectance; bright green, high temperature. See Paragraph 8.4.1 for detailed comments. For location, see Map of geographical locations of satellite images

Plate 4. METEOSAT-TIR image of Qarqaf, Wadi Ash Shati, Idehan Awbari and Idehan Marzuq (see Fig. 1.4), as taken on 18 February 1978 (7.45 h LMT). The observed range of T_0 is 10 K, i.e. between 268 K (red) and 278 K (yellow). See Paragraph 8.4.1 for detailed comments. For location, see Map of geographical locations of satellite images

Table 7.7. Indetermination of I_λ^{top} due to different choices of $\hat{\Gamma}_v$ and specifications of its dependence on T, P, e. Two sun zenith angles Φ_{su} are considered, T_0 = 303 K, τ_v is the optical depth, I_λ^a the atmospheric contribution to total outgoing radiation I_λ^{top}. For cases 1 through 4, see text

Absorption coefficients		τ_v (-)	I_λ^a (W·m⁻²·sr⁻¹·μm⁻¹)	I_λ^{top} (W·m⁻²·sr⁻¹·μm⁻¹)
$\Phi_{su} = 0°$				
1. $\hat{\Gamma}_v^{for} = 0.0$	$\hat{\Gamma}_v^{self} = 8.622$ at 303 K	0.2386	1.769	9.465
2. $\hat{\Gamma}_v^{for} = 0.01$	$\hat{\Gamma}_v^{self} = 8.622$ at 303 K	0.2559	1.878	9.442
3.	$\hat{\Gamma}_{dim} = 259$	0.2973	2.099	9.351
4.	$\hat{\Gamma}_{dim} = 265$	0.3042	2.140	9.348
$\Phi_{su} = 30°$				
1. $\hat{\Gamma}_v^{for} = 0.0$	$\hat{\Gamma}_v^{self} = 8.622$ at 303 K	0.2755	2.005	9.422
2. $\hat{\Gamma}_v^{for} = 0.01$	$\hat{\Gamma}_v^{self} = 8.622$ at 303 K	0.2955	2.125	9.396
3.	$\hat{\Gamma}_{dim} = 259$	0.3433	2.369	9.300
4.	$\hat{\Gamma}_{dim} = 265$	0.3513	2.414	9.290

with the aid of Fig. 5.4. Namely I_λ^{top} (case c) less I_λ^{top} (case a) divided by the mean I_λ^{top} gives 9.7°/oo. At the same temperature (313 K) one finds from Fig. 5.4 (B'/B) = 13°/oo. Thus (9.7/13) = 0.8, i.e. the indetermination of the T, P, e profile implies an indetermination of T_{top}^0 of 0.8 K. Finally in Table 7.6 values of $(T_0 - T_{top}^0)$ for four sun zenith angles Φ_{su} are presented. In this case the calculations were carried out by applying eqs. (5.21) and (5.22) with $\hat{\Gamma}_{dim} = 259$ cm²·g⁻¹.

A d B. As already shown in Paragraph 5.2.3, a relatively large number of different choices are possible for the absorption coefficient of atmospheric water vapour. Calculations of absorption have been performed with four values of $\hat{\Gamma}_v$, and two sun zenith angles Φ_{su}; these values are given in Table 7.7. There the calculated values of the optical depth τ_v, of the spectral radiant intensity emitted by the atmosphere I_λ^a and of the spectral radiant intensity at the top of the atmosphere I_λ^{top} also are given. The dependence of $\hat{\Gamma}_v$ on T, P and e has been calculated by eqs. (5.18) and (5.20) for the cases 1 and 2, and by eqs. (5.21) and (5.22) for the cases 3 and 4. From the I_λ^{top}-values it can be seen that I_λ^{top} decreases nonlinearly with increasing τ_v. As already done with the data in Table 7.5, the difference between the highest and the lowest value of I_λ^{top} can be expressed by means of Fig. 5.4 in terms of indetermination of I_λ^{top} itself, and accordingly of T_{top}^0. For example, from the values in Table 7.7 pertaining to $\Phi_{su} = 0°$, one finds that 9.465 - 9.348 = 0.117, which divided by the mean

value 9.4015, gives 12.5°/oo. At T_0 = 303 K and with the aid of Fig. 5.4 one finds that the indetermination of T_{top}^0 is 0.9 K. The latter value due to differences in $\hat{\Gamma}_v$ must be added to the previously (ad A) given 0.8 K. The maximum contribution of the effects discussed under ad A and ad B is, therefore, 1.7 K.

It should be noted that the selection of the absorption coefficients in Table 7.7 has been rather conservative by taking those reported in most of the recent literature on the subject. Many different values have been reported, however, although with unclear specifications of the T, P, e conditions applying to the particular experiment.

An additional source of indetermination relates to possible inconsistencies between the calibration relationships, as for example given for the HCMM radiometer as applying to T_{top}^0 respectively I_λ^{top}. It has been found by the present author that for $T_0 \geq 310$ K a difference of 0.5 K is observed between the value of T_{top}^0 calculated via the radiation transfer model and the value $\tilde{T}_{top}^0$ obtained from the I^{top}-value (as corresponding to that calculated T_{top}^0) through the HCMM calibration equations for I_λ and T.

Until now only the indeterminations of calculations with variables which are not exactly known, have been discussed. Summing up, one may conclude that an a-priori inaccuracy of calculated T_{top}^0-values, as obtained from radiosonde data by means of the radiation transfer model, can be estimated as being approximately 2 K.

A few authors have compared c a l c u l a - t i o n s of the type as presented in Tables 7.5

Table 7.8. Values of the difference $T_0 - T_{top}^0$ (in K) as calculated with $\hat{r}_{dim} = 259$ cm$^2 \cdot$g^{-1} with eqs. (5.21), (5.22) for five surface temperatures and two sun zenith angles Φ_{su}

	T_0 (K)				
	283	293	303	313	323
$\Phi_{su} = 0°$					
16 Feb. 1978	0.3	0.6	0.9	1.1	1.4
18 Feb. 1978	0.3	1.4	2.5	3.6	4.6
17 Sept. 1978	-0.2	2.0	4.3	6.4	8.5
18 Sept. 1978	-2.0	0.6	3.1	5.4	7.7
$\Phi_{su} = 30°$					
16 Feb. 1978	0.4	0.7	1.0	1.3	1.6
18 Feb. 1978	0.2	1.6	2.9	4.1	5.2
17 Sept. 1978	-0.3	2.3	4.9	7.3	9.6
18 Sept. 1978	-2.2	0.7	3.5	6.2	8.7

through 7.7 with m e a s u r e m e n t s of I_λ^{top}. Differences even larger than above indicated were found. Analyses of the Nimbus-4 infrared spectroscopy experiment in the range 6.9 tot 2.2 µm have been presented by KUNDE et al. (1974). In the range between 10.5 and 13.3 µm a constant underestimation of 5% in I_λ^{top} (or 4 to 5 K on T_{top}^0 according to Fig. 5.4) was observed. In theoretical calculations these authors applied $\hat{r}_v$ in a form similar to eq. (5.20) with $\hat{r}_v^{for} = 0.0$. Their findings confirmed the earlier results obtained by HOUGHTON and LEE (1972). KUNDE et al. (1974) gave for the standard deviation of measured T_{top}^0 at 11.1 µm a value of 3 K. Another very useful analysis of spectral radiant intensity data in the 10 to 12 µm spectral range was presented by PLATT (1972). The absorption coefficient $\hat{r}_v$ as given by BIGNELL (1970) was compared with values of $\hat{r}_v$ calculated from the decrease with height of measured spectral radiant intensity.

The agreement was found to be only qualitative and a large scatter was observed when plotting $\hat{r}_v$ from the I_λ^--measurements versus vapour pressure e.

The overall conclusion on the calculation of $T_0 - T_{top}^0$ is, that it is impossible to achieve an accuracy better than 5 K, say.

This must be taken into account when reading the figures presented in Table 7.8. Calculations were carried out by the present author with Γ_v given by eqs. (5.21) and (5.22) and $\hat{r}_{dim} = 259$ cm$^2 \cdot$g^{-1}. Surface temperatures between 283 and 323 K and two sun zenith angles, $\Phi_{su} = 0°$ and $30°$, were considered. The $T_0 - T_{top}^0$ values have been calculated from radiosonde data at Sabhah on the four days corresponding with the IRLS survey and the HCMM overpasses. It is clear that since the indetermination of the calculated values is comparable with, or even larger than, the results themselves, the latter are of no operational value whatsoever.

7.4.3. Dust

Atmospheric transmittance of solar radiation in desert regions is strongly affected by the presence of dust. To quantitatively evaluate such an effect the concentration and size distribution of dust also must be known (see Paragraphs 5.2.2 and 5.2.3). Particularly in Pagragraph 5.2.2 it was anticipated that when surface reflectance and its view angle dependency are known very accurately, atmospheric transmittance can be inferred from reflected radiance. This definitely is not true for undulated and rugged land surfaces, e.g. dunes and playas (see Fig. 6.9).

The following points now will be discussed in relation to the effect of dust on the remotely sensed data for the Wadi Ash Shati basin:

Fig. 7.7. Sandstorm at Brak, Wadi Ash Shati, April 1978
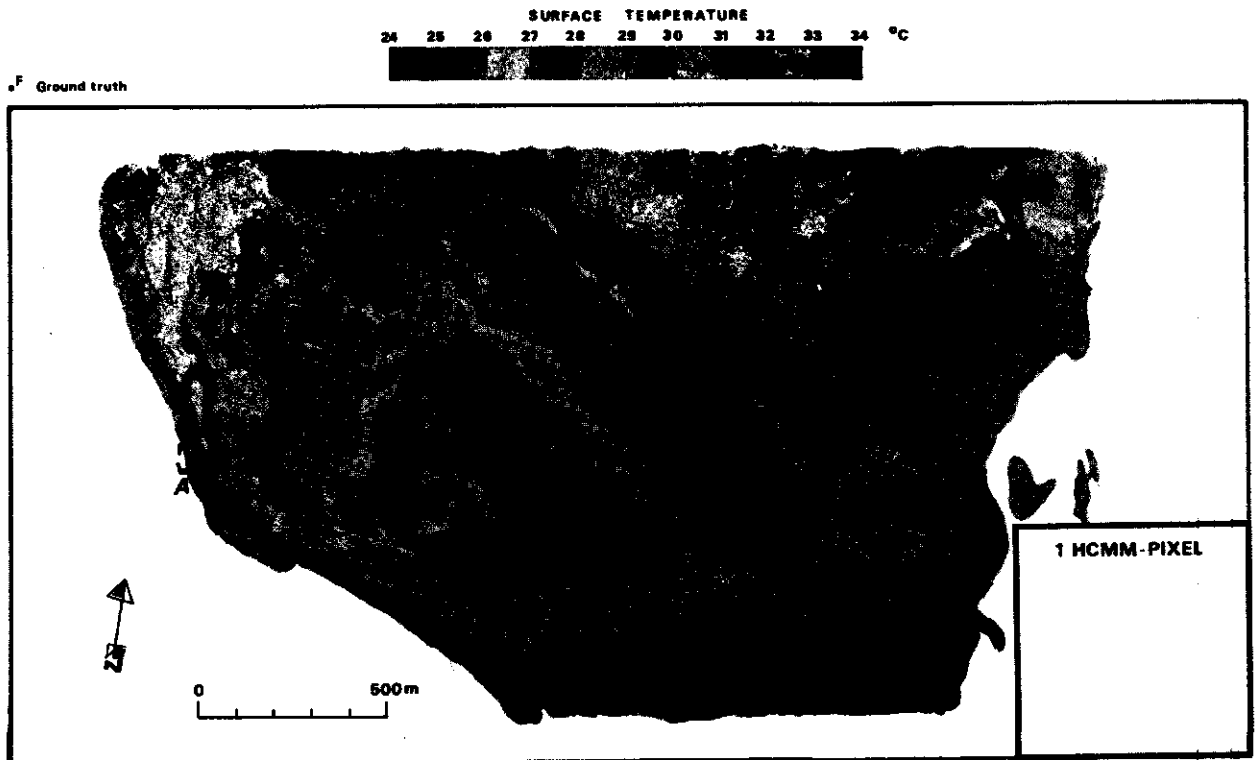
Plate 5. Surface temperature map of the playa West-Idri (see Fig. 6.12) on 16 February 1978 at 13.00 h LMT. The cross-section A - A' is considered in Fig. 7.22 (Paragraph 7.5.2); the size of one HCMM pixel also is indicated. See Paragraph 8.4.1 for detailed comments. For location, see Map of geographical locations of satellite images

Plate 6. Colour composite of LANDSAT Band 7 (red), Band 5 (green), Band 4 (blue). Left, 12 March 1978 and right, 26 September 1978. In the bottom-right of the image on the left side a salt crust is seen, which is not present in the right hand image. Oases shown in red. See also Plate 7. See Paragraph 8.4.1 for detailed comments. For location, see Map of geographical locations of satellite images

130
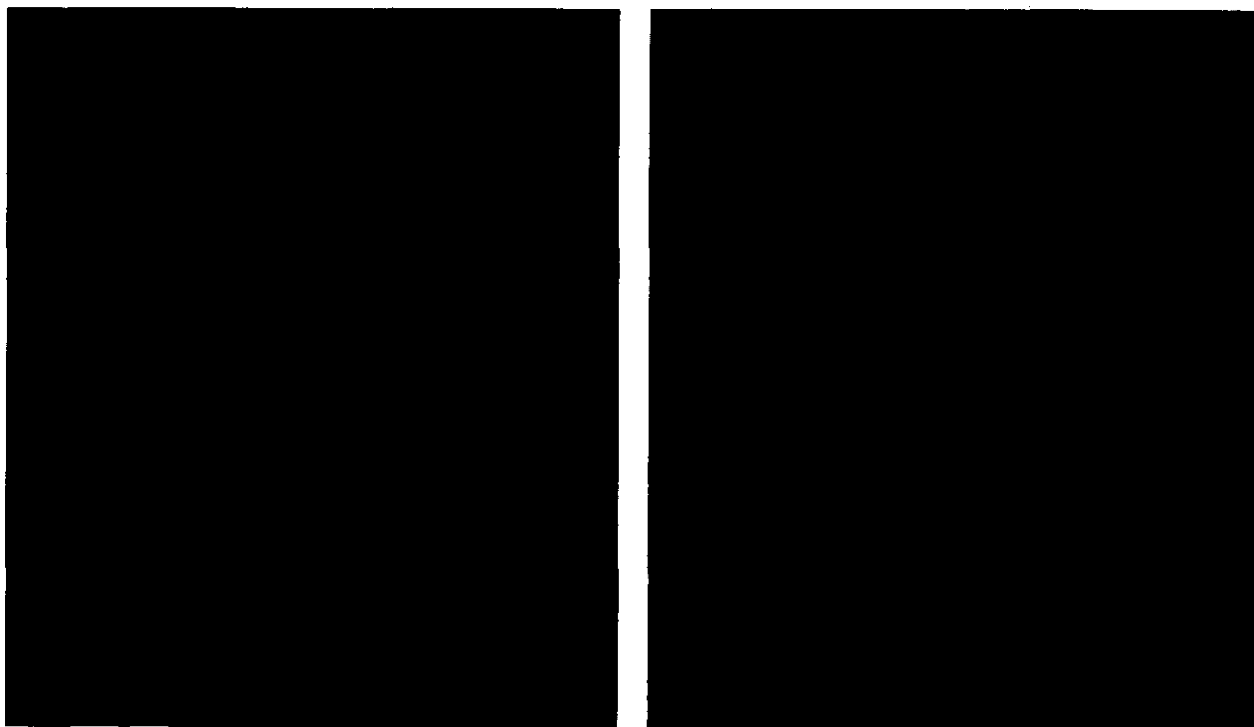
Plate 7. Areas where evaporation takes place at the soil surface, $z_E = 0$ and $\alpha_0 > \alpha_{0E}$ displayed in the green colour scale, areas where $z_E > 0$ and $\alpha_0 < \alpha_{0E}$ in the red colour scale, black are areas where $z_E = 0$ and $\alpha_0 = \alpha_{0E}$. Left, 12 March 1978 and right, 26 September 1978. The Idehan Awbari and the Idri village are shown. See also Plate 6. See Paragraph 8.4.1 for detailed comments. For location, see Map of geographical locations of satellite images
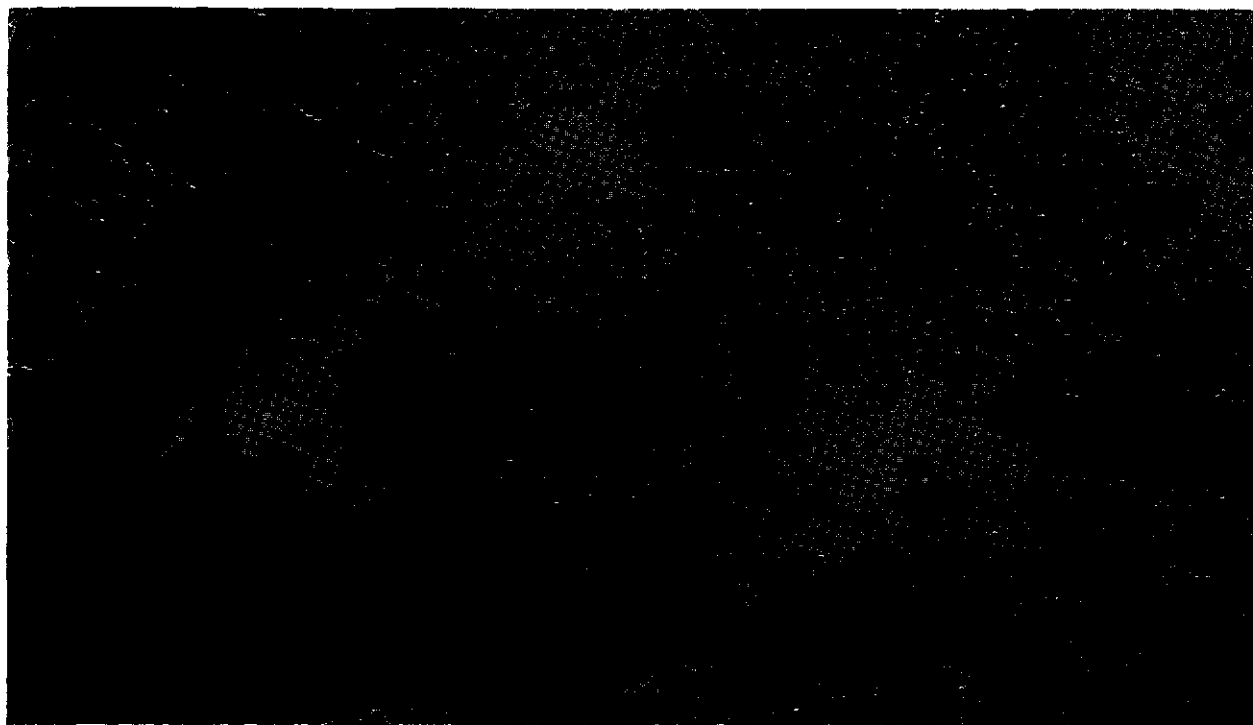
Plate 8. Sensible heat flux H as calculated from the HCMM-image on 18 September 1978, 13.45 h local time for a part of the Fezzan area in Libya. A 36,000 km area including the Qarqaf highland and the Wadi Ash Shati basin is shown (see Fig. 6.4). Black and blue: clouds; yellow: semitransparent clouds and $0 < H < 200$ W·m^{-2}; green: $200 < H < 600$ W·m^{-2}; red: $600 < H < 750$ W·m^{-2}. See Paragraph 8.4.1 for detailed comments. For location, see Map of geographical locations of satellite images

Table 7.9. Solar radiation in the spectral range 0.4 - 2 µm. $\overline{R}_{sw}^{out}$ is the mean total solar radiation at the top of the atmosphere (Table 132, Smithsonian Meteorological Tables, 1951). $\overline{R}_{sw}$ is the mean monthly value at ground level as measured at Idri weather station. Atmospheric transmittance (exp -τ) is equal to $\overline{R}_{sw}/\overline{R}_{sw}^{out}$

	1978											1979		
	Feb.	Mar.	Apr.	May	June	July	Aug.	Sept.	Oct.	Nov.	Dec.	Jan.	Feb.	Mar.
$\overline{R}_{sw}^{out}$ (W·m^{-2})	313.7	378.1	428.5	462.1	470.6	467.8	439.7	397.7	338.9	280.0	249.3	263.3	313.7	378.1
$\overline{R}_{sw}$ (W·m^{-2})	187.7	221.3	257.7	238.0	282.9	288.5	268.9	243.7	193.3	156.9	154.0	149.7	190.5	193.3
exp -τ	0.598	0.585	0.601	0.515	0.601	0.617	0.612	0.613	0.57	0.56	0.618	0.607	0.607	0.511
τ	0.51	0.54	0.51	0.66	0.51	0.48	0.49	0.49	0.56	0.58	0.48	0.50	0.50	0.67

Table 7.10. As Table 7.9 for the days on which remotely sensed data have been considered for detailed analysis

	16 Feb. 1978	17 Feb. 1978	18 Feb. 1978	15 Sept. 1978	16 Sept. 1978	17 Sept. 1978	18 Sept. 1978
$\overline{R}_{sw}^{out}$ (W·m^{-2})	315.8	318.0	320.2	391.8	390.1	388.4	386.7
$\overline{R}_{sw}$ (W·m^{-2})	201.8	206.9	203.2	254.0	252.2	246.2	244.4
exp -τ	0.64	0.65	0.63	0.65	0.65	0.63	0.63
τ	0.45	0.43	0.46	0.43	0.43	0.46	0.46

Table 7.11. Drift potential DP in arbitrary units as calculated from weather observations at Sabhah and assumed to apply to the Idehan Awbari (after Fryberger, 1979)

Jan.	Feb.	Mar.	Apr.	May	June	July	Aug.	Sept.	Oct.	Nov.	Dec.
17	21	38	30	54	26	8	7	11	24	20	13

A. indirect detection of dust from meteorological data data;

B. estimation of τ_d from remotely sensed data in the 0.6 to 0.7 µm spectral range;

C. required accuracy of τ_d to obtain reliable estimates of the effect of dust on satellite-measured surface temperatures.

A d A. The most direct indication of dust is the reduced atmospheric transmittance of solar ratiation. During a sandstorm (see Fig. 7.7) this is quite clear. Under less severe conditions a more refined assessment is required.

In Table 7.9 calculated values (SMITHSONIAN MEMEOROLOGICAL TABLES, 1951) of solar radiation at the top of the atmosphere $\overline{R}_{sw}^{out}$, measured $\overline{R}_{sw}$-values at Idri and calculated atmospheric transmittances exp -τ, i.e. $\overline{R}_{sw}/\overline{R}_{sw}^{out}$, and calculated optical depths (τ-values) are given. In Table 7.10 the corresponding data at some dates corresponding with the HCMM overpasses and the IRLS airborne survey are presented. The τ-values in both tables have only a qualitative meaning, since the transmittance of direct solar radiation and the scattering of diffuse radiation should be separated explicitly (see BOLLE, 1982). Nevertheless the optical depth τ, as given in Tables 7.9 and 7.10, is a measure

of the overall effect of dust on global solar radiation and this meaning will be applied here.

To give an impression of the variability in atmospheric transmittance, it is recalled that in the spectral range 0.2 to 2 µm (SMITHSONIAN METEOROLOGICAL TABLES, 1951) a pure, dry and dust free atmosphere has a transmittance of 0.9 and that an average figure for the entire earth is 0.5 (SELLERS, 1965). The values of atmospheric transmittance given in Tables 7.9 and 7.10 show that the atmosphere was not entirely pure. A most likely reason for this behaviour is dust.

In Table 7.11 values of the drift potential (DP) of sand as calculated by FRYBERGER (1979) from weather observations at Sabhah are given. As can be seen the largest drift potentials are present in May and March, while in Table 7.9 it was shown that the lowest transmittances were observed in May 1978 and March 1979. Conversely, the lowest drift potentials (Table 7.11) are in July and August, and the largest transmittances (Table 7.9) at Idri were observed in July, August and December 1978.

On the other hand, by comparing the values of atmospheric transmittance given in Table 7.10 with Fig. 7.2, it is seen that the c l o u d s detected on
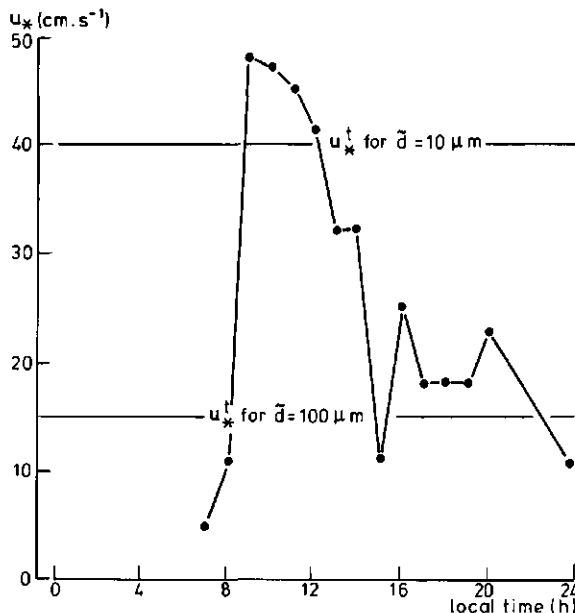
Fig. 7.8. Friction velocity u_*, as obtained from micrometeorological data in the playa West-Idri on 18 September 1978, plotted versus local time. Two values of the threshold friction velocity u_*^t, for lifting of dust particles also are shown

16 September 1978 on the METEOSAT-TIR image, and also evident in the DMSP-TIR (see also Table 6.11) photographic product, did not yield a very sensible effect on the atmospheric transmittance. On 15, 17 and 18 September the area essentially was cloud free.

Another possible way of assessing the rôle of d u s t is by establishing on the basis of micrometeorological observations whether dust particles can be lifted from the ground surface. Then relative increases in dust load can in principle be calculated.

The theory of sand lift and transport has made little fundamental progress after the textbook of BAGNOLD (1954). This author gave a formula to estimate the threshold friction velocity u_*^t (cm·s^{-1}) for lifting a particle, with diameter $\tilde{d}$ (cm) and density ρ_{si} (g·cm^{-3}), from the surface. In Fig. 7.8 the friction velocity u_*, as obtained by the present author from data collected on 18 September 1978 in the playa West-Idri (see Table 6.9), is shown. This friction velocity was calculated with the equation:

$$u^* = k(z - d)\phi_m^{-1} \frac{\partial u}{\partial z} \quad (cm·s^{-1}) \qquad (7.11)$$

where for a nearly flat surface the zero-plane displacement $d \ll z$, since the lowest measuring level was $z = 0.5$ m. The values of the Monin-Obukhov's function, ϕ_m, were calculated by $0.95(1 + 16$ Ri$)^{1/3}$ for stable conditions, and by $(1 - 16$ Ri$)^{-1/4}$ for unstable conditions. The Richardson number, Ri, at 1 m height has been calculated according eq. (2.29). Val-

ues of the threshold friction velocity u_*^t according to to BAGNOLD (1954) can be calculated as:

$$u_*^t = A(\frac{\rho_{si} - \rho_a}{\rho_a} \tilde{d}g)^{\frac{1}{2}} \qquad (cm·s^{-1}) \qquad (7.12)$$

where A is a constant for a particular $\tilde{d}$. The value of A is about 0.1 for particles with a diameter $\tilde{d}$ of about 100 μm; it increases with lower particle size. For the numerical values $\tilde{d} = 10$ μm and $\rho_{si} = 2.65$ g·cm^{-3} a value of $u_*^t \cong 40$ cm·s^{-1} is obtained by means of eq. (7.12) and for $\tilde{d} = 100$ μm, $u_* = 15$ cm·s^{-1}. These threshold values also have been plotted in Fig. 7.8. It should be pointed out that the eq. (7.12) has been obtained by BAGNOLD (1954) by assuming that the particles are lying loose. In reality smaller particles of desert soils may stick to the larger ones, as shown by the photomicrographs of sand particles from Fezzan, Libya presented by WALKER (1979). Fig. 7.8 gives a reliable indication that during daytime particles with diameters of some 100 μm will be lifted from the soil surface. It appears rather difficult to predict what happens to the small particles: they can be detached from the larger ones either during each 'flight' or at the following impact with the soil surface. The threshold friction velocity relates to a particular particle diameter. With a real sand, lifting of larger particles will occur before the higher threshold friction velocity of smaller particles is attained. Saltation of the larger particles will occur, and their impact on the surface would lift particles of any diameter. As shown by BAGNOLD (1954) the threshold impact energy decreases linearly with decreasing particle diameter and, at $\tilde{d} < 0.1$ mm, the threshold impact energy is smaller than the threshold fluid energy. So there is no clear-cut criterion to decide whether sand lifting will occur at a relevant extent under given weather conditions. As regards experimental evidence SCHÜTZ and JAENICKE (1974) did show on the basis of measurements, that the number of particles in the air flow in the $\tilde{d}$-range 1 to 10 μm increased by one order of magnitude when wind speed increased from 7.6 to 8.7 m·s^{-1}. Their data were collected in the Fezzan region. Hence it can be concluded that determination of u_*^t is rather critical.

By observing wind direction both at the Idri weather station and the playa West-Idri it appeared that a sea-breeze-like circulation if often established. During daytime wind velocities then are large enough to induce sand lifting and transport; see Fig. 7.8 relating to such a day.

In the early morning shortwave incoming radiation gets easily through the clear air. Then, because of the difference in thermal characteristics, the difference in surface temperature between the Idehan Awbari and the rocky Qarqaf rapidly increases. This

increasing temperature difference triggers off a breeze at ground level from the cooler Idehan Awbari to the warmer Qarqaf. Thus the temperature difference between the sandy and rocky regions is reduced by the heat exchange between the cooler air and warmer surface of the Qarqaf. The air then rises above the Qarqaf and after circulation at higher levels feeds the air flow above the Idehan Awbari. Around 10 o'clock local time the temperature difference between the dunes and the rocks starts to decrease and the breeze circulation slows down. In the late afternoon and evening a light breeze is established in the opposite direction (from Qarqaf towards Idehan Awbari).

A d B. It has now to be discussed whether the actual determination of τ_d, the purely dust-related atmospheric optical depth, is feasible by means of procedures using satellite data only (see Paragraph 5.2.2).

If τ_d could be obtained at a particular wavelength, then the corresponding τ_d in the thermal infrared spectral range could be inferred on the basis of dust optical properties and size distribution. Available measurements of the refraction index of dust at different wavelengths were reviewed and compared by CARLSON and BENJAMIN (1980). Dust particle size distribution in the size range from 1 to 10^3 µm in the Libyan desert was measured by SCHÜTZ and JAENICKE (1974). They collected samples at one site in the northeastern part of Hamada al Hamra and one near Sabhah. If dust distribution with height is known a relationship exists between the optical depth τ_d at 0.5 µm, independent of temperature, applied as an index of dust amount and the optical depth τ_d between 10 and 13 µm, dependent of temperature (see also eqs. 5.14 and 5.15).

As calculated by CARLSON and BENJAMIN (1980) the atmospheric optical depth τ_d in the thermal infrared range, at $\tilde{\lambda} = 11.5$ say, is a fraction of the τ_d-value at shorter wavelengths (see also Paragraph 5.2.3). The following relationship holds:

$$\tau_d \ (\tilde{\lambda} = 11.5 \ \mu m) = 0.73 \ \tau_d \ (\tilde{\lambda} = 0.5 \ \mu m) \qquad (-)(7.13)$$

An empirical relationship to infer τ_d at $\tilde{\lambda} = 0.66$ µm from Very High Resolution Radiometer (VHRR) reflected radiance data has been presented by CARLSON and WENDLING (1977). That relationship reads:

$$\tau_d \ (\tilde{\lambda} = 0.66 \ \mu m) = 0.005 \ R_5^2 + 0.38 \ R_5 - 0.15 \qquad \begin{array}{c} (-) \\ (7.14) \end{array}$$

where R_5 is the reflected radiance $(W \cdot m^{-2} \cdot sr^{-1})$ in the VHRR-Band 5 (0.6 to 0.7 µm). Note that wavelength $\tilde{\lambda} = 0.65$ µm lies in the center of the LANDSAT MSS-Band 5. The eq. (7.14) was established by making use of data
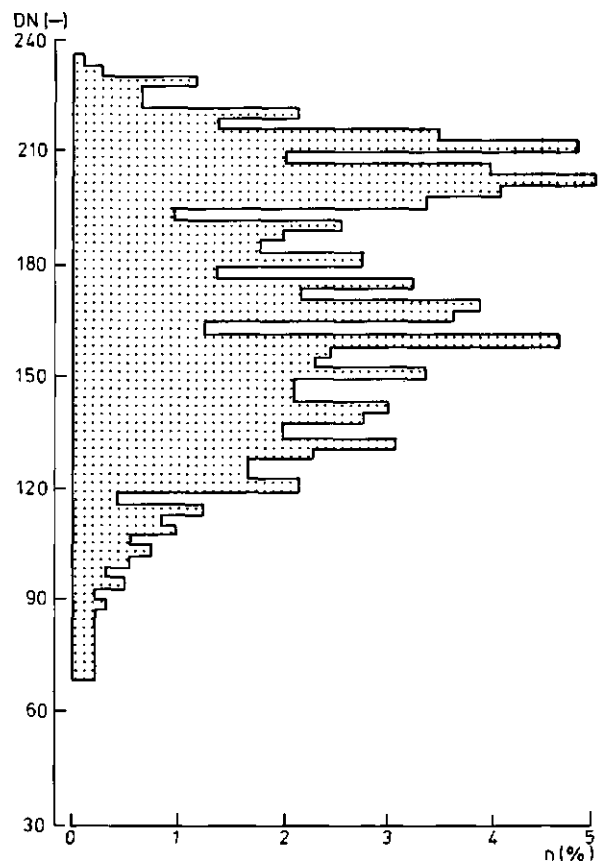
Fig. 7.9. Histogram of DN-values in the LANDSAT-MSS Band 5 on 27 February 1977, Idehan Awbari - Idri area; n, pixel frequency; the number of pixels is $2.5 \cdot 10^5$ and the area 1200 km².

relating to the ocean surface. A correction, therefore, has been tentatively applied by the present author to eq. (7.14) and the result has been used to estimate τ_d ($\tilde{\lambda} = 0.65$ µm) from a LANDSAT-MSS image of the Idri area. Such correction has been calculated by taking into account the difference in reflectance between the ocean and the desert surface. Representative figures are $\alpha_0 = 0.08$ for the ocean respectively 0.28 for the desert (see also Paragraphs 5.2.2 and 5.3.1). Accordingly one finds a different zero-value for the R_5-values in eq. (7.14), when the latter is applied to the two different surfaces mentioned above.

For a LANDSAT image of the Idri area, the present author estimated the zero R_5-value, i.e. corresponding to the lowest τ_d, in eq. (7.14) for the desert case at 5.2 $W \cdot m^{-2} \cdot sr^{-1}$, or 3.7 $W \cdot m^{-2} \cdot sr^{-1}$ higher than for the ocean case. Now the DN-values in Fig. 7.9 can be applied to calculate R_5 by means of Table 7.2 and eq. (7.2), and then τ_d ($\tilde{\lambda} = 0.65$ µm) by means of eq. (7.14).

The mean $\overline{DN}$ in the entire image is $\overline{DN} = 171$ (see the histogram of Fig. 7.9). Then by entering $R_5(\overline{DN})$ -

Fig. 7.10. LANDSAT-MSS image of the Idehan Awbari - Idri area on 27 February 1977; same area as in Fig. 7.9

$3.7 = 6.3 \text{ W} \cdot \text{m}^{-2} \cdot \text{sr}^{-1}$ in eq. (7.14) one finds τ_d ($\tilde{\lambda} = 0.65 \text{ μm}$) = 2.4, which is rather high but still reasonable. The use of eq. (7.14) is tricky, however, even when corrections for differences in α_0 are applied as indicated above.

A d C. A very likely error source in the procedure presented above relates to dip and orientation of sloping surfaces. The linear dunes in the Idehan Awbari near Idri, provide an excellent example. As can be seen in the LANDSAT-MSS image presented in Fig. 7.10, the sun-facing side of the dunes has a high reflectance; the DN-values of these surfaces (see Fig. 7.9) are about DN = 246. By applying eq. (7.14) as discussed under A d B , one finds τ_d ($\tilde{\lambda} = 0.65 \text{ μm}$) = 4.8, an unreasonably high value (no sandstorm taking place!). If dip and orientation are properly related to the sun zenith Φ_{su} and azimuth $\tilde{a}_{su}$ angle, the very high reflectance of dunes can easily be explained. In Fig. 7.11 the relevant angular coordinates: surface dip Φ_0, surface azimuth $\tilde{a}_0$, sun zenith Φ_{su} and sun azimuth $\tilde{a}_{su}$ are shown. According to MARTINELLI (1967) the following equation holds for the cos Φ_{rn} of the angle Φ_{rn} between a straight line r intersecting a plane and the normal n to this plane:
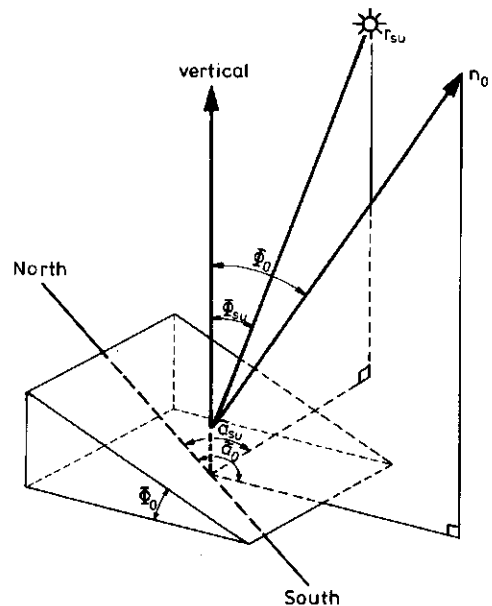
Fig. 7.11. Sketch showing the angular coordinates of an inclinated surface and their relationship with the angular coordinates of the sun. Surface dip Φ_0 and azimuth $\tilde{a}_0$, sun zenith Φ_{su} and azimuth $\tilde{a}_{su}$ are indicated; r_{su} is the line connecting the sun to the observer point O, n_0 is the normal to the surface at O

135

$$\cos \Phi_{rn} = \cos \Phi_{rx} \cos \Phi_{nx} + \cos \Phi_{ry} \cos \Phi_{ny} +$$

$$+ \cos \Phi_{rz} \cos \Phi_{nz} \qquad (-) \qquad (7.15)$$

where x, y and z are the unit-vectors of the coordinate axes X, Y and Z. When r_{su} is the line connecting the sun to the observer point O (Fig. 7.11) and n_0 is the normal to dune surface at the point 0, $\Phi_{r_{su}n_0}$ is the actual sun zenith angle for the inclinated face of the dune. Therefore for $\Phi_{r_{su}n_0}$, eq. (5.26) and the relationships presented in Fig. (5.3) hold true. The angle Φ_0 can be estimated to be $33°$, the angle of repose for sand according to BAGNOLD (1966), while $\tilde{a}_0$ has been determined by the present author from the LANDSAT image in Fig. 7.10. Accordingly by means of eq. (7.15) $\cos \Phi_{r_{su}n_0} = 0.42$ is obtained. Then the value of $\alpha_p = 0.48$ obtained from DN = 246, can be corrected first by means of Fig. 5.3, then by eq. (5.26), to obtain $\alpha_0 = 0.36$, which is somewhat on the high side, but not as unreasonable as the 0.48 mentioned above. For a detailed analysis of the relationship between satellite measured radiance, terrain orientation and sun position see DAVE and BERNSTEIN (1982), KOWALIK et al. (1982).

It is understood that the assessment of the relationship between surface dip, azimuth and the reflected radiance, is not always as easy as with the dunes in Fig. 7.10. As can be seen in Fig. 5.5, an indetermination on τ_d of 0.5 say, corresponds to an indetermination of 5 K on $T_0 - T_{top}^0$. The indetermination of τ_d can be larger than 0.5 as shown above ($\tau_d = 4.8$). It should be noted that the graphs in Fig. 5.5 can be entered with τ_d obtained by means of eq. (7.14), because τ_d ($\tilde{\lambda} = 0.65$ µm) = τ_d ($\tilde{\lambda} = 0.5$ µm) according to CARLSON and BENJAMIN (1980).

Thus it must be concluded, as has earlier been done for calculations on the effect of atmospheric water vapour, that procedures to correct satellite measured surface temperatures for the effect of dust have not yet achieved the accuracy required by operational use of such methods.

7.4.4. Feasibility of operational calculations

In the preceding paragraphs some of the difficulties encountered in the analysis of satellite data of the Wadi Ash Shati basin have been discussed. It has already been stated that calculation procedures to correct thermal infrared satellite data cannot achieve the accuracy required for quantitative application of such data. This point can clearly be made by recalling that an accuracy of 1 K on T_0, implies an accuracy of 20% on τ_v. The results presented in Table 7.7, for example, show that the indeterminations discussed in

Paragraph 7.4.2 induce uncertainties of this magnitude. Furthermore the accuracy of the radio-soundings required to calculate τ_v and I_λ^{top} has not yet be taken into account. In the author's opinion a 10% accuracy on I_λ^{top} is a conservative estimation, which implies a 10 K accuracy on T_0 according to Fig. 5.4.

As regards dust it has already be mentioned in Paragraph 5.2.3 that τ_d is to be known with a 0.1 accuracy in its value, if the effect of dust on the satellite measured T_{top}^0 is to be calculated with a 1 K absolute accuracy.

Finally it should be realized that clouds (see Paragraph 5.4.1) are a very good reason for T_{top}^0 being lower than T_0. It is easily understood that it is difficult to ascertain whether a pixel showing a particular ($T_0 - T_{top}^0$)-value (see Fig. 7.2 for example) relates to one or more of the effects mentioned above. A 5 K difference in $T_0 - T_{top}^0$ could be ascribed to any of the following reasons:

- clouds at some 1000 m height, or
- optical depth τ_d higher by some 0.5, or
- a 5% decrease in I_λ^{top} due to atmospheric water vapour.

It is, therefore, the present author's opinion that ground measurements are definitely needed to assess how relevant the differences between satellite and ground measurements are. The calculation methods discussed above have of course their merits for analyzing the different aspects of the problem, but they do not appear to improve the accuracy of satellite data.

7.5. GROUND AND SPACE MEASUREMENTS OF SURFACE REFLECTANCE AND TEMPERATURE

In Section 7.4 it has been shown that one cannot assess the accuracy of remotely sensed data on theoretical grounds only. In the following pages the data collected in the Wadi Ash Shati basin (see Paragraph 6.2.4) will be compared with reflectances and blackbody equivalent temperatures as measured by radiometers on-board the LANDSAT, HCMM and METEOSAT satellites (see also Table 6.11).

7.5.1. Surface reflectance

G r o u n d   m e a s u r e m e n t s. Solar incoming and reflected radiation has been measured at a number of sites, as listed in Table 6.9. Hourly total radiation data were used to obtain the surface reflectance of these sites as a function of local mean time. In Fig. 7.12 the results obtained for the sites studied
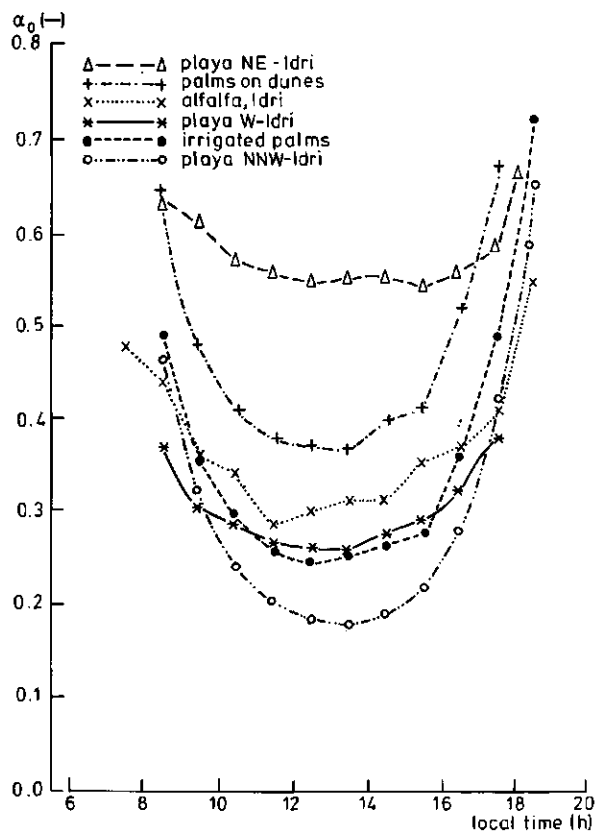
Fig. 7.12. Measured surface reflectance of different surfaces plotted versus local time in February 1978. For the description of sites and data see Paragraph 6.2.4

Fig. 7.13. Measured surface reflectance of different surfaces plotted versus local time in September 1978. For the description of sites and data see Paragraph 6.2.4

in February 1978 are presented. A characteristic shared by all the curves is the clear dependence on Φ_{su}, of the type discussed in Paragraph 5.3.1 and presented in Fig. 5.6. The curve given for the playa NNW-Idri relates to an open water surface (see Figs. 6.12 and 6.17) and the relatively high reflectance, at least for water, is probably due to the shallowness and transparency of that pool. The difference between the reflectance of palms in an irrigated plot of the Idri oasis and of the palms on a dune outside the oasis is quite marked, and a good measure of the evidently different vigour of palms in the two plots. As regards the alfalfa curve it is interesting to note that the oscillations are probably due to the soil contribution: in that small plot alfalfa was being grown as a row crop to allow furrow irrigation. The very large difference in α_0 between the wet soil of the playa West-Idri (see also Figs. 6.8 and 6.12) and the dry soil of the playa NE-Idri (see also Figs. 6.11 and 6.12) can be explained by the different moisture content and by the whitish salt crust in the playa NE-Idri.

In Fig. 7.13 the α_0-curves for the sites (see Table 6.9) studied in September 1978 are presented.

It is immediately seen that the reflectance of the open water surface in the playa NNW-Idri was close to normal values for water: in September water turbidity was much higher than in February. The reflectance of both Calligonum and palms was relatively similar and quite close to α_0-values usually ascribed to deserts (see also Paragraph 5.2.2). The α_0-curve of alfalfa now relates to a homogeneously covered plot and the oscillations noticed in Fig. 7.12 do not occur. The salt crust in the playa NE-Idri (see Plate 7) disappeared between February and September 1978 and the corresponding decrease of α_0 is quite evident when comparing the curves for this site in Fig. 7.12 and in Fig. 7.13. The higher reflectance of the playa West-Idri in Fig. 7.13, as compared with the corresponding curve in Fig. 7.12, only relates to the different surface studied in September 1978 (see also Tables 6.9 and Fig. 6.10).

A more interesting feature of the α_0-curve in Fig. 7.13 of this site is that the minimum value is attained somewhat earlier than noon (13.00 hrs Libyan LMT). It can also be seen that at the same Φ_{su} higher α_0-values are measured in the afternoon than in the morning. This behaviour can be explained by

137
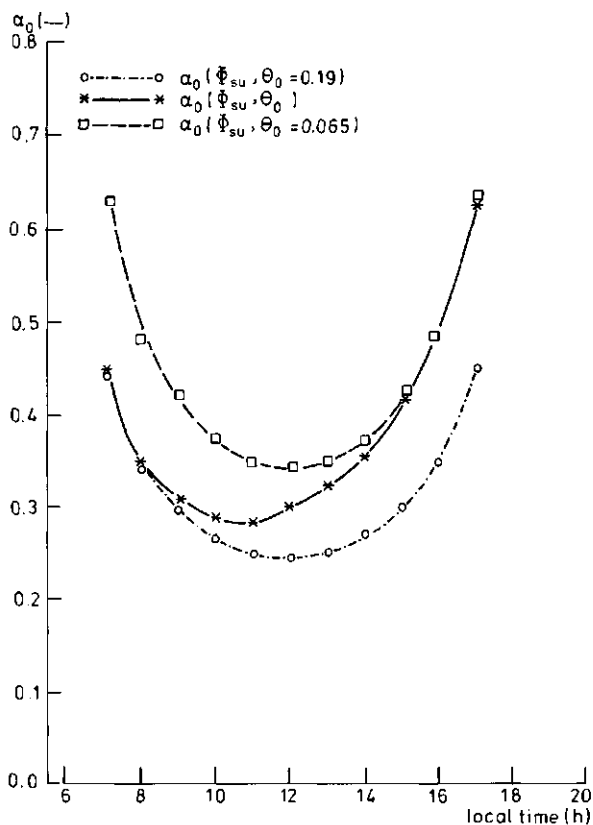
Fig. 7.14. Calculated surface reflectance by means of eq. (5.26) combined with eq. (5.28) for two constant surface moisture contents θ_0 and for a soil surface drying during daytime

Fig. 7.15. Measured surface reflectances of different playa surfaces in the Idri area (see also Fig. 6.12 and Table 6.9), Wadi Ash Shati basin, plotted versus local time in 1978

taking into account the variability during daytime of both the surface moisture content θ_0 and of Φ_{su}. Namely the eqs. (5.26) and (5.28) can be combined to predict the α_0-curve applying to a particular progression of θ_0 and Φ_{su}. JACKSON (1973) measured θ_0 during 24-hour periods and observed a quasi-linear decrease of α_0 during the daytime, with a re-wetting of the soil surface during the night.

From the data presented by this author the following values can be chosen for the progression of soil moisture content: $\theta_0 = 0.19$ in the early morning and $\theta_0 = 0.065$ in the late afternoon. These values have been applied by the present author to calculate by means of eqs. (5.26) and (5.28) three α_0-curves for:

$\alpha_0 = \alpha_0 (\Phi_{su}, \theta_0 = 0.19)$, i.e. with θ_0 kept constant and equal to the early morning value;

$\alpha_0 = \alpha_0 (\Phi_{su}, \theta_0 = 0.065)$, i.e. with θ_0 kept constant and equal to the late afternoon value;

$\alpha_0 = \alpha_0 (\Phi_{su}, \theta_0)$, i.e. with θ_0 decreasing during daytime from 0.19 to 0.065.

The three curves have been plotted in Fig. 7.14. It is immediately appreciated that the behaviour of

the α_0-curve of the playa West-Idri in Fig. 7.13 can indeed be explained by the drying of the soil surface, in combination with the dependence of α_0 on Φ_{su}.

Finally in Fig. 7.15 the α_0-curves of the different surfaces present in the playas around Idri are given. The observed range of α_0 from the 0.1-value applying to water in the playa NNW-Idri (September) to that of the whitish salt crust in the playa NE-Idri (February), i.e. 0.55, aptly emphasizes the need for such data to study the energy balance of playas. In this respect it should be taken into account, as for example by means of eq. (5.25), that α_0 also depends on the ratio of direct to diffuse solar radiation (Paragraph 5.3.1) and this ratio depends on the presence of clouds and dust.

S a t e l l i t e   m e a s u r e m e n t s . The α_0-data presented above give an excellent opportunity to test the capability of satellite data to provide reasonably accurate measurements of α_0. Accordingly satellite-measured α_p-values will now be compared with the measured α_0-values to assess whether the α_p-values can directly be applied to estimate the surface energy balance terms. The satellite measured values

138
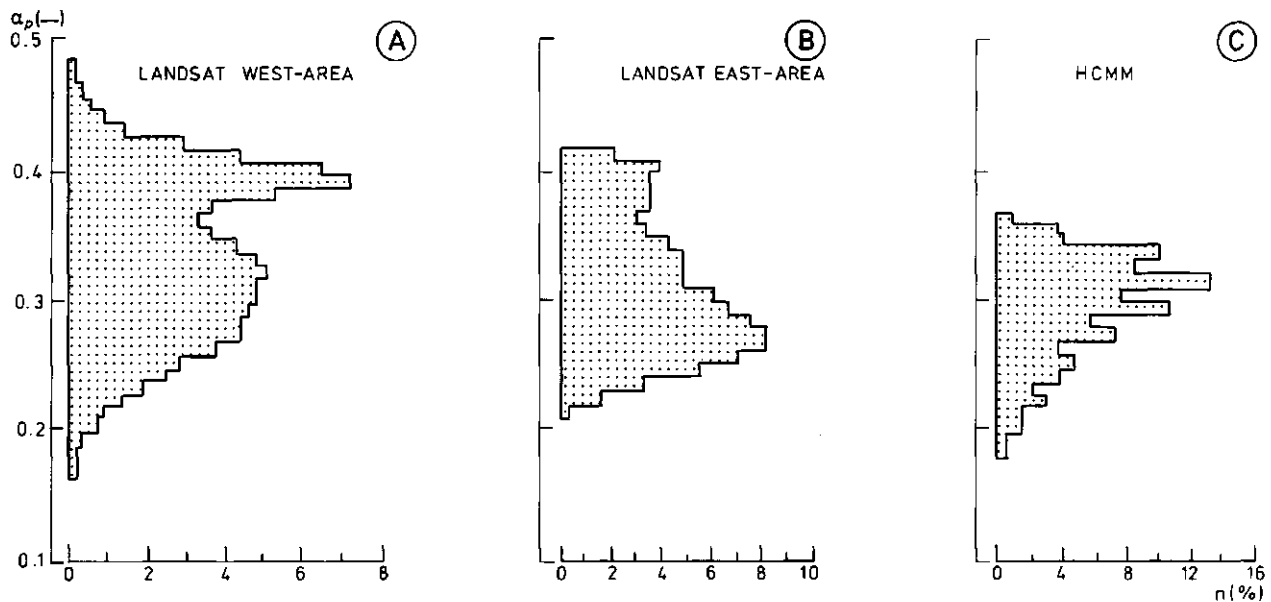
Fig. 7.16. Histogram of surface reflectances as calculated from LANDSAT-MSS data for A the western part of the Wadi Ash Shati basin (1200 km²), B its eastern part (890 km²) and C from HCMM (0.4 to 1.1 μm) data for the Qarqaf highland and the Wadi Ash Shati basin (36,000 km²); n, pixel frequency

have been obtained as described in Section 7.3: therefore no correction has been applied to account for atmospheric effects.

Although such effects have been discussed in paragraph 7.4.3 and a specific discussion concerning satellite measured radiances in the LANDSAT Band 5 and 7 can be found in SLATER and JACKSON (1981), it is the opinion of the present author, as clearly stated in Paragraph 7.4.4, that atmospheric effects can only be taken into account if many additional data are available. As regards dust such data are scarce and specific measurements, either of dust properties or of atmospheric turbidity, should be collected for each separate case.

The range of variability of α_p-values as observed in satellite measurements can be compared with α_0 ground measurements by means of histograms of α_p-images as calculated from LANDSAT-MSS and HCMM data relating to the Qarqaf highland and Wadi Ash Shati basin.

The histogram in Fig. 7.16A relates to the western part of the basin and in Fig. 7.16B to the eastern part. Both histograms were calculated from LANDSAT-MSS data. In Fig. 7.16C the histogram relates to the entire basin and it was calculated from HCMM data. It appears that in all cases the range, mean (A: 0.33; B: 0.30; C: 0.29) and standard deviations (A: 0.06; B: 0.05; C: 0.04) are relatively close to each other. The tenfold increase in pixel size of the HCMM data as compared with the LANDSAT-MSS data does not yield very large effects as regards the total range. In Fig. 7.16C the mean and standard deviation are slightly

lower than in Figs. 7.16A and B. More significant is the difference in shape: the histogram in Fig. 7.16A shows two peaks while in Fig. 7.16C there is only one. Note that the three mean values are very close to the values given in Paragraph 5.2.2 as being typical of deserts.

The histograms presented in Fig. 7.16 show that the variability of surface reflectance in deserts is large and is comparable with the differences observed in ground measurements such as in Figs. 7.12 and 7.13. Now the problem is how to establish a relationship between the surface reflectance as measured from space for relatively large pixels and the point measurements performed on the ground. In some cases this may be easy: the peak at $\alpha \cong 0.40$ in Fig. 7.16A relates to the dunes in Fig. 7.10. This surface type is a rather extensive one, homogeneous and very clearly defined on the image. Thus it is possible to compare safely ground measurements with the α_p-value pertaining to that particular surface. When different surface types occur in small areas, the relationship between a particular α_p-value and a specific surface type is difficult to establish. For this purpose the α_p-data derived from LANDSAT-MSS images can be considered.

A number of image-samples have been analyzed and in Table 7.12, the corresponding α_p-range, the mean reflectance $\bar{\alpha}_p$, the standard deviation at different sample sizes, the number of pixels in, and the area covered by each sample are given. Only the results presented for the category 'playas' (having a relatively large extension) can directly be compared with

Table 7.12. Variability of surface reflectance α_p as measured by the LANDSAT-MSS (0.5 to 1.1 μm), Wadi Ash Shati basin. For each image sample mean reflectance $\bar{\alpha}_p$, standard deviation $\tilde{\sigma}_{\alpha_p}$, number of pixels N_{pix} and area are given

Description	Range of α_p	$\bar{\alpha}_p$	$\tilde{\sigma}_{\alpha_p}$	N_{pix}	Area (km²)
Rocks					
weathered rocks, Qarqaf (Ashkidah area)	0.22 – 0.26	0.233	0.009	306	1.38
weathered rocks, East of Idri	0.15 – 0.27	0.214	0.039	24	0.11
light coloured rocks (Ashkidah area)	0.26 – 0.33	0.298	0.014	572	2.57
darkest rocky area	0.13 – 0.18	0.149	0.019	9	0.04
Playas					
area of highest reflectance in playa E-Idri	0.27 – 0.37	0.331	0.024	80	0.36
area of highest reflectance in playa W-Idri	0.32 – 0.41	0.370	0.026	63	0.28
darkest area in playas	0.27 – 0.30	0.287	0.009	35	0.16
playa W-Idri	0.21 – 0.43	0.300	0.054	396	1.78
high reflecting part of playa, W-Idri	0.32 – 0.38	0.352	0.013	30	0.14
high reflecting part of playa, W-Idri	0.30 – 0.36	0.332	0.016	36	0.16
hard salty crust in the central part of the playa W-Idri	0.36 – 0.38	0.371	0.008	20	0.09
wet part, playa West of Idri	0.21 – 0.33	0.253	0.032	15	0.07
Dunes					
sandy flat area	0.36 – 0.40	0.377	0.009	550	2.48
interdune depression	0.32 – 0.44	0.393	0.015	576	2.59
interdune depression	0.36 – 0.44	0.393	0.016	230	1.04
dune top and depression	0.27 – 0.50	0.408	0.030	2700	12.15
dune top and depression	0.27 – 0.50	0.407	0.039	672	3.02
sun-facing side of dunes	0.38 – 0.40	0.389	0.007	25	0.11
Vegetation					
Ashkidah irrigation scheme	0.27 – 0.38	0.335	0.023	868	3.91
palms and fields, E-Idri oasis	0.19 – 0.22	0.204	0.012	9	0.04
water and vegetation North of Ashkidah	0.22 – 0.31	0.256	0.017	143	0.64
Idri village and outskirts (including oasis)	0.18 – 0.37	0.284	0.042	1581	7.11

Table 7.13. Variability of surface reflectance α_p as measured by the HCMM-radiometer (0.4 to 1.1 μm), Wadi Ash Shati basin. For each sample the mean reflectance $\bar{\alpha}_p$, the standard deviation $\tilde{\sigma}_{\alpha_p}$, the number of pixels N_{pix} and the area are given

Description	Range of α_p	$\bar{\alpha}_p$	$\tilde{\sigma}_{\alpha_p}$	N_{pix}	Area (km²)
Rocks					
light coloured rocks, Qarqaf	0.20 – 0.35	0.309	0.019	1882	677.5
light coloured rocks, Qarqaf	0.29 – 0.34	0.316	0.009	140	50.4
weathered rocks, Qarqaf	0.15 – 0.34	0.256	0.037	2777	999.7
weathered rocks, Qarqaf	0.18 – 0.31	0.246	0.035	178	64.1
Playas					
	0.20 – 0.28	0.245	0.018	282	101.5
	0.20 – 0.28	0.241	0.018	73	26.3
	0.15 – 0.29	0.229	0.024	1670	601.2
Dunes					
	0.27 – 0.34	0.307	0.012	702	252.7
	0.28 – 0.37	0.332	0.016	462	166.3
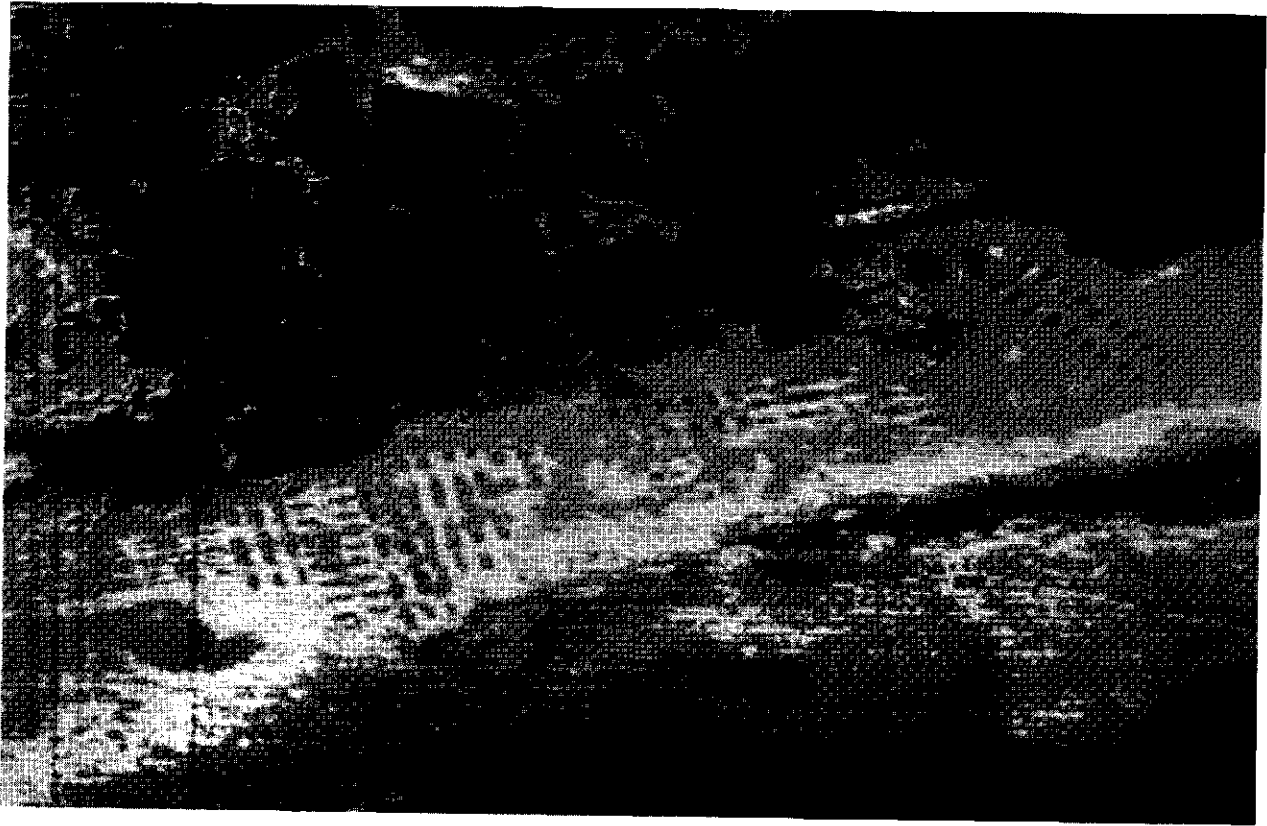
Fig. 7.17. LANDSAT-MSS image of the Ashkidah irrigation scheme, Wadi Ash Shati basin

ground measurements. It appears that the same range of variability in α_p as observed for α_0 in the Figs. 7.12 and 7.13, is also found in the satellite measured data. In the LANDSAT image, however, reflectances as high as the 0.55-value measured in the playa NE-Idri in February 1978 (Fig. 7.12) were not observed. Note the good agreement between the results referred to in Fig. 7.13 as 'playa West-Idri' and those in Table 7.12 indicated as 'hard salty crust in the central part of the playa W-Idri'. In this case the experimental site (playa West-Idri) could be located on the LANDSAT image, because of the relatively large extension of that particular homogeneous surface (see also Fig. 6.11). The rather high α_p-value measured for the Ashkidah irrigated area can easily be explained by the alternation of cultivated and bare soil parcels, as is quite clearly shown on the LANDSAT image of Fig. 7.17.

In Table 7.13 surface reflectances α_p as measured by the HCMM-radiometer, relating to the same region that was considered in Table 7.12, are presented. It appears that the α_p-values found for playas are somewhat lower than in Table 7.12, while those applying to rocks agree with each other. The difference in the reflectance of dunes can be explained by the effect of the variable sun zenith angle on inclinated surfaces (see Paragraph 7.4.3). By comparing the $\bar{\alpha}_p$-value
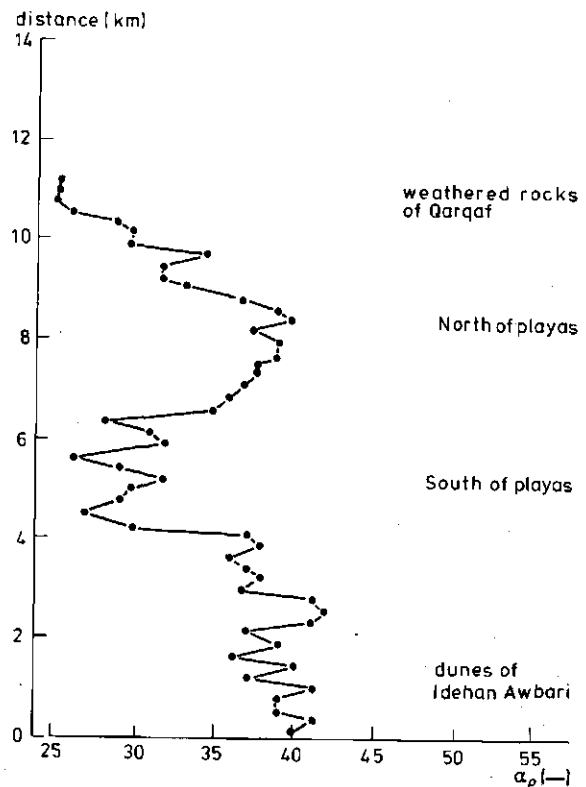
Fig. 7.18. Cross section of a surface reflectance map calculated from LANDSAT-MSS data; the cross-section goes from the dunes in the Idehan Awbari across the Idri playas towards the Qarqaf highland

141

α_ρ (—)

A N = 396 1.4 km²

B N = 15 0.05 km²

C N = 36 0.13 km²

D N = 20 0.07 km²

E N = 63 0.23 km²

n (%)
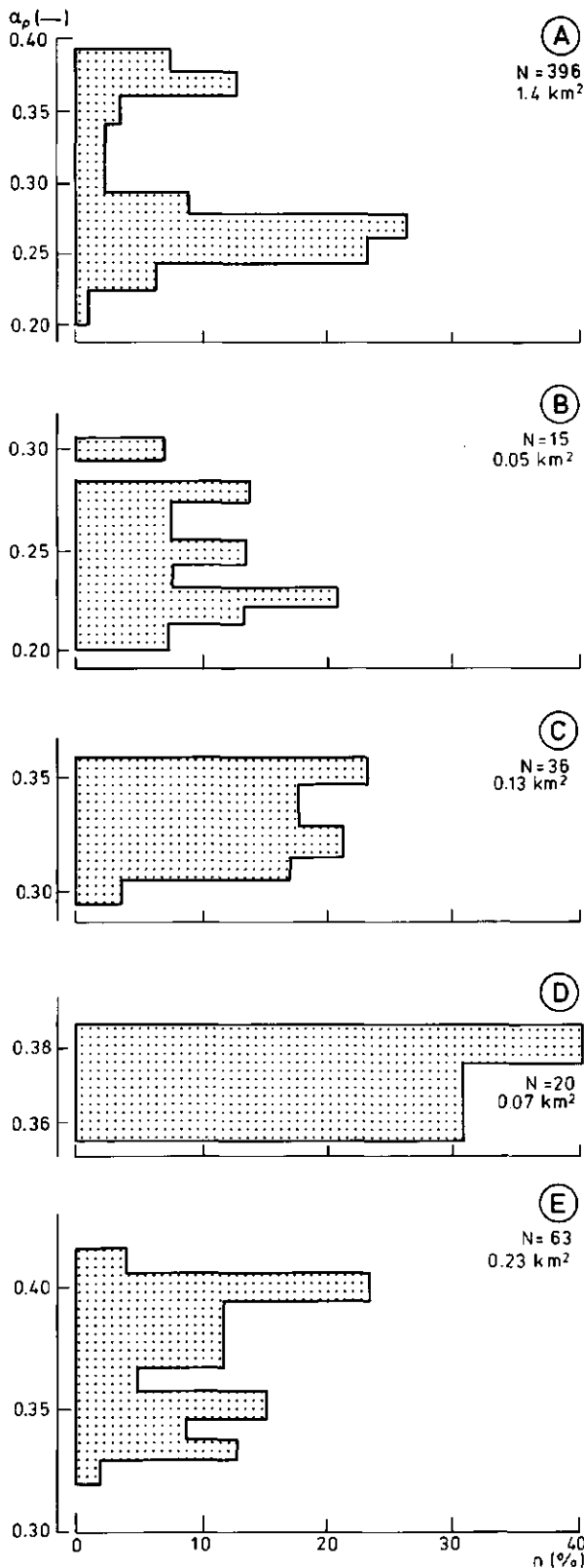
Fig. 7.19. Histograms of surface reflectance as calculated from LANDSAT-MSS data for a number of image samples. n, pixel frequency; N, number of pixels in image sample, the size of each sample also is indicated. A, playa West-Idri; B, wet part playa West-Idri; C, high reflecting part of playa West-Idri; D, hard salty crust in the central part of the playa West-Idri; E, area of highest reflectance in playa West-Idri

given in Table 7.12 for the sun-facing side of dunes, with those in Table 7.13 for dunes it can be seen that the much lower resolution of HCMM data smooths out the slope-dependent variations in reflectance.

The contrast in surface reflectance across the dunes - playa and the playa - rocks boundaries is clearly shown in Fig. 7.18. Here the data obtained from the LANDSAT image of Fig. 7.10 are presented along a cross-section from dunes to rocks. Finally a few histograms of surface reflectance as measured by the LANDSAT-MSS and applying to different parts of the playas present around Idri are given in Fig. 7.19A through E. It can be seen that the variability of α_p is large even in small (Fig. 7.19A) and in very small areas. The case of Fig. 7.19E is of particular relevance for the use of HCMM-derived reflectances; this image sample relates to a 0.3 km² area, therefore smaller than one HCMM pixel of 0.36 km². Nevertheless, a relatively large variability of α_p is still observed in the LANDSAT image sample. The results presented in Fig. 7.19 provide a kind of measure of the difficulties involved in comparing ground and detailed satellite measured surface reflectances. It can be seen that even in a relatively homogeneous area, such as the playa West-Idri, the probability of rejecting as unreliable the satellite based data on the ground of a single-site experiment, is relatively high. The results given in Fig. 7.19B for the wet part of the playa West-Idri compare well with the wet-soil curve in Fig. 7.15 and those in Fig. 7.19D for the salty hard crust in the central part of the playa West-Idri with the curve in Fig. 7.15 for the dry-soil playa West-Idri.

From the data presented insofar, it can be concluded that satellite measured α_p-values give a representative and reasonably accurate picture of reality. This is especially true as regards the areal variability of α_p. It should be noted that in the case of rocks (see Tables 7.12 and 7.13) low reflectances can be found. Such low reflectances are due to weathering of the rock materials (Brak means black in the aboriginal language Tamahak) and these α_p-values can be misleading when satellite data are applied to estimate evaporation losses for those sites (compare Fig. 5.2). The rock-data show, however, that PLINIUS (77) was right in describing the dark Qarqaf (mons Ater) at the beginning of this chapter and in relating the colour of those rocks to the effect of sun rays.

7.5.2. Surface radiation temperature

Surface radiation temperature and soil temperature measurements have been collected at a number of sites (see Table 6.9). Some additional data have been

Fig. 7.20. Surface radiation tempera-
ture T_0 as measured by the METEOSAT
radiometer, an airborne thermal infra-
red scanner flown at 4000 respective-
ly 7500 m height and on the ground
by a hand-held infrared thermometer.
The soil temperature at two depths,
0.3 respectively 0.8 m below the soil
surface also is shown. Sand dune area
in the Idehan Awbari near Idri on 16
through 18 February 1978
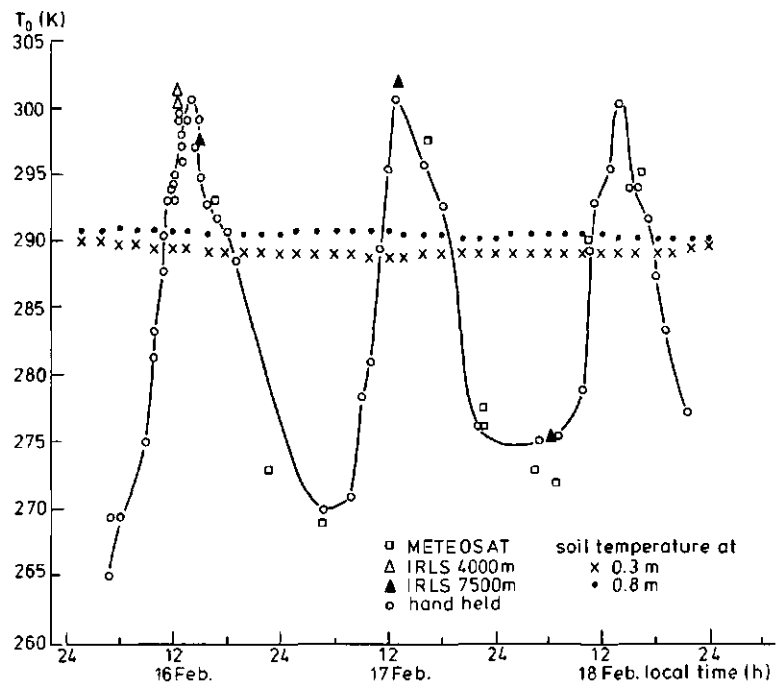
collected with the explicit purpose of checking the
remotely sensed data listed in Tables 6.10 and 6.11.
As test-site a dune area near Idri in the Idehan
Awbari was chosen. This because of the homogeneity
as well as the extension of that surface type. Even
then a comparison between surface radiation tempera-
ture data of very different resolution, i.e. from
7 m of the lower height IRLS flight to 5 km of the
METEOSAT-TIR data, is not straightforward.

The IRLS flights were carried out in February
1978, while HCMM data were available only for Septem-
ber 1978. These data will therefore be separately com-
pared with the other measurements. Soil temperatures
as measured in the dunes, will be applied to compare
satellite mean radiation temperatures with mean soil
temperatures, after correcting the surface radiation
temperature for surface emissivity.

In Fig. 7.20 surface radiation and soil tempera-
ture data as collected on 16, 17 and 18 February 1978
are presented. The overall conclusion is that both
METEOSAT-TIR and airborne IRLS data compare rather
well with ground measurements. The large temperature
amplitudes, as typical for desert climates, make the
comparison of the data more difficult. The ground
measurements shown in Fig. 7.20 were either sampled
at only approximately equal time intervals or record-
ed on paper charts with a poor time resolution. It is
therefore difficult to accurately establish the cor-
respondence in time between ground and satellite data.
This problem can influence the agreement between the
different data. For example the 6 K difference observed
on 16 February at 23.00 h between the ground measured

radiation temperature and the METEOSAT-TIR value is
likely to be due to the lack of ground data between
19.00 h on 16 February and 5.00 h on 17 February. This
circumstance does not allow for the cooling branch
of the T_0 graph to be accurately known. As it can be
seen from the early morning values on 17 February the
agreement between the ground and satellite data is
much closer. It is also clear that no systematic dif-
ference between high altitude and ground based mea-
surements is observed, such as expected from calcula-
tions of atmospheric effects (see Section 7.4 and
Table 7.8). To stress the range of variability in
surface radiation temperature even for large, homoge-
neous areas such as the Idehan Awbari and Idehan
Marzuq, the METEOSAT-TIR image taken on 18 February
1978 (slot 12, i.e. 7.45 LMT in Fezzan) and presented
in Plate 4 should be considered. The range of vari-
ability of T_0 is from 268 to 278 K and the difference
in the image between the Idehan Awbari (272 to 273 K)
and the Idehan Marzuq (268 to 273 K) is evident. Such
differences, comparable with the accuracy of the sat-
ellite data, cannot easily be explained. An explana-
tion might be based on the higher thermal conductivity
of the shallow water-saturated sand layers present in
the Idehan Awbari. According to the concepts discuss-
ed in Paragraph 5.4.2 this fact would induce a higher
mean surface temperature.

To compare the HCMM-TIR data with ground measure-
ments, the experiments carried out during September
1978 must be considered. In Fig. 7.21 surface radia-
tion temperature as measured by the METEOSAT and
HCMM satellites and by an infrared radiation thermo-

143
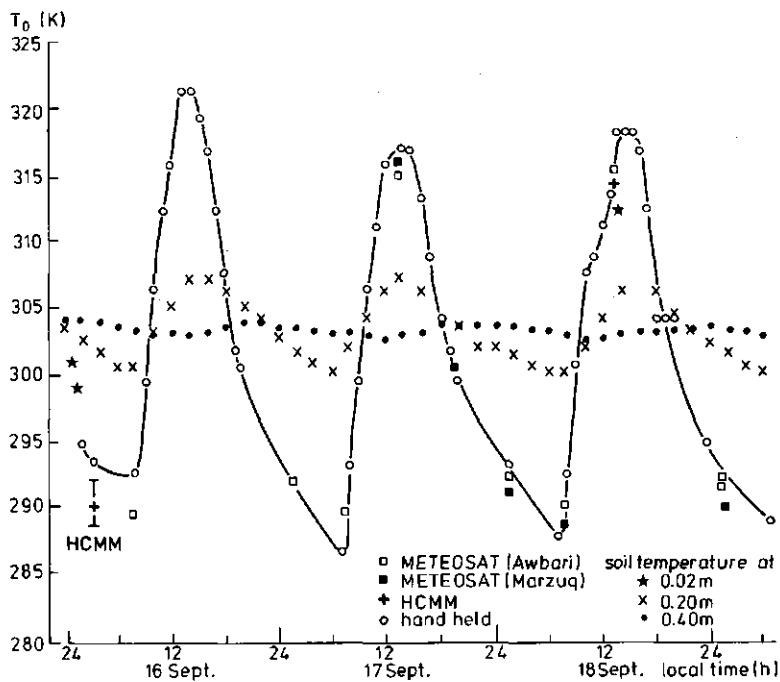
Fig. 7.21. Surface radiation temperature T_0 as measured by the METEOSAT and HCMM radiometers and, on the ground by a hand-held infrared thermometer. Soil temperature at two depths, 0.2 respectively 0.4 m below the soil surface also is shown, along with three spot measurements at a 0.02 m depth. Furthermore the range of the night-time HCMM data is given. Sand dune area in the Idehan Awbari near Idri on 16 to 19 September 1978

meter just above the ground surface are compared; soil temperature at the 0.2 and 0.4 m depths also is shown. Here, as already shown in Fig. 7.20, an overall agreement between the various groups of data is observed. The Idehan Marzuq is still found to be slightly (2 K) cooler than the Idehan Awbari, as already observed in Plate 4. The agreement between the HCMM and METEOSAT-derived surface radiation temperature is quite good (for details on the calibration relationships see Section 7.3). No explanation can be given for the difference between these satellite data and the ground measurements observed in the night and early morning of 16 September 1978. The spatial variability of surface temperature should anyhow be taken into account. The range in temperature (including a 1 K accuracy) is indicated in Fig. 7.21 for the HCMM image sample (120 km^2) which had a $\overline{T}_0$ = 290.6 K; this sample was taken from the image presented in Plate 2.

The HCMM data have also been compared with surface radiation temperatures as measured on the ground in playas. The result is shown in Table 7.14, from which it can be seen that the agreement is excellent when the night-time data are considered. During day-

time, however, the picture is not that clear, since at one site a much lower temperature is present than was observed in the HCMM image. This behaviour is to be ascribed to the variability of T_0, which is quite large even within restricted areas. In Plate 5 a map of T_0 as measured by means of the airborne thermal infrared scanner (see Table 6.10) for the test site playa West-Idri is shown. The size of one HCMM pixel (0.6 x 0.6 km) is indicated to point out the variability of T_0 within this pixel: a full 10 K range within
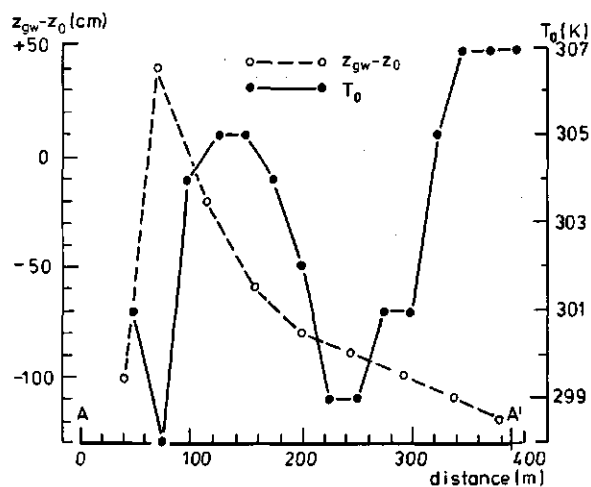
Fig. 7.22. Variation of surface radiation temperature T_0, as obtained on 16 February 1978 at 13.00 h LMT from the 4000 m height IRLS data, and the depth of shallow groundwater table relative to the ground surface along the cross section A - A' in Plate 5 (see also Figs. 6.14 and 6.16); both variables plotted versus the distance from point A

Table 7.14. Variability of surface radiation temperature T_0 in playas as measured by infrared radiation thermometers (at ground level) and by the HCMM satellite

Time	Ground data (K)	HCMM data (K)
Night (3.00 a.m.)	288 - 292	289.8
Day (14.00 p.m.)	309 - 316	315 - 317

a 0.5 km distance. Furthermore the variation of T_0
across this playa is not related in a simple way to
soil moisture content and to the shallow groundwater
table depth. This is quite clearly depicted by Fig.
7.22, where T_0 and z_{gw} are plotted, as measured along
the cross-section A - A' (see Plate 5, also Figs.
6.14 and 6.16). It can be seen that the lowest temper-
ature is found at the open water surface and the over-
all trend of T_0 is to increase with increasing z_{gw}.
Between 160 m and 260 m distance, however, T_0
decreases steeply. A most likely explanation is to be
found in the sharp variations in soil properties, as
illustrated by Fig. 6.8 in comparison with Fig. 6.9.
The salt crust is the result of the slightly deeper
water table, but the thermal admittance of the soil
surface increases dramatically because of the wide
cracks. In this situation convection of soil air oc-
curs, as has been shown in Chapter 3.

One should realize that physically meaningful
details, as discussed above, may be lost in thermal
infrared images of lower resolution. This is a major
difficulty in the interpretation and use of thermal
infrared satellite data because one tries to correlate
them with ground-established knowledge of particular
transfer processes, the effect of which has been wiped
out by the poor resolution. This can be illustrated
by the cross-sections of T_0 images presented in Fig.
7.23. The variation of T_0 from the dunes of the Idehan
Awbari, across the playas on the western side of Idri
and towards the Qarqaf highland is presented as obtain-
ed from data of different resolution (see also Para-
graph 6.2.5).

In Fig. 7.23 the approximate position of the
southern boundary of the playas is indicated in the
4000 m height airborne IRLS data (top), in the 7500 m
height airborne IRLS data (centre) and in the METEOSAT-
TIR data (bottom). The absolute T_0-values differ be-
cause of the difference in time between the three im-
ages. By comparing Fig. 7.23A with B it can be seen
that the slightly lower resolution of the 7500 m
height flight does smooth out the fine structure ob-
served in Fig. 7.23A. Moreover, the 5 km resolution
METEOSAT data show a completely different variation of
T_0, with the exception of the dunes which remain
cooler than the northern side of playas and the bound-
ary between playas and rocks (Qarqaf). When the mean
surface temperature of relatively large areas is con-
sidered, a close agreement between different data is
observed. As an example in Fig. 7.24 the histogram and
mean of the T_0-image samples of the Idehan Awbari are
presented, as obtained from METEOSAT-TIR data on 16
September 1978 (slot 10, 7.45 LMT) and from HCMM-TIR
data in the same night at 2.30 LMT. It can be seen
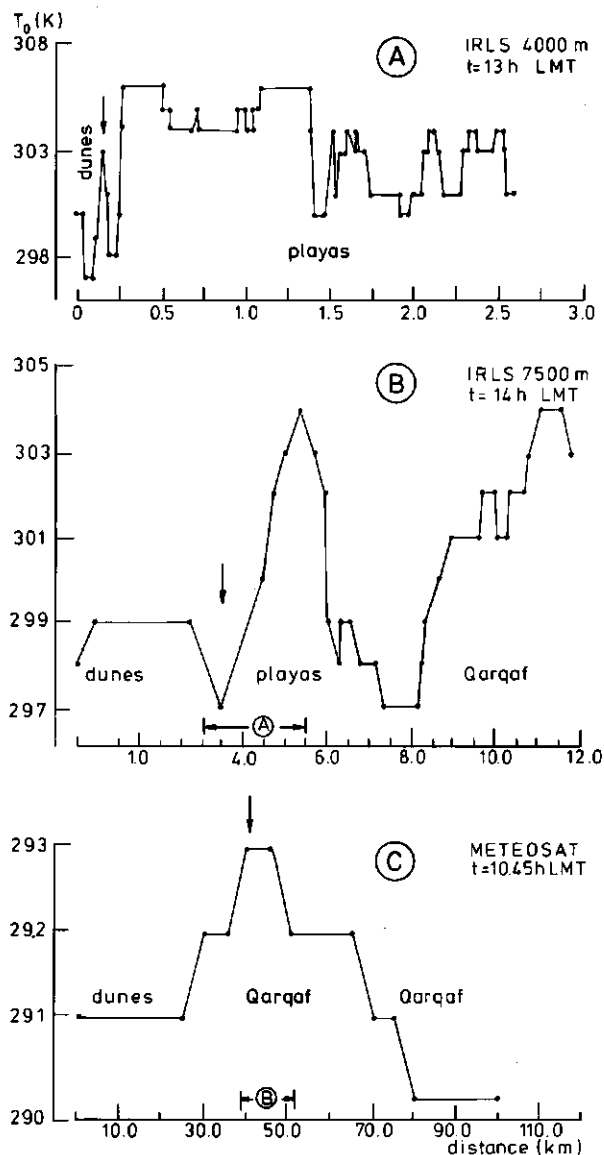
Fig. 7.23. Surface radiation temperature on 16 Feb-
ruary 1978 along cross-sections of decreasing length
of: A, the 4000 m height IRLS image; B, the 7500 m
height IRLS image; C, the METEOSAT-TIR data. The
three curves relate to the boundary between the
Idehan Awbari and the Qarqaf highland and across the
playas on the western side of Idri

that the $\overline{T}_0$-values are very close to each other (only
0.8 K difference), even although areas of different
extension have been considered: 1800 km^2 for the
METEOSAT data and 119 km^2 for the HCMM data.

Ground measurements can also be applied to check
the satellite measured surface radiation temperature.
For this purpose the data already presented in Figs.
7.20 and 7.21 can be applied. Because of the concepts
discussed above, some kind of average value of the
ground measurements is more suitable for the comparison
with satellite data than instantaneous measurements.

145
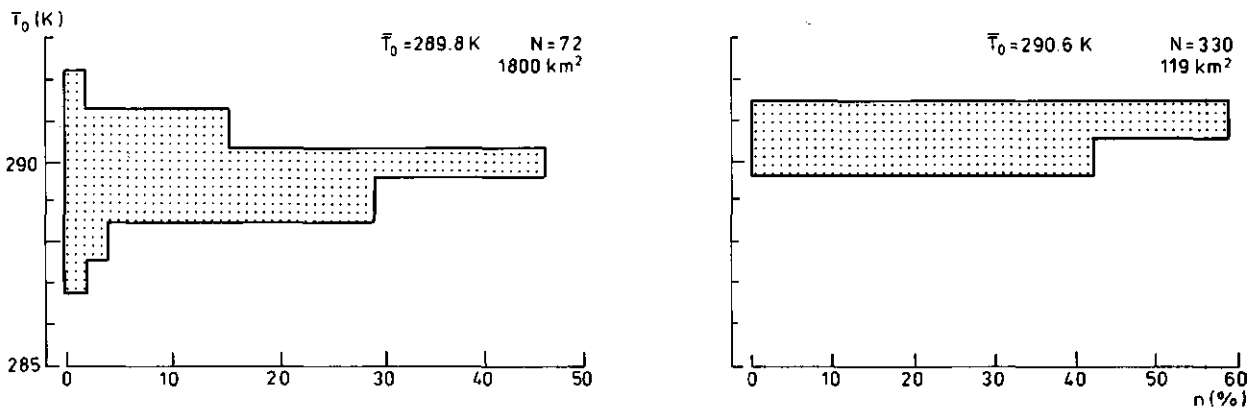
Fig. 7.24. Histogram of T_0-values for a dune area in the Idehan Awbari as obtained from: left, the METEOSAT-TIR image on 16 September 1978 (7.45 h LMT) and right, from the HCMM-TIR image on 16 September 1978 (2.30 h LMT); T_0, mean surface temperature; n, pixel frequency; N, number of pixels in image sample; sample area also indicated

The black-body equivalent surface temperatures, as measured by the satellite, must be corrected for the surface emissivity, $\varepsilon = 0.97$ say (see also Paragraphs 5.2.3 and 5.3.2). Then daily averages of satellite measured surface temperatures can be compared with the daily mean soil temperature, as measured at shallow depths (0.4 m in Fig. 7.20 and 0.2 m in Fig. 7.21) in the dunes. As shown in those figures comparable values are found. Another 'common-sense' check can be applied, by calculating by means of eq. (3.60) the soil thermal diffusivity, a, from the amplitudes of the temperature oscillations at different depths. Namely, the amplitude of surface temperature as obtained above can be used in combination with the amplitude of soil temperature at the 0.4 m or 0.2 m depths. Values of a calculated in this way with the data in Figs. 7.20 and 7.21 have been found by the present author to compare well with figures known to apply to dry sand (see Table 4.1). This result confirms that satellite measured surface temperatures can be applied to study the soil apparent thermal admittance (see Chapter 4). In relation to this topic it must be pointed out that two thermal infrared im-

ages, as for example taken in the early afternoon and early morning (pre-dawn), may not give accurate values of the T_0-amplitude of very different surfaces.

A sensible shift in time between the highest T_0-values in the day may be present, because of the dependence of $z/d = \Omega$ on thermal properties (see eq. 3.57). This effect is quite clear in Fig. 7.25, where surface radiation temperatures of different surfaces, as measured in February 1978 in the surroundings of Idri, are presented. It can be seen that the maximum T_0-value for water was measured 2½ hours later than for dry sandstone.

According to the above it can be concluded that remotely sensed surface radiation temperatures have been found to agree with ground measurements within the relatively poor accuracy of both data, arising as regards remotely sensed data from the mis-registration and spatial resolution of these data. This conclusion particularly applies to the 5 km resolution of the METEOSAT data.
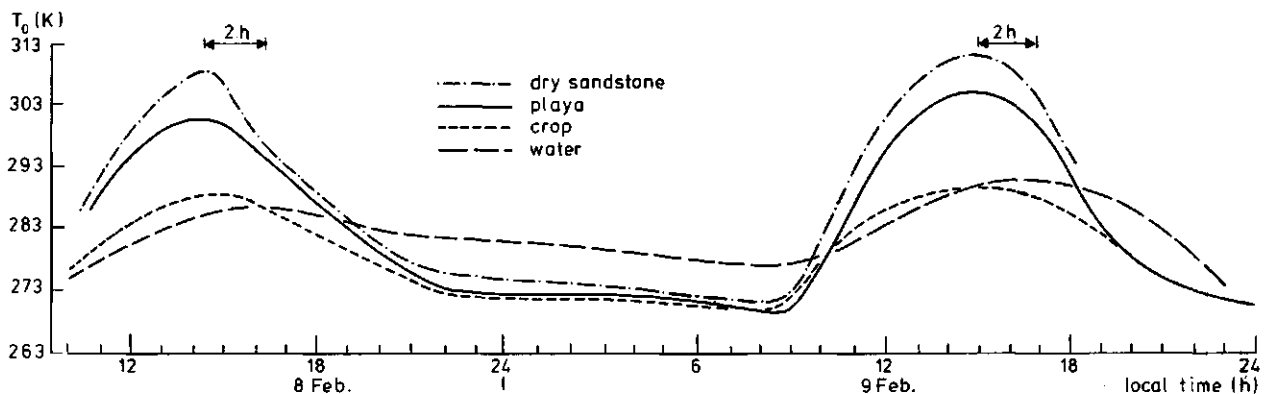
Fig. 7.25. Progression of surface radiation temperature as measured on the ground for different surfaces in the surroundings of Idri; February 1978

146

7.6. AREAL COHERENCE OF SURFACE RADIATION TEMPERATURE AND REFLECTANCE AS MEASURED BY SATELLITES

So far in Chapter 7 many examples of satellite images have been presented. Particular problems have been discussed and some kind of comparison between the different kinds of data has been put forward. It is, however, impossible to assess the potentiality of different types of satellite data without defining some criterion to compare them in mathematical terms. One possibility is to apply features as defined for image texture analysis (BALLARD and BROWN, 1982). Here only the areal correlation function $r(T)$ will be considered, because it is related to the turbulent heat exchange at the soil - atmosphere interface.

The areal correlation function of the gray-levels being present in a digital image can be defined as:

$$r(T_k) = \frac{\sum_{i,j}^{N} (i - \bar{i})(j - \bar{j})p(i,j|T_k)}{\sigma_1 \sigma_2} \quad (-) \quad (7.16)$$

where

T_k = distance expressed in pixels between (x_1,y_1) and (x_h,y_h)

i resp. $\bar{i}$ = gray-level respectively mean gray-level in the set $\{g_1\} = 0, \ldots, N$

j resp. $\bar{j}$ = gray-level respectively mean gray-level in the set $\{g_2\} = 0, \ldots, N$

$p(i,j|T_k)$ = probability of finding gray-levels i and j at a distance T_k

σ_1 resp. σ_2 = standard deviation of gray-level in $\{g_1\}$ respectively $\{g_2\}$

Reflectance images (LANDSAT and HCMM-VIS data) and thermal infrared images (HCMM-TIR and METEOSAT-TIR data) were used to calculate the function $r(T_k)$ with eq. (7.16) for some seventy image samples. Distances up to 10 pixels around each sample were considered, i.e. $T_k = 1, \ldots, 10$ pixels.

In a preliminary analysis of the results it appeared that according to the resolution, systematic differences existed between thermal images. For METEOSAT-TIR samples of homogeneous surfaces $r(T)$ was consistently around zero. Accordingly a detailed analysis of the correlation function of image samples relating to the categories 'dunes' and 'dunes - playa boundary' was carried out. The dunes category is taken to be a good example of a homogeneous surface. Each sample of the second category includes a share as close as possible to 50% of the two neighbouring surfaces. In Fig. 7.26 a view of such a dune area near the boundary with the playas around Idri is given. The few plants that can be seen in this picture disappear a few hundred meters away from the boundary.

In Fig. 7.27 the $r(T)$ function has been calculated from dune samples of METEOSAT-TIR images taken on 17 September 1978 (slot 10, night, and slot 22, day) and of HCMM-TIR images taken on 16 September (night) and 18 September (day). It can be seen that the METEOSAT derived $r(T)$-values are essentially zero, so much lower, up to a distance of 5 pixels, than the HCMM-derived values. When viewing the results for dunes - playa boundaries in Fig. 7.28, obtained from the same images as those of Fig. 7.27, one notices some important differences with Fig. 7.27. The $r(T)$-values are similar for all the samples which have been considered and they also are high for METEOSAT data. Again higher values are observed for the daytime image samples.

Fig. 7.26. A view of the dunes in the Idehan Awbari on the southern side of the playa West-Idri
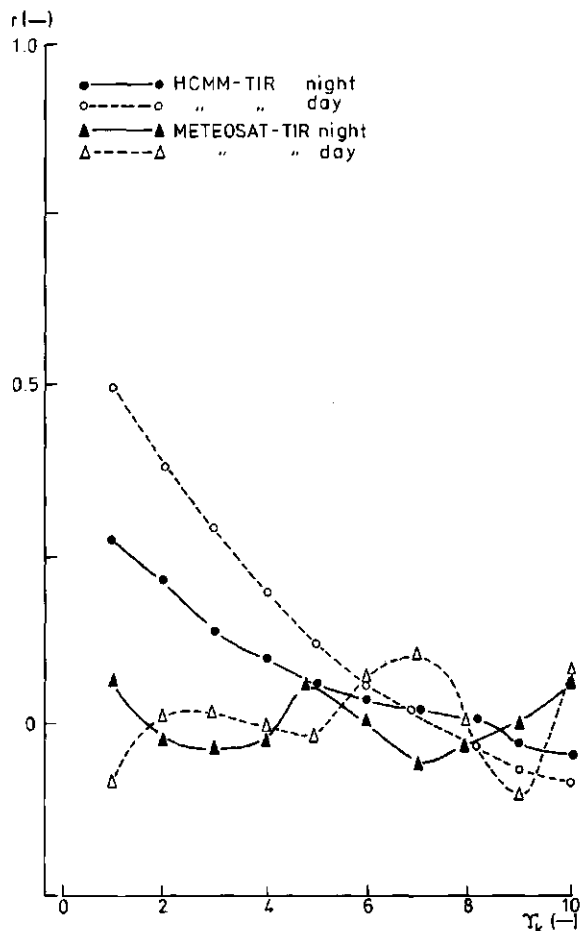
Fig. 7.27. Areal correlation function $r(T_k)$ as calculated from different thermal infrared satellite data for image samples of a homogeneous dune area
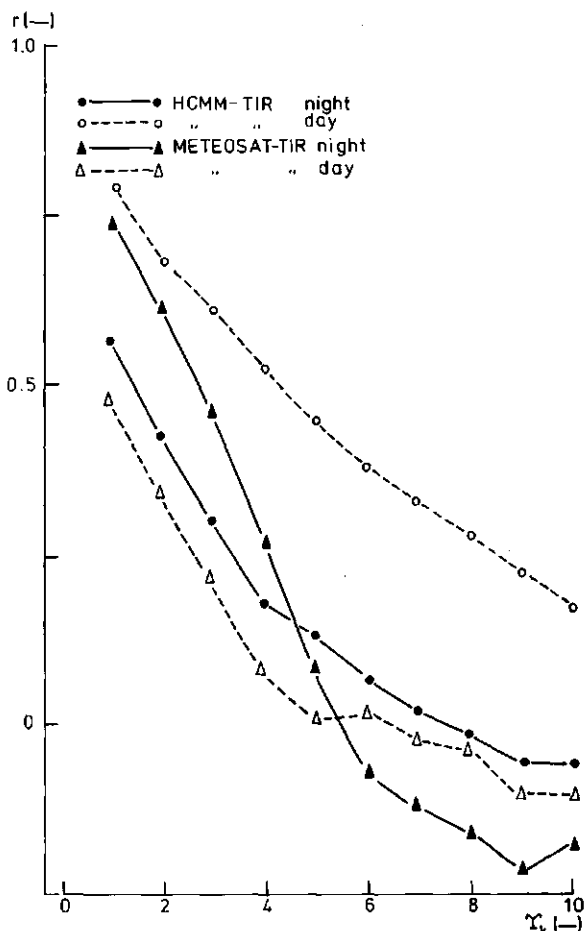
Fig. 7.28. Areal correlation function $r(T_k)$ as calculated from different thermal infrared satellite data for image samples of the boundary between dunes and playas

The conclusion is that surface radiation temperatures within homogeneous surfaces have a lower areal correlation than those within non-homogeneous surfaces! In the latter case a strong signal, i.e. the sharp boundary between playas and dunes is present in each of the samples around which $r(T_k)$ was calculated. At first glance this result may look strange. A possible reason for such behaviour, however, can be given by considering the nature of sensible heat exchange between a turbulent atmosphere and a hot surface.

Recent research on turbulence in the planetary boundary layer clearly did show the existence of coherent structures as earlier observed during laboratory experiments on turbulent boundary layers.

Sensible heat transport in the planetary boundary layer was studied by SCHOLS (1983). The sensible heat flux H can be written as $\rho_a c_p \overline{w'T_a'}$ and the relevant frequency range, i.e. where fluctuations of w and T_a contributing to H in the surface layer take

place, is from 10^{-3} to 10 Hz at 1 m height. Fluctuations in this frequency range accounts for some 90% of the sensible heat flux. The intensity of sensible heat transport varies unevenly in time and space. The intensity is high during relatively short time periods and much lower during longer periods. The length scale of the large flux spots on the surface is very loosely known. It is, however, possible to obtain an estimation of it by means of the Taylor hypothesis. By taking into account the different duration of the periods of peak respectively low intensity, one finds that the order of magnitude of the length scale is 10^2 m for the peak-intensity spots and 10^3 m for the low-intensity spots.

Before proceeding further it might be helpful to give a few comments on the peculiar nature of thermal infrared data as collected by satellite sensors. The optical-mechanical scanners that are installed on the METEOSAT and HCMM space platforms have a very small

148

sampling interval (10^{-5} to 10^{-4} s). Such a time period is short enough to freeze at a given instant the convective structure of the atmosphere. With the term 'instant' is meant a time interval defined by the highest frequency of fluctuations contributing to the intermittent sensible heat transport, 10 Hz say. A sampling interval of 10^{-5} to 10^{-4} s (or some 10^4 Hz) is therefore that small that it allows to measure the surface temperature of more than 10^3 pixels before any change occurs. As regards spatial resolution there is an important difference between HCMM and METEOSAT pixels in relation with the comments given above on the mechanism of heat transport in the surface layer.

One HCMM-TIR pixel is $6 \cdot 10^2$ m in size, and one METEOSAT-TIR $5 \cdot 10^3$ m. Accordingly a single HCMM pixel is of the order of magnitude of a single large-flux spot, while a single METEOSAT pixel may include a (with time) varying number of large-flux spots. A reasonable working hypothesis is that these spots are located at random on a homogeneous surface. It can therefore be understood that the coherence of surface temperature (Fig. 7.27) is higher for the HCMM data. At their spatial resolution in principle either a single pixel relates to a single active spot or many pixels belong to the same non-active spot. Conversely METEOSAT pixels in principle include a number of active spots because of their random spatial distribution. So a low correlation is to be expected.

When the preceding reasoning is tentatively accepted, the length scale of the active spots can be estimated from Fig. 7.27 as being 10^3 m to $2 \cdot 10^3$ m (WARTENA, personal communication).

Some support to the concepts given above is obtained from literature, although no single result can be considered to be of general significance. In a desert environment at White Sands (New Mexico) PIELKE and PANOFSKY (1970) observed that areal coherence of velocity spectra increases under unstable conditions. The scale of the horizontal cross-section of 'convective coherent plumes' was determined by MANTON (1976) to be $1.5 \cdot 10^5$ m^2, or a length scale of 400 m. Air temperature spectra were found by ASIMAKOPOULOS et al. (1976) to attain their maximum amplitude at a frequency between $1 \cdot 10^{-2}$ and $2 \cdot 10^{-2}$ Hz, according to atmospheric thermal stratification. Sawtoothed temperature fluctuations were studied by PHONG-ANANT et al. (1981). In the wind direction the decay-constant of the coherence spectra for air temperature was around 1, and the related frequency band was $5 \cdot 10^{-3}$ Hz. From their results one finds a coherence level of 0.22 at T = 600 m (one HCMM pixel),

which figure can be compared with the curves plotted in Figs. 7.27 and 7.28 taking into account the proper pixel size.

So it can be concluded that the preceding reasoning is at least a likely interpretation of the results presented in Figs. 7.27 and 7.28. It remains to be discussed whether the amplitude of these short term variations of sensible heat flux may induce noticeable variations of T_0.

An estimation of the amplitude of H can be obtained according to the following argument, as proposed by WARTENA (1983, personal communication). Let us assume that the, say hourly, mean sensible heat flux is 400 W·m^{-2} and that a fraction 0.75 of this transport takes place in a fraction 0.25 of the time. Then the peak H-value would be $(0.75 \cdot 400)/0.25 = 1200$ W·m^{-2}, while in the low intensity periods H $\cong$ 130 W·m^{-2}. Then the amplitude is $H_0' = (1200 - 130)/2 \cong 530$ W·m^{-2}. To estimate the frequency of such oscillations, one may argue that the interval between two successive peaks is 600 s (10 minutes) and take this figure as an estimation of the length of the period of the heat wave with amplitude 530 W·m^{-2}.

The thermal admittance of the soil surface for a temperature wave with period P = 600 s can be calculated by means of eq. (4.16) and taking from Table 4.1 the λ_s and $(\rho c)_s$-values relating to the convection-enhanced soil heat flow (case B1). Accordingly $|y_0| = 130$ W·m^{-2}·K^{-1}. Next, by means of eq. (4.17) an estimation of the fluctuation of surface temperature can be obtained, in this case: $T_0' = H_0'/|y_0| = 530/130 \cong 4$ K. So it can be concluded that meaningful oscillations in surface temperature may occur as a consequence of the high-frequency variability of sensible heat transport in the atmospheric surface layer. The pulsating nature of sensible heat transport further complicates the estimation of actual evaporation by the procedures presented in Chapters 2 and 5. The equations presented there, therefore, are intended to describe the mean intensity of sensible heat transport.

There are two possible objections to the preceding reasoning. The first relates to the homogeneity of the dunes in Fig. 7.26 and whether this is true. The point is that the damping depth (eq. 3.59) of dry sand (see also Table 4.1) at a frequency of some 10^{-2} Hz is 5 mm only. It appears that the upper few millimeters of a sand dune, where the wind action greatly facilitates the mixing of soil constituents, are a good example of a homogeneous, constant moisture top soil layer.

The second objection relates to whether the low values of r(T) as observed in Figs. 7.27 and 7.28, are also obtained from satellite data in a different

r (—)
1.0

●——● HCMM-VIS

o------o LANDSAT

0.5

0

0   2   4   6   8   10
                         T_k (—)

r (—)
1.0

●——● HCMM-VIS

o---o LANDSAT

0.5

0

0   2   4   6   8   10
                         T_k (—)
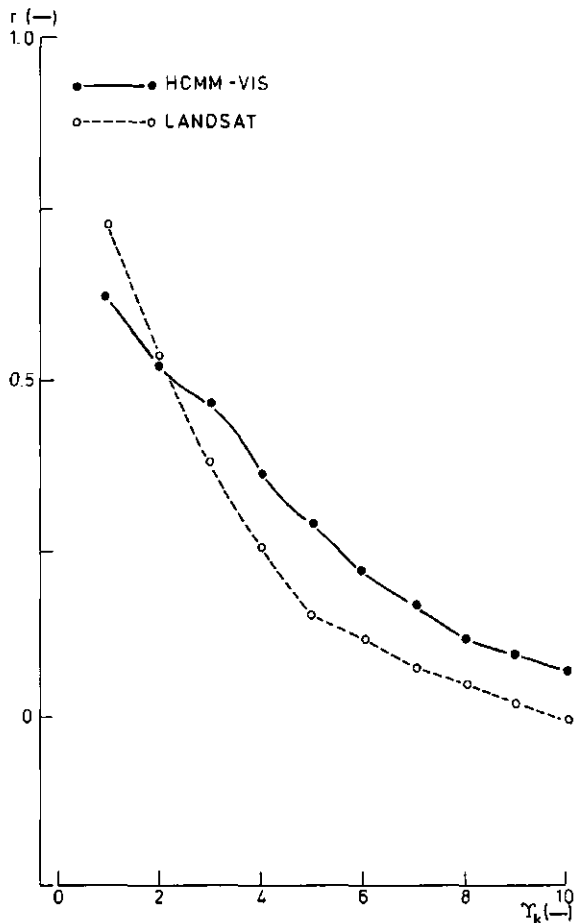
Fig. 7.29. Areal correlation function $r(T_k)$ as calculated from different α_p-images for a homogeneous dune area

Fig. 7.30. Areal correlation function $r(T_k)$ as calculated from different α_p-images for the boundary between dunes and playas

spectral range. By considering the reflectance images as calculated from LANDSAT and HCMM-VIS data, it can be shown that the above discussed values of the $r(T)$-function are only found in thermal infrared data. In Fig. 7.29 values of $r(T)$, as obtained from a HCMM-VIS image on 18 September 1978 and a LANDSAT image on 27 February 1977, are presented for the category dunes. It appears that the ten-fold increase in pixel size when changing from LANDSAT to HCMM data does not affect the coherence level in these images. Results for the category boundary between dunes and playas are given in Fig. 7.30. Even higher correlated values than in all the preceding figures are found. It should be noted that the steeper decay of LANDSAT derived curves is consistent with the intuitive concept that higher resolution allows for better sensing the noise contribution due to terrain exposure.

The results presented in this section should be considered together with the discussion given in Sec-

tion 5.4 on the time-dependent and time-independent parts of the surface temperature patterns. It appears that temperature patterns observed in thermal infrared images are a superposition of:

- very large scale features due to differences in thermal conductivity of deeper layers and perhaps to geothermal heat flux;
- large scale features due to temperature cycles at relatively low frequency, modulated by the thermal admittances of layers in the upper few meters;
- small scale features due to the daily temperature cycle and modulated by the apparent thermal admittance of the upper 20 cm-layer, say;
- microscale noise due to the pulsation of sensible heat transport in the air.

As regards the first mentioned aspect, the best proof of this statement should be based on the analysis of a relatively long time series, e.g. the METEOSAT images listed in Table 6.11. Because of dif-
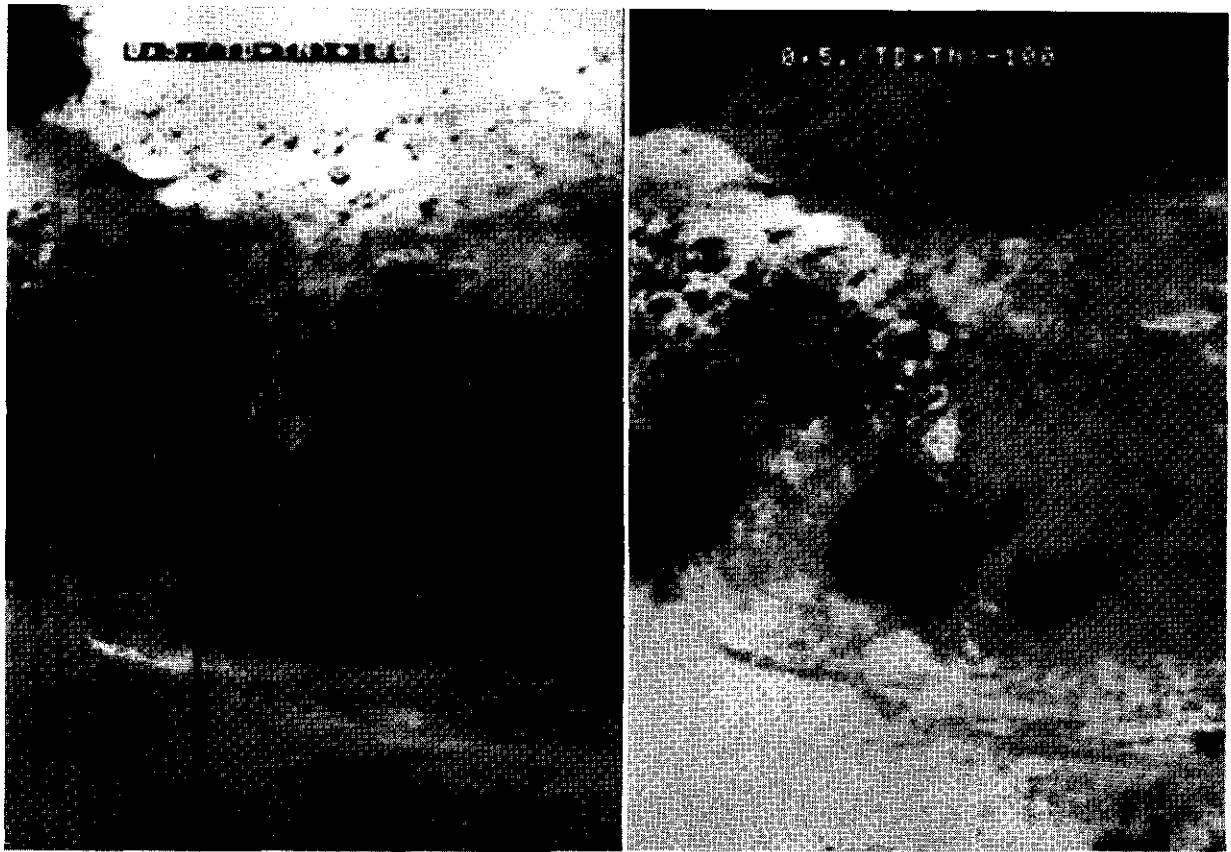
Fig. 7.31. Difference (left) between daytime (18 September 1978) and night-time (16 September 1978) surface temperature as obtained from the HCMM images. Mean surface temperature (right) calculated from the same images

ficulties in the process of mutual registration of these images such an analysis proved to be impossible. A proof can be given, however, of the fact that a day and night pair of thermal infrared images bears a comparable quantity of information both on the image showing the difference and on the image of the mean temperature. In Fig. 7.31 (left) the difference in T_0 between the daytime and night-time HCMM-TIR images (see Table 6.11) is compared with (right) the $\bar{T}_0$-image. It can be seen that the same patterns and details show up on both images.

It should be noted that before a specific, quantitative analysis procedure can be applied, one has to find out which of the above aspects apply to that particular image.

7.7. SUMMARY

In Section 7.1 a short overview has been given on reported applications of satellite imagery to study the Libyan desert. As regards thermal infrared data, the broader topic of deserts in general has been considered.

In Section 7.2 the procedure followed in the present investigation to co-registrate different satellite images has been outlined. Specific results for a HCMM day - night pair of images were given.

In Section 7.3 the procedure applied to transform the standard pixel values, as usually provided in satellite digital data products, into calibrated data has been presented. As in Section 7.2, the case of LANDSAT, HCMM and METEOSAT data has separately been discussed.

In Section 7.4 the atmospheric effects on the specific satellite data of the Wadi Ash Shati area (as described in Chapter 6), were assessed. The effect of clouds, atmospheric water vapour and dust was discussed, following the concepts presented in Section 5.2. As regards clouds it has been shown that by combining thermal infrared satellite data with radio soundings of the atmosphere, a threshold temperature can be established for each particular image. In this way the pixels showing a temperature lower than the established threshold are excluded from further calculations involving satellite data and relating to the ground surface. More difficult is the analysis of the effect of atmospheric water vapour. Many uncertainties, some of a rather fundamental character, are involved. The relative weight of these uncertainties

has been assessed by means of the radiation transfer model described in Paragraph 5.2.3. It was concluded that such a calculation procedure cannot achieve an accuracy better than 5 K, which figure regrettably quite often is comparable with the calculated correction to be applied to the satellite measured surface radiation temperature. The effect of dust on the emitted radiation has been discussed next. It has been shown that the presence of dust can be detected by using ground meteorological data, as collected at the Idri weather station and in the playas around that village. It was, however, impossible to estimate the atmospheric optical depth due to dust. In principle satellite measured reflected radiance could be used for this purpose, but both the reflectance and the exposure of the surface have to be known. The overall conclusion was that the accuracy of the correction procedures still is poor. So the accuracy of satellite measured surface reflectance and surface radiation temperature can be better assessed on the basis of ground reference measurements of these variables.

In Section 7.5 ground measurements of surface reflectance and temperature have been compared with the values obtained from the LANDSAT, HCMM and METEOSAT data described in Section 6.2. As regards the ground based measurements of surface reflectance it has been shown how the equations as given in Section 5.3 to account for the dependence of surface reflectance on surface moisture content and on sun zenith angle can be combined. The result was that the observed variation in surface reflectance during the day in the playa West-Idri (September 1978) could be explained by the drying of the soil surface. A detailed conspectus of satellite measured surface reflectances has been given as relating to the LANDSAT and HCMM data. It was shown that comparable mean values for the different surface types are found. The range of the observed values for each particular surface was narrower when HCMM data were used. Surface radiation temperatures as measured by means of an airborne scanning radiometer, of the HCMM-TIR and the METEOSAT-TIR channels have been compared with surface radiation temperatures as measured on the ground and with soil temperatures. A dune area in the Idehan Awbari was chosen as test area. The amplitude of surface radiation temperature also was compared with soil temperature at different depths in the sand dunes. Comparison of the values in the non-cloudy pixels (see Section 7.4) with ground measurements gave a good agreement for the different kinds of remotely sensed data. On very few occasions the differences with the ground based data were large, although no systematic deviation

was observed. Such deviations, however, remained well below the areal variability of surface radiation temperature, as observed in the remotely sensed data of different resolution.

In Section 7.6 the areal variability of surface radiation temperature and surface reflectance has been studied in more detail by calculating the areal correlation function for a number of samples of the images available for the Wadi Ash Shati area. A somewhat surprising result was obtained in that the areal coherence was lower for homogeneous surfaces than for non-homogeneous ones. An explanation for this finding has been given on the basis of the pulsating nature of heat exchanges at the soil - air interface. Finally it has been shown that HCMM images give a comparable detail on the features of the area, as well when showing the day - night temperature difference as when showing the mean temperature.

The overall conclusion to be drawn from the data having been presented in this chapter is that their accuracy is acceptable for the applications that are to be presented in Chapter 8. The more so when it is realized that the relatively poor accuracy of remotely sensed data is outweighed by their capability of providing essential information over the large expanses of the Libyan desert in general and particularly on the playas which are scattered there.

8. CALCULATION OF REGIONAL ACTUAL EVAPORATION FROM DESERTS, AS EXEMPLIFIED FOR PART OF THE LIBYAN DESERT

'Sunt et in Africa lacus, et quidem turbidi, salem ferentes. ..... Nam et Cyrenaici tractus nobilitantur Hammoniaco et ipso, quia sub harenis inveniatur, appellato.'

(PLINIUS, Naturalis Historia, Liber XXXI:76,79)

8.1. USE OF SATELLITE DATA

8.1.1. Linear approximation of the surface energy balance equation

In the Sections 5.1 and 5.6 it has already been discussed how the energy balance equation can be reduced to a linear form and which consequences are implied by this procedure. It will now be shown that useful formulas to calculate LE will be obtained from the following approaches:

- Approximation of the LE-surface of Fig. 5.2 by using the plane tangent to the LE-surface at a reference point $\tilde{P}^*$, where $LE = \tilde{LE}$. The equation of the tangent plane can be calculated from the derivatives $D_{\alpha_0}(LE)$, eq. (5.5), and $D_{T_0}(LE)$, eq. (5.6).
- Approximation of the LE-surface by using an intersecting plane. The equation of the plane is obtained by means of eq. (5.55) from specific 3-strings (see Section 5.6).

The first approach is most suitable when, on the surface depicted in Fig. 5.2 the evaporation rates to be calculated fall within a short distance from $\tilde{P}^*$. The second approach, conversely, fares better when the expected evaporation rates tend to form separate clusters on the surface. This situation is likely to occur when soil surface properties are considerably modified by weathering of the soil (Fig. 5.11) or by salt crusts (Section 1.2 and Paragraph 7.5.1). A specific example dealing with the relationship between the estimation of actual evaporation rate and the presence of salt crusts will be presented later in this paragraph.

T a n g e n t   p l a n e. The total differential of $LE = LE(\alpha_0, T_0)$ can be obtained as the sum of partial differentials. The equation of the plane tangent to LE at some reference point $\tilde{P}^*$, where $LE = \tilde{LE}$ can be

written as:

$$LE(\alpha_0,T_0) = \tilde{LE} + D_{\alpha_0}(LE) + D_{T_0}(LE) \qquad (8.1)$$

or, see eqs. (5.5) and (5.6), by introducing small increments $\delta\alpha_0$ and δT_0:

$$LE(\alpha_0,T_0) = \tilde{LE} + R_{sw}\delta\alpha_0 + (4\varepsilon\sigma T_0^3 + \frac{\rho_a c_p}{r_a})\delta T_0 \quad (W\cdot m^{-2}) \qquad (8.2)$$

where fluxes away from the soil surface are negative. Eq. (8.2) illustrates how satellite measured α_0 and T_0-values have to be combined with ground reference measurements. The reference value $\tilde{LE}$ is most aptly obtained by means of ground based measurements for a surface type representative of the area to be investigated. The value of variables like r_a which cannot be measured areally, also is to be obtained from ground based measurements. Then the satellite data can be applied to establish the required areal pattern of LE.

The term $4\varepsilon\sigma T_0^3$ in eq. (8.2), the so-called 'radiative transfer coefficient', changes little with varying T_0, so such a variation will have a minor effect on the corresponding variation of the calculated LE. To illustrate this point, in Table 8.1 the values of $4\varepsilon\sigma T_0^3$ as calculated for different surface temperatures are given. By making use of these values it can immediately be shown that the mean in the T_0-range 270 to 330 K is a safe approximation with which to calculate $D_{T_0}(LE)$. Namely the term $4\varepsilon\sigma T_0^3 \cdot \delta T_0$ can be calculated, e.g. for a T_0-range from 270 to 310 K,

Table 8.1. Values of the radiative transfer coefficient $4\varepsilon\sigma T_0^3$, see eq. (8.2), at different surface temperatures

T_0 (K)	270	290	310	330
$4\varepsilon\sigma T_0^3$ ($W\cdot m^{-2}\cdot K^{-1}$)	4.33	5.37	6.56	7.91

by applying the value of $4\varepsilon\sigma T_0^3$ at 290 K or for example the values at $T_0 = 270$, 290 and 310 K. Accordingly it is found that $(4\varepsilon\sigma T_0^3 \cdot \delta T_0) = 214.8$ $W\cdot m^{-2}$ in the first case and 216.3 $W\cdot m^{-2}$ in the second case. As regards r_a it should be recalled that it depends on atmospheric stability as expressed by means of the ϕ_h-functions, see eq. (2.33), and therefore also on T_0. It is, however, impossible to determine r_a areally, and so it has to be kept constant in eq. (8.2). Corrections can eventually be applied by means of eq. (5.57) as discussed in Section 5.6. A final remark about eq. (8.2) relates to R_{sw}. Under clear sky conditions it can be kept constant for an entire image, otherwise the procedure briefly described in the Paragraph 5.2.1 should be applied. Under partly cloudy conditions relatively large variations of R_{sw} may occur over short distances and, therefore, they are at least as important as the variations of α_0 and T_0.

A first linear formula to calculate LE from α_0 and T_0 can be obtained by substitution of the data collected during the experiments listed in Table 6.9 into eq. (8.2). If only the winter data are taken, the solution is:

$$LE = -135 + 218\ \delta\alpha_0 + 11.2\ \delta T_0 \qquad (W\cdot m^{-2}) \qquad (8.3)$$

and the reference point now is $\tilde{P} \equiv (\tilde{\alpha}_0, \tilde{T}_0, \tilde{LE}) \equiv (0.32, 291.4, -135)$. If only the summer data are considered, the result reads:

$$LE = -87 + 267\ \delta\alpha_0 + 12.0\ \delta T_0 \qquad (W\cdot m^{-2}) \qquad (8.4)$$

with $\tilde{P} \equiv (0.386, 306.2, -87)$.

It should be recalled that, according to the description of the experiment sites given in Section 6.2, there are important differences between the summer and winter data sets. First of all most of the winter data originate from the wet part of the playa West-Idri, while the summer data-set mostly relates to the very dry part of that playa. After the experiments performed in February 1978, it was realized that the dry type of playa surface had a much larger extension than the wet type. Therefore the summer-formula, eq. (8.4), must be considered to give a better picture of the a r e a l   d i s t r i b u - t i o n of evaporation in playas. This explains the lower mean evaporation rate in the summer data-set.

I n t e r s e c t i n g   p l a n e. According to the concepts discussed at the beginning of this paragraph, the differences that exist between the experimental sites suggest that a plane intersecting the LE-surface can give a better approximation than a

plane tangent to this surface. By using a representative point on the LE-surface of Fig. 5.2, for each separate cluster the approximation now will be satisfactory around three points. To obtain specific formulae to calculate LE eq. (5.55) must be applied. Again the data listed in Table 6.9 will be used. As a first example the following points will be considered: $P_1 \equiv (0.267, 288.2, -150)$, playa West-Idri on 16 February; $P_2 \equiv (0.583, 282.9, -95)$, playa NE-Idri on 16 February; and $P_3 \equiv (0.376, 293.8, -195)$, palms on dunes, on 17 February. By substitution of these values in eq. (5.55) the following solution is obtained:

$$LE = 2330.98 + 29.70\ \alpha_0 - 8.637\ T_0 \qquad (W\cdot m^{-2}) \qquad (8.5)$$

It can be shown that a completely different solution is obtained when considering the data relating to the dry part of the playa West-Idri, to the playa NE-Idri without the salt puffy crust and to the palms on dunes (all in September 1978). Accordingly the following points were chosen: $P_1 \equiv (0.383, 301.2, -61)$, playa West-Idri on 15 September; $P_2 \equiv (0.436, 316, -106)$, playa NE-Idri on 4 September; and $P_3 \equiv (0.303, 309.9, -178.5)$, palms on dunes on 7 September. By substitution of these values in eq. (5.55) the following solution is obtained:

$$LE = 1426.748 + 819.149\ \alpha_0 - 5.98\ T_0 \qquad (W\cdot m^{-2}) \qquad (8.6)$$

It can be seen that in eqs. (8.5) and (8.6) the sign of the coefficient of α_0 is opposite to the sign of the coefficient of T_0. The reason for this seemingly unreasonable result is that, in the intersecting plane approach, equations of planes intersecting the LE surface (Fig. 5.2) are being sought. There is no reason, therefore, to expect that the sign of the α_0 and T_0 terms in eqs. (8.5) and (8.6) is equal to that of the differential terms in the tangent plane approach, where the coefficients of α_0 and T_0 are always positive. The case of evaporation increasing with increasing T_0 has already been discussed in Section 5.1 (see Fig. 5.2).

The difference in size between the coefficients of α_0 in the eqs. (8.5) and (8.6) is remarkable. The explanation is the very high reflectance observed at the playa NE-Idri during the winter experiments. The extension of the crust and the contrast between the salty crust of this playa and the entire area surrounding the village of Idri, are quite evident in the LANDSAT image presented in Plate 6, left. This image, a colour composite of the LANDSAT bands 7, 5 and 4, was taken on 12 March 1978 (see Table 6.11). The variability of surface reflectance of playas with

time, as shown by the ground measurements presented in Section 7.5, can greatly modify the surface energy balance. These modifications can affect large areas and contribute to the variability in space of the surface energy balance, as depicted by the LANDSAT colour composite presented in Plate 6, right, applying to 26 September 1978.

Eq. (5.55) can be helpful in accounting for such a variability, because the number of field experiments can be restricted to areas where such modifications occur. The results of those experiments can be substituted in eq. (5.55) when expressed in terms of the coordinates α_0, T_0, LE. For example MENENTI (1980) obtained a formula to calculate LE by making use of data of the playa NE-Idri on 16 February 1978. The coordinates of this point were substituted in eq. (5.55), together with an average point $P_1 \equiv (0.25, 280.0, -184)$ obtained from the experiments described in Paragraph 6.2.4 and a point calculated from P_1 by means of the differential D_{T_0} (LE), to account for the variation of LE due to an increase of T_0 only. The reflectance α_0 was kept constant and T_0 chosen as corresponding to the higher values in the summer data-set. Accordingly $P_2 \equiv (0.25, 300.8, -111.6)$ was obtained.

By substitution of these points in eq. (5.55), the following solution is obtained:

$$LE = -1217.85 + 236.954\ \alpha_0 + 3.481\ T_0 \qquad (W \cdot m^{-2})\ (8.7)$$

The equations to calculate LE as given insofar relate to daily (24 hours) mean evaporation rates. They can be applied to a relatively wide spectrum of desert surfaces, i.e. of different LE, α_0 and T_0. It is understood that although they are of empirical nature, they allow for straightforward transformations of satellite measured α_0 and T_0-images to LE-values.

8.1.2. Threshold values of θ_E and α_{0E} at the evaporation front

It has already been discussed in Paragraph 5.4.4 that it would be quite helpful to establish whether

evaporation takes place at the soil surface or inside the soil. This now will be done.

The theoretical concepts presented in Paragraphs 3.3.1 and 3.3.3 will be now combined with eq. (5.28) to establish the moisture content θ_E at the evaporation site and the pertaining reflectance α_{0E}. According to the definition of evaporation sites given in Paragraph 3.3.3, they are found in pores where the mean free path of water vapour $\ell_m \cong$ the pore radius r_m. The value of ℓ_m must be calculated as a function of temperature. Then the surface tension σ_{wa} also must be known to be able to calculate the matric pressure head at the evaporation site h_{mE} by means of eq. (3.7). Finally the value of θ_E is obtained through the moisture retention curve $h(\theta)$; see also Paragraph 3.5.3. To obtain the θ_E-values in Table 8.2 the $h(\theta)$ curve applying to the playa NE-Idri has been used. The results of these calculations are presented in Table 8.2, where it can be seen that the moisture content θ_E only slightly increases with temperature. It can therefore be concluded that at the evaporation sites $\overline{\theta}_E = 0.048$, with a resulting temperature coefficient of $6 \cdot 10^{-5}$ K^{-1}. So the moisture content θ_E increases linearly with temperature by a factor $6 \cdot 10^{-5}$ per 1 K.

If the $h(\theta)$ curve of the soil profile in the Ashkidah oasis is applied, then $\overline{\theta}_E = 0.062$ with a resulting temperature coefficient of $1 \cdot 10^{-4}$ K^{-1}.

It should be noted that in the calculation of θ_E the osmotic pressure head h_o must not be added to h_m. It is only in the calculation of soil air relative humidity U, when for example required at the evaporation site, that h_o must be included in the h-value entered in eq. (3.21). In principle the effect of salts on σ_{wa} should be taken into account, but only very slight variations of θ_E are found. If a NaCl-saturated solution is considered (see also Table 3.3), $\overline{\theta}_E = 0.047$ when taking the $h(\theta)$ curve of the NE-Idri soil and 0.060 when taking the $h(\theta)$ curve of the Ashkidah soil. It can therefore be concluded that salts do not significantly affect the value of θ_E.

The value of the surface reflectance that corresponds to $\overline{\theta}_E$ can now be calculated by means of eq.

Table 8.2. Mean free path of water vapour ℓ_m, surface tension of water against air σ_{wa}, matric pressure head h_{mE} and moisture content at the evaporation sites θ_E at various temperatures T. The $h(\theta)$ curves of the soils in the playa NE-Idri and in the Ashkidah oasis have been used to obtain θ_E; ℓ_m values calculated according to Forsythe (1964)

T	ℓ_m	σ_{wa}	h_{mE}	θ_E (-)	
(K)	(m)	(N·m^{-1})	(m)	NE-Idri	Ashkidah
280	$4.0 \cdot 10^{-8}$	$7.48_5 \cdot 10^{-2}$	382.9	0.046	0.059
300	$4.5 \cdot 10^{-8}$	$7.16 \cdot 10^{-2}$	324.7	0.047	0.061
310	$4.7 \cdot 10^{-8}$	$7.00 \cdot 10^{-2}$	304.0	0.048	0.062
320	$5.0 \cdot 10^{-8}$	$6.84 \cdot 10^{-2}$	279.2	0.049	0.063
330	$5.3 \cdot 10^{-8}$	$6.68 \cdot 10^{-2}$	257.2	0.049	0.064

(5.28), thereby obtaining for the playa NE-Idri soil $\alpha_{OE} = \alpha_0(\bar{\theta}_E) = 0.34$ and for the Ashkidah soil $\alpha_{OE} = 0.33$. The value of α_{dry}^0 required in eq. (5.28) has been chosen to be 0.38, since it was measured for the dry soil surface in the playa West-Idri (September 1978). There the surface moisture content θ_0 was measured to be lower than 0.02 on weight basis.

The α_{OE}-values of 0.33 and 0.34 mentioned above were obtained by applying the definition of the evaporation site given in Section 3.3 in a somewhat restrictive manner by taking $r_m = \ell_m$. It can clearly be seen in Fig. 3.7, however, that at capillary radii larger than ℓ_m, $D_{eff} \gg D_a$. Let us assume that pores of $r_m = 2 \ell_m$ also are suitable sites of evaporation. Then the values of h_m would be half (see eq. 3.7) of those given in Table 8.2. Accordingly one would find for the playa NE-Idri soil $\bar{\theta}_E' = 0.054$ and for the Ashkidah soil $\bar{\theta}_E' = 0.07$. These $\bar{\theta}_E$-values yield a α_{OE} of 0.33 for the first case respectively 0.32 for the second case. It can therefore be concluded that for both soils an average surface reflectance value pertaining to the moisture content at the evaporation site $\alpha_{OE} = 0.33$ can be taken.

Finally it might be useful to point out that once α_{dry}, α_{OE} and θ_E are known one is able to calculate, from the surface reflectance for k pixels α_{Ok}, the surface moisture content θ_{Ok} by rearranging eq. (5.28) into the expression:

$$\theta_{Ok} = \frac{\chi(\alpha_{OE} - \alpha_{Ok}) + \theta_E(\alpha_{dry}^0 - \alpha_w)}{\alpha_{dry}^0 - \alpha_w} \quad (-) \qquad (8.8)$$

The α_{OE}-values obtained above greatly enhance the scope for the application of remotely sensed data to study the surface energy balance. Namely these α_{OE}-values can now be used to split up a map of surface reflectance (e.g. as calculated from LANDSAT data) into two surface types: one where $z_E = 0$, i.e. $\alpha_0 \leq \alpha_{OE}$ and a second one where $z_E > 0$, i.e. $\alpha_0 > \alpha_{OE}$. As discussed in Paragraph 5.4.4 and Section 5.5 such zoning greatly simplifies the estimation of fluxes contributing to the surface energy balance.

Before a specific example of the procedure can be presented one more intermediate step ought to be discussed. To obtain the reflectance at the top of the cloud-free atmosphere α_{pE} that corresponds to α_{OE} for a specific image, i.e. for a specific ϕ_{su}, one has to apply the curves of Fig. 5.3. In Plate 7 an example of the results which can be obtained by means of this procedure is given. There two images are presented that relate to the Idri area. The α_{pE}-value is 0.29. As can be seen most of the area where $z_E > 0$, because $\alpha_0 > \alpha_{OE}$, relates to the dunes of the Idehan

Awbari. This is of course reasonable as they are the driest surface in the area. It has, however, been made clear in Paragraph 7.4.3 that large α_0-values also can be measured because of a particular exposure. Such problems obviously make it more difficult to apply the procedure presented here without having some ground information.

The images shown in Plate 7 demonstrate that satellite measured surface reflectances can successfully be applied to establish whether evaporation takes place at the soil surface or inside the soil. It must be emphasized that the fundamental character of the definition of evaporation sites as given in Paragraph 3.3.3 is the key-factor in making the procedure presented in this paragraph straightforward.

8.1.3. Calculation of instantaneous images of the different terms of the surface energy balance

It now will be shown how the areal distribution of instantaneous values of the fluxes in the surface energy balance equation can be calculated by applying satellite measured surface radiation temperatures and reflectances.

To calculate R_n by means of eq. (5.2) the values of α_0 and T_0 must be measured areally by satellite-borne radiometers (Chapter 7). The R_{sw}-term can eventually be estimated areally as shown in Paragraph 5.2.1. It should be noted that even if the evaporation site is located at the soil surface, the dependence of α_0 on θ_0, as described by eq. (5.28), implies a tendency towards lower LE-values with decreasing θ_0. For example with $R_{sw} = 863.9$ W·m^{-2}, as measured on 18 September 1978 at 14.00 h in the playa West-Idri, the difference in reflectance between the wet part of the playa, i.e. $\alpha_0 = 0.26$ (see Fig. 7.15), and the threshold value $\alpha_{OE} = 0.33$ (see Paragraph 8.1.2) implies 60 W·m^{-2} less available energy in the second case. Between an open water surface with $\alpha_w = 0.1$, as measured in the playa NNW-Idri (see Fig. 7.13) and a soil surface where $\alpha_{OE} = 0.33$ the latter soil surface has 199 W·m^{-2} less available energy.

The term $\varepsilon\sigma T_0^4$ in eq. (5.2) can directly be calculated for each pixel of a satellite image (thermal infrared spectral range). For each pixel the value of the black-body equivalent surface temperature T^* is obtained, hence the emitted radiation term is obtained as $\sigma(T_0^*)^4$. More troublesome is the calculation of the term $\varepsilon'\sigma T_a^4$. The apparent emissivity ε' depends that much on weather conditions that it is of critical importance for the calculation of $(\varepsilon'\sigma T_a^4 - \varepsilon\sigma T_0^4)$ in eq. (5.2). This can easily be shown by calculating

Table 8.3. Net radiation R_n, surface radiation temperature T_0^*, incoming R_{sw} and reflected solar radiation R_{swr}, air temperature T_a, apparent radiation temperature of the atmosphere T_{sky} and apparent emissivity of the atmosphere ε', as determined from data measured on 16 (night) and 18 September (day) 1978 in the playa West-Idri

Local time	R_n	T_0^*	R_{sw}	R_{swr}	T_a	T_{sky}	$T_a - T_{sky}$	ε'
	$(W \cdot m^{-2})$	(K)	$(W \cdot m^{-2})$	$(W \cdot m^{-2})$	(K)		(K)	(-)
16 September 2.15 h	-57.1	289.2	-	-	295	278.2	16.8	0.79
18 September 13.45 h	399	309.2	755.4	313.6	305.1	303.1	2	0.97

the values of ε' on 16 September 1978 (night) and on 18 September 1978 (day), using the ground data collected at these times in the playa West-Idri (see Paragraph 6.2.4). To calculate ε', or alternatively the apparent radiation temperature of the atmosphere T_{sky} (defined by $\varepsilon'\sigma T_a^4 = \sigma T_{sky}^4$), night measurements of R_n and T_0^* are required, while day measurements of incoming and reflected solar radiation also are needed. The results are presented in Table 8.3, where it can be seen that during the night $\varepsilon' = 0.79$ and during the day $\varepsilon' = 0.97$. In terms of T_{sky} the difference is perhaps more impressive: $T_a - T_{sky}$ is 16.8 respectively 2 K, which further emphasizes the need for ground measurements. The difference between day and night is due to clouds, to dust and to the thermal infrared tail of solar radiation. Some 29.4 $W \cdot m^{-2}$ belong to the spectral region $\tilde{\lambda} > 3$ μm (THEKAEKARA, 1973), and with a transmittance of 0.75 this amounts to some 5% of R_n (Table 8.3, daytime). With the ε'-values in Table 8.3, R_n-values were calculated for each pixel of the HCMM-images (see Table 6.11).

Now the determination of the sensible heat term H in eqs. (5.1) and (5.3) will be discussed. In principle eq. (2.15) can be applied, but the surface temperature T_0 must be obtained from the surface radiation temperature T_0^*. Moreover, the resistance for sensible heat transport $r_{ah} = r_a$ must be determined. The first problem is easily solved by recalling that $\varepsilon = 0.97$ for desert and playa surfaces, as shown in Paragraph 5.3.2 and Fig. 5.12. Then eq. (5.23) can be applied.

The resistance r_a can be obtained by means of eq. (2.33). The values of ϕ_h and u_* can be calculated if the value of Ri is known (see Section 2.5). To

Table 8.4. Richardson number Ri, surface temperature T_0, friction velocity u_* and aerodynamic resistance r_a, as determined from data measured on 16 (night) and 18 September (day) 1978 in the playa West-Idri

Local time	Ri	T_0	u_*	r_a
	(-)	(K)	$(m \cdot s^{-1})$	$(s \cdot m^{-1})$
16 September 2.15 h	0.094	291.4	0.35	66
18 September 13.45 h	-0.1	311.5	0.21	40

derive u_* by means of eq. (7.11), the value of ϕ_m is required in addition to $\partial u/\partial z$. To calculate Ri by means of eq. (2.29) the gradient term $\partial \overline{T}_a/\partial z$ also is required. All these data were collected in the playa West-Idri in connection with the HCMM overpasses. In Table 8.4 the values of u_* and r_a for the same time periods as considered in Table 8.3 are presented. The ϕ-functions have been chosen, see Fig. 2.4 and PRUITT et al. (1973), as follows:

$\phi_m = 0.95(1 + 16 \text{ Ri})^{1/3}$ for stable and $\phi_m = (1 - 16 \text{ Ri})^{-1/4}$ for unstable conditions;

$\phi_h = 0.885(1 + 34 \text{ Ri})^{0.4}$ for stable and $\phi_h = 0.885(1 - 22 \text{ Ri})^{-0.4}$ for unstable conditions.

For pixels where $\alpha_0 > \alpha_{0E}$ the latent heat flux is zero at the soil surface. Since R_n and H have been obtained, the soil heat flux G_0 can be determined as the only unknown term of the surface energy balance equation eq. (5.43).

For pixels where $\alpha_0 \leq \alpha_E$ the surface energy balance equation holds in the form eq. (5.44). In this case the latent heat flux is to be calculated by means of eq. (2.18), where the vapour pressure at the soil surface e_0 can easily be calculated from T_0 and air relative humidity U_0. Namely $U_0 \geq 0.97$ (Paragraph 3.3.3), because $\alpha_0 \leq \alpha_E$. When salts are present U_0 will be lower (see also Section 2.2 and Paragraph 3.5.3). Hence, if the soil liquid phase is a salt saturated solution, as holds true for the playas around Idri (see Tables 6.6 and 6.7) then, with 0.75 as the relative humidity of air in equilibrium with a NaCl-saturated solution, $U_0 = 0.97 \cdot 0.75 = 0.73$. The resistance r_{av} in eq. (2.18) is taken equal to r_{ah}, thus also to r_a (see Section 2.5). Once the value of LE in eq. (5.44) is known, then G_0 can also be determined. The night- and daytime G_0-images can be combined with T_0-images to apply the procedures of Chapter 4. Some results will be given in Paragraph 8.4.2.

The procedures presented in this section have been applied to the HCMM images on 16 and 18 September 1978. The image of the sensible heat flux H on 18 September 1978 is presented as Plate 8. The reader should recall the discussion presented in Section 7.6 on the nature of sensible heat transport. The quick fluctua-

tions in surface temperature, e.g. ≈ 4 K, are a relevant percentage of the difference $T_0 - T_a = 6.4$ as given in Tables 8.4 and 8.3. Hence, see eq. (2.15), quite large fluctuations in H, 530 $W \cdot m^{-2}$ say, can be present in the pixels of Plate 8. Namely the H-value for the playa West-Idri calculated by that equation with the data in Tables 8.3 and 8.4 is 185 $W \cdot m^{-2}$, while in Plate 8 this playa lies in the green part, i.e. with H between 200 and 600 $W \cdot m^{-2}$.

8.2. USE OF GROUND REFERENCE MEASUREMENTS

8.2.1. Soil water balance at some specific points

Soil moisture content has been measured at a number of sites in the Wadi Ash Shati area. The data collection programme has been described in Paragraph 6.2.3 (see in particular Table 6.8). Locations of the sites are shown in Figs. 6.4, 6.12, 6.14 and 6.15. From these data the variation in soil moisture storage and the flux of capillary rise can be calculated and, therefore, the mean evaporation rate during relatively long time periods.

Measurement of soil moisture content. Because of the deadlines of the study as mentioned in Chapter 6, soil moisture data had to be collected within a relatively short time period, i.e. ten months.

In connection with the calibration procedure of the neutron probe used to determine θ, the values of $\chi = (1 - \chi_s)$, i.e. the total pore volume and of ρ_s, the soil dry bulk density are required. In Table 8.5

Table 8.5. Total pore volume χ and dry bulk density ρ_s as obtained for a number of undisturbed soil cores at different sites in the Wadi Ash Shati basin; for the location of the sites and the access tubes see Table 6.8 and Figs. 6.4, 6.12, 6.14 and 6.15

Access tube	Depth (m)	χ (-)	ρ_s ($kg \cdot m^{-3}$)
306	0.5	0.35	$1.50 \cdot 10^3$
	1.0	0.34	$1.59 \cdot 10^3$
701	0.5	0.45	$1.14 \cdot 10^3$
	1.0	0.47	$1.19 \cdot 10^3$
	1.5	0.38	$1.38 \cdot 10^3$
801	0.5	0.29	$1.80 \cdot 10^3$
901	0.5	0.28	$1.75 \cdot 10^3$
	1.0	0.26	$1.80 \cdot 10^3$
	1.5	0.25	$1.79 \cdot 10^3$
1201	0.2	0.30	$1.68 \cdot 10^3$
	0.4	0.38	$1.62 \cdot 10^3$
1301	0.5	0.36	$1.44 \cdot 10^3$
	1.0	0.42	$1.3 \cdot 10^3$
	1.5	0.39	$1.46 \cdot 10^3$

some values for a number of sites are presented. The χ-values have been used to obtain from determinations on weight basis the θ-values on volume basis. From these θ-data two calibration relationships were established: one for the soil layer between the surface and the 110 cm depth and a second one for the soil layer below 110 cm depth. The separation in these two layers has been done on the basis of the soil hydrological properties to be discussed below.

An example of some observed soil moisture pro-
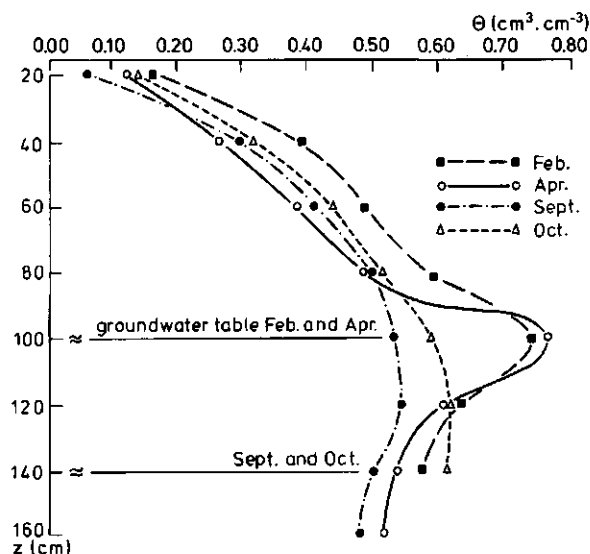
Fig. 8.1. Soil moisture content as measured in the playa West-Idri in access tube 104 during February through October 1978
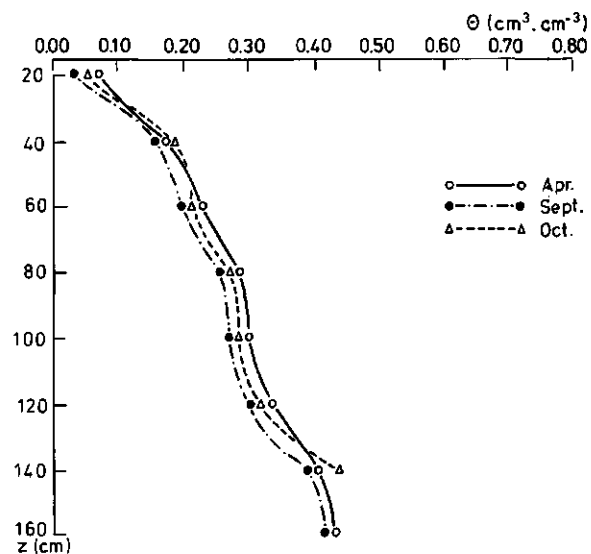
Fig. 8.2. Soil moisture content as measured in the playa NE-Idri in access tube 307 during April through October 1978

files has already been given in Fig. 4.5 for a sand dune. Here two more examples will be presented applying to the playas West and NE-Idri with a relatively high and a low groundwater table respectively. In Fig. 8.1 soil moisture content as measured in the access tube 104 in playa West-Idri is shown. The exceedingly high values observed at 1 m depth in February and April 1978 are probably due to the presence of the 1 m deep groundwater table in combination with a salt crust, as discussed below. Between February and September the shallow groundwater table was observed to draw down some 40 cm. Relatively high water tables, i.e. the February situation, tend to dissolve previously established crystallized salt layers and, therefore, to increase the total pore volume of the soil. The depth where such layers grow depends on the history of the shallow groundwater table depth. In Fig. 8.2 the results obtained in the playa NE-Idri for the access tube 307 are given. Here the depth of the groundwater table is about 1.60 m. It can clearly be seen that the soil moisture content remains fairly constant during the observation period. Such a conclusion is of particular relevance for the accuracy of the capillary rise approach (Paragraph 3.2.3) in determining evaporation in playas. The reader should be reminded here of the description given in Section 1.2 about the relation between groundwater table depth and surface characteristics of playas.

Soil hydrological properties. Soil hydrological properties (see Paragraph 3.5.3) have been determined for a number of undisturbed soil cores as described in Paragraph 6.2.3. A gradual variation with depth of the h(θ) relationship was observed in the soil profile sampled in the playa NE-Idri. This soil has at the 45 cm depth the h(θ)-curve characteristic of sandy soils, while at deeper depths ρ_s and clay content increase. At 180 cm depth this soil contains some 15% of clay particles. On the basis of these laboratory analyses the h(θ)-curves in Fig. 8.3 were chosen to be representative of the 110 cm upper soil layer respectively of the soil layer below this depth. In Fig. 8.4 the laboratory determined κ(h)-curves corresponding to the soil layers shown in Fig. 8.3 are presented. As can be seen κ(h)-values could be measured only up to $|h| = 210$ cm. Accordingly, and as already been discussed in Paragraph 3.5.3, κ(h) can safely be used for playa soils with shallow ground groundwater tables.

The θ(z) and h(z) profiles in playa soils relate to steady-state conditions, the rôle of hysteresis (see also Paragraph 3.5.3) is neglected and κ(θ) = κ(h).
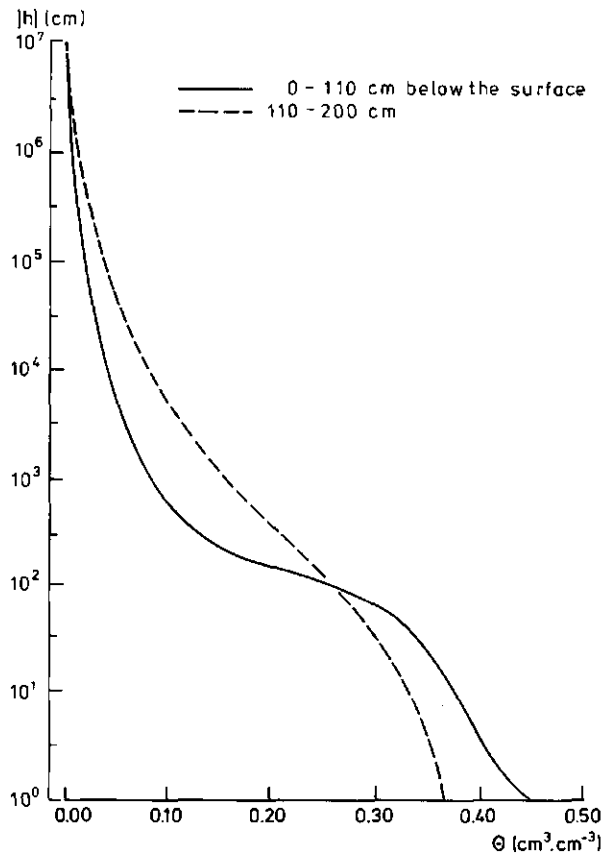
Fig. 8.3. Soil water retention curves h(θ) of a soil profile (see Paragraph 6.2.3) in the playa NE-Idri: layer between the soil surface and 110 cm depth respectively between the 110 cm and 200 cm depth

Capillary rise and evaporation. The curves presented in Figs. 8.3 and 8.4 have been determined under laboratory conditions, i.e. at 20°C and zero solute concentration. Therefore to account for the different soil temperatures and salt concentrations occurring in the playas around Idri, corrections must be applied by means of the equations given in Paragraphs 3.2.1 and 3.5.3. According to the soil temperature data collected at the Idri weather station (see Paragraph 6.2.2 and Fig. 6.12) in the time span applying to the soil moisture data collection, the mean soil temperature (at 90 cm depth) was about 30°C. The correction that must be applied to the κ(h)-curve can be obtained from Table 3.3, as applying to the NaCl-saturated soil liquid phase. The resulting correction is 0.93. Now z(h)-functions can be calculated by means of eq. (3.23) for various fluxes $v_{w,i}$. The graphs of these functions are presented in Fig. 8.5. The nomogram allows to determine a particular liquid water flux corresponding with a particular $|h|$-value measured at a specific distance above the water table. Since θ is measured in the field instead of h, the h(θ) curves in Fig. 8.3 are needed

159
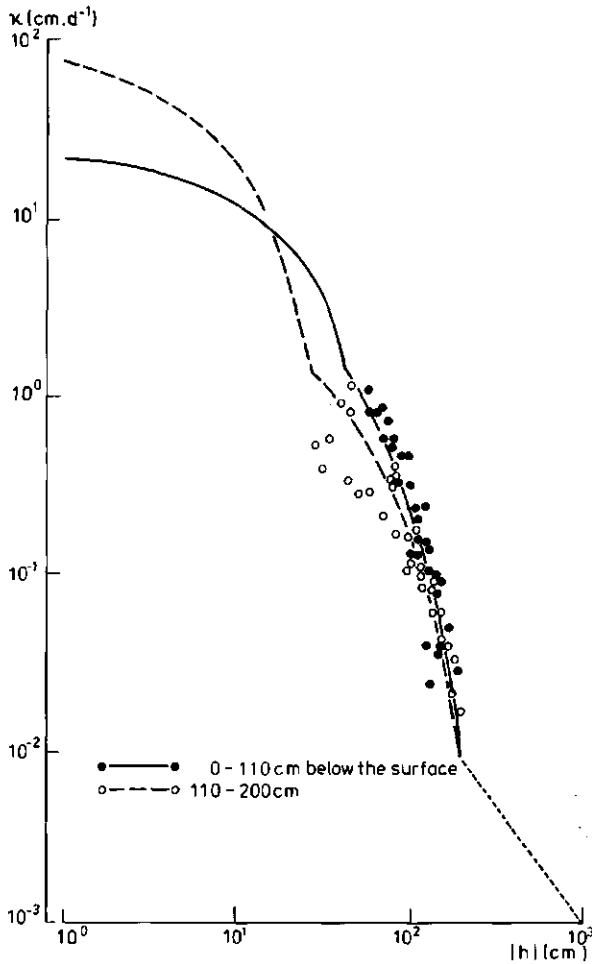
Fig. 8.4. Unsaturated capillary conductivity $\kappa(h)$-curves of the soil profile in the playa NE-Idri mentioned in Fig. 8.3: layer between soil surface and 110 cm depth respectively between the 100 cm and 200 cm depth

to enter Fig. 8.5. Here, as above for $\kappa(h)$, a correction must be applied to $|h|$ to account for the difference between playa and laboratory conditions. For example the correction coefficient for $|h| \approx 10^2$ cm, $T \approx 30°C$ and a NaCl-saturated soil liquid phase, is 0.95.

This approach remains reliable insofar the soil moisture distribution corresponds to a steady state. The soil moisture profiles given in Figs. 4.5, 8.1 and 8.2 indicate that this is true indeed. A further proof of this statement is provided by the results obtained by means of the soil water flow simulation model SWATR of FEDDES et al. (1978). The progression in soil moisture content was simulated under constant boundary conditions: a constant groundwater table depth z_{gw} and constant potential evaporation, with as initial condition $h = z - z_{gw}$. After a three-month simulation period the calculated $h(z)$ and $\theta(z)$-profiles were found to attain a constant configuration. The simulation study was carried out for various z_{gw}-values. In Fig. 8.6 the calculations are compared with the measured $\theta(z)$-profile for the access tube 305 (see Table 6.8 and Fig. 6.15) in the playa NE-Idri. The fair agreement between calculations and measurements definitely confirms that the steady state approximation of soil water flow in playas is correct.

An additional, useful result obtained by means of the soil water flow simulation model is a relationship between the shallow groundwater table depth and the ratio of actual to potential evaporation (relative evaporation). The latter ratio is a direct output of the SWATR model calculations. The values of the relative evaporation against the z_{gw}-values are presented in Fig. 8.7. It can be seen that soil water flow keeps pace with the potential evaporation rate up to
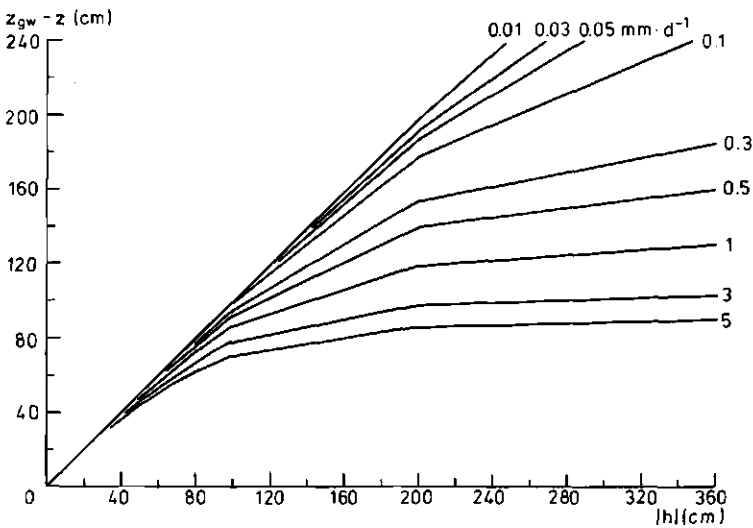
Fig. 8.5. Steady-state solutions $z_{gw} - z(h)$ of eq. (3.1) for various fluxes of capillary rise; soil hydrological properties of the soil profile in the playa NE-Idri mentioned in Figs. 8.3 and 8.4
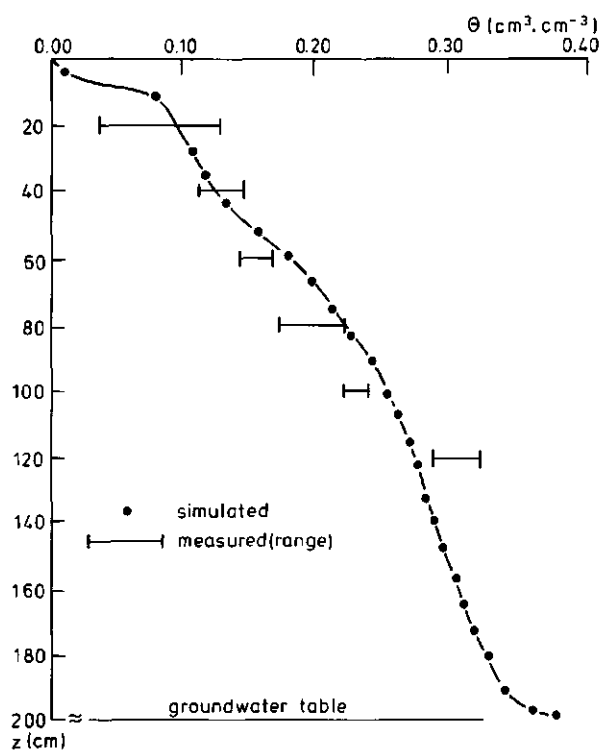
Fig. 8.6. Comparison between soil moisture content as measured on 18 through 25 February 1978 in the playa NE-Idri (access tube 305) and calculated for the same period by the soil water flow simulation model SWATR
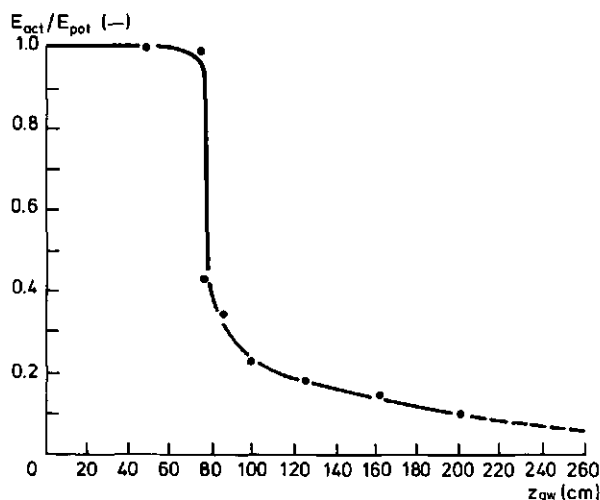
Fig. 8.7. Ratio of actual to potential evaporation versus groundwater table depth, as calculated by means of the soil water flow simulation model SWATR

a 70 cm deep groundwater table, then a sharp drop in relative evaporation occurs.

Actual soil evaporation was calculated by the soil water balance method (see for instance FEDDES, 1971) at a number of sites, where soil moisture content was measured and the contribution of capillary

Table 8.6. Actual soil evaporation as determined by the soil water balance method at a number of sites in the Idri playas in the period February through October 1978; z_{gw} for playa West-Idri ≈ 1 m, for NE-Idri ≈ 2 m; for location of access tubes see Figs. 6.14 and 6.15

	Site						
	playa West-Idri in access tube				playa NE-Idri in access tube		
	102	103	104	105	301	302	307
E_{act} (mm·d^{-1})	2.6	2.9	2.6	3.9	0.2	1.1	1.1

rise taken into account as described above. The results are presented in Table 8.6. The reduction in soil evaporation due to the deeper groundwater table in the playa NE-Idri is quite evident. No explanation can be given for the lower evaporation rate obtained for the access tube 301 in comparison with the values obtained at the other sites. In all the cases which were considered the contribution to evaporation due to variations in soil water content was found to be much smaller than the contribution due to capillary rise from the groundwater table.

8.2.2. Energy balance, soil heat flux and actual evaporation in a playa soil

In Section 2.5 it was shown that for desert conditions the Bowen ratio - energy balance method (described in Section 2.3) can be used to measure actual evaporation.

The following scheme for the calculation procedure is to be considered:

- if $z_E = 0$ $(\theta_0 \geq \theta_E)$ eqs. (2.6) and (2.27) must be applied to calculate potential evaporation, with heat flux G_0;
- if $z_E > 0$ $(\theta_0 < \theta_E)$ eqs. (2.14) and (2.25) must be applied to calculate actual evaporation, with heat flux G_E.

In the latter case calculations can in principle only be worked out over periods in which heat storage between soil surface and depth z_E can be neglected.

From the data listed in Paragraph 6.2.4 one is able to calculate evaporation from the soil by means of the eqs. (2.6), (2.14), (2.25) and (2.27) following the scheme given here above. The bottle-neck in these procedures is the determination of the soil heat fluxes G_E and G_0. In this respect direct measurements by means of heat flux plates are not of much help as has been discussed in Paragraph 4.1.1. The point is that whatever method is followed the value
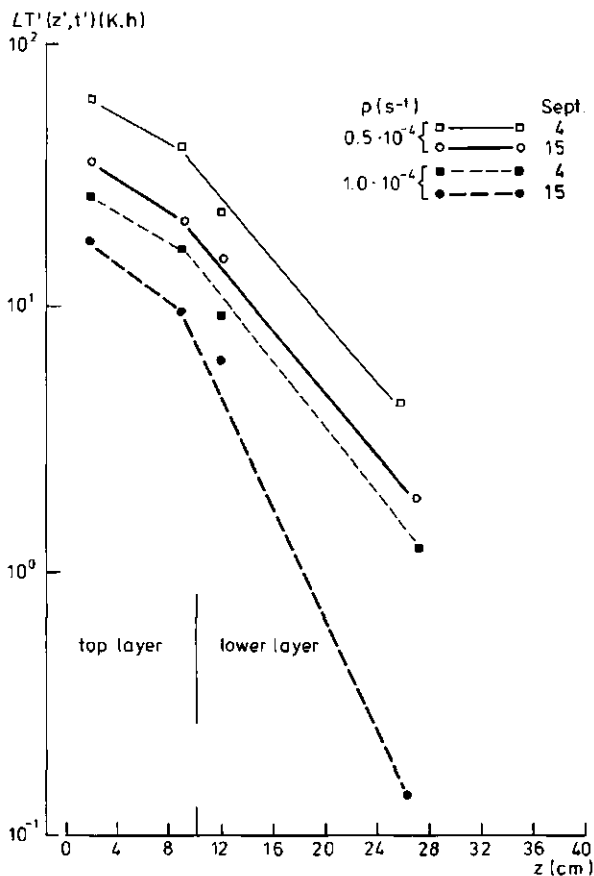
Fig. 8.8. Laplace transform $LT'(z',t')$ of temperature measurements at different soil depths in the playa West-Idri, September 1978

of the apparent soil thermal conductivity λ'_s always is to be known. This conductivity is needed either to correct the measured heat flux through a transducer G_{me} by means of eq. (4.1), or to calculate the flux from measured soil temperature gradients (Section 3.4). Moreover, the conductivity λ'_s as defined by eq. (3.53) is related to the convective heat transfer in the soil by eq. (3.49). As already has been shown in Paragraph 4.1.1, the determination of λ'_s on some routine basis and under the conditions actually present in the field, does not seem to be feasible. Determination of the apparent soil thermal diffusivity $a = \lambda'_s/(\rho c)'_s$ from soil temperature measurements is a much more promising approach (see Paragraph 3.5.1) to derive the soil heat fluxes G_E and G_0.

Calculation of the apparent soil thermal diffusivity a.
The line of attack is to apply the procedure C of Paragraph 3.5.1 to obtain the apparent soil thermal diffusivity a at different depths by calculating the Laplace transform $LT'(z',t')$ of the soil temperature measurements. In Fig. 8.8 the values of this trans-

form at the 2, 4, 9, 12 and 27 cm depths are shown, as calculated from soil temperature data collected by the present author in the playa West-Idri on 4 and 15 September 1978. The transforms of these temperature measurements have been calculated according to eq. (3.65) using two values for the exponent p. It can clearly be seen that for the four lines relating to these dates the difference in slope above and below 9 cm depth indicates the presence of an upper and lower soil layer (9 to 27 cm), showing different thermal diffusivities. The a-values obtained by means of eq. (3.66) are presented in Table 8.7. Other ways of deriving a, are through the Green's function of the eq. (3.53), i.e. by means of eq. (3.63) and through the ratio of the temperature amplitudes, eq. (3.60). The results of these calculations also are presented in Table 8.7. As the Green's function method applies to the entire measured temperature profile only one a-value can be derived. The results obtained from the ratio of temperature amplitudes are quite different from the ones obtained by the first mentioned method. The reason is that the temperature fluctuations in the test-site area cannot be approximated by a single-frequency harmonic, as for instance shown in Fig. 7.25. Although the a-values found by the various methods differ from each other, the difference in apparent thermal diffusivity between the top and lower soil layer is confirmed. This conclusion is supported by results obtained from temperature data collected by the present author in playas West and NE-Idri on other days. Because the Laplace transform method is suitable for transient temperature variations and a-values are obtained at different soil depths, which is impossible with the Green's function method, the first mentioned method must be considered the most convenient one to determine the thermal diffusivity a.

From the obtained values of a, the required values of the apparent soil thermal conductivity λ'_s can be calculated. The soil heat capacity $(\rho c)_s$ in $\lambda'_s = a(\rho c)_s$ is calculated by means of eq. (3.54), but two

Table 8.7. Soil apparent thermal diffusivity a $(m^2 \cdot s^{-1})$ as determined from soil temperature measurements at different depths in the playa West-Idri in September 1978

Method	Top layer (0-9 cm)		Lower layer (9-27 cm)
Laplace transform by eq. (3.66)	$1.5 \cdot 10^{-6}$		$2.7 \cdot 10^{-7}$
Green's function by eq. (3.63)		$4.5 \cdot 10^{-7}$	
Ratio of temperature amplitudes by eq. (3.60)	$0.6 \cdot 10^{-6}$		$1 \cdot 10^{-7}$

Fig. 8.9. Soil heat flux G in the playa West-Idri on 11 September 1978, as calculated according to four procedures: G_0' by means of eq. (4.1), with λ_s' obtained by means of eqs. (3.66) and (3.54); G_0'' from soil temperature measurements, with λ_s' calculated by means of eq. (3.49) to account for thermal convection of soil air; G_0''' from soil temperature measurements, with λ_s' obtained by means of eqs. (3.66) and (3.54); G_E from soil temperature measurements with λ_s' obtained by means of eqs. (3.66) and (3.54). The soil heat flux measured in the top soil layer G_{me} also is shown
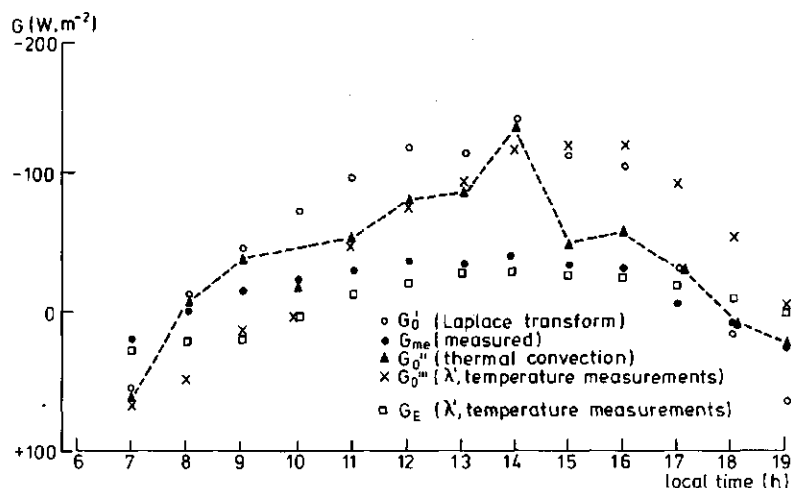
simplifying hypotheses then have to be accepted. Firstly the possibility of heat storage in the adsorbed water phase (see Paragraph 3.5.2 and Fig. 3.17) is neglected. Secondly, for the case $z_E > 0$ the contribution of evaporation to the apparent soil heat capacity $(\rho c)_s'$, as defined by eq. (3.50), also is considered negligible. In accordance with these two simplifications, the following values of λ_s' have been obtained:

- for the 0 to 9 cm soil layer: $\lambda_s' = 1.6 \text{ W·m}^{-1}\text{·K}^{-1}$;
- for the 9 to 27 cm soil layer: $\lambda_s' = 0.33 \text{ W·m}^{-1}\text{·K}^{-1}$.

The value applying to the actually dry top layer is much larger than the values known to apply to dry soils. The reason is to be sought in the rôle of the thermal convection above the evaporation front (see Paragraph 3.4.4).

Calculation of the soil heat fluxes G_0 and G_E. The λ_s'-values derived so far can now be applied to calculate the soil heat flux above and below the 9 cm depth. Two approaches will be followed:

- application of eq. (4.1) to correct the soil heat flux G_{me}, as measured by plate transducers in the 0 to 9 cm depth layer; the correction factor to be obtained will be either a constant when taking $\lambda_s' = 1.6 \text{ W·m}^{-1}\text{·K}^{-1}$, or a function of time when calculating λ_s' from measurements by means of eq. (3.49);
- calculation of the heat flux G_0 from soil temperature measurements taking $\lambda_s' = 1.6 \text{ W·m}^{-1}\text{·K}^{-1}$ and calculation of the heat flux G_E taking $\lambda_s' = 0.33 \text{ W·m}^{-1}\text{·K}^{-1}$.

In Fig. 8.9 soil heat fluxes calculated according to the procedures mentioned above are presented, along

with the measured flux G_{me}. All the data relate to the playa West-Idri on 11 September 1978.

The flux G_0', above z = 9 cm, has been calculated from the soil heat flux measurements. Taking into account the thermal conductivity and the shape of the particular heat flux plate used in the field experiments, and using $\lambda_s' = 1.6 \text{ W·m}^{-1}\text{·K}^{-1}$ (see eq. 4.1), a value of about 3 was obtained for the ratio G_0/G_{me}. If the same plate had been placed in the lower 9 to 27 cm layer, the ratio G_s/G_{me} would have been 0.8.

The flux G_0'' in the 0 to 9 cm layer, has been calculated from the same soil heat flux measurements, but applying eq. (3.49) to calculate λ_s'. Accordingly a time dependent correction is obtained by means of eq. (4.1). As regards the use of eq. (3.49) two points have to be made clear. The first is that this equation, as it is written, applies to dry air. For moist soil air, therefore, first the virtual temperature T_{vi} must be calculated from T_s and then ρ_a calculated at T_{vi}. The second point relates to the simultaneous and contrary transport of heat and vapour, the working of which has been depicted in Fig. 3.14. The convective coils shown in that figure are not a rigid and stable structure (see the discussion on the fast variability of heat exchanges at the soil surface, presented in Section 7.6). Soil temperature measurements collected at a fixed point, as applied in this paragraph, will therefore relate at different time instants to either the upwelling or to the downwelling branch of the thermal convective coil. Hence when such measurements are entered in the one-dimensional eqs. (3.46) and (3.48) (see Paragraph 3.4.2 and Fig. 3.10) either a negative or a positive velocity v_{za} will be obtained. Notwithstanding this the convective coil is still carrying heat downwards and vapour upwards. It can therefore be concluded that when fixed

163

point measurements are being used to calculate λ'_s from eq. (3.49), the absolute value of the first term at the right hand side must be taken. The λ'_s-values obtained in this way were found to be comparable with the figures obtained via the Laplace transform method.

Accordingly it can be concluded that z_E = 9 cm and that above this depth the thermal convective process as described in Paragraph 3.4.4 occurs. Thus to calculate the virtual temperature T_{vi} of soil air, the relative humidity at z = z_E will be taken to be equal to 0.97 ·0.75 = 0.73. The humidity value of 0.97 is obtained with r_m = $5 \cdot 10^{-8}$ m (see Paragraph 3.3.3). The humidity value of 0.75 accounts for the soil liquid phase in the Idri playas being a NaCl saturated solution (see also Table 3.3). At the soil surface the vapour pressure e, as needed in eq. (3.39) has been obtained by assuming that the saturation deficit of the soil air at the surface was equal to the deficit of the air as measured 30 cm above the soil surface. The value of the specific permeability K in eq. (3.49) has been taken to be the mean of the K-values considered in the text relating to Figs. 3.15 and 3.16. The λ'_s-values thus obtained are a function of time, because the gradient term in eq. (3.49) is time dependent. The correction obtained by means of eq. (4.1) therefore also is time dependent.

Back again to Fig. 8.9: the soil heat flux G_0''' has been calculated from soil temperature measurements on 11 September 1978 by applying the λ'_s = 1.6 $W \cdot m^{-1} \cdot K^{-1}$ value obtained via the Laplace transform of the data on 15 September 1978.

Finally the soil heat flux G_E (see eq. 2.13), has been calculated from the soil temperature measurements on 11 September 1978 with λ'_s = 0.33 $W \cdot m^{-1} \cdot K^{-1}$.

The most important conclusion that can be drawn from Fig. 8.9 is that the complications concerning the determination of the soil heat flux are no minor nuisances. Secondly, eq. (3.49) properly accounts for the effect of thermal convection on G_s, with K =

$1.8 \cdot 10^{-9}$ m^2. Furthermore, at least in this case the uncorrected measurements of the soil heat flux G_{me}, at some 1 to 2 cm depth, give an indication of G_E at z_E = 9 cm. This, however, holds true only for the particular plate which was used.

In Paragraph 8.1.3 it was shown that the soil heat flux G_0 can be calculated from a combination of satellite data and ground measurements. It is, however, clear that in the areas where z_E > 0 (the boundaries of which can be established by means of the procedure presented in Paragraph 8.1.2), the heat flux G_E is needed for the calculation of the latent heat flux LE by the Bowen ratio method (eq. 2.14). One possible solution of this problem is the application of the apparent soil thermal admittance approach as presented in Chapter 4 and as further discussed in Paragraph 5.4.4 and Section 5.5. A second, much simpler, solution is by making use of soil temperature measurements for the evaluation of the ratio G_E/G_0 and next to apply this ratio to the G_0-images obtained from satellite data, by means of the procedure presented in Paragraph 8.1.3. From the data collected in the playa West-Idri the present author found that on a daily basis (24 hours) $G_E \cong 0$ and that the value of G_E/G_0 for shorter time periods varies between 0.15 and 0.20.

Calculation of actual soil evaporation LE. It is now possible to calculate the latent heat flux according to the scheme given at the beginning of this paragraph. The different determinations of the soil heat flux G_s, discussed above and presented in Fig. 8.9 will be applied in the calculation of LE. To obtain hourly values of LE, the Bowen ratio energy balance method, see eqs. (2.6) and (2.14) will be applied. For daily (24 hours) values the combination equation, eq. (2.25), will be used.
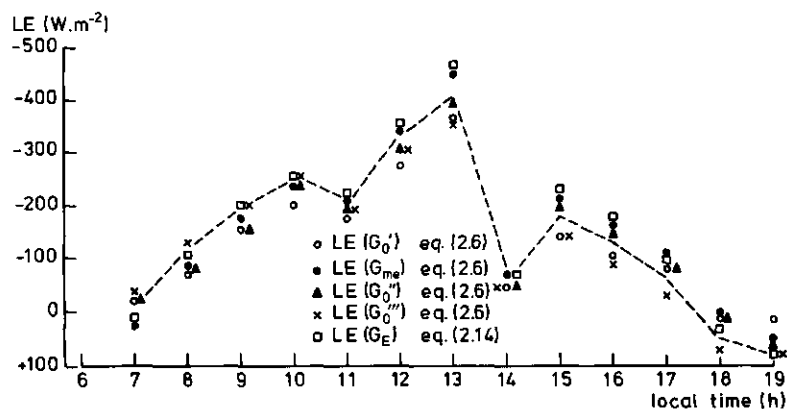
Fig. 8.10. Latent heat flux LE in the playa West-Idri on 11 September 1978, as calculated by means of the Bowen ratio energy balance method, taking the soil heat flux as given in Fig. 8.9

In Fig. 8.10 the LE-values as calculated by means of eq. (2.6) and eq. (2.14) from the data collected on 11 September 1978 in the playa West-Idri are presented. As soil evaporation took place below the soil surface, eq. (2.6) does not apply. Calculations by means of eq. (2.6) are only presented to illustrate what size the deviations in LE may have due to wrong assessment of the depth of the evaporation front z_E. When looking at the data in Fig. 8.10, one sees that the largest difference between the various calculation procedures is 100 $W \cdot m^{-2}$.

On a daytime basis (7 through 19 h local time), the evaporation rate amounts to 2.5 mm with G_E and 3.0 mm with G_0. A difference in the daytime evaporation of 0.5 mm is within the accuracy of the Bowen ratio energy balance method used and therefore may look not relevant. This, however, is definitely not the case. As discussed in Section 1.1 a difference of 0.5 mm in the mean actual daily evaporation rate is a full order of magnitude larger than the accuracy required to judge projected water consumptions in deserts.

From Fig. 8.10 it can be seen that the means of the $LE(G_0'')$ values, i.e. eq. (2.6), and the $LE(G_E)$ values, i.e. eq. (2.14), are close to the $LE(G_0'')$ values, i.e. with the soil heat flux calculated by means of eq. (3.49).

The means of $LE(G_0'')$ and $LE(G_E)$ give the best estimation of LE for the following reasons. $LE(G_0'')$, as calculated by means of eq. (2.6), yields an underestimation of LE, when evaporation takes place inside the soil. On the other hand the $LE(G_E)$ values are overestimates of LE. To understand why this occurs, one should recall (see Section 2.3) that $G_0 = LE + G_E +$ + storage. So $G_0 > (G_E + \text{storage})$, which implies that $R_n + G_0$, to be used in eq. (2.6), is a quantity lower than the correct one, i.e. $R_n + G_E$ - storage. When eq. (2.14) is used with G_E the quantity $R_n + G_E$, contrariwise, is larger than it should be, i.e. $R_n + G_E$ - storage.

Another important conclusion which can be drawn from Fig. 8.10 relates to the thermal convection model of evaporation as presented in Paragraph 3.4.4. Firstly it should be noted that the larger part of evaporation losses occurs from 7.00 to 13.00 hours. This is to be expected from the theory discussed there, because in that part of the day the largest differences in virtual temperature exist between the evaporation front and the soil surface. Secondly the LE-values, relating to λ_s' from eq. (3.49), agree quite well with the means of $LE(G_0'')$ and $LE(G_E)$ presented in this paragraph. It might be helpful for the reader to recall that the values of thermal conductivity λ_s', and thus of G_s, as obtained by means of eq. (3.49), do not involve the use of either the results of the Laplace transform

method or the field measurements of the soil heat flux.

To conclude the discussion on the application of micro-meteorological methods to determine actual evaporation in playas it will now be shown how the combination method, eq. (2.25), is to be applied. Because in the derivation of this equation the heat storage in the soil layer above the evaporation front has been neglected, eq. (2.25) can only be used when taking the daily mean values of the variables involved. The determination of the resistances $r_{ah} = r_{av} = r_a$ has already been discussed in Paragraphs 2.5 and 8.1.3. The resistance r_{sh} can directly be obtained by means of eq. (2.17) with $z_E = 0.09$ m and $\lambda_s' = 1.6$ $W \cdot m^{-1} \cdot K^{-1}$, $r_{sh} = 5.62 \cdot 10^{-2}$ $W^{-1} \cdot m^2 \cdot K$. The resistance r_{sv} can be calculated as $r_{sv} = z_E / D_{eff}$, where the soil effective vapour diffusivity D_{eff} can be obtained from the convective velocity of soil air v_{za}, calculated from λ_s' by means of eq. (3.45). The vapour flux through the soil surface can be determined as $\rho_v v_{za}$ and D_{eff} is finally estimated by inverting eq. (3.13). The result is $r_{sv} = 41$ $s \cdot m^{-1}$ which applies to the data collected in the playa West-Idri on 11 September 1978.

In Table 8.8 the mean LE-values as calculated according to the three procedures mentioned are presented. It can be seen that the $\overline{LE}$-value obtained through the thermal convection model agrees quite well with the mean of $LE(G_E)$ and $LE(G_0'')$, i.e. with eqs. (2.14) and (2.6). The difference with the result of eq. (2.25), which is an average figure pertaining to 24 hours, is likely to be due to the different time period.

Table 8.8. Daily integrals of latent heat flux LE and actual soil evaporation E_{act}, as calculated with the data collected in the playa West-Idri on 11 September 1978, according to three different procedures

	Method		
	mean of $LE(G_E)$ and $LE(G_0'')$ (eq. 2.14 resp. 2.6)	mean of $LE(G_0'')$, with λ_s' from thermal convection model (eq. 3.49)	daily mean of LE by combination equation (eq. 2.25)
$\int LE$ ($J \cdot m^{-2} \cdot d^{-1}$)	$6.6 \cdot 10^6$	$6.6 \cdot 10^6$	$8.0 \cdot 10^6$
E_{act} (mm)	2.7	2.7	3.3

8.3. COMBINED APPLICATION OF SATELLITE AND GROUND REFERENCE MEASUREMENTS

In Paragraph 8.1.3 use of ground reference mea-surements has already been made to determine some of the coefficients and variables required to calculate areal patterns of the terms in the surface energy balance equation. After the results presented in Section 8.2, as obtained from ground-based measure-ments, it is now possible to illustrate in more detail the combined use of satellite and ground reference data. Such a discussion is very much needed before the results of calculations involving satellite data can be presented (Section 8.4). In that stage the reader must have not only a clear notion of the direct outcome of the satellite data, but also of how dead-end steps in calculations relying on satellite data only, are solved by making use of ground-based data. It must be stated clearly that not a single one of the fluxes appearing in the surface energy balance equation can be calculated directly from satellite data only. Additional data must either be measured at the ground or guessed.

Requirements of ground reference data differ ac-cording to the procedures presented in Paragraphs 8.1.1 through 8.1.3. In Paragraph 8.1.1 ground-based measurements of surface reflectance, surface radia-tion temperature and actual evaporation were used to derive by means of eqs. (5.55) and (8.2) simple ex-pressions to calculate actual evaporation from satel-lite data.

In this way the separation in two subsequent steps, the first involving ground-based data, the second requiring satellite data, is clear-cut. The coefficients of α_0 and T_0 in the eqs. (8.3) through (8.7) have been determined by measuring on the ground the latent heat flux LE together with α_0 and T_0. The LE-values have been measured by means of the Bowen ratio energy balance method, as described in Paragraph 8.2.2. Next the areal pattern of actual evaporation can be calculated from satellite data only. The accu-racy obtained in the areal pattern of LE is satisfac-tory for the kind of surfaces which have been covered by the ground experiments. In Fig. 8.11 for example, actual evaporation rates, as calculated for a specific case (see Paragraph 8.1.1) by means of eq. (8.7), which was derived with the aid of eqs. (5.55) and (8.2), are compared with values measured by applying the Bowen ratio energy balance method. The data in Fig. 8.11 relate to the sites and periods given in Table 6.9. It can be seen that the agreement is rather satisfactory, especially when recalling that these data apply to quite different surface types and peri-
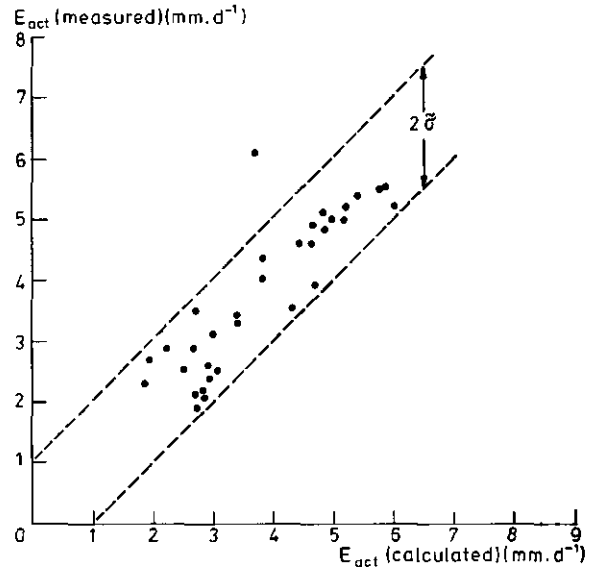
Fig. 8.11. Measured versus calculated (eq. 8.7) evap-oration rates. A spread equal to twice the standard deviation also is shown (broken lines)

ods of the year. It must be borne in mind that the lin-ear approximation procedure of the energy balance equation as presented in Paragraph 8.1.1 relies for its accuracy entirely on ground reference data. This procedure, however, is quite straightforward to apply to α_0- and T_0-images calculated from satellite data in the 0.4 to 1.1 µm respectively the 10.5 to 12.5 µm spectral range.

The 'θ_E and α_{0E}' procedure as presented in Para-graph 8.1.2 to establish whether in a given area evap-oration takes place at the soil surface or below it, makes a rather different use of ground reference data. The ground segment of the procedure ends with the determination of the threshold reflectance α_{0E}. Next an α_0-image calculated from satellite data only, can be divided in two parts as shown in Plate 7: pixels where $z_E = 0$ belong to a class and pixels where $z_E > 0$ to a second class. The data required in going through the ground segment of the procedure cannot be related to satellite data. Namely both the h(θ) curves, as needed to obtain θ_E, and the total pore volume, as required to calculate α_{0E} by means of eq. (5.28), must be known.

Only the value of α^0_{dry}, which also is required in eq. (5.28), can in principle be obtained from both satellite and ground reference measurements. As re-gards satellite data one can choose a dry-surface-sample in an α_0-image and use the mean α_0 in this sample as α_{dry}. A more reliable solution remains that of taking the ground measured surface reflectance and moisture content.

Point ground reference data always are needed to verify whether the established partition of the territory into areas where $\alpha_0 \leq \alpha_{0E}$ and where $\alpha_0 > \alpha_{0E}$ is correct. This can be illustrated by the ground measured reflectances of playa surfaces presented in Fig. 7.15. There it can be seen that the variation in α_0 when going from wet (playa NNW-Idri) to dry playas (playa NE-Idri), confirms the concept underlying eq. (5.28), but it also is clear that large variations in surface reflectance bearing no relationship with moisture content at all, may occur. The reflectance of the playa NNW-Idri is much lower in September because of the greater turbidity of the water. The reflectance of the playa NE-Idri also was lower in September, because the salt crust was not present anymore (see also Plate 6).

When α_p-values, i.e. satellite data, as shown in Plate 7, are used to define the above described partition, the ground-reference measurements are needed to assess the differences between α_0 and α_p-values (see also Sections 5.2 and 7.5).

To conclude the comments on the mapping of areas with sub-surface evaporation, it must be recalled that the resolution of the particular satellite data to be used, is of relevance. As can be seen in Tables 7.12 and 7.13, the variation in $\overline{\alpha}_p$-values over the Idri playas as measured by the LANDSAT respectively HCMM satellite is rather different. It is largest in the LANDSAT data. Again the readiest help at hand is to be expected from ground measured α_0-values.

The integration of ground and satellite measured data is at its best when applying the procedure described in Paragraph 8.1.3. There, in the outline of the procedure, use of some particular ground reference data has already been mentioned. In the following, more attention will be paid to the extrapolation of point ground estimated transport coefficients for heat and vapour flow, to different parts of the area covered by a particular satellite image.

As regards weather data it has already been stated that air temperature T_a and humidity U always are needed. The apparent emissivity of the atmosphere ε' can in principle be calculated from T_a and U by means of various formulae proposed in literature. The present author observed, however, for the specific case of the HCMM images in Plate 2 (16 September 1978, night) that unreliable results then may be obtained. Namely, the longwave radiation flux calculated from HCMM-TIR data was directed towards the surface while the ground measured flux was directed outwards. Such a result is of course due to the values of either ε', or T_{sky} calculated too high (see Paragraph 8.1.3). Only by making use of ground reference data (see Table

8.3), correct results could be obtained.

The main difficulty in applying the surface energy balance equation (eq. 5.4) to calculate latent heat flux, is the determination of the resistance r_a to transport of heat and vapour in the atmosphere and of the coefficient of heat transfer in the soil (the latter is required to obtain G_E from G_0, see Paragraph 8.2.2). There is no rigorous solution to this problem. Therefore a practical solution, relying on ground reference data, now will be proposed.

In literature some models have been presented (see Paragraph 5.4.3) to calculate from the satellite measured surface temperature either actual evaporation or surface moisture content. Usually two key-assumptions then are made: the soil thermal properties have to be specified to simulate the progression of soil temperature, and the surface temperature (of each pixel) is used in combination with air temperature (at a single weather station, at one height) to calculate r_a by means of flux - profile relationships (see Section 2.5). By making use of the data collected in the Idri playas it easily can be shown that with this approach unreasonable values for stability parameters as the Richardson number Ri are obtained. This result is already to be expected on theoretical grounds.

The use of data helps to clarify this even more. For that purpose the air temperature and wind speed data as measured on 3 September 1978 at heights of 0.3 and 2 m above the soil surface respectively in the playas West and NE-Idri have been used by the present author. It was found that during the hottest part of the day (large atmospheric instability) in the playa West-Idri, Ri was between -0.2 and -0.5 and in the warmer playa NE-Idri, Ri varied between -0.1 and -1.0. At the latter site surface radiation temperature was as high as 333 K. When Ri was calculated taking the soil surface as the lowest level and applying the same wind velocity gradient as present at the given heights above the soil surface, unreasonably large Ri-values were obtained. If the wind velocity at some level very close to the soil surface was assumed to be zero, unreasonably small Ri-values (near neutral conditions) were obtained. Accordingly, in the present author's opinion, there is little point in setting up involved data-crunching procedures in order to balance the energy fluxes at the soil surface, when solving eq. (5.4) to obtain the latent heat flux.

A more correct solution proposed by the present author is by directly applying ground measurements of T_a and u at two heights. From these data, the mean friction velocity $\overline{u}_*$ (calculated as described in Paragraph 8.1.3) and the mean resistance value $\overline{r}_a$ have

Table 8.9. Mean values of friction velocity $\bar{u}_*$, re-sistance to transfer of heat and vapour in the atmo-sphere $\bar{r}_a$, air temperature $\bar{T}_a$ and surface radiation temperature $\bar{T}_0$, as determined from data collected in the playa West respectively NE-Idri between 12.00 and 15.00 hrs on 3 september 1978

Site	$\bar{u}_*$	$\bar{r}_a$	$\bar{T}_a$	$\bar{T}_0$
	$(cm \cdot s^{-1})$	$(s \cdot m^{-1})$	(K)	(K)
Playa West-Idri	17	35.5	313.3	316.2
Playa NE-Idri	13	11.5	312.7	327.2

been obtained on 3 September 1978 for the period 12.00 through 15.00 hrs for the playas West and NE-Idri. The data $\bar{u}_*$, $\bar{r}_a$ and the measured $\bar{T}_0$ are present-ed in Table 8.9. It can be seen that the $\bar{r}_a$-value of the playa NE-Idri is much lower than the one above the playa West-Idri. This result was to be expected because of the larger differences between surface and air temperature observed in the playa NE-Idri. The $\bar{r}_a$-values in Table 8.9 can be applied to estimate the variation of $\bar{r}_a$ across a thermal infrared image of playas. From the $\bar{r}_a$ and $\bar{T}_0$-values one immediately can derive that the ratio $\delta\bar{r}_a/\delta\bar{T}_0 = -2.2$ $s \cdot m^{-1} \cdot K^{-1}$. This figure can be applied to calculate from satellite data images of the terms in the surface energy bal-ance equation. Results of such calculations will be presented in Section 8.4.

The second point to be adressed relates to the areal variability of soil thermal properties. An ap-proach to tackle this problem has been presented in Chapter 4. Since the soil heat flux can be calculated (see Paragraph 8.1.3) from satellite data without re-quiring that soil thermal properties are preliminarily known, the apparent thermal admittance can be obtain-ed by means of eq. (4.17). An example will be given later on in Section 8.4. Here it is only mentioned that the multi-temporal approach (see Section 4.3) could not be applied because of inherent difficulties in the mutual registration of METEOSAT-TIR images (see Section 7.2). It has, however, been possible to determine the soil apparent thermal diffusivity from soil temperature measurements collected at two sites, as described in Paragraph 8.2.2. In Table 8.10 the values of the mean resistances to transport of heat $\rho_a c_p r_{sh}$ and of vapour in the soil r_{sv} are shown, to-gether with the estimated depth of the evaporation front z_E. To calculate $\rho_a c_p r_{sh}$, the λ_s'-value has been calculated from thermal diffusivity and heat capacity: $\lambda_s' = a(\rho c)_s$. Then the velocity $\bar{V}_{za}$ has been obtained by means of eq. (3.45). Finally r_{sv} has been deter-mined by means of eq. (3.13) as described in Paragraph 8.2.2. To give an impression of the effect of r_{sh} and r_{sv} on the actual evaporation rate, the value of LE

Table 8.10. Mean resistances to transfer of heat in the soil $\rho_a c_p r_{sh}$ and of vapour in the soil r_{sv}. The depth of the evaporation front z_E and the actual evap-oration rate LE, as calculated by means of eq. (2.25) also are given. Measurements used, have been collect-ed in the playa West respectively NE-Idri on 3 Sep-tember 1978

Site	$\rho_a c_p r_{sh}$	r_{sv}	z_E	LE (eq. 2.25)
	$(s \cdot m^{-1})$	$(s \cdot m^{-1})$	(cm)	$(W \cdot m^{-2})$
Playa West-Idri	65	41	9	-103
Playa NE-Idri	194	345	12	- 30

calculated according to eq. (2.25) has also been pre-sented in Table 8.10. It can be seen that for the proper use of the combination equation eq. (2.25), knowledge of r_{sh} and r_{sv} is essential. This point will be discussed in more detail in Section 8.4, where other LE-values calculated in this way from satellite data are presented.

A point which has not yet been mentioned is the extrapolation in time of the results obtained by means of calculations involving satellite data. Such calcu-lations will, by necessity, be restricted to a number of short periods over the year. Such a necessity arises not so much from the amount of work involved in pro-cessing large amounts of data as from the change in weather conditions (e.g. cloudiness). Therefore only a selected number of images is suitable for the appli-cations described here.

For the ultimate goal set forward in Chapter 1, however, total evaporation losses over relatively long time periods are required. For this purpose the LE-images can be transformed into images of relative evaporation by dividing the LE-value calculated for each pixel by either the result of a formula for po-tential evaporation, e.g. eq. (2.27), or by a measured pan-evaporation. These two climatological indexes, potential and pan evaporation, vary over the year. The relative evaporation figures, as obtained from only a very few data-sets, would therefore yield over long time periods a varying soil actual evaporation. This does not apply, however, when evaporation from bare soil takes place under more or less steady state con-ditions, as for the Idri-playas (see Paragraph 8.2.1). Then the relative evaporation concept fails and one better can take a constant evaporation rate at each point, e.g. the mean value over a few separate days considered in the calculations with satellite data. Again it clearly appears that total evaporation losses cannot be calculated from satellite data only. Such data, however, add the areal dimension to the experi-ments performed on the ground and represent the only

possibility to work out the required calculations of total evaporation losses from large desert expanses.

8.4. REGIONAL ACTUAL EVAPORATION

8.4.1. Comments on the satellite images

The characteristics of the Qarqaf and Wadi Ash Shati area as seen in the satellite images are presented in Plates 1 through 8. The characteristics of the different satellite data are given in Table 6.11. The images, in particular the HCMM-images shown in Plates 1, 2, 3 and 8, give data to be used in Paragraph 8.4.2 to calculate the different terms of the surface energy balance equations. There are two reasons for giving some general comments about these images. The first is to recall that these images actually are used as arrays of surface temperature and surface reflectance data (see also Section 7.5). The second is to point out the difficulties to be expected when making calculations based on these data. The different terms in the surface energy balance do not always change with surface temperature and surface reflectance in a predictable way. In particular the latent heat flux may change with α_0 and T_0 in a way different from the expected behaviour for homogeneous surfaces. This kind of deviations has already been depicted in Fig. 5.2 and discussed in Paragraph 8.1.1.

The values of surface reflectance, already presented in Paragraph 7.5.1 as obtained from HCMM-VIS data, have been calculated from the image shown in Plate 1. The calibration relationship was given in Section 7.3. In Plate 1 it can be seen that low surface reflectances (black) are found not only in the playas along the southern side of the Qarqaf highland (see Fig. 6.4), bus also on the highland itself and on the Jabal as Sawda (top right in Plate 1). The α_0-values of weathered rocks and of the wet part of playas are quite close, as shown in Table 7.13. More comments on the low reflectances of weathered rocks have been given in Paragraphs 5.3.1 and 7.5.1 (see Fig. 7.18). When the simple linear equations given in Paragraph 8.1.1 are used, the low surface reflectances of rocks yield a tendency for translating them towards higher evaporation rates. If a complete calculation of the surface energy balance is worked out, as described in Paragraph 8.1.3, such a tendency can be compensated for by variations in the transfer coefficients involved. Then, however, a better knowledge of the area and more data are needed. On Plate 1, it can be seen that other dry surfaces, i.e. part of the Qarqaf and the dunes in the Idehan Awbari (bottom

left) behave in a more reasonable way. There the reflectance (white and whitish) is, as expected, on the high side. The intensity of the red colour indicates increasing surface reflectances, from black over light to dark red, to white.

In Plate 2, covering the same area as Plate 1, the HCMM-TIR image earlier mentioned in Paragraph 7.5.2 is presented. This image has been used to establish the boundary, and therefore the extension, of the playa area. The playas (see Fig. 6.19), in dark red, are cooler than both the Qarqaf (white to whitish) and the dunes in the Idehan Awbari (light red). Some troubles arise with the southern part of the Hamada al Hamra (for location see Fig. 6.1), which is the coldest surface (black) in the image. Again some knowledge of the area is needed to avoid gross misinterpretations of these satellite data. It should be noted that playas have high surface temperatures during the day (see also Figs. 7.23 and 7.25) and low ones at night. This is in open contradiction with the working-hypothesis (small amplitudes) for using thermal infrared data to detect moist areas. A numerical example to show how this behaviour may occur, has been given in Paragraph 4.1.4 (see also Table 4.1). The point is that the enhanced heat transport in the top soil layer may not be completely compensated by an increase in the. thermal admittance $|y_0|$. So relatively large amplitudes of surface temperature may be observed. It must be mentioned that small day – night amplitudes of the surface temperature have been observed in flooded playas, which are present in parts of the full-frame HCMM-TIR image not shown in Plate 2.

In Plate 3, covering almost the same area as Plates 1 and 2, a colour composite of the HCMM-VIS (red) and HCMM-TIR (green) daytime images is shown. The intensity of the red hue increases with increasing reflectance and the intensity of the green hue increases with increasing radiation temperatures. So brilliant red objects are cold and highly reflective, while the brilliant green ones are warm and dark. In Plate 3 it can be seen that the Wadi Ash Shati basin (see also Figs. 1.4, 1.6 and 6.19) is characterized by high temperatures (green). The boundaries are quite clear and one might be tempted to conclude that the entire green area is the area where evaporation of groundwater takes place (see also Fig. 1.5, cross section C - C'). It is clear in Plate 3, however, that also the dry Qarqaf highland has high temperatures and a low surface reflectance. The temperature of the Qarqaf surface is even somewhat lower than that of the playas. It is therefore clear that a higher evaporation rate would be calculated, unless the variations

in r_a and r_{sh} (see eq. 2.25) properly are taken into account. The resistance r_a on the Qarqaf is lower than on the playas, because of the elements with higher surface roughness. Fragments of rocks cover the surface, thus giving it a rather hummocky aspect. Such an explanation, however, is of no help if one cannot specify how large the resistances r_a and r_{sh} are, the latter being equivalent to the thermal admittance $|y_0|$. Interpretation problems, as above with the Qarqaf, also arise with clouds. The high clouds (brilliant red) are easily identified (see also Paragraphs 5.2.1 and 7.4.1, Fig. 7.2). It is with the fringes of the semi-transparent lower clouds (see also Fig. 7.3) that problems arise. If one tries to calculate LE-values for these pixels where the reflectance is comparable with that of the surface and where temperature is lower than the surface, high LE-values will of course be obtained. The pixels relating to these fringes cannot easily be separated from non-contaminated pixels (see also Paragraph 7.4.4). The resulting LE-values, as well as the values of the other fluxes that contribute to the energy balance of the surface, will not be that unreasonable to be rejected right away. To overcome this difficulty, ground reference data are invaluable.

In Plate 4 a METEOSAT-TIR image is shown, which confirms the occurrence of lower temperatures in the playas (green and black) than in the Qarqaf (274 to 278 K, yellow). Still lower surface temperatures (red), i.e. between 268 and 270 K, are observed in the Hamada al Hamra and in the Idehan Marzuq. The occurrence of large surface temperature amplitudes in playas was confirmed by the other thermal infrared satellite data listed in Table 6.11.

The thermal infrared high resolution image presented in Plate 5 obtained by means of an airborne scanner, shows how dramatic the smoothing effect of low resolution satellite images can be. As it can be seen a full 10 K range may be present in an area with the size of one HCMM pixel (0.6 by 0.6 km). This smoothing effect and the relation between the areal variability of surface temperature, as observed with different resolutions has been discussed in detail in Paragraph 7.5.2 (see, for example, Fig. 7.23). In particular the relationship between surface temperature and shallow groundwater table depth along the cross section A - A' in Plate 5 has been presented in Fig. 7.22.

A comparable smoothing effect is observed in satellite data in the 0.4 to 1.1 μm spectral range. In Plate 6 a colour composite of LANDSAT bands 7, 5 and

4 is presented. Many tiny details can be seen around the Idri village (the light spot in the dark surroundings at the center bottom of the images), around which the vegetation (red) shows up, and in the Qarqaf to the North of Idri. Furthermore a large variation in surface reflectance between March and September occurs in the area where the white salt crust is present in the March image. Comments on the consequences of this variation in surface reflectance have already been given in Paragraph 8.1.1. The test site 'playa West-Idri' (see also Fig. 6.12) can be recognized, especially in the March (left) image when the salt crust was present along the boundary between the playa and the dunes of the Idehan Awbari. The details in surface characteristics of the area shown in Plate 6 are almost completely lost in Plate 1 (same spectral range), where the Idri area can be recognized in the lower part of the image on the left hand side, as a small red spot in the dark playa area and close to the dunes.

The procedure applied to obtain Plate 7 (covering almost the same area as Plate 6) has been described in Paragraph 8.1.2. Here only two additional remarks will be given. Firstly, the α_{pE}-value corresponding to α_{0E} was obtained by making use of the curves in Fig. 5.3. In principle different sets of these curves should be used, even under relatively cloud- and dust-free conditions. As discussed in Section 7.4, calculations of the atmospheric effects on remotely sensed data, cannot be accurate unless the atmospheric transmittance is measured. As an alternative, one should determine the ratio α_p/α_0 by making use of ground measurements and then apply the value of this ratio in the procedure described in Paragraph 8.1.2. The second remark relates to the separation of the α_0-image into the green part $(\alpha_0 < \alpha_{0E})$ and the black $(\alpha_0 = \alpha_{0E})$ to red part $(\alpha_0 > \alpha_{0E})$. This partition is misleading when applied to the dark, rocky surfaces. Furthermore many pixels where $\alpha_0 > \alpha_{0E}$ are present in the playa area. In these pixels, however, the value of α_0 is close to α_{0E} and only could have been displayed by using a density slicing representation for this image. The separation in two, green and black to red, hues has been preferred because then the image looks more natural than the density sliced one.

In Plate 8 (giving the same area as Plates 1 and 2) an image depicting the areal pattern of the sensible heat flux H (see Section 2.3) is presented. This image has been calculated by combining the daytime HCMM-TIR image, already used to obtain Plate 3, with ground measurements applying the procedure presented in Paragraph 8.1.3. The reason for presenting this

H-image is twofold. Firstly, the sensible heat term
takes the largest share of the available radiative
energy and it is, therefore, necessary to determine
it with the best possible accuracy if reasonable val-
ues for LE and G_0 are being sought. Secondly, the
large H-values present in Plate 8, as well as their
areal variability, give an actual image of the areal
coherence of the surface radiation temperature and of
the pulsation of soil - air heat exchanges, as
discussed in Section 7.6. As r_a is required to calcu-
late the H-image (see Paragraphs 8.1.3 and 8.2.2), it
must be added that the values given in Section 7.6 of
the frequency of the thermal pulsation at the
soil - air interface, support this use of the measure-
ments collected in the Idri playas. This holds true
at frequencies of 10^{-2} to 10^{-3} Hz, at which frequen-
cies the thermal bursts occur, according to the lit-
erature mentioned in Section 7.6. In the present
author's opinion H-images, as presented in Plate 8,
provide useful information for meteorological research,
since they give a vivid picture of intricate patterns
of turbulent soil - air heat exchange.

8.4.2. Results

C a l c u l a t i o n   o f   t h e   s u r f a c e
e n e r g y   b a l a n c e   w i t h   t h e   a i d
o f   s a t e l l i t e   d a t a . The HCMM data de-
scribed in Paragraph 8.4.1 have been combined with
point ground reference measurements to calculate areal
patterns of net radiation R_n, sensible heat flux H,
soil heat flux at the soil surface G_0 and latent heat
flux LE. The images relate to instantaneous values of
R_n, H and G_0 and to either daily totals or mean daily
fluxes for LE. The calculation procedure has already
been described in Paragraph 8.1.3. Here the successive
steps will only be recalled in short.

The day image of net radiation R_n has been calcu-
lated by means of eq. (5.2) taking shortwave radia-
tion R_{sw} from ground measurements (see Table 6.9). The
surface reflectance α_0 has been calculated from the
HCMM-VIS image (see Plate 1 and Section 7.3). The at-
mospheric emission term $\epsilon'\sigma T_a^4$ has been calculated with
the air temperature T_a as measured at the playa West-
Idri and at the Idri meteorological station (see Fig.
6.12). The apparent emissivity of the atmosphere ϵ'
is as given in Table 8.3. The emissivity of the sur-
face here has been taken equal to 1, since the surface
radiation temperature T_0 is directly obtained from the
HCMM-TIR data. The difficulties with the calibration
of these HCMM-TIR data have been given full attention
in Section 7.3. As regards the night R_n-image, the
same calculation procedure as for the day R_n-image has
been applied, by taking into account the proper ϵ'-

value given in Table 8.3.

The day image of the sensible heat flux H has
been calculated by means of eq. (2.15) and applying
(see Table 8.4) $r_a = 40$ s·m^{-1}. Air temperature T_a
has been measured on the ground at the playa West-
Idri and the Idri meteorological station. The night
H-image also has been calculated by means of eq. (2.15),
but with $r_a = 66$ s·m^{-1} as given in Table 8.4.

The images of the soil heat flux G_0 have been
calculated by means of eq. (5.43) as the only remain-
ing unknown term in the energy balance equation. Eq.
(5.43) applies to the case of evaporation taking place
below the soil surface, so $G_0 = -R_n - H$ can be calcu-
lated for each pixel of the R_n- and H-images. The same
calculation procedure was applied to derive the night
image of G_0, from the night images of R_n and H.

The HCMM-VIS subscene has not been separated into
two parts, i.e. where $z_E = 0$ and where $z_E > 0$, as
was done with the LANDSAT data presented in Plate 7.
One reason is that the HCMM-VIS image contains a large
percentage of cloud contaminated pixels. These pixels,
as mentioned in the description of Plate 3, would be
erroneously assigned to the category 'evaporation
from below the soil surface'. Conversely the pixels
belonging to the dark part of the Qarqaf (see again
Plate 1) would be erroneously classified as 'evapora-
tion at the soil surface'. In principle the LANDSAT
image, taken on 26 September 1978, eight days later
than the HCMM-VIS image of 18 September 1978, might
have provided a solution. This LANDSAT image, however,
covers only a small part of the HCMM subscenes which
have been applied here. Moreover, the same difficul-
ties would arise with the weathered dark rocks in the
Qarqaf.

The only consequence of assuming that everywhere
evaporation takes place below the soil surface, is
that some of the G_0-values in the G_0-images include
both the latent heat flux LE and the heat flux which
actually penetrates below the soil surface, i.e. the
true G_0. In such cases one should apply eq. (5.44)
$G_0 + LE = -R_n - H$. Since this occurs in only a small
part of the area covered by both the LANDSAT and HCMM
images, the case of eq. (5.44) has not been considered.

The results of the calculations, i.e. the daytime
R_n, H and G_0-images, will now be given and compared
with measurements of these variables, as collected in
the playa West-Idri at the moment of the HCMM over-
passes during daytime.

The measured LE and G_0-values, as given in Table
8.11 for the test site, have been obtained indepen-
dently from the R_n and H-values. The latent heat flux
LE has been obtained by the Bowen ratio energy balance
method. The G_0-term has been calculated from soil heat

Table 8.11. Areal means of net radiation R_n, sensible heat flux H, soil heat flux at the soil surface G_0, as calculated from HCMM-VIS and HCMM-TIR subscenes at 13.45 h LMT on 18 September 1978 (see Plates 1, 3 and 8). To calculate R_n and H instantaneous images ground reference measurements have been combined with satellite data as described in Paragraph 8.1.3. The standard deviations σ and the number of pixels N_{pix} are shown to illustrate the areal variability and the representativeness of the R_n, H and G_0 values. The entire subscene includes the Qarqaf highland and the Wadi Ash Shati basin. Independent ground reference measurements of R_n, H, G_0 and LE were collected in the playa West-Idri at the same moment

Data on	Origin of data	R_n (W·m^{-2})	σ_{R_n} (W·m^{-2})	N_{pix}	H (W·m^{-2})	σ_H (W·m^{-2})	N_{pix}	G_0 (W·m^{-2})	σ_{G_0} (W·m^{-2})	N_{pix}	LE (W·m^{-2})
Entire subscene (36,000 km²)	satellite + ground	480	40	10^5	-230	120	10^5	-240	130	10^5	
Playa samples (1 pixel = 0.36 km²)	satellite + ground	475	10	240	-360	40	192	-110	30	110	
Playa West-Idri	ground	399			-183			-150			-130

flux measurements. Both LE and G_0 were obtained as described in Paragraph 8.2.2.

For the satellite derived values a measure of variability, i.e. the standard deviation, and a measure of representativeness, i.e. the number of pixels, have been given, which is impossible for the point ground reference measurements. Such a difference underlines the areal character of the satellite-derived values. The R_n, H and G_0-values applying to the entire 36,000 km² subscene include the contribution of cloud-contaminated pixels and therefore also are affected by this error. The image samples relating to the playas include only non-contaminated pixels.

The lower standard deviations of the R_n, H and G_0-values for the image samples of playas are due to the homogeneity of the smaller surface. It is worthwhile to mention that the standard deviation of the H-values, as a fraction of H, is larger than that of the R_n-values. The large σ_H-values confirm the interpretation of the areal variability of H, which has

been given in Section 7.6 and in Paragraphs 8.1.3 and 8.4.1; an interpretation relying on the thermal pulsation mechanism. The H-flux in playa samples takes a larger share of the available energy R_n than in the entire subscene. The H-term is in any case much larger than the latent heat flux LE, given in Table 8.11 as measured in the playa West-Idri at the moment of the HCMM overpass.

The energy balance equation at the soil surface (eq. 5.43) is not verified when the fluxes given in Table 8.11 for the playa West-Idri are substituted into it. Namely according to that table R_n + H + G_0 = 399 - 183 - 150 = 66 W·m^{-2} instead of zero. A first reason for this difference stems from plain inaccuracies, which include both the instrument inaccuracies and the approximative character of the equations which have been used. Assuming a 20% inaccuracy in each term of the given energy balance, the absolute indetermination of this equation would be 146 W·m^{-2}. There is, however, a second point concerning the difference of 66 W·m^{-2}

Table 8.12. Areal means of net radiation R_n, sensible heat flux H, soil heat flux at the soil surface G_0, as calculated from a HCMM-TIR subscene at 2.00 h LMT on 16 September 1978 (see also Plate 2). To calculate R_n and H instantaneous images ground reference measurements have been combined with satellite data as described in Paragraph 8.1.3. The standard deviations σ and number of pixels N_{pix} are shown to illustrate the areal variability and the representativeness of the R_n, H and G_0-values. The subscene includes the Qarqaf highland and the Wadi Ash Shati basin. Independent ground reference measurements of R_n, H, G_0 and LE were collected in the playa West-Idri at the same moment

Data on	Origin of data	R_n (W·m^{-2})	σ_{R_n} (W·m^{-2})	N_{pix}	H (W·m^{-2})	σ_H (W·m^{-2})	N_{pix}	G_0 (W·m^{-2})	σ_{G_0} (W·m^{-2})	N_{pix}	LE (W·m^{-2})
Entire subscene (36,000 km²)	satellite + ground	-65	6	10^5	29	17	10^5	26	23	10^5	
Playa samples (1 pixel = 0.36 km²)	satellite + ground	-54	3	60	64	14	49	-16	16	56	
Playa West-Idri	ground	-57			62			20			-55

between R_n and $(H + G_0)$ which ought to be mentioned. The energy balance equation at the evaporation front according Table 8.11 reads $G_E = G_0 - LE = -150 + 130 = -20$ W·m^{-2}, which is in agreement with the results presented in Paragraph 8.2.2 (see Fig. 8.9). So if the 66 W·m^{-2} is not accepted as a plain experimental error, at the surface an additional sink of energy must be present. An additional contribution to LE might arise from the rim of the cracks being present in the playa West-Idri. The one-dimensional model of the evaporation front would account for evaporation from within the cracks without taking account of the rim-effect. It is understood that the partition of an area in two parts, i.e. with $z_E = 0$ and with $z_E > 0$ (see Plate 7), is approximated, because of the smoothing of any deviations, such as the rim-effect, caused by the resolution of the satellite data.

The results obtained by combining the night HCMM-TIR image on 16 September 1978 with the required ground measurements, are given in Table 8.12. The agreement between the satellite derived values for the playa samples and the independent ground measurements of R_n and H of the playa West-Idri is remarkable. Because of this result and of the very sharply defined boundaries of the playa area in the Wadi Ash Shati basin, the extent of the evaporation area has been obtained from the night R_n and H-images. Accordingly it has been established that 10,500 HCMM-pixels, so a 3800 km^2 area, belong to the area where evaporation of groundwater takes place.

The areal mean G_0-value for the playa image samples is negative which looks somewhat unreasonable in regard of the positive measured value of 60 W·m^{-2}. Furthermore the measurements given in Table 8.12 for

the test site indicated that evaporation, LE = -55 W·m^{-2}, was taking place. The discrepancy between the satellite derived values of G_0 and the ground measurements of G_0 together with the measurement of LE can be explained by recalling how the G_0 (satellite) values have been obtained. As already mentioned above, eq. (5.43) has been applied: G_0 (satellite) = R_n (satellite) + H (satellite). If evaporation takes place at the soil surface, eq. (5.44) should be used and R_n + H = G_0 + LE, so G_0 (satellite) = G_0 + LE = 20 - 55 = -35. The latter result does not contradict the value of G_0 (satellite) given in Table 8.12, i.e. G_0 (satellite) = -16 W·m^{-2}, with a standard deviation $\tilde{\sigma}_{G_0}$ = 16 W·m^{-2}.

As regards the satellite derived values in both Table 8.11 and 8.12 it must be added that in the calculation procedure some accuracy has been lost. Because the calculated values for the different fluxes have to be handled as images, they must be made to fall in the numerical 0 to 255 range. This implies a contraction of the flux scale and, therefore, a loss in accuracy. For example for a H-range of 500 W·m^{-2}, one must use a 2 W·m^{-2} unit.

Calculation of soil apparent thermal admittance. The day and night G_0-images have also been applied to calculate an image of the apparent soil thermal admittance $|y_0|$. The related theory has been presented in Chapter 4. To calculate $|y_0|$ by means of eq. (4.17), images depicting the amplitudes of the heat flux at the soil surface G_0 and of surface temperature T_0 have to be calculated. These calculations could only be carried out with the day and night HCMM-TIR images for the 24-hour temperature wave. The main difficulty with the METEOSAT-
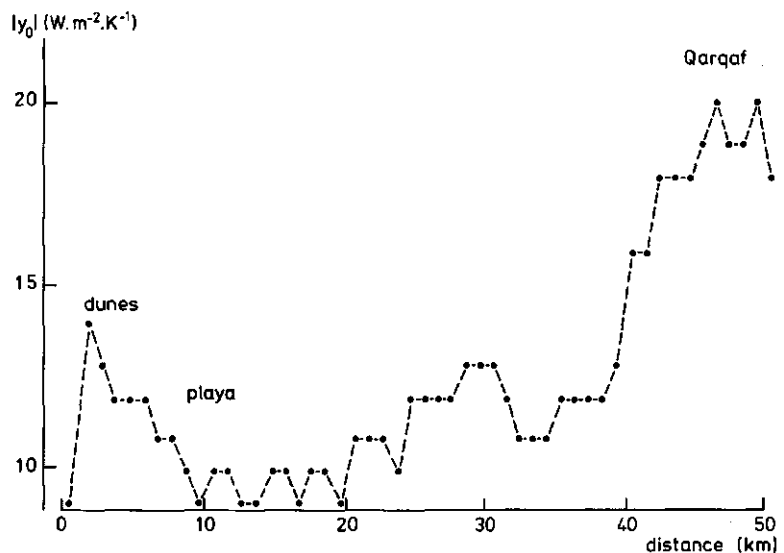
Fig. 8.12. Cross section of an image of the apparent thermal admittance of the soil surface $|y_0|$. For the calculation procedure see text. The cross section goes from the dunes of the Idehan Awbari, across the playas and towards the Qarqaf highland. Day HCMM-VIS and HCMM-TIR, and night HCMM-TIR data of 18 respectively 16 September 1978 have been applied

-TIR data collected for the Libyan desert (see Table 6.11 and Section 7.2) which could not be overcome was the impossibility of mutual registration of the images in the time series.

In Fig. 8.12 a cross section of the $|y_0|$ image calculated from the HCMM day and night images (18 respectively 16 September 1978) that also were applied in the calculations concerning the surface energy balance, is presented. The values of $|y_0|$ obtained in the dunes are somewhat higher than expected for dry sand. This result explains the much lower amplitudes of surface temperature observed in the dunes as compared with the playas (Section 7.1). The values obtained in the playas are in excellent agreement with the results obtained from ground measurements as described in Paragraph 8.2.2, i.e. $|y_0| = 11 \ W\cdot m^{-2}\cdot K^{-1}$ (see Table 4.1). The Qarqaf-values are also in excellent agreement with literature values for the thermal properties of sandstone, from which it can be calculated that $|y_0| = 19 \ W\cdot m^{-2}\cdot K^{-1}$ (REEVES et al., 1975). As will be shown in the flow chart presented in Fig. 8.16, the determination of $|y_0|$-images is fed-back into the calculation of the various surface energy

balance terms from satellite data. The reason for this feed-back connection stems from eq. (4.17): if $|y_0|$ is known for a given area, eq. (4.17) can be applied to calculate G_0 from T_0-images. As, however, only one suitable set of images (HCMM), already used for the calculation of the $|y_0|$-image, was available it was impossible in the here presented case to make use of the feed-back sequence.

Calculation of regional actual evaporation. The linear equations presented in Paragraph 8.1.1 have been applied to calculate the areal pattern of actual evaporation from the HCMM data already mentioned (16 September, night, and 18 September, day). As explained these simple linear equations can directly be applied to the satellite data.

In Fig. 8.13 a detail of a LE-image (11,000 km²) is presented, as calculated from the day HCMM-VIS and HCMM-TIR images by means of eq. (8.7), rewritten to obtain actual evaporation in $mm\cdot d^{-1}$ units. The playa area is the transversal, white to light-gray portion of the image. In the central zone of the

Fig. 8.13. Image depicting the areal pattern of actual evaporation on 18 September 1978, as calculated by means of eq. (8.7) from the daytime HCMM-VIS and HCMM-TIR data for a part of the playa area surrounding Idri, Wadi Ash Shati. At the point indicated by the cross-hair cursor actual evaporation is 2 $mm\cdot d^{-1}$
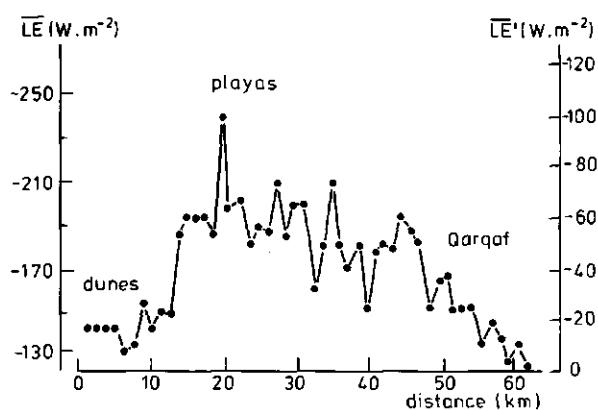
Fig. 8.14. Cross section of an image depicting the areal pattern of the mean latent heat flux $\overline{LE}$ $(W \cdot m^{-2})$ as calculated by means of eq. (8.6) from daytime (18 September 1978) HCMM-VIS, HCMM-TIR, and night-time (16 September 1978) HCMM-TIR data. The cross section goes from the dunes in the Idehan Awbari across the playas and towards the Qarqaf highland. The additional $\overline{LE}'$-axis has been obtained taking $\overline{LE}$ = 0 in the Qarqaf

playa area actual evaporation is 2 $mm \cdot d^{-1}$, a value supported by the ground measurements in Tables 8.6 (soil water balance method) and 8.8 (Bowen ratio energy balance method). It can be seen that the calculated evaporation rate is much lower, dark to black, in the dunes (bottom) and in part of the Qarqaf (top left) than in the playa area. In the top center part, because of clouds, unreasonable figures of up to 8 $mm \cdot d^{-1}$ are obtained. It is quite clear that when the evaporation rate decreases steeply or less steeply outwards of the playas, different estimates of the total groundwater losses are obtained. This aspect of the areal variation of evaporation is the main difficulty in assessing the total groundwater losses by evaporation. It must be stressed that the determination of functions

to map the areal variation of actual evaporation is even more important than measuring the actual evaporation at some specific sites.

This point will be discussed further in relation to Fig. 8.14. There a cross section of an LE-image is presented, as calculated by means of eq. (8.6) from the HCMM-VIS data and the mean surface temperature, the latter as obtained from the day - night pair of HCMM-TIR images. As can be seen the contrast of the playas, at the center of the cross section, and both the dunes (left hand side) and the rocks (right hand side), is large. In this image the difficulties with the Qarqaf area, which already have been mentioned in the comments on Plate 3 given in Paragraph 8.4.1, could be overcome with eq. (8.6). It can be seen, however, that the calculated evaporation rates are unreasonably large. It is only by arbitrarily assuming that the base line value corresponds to a zero evaporation rate (see the $\overline{LE}'$-scale), that acceptable results are obtained.

Finally total daily evaporation has been calculated by means of the combination equation, eq. (2.25). The determination of r_a, r_{sh}, r_{sv} has already been discussed at length in Paragraph 8.2.2 and Section 8.3. Here it will only be mentioned that in the calculations the following values have been taken: r_a = 40 $s \cdot m^{-1}$, $\rho_a c_p r_{sh}$ = 65 $s \cdot m^{-1}$ and r_{sv} = 41 $s \cdot m^{-1}$. The mean $\overline{R}_n$-image has been calculated from the R_n-images, i.e. day and night, presented at the beginning of this paragraph. The mean $\overline{G}_E$-image has been calculated in the same way, taking $\overline{G}_E$ = 0.18 $\overline{G}_0$, as discussed in Paragraph 8.2.2, for both the day and night G_0-image. In Fig. 8.15 a cross-section of this $\overline{LE}$-image, approximately along the same line as in Figs. 8.12 and 8.14,
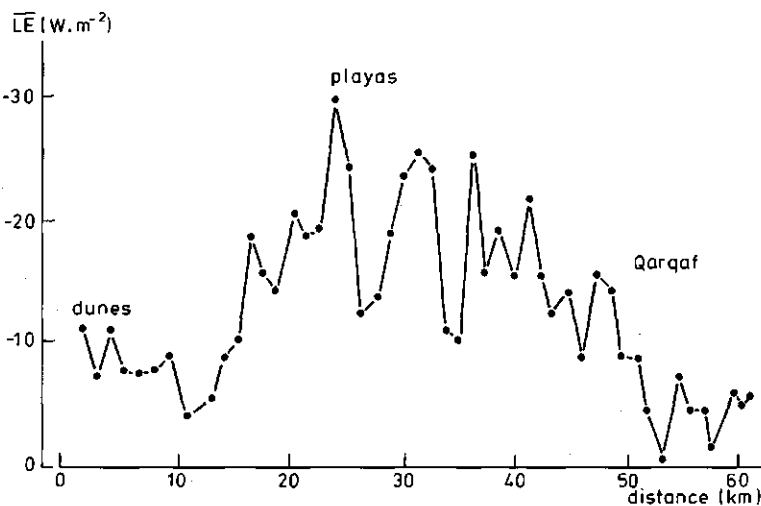
Fig. 8.15. Cross section of an image depicting the areal pattern of the mean latent heat flux as calculated by means of the combination equation (2.25) from R_n and G_0-images and ground reference measurements. The cross section goes from the dunes in the Idehan Awbari, across the playas and towards the Qarqaf highland. The HCMM data used were collected on 16 and 18 September 1978

175

is presented. As can be seen much lower values are found than in Fig. 8.14. The $\overline{LE}$-values given in Fig. 8.15 are comparable, however, with the ground measurements at the test site playa NE-Idri (see Tables 8.6 and 8.10). The cross section presented in Fig. 8.15 correctly accounts for the evaporation being negligible in the dunes and on the rocks. Furthermore the decrease in evaporation from the wetter southern boundary to the drier northern boundary of the playas (see also Plates 6 and 7 and Fig. 7.18) is properly depicted. Note that this result is the outcome of spatial variations in the R_n, H and G_0 areal patterns, since constant values for r_a, r_{sh} and r_{sv} were taken.

The $\overline{LE}$-image out of which the cross section of Fig. 8.15 was extracted also contains a large quantity of cloud contaminated pixels. Therefore, to determine the areal mean actual evaporation rate of playas image-samples of the cloud free areas have to be considered. Accordingly $\overline{LE}$ = 17 $W \cdot m^{-2}$ has been obtained for the playas. This result can be now multiplied with the area of playas, as determined from the R_n and H night-images on the basis of the reasoning presented in the first part of this paragraph.

The estimated groundwater losses by evaporation in the part of the West-Libyan aquifer system included in the HCMM subscene shown in Plates 1, 2, 3 and 8, in this manner can be calculated as being $8.5 \cdot 10^8$ $m^3 \cdot a^{-1}$. This figure applies to steady state conditions (see Paragraph 8.2.1). In the following paragraph this figure will be compared with the estimated artificial discharge and recharge, as given in Chapter 6.

8.4.3. Conclusions

The estimate, as given in the previous paragraph, of groundwater losses by evaporation from the playas in the Wadi Ash Shati basin will now be compared with the data on artificial discharge and recharge given in Chapter 6. The data given there on artificial groundwater discharge apply only to the area covered by the Aquater study, as indicated in Fig. 6.1. The data on the recharge to the aquifer relate to the entire system, as depicted in Figs. 1.4 and 6.1.

In the Aquater study the area of playas was established on the basis of morphological features only. Moreover, as shown in Fig. 6.19, the carried out IRLS survey covered only part of the playa area. It therefore can be understood that in the mentioned study only part of the playas could have been included to estimate the groundwater losses. Only those playas lying in the lowest topographic positions and with the morphological features described in Section 1.2, were included in the final Aquater calculation of evapora-

Table 8.13. Yearly evaporation from the playas in the Wadi Ash Shati basin, as estimated by the present author on the basis of the here presented investigations and as given by Aquater (1980). Also shown is the area from which evaporation was considered to take place in the two studies

Source	Area of evaporation (km^2)	Evaporation (mm·a^{-1})	Evaporation losses (m^3·a^{-1})
Present report	3800	220	$8.5 \cdot 10^8$
Aquater (1980)	194.1	400	$0.8 \cdot 10^8$

tion losses. The playas depicted in Fig. 6.19 are situated in the area shown in the green hue at the bottom of Plate 3. The colour composite of the daytime HCMM-VIS and HCMM-TIR, however, provides a more accurate determination of the extension of playas, which is a strong point in favour of the use of these HCMM images (see also Paragraph 8.4.2).

In Table 8.13 the yearly overall evaporation from the playas being present in the Wadi Ash Shati basin is given, according to the present investigation as well as according to the AQUATER (1980) one. It can be seen that the higher value of evaporation per unit area of the earlier estimates (AQUATER, 1980) confirms that in the study of AQUATER (1980) the boundaries of playas were defined too narrowly. Only those surface units which most clearly appeared as 'real' playas, were included. The results in Table 8.13 show that satellite data of reasonable resolution, such as the HCMM data, are most suitable to solve the kind of large-scale problems here being considered.

To conclude the presentation of the given results, they will be related to the West-Libyan aquifer system, although in the manner of an educated guess. In Table 8.14 groundwater losses by evaporation are compared with the actual artificial discharge and the recharge of this aquifer system. The estimated losses by evaporation relate only to the playas in the Wadi Ash Shati basin. For an overview of the, larger, total natural discharge from the West-Libyan aquifer system see Section 1.3.

The available data on artificial groundwater discharge have been briefly summarized in Paragraph 6.1.4 (see Fig. 6.5) and the estimation of recharge has been discussed in Paragraph 6.1.3. The estimated net depletion of the groundwater reservoir has been obtained as:

net depletion = evaporation + artificial discharge + - recharge

Table 8.14. Estimated evaporation from playas, artificial discharge, recharge and net depletion of the West-Libyan aquifer system. Evaporation has been calculated as described in Paragraph 8.4.2; for the other data see Paragraphs 6.1.3 and 6.1.4

Evaporation losses	Artificial discharge	Recharge	Net depletion	
			total	per unit area of aquifer outcrops
$(m^3 \cdot a^{-1})$	$(m^3 \cdot a^{-1})$	$(m^3 \cdot a^{-1})$	$(m^3 \cdot a^{-1})$	$(mm \cdot a^{-1})$
$8.5 \cdot 10^8$	$1.6 \cdot 10^8$	$6 \cdot 10^8$	$4 \cdot 10^8$	4

The net depletion values in Table 8.14 are given both as total amount and per unit area of aquifer outcrops (see Fig. 6.1). The 4 $mm \cdot a^{-1}$ value of net depletion given for the outcrop area is worth an additional remark. This value has been obtained by considering the outcrops of the aquifer system (see Fig. 6.1) which stretch over 104,500 km^2 of a void desert. It is, accordingly, to be understood that the amount of available hydrological data, and more specifically the areal density of rainfall measuring points, is low by any standard. So the indetermination of measured rainfall is probably much greater than this 4 $mm \cdot a^{-1}$ figure. Still the values in Table 8.14 are the outcome of a rather unusual wealth of data, at least by desert-hydrology standards.

According to the data in Table 8.14 the aquifer system is undergoing natural depletion (see also Section 1.3). This conclusion also relies on the thorough analysis presented by AQUATER (1980), where it has been concluded that during the last 10,000 years the piezometric levels in this aquifer have quasi-steadily been drawing down. Moreover, the effect of natural groundwater discharge in the form of evaporation from playas is quite evident in the distribution of piezometric head, as presented in Fig. 1.6.

It might be of interest to show that the 4 $mm \cdot a^{-1}$ natural depletion in Table 8.14 is of the proper order of magnitude. According to AQUATER (1980) the storage coefficient of the aquifer outcrops is 10^{-1}. Thus a 4 $cm \cdot a^{-1}$ drawdown of the piezometric head in the aquifer outcrops is implied by the data in Table 8.14. Let us assume that this rate has been the mean yearly drawdown since the Makalian Pluvial, 11,000 year B.P., see Section 1.1, and that the groundwater table at that time was situated at the surface of the aquifer outcrops. Accordingly one would expect, nowadays, to find piezometric head values 440 m lower than the elevation of the ground surface in the outcrops (see Fig. 6.1). As can be seen in Fig. 1.5 the elevation of the Tassili N'Ajjer, for example, is some 1000 to 1500 m above O.D. Fig. 1.6 shows that the piezometric head is some 750 m above O.D. which values, i.e. 1250 - 750, compare fairly well with the 440 m estimated drawdown.

8.4.4. Epilogue

As regards the general significance of the results presented in this Report, the reader should recall the map of the desert areas in the world, presented in Fig. 1.1. In this study groundwater losses by evaporation have been shown to be a rather entangled matter and a challenge to existing knowledge on transport phenomena in soils. A host of problems has been left open. In the present author's opinion, however, sufficient evidence has been brought to light that estimation of groundwater losses by evaporation in deserts is a real exigency and that a systematic use of satellite data would help considerably to fulfill it.

The reader may have received the impression that this book proposes new techniques to study newly discovered physical processes. The latter may not entirely be true: the primeval essentials of these processes and their relevance for the ordinary, strongly on water-dependent life of Saharan people was appreciated long ago. The quotations given at the beginning of each chapter, all of them originally dealing with the Libyan desert, are intended to underscore a much needed historical perception of water management in deserts. The toponymy itself of the Libyan desert spotlights this concept. According to MERCIER (1924) the aboriginal root of Idri, the name of the village in the Wadi Ash Shati means in tamahak 'alive'.

177

8.5. SUMMARY

In Chapter 8 the approach proposed in this book to calculate regional actual evaporation from deserts has been clearly indicated and applied to part of the Libyan desert.

As this chapter is in itself a kind of summary of the entire book, it has therefore been presumed that more helpful than a written summary will be a chart showing the connections between the four sections of this last chapter and the other chapters respectively sections or paragraphs of the book. Such a chart if given in Fig. 8.16.
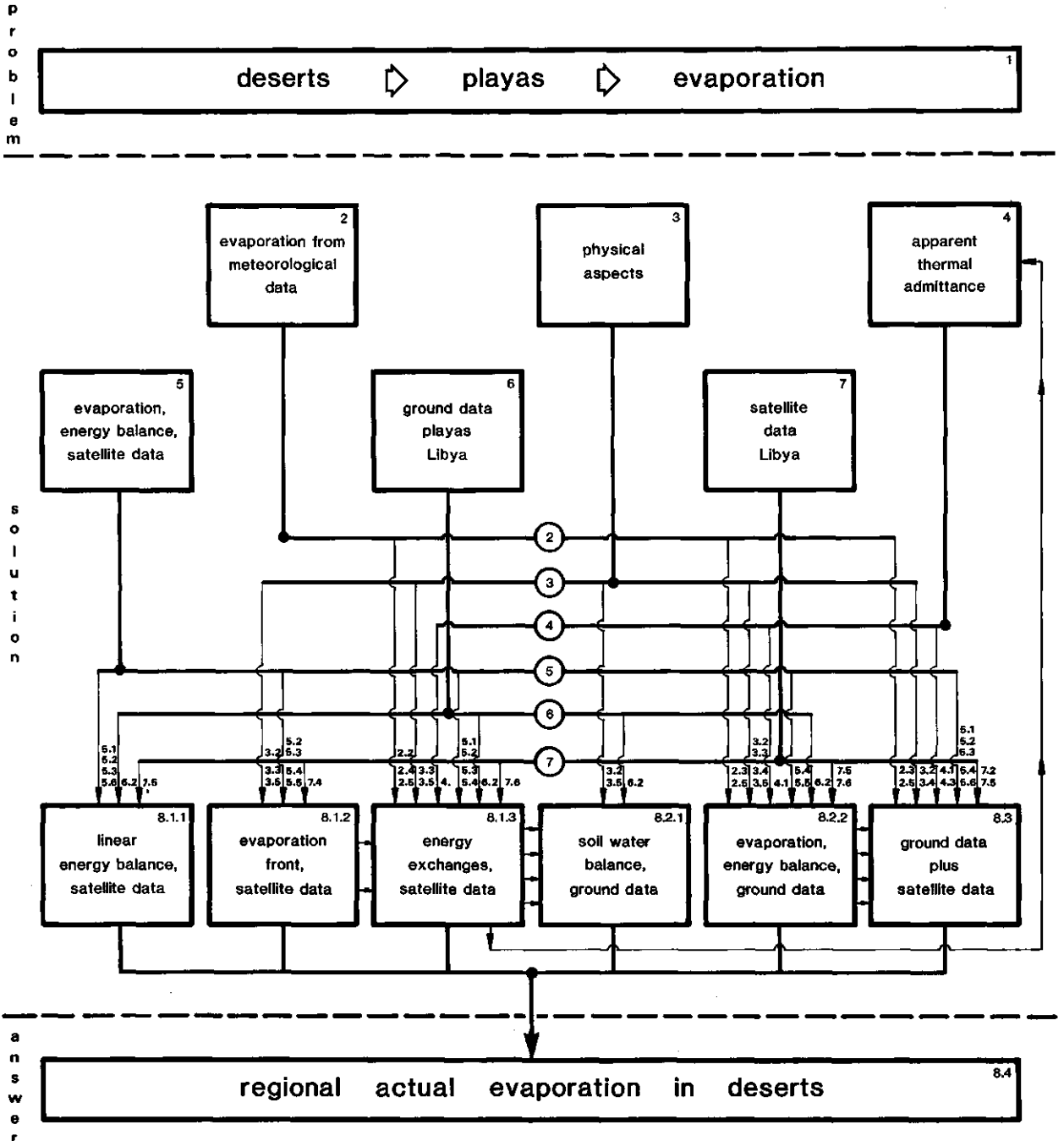
Fig. 8.16. Conspectus of the approach to assess the regional actual evaporation from deserts. The numbers relate to respectively chapters, sections and paragraphs (see list of Contents)

MAP OF GEOGRAPHICAL LOCATIONS OF SATELLITE IMAGES
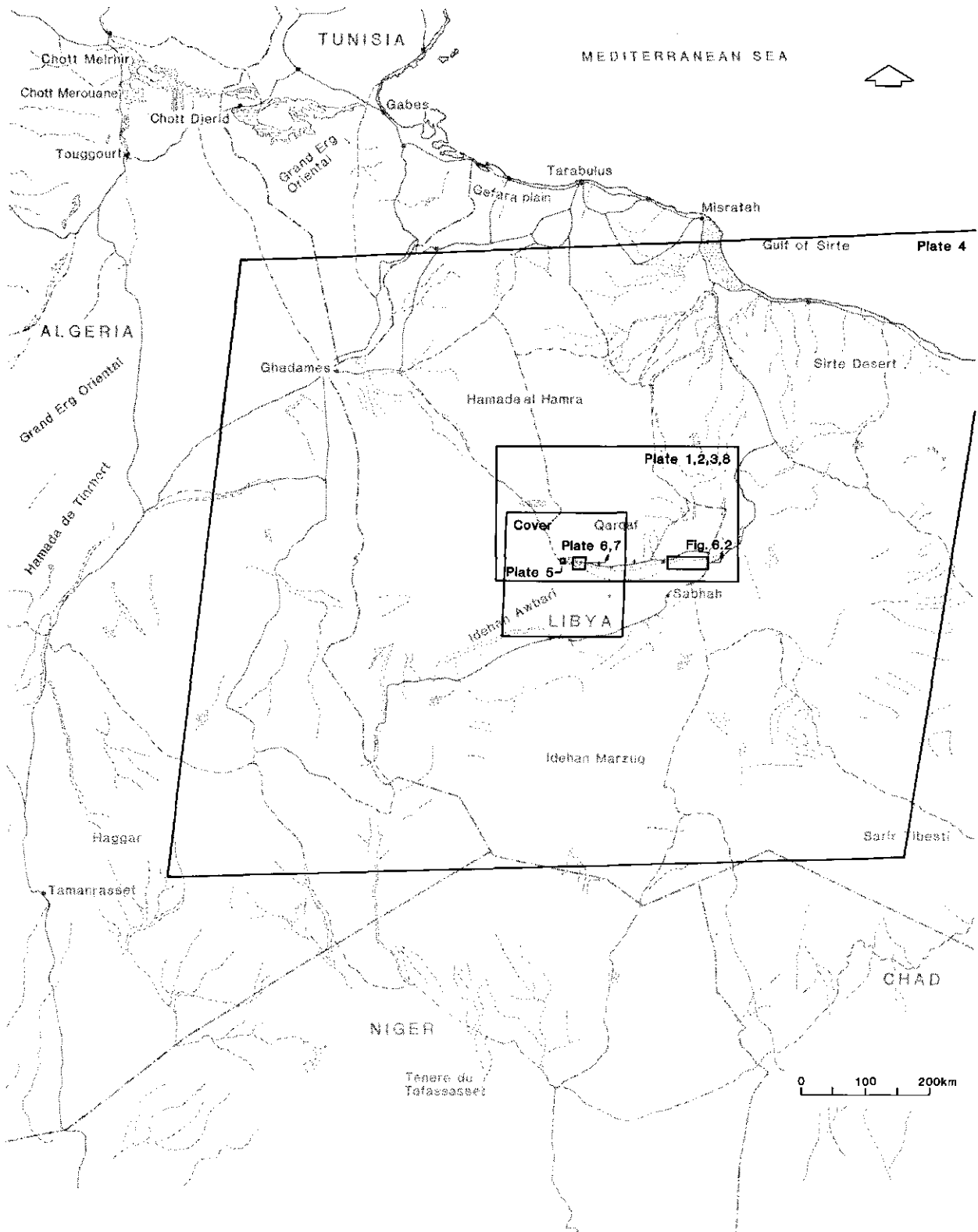
SUMMARY

'Nec de Africa plura quae memorentur occurrunt.'

(PLINIUS, Naturalis Historia, Liber V:46)

This Report is an attempt to answer the following questions:

A. What is the practical scope for the estimation of groundwater losses by evaporation in large desert expanses? Which kind of difficulties have to be expected in relation to soil types, and their thermal and hydrological regime, present in the desert areas where evaporation takes place?

B. Are the present meteorological methods for calculating actual evaporation suitable for desert conditions?

C. Is heat and moisture transfer in nearly dry, hot soils with a very high salt content and a rather complex structure a process sufficiently understood?

D. Which techniques of data collection and data interpretation are suitable for the peculiar characteristics of very large desert areas with a very low density of measuring points at ground surface?

In Chapter 1 an answer has been given to question A. It has been shown that natural groundwater losses by evaporation have all too often been underrated in water management studies of deserts. Groundwater losses by evaporation take place in playas, which are a morphological feature typical of deserts. Besides being affected by large temperature amplitudes and by the presence of shallow water tables, playa soils have salts as a relevant, or dominant, constituent. These three characteristics imply a very close relationship of the surface properties and structure of playa soils with the hydrological regime of playas. The rôle of groundwater evaporation in playas has been illustrated by describing, as an example, the West-Libyan aquifer system.

In Chapter 2 a short overview of literature has been presented to maintain that the usual concept of potential evaporation is an immaterial quantity for desert surfaces. To overcome this difficulty and to answer question B, a new combination formula has been derived to account for evaporation when it takes place below the soil surface. It has also been shown that the limit of this equation for zero depth of the evaporation front, is the well known combination equation for potential evaporation of bare soil. Accordingly a clear separation between actual and potential evaporation was established. When evaporation takes place below the soil surface, the new combination equation can only be used when the transfer coefficients for heat and vapour in the soil are known. As has been shown in Chapter 2 these transfer coefficients are very closely related to the evaporation rate and to the vertical distribution of the moisture content above the evaporation front, preventing a circumvention of this problem. The answer to question B therefore is that the calculation of evaporation with meteorological data is possible only if an in-depth analysis of heat and moisture flow in soils yields a procedure to determine the transfer coefficients.

The answer to question C has been given in Chapter 3. There it has been shown that different enhancement mechanisms contribute to heat and moisture transfer in playa soils. These enhancement mechanisms may be relatively irrelevant under the usual temperature and moisture conditions of non-structured soils outside desert regions. So relatively little is known about the actual quantitative rôle of these mechanisms. In Chapter 3 it has been proven and emphasized that vapour flow can significantly deviate from the diffusive behaviour one often thinks of. Such a deviation stems from the in deserts prevailing dry range of moisture content and from the presence of cracks in the salt crusts of playas. The most important conclusions with regard to heat and moisture flow in desert soils given in Chapter 3 are:

- when evaporation takes place below the soil surface, vapour flow in the top soil may be contrary to heat flow because of thermal convection of moist soil air;
- when the menisci in small pores achieve a radius comparable with the mean molecular free path of water vapour, the outflow of vapour from these micro-

pores is orders of magnitude faster than by diffu-
sion. On this process relies the new definition of
evaporation sites given in Chapter 3.

The effects of enhanced moisture and heat flow
are more easily disclosed by their influence on soil
thermal properties that can be derived from soil tem-
perature measurements by means of procedures discussed
in Chapter 3. If only traditional field-scale data
had to be applied, the concepts and methods presented
in the Chapters 2 and 3 would hardly be useful to es-
timate groundwater losses by evaporation.

The answer to question D has been given in Chap-
ters 4 and 5, where methods to collect areal data have
been presented. In Chapter 4 a new method has been
presented to infer the thermal properties of the soil
layers by means of remote measurements of surface tem-
perature at different frequencies of the incoming tem-
perature wave. This method is particularly suited for
the multi-temporal data provided by geostationary sat-
ellites. The basic concept of the method is to make
use of the explicit relationship between the apparent
soil thermal admittance, the thermal properties and
thickness of the various soil layers. For a soil
layering with specified layer thicknesses and thermal
properties the apparent soil thermal admittance is a
one-value function of the frequency of the incoming
surface temperature wave. This means that remote mea-
surements of the apparent soil thermal admittance can
be applied to infer to a certain depth the thermal
properties and thickness of soil layers.

In Chapter 5 a somewhat more detailed answer to
question D has been given. It was shown that in des-
erts satellite data can be used to measure areally
surface reflectance and surface temperature. Ground
reference measurements still are needed, however, to
be able to determine all the terms in the surface
energy balance equation. In particular it has been
shown that the latent heat flux is a function of six
variables, out of which at best only two can be mea-
sured by remote sensors. Thus only by applying ground
reference measurements, the dimensionality of this
function can be reduced and latent heat flux be
calculated areally from satellite data on surface re-
flectance and surface temperature.

Furthermore, in Chapter 5, it has been shown that
the dependence of surface reflectance on surface
moisture content can be described by a simple linear
function. Total pore volume, the reflectance of the
dry soil and the reflectance of open water are the
parameters of this function.

In Chapter 6 the data applied in Chapters 7 and

8, were presented. These data relate to the West-
Libyan aquifer system.

In Chapters 7 and 8 the methods presented in
Chapters 2 through 5 have been applied. In Chapter 7
the remotely sensed data of the Wadi Ash Shati basin
in Libya have been analyzed. The key issues were
the assessment firstly of atmospheric effects on the
remotely sensed data and secondly of the areal vari-
ability of surface temperature and reflectance.

As regards the first point it was concluded
that to correct the remotely sensed data, the sole
use of radiation transfer models cannot achieve the
required accuracy. To reach that accuracy many addi-
tional data have to be available. By comparing ground
measurements with satellite measurements of surface
temperature and reflectance it was found that, at
least under the atmospheric conditions present in the
Wadi Ash Shati, the satellite data have an acceptable
accuracy, comparable with the one of the radiation
transfer models.

As regards the second point (areal variability)
it has been shown in Chapter 7 that the smoothing
effect of poorer resolutions of satellite data, makes
the combination of data of different resolution some-
what tricky. A rather surprising result was obtained
by studying the areal coherence of surface tempera-
ture. It was found that the areal coherence is lower
in homogeneous areas than in heterogeneous areas. An
explanation of this finding has been proposed on the
basis of the existing pulsation of sensible heat
transport.

In Chapter 8 the procedures to areally estimate
actual evaporation and to study the surface energy
balance with remotely sensed data, were summarized.
A major bottle-neck was overcome by combining the
definition of evaporation sites given in Chapter 3
with the relationship between surface reflectance
and moisture content as given in Chapter 5. These
procedures were applied to satellite data of a
36,000 km^2 area in the Libyan desert and to point
ground reference measurements collected in this area.
Estimations of the apparent soil thermal admittance
and of actual evaporation for each pixel of the sat-
ellite images were made. Finally the impact of the
groundwater losses by evaporation from playas on the
water balance of the West-Libyan aquifer system was
discussed.

SAMENVATTING

FYSISCHE ASPECTEN EN BEPALING VAN DE VERDAMPING IN WOESTIJNEN ONDER TOEPASSING VAN VERTE-WAARNEMINGEN

Gepoogd is een antwoord te geven op de volgende vragen:

A. Welk praktisch belang heeft de schatting van de grondwaterverliezen door verdamping in uitgestrekte woestijngebieden en welke aard van moeilijkheden kunnen daarbij worden verwacht in verband met de op plaatsen met verdamping in woestijnen voorkomende bodemtypen, waarbij inbegrepen hun warmte- en waterhuishouding?

B. Zijn de huidig gebruikte meteorologische methoden om de werkelijke verdamping te berekenen, geschikt voor woestijnomstandigheden?

C. Is het proces van warmte- en vochtoverdracht in bijna droge, hete gronden met een hoog zoutgehalte, voldoende bekend?

D. Welke technieken zijn bruikbaar voor het verzamelen en interpreteren van gegevens onder de bijzondere omstandigheden die zich voordoen in grote woestijngebieden met een gering aantal grond-meetpunten?

In Hoofdstuk 1 is een antwoord gegeven op vraag A. Daarin is aangetoond dat in waterhuishoudkundige studies van woestijnen de natuurlijke grondwaterverliezen door verdamping, te vaak zijn onderschat. Deze grondwaterverliezen treden op in playa's, morfologische landschapsvormen die typisch zijn voor woestijnen. Playagronden worden, behalve door grote temperatuurwisselingen en grondwater op geringe diepte, gekenmerkt door de aanwezigheid van zouten als belangrijk- of hoofdbestanddeel. Deze drie factoren hebben tot gevolg dat er een nauw verband bestaat tussen de oppervlakte-eigenschappen en -structuur, en hun waterhuishouding. In Hoofdstuk 1 is de rol van de grondwaterverdamping via playa's toegelicht aan de hand van een beschrijving van het systeem van watervoerende lagen in West-Libië.

In Hoofdstuk 2 is een kort literatuuroverzicht

gegeven om aan te tonen dat het gebruikelijke concept van potentiële verdamping, niet van toepassing is voor woestijnoppervlakten. Ten einde dit probleem op te lossen en om vraag B te beantwoorden, is een nieuwe combinatievergelijking afgeleid waardoor de verdamping die beneden de grondoppervlakte optreedt, in rekening kan worden gebracht. Bovendien is aangetoond dat de limiet van deze vergelijking voor een diepte nul van het verdampingsfront, overeenkomt met de algemeen bekende combinatievergelijking voor verdamping van kale grond. Op deze wijze is een duidelijke scheiding gemaakt tussen de werkelijke en de potentiële verdamping. Wanneer de verdamping beneden de grondoppervlakte plaatsvindt, kan de nieuwe combinatievergelijking echter alleen worden toegepast indien de coëfficiënten voor overdracht van warmte en van damp in de grond, bekend zijn. Zoals in Hoofdstuk 2 is aangetoond, staan deze coëfficiënten in nauw verband met de verdampingssnelheid en met de vertikale verdeling van het vochtgehalte boven het verdampingsfront, hetgeen een omzeilen van bovengenoemd probleem verhindert. Daarmee is het antwoord op vraag B: dat een verdampingsberekening uit meteorologische gegevens slechts mogelijk is indien een diepgaande analyse van de warmte- en vochtstroming in de bodem een methode oplevert waarmee de overdrachtscoëfficiënten kunnen worden bepaald.

Het antwoord op vraag C is gegeven in Hoofdstuk 3. Daarin is aangetoond dat verschillende mechanismen de warmte- en vochtoverdracht in playagronden doet toenemen. Deze intensiverende processen zijn veelal van weinig belang onder de temperatuur- en vochtomstandigheden die gewoonlijk optreden in niet-gestructureerde bodems buiten de woestijnen. Daarom is over hun praktisch-kwantitatieve rol weinig bekend. In Hoofdstuk 3 is echter bewezen dat de vochtstroom duidelijk kan afwijken van het diffusiekarakter, waaraan men gewoonlijk denkt. Dit afwijkende gedrag is een gevolg van de in woestijnen overwegend voorkomende lage vochtgehalten en van de aanwezigheid van spleten in de zoutkorsten van playa's. De belangrijkste in Hoofdstuk 3 gegeven conclusies over de warmte- en vochtstroming in woestijngronden zijn:

- wanneer de verdamping beneden de grondoppervlakte plaatsvindt, kan de vochtstroom tegengesteld aan de warmtestroom verlopen als gevolg van thermische convectie van de vochtige bodematmosfeer;
- wanneer de vloeistofmenisci in de kleine poriën een straal hebben die vergelijkbaar is met de gemiddelde vrije lengte van waterdampmoleculen, is de vocht- stroom uit deze poriën orden van grootte sneller dan bij diffusie. Dit proces ligt ten grondslag aan de nieuwe definitie van de verdampingsplaatsen die in Hoofdstuk 3 is gegeven.

De effecten van de geïntensiveerde vocht- en warmtestroom komen duidelijker tot uiting door hun in- vloed op de thermische bodemeigenschappen die kunnen worden afgeleid uit bodemtemperatuurmetingen volgens de methoden die in Hoofdstuk 3 zijn besproken. Indien alleen plaatselijke veldgegevens ter beschikking zou- den staan, zouden de achtergronden en methoden die in Hoofdstuk 2 en 3 zijn gegeven nauwelijks bruikbaar zijn voor het schatten van grondwaterverliezen door verdamping.

Het antwoord op vraag D is gegeven in Hoofdstuk 4 en 5, waarin de methoden voor het verzamelen van ge- biedsgegevens zijn gepresenteerd. In Hoofdstuk 4 wordt een nieuwe methode besproken om de thermische eigen- schappen van bodemlagen af te leiden uit verte-waarne- mingen van de oppervlaktetemperatuur voor verschillen- de frequenties van de inkomende temperatuurgolf. Deze methode is vooral geschikt bij gebruik van regelmatig verkregen gegevens van geostationaire satellieten. De grondslag van de methode is het gebruik-maken van het expliciete verband tussen de schijnbare warmte-opname- coëfficiënt van de grondoppervlakte en de thermische eigenschappen en dikte van de verschillende bodemla- gen. Voor een bodem met lagen van bekende dikte en be- kende thermische eigenschappen is de schijnbare warm- te-opnamecoëfficiënt een eenduidige functie van de frequentie van de aan de grondoppervlakte inkomende temperatuurgolf. Dit betekent dat verte-waarnemingen van de schijnbare warmte-opnamecoëfficiënt van de grondoppervlakte kunnen worden gebruikt om tot een ze- kere diepte de thermische eigenschappen en dikte van bodemlagen af te leiden.

In Hoofdstuk 5 is een meer uitgebreid antwoord op vraag D gegeven. Aangetoond wordt dat satellietge- gevens kunnen worden gebruikt om in woestijnen de op- pervlaktereflectie en de oppervlaktetemperatuur ge- biedsgewijze te meten. Referentiemetingen op de grond blijven echter nodig om alle termen van de energieba- lans aan de grondoppervlakte te kunnen bepalen. Spe- ciaal is aangetoond dat de latente warmtestroom een functie is met zes variabelen waarvan hoogstens twee

door sensoren in de ruimte kunnen worden gemeten. Slechts door gebruik te maken van referentiemetingen op de grond kan de dimensie van deze functie worden verkleind en de warmtestroom gebiedsgewijze worden be- rekend uit satellietgegevens van oppervlaktereflectie en oppervlaktetemperatuur.

In Hoofdstuk 5 is ook aangetoond dat de onderlinge afhankelijkheid van oppervlaktereflectie en vochtgehal- te aan de grondoppervlakte kan worden beschreven met een eenvoudige lineaire functie. Het totale poriënvo- lume, de reflectie van droge grond en de reflectie van water zijn de parameters in deze functie.

In Hoofdstuk 6 zijn de gegevens gepresenteerd die in Hoofdstuk 7 en 8 worden gebruikt. Zij betreffen het systeem van watervoerende lagen in West-Libië.

In Hoofdstuk 7 en 8 zijn de methoden die in Hoofd- stuk 2 tot en met 5 zijn besproken, toegepast. In Hoofdstuk 7 zijn de verte-waarnemingen van het Wadi Ash Shati bekken in West-Libië geanalyseerd. Belang- rijk was het vaststellen van de effecten van de atmos- feer op de verte-waarnemingen en de ruimtelijke varia- tie in oppervlaktetemperatuur en oppervlaktereflectie.

Wat betreft het eerste is vastgesteld dat verte- waarnemingen niet met voldoende nauwkeurigheid kunnen worden gecorrigeerd door alleen stralingsoverdrachtmo- dellen te gebruiken. Om de nodige nauwkeurigheid te bereiken dienen dan nog vele additionele gegevens be- schikbaar te zijn. Overigens is, tenminste voor de at- mosferische omstandigheden die in de Wadi Ash Shati voorkomen, bij een vergelijking van grondmetingen met verte-waarnemingen gebleken dat verte-waarnemingen een acceptabele nauwkeurigheid bezitten die vergelijkbaar is met die van stralingsoverdrachtmodellen.

Ten aanzien van de ruimtelijke variatie in opper- vlaktetemperatuur is in Hoofdstuk 7 aangetoond dat het vereffenende effect van het geringere oplossend vermo- gen van verte-waarnemingen, het combineren daarvan met gegevens met een andere nauwkeurigheidsgraad enigszins verraderlijk maakt. Een vrij verrassend resultaat had het onderzoek naar de ruimtelijke samenhang van opper- vlaktetemperaturen. Het bleek dat deze samenhang in morfologisch homogene gebieden lager was dan die in morfologisch heterogene gebieden. Gebaseerd op het voorkomen van sterke fluctuaties in intensiteit van het transport van voelbare warmte is een voorstel tot een verklaring van dit fenomeen gegeven.

In Hoofdstuk 8 is een samenvatting gegeven van de ontwikkelde methoden om met behulp van verte-waar- nemingen de werkelijke verdamping gebiedsgewijze te schatten en de energiebalans aan de grondoppervlakte te onderzoeken. Een belangrijk obstakel daarbij werd

uit de weg geruimd door de in Hoofdstuk 3 gegeven de-
finitie van de plaatsen van verdamping te combineren
met het in Hoofdstuk 5 gegeven verband tussen opper-
vlaktereflectie en het vochtgehalte aan de grondopper-
vlakte. De besproken methoden werden toegepast op
verte-waarnemingen van een 36 000 km^2 groot gebied in
de Libische woestijn en op veldgegevens verzameld in
dat gebied. Schattingen werden gemaakt van de schijn-
bare warmte-opnamecoëfficiënt van de grond en van de
werkelijke verdamping voor elke pixel van de satel-
lietopnamen. Ten slotte is de invloed besproken van
de door verdamping uit playa's optredende grondwater-
verliezen op de waterbalans van het systeem van water-
voerende lagen in West-Libië.

REFERENCES

'Quapropter auctorem neminem unum sequar, sed ut quemque verissimum in quaque parte arbitrabor, quoniam commune ferme omnibus fuit ut eos quisque diligentissime situs diceret in quibus ipse prodebat.'

(PLINIUS, Naturalis Historia, Liber III:1)

ADAMS, J.E., J.T. RITCHIE, E. BURNETT and D.W. FRYREAR, 1969. Evaporation from a simulated soil shrinkage crack. Soil Sci. Soc. Amer. Proc. 33: 609-613.

AL-NAKSHABANDI, G.A. and J.W. KIJNE, 1974. Potential evapotranspiration in central Iraq using the Penman method with modified wind function. J. Hydrol. 23: 319-328.

ANDERSON, R.N. and J.H. SKILBECK, 1980. Oceanic heat flow. In: C. Emiliani (ed.). The Sea 7. Wiley - Interscience, New York: 489-523.

ÅNGSTRÖM, A., 1925. The albedo of various surfaces of ground. Geografiska Ann. 7: 323.

AQUATER, 1980. Hydrogeological study of Wadi Ash Shati, Al Jufrah and Jabal Fezzan area. Final report.

ARYA, L.M., D.A. FARRELL and G.R. BLAKE, 1975. A field study of soil water depletion patterns in presence of growing soybean roots. I. Determination of hydraulic properties of the soil. Soil Sci. Soc. Amer. Proc. 39: 424-430.

ASHBURN, E.W. and R.G. WELDON, 1956. Spectral diffuse reflectance of desert surfaces. J. Opt. Soc. Am. 46(8): 583-586.

ASIMAKOPOULOS, D.N., R.S. COLE, S.J. CAUGHEY and B.A. CREASE, 1976. A quantitative comparison between acoustic sounder returns and the direct measurement of atmospheric temperature fluctuations. Boundary-Layer Meteorol. 10: 137-147.

BAGNOLD, R.A., 1954. The physics of blown sand and desert dunes. Methuen, London. 265 p.

——, 1966. An approach to the sediment transport problem from general physics. US Geol. Survey Professional Paper 422-I. 37 p.

BALLARD, D.H. and C.M. BROWN, 1982. Computer vision. Prentice Hall Inc., Englewood Cliffs, N.J. 523 p.

BARDINET, C., J.M. MONGET and Y. PATOUREAUX, 1982. Combined use of daily thermal cycle of METEOSAT imagery and multispectral LANDSAT data: application to the Bandiagara Plateau, Mali. Proc. EARSel-ESA Symposium, Igls, Austria, 20-21 April 1982. ESA SP-175: 95-101.

BARTMAN, F.L., 1980. A time variable model of earth's albedo. NASA CR-159259. 123 p.

BAVEL, C.H.M. van, 1966. Potential evaporation. The combination concept and its experimental verification. Water Resour. Res. 2(3): 455-467.

—— and D.I. HILLEL, 1976. Calculating potential and actual evaporation from a bare soil surface by simulation of concurrent flow of water and heat. Agric. Meteorol. 12: 361-369.

BEAR, J., D. ZASLAVSKY and S. IRMAY, 1968. Physical principles of water percolation and seepage. Arid Zone Research XXIX. UNESCO, Paris. 465 p.

BENEDICT, W.S. and L.D. KAPLAN, 1964. Calculation of line widths in H_2O - H_2O and H_2O - O_2 collisions. J. Quant. Spectrosc. Radiat. Transfer. 4: 453-469.

BEUKEMA, K.J., 1980. Heat and mass transfer during cooling and storage of agricultural products as influenced by natural convection. Agric. Res. Report 897. PUDOC, Wageningen. 159 p.

BIGNELL, K.J., 1970. The water - vapour infra-red continuum. Quart. J. R. Met. Soc. 96: 390-403.

BLANEY, H.F., 1957. Evaporation study at Silver Lake in the Mojave Desert, California. Trans. Amer. Geophys. Union 38(2): 209-215.

BOELS, D., J.B.H.M. VAN GILS, G.J. VEERMAN and K.E. WIT, 1978. Theory and system of automatic determination of soil moisture characteristics and unsaturated hydraulic conductivities. Soil Sci Science 126(4): 191-199.

BOHLANDER, R.A., R.J. EMERY, D.T. LLEWELLYN-JONES, G.G. GIMMESTAD, H.A. GEBBIE, O.A. SIMPSON, J.J. GALLAGHER and S. PERKOWITZ, 1980. Excess absorption by water vapor and comparison with theoretical dimer absorption. In: A. Deepak et al., 1980. Atmospheric water vapor. Academic Press, London: 241-254.

BOLLE, H.J., 1982. Radiation and energy transport in the earth - atmosphere system. In: O. Hutzinger (ed.). The handbook of environmental chemistry 1, Part B: 131-303. Springer Verlag, Heidelberg.

BOLT, G.H., 1976. Surface interaction between the soil solid phase and the soil solution. In: G.H. Bolt and M.G.M. Bruggenwert (eds.). Soil chemistry. A. Basic elements. Elsevier, Amsterdam: 43-53.

BOUCHET, R.J., 1963. Evapotranspiration réelle et potentielle, signification climatique. Int. Assoc. Sci. Hydrol. 62: 134-142.

BOWEN, I.S., 1926. The ratio of heat losses by conduction and by evaporation from any water surface. Phys. Rev. 27: 779-787.

BOWERS, S.A. and R.J. HANKS, 1965. Reflection of radiant energy from soils. Soil Sci. 100(2): 130-138.

BRAKEL, J. VAN and P.M. HEERTJES, 1974. Analysis of diffusion in macroporous media in terms of a porosity, a tortuosity and a constrictivity factor. Int. J. Heat Mass Transfer 17: 1093-1103.

BREED, C.S., S.G. FRYBERGER, S. ANDREWS, C. McCAULEY, F. LENNARTZ, D. GEBEL and K. HORTSMAN, 1979. Regional studies of sand seas using LANDSAT (ERTS) imagery. In: E.D. McKee (ed.), 1979. A study of global sand seas. USGS Prof. paper 1052: 305-397.

BRESLER, E., H. BIELORAI and A. LAUFER, 1979. Field test of solution flow models in a heterogeneous irrigated cropped soil. Water Resour. Res. 15(3): 645-652.

BROST, R.A., 1979. Some comments on the 'Turbulent exchange coefficients for sensible heat and water vapor under advective conditions'. J. Appl. Meteor. 18: 378-380.

BRUTSAERT, W., 1976. The concise formulation of diffusive sorption of water in dry soil. Water Resour. Res. 12(6): 1118-1124.

——, 1979. Universal constants for scaling the exponential soil water diffusivity? Water Resour. Res. 15(2): 481-483.

——, 1981. Vertical flux of moisture and heat at a bare soil surface. Study conference on land-surface processes in atmospheric general circulation models. NASA - Goddard Space Flight Center, Greenbelt, Maryland, 5-10 Jan. 1981. 51 p.

——, 1982. Evaporation into the atmosphere. Theory, history and applications. D. Reidel Publishing Co., Dordrecht. 299 p.

—— and J.A. MAWDSLEY, 1976. The applicability of planetary boundary layer theory to calculate regional evapotranspiration. Water Resour. Res. 12(5): 852-858.

—— and H. STRICKER, 1979. An advection - aridity approach to estimate actual regional evapotranspiration. Water Resour. Res. 15(2): 443-450.

BUCKINGHAM, E., 1907. Studies on the movement of soil moisture. Bull. 38, Bureau of soils, US Department of Agriculture, Washington DC. 61 p.

BURCH, D.E. and D.A. GRYVNAK, 1980. Continuum absorption by H_2O vapor in the infrared and millimeter regions. In: A. Deepak et al. (eds.), 1980. Atmospheric water vapor. Academic Press, London: 47-76.

BYRNE, G.F. and J.R. DAVIS, 1980. Thermal inertia, thermal admittance, and the effect of layers. Remote Sens. Environ. 9: 295-300.

CABANISS, G.H., 1965. Geophysical studies of playa basins. In: J.T. Neal (ed.). Geology, mineralogy and hydrology of US playas. Air Force Cambridge Research Labs., Env. Res. Paper 96, Bedford, Mass.: 123-148.

CAMILLO, P.J., R.J. GURNEY and T.J. SCHMUGGE, 1983. A soil and atmospheric boundary layer model for evapotranspiration and soil moisture studies. Water Resour. Res. 19(2): 371-380.

CARLSON, T.N. and S.G. BENJAMIN, 1980. Radiative heating rates for Saharan dust. J. Atmos. Sci. 37: 193-213.

—— and R.S. CAVERLY, 1977. Radiative characteristics of Saharan dust at solar wavelengths. J. Geophys. Res. 82: 3141-3152.

—— and P. WENDLING, 1977. Reflected radiance measured by NOAA 3 VHRR as a function of optical depth for Saharan dust. J. Appl. Meteor. 16: 1368-1371.

CARMAN, P.C., 1956. Flow of gases through porous media. Butterworths, London. 182 p.

—— and F.A. RAAL, 1951. Physical adsorption of gases on porous solids. I. Proc. Royal Soc., London, Serie A209: 59-69.

CARSLAW, H.S. and J.C. JAEGER, 1959. Conduction of heat in solids. 2nd Ed., Clarendon Press, Oxford. 510 p.

CARY, J.W., 1971. Calibration of soil heat and water flux meters. Soil Sci. 111(6): 399-400.

——, 1979. Soil heat transducers and water vapor flow. Soil Sci. Soc. Am. J. 43: 835-839.

——, R.A. KOHL and S.A. TAYLOR, 1964. Water adsorption by dry soil and its thermodynamic functions. Soil Sci. Soc. Amer. Proc. 28: 309-314.

—— and S.A. TAYLOR, 1962a. The interaction of the simultaneous diffusions of heat and water vapor. Soil Sci. Soc. Amer. Proc. 26: 413-416.

—— and S.A. TAYLOR, 1962b. Thermally driven liquid and vapor phase transfer of water and energy in soil. Soil Sci. Soc. Amer. Proc. 26: 417-420.

CHAMBOULEYRON, J., M. MENENTI, L. FORNERO, J. MORABITO and L. STEFANINI, 1983. Evaluación y optimización del uso del agua en grandes redes de riego. Instituto Italo-Latino Americano (IILA), Rome. 176 p.

CHILDS, E.C., 1969. An introduction to the physical basis of soil water phenomena. John Wiley and Sons, London. 493 p.

—— and N. COLLIS-GEORGE, 1950. The permeability of porous materials. Proc. Royal Soc., London, Serie A201: 392-405.

CHIN, L.T., 1977. Calculation of crop evapotranspiration, ET (crop) for alfalfa, wheat and maize to be grown at Sebha - Fezzan. Techn. Report 3, Agricultural Research Council (ARC) - LAR, Sebha. 15 p.

CHO, S.H., 1975. An exact solution of the coupled phase change problem in a porous medium. Int. J. Heat Mass Transfer 18: 1139-1142.

CHU, SHU-YAN, G. SPOSITO and W.A. JURY, 1983. The cross-coupling transport coefficient for the steady flow of heat in soil under a gradient of water content. Soil Sci. Soc. Am. J. 47:21-25.

CHUDNOVSKII, A.F., 1962. Heat transfer in the soil. Israel program for scientific translations, Jerusalem. 163 p.

CHURAEV, N.V., 1975. Surface phenomena connected with evaporating water and condensing water vapour in thin capillaries. In: D.A. de Vries and N.H. Afgan (eds.). Heat and mass transfer in the biosphere. Part 1. Transfer processes in the plant environment. Scripta Book Company, Washington DC: 5-28.

CLOUGH, S.A., F.X. KNEIZYS, R. DAVIES, R. GAMACHE and R. TIPPING, 1980. Theoretical line shape for H_2O vapor; application to the continuum. In: A. Deepak et al. (eds.), 1980. Atmospheric water vapor. Academic Press, London: 25-46.

COLEMAN, G. and D.G. DE COURSEY, 1976. Sensitivity and model variance analysis applied to some evaporation and evapotranspiration models. Water Resour. Res. 12(5): 873-879.

COMBARNOUS, M.A. and S.A. BORIES, 1975. Hydrothermal convection in saturated porous media. Adv. in Hydrosc. 10: 231-307.

CONDIT, H.R., 1970. The spectral reflectance of American soils. Photogramm. Eng. 36: 955-966.

CONSTANZ, J., 1982. Temperature dependence of unsaturated hydraulic conductivity of two soils. Soil Sci. Soc. Am. J. 46(3): 466-470.

CORNILLON, P., 1982. A guide to environmental satellite data. Univ. of Rhode Island, Marine Techn. Report 79. 470 p.

COX, S.K., 1973. Infra-red heating calculations with a water vapour pressure broadened continuum. Quart. J. R. Met. Soc. 99: 669-679.

CRANK, J., 1956. The mathematics of diffusion. Oxford Univ. Press, London. 339 p.

CROSS, M., R.D. GIBSON and R.W. YOUNG, 1979. Pressure generation during the drying of a porous half space. Int. J. Heat Mass Transfer 22: 51-60.

CURRIE, J.A., 1960. Gaseous diffusion in porous media. Brit. J. Appl. Phys. 11: 314-324.

DANE, J.H. and A. KLUTE, 1977. Salt effects on the hydraulic properties of a swelling soil. Soil Sci. Soc. Am. J. 41: 1043-1049.

DAVE, J.V. and R. BERNSTEIN, 1982. Effect of terrain orientation and solar position on satellite-level luminance observations. Remote Sens. Environ. 12: 331-348.

DEEPAK, A., T.D. WILKERSON and L.H. RUHNKE, 1980. Atmospheric water vapour. Academic Press, London. 695 p.

DIJK, C. van, C.J. MULDER, J.Ph. POLEY and J. van STEVENINK, 1971. Exploration for (shallow) geological structures with the thermal infrared imagery technique in some desert areas of Oman. Proc. 7th Intern. Symp. on Remote Sensing of Environment III: 2115-2131.

DINCER, T., A. AL-MUGRIN and U. ZIMMERMANN, 1974. Study of the infiltration and recharge through the sand dunes in arid zones with special reference to the stable isotopes and thermonuclear tritium. J. Hydrol. 23: 79-109.

DUIN, R.H.A. van, 1963. The influence of soil management on the temperature wave near the soil surface. Techn. Bull. 29 Inst. for Land and Water Manag. Res., Wageningen. 20 p.

DULLIEN, F.A.L., 1979. Porous media. Fluid transport and porous structure. Academic Press, London. 396 p.

DUTCHER, L.C. and H.E. THOMAS, 1967. Surface water and related climate features of the Sahil Susah area, Tunisia. US Geological Survey, Water Supply Paper 1757-E. 40 p.

DYER, A.J., 1974. A review of flux - profile relationships. Boundary-Layer Meteorol. 7: 363-372.

EDMUNDS, W.M. and E.P. WRIGHT, 1979. Groundwater recharge and paleoclimate in the Sirte and Kufra basins, Libya. J. Hydrol. 40: 215-241.

EGELSTAFF, P.A., 1967. Introduction to the liquid state. Academic Press, London. 236 p.

EHLERS, W., 1976. Rapid determination of unsaturated hydraulic conductivity in tilled and untilled loess soil. Soil Sci. Soc. Am. J. 40: 837-840.

EISENBERG, D. and W. KAUZMANN, 1969. The structure and
properties of water. Clarendon Press, Oxford.
296 p.

ELDBLOM, L., 1961. Quelques points de vue comparatifs
sur les problèmes d'irrigation dans les trois
oasis libyennes de Brak, Ghadames et particuliè-
rement Mourzouq. Lund studies in geography, Ser.
B. Human geography 22. 22 p.

EL-SHAZLY, E.M., M.A. ABDEL-HADY and M.A. MORSY, 1973.
Geologic interpretation of infrared thermal im-
ages in East Qatrani area, Western Desert, Egypt.
Proc. 9th Int. Symp. Remote Sens. Environ.: 1877-
1889.

ENNABLI, M., 1981. Vulnerability study of an overex-
ploited aquifer to the saline contamination from
a sebkhat by mathematical model: Sedjoumi's aqui-
fer's case in Tunisia. In: Quality of Groundwater.
Proceedings of an intern. symposium, Noordwijker-
hout, The Netherlands, 23-27 March 1981. W. van
Duijvenbooden, P. Glasbergen and H. van Lelyveld
(eds.). Studies in environmental science 17: 897-
907. Elsevier Scientific Publishing Company.

ERGUN, S., 1952. Fluid flow through packed columns.
Chem. Engng. Prog. 48: 89-94.

ERH, K.T., D.R. NIELSEN and J.W. BIGGAR, 1971. Two
dimensional heat transfer in porous media with
steady-state water flow. Soil Sci. Soc. Amer.
Proc. 35(2): 209-214.

ESOC, 1980a. Use of Meteosat high resolution format
interpretation data. European Space Operations
Centre (ESOC), Darmstadt. 31 p.

———, 1980b. Magnetic tape and file descriptions.
Meteosat system guide 12. European Space Opera-
tions Centre (ESOC), Darmstadt. 71 p.

———, 1981. METEOSAT system guide 6, annex A - METEOSAT
1.

EUGSTER, H.P. and G.I. SMITH, 1965. Mineral equilibria
in Searles Lake evaporites, California. J. Petr.
6(3): 473-522.

EVANS, D.D., T.W. SAMMIS and D.R. CABLE, 1981. Actual
evapotranspiration under desert conditions. In:
D.D. Evans and J.L. Thames (eds.). Water in desert
ecosystems. Dowden, Hutchinson and Ross, Inc.,
Stroudsburg, Pennsylvania: 195-218.

——— and J.L. THAMES (eds.), 1981. Water in desert
ecosystems. Dowden, Hutchinson and Ross, Inc.,
Stroudsburg, Pennsylvania. 280 p.

FALCKENBERG, G., 1928. Die Absorptionskonstanten eini-
ger meteorologisch wichtigen Körper für infrarote
Wellen. Met. Z.: 334-337.

FANTOLI, A., 1967. Contributo alla climatologia della
Tripolitania. Parte I. Min. degli Aff. Esteri
(MAE), Rome. 640 p.

FAO, 1975. Crop water requirements. Irr. Drain. Paper
24 (1st ed.). 179 p.

———, 1977. Crop water requirements. Irr. Drain. Paper
24 (2nd ed.). 144 p.

———, 1981. Arid zone hydrology for agricultural devel-
opment. Irr. Drain. Paper 37. 367 p.

FARRELL, D.A., E.L. GREACEN and C.G. GURR, 1966. Vapor
transfer in soil due to air turbulence. Soil Sci.
102(6): 305-313.

FEDDES, R.A., 1971. Water, heat and crop growth. Thesis,
Agricultural University, Wageningen, The Nether-
lands. H. Veenman & Zonen, Wageningen. 184 p.

———, P.J. KOWALIK and H. ZARADNY, 1978. Simulation of
field water use and crop yield. Simulation mono-
graphs. PUDOC, Wageningen. 188 p.

FERMI, E., 1968. Termodinamica (7th unrevised edition,
1st ed. 1958). Boringhieri, Torino. 179 p.

FINK, D.H. and R.D. JACKSON, 1973. An equation for de-
scribing water vapor adsorption isotherms of soils.
Soil Sci. 116(4): 256-261.

FORSYTHE, W.E., 1964. Smithsonian physical tables (9th
revised edition - 3rd reprint). Smithsonian In-
stitution, Washington DC. 827 p.

FRASER, R.S., 1976. Satellite measurements of mass of
Sahara dust in the atmosphere. Appl. Opt. 15(10):
2471-2479.

FRITTON, D.D., D. KIRKHAM and R.H. SHAW, 1970. Soil
water evaporation, isothermal diffusion and heat
and water transfer. Soil Sci. Soc. Amer. Proc.
34(2): 183-189.

FRYBERGER, S.G., 1979. Dune forms and wind regime. In:
E.D. McKee (ed.), 1979. A study of global sand
seas. USGS Prof. paper 1052: 137-169.

FUCHS, M. and A. HADAS, 1972. The heat flux density in
a non-homogeneous bare loessial soil. Boundary-
Layer Meteorol. 3: 191-200.

——— and C.B. TANNER, 1968. Calibration and field test
of soil heat flux plates. Soil Sci. Soc. Amer.
Proc. 32: 326-328.

GAEVSKY, V.L., 1951. Surface temperature over large
territories. Trudy GGO 26(88) (in Russian).

GARDNER, H.R. and R.J. HANKS, 1966. Evaluation of the
evaporation zone by measurement of heat flux.
Soil Sci. Soc. Amer. Proc. 30(4): 425-433.

GARTLING, D.K., 1982. Finite element analysis of ther-
mal convection in deep ocean sediments. Adv. Wa-
ter Resources 5: 136-141.

GAY, L.W., 1981. Potential evapotranspiration for des-
erts. In: D.D. Evans and J.L. Thames (eds.). Wa-
ter in desert ecosystems. Dowden, Hutchinson and
Ross, Inc., Stroudsburg, Pennsylvania: 172-194.

GERMANCONSULT, 1975. Groundwater resources development.
Ummal Djadawel and Hatteyat-Barken. Counc. of
Agric. Dev. LAR, Tripoli 1 and 2.

GILLESPIE, A.R. and A.B. KAHLE, 1977. Construction and interpretation of a digital thermal inertia image. Photogramm. Eng. Remote Sens. 43(8): 983-1000.

GOUDARZI, G.H., 1962. Idri salt deposits, Fezzan province, Libya. US Geological Survey - open file report. 36 p.

——, 1970. Geology and mineral resources of Libya. A reconnaissance. US Geological Survey Prof. paper 660: 104 p + 13 plates.

GRIFFITHS, J.F. and K.H. SOLIMAN, 1972. Climates of Africa: the Northern Desert. In: J.F. Griffiths (ed.). Climates of Africa. World Survey of climatology (H.E. Landsberg, ed.) 10: 75-131. Elsevier, Amsterdam.

GRUBER, A., 1981. An earth-radiation budget data set and its potential for determining surface radiation budget characteristics. Study conference on land surface processes in atmospheric general circulation models. Greenbelt, USA, 5-10 January 1981: 541-560.

GUBE, M., 1982. Computation of the earth's radiation budget from spectral radiance measurements of the satellite Meteosat. ESA STR-210, European Space Agency, Paris. 66 p.

GUPTA, J.P., 1979. Some observations on the periodic variations of moisture in stabilized and unstabilized sand dunes of the Indian Desert. J. Hydrol. 41: 153-156.

HADAS, A., 1969. A comparison between predicted and measured values of the thermal conductivity of a moist soil under steady and fluctuating thermal regimes. Israel J. Agric. Res. 19: 151-160.

——, 1973. Evaluation of the block method for determining the thermal properties of the top soil. Agric. Meteorol. 11: 269-276.

——, 1977a. Evaluation of theoretically predicted thermal conductivities of soils under field and laboratory conditions. Soil Sci. Soc. Amer. Proc. 41: 460-466.

——, 1977b. Heat transfer in dry aggregated soil. I. Heat conduction. Soil Sci. Soc. Am. J. 41: 1055-1059.

—— and D. HILLEL, 1972. Steady-state evaporation through non homogeneous soils from a shallow water table. Soil Sci. 113(2): 65-73.

HANEGHEM, I.A. van, 1981. Een niet-stationaire naald-methode (warmtegeleiding, warmtecapaciteit, contactweerstand). Thesis, Agricultural University, Wageningen, The Netherlands. 187 p.

HANKS, R.J. and C.B. TANNER, 1972. Calorimetric and flux meter measurements of soil heat flow. Soil Sci. Soc. Amer. Proc. 36: 537-538.

HARBECK, G.E. Jr., 1955. The effect of salinity on evaporation. US Geol. Survey Prof. paper 272-A. 6 p.

HASSAN, F.A. and A.S. GHAIBEH, 1977. Evaporation and salt movement in soils in the presence of water table. Soil Sci. Soc. Amer. Proc. 20(3): 470-478.

HELLWIG, D.H.R., 1973. Evaporation of water from sand. 2. Diurnal variations. J. Hydrol. 18: 109-118.

——, 1974. Evaporation of water from sand. 5. The effect of evaporation on the precipitation of salts dissolved in water stored in sand. J. Hydrol. 21: 101-110.

——, 1978. Evaporation of water from sand. 6. The influence of the depth of the water table on diurnal variations. J. Hydrol. 39: 129-138.

——, 1979. Evaporation of water from sand. The effect of evaporation on the precipitation of salts dissolved in water stored in sand. J. Hydrol. 41: 149-151.

HEM, J.D., 1967. Composition of saline residues on leaves and stems of saltcedar (Tamarix pentandra Pallas). US Geol. Survey Prof. paper 491-C. 9 p.

HERZEN, R.P. von, H. HOSKINS and T.H. van ANDEL, 1972. Geol. Soc. America Bull. 83: 1901-1910.

HICKS, B.B. and R.G. EVERETT, 1979. Comments on 'Turbulent exchange coefficients for sensible heat and water vapor under advective conditions'. J. Appl. Meteor. 18: 381-382.

HILLEL, D., 1980. Applications of soil physics. Academic Press, New York. 385 p.

—— and A. HADAS, 1972. Isothermal drying of structurally layered soil columns. Soil Sci. 113(1): 30-35.

HISER, H.W. and H.V. SENN, 1980. Mesoscale mapping of available solar energy at the earth's surface by use of satellites. Solar Energy 24: 129-141.

HORTON, R. Jr., 1982. Determination and use of soil thermal properties near the soil surface. Ph.D. Dissertation. New Mexico State Univ. Univ. Microfilms. Ann Arbor, Mich. (Diss. Abstr. DA 82-03096). 132 p.

——, P.J. WIERENGA and D.R. NIELSEN, 1983. Evaluation of methods for determining the apparent thermal diffusivity of soil near the surface. Soil Sci. Soc. Am. J. 47: 25-32.

HOUGHTON, J.T. and A.C.L. LEE, 1972. Atmospheric transmission in the 10-12 μm window. Nature - Physical Science 238: 117-118.

HOVIS, W.A. Jr., 1966. Infrared reflectance of some common minerals. Appl. Opt. 5(2): 245-248.

——, L.R. BLAINE and W.R. CALLAHAN, 1968. Infrared aircraft spectra over desert terrain 8.5 to 16 μm. Appl. Opt. 7: 1137-1140.

HOVIS, W.A. Jr. and W.R. CALLAHAN, 1966. Infrared reflectance spectra of igneous rocks, tufts and red sandstone from 0.5 to 22 μ. Opt. Soc. Amer. 56(5): 639-643.

HUANG, C.L.D., 1979. Multi-phase moisture transfer in porous media subjected to temperature gradients. Int. J. Heat Mass Transfer 22: 1295-1307.

———, H.H. SIANG and C.H. BEST, 1979. Heat and moisture transfer in concrete slabs. Int. J. Heat Mass Transfer 22: 257-265.

HUNT, C.B., 1960. The Death Valley salt pan, a study of evaporites. US Geol. Survey Prof. paper 400-B: 456-458.

HUNT, G.E., 1973. Radiative properties of terrestrial clouds at visible and infra-red thermal window wavelengths. Quart. J. R. Met. Soc. 99: 346-369.

HUYGEN, J. and P. REINIGER, 1979. A test of the TELL-US model for the conditions of the Grendon test-site. Tellus Newsletter 8. JRC, Ispra. 16 p.

HYLCKAMA, T.E.A. van, 1970. Water use by salt cedar. Water Resour. Res. 6(3): 728-735.

———, 1974. Water use by salt cedar as measured by the water budget method. US Geol. Survey Prof. paper 491-E. 30 p.

———, 1980. Weather and evapotranspiration studies in a salt cedar thicket, Arizona. US Geol. Survey Prof. paper 491-F. 78 p.

IDSO, S.B., 1972. Calibration of soil heat flux plates by a radiation technique. Agric. Meteorol. 10: 467-471.

———, R.D. JACKSON, R.J. REGINATO, B.A. KIMBALL and F.S. NAKAYAMA, 1975. The dependence of bare soil albedo on soil water content. J. Appl. Meteor. 14(1): 109-113.

———, R.J. REGINATO, R.D. JACKSON, B.A. KIMBALL and F.S. NAKAYAMA, 1974. The three stages of drying of a field soil. Soil Sci. Soc. Amer. Proc. 38(5): 831-837.

INTERAGENCY TASK FORCE ON IRRIGATION EFFICIENCIES, 1979. Irrigation water use and management. US Government Printing Office, Washington DC. 133 p.

ITALCONSULT, 1969. Water and agricultural development studies for Area IV. Final report: Climate and surface hydrology. Italconsult, Rome. 83 p, 5 appendices.

———, 1975. Fezzan land reclamation project. Wadi Shatti - Eshkeda area. Hydrogeological survey. Part 2. Min. Agric. Dev., Tripoli. 70 p.

ITIER, B., 1977. Determination des corrections à apporter aux mesures et aux estimations de l'évapotranspiration en régime advectif. La Météor., VIth Ser., no. 11: 55-60.

ITTEN, K.I., 1981. Possibilities for remote sensing of surface characteristics. Study conference on land surface processes in atmospheric general circulation models. Greenbelt, USA, 5-10 January 1981: 541-560.

JACKSON, R.D., 1964a. Water vapor diffusion in relatively dry soil. I. Theoretical considerations and sorption experiments. Soil Sci. Soc. Amer. Proc. 28(2): 172-176.

———, 1964b. Water vapor diffusion in relatively dry soil. II. Desorption experiments. Soil Sci. Soc. Amer. Proc. 28(4): 464-466.

———, 1964c. Water vapor diffusion in relatively dry soil. III. Steady-state experiments. Soil Sci. Soc. Amer. Proc. 28(4): 467-470.

———, 1965. Water vapor diffusion in relatively dry soil. IV. Temperature and pressure effects on sorption diffusion coefficients. Soil Sci. Soc. Amer. Proc. 29(2): 144-148.

———, 1973. Diurnal changes in soil water content during drying. In: R.R. Bruce et al. (eds.). Field soil water regime. Special Pub. 5, Soil Sci. Soc. Amer. Proc.: 37-55.

———, B.A. KIMBALL, R.J. REGINATO and F.S. NAKAYAMA, 1973. Diurnal soil-water evaporation: time - depth - flux patterns. Soil Sci. Soc. Amer. Proc. 37: 505-509.

———, R.J. REGINATO, B.A. KIMBALL and F.S. NAKAYAMA, 1974. Diurnal soil-water evaporation: comparison of measured and calculated soil-water fluxes. Soil Sci. Soc. Amer. Proc. 38(6): 861-866.

JONES, J.E., 1977. Calculation of evapotranspiration using color-infrared photography. US Geological Survey Prof. paper 655-0. 45 p.

JONES, J.R., 1964. Ground-water maps of the Kingdom of Libya. US Geological Survey, open-file report. 24 p.

———, 1971. Ground-water provinces of Libyan Arab Republic. In: Carlyle Gray (ed.), 1971. Symposium on the geology of Libya, April 14-18, 1969. Tripoli: 449-457.

JONES, M., 1981. Navigation and deformation modelling for Meteosat Imagery. ESA Journal 5: 287-304.

JONGERIUS, A. and E.B.A. BISDOM, 1981. Porosity measurements using the Quantimet 720 on backscattered electron scanning images of thin sections of soils. In: E.B.A. Bisdom (ed.). Submicroscopy of soils and weathered rocks. PUDOC, Wageningen: 207-216.

JURY, W.A., R. GROVER, W.F. SPENCER and W.J. FARMER, 1980. Modeling vapor losses of soil-incorporated triallate. Soil Sci. Soc. Am. J. 44(3): 445-450.

JURY, W.A., J. LETEY Jr. and L.H. STOLZY, 1981. Flow of water and energy under desert conditions. In: D.D. Evans and J.L. Thames (eds.). Water in desert ecosystems. Dowden, Hutchinson and Ross, Inc., Stroudsburg, Pennsylvania: 92-113.

—— and E.E. MILLER, 1974. Measurement of the transport coefficients for coupled flow of heat and moisture in a medium sand. Soil Sci. Soc. Amer. Proc. 38: 551-557.

JUTSON, J.T., 1918. The sand ridges, rock floors and other associated features at Goongarrie in subarid Western Australia, and their relation to the growth of Lake Goongarrie, a 'dry' lake or playa. Royal Society of Victoria, Proceedings 31: 113-128.

KATTO, Y. and T. MASUOKA, 1967. Criterion for the onset of convective flow in a fluid in a porous medium. Int. J. Heat Mass Transfer 10: 297-309.

KAWABATA, Y., F. OOMORI and T. HATTORI, 1951. Radiation properties of some soils. J. Agric. Meteorol. 6(3-4)

KEEY, R.B. and M. SUZUKI, 1974. On the characteristic drying curve. Int. J. Heat Mass Transfer 17: 1455-1464.

KERR, P.F. and A.M. LANGER, 1965. Mineralogical feature of Mojave Desert playa crusts. In: J.T. Neal (ed.). Geology, mineralogy and hydrology of US playas. Air Force Cambridge Research Labs, Env. Res. Paper 96, Bedford, Mass.: 31-72.

KEULEN, H. van and D. HILLEL, 1974. A simulation study of the drying-front phenomenon. Soil Sci. 118(4): 270-273.

KIMBALL, B.A., 1973. Water vapor movement through mulches under field conditions. Soil Sci. Soc. Amer. Proc. 37(6): 813-818.

—— and R.D. JACKSON, 1975. Soil heat flux determination: a null alignment method. Agric. Meteorol. 15: 1-9.

—— and E.R. LEMON, 1971a. Air turbulence effects upon soil gas exchange. Soil Sci. Soc. Amer. Proc. 35: 16-21.

——, 1971b. Theory of soil air movement due to pressure fluctuations. Agric. Meteorol. 9: 163-181.

KLUTE, A., 1972. The determination of the hydraulic conductivity and diffusivity of unsaturated soils. Soil Sci. 113(4): 264-276.

KONDRATYEV, K.Ya., 1954. Radiative solar energy. Gidrometeoizdat, Leningrad. 692 p. (in Russian).

——, 1969. Radiation in the atmosphere. Academic Press, New York. 912 p.

——, V.I. KORZOV, V.V. MUKHENBERG and L.N. DYACHENKO, 1981. The shortwave albedo and the surface emissivity. Study conference on land surface processes in atmospheric general circulation models. Greenbelt, USA, 5-10 January 1981: 463-514.

KÖPKE, P., 1980. Absolute calibration of METEOSAT-VIS and IR-channel by ground measurements. The Second Scientific User Meeting, London, 26-27 March 1980. European Space Operations Centre (ESOC), Darmstadt: E1-E7.

KOWALIK, W.S., S.E. MARSH and R.J.P. LYON, 1982. A relation between Landsat digital numbers, surface reflectance and the cosine of the solar zenith angle. Remote Sens. Environ. 12: 39-55.

KRISCHER, O. and H. ROHNALTER, 1940. Wärmeleitung und Dampfdiffusion in feuchten Gutern. Verein Deut. Ing. Forschungsheft 402.

KUNDE, V.G., B.J. CONRATH, R.A. HANEL, W.C. MAGUIRE, C. PRABHAKARA and V.V. SALOMONSON, 1974. The Nimbus 4 infrared spectroscopy experiment. 2. Comparison of observed and theoretical radiances from 425-1450 cm^{-1}. J. Geophys. Res. 79(6): 777-784.

LANGER, A.M. and P.F. KERR, 1966. Mojave playa crust: physical properties and mineral content. Jour. Sedimentary Petrology 36(2): 377-395.

LARSON, J.C. and B.R. BARKSTROM, 1977. Effects of realistic angular reflection laws for the earth's surface upon calculations of the earth - atmosphere albedo. Proc. Symp. on radiation in the atmosphere, 19-23 Aug. 1976: 451-453. Science Press, Princeton, N.Y.

LAWSON, M.L. and W.J. YANG, 1975. Thermal stability of binary gas mixtures in a porous medium. J. Heat Transfer 97: 378-381.

LEBEDEV, A.N. (ed.), 1968. The climate of Africa I. Israel program for scientific translations. 482 p.

LEE, A.C.L., 1973. A study of the continuum absorption within the 8-13 µm atmospheric window. Quart. J. R. Met. Soc. 99: 490-505.

LEE, T.C., 1975. Focusing and defocusing of heat flow by a buried sphere. Geophys. J. R. Astr. Soc. 43: 635-641.

—— and T.L. HENVEY, 1974. Heat-flow refraction across dissimilar media. Geophys. J. R. Astr. Soc. 39: 319-333.

LI, H.H., 1980. The infrared absorption coefficients of Alkali Halides. Int. J. of Thermophysics 1(1): 97-133.

LIOU, K.N., 1980. An introduction to atmospheric radiation. Academic Press, London. 392 p.

LLEWELLYN-JONES, D.T., 1980. Laboratory measurements of absorption by water vapour in the frequency range 100 to 1000 GHz. In: A. Deepak et al. (eds.), 1980. Atmospheric water vapour. Academic Press, London: 255-264.

LOW, P.F., 1979. Nature and properties of water in montmorillonite - water systems. Soil Sci. Soc. Am. J. 43: 651-658.

LUIKOV, A.V., 1966. Heat and mass transfer in capillary porous bodies. Pergamon Press, London. 523 p.

——, T.L. PERELMAN, V.V. LEVDANSKY, V.G. LEITSINA and N.V. PAVLYUKEVICH, 1974. Theoretical investigation of vapour transfer through a capillary porous body. Int. J. Heat Mass Transfer 17: 961-970.

LYON, R.J.P. and J.W. PATTERSON, 1969. Airborne geological mapping using infrared emission spectra. Proc. 6th Symp. on Remote Sensing of Environment. Univ. of Mich., Ann Arbor 1: 527-552.

MAKAROVA, N.M., A.E. MIKIROV and V.A. SMERKALOV, 1973. Generalized dependence of land and sea surfaces' albedos on sun elevation. Trudy IPG 17: 203-210 (in Russian).

MANTON, M.J., 1976. On the structure of free convection near the surface. Boundary-Layer Meteorol. 10: 347-352.

MARSHALL, T.J. and J.W. HOLMES, 1979. Soil physics. Cambridge Univ. Press. 345 p.

MARTINELLI, E., 1967. Lezioni di geometria I. Veschi, Rome. 722 p.

MASON, E.A., A.P. MALINAUSKAS and R.B. EVANS, 1967. Flow and diffusion of gases in porous media. J. Chem. Phys. 46(8): 3199-3216.

MAUNY, R., 1961. Tableau géographique de l'Ouest Africain au moyen age. Institut Français d'Afrique Noire (IFAN), Dakar. 575 p.

MAY, G.A. and G.W. PETERSEN, 1975. Spectral signature selection for mapping unvegetated soils. Remote Sens. Environ. 4: 211-220.

McCUEN, R.H., 1974. A sensitivity and error analysis of procedures used for estimating evaporation. Water Resour. Bull. 10(3): 486-497.

MEIGS, P., 1953. World distribution of arid and semi-arid homoclimates. In: Arid Zone Programme 1: Reviews of research on arid zone hydrology. UNESCO, Paris: 203-210.

MEINZER, O.E., 1927. Plants as indicators of ground water. US Geol. Survey water-supply paper 577. 95 p.

McGINNIES, W.G., B.J. GOLDMAN and P. PAYLORE (eds.), 1968. Deserts of the world. Univ. of Arizona Press. 788 p.

—— and B.J. GOLDMAN (eds.), 1969. Arid lands in perspective. Univ. of Arizona Press. 421 p.

McKEE, E.D. (ed.), 1979. A study of global sand seas. US Geological Survey Prof. paper 1052. 429 p.

MENENTI, M., 1980. Defining relationships between surface characteristics and actual evaporation rate. TELLUS Newsl. 15, JRC Ispra. 21 p.

MERCIER, M.G., 1924. La langue libyenne et la toponymie antique de l'Afrique du Nord. Journal Asiatique, tome CCV: 189-320.

MIKHAILOV, M.D., 1975. Exact solutions of temperature and moisture distributions in a porous half-space with moving evaporation front. Int. J. Heat Mass Transfer 18: 797-804.

MOGRO-CAMPERO, A. and R.L. FLEISCHER, 1977. Subterrestrial fluid convection: a hypothesis for long distance migration of radon within the earth. Earth and Pl. Sc. Lett. 34: 321-325.

MOLINEUX, C.E., E.E. BLIAMUTIS and J.T. NEAL, 1971. A remote sensing investigation of four Mojave playas. Air Force Cambridge Research Labs. Env. Res. paper 352. 70 p.

MONTEITH, J.L., 1973. Principles of environmental physics. Edward Arnold, London. 241 p.

——, 1981. Evaporation and surface temperature. Quart. J. R. Met. Soc. 107: 1-27.

MONTGOMERY, G.P. Jr., 1978. Temperature dependence of infrared absorption by the water vapor continuum near 1200 cm^{-1}. Applied Optics 17(15): 2299-2303.

MORROW, N.R., 1970. Physics and thermodynamics of capillary action in porous media. Ind. Eng. Chem. 62(6): 32-56.

MORTON, F.J., 1978. Estimating evapotranspiration from potential evaporation: practicality of an iconoclastic approach. J. Hydrol. 38: 1-32.

MOTHA, R.P., S.B. VERMA and N.J. ROSENBERG, 1979a. Turbulence spectra above a vegetated surface under conditions of sensible heat advection. J. Appl. Meteor. 18: 317-323.

——, S.B. VERMA and N.J. ROSENBERG, 1979b. Exchange coefficients under sensible heat advection determined by eddy correlation. Agric. Meteor. 20: 273-280.

MOTTS, W.S., 1965. Hydrologic types of playas and closed valleys and some relations of hydrology to playa geology. In: J.T. Neal (ed.). Geology, mineralogy and hydrology of US playas. Air Force Cambridge Research Labs. Env. Res. paper 96, Bedford, Mass.: 73-104.

MUALEM, Y., 1976. A new model for predicting the hydraulic conductivity of unsaturated porous media. Water Resour. Res. 12(3): 513-522.

—— and G. DAGAN, 1978. Hydraulic conductivity of soils: unified approach to the statistical models. Soil Sci. Soc. Am. J. 42: 392-395.

NACK, M.L. and R.J. CURRAN, 1978. Transformation of surface albedo to surface atmosphere albedo and irradiance, and their spectral and temporal averages. Third Conference on atmospheric radiation of the American Meteorological Society, June 27-30, 1978. Davis, Calif.

NAKANO, Y., 1980. Traveling wave solutions of saturated - unsaturated flow through porous media. Water Resour. Res. 16(1): 117-122.

——, 1981. A traveling wave solution to the problem of simultaneous flow of water and air through homogeneous porous media. Water Resour. Res. 17 (1): 57-64.

NAKANO, M. and T. MIYAZAKI, 1979. The diffusion and nonequilibrium thermodynamic equations of water vapor in soils under temperature gradients. Soil Sci. 128(3): 184-188.

NAKAYAMA, F.S., R.D. JACKSON, B.A. KIMBALL and R.J. REGINATO, 1973. Diurnal soil water evaporation: chloride movement and accumulation near the soil surface. Soil Sci. Soc. Amer. Proc. 37: 509-513.

NASA, 1980. Heat capacity mapping mission. User's guide. 2nd Revision. Goddard Space Flight Center, Greenbelt, Maryland. 120 p.

NEAL, J.T. (ed.), 1965a. Geology, mineralogy and hydrology of US playas. Air Force Cambridge Res. Labs. Env. Res. paper 96, Bedford, Mass. 176 p.

——, 1965b. Airphoto characteristics of playas. In: J.T. Neal (ed.). Geology, mineralogy and hydrology of US playas. Air Force Cambridge Res. Labs. Env. Res. paper 96, Bedford, Mass.: 149-176.

——, 1969. Playa variation. In: W.G. McGinnies and B.J. Goldman (eds.). Arid lands in perspective. Univ. of Arizona Press: 13-44.

——, 1972. Playa surface features as indicators of environment. I. CASALS pub. 4, Texas Tech. Univ., Lubbock, Texas: 107-131.

——, 1975. Playas and dried lakes. In: R.W. Fairbridge (ed.). Benchmark papers in geology 20. Dowden, Hutchinson and Ross, Inc. 401 p.

—— and W.S. MOTTS, 1967. Recent geomorphic changes in playas of western United States. Jour. Geol. 75(5): 511-526.

NIELD, D.A., 1968. Onset of thermohaline convection in a porous medium. Water Resour. Res. 4: 553-560.

NIELSEN, D.R., J.W. BIGGAR and K.T. ERH, 1973. Spatial variability of field measured soil-water properties. Hilgardia 42: 215-259.

OGUNTOYINBO, J.S., 1970. Reflection coefficient of natural vegetation, crops and urban surface in Nigeria. Quart. J. Roy. Met. Soc. 96(409): 430-441.

ONCHUKOV, D.N., 1957. The phenomenon of heat and moisture transmission in soils and subsoils. Moskov. Technol. Inst. Pishch. Promysh. Trudy: 55-63.

OTTERMAN, J. and R.S. FRASER, 1976. Earth - atmosphere system and surface reflectivities in arid regions from Landsat MSS data. Remote Sens. Environ. 5: 247-266.

OVERGAARD MOGENSEN, V., 1970. The calibration factor of heat flux meters in relation to the thermal conductivity of the surrounding medium. Agr. Meteorol. 7: 401-410.

PALLAS, P., 1977. Evaluation of groundwater resources - Fezzan. Secretary of Dams and Water Resources (SDWR), LAR, Tripoli. 23 p.

PARIKH, J.A., 1977. A comparative study of cloud classification techniques. Remote Sens. Environ. 6: 67-81.

—— and J.T. BALL, 1980. Analysis of cloud type and cloud amount during GATE from SMS-1 IR data. Remote Sens. Environ. 9: 225-245.

PEIXOTO, J.P., R.D. ROSEN and M.F. WU, 1976. Seasonal variability in the Pole-to-Pole water balance during the IGY. Nordic Hydrology 7: 95-114.

——, D.A. SALSTEIN and R.D. ROSEN, 1981. Intra-annual variation in large-scale moisture fields. J. Geophys. Res. 86(C2): 1255-1264.

PENMAN, H.L., 1948. Natural evaporation from open water, bare soil and grass. Proc. Roy. Soc., Ser. A, vol. 193: 120-146.

PHILIP, J.R., 1957. Evaporation, and moisture and heat fields in the soil. J. Meteorol. 14: 354-366.

——, 1961. The theory of heat flux meters. J. Geophys. Res. 66(2): 571-579.

——, 1969. Theory of infiltration. Adv. Hydroscience 5: 215-296.

——, 1975. Water movement in soils. In: D.A. de Vries and N.H. Afgan (eds.). Heat and mass transfer in the biosphere. Part 1. Transfer processes in the plant environment. Scripta Book Company, Washington DC: 5-28.

——, 1982a. Free convection at small Rayleigh number in porous cavities of rectangular, elliptical, triangular and other cross-sections. Int. J. Heat Mass Transfer 25(10): 1503-1509.

——, 1982b. Axisymmetric free convection at small Rayleigh number in porous cavities. Int. J. Heat Mass Transfer 25(11): 1689-1699.

—— and D.A. de VRIES, 1957. Moisture movement in porous materials under temperature gradients. Trans. Amer. Geophys. Union 38(2): 222-232.

PHONG-ANANT, D., A.J. CHAMBERS and R.A. ANTONIA, 1981. Spatial coherence of temperature fluctuations in the atmospheric surface layer. Boundary-Layer Meteorol. 21(4): 464-475.

PIELKE, R.A. and H.A. PANOFSKY, 1970. Turbulence characteristics along several towers. Boundary-Layer Meteorol. 1(2): 115-130.

PIKE, J.G., 1970. Evaporation of groundwater from coastal playas (sabkhah) in the Arabian Gulf. J. Hydrol. 11(72): 79-88.

PIZZI, G. and E. PONE, 1978. Hydrogeology of the western Libya regional aquifer system. Internal report 18, Idrotecneco, Pesaro. 45 p.

PLANET, W.G., 1970. Some comments on reflectance measurements of wet soils. Remote Sens. Environ. 1: 127-129.

PLATT, C.M.R., 1972. Airborne infrared radiance measurements (10 to 12 micron wavelength) off tropical east-coast Australia. J. Geophys. Res. 77(9): 1597-1609.

———, 1981. Two dimensional histograms of GMS-1 satellite visible albedo and infrared temperature for selected cloud systems. CSIRO Aust. Div. Atmos. Phys. Tech. paper 40: 1-43.

PLINIUS, 77. Naturalis Historia. Editions: Liber V and XXXI: J. Desarges; Société d'Edition 'Les Belles Lettres', Paris 1980. Liber III: H. Rackham. W. Heinemann Ltd., London 1947.

POHN, H.A., T.W. OFFIELD and K. WATSON, 1974. Thermal inertia mapping from satellite - discrimination of geologic units in Oman. Jour. Research US Geol. Survey 2(2): 147-158.

PORTMAN, D.J., 1958. Conductivity and length relationships in heat flow transducer performance. Trans. Amer. Geophys. Union 39(6): 1089-1094.

PRATT, D.A., 1980. Two dimensional model variability in thermal inertia surveys. Remote Sens. Environ. 9: 325-338.

——— and C.D. ELLYETT, 1979. The thermal inertia approach to mapping of soil moisture and geology. Remote Sens. Environ. 8: 151-168.

PRICE, J.C., 1977. Thermal inertia mapping: a new view of the earth. J. Geophys. Res. 82(18): 2582-2590.

———, 1980. The potential of remotely sensed thermal infrared data to infer surface soil moisture and evaporation. Water Resour. Res. 16(4): 787-795.

———, 1982. On the use of satellite data to infer surface fluxes at meteorological scales. J. Appl. Meteor. 21(8): 1111-1122.

PRUITT, W.O., D.L. MORGAN and F.J. LOURENCE, 1973. Momentum and mass transfers in the surface boundary layer. Quart. J. R. Met. Soc. 99: 370-386.

PUPISKY, H. and I. SHAINBERG, 1979. Salt effects on the hydraulic conductivity of a sandy soil. Soil Sci. Soc. Am. J. 43(3): 429-433.

QUIEL, F., 1975. Thermal IR in geology. Photogramm. Eng. Remote Sens. 41(3): 341-346.

REEVES, R.G., A. ANSON and D. LANDEN (eds.), 1975. Manual of remote sensing I and II. Amer. Soc. of photogrammetry, Falls Church, Virginia. 867 p. (I), 2144 p. (II).

REGWA, 1973. Studies in Wadi al Ajal, el Shatti and Traghen. Min. Agric. Dev. LAR, Tripoli. 15 vol. (unpublished).

REICHARDT, K., D.R. NIELSEN and J.W. BIGGAR, 1972. Scaling of horizontal infiltration into homogeneous soils. Soil Sci. Soc. Amer. Proc. 36: 241-245.

REINIGER, P., 1981. HCMM satellite data calibration and atmospheric corrections. TELLUS Newsletter 25. Joint Res. Centre, Ispra. 16 p.

RIBANDO, R.J. and K.E. TORRANCE, 1976. Natural convection in a porous medium: effects of confinement, variable permeability and thermal boundary conditions. J. Heat Transfer 98: 42-48.

RICHARDS, L.A., 1931. Capillary conduction of liquids through porous mediums. Physics 1: 318-333.

———, W.R. GARDNER and G. OGATA, 1956. Physical processes determining water loss from soil. Soil Sci. Soc. Amer. Proc. 20(3): 310-314.

RIDDER, N.A. de and A. EREZ, 1977. Optimum use of water resources. Publ. 21 ILRI, Wageningen. 250 p.

RIJTEMA, P.E., 1969. Soil moisture forecasting. Nota 513, Inst. for Land and Water Manag. Res., Wageningen. 28 p.

RITCHIE, J.T. and J.E. ADAMS, 1974. Field measurements of evaporation from soil shrinkage cracks. Soil Sci. Soc. Amer. Proc. 38(1): 131-134.

RNEA (Regional Near EAst office, FAO), 1976. Desert creep and range management in the Near East. Mission report, March-April 1976. Cairo.

ROBERTS, R.E., J.E.A. SELBY and L.M. BIBERMAN, 1976. Infrared continuum absorption by atmospheric water vapor in the 8-12 μm window. Appl. Opt. 15(9): 2085-2094.

ROBINSON, T.W., 1958. Phreatophytes. US Geol. Survey Water supply paper 1423. 84 p.

——— and A.O. WAANANEN, 1970. Evapotranspiration by woody phreatophytes in the Humboldt River valley near Winnemucca, Nevada. US Geol. Survey Prof. paper 491-D. 41 p.

ROSE, C.W., 1968. Water transport in soil with a daily temperature wave. II. Analysis. Aust. J. Soil Res. 6: 45-57.

ROSEMA, A., 1982. Group Agromet Monitoring Project (GAMP)-Final report, chapter 7. Contract M 4660/ 81/D/IM(SC), European Space Agency (ESA), Paris.

——, J.H. BIJLEVELD, P. REINIGER, G. TASSONE, K. BLYTH and R.J. GURNEY, 1978. 'TELL-US' a combined surface temperature, soil moisture and evaporation mapping approach. Proc. 12th Int. Symp. on Remote Sensing of Environment, Environmental Res. Inst. of Michigan: 2267-2276.

ROWLINSON, J.S., 1949. The second virial coefficient of polar gases. Trans. Faraday Soc. 45: 974-984.

ROYER, J.M. and G. VACHAUD, 1975. Field determination of hysteresis in soil - water characteristics. Soil Sci. Soc. Amer. Proc. 39(2): 221-223.

SALEM, O. and J.H. VISSER, 1977. Mission report on visit to the Intern. Atomic Energy Agency (IAEA), Vienna. Secret. of Dams and Water Resourc. (SDWR) LAR, Tripoli. 5 p.

SALTZMAN, B. and S. ASHE, 1976. The variance of surface temperature due to diurnal and cyclone-scale forcing. TELLUS 28: 307-322.

—— and J. POLLACK, 1977. Sensitivity of the diurnal surface temperature range to changes in physical parameters. J. Appl. Meteor. 16: 614-619.

SCHOLS, J.L.J., 1983. The detection and measurement of turbulent structures in the atmospheric surface layer. Submitted to: Boundary Layer Meteorology.

SCHOONDERBEEK, D., F. THIEL and E.B.A. BISDOM, 1983. Quantimet 720 analysis of porosities in back-scattered electron scanning images made with different photo-techniques. Geoderma 30(1-4): 271-275.

SCHÜTZ, L. and R. JAENICKE, 1974. Particle number and mass distributions above 10^{-4} cm radius in sand and aerosols of the Sahara desert. J. Appl. Meteor. 13: 863-870.

SCOTTER, D.R. and P.A.C. RAATS, 1969. Dispersion of water vapor in soil due to air turbulence. Soil Sci. 108(3): 170-176.

——, G.W. THURTELL and P.A.C. RAATS, 1967. Dispersion resulting from sinusoidal gas flow in porous materials. Soil Sci. 104(4): 306-308.

SELIM, H.M. and D. KIRKHAM, 1970. Soil temperature and water content changes during drying as influenced by cracks: a laboratory experiment. Soil Sci. Soc. Amer. Proc. 34: 565-569.

SELLERS, W.D., 1965. Physical climatology. The Univ. of Chicago Press. 272 p.

SEPASKHAH, A.R. and L. BOERSMA, 1979. Thermal conductivity of soils as a function of temperature and water content. Soil Sci. Soc. Am. J. 43: 439-444.

SHARMA, M.L., G. UEHARA and J.A. MANN Jr., 1969. Thermodynamic properties of water adsorbed on dry soil surfaces. Soil Sci. 107(2): 86-93.

SINGH, S.R. and B.K. SINHA, 1977. Soil thermal diffusivity determination from overspecification of boundary data. Soil Sci. Soc. Am. J. 41(5): 831-834.

SLATER, P.N. and R.D. JACKSON, 1981. Transforming ground-measured reflectances to radiances measured by various space sensors through clear and turbid atmospheres. Colloque international: Signatures spectrales d'objects en télédétection, Avignon 8-11 Sept. 1981: 531-542.

SLATYER, R.O. and I.C. McILROY, 1961. Practical microclimatology. CSIRO, Melbourne. 310 p.

SMIRNOFF, T.P. and J.A. HRIBAR, 1970. The steady state in soil subjected to several coupled forces. I. A finite element formulation. Soil Sci. 110(3): 183-190.

SMITHSONIAN METEOROLOGICAL TABLES, R.J. List (ed.), 1951. 6th rev. edition. Smithsonian Institution, Washington DC. 527 p.

SOER, G.J.R., 1980. Estimation of regional evapotranspiration and soil moisture conditions using remotely sensed crop surface temperatures. Remote Sens. Environ. 5: 137-145.

STAKMAN, W.P. and G.G. van der HARST, 1969. Determination of soil moisture retention curves. II. Pressure membrane apparatus; range pF 3.0 to 4.2. Inst. for Land and Water Manag. Res., Wageningen. 10 p.

——, G.A. VALK and G.G. van der HARST, 1969. Determination of soil moisture retention curves. I. Sand box apparatus; range pF 0 to 2.7. Inst. for Land and Water Manag. Res., Wageningen. 19 p.

STANGHELLINI, C., 1981. A simple method for evaluating sunshine duration by cloudiness observations. J. Appl. Meteor. 20(3): 320-323.

STANHILL, G., 1965. The concept of potential evapotranspiration in arid zone agriculture. Proc. Montpellier symposium, UNESCO: 109-117.

——, 1973. Evaporation, transpiration and evapotranspiration: a case for Ockam's razor. In: A. Hadas, D. Swartzendruber, P.E. Rijtema, M. Fuchs and B. Yaron (eds.). Physical aspects of soil water and salts in ecosystems. Springer Verlag, Berlin: 207-220.

STEPANOV, I.S., 1974. Interpretation of infrared soil spectra. Soviet Soil Sci. 6: 354-367.

STIGTER, C.J., 1969. On measuring properties of soils by thermal methods with special reference to the contact method. Neth. J. Agric. Sci. 17: 41-49.

SUBBARAYUDU, J., 1979. Heat capacity mapping mission (HCMM). Validation study. Final report. Report R-SAG-3/79-01 Systems and Applied Sciences Corporation, Riverdale, Maryland 20840. 38 p.

SUTCLIFFE, J.V. and C.H. SWAN, 1970. The prediction of actual evaporation in semi-arid areas. IASH, Proc. Reading Symposium July 1970: 213-224.

SUTHERLAND, R.A., J.F. BARTHOLIC and J.F. GERBER, 1979. Emissivity correction for interpreting thermal radiation from a terrestrial surface. J. Appl. Meteor. 18: 1165-1171.

SZABOLCS, I., 1979. Review of research on salt affected soils. UNESCO, Paris. 137 p.

TANNER, C.B. and M. FUCHS, 1968. Evaporation from unsaturated surfaces: a generalized combination method. J. Geophys. Res. 73(4): 1299-1304.

TARPLEY, J.D., 1979. Estimating incident solar radiation at the surface from geostationary satellite data. J. Appl. Meteor. 13: 289-297.

TAYLOR, S.E., 1979. Measured emissivity of soils in the southeast United States. Remote Sens. Environ. 8: 359-364.

TELESPAZIO, 1976. Format specifications for LANDSAT-MSS System Corrected Computer Compatible Tape. Telespazio s.p.a., Rome. 36 p.

——, 1979. Format specifications for LANDSAT-MSS System Corrected Computer Compatible Tape. Rev. Oct. 1979. Telespazio, s.p.a., Rome. 36 p.

THEKAEKARA, M.P., 1973. Solar energy outside the earth's atmosphere. Solar energy 14: 109-127.

THOM, A.S. and H.R. OLIVER, 1977. On Penman's equation for estimating regional evaporation. Quart. J. R. Met. Soc. 103: 345-357.

TIBBITS, G.C., 1966. Ground-water resources of Ash Shati area, King. US Geol. Survey open file report. 184 p.

TSCHAPEK, M., C.O. SCOPPA and C. WASOWSKI, 1978. The surface tension of soil water. J. Soil Sci. 29(1): 17-21.

UMURZAKOV, T.S., 1980. Landscape water indicators on inselbergs of central Asian deserts. Problemy Osvoeniya Pustyn 1: 83-85. Transl. in: Problems of desert development.

UNESCO, 1972. Etude des ressources en eau du Sahara septentrional. Rapport final, UNESCO, Paris. 78 p.

UTEPBERGENOV, D., 1980. Problems of afforestation of the margins of closed playa depressions of Ustyurt. Problemy Osvoeniya Pustyn 1: 80-83. Transl. in: Problems of desert development.

VACHAUD, G., M. VAUCLIN and J. COLOMBANI, 1981. Bilan hydrique dans le sud-Tunisien. I. Caracterisation expérimentale des transferts dans la zone non-saturée. J. Hydrol. 49: 31-52.

VAUCLIN, M. and G. VACHAUD, 1981. Bilan hydrique dans le sud-Tunisien. II. Modelisation numérique et prévision des transferts hydriques en sol stratifie. J. Hydrol. 49: 53-73.

VERGOUWEN, L., 1981. Salt minerals and waters from soils in Konya and Kenya. Thesis, Agricultural Univ., Wageningen. 139 p.

VERSLUYS, J.M.I., 1916. De capillaire werkingen in den bodem. Thesis Techn. Univ., Delft. 136 p.

VINCENT, R.K., 1975. The potential rôle of thermal infrared multispectral scanners in geological remote sensing. Proc. IEEE 63: 137-147.

——, L. ROWAN, R.E. GILLESPIE and C. KNAPP, 1975. Thermal infrared spectra and chemical analyses of twenty-six igneous rock samples. Remote Sens. Environ. 4: 199-209.

VOGEL, J.C., L. THILO and M. van DIJKEN, 1974. Determination of groundwater recharge with tritium. J. Hydrol. 23: 131-140.

VONDER HAAR, T.H., 1980. Earth radiation budget measurements from satellites and their interpretation for climate modeling and studies. Contract NAS1-15553. Res. Inst. of Colorado, Fort Collins. 58 p.

VRIES, D.A. de, 1952. Het warmtegeleidingsvermogen van grond. Meded. Landbouwhogeschool, Wageningen 52(1). 73 p.

——, 1963. Thermal properties of soils. In: W.R. van Wijk (ed.). Physics of plant environment. John Wiley & Sons, Inc., New York: 210-235.

——, 1975. Heat transfer in soils. In: D.A. de Vries and N.H. Afgan (eds.). Heat and mass transfer in the biosphere. Part 1. Transfer processes in the plant environment. Scripta Book Company, Washington DC: 5-28.

WALKER, T.R., 1979. Red colour in dune sand. In: E.D. McKee (ed.). A study of global sand seas. USGS Prof. paper 1052: 61-81.

WARD, R.C., 1971. Measuring evapotranspiration; a review. J. Hydrol. 13: 1-21.

WARHAFT, Z., 1976. Heat and moisture flux in the stratified boundary layer. Quart. J. R. Met. Soc. 102: 703-707.

WARRICK, A.W., G.J. MULLEN and D.R. NIELSEN, 1977. Scaling field measured soil hydraulic properties using a similar media concept. Water Resour. Res. 13(2): 355-362.

WARTENA, L., 1959. Het klimaat en de verdamping van een meer in centraal Irak. Meded. Landbouwhogeschool, Wageningen 59(9). 92 p.

WATSON, K., 1975. Geologic applications of thermal infrared imagery. Proc. IEEE 63: 128-137.

WEBER, J.E., 1973. On thermal convection between non-uniformly heated planes. Int. J. Heat Mass Transfer 16: 961-970.

———, 1974. Convection in a porous medium with horizontal and vertical temperature gradients. Int. J. Heat Mass Transfer 17: 241-248.

WEDMAN, E.J., 1963. Geohydrology of Sebkra Sedjoumi (Tunisia). IASH publ. 64: 50-67.

WEEKS, L.V., S.J. RICHARDS and J. LETEY, 1968. Water and salt transfer in soil resulting from thermal gradients. Soil Sci. Soc. Amer. Proc. 32: 193-197.

WHALEN, J.W., 1961. Thermodynamic properties of water adsorbed on quartz. J. Phys. Chem. 65: 1676-1681.

WHITCOMB, H.A., 1956. Geology and hydrology of the western part of the province of Fezzan, United Kingdom of Libya. US Geol. Survey Prof. paper 102. 124 p.

WIEGAND, C.L. and S.A. TAYLOR, 1961. Evaporative drying of porous media. Utah State Univ. Agricultural exp. station, Logan. Spec. rep. 15. 28 p.

WIERENGA, P.J., D.R. NIELSEN and R.M. HAGAN, 1969. Thermal properties of a soil based upon field and laboratory measurements. Soil Sci. Soc. Amer. Proc. 33: 354-360.

WIJK, W.R. van and P.J. BRUIJN, 1964. Determination of thermal conductivity and volumetric heat capacity of soils near the surface. Soil Sci. Soc. Amer. Proc. 28(4): 461-464.

——— and W.J. DERKSEN, 1963. Sinusoidal temperature variation in a layered soil. In: W.R. van Wijk (ed.). Physics of plant environment. John Wiley & Sons, Inc., New York: 171-209.

——— and W.J. DERKSEN, 1966. Thermal properties of a soil near the surface. Agric. Meteorol. 3: 333-342.

WILLIAMSON, E.J. and G.G. WILKINSON, 1980. Sea surface temperature measurements from METEOSAT. The 2nd Meteosat Scientific User Meeting. London 26-27 March 1980. Eur. Space Operations Centre (ESOC), Darmstadt: J1-J20.

WOODSIDE, W. and J.H. MESSMER, 1961. Thermal conductivity of porous media. 1. Unconsolidated sands. J. Appl. Physics 32: 1683-1699.

WRIGHT, E.P. and W.M. EDMUNDS, 1971. Hydrogeological studies in Central Cyrenaica. In: Carlyle Gray (ed.). Symposium on the geology of Libya, April 14-18 1969, Univ. of Libya, Tripoli: 459-481.

YAGLOM, A.M., 1977. Comments and temperature flux - profile relationships. Boundary-Layer Meteorol. 11: 89-102.

ZUIDAM, R.A. van, 1971. Orbital photography as applied to natural resources survey. Int. Inst. for Aerial Survey and Earth Sci. (ITC). Publ. 61, series B. Enschede. 59 p.

FREE TRANSLATION OF THE LATIN QUOTATIONS
as taken from Plinius' Naturalis Historia and given in this Report

Preface

'Nunc de partibus, quamquam infinitum id
quoque existimatur nec temere sin aliqua
reprehensione tractatum, ...'
(Liber III:1)

Now the different parts will be dealt
with, although they appear to be of over-
whelming extent, and without fearing any-
body's reprehension, ...

Chapter 1

'... harenis circumdati, puteos tamen
haut difficile binum fere cubitorum
altitudine inveniunt, ibi restagnantibus
Mauretaniae aquis.'
(Liber V:34)

... surrounded by the sandy expanses,
however, groundwater reservoirs, the
stagnating waters from Mauritania, can be
reached by digging wells to a depth sel-
dom deeper than 0.9 m.

Chapter 2

'... fontem eius, mergique in cuniculos
ipsum amnem vapore anhelantem fumidis
cautibus ubi conditur;...'
(Liber V:55)

... (the Nile) downstream of the springs,
the stream dives into underground channels
where it mixes with its own vapour, pro-
duced because of the hot rocks; ...

Chapter 3

'... adfuso fonte a medio die ad mediam
noctem aquis ferventibus totidemque
horis ad medium diem rigentibus, ...'
(Liber V:36)

... (with) a permanent spring, where wa-
ter is warm between noon and midnight and
cool from midnight to noon, ...

Chapter 4

'... per solitudines nigri pulveris,
eminentibus interdum velut exustis
cautibus, loca inhabitabilia fervore,
quamquam hiberno tempore experto.'
(Liber V:15)

... amidst the stretched expanses covered
by dark dust, baked-like rocks project
from the ground surface, and these places
cannot be lived in because of the heat,
unbearable even in wintertime.

Chapter 5

'... et solem orientem occidentemque
dira inprecatione contuentur ut
exitialem ipsis agrisque, ...'
(Liber V:45)

... they throw angry insults at the sun
in its course from East to West, because
of its deadly effect on their field crops,
...

Chapter 6

'Ultra eum deserta, mox Thelge oppidum
Garamantum itemque Dedris adfuso fonte
... eius puteos - qui sunt non alte
fodiendi, si locorum notitia adsit -
harenis operientibus.'
(Liber V:36,38)

Beyond it (there are) deserts, and next
Thelge, town of the Garamantes, and also
Dedris with a permanent spring ... their
wells are covered with sand, but can be
found at shallow depths, if (enough) in-
formation about the region is available.

Chapter 7

'Ab his mons longo spatio in occasum ab
ortu tendit, Ater nostris dictus a
natura, adusto similis aut solis
repercussu accensus.'
(Liber V:35)

Outwards of these regions a mountain
stretches over a large expanse from East
to West, which is named Black because of
its baked appearance, but is also shining
because of the reflected sun rays.

Chapter 8

'Sunt et in Africa lacus, et quidem
turbidi, salem ferentes. ..... Nam et
Cyrenaici tractus nobilitantur
Hammoniaco et ipso, quia sub harenis
inveniatur, appellato.'
(Liber XXXI:76,79)

There are lakes in Africa, some of them
turbid, where salts are present .... More-
over the stretches of Cyrenaica are re-
nowned for the ammonium salt, so named
because it can be found below the sand
surface.

Summary
Samenvatting

'Nec de Africa plura quae memorentur
occurrunt.'   (Liber V:46)

About Africa there is not anything more
worth mentioning.

References

'Quapropter auctorem neminem unum
sequar, sed ut quemque verissimum in
quaque parte arbitrabor, quoniam commune
ferme omnibus fuit ut eos quisque
diligentissime situs diceret in quibus
ipse prodebat.'   (Liber III:1)

Thereby I will not follow a single spe-
cific author, because I am convinced, as
it is a widespread and firm opinion, that
anybody proves most reliable when de-
scribing those areas which he himself did
traverse.

LIST OF SYMBOLS

Some of the symbols used in a few consecutive equations falling outside the main line of argument are defined in the text only.

Symbol	Interpretation	Units	Dimensions
a	thermal diffusivity	$m^2 \cdot s^{-1}$	$L^2 \cdot t^{-1}$
$\tilde{a}$	azimuth angle	rad	-
B	Planck's function	$W \cdot m^{-2} \cdot sr^{-1} \cdot \mu m^{-1}$	$M \cdot L^{-1} \cdot t^{-3}$
c	specific heat	$J \cdot kg^{-1} \cdot K^{-1}$	$L^2 \cdot t^{-2} \cdot T^{-1}$
c_p	air specific heat at constant pressure	$J \cdot kg^{-1} \cdot K^{-1}$	$L^2 \cdot t^{-2} \cdot T^{-1}$
D	diffusivity	$m^2 \cdot s^{-1}$	$L^2 \cdot t^{-1}$
DN	digital count number in CCT satellite data	-	-
d	zero-plane displacement	m	L
$\tilde{d}$	diameter	m	L
d	damping depth, see eq. (3.59)	m	L
E	evaporation	$kg \cdot m^{-2} \cdot s^{-1}$	$M \cdot L^{-2} \cdot t^{-1}$
EC	electrical conductivity	$S \cdot m^{-1}$	$Q^2 \cdot t \cdot M^{-1} \cdot L^{-3}$
ET0	reference crop evapotranspiration	$mm \cdot d^{-1}$	$L \cdot t^{-1}$
e	vapour pressure	mbar	$M \cdot L^{-1} \cdot t^{-2}$
F	amplification factor	-	-
G	soil heat flux	$W \cdot m^{-2}$	$M \cdot t^{-3}$
g	acceleration due to gravity	$m \cdot s^{-2}$	$L \cdot t^{-2}$
H	sensible heat flux	$W \cdot m^{-2}$	$M \cdot t^{-3}$
h	pressure head	m	L
I	radiant intensity	$W \cdot m^{-2} \cdot sr^{-1} \cdot \mu m^{-1}$	$M \cdot L^{-1} \cdot t^{-3}$
K	specific permeability	m^2	L^2
$\hat{K}$	transfer coefficient	$m^2 \cdot s^{-1}$	$L^2 \cdot t^{-1}$
k	ratio of apparent and actual soil thermal admittance	-	-
k	von Karman's constant	-	-
L	latent heat of vaporization of water	$J \cdot kg^{-1}$	$L^2 \cdot t^{-2}$
LE	latent heat flux	$W \cdot m^{-2}$	$M \cdot t^{-3}$
ℓ_m	mean molecular free path	m	L
M	weight of a mole of water	$kg \cdot mol^{-1}$	M
molec	molecule	-	-
N	integer	-	-
n	frequency	-	-
P	pressure	$N \cdot m^{-2}$	$M \cdot L^{-1} \cdot t^{-2}$
P	period	s	t
Q	heat amount	J	$M \cdot L^2 \cdot t^{-2}$
$\dot{Q}$	volumetric heading rate	$J \cdot m^{-3} \cdot s^{-1}$	$M \cdot L^{-1} \cdot t^{-3}$
q	moisture mass flux	$kg \cdot m^{-2} \cdot s^{-1}$	$M \cdot L^{-2} \cdot t^{-1}$
$\tilde{q}$	moisture flux density	$m \cdot s^{-1}$	$L \cdot t^{-1}$
q_a	air specific humidity	-	-
R	radiance	$W \cdot m^{-2}$	$M \cdot t^{-3}$
$\hat{R}$	gas constant	$J \cdot mol^{-1} \cdot K^{-1}$	$M \cdot L^2 \cdot t^{-2} \cdot T^{-1}$

Symbol	Interpretation	Units	Dimensions
Ra	Rayleigh number	-	-
Re	Reynolds number	-	-
Ri	Richardson number	-	-
r	resistance to transport	$s \cdot m^{-1}$	$t \cdot L^{-1}$
$\tilde{r}$	mixing ratio	-	-
r_m	pore radius	m	L
S	source term, see eq. (3.68)	$K \cdot m^{-2}$	$T \cdot L^{-2}$
s	slope of $e_{sat}(T)$	$mbar \cdot K^{-1}$	$M \cdot L^{-1} \cdot t^{-2} \cdot T^{-1}$
T	temperature	K	T
U	air relative humidity	-	-
U	energy	J	$M \cdot L^{2} \cdot t^{-2}$
u	horizontal wind velocity	$m \cdot s^{-1}$	$L \cdot t^{-1}$
u_*	friction velocity	$m \cdot s^{-1}$	$L \cdot t^{-1}$
v	flux density or filtration velocity	$m \cdot s^{-1}$	$L \cdot t^{-1}$
w	vertical wind velocity	$m \cdot s^{-1}$	$L \cdot t^{-1}$
$\tilde{w}$	precipitable water vapour	$cm^{3} \cdot cm^{-2}$	L
y	thermal admittance	$W \cdot m^{-2} \cdot K^{-1}$	$M \cdot t^{-3} \cdot T^{-1}$
z	vertical distance	m	L
z_0	roughness length	m	L
α	surface reflectance	-	-
β	Bowen ratio	-	-
Γ	extinction coefficient	cm^{-1}	L^{-1}
$\hat{\Gamma}$	absorption coefficient	$cm^{2} \cdot g^{-1}$	$L^{2} \cdot M^{-1}$
γ	see eq. (4.5)	m^{-1}	L^{-1}
$\tilde{\gamma}$	psychrometric constant	$mbar \cdot K^{-1}$	$M \cdot L^{-1} \cdot t^{-2} \cdot T^{-1}$
δ	variation of a quantity	-	-
ϵ	surface emissivity	-	-
ϵ'	apparent emissivity of atmosphere at ground level	-	-
ζ	Monin-Obukhov's stability parameter	-	-
η	viscosity	$N \cdot s \cdot m^{-2}$	$M \cdot L^{-1} \cdot t^{-1}$
θ	moisture content (volume)	$cm^{3} \cdot cm^{-3}$	-
κ	capillary conductivity	$m \cdot s^{-1}$	$L \cdot t^{-1}$
λ	thermal conductivity	$W \cdot m^{-1} \cdot K^{-1}$	$M \cdot L \cdot t^{-3}$
λ'	apparent thermal conductivity	$W \cdot m^{-1} \cdot K^{-1}$	$M \cdot L \cdot t^{-3}$
$\tilde{\lambda}$	wave length	μm	L
Λ	thermal conductivity tensor	$W \cdot m^{-1} \cdot K^{-1}$	$M \cdot L \cdot t^{-3}$
μ	weighting coefficient	-	-
$\tilde{\upsilon}$	wave number	cm^{-1}	L^{-1}
ξ	fraction of a quantity	-	-
ρ	density	$kg \cdot m^{-3}$	$M \cdot L^{-3}$
$(\rho c)'$	apparent heat capacity	$J \cdot m^{-3} \cdot K$	$M \cdot L^{-1} \cdot t^{-2} \cdot T^{-1}$
σ	Stefan Boltzmann constant	$W \cdot m^{-2} \cdot K^{-4}$	$M \cdot t^{-3} \cdot T^{-4}$
$\tilde{\sigma}$	standard deviation	-	-
σ_{wa}	surface tension of water against air	$N \cdot m^{-1}$	$M \cdot t^{-2}$
τ	optical depth	-	-
T	distance in arbitrary units		
Φ	angle	rad	-
ϕ	Monin-Obukhov's function	-	-
χ	volumetric concentration	-	-
Ω	phase angle	rad	-

SUBSCRIPTS

Symbol	Interpretation
a	air
act	actual
ad	adsorbed
bot	bottom, where z = 0
c	cloud
conv	convective
cr	critical
d	dust
diff	diffusion
dim	dimer, $(H_2O)_2$
dry	dry soil
E	evaporation front, respectively site
encl	enclosure
gw	groundwater
h	heat
k,i,r	integers
ℓ	liquid
m	momentum
me	measured
mo	moisture
mon	monomer, H_2O
n	net
o	osmotic
out	outside the atmosphere
p	planetary
pix	pixel
pot	potential
ref	reference
s	soil
sat	at saturation
so	solid
su	sun
sw	shortwave
swd	direct solar radiation
swr	reflected shortwave solar radiation
swdf	diffuse shortwave solar radiation
top	top atmospheric layer where P = 100 mbar
u	upper
v	vapour
vi	virtual
vol	volume
w	water
X	maximum value
0	ground surface
θ	moisture
λ	spectral quantity

SUPERSCRIPTS

Symbol	Interpretation
'	fluctuation
.	derivative with respect to time
*	effective property
0	ground surface
out	outside the atmosphere
sat	at saturation
self	self-broadening
for	foreign-broadening
t	threshold